EXPO Ingeniería

Engineering for **Transformation**

ENERGY

INFRASTRUCTURE

4.0 TECHNOLOGY

VITAL ENGINEERING

FONDO EDITORIAL EIA

Colección EUREKA

UNIVERSIDAD DE ANTIOQUIA
Facultad de Ingeniería

EXPO Ingeniería

Engineering for **Transformation**

ENERGY

INFRASTRUCTURE

4.0 TECHNOLOGY

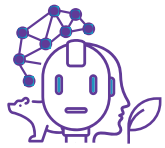

VITAL ENGINEERING

FONDO EDITORIAL EIA

Colección EUREKA

UNIVERSIDAD DE ANTIOQUIA
Facultad de Ingeniería

Colección Eureka

ISBN Digital:978-628-95287-1-8
Queda hecho el depósito que ordena la Ley
(Ley 44 de 1993 / Decreto 460 de 1995)

Dirección editorial: Mauricio Andrés Misas Ruiz
Dirección de Colección: Nathalia Vélez López de Mesa
Diseño de cubierta y diagramación: Maria Fernanda Perez A.

Fondo Editorial EIA
Calle 23 AA Sur Nro. 5-200, Kilómetro 2+200 vía al Aeropuerto José María Córdova. Envigado,
Colombia.
Código Postal: 055428
Tel.: (60+4) 3549090 - opc. 1. Ext. 223 - 218
Correo electrónico: editorial@eia.edu.co
http://www.eia.edu.co/fondoeditorial

IC-EXPOI
Congreso Internacional de Ingeniería

Un evento de:
Expo Ingeniería

ORGANIZADORES

cpm Central Promotora de Medios S.A.S
ImaGroup Soluciones inteligentes
Plaza Mayor Medellín Convenciones y Exposiciones
Universidad de Antioquia

ALIADOS

Túnel Guillermo Gaviria Echeverri
Alcaldía de Medellín Distrito de Ciencia, Tecnología e Innovación
Gobernación de Antioquia
UNIDOS

Contenido

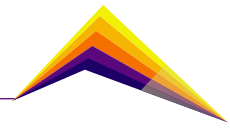

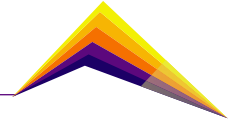

Preface

Engineering for Transformation contains a series of papers presented at the International Congress EXPOIngenieria 2022 (IC-EXPOI 2022). The Event was held at the Green Pavilion of Plaza Mayor, Medellín, Colombia, from October 27th to 29th, 2022. The International Congress was organized by the Engineering Faculty of Universidad de Antioquia, Plaza Mayor, IMAGROUP and CPM logística, with the support of Alcaldía de Medellín and Gobernación de Antioquia.

This book covers papers from four areas: energy, infrastructure, 4.0 technology and vital engineering. These areas were selected as the main thematic axes of the congress because of their current importance and their short- and long-term relevance on the developing of engineering and society.

The series of papers in this book, encompasses a long range of topics, such as conventional sources of energy, solar energy, hydrogen, biomass, urbanistic processes, structural materials, materials degradation, thermal spray coatings, artificial intelligence, nanotechnology, additive manufacturing, socioenvironmental sustainability and life cycle analysis, and engineering for health, among others. They have been organized by grouping those that treat similar topics in sections, according with the four thematic axes of the congress. It may appear sometimes, that a paper that has been classified in the energy area belongs to the vital engineering area or, a paper found in the section of infrastructure belongs to 4.0 technology. This is because the topics are highly interconnected, for example nanotechnology, which belongs 4.0 technology, is currently used and investigated to improve the performance of materials used for infrastructure or human health. Also, for example, life cycle analysis, which belongs to vital engineering, can be applied to solar cells that belongs to the energy area. The bottom line is that, all the papers approach issues currently relevant and show how applied science and engineering can contribute to transform society and human life quality.

We hope this book will serve as a reference for undergrad and grad engineering students, engineers and scientist working on the four main areas discussed during the congress.

Finally, we would like to acknowledge our invited speakers for their valuable conferences, the authors of the papers for their significant contributions, the members of the scientific committee and the pool of reviewers and sub-reviewers for their effort selecting and organizing the best papers submitted to the congress, the English for Engineers team from the Engineering Faculty of Universidad de Antioquia for proofreading the papers, DRAI (Department of resources and informatic support) of the Engineering Faculty of Universidad de Antioquia team for taking care of the logistic, experience design and congress assembly, and the Editorial EIA team for accepting joining us at the publication of this book.

Ricardo Aristizábal-Sierra
Coordinator of the Scientific Committee
International Congress EXPOIngeniería 2022

General Committee

Jesús Francisco Vargas Bonilla
Dean, Facultad de Ingeniería, Universidad de Antioquia

Tatiana Marcela Gómez Bustamante
EXPOIngeniería Director

Mauricio Andrés Correa-Ochoa
CESET Director, Engineering Faculty, Universidad de Antioquia

Juan Diego Velez
DRAI Director, Engineering Faculty, Universidad de Antioquia

Lyda Janeth Contreras Olivares
Logistic, design and assembly Director, International Congress EXPOIngeniería 2022

Víctor Hugo Zapata Madrigal
Representative of “Plaza Mayor”

Juan Esteban Taborda Grisales
Representative of “IMAGROUP”

Víctor Manuel Gámez Fonseca
Representative of “CPM Logística”

Academic Committee

Sergio Cipriano Agudelo
Vice-Dean, Engineering School, Universidad de Antioquia

Mauricio Andrés Correa-Ochoa
CESET Director

Tatiana Marcela Gómez Bustamante
EXPOIngeniería Director

Ricardo Aristizábal-Sierra
Scientific Committee Coordinator

Sara Cristina Vieira Agudelo
Research Director, Engineering School, Universidad de Antioquia

Maryory Astrid Gómez
"Facultad de Ingeniería UdeA" Journal, Director. Professor, Researcher

Andrea Rodríguez Sánchez
International Congress EXPOIngeniería 2022, Administrative support

Lina Herrera Moncada
Communicator International Congress EXPOEngineering

Astrid Marcela Mira Hincapié
Coordinator, Continuing Education and Events, Engineering Faculty,
Universidad de Antioquia

Scientific Committee

Aida Luz Villa
Universidad de Antioquia
Colombia

Ainhoa Rubio Clemente
Universidad de Antioquia
Colombia

Ana María Cárdenas
Universidad de Antioquia
Colombia

Ana María Pérez Ceballos
Universidad Industrial de Santander
Colombia

Ángela Rendón
Universidad de Antioquia
Colombia

Carlos Serna Giraldo
Universidad UNIRB
Brazil

Carlos Alberto Palacio
Universidad de Antioquia
Colombia

Carlos Rivero
Universidad de Antioquia
Colombia

Celia Malfatti
Universidad de Antioquia
Brazil

Claudia Patricia Serna
Universidad de Antioquia
Colombia

Daniel Estiben Ramírez
Universidad de Antioquia
Colombia

Danny Múnera
Universidad de Antioquia
Colombia

Diana Catalina Rodríguez
Universidad de Antioquia
Colombia

Edison Gustavo Cueva
Universida de Brasília
Brasil

Edwin Chica
Universidad de Antioquia
Colombia

Esperanza López Gómez
Universidad de Antioquia
Colombia

Fernando Juan Beltran
Universidad de Extremadura
Spain

Gianpaolo Vitale
National Research Council of Italy
Italy

Henry Colorado
Universidad de Antioquia
Colombia

Javier Rivero
Universidad de Antioquia
Colombia

Jhon Fredy Vélez
CARTIF Technological Center
Spain

John Ramiro Agudelo
Universidad de Antioquia
Colombia

Juan Guillermo Villegas
Universidad de Antioquia
Colombia

Juan Marcelo Rojas
Universidad de Antioquia
Colombia

Juan Sebastián Botero
Institución Universitaria ITM
Colombia

Juliana Uribe
Universidad de Antioquia
Colombia

Lina Berrouet
Universidad de Antioquia
Colombia

Luis Alejandro Fletscher
Universidad de Antioquia
Colombia

María Esperanza López
Universidad de Antioquia
Colombia

María Teresa Hernández
Ministry for The Ecological Transition
and the Demographic Challenge
Spain

Maryory Astrid Gómez
Universidad de Antioquia
Colombia

Melissa Barrera Durango
Universidad de Antioquia
Colombia

Nataly Carolina Rosero
Institute of Ceramic and Glass
Spain

Néstor Aguirre
Universidad de Antioquia
Colombia

Nuria Vela de Oro
Universidad Católica de Murcia
Spain

Pablo Andrés Maya
Universidad de Antioquia
Colombia

Rafael Orozco
Universidad de Antioquia
Colombia

Raquel Lebrero Fernández
University of Valladolid
Spain

Valeria Chávez Cerón
UNAM
Mexico

Invited reviewers and subreviewers

Sara Aguilar
Universidad de Antioquia

Claudia Aldana
Universidad de Antioquia

Luis Castaño-Londoño
Institución Universitaria ITM

Claudia Elena Echeverri
Universidad EIA

Carmiña Gartner
Universidad de Antioquia

Diego Hernán Giraldo
Universidad de Antioquia

Cristian Guarnizo-Lemus
Institución Universitaria ITM

Francisco López
Institución Universitaria ITM

David Márquez-Viloria
Institución Universitaria ITM

Luis Morantes-Guzmán
Institución Universitaria ITM

Juan Guillermo Muñoz
Universidad Nacional

Gustavo Patiño
Universidad de Antioquia

Edward Restrepo
Universidad de Antioquia

Erick Reyes
Institución Universitaria ITM

Oscar Ríos-Diez
Universidad de Antioquia

Daniel Tobón
Universidad de Antioquia

Juliana Valencia-Aguirre
Institución Universitaria ITM

Fabio Vargas
Universidad de Antioquia

Juan Camilo Villegas
Universidad de Antioquia

Juan Felipe Montoya Arango
Universidad de Antioquia

Franky Bedoya
EPFL, Suiza

Claudia Patricia Ossa Orozco
Universidad de Antioquia

Jonathan Gallego
Universidad de Antioquia

Fabián Castaño
Universidad de Antioquia

Ana María Torres López
Universidad de Antioquia

Isabel Cristina Muñoz Ortega
Universidad de Antioquia

English for Engineers Team

Alejandra Ramos Osorio
Coordinator, Universidad de Antioquia

Jorge Humberto Guerra Torres
Universidad de Antioquia

Laura Victoria Toro Zapata
Universidad de Antioquia

Ever de Jesús Bedoya Bedoya
Universidad de Antioquia

Barbara Vanessa Henao Gómez
Universidad de Antioquia

Jaime Alberto Navas Mira
Universidad de Antioquia

Design, Logistic and Assembly Congress Team

Lyda Yaneth Contreras Olivares
Director

Luisa Fernanda Clavijo Cuartas
Communication and creation of content

Juan David Domínguez
Digital communication Coordinator

David Cano
Graphic Design

Key note speakers

Dr. Steven Latré
Imec and University of Antwerp, Belgium.

Dr. Antonio Bula
Universidad del Norte, Colombia.

Dr. Debashis Chanda
University of Central Florida, USA.

Dr. Valeria Chávez Cerón
UNAM, Mexico.

Dr. Gonzalo Mejía
Universidad de la Sabana, Colombia.

Dr. Pablo Maya
Universidad de Antioquia, Colombia.

Dr. Juan Saldarriaga
Universidad de los Andes, Colombia.

Dr. Paola Arias-Gómez
Universidad de Antioquia, Colombia.

Dr. André Boehman
University of Michigan, USA.

Dr. Paulina Aldunce
Universidad de Chile, Chile.

ENERGY

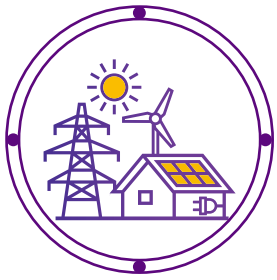

Reducing GHG Emissions via Low Carbon Fuels: Challenges and Opportunities

André L. Boehman

E-mail: boehman@umich.edu

Professor of Mechanical Engineering, University of Michigan

Abstract

We will address the role that low carbon fuels (not strictly "carbon free" fuels, but those with low carbon intensity) can and should play in reducing greenhouse gas emissions. To some, it seems a foregone conclusion that the days of the internal combustion engine are nearing an end, and that the fastest path to "zero carbon emissions" is through adoption of electric vehicles. But bringing down fossil carbon emissions immediately can yield tremendous improvements with regard to the climate crisis, in contrast with waiting for electric vehicles to penetrate the market, and electricity production to be deeply de-carbonized. Widespread and immediate adoption of low carbon intensity renewable fuels can provide dramatic carbon intensity reductions, overnight, when used in the vehicles we drive today. But both the pursuit of electrification of the transportation sector and adoption of low carbon fuels runs into a major practical challenge – achieving major reductions in reducing fossil carbon emissions at scale. Replacing 20 million barrels a day of petroleum presents a daunting barrier to addressing the climate crisis. We will take a realistic look at these questions, and recommend a path forward that uses both strategies, based on life cycle analysis and experimental studies with engines and vehicles.

Correspondent author

Keywords: transportation, decarbonization, renewable fuel, low carbon intensity

Introduction

In this extended abstract, we will cover the outcomes from a specific project that will be discussed in the presentation, a vehicle demonstration performed at the University of Michigan.

Next generation renewable fuels represent the fastest path to ultra low carbon emissions for the transportation sector. Renewable fuels, particularly renewable hydrocarbon fuels, can in some cases serve as drop-in fuels and immediately provide dramatic (>70%) reductions in carbon footprint. There is no new infrastructure that has to be created from scratch such as with hydrogen, or that requires the dramatic expansion of mineral resource extraction (lithium) and carbon-intensive manufacturing such as with lithium-ion battery electric vehicles. The challenges are with finding the feedstocks to produce the renewable fuels in large quantities sustainably, and developing end-user confidence and familiarity with the implementation of drop-in advanced renewable fuels.

Methodology

We will analyze results from an ongoing field vehicle demonstration of renewable diesel fuel (hydrodeoxygenated vegetable oil, HVO) as a drop-in low carbon fuel that is being pursued on the UM campus through the Department of Mechanical Engineering, General Motors, and the Top Tier fuel quality program. Bio-hydrocarbon fuels such as renewable diesel fuel and Fischer-Tropsch fuels from certain pathways can deliver a drop-in solution and potentially can be used with the existing infrastructure for fuel handling, including refining processes, fuel pipelines, and fuel dispensers. In a demonstration activity at the University of Michigan, we have been operating a 2014 Chevy Cruze turbodiesel vehicle on 100% renewable diesel fuel. The test vehicle is shown in Figure 1, along with a 2012 Chevy Volt, which is used for comparison between a drop-in low carbon fuel and vehicle electrification.

(a)

(b)

Figure 1. Different vehicle options for reducing fossil fuel consumption: (a) Chevy Cruze (MY2014) operating on 100% renewable diesel fuel, (b) Chevy Volt plug-in hybrid (MY2012).

Results and analysis

Table 1 compares the carbon emissions per mile for a 40 mile trip with mixed city and highway driving, for which published fuel economy or measured fuel economy data are used. In this case, we differentiate between fossil carbon-derived CO_2 and renewable carbon, and address the carbon intensity of the energy sources.

Vehicle	MPG (60% city, 40% hwy)	Energy (kWh) or Fuel (kg) Used over 40 miles	Fossil CO_2 Emitted (kg)**	Fossil CO_2 emitted per mile (kg/mile)	% GHG Footprint Compared to 2005 Baseline
2005 Chevy Cavalier*	25	5	3.91	0.36	----
2014 Chevy Cruze Diesel	35	4	1.88	0.047	13
2012 Chevy Volt† (2020 electricity CI)	----	8	3.01	0.075	21
2012 Chevy Volt†† (2050 electricity CI)	----	8	1.86	0.047	13

* Baseline case, using the Obama Administration GHG emissions target of 83% reduction relative to 2005 baseline GHG emissions

**Using minimum carbon intensity for Neste Oil renewable diesel fuel (16.9 gCO2e/MJ) from a range of 16.9 to 39 reported by Neste.

†Using 2020 U.S. average carbon intensity for electricity production (see Figure 3.26), 375 g/kWh [1]

††Using 2050 U.S. average carbon intensity for electricity production (see Figure 3.26), 225 g/kWh [1]

Conclusions or summary

We can achieve faster and deeper GHG footprint reduction with drop-in low carbon fuels than can be achieved via vehicle electrification and deliver a lower cost of ownership that via electrification when one accounts for the capital expense for charging infrastructure.

Acknowledgment

The author gratefully acknowledges support for this vehicle demonstration activity from Shailesh Lopes of General Motors and the Top Tier fuel quality program.

References

[1] Energy Information Agency, Annual Energy Outlook 2021, Washington, D.C., 2021.

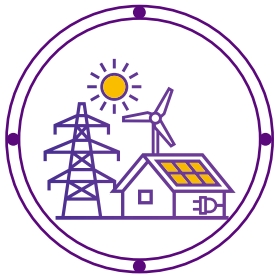

Comparison of the performance of hydrofoils used in vertical-axis hydrokinetic turbines (VAHT) using computational fluid dynamics

Andrés Jahir Chalaca Salas[1] *E-mail: aandres.chalaca@udea.edu.co*

Laura Isabel Velásquez,[1] *E-mail: blisabel.velasquez@udea.edu.co*

Edwin Chica[1] *E-mail: cedwin.chica@udea.edu.co*

[1] *Grupo de Investigación Energía Alternativa (GEA), Facultad de Ingeniería, Universidad de Antioquia, Calle 70 N° 52-21, Medellín 050010, Colombia.*

Abstract

A non-conventional alternative for power generation is the use of water potentials through power generation systems equipped with hydrokinetic turbines, which can operate in axial flow (HAHT) or crossflow (VAHT). The rotors of such turbine have hydrofoils that play an important role in the performance of the turbine. This work compared the performance of 5 hydrofoils used in the design of a VAHT, which were subjected to 3 hydrodynamic analyses: i) the quantification of the highest ratio between lift (C_L) and drag (C_D) coefficients; ii) the cavitation analysis considering the environmental conditions that can be experienced in the rivers of Colombia; and, finally, iii) the determination of the pressure coefficient () along the chord length of the hydrodynamic profiles. These analyses were carried out using numerical simulation based on the Reynolds Averaged Navier-Stokes (RANS). The results allowed to choose the NACA 0015 hydrofoil due to its performance, i.e., the highest C_L/C_D

Correspondent author

ratio, the minimum affectation by the cavitation phenomenon, and the best distribution of the () along the chord length was achieved. The selected hydrofoil can be used in the design of a Gorlov-type vertical-axis hydrokinetic turbine.

Keywords: Hydrokinetic turbine, pressure coefficient, cavitation, hydrofoil, CFD, RANS.

Introduction

The population growth and economic development of countries have increased world energy demand in the last decades [1]. The increase in energy demand means adverse effects on the environment (global warming, greenhouse emissions) because conventional energy sources (oil, gas, carbon) occupy about 70% of the world power generation matrix and the economic world depends on these [2]. This context presents a great opportunity to diversify the global power generation matrix by searching for alternative energy sources efficiently and with low environmental impact, ensuring the sustainability of the planet for future generations.

A non-conventional alternative for power generation is the use of water potentials through power generation systems equipped with hydrokinetic turbines, which can operate in axial flow (HAHT) or cross-flow (VAHT)[3]. These are a great promise to alleviate the global crisis in energy use as they allow generating energy economically and ecologically in almost any place with water flows; they are sustainable and competitive systems that allow reducing dependence on fossil fuels in a context of increasing scarcity of resources [4]. In Colombia, this type of technology under development can be an opportunity for the diversification of the energy matrix and the reliable supply of energy to areas that are not interconnected to the national system, since civil works (dams, reservoirs, canals, and load tunnels) are not required in contrast to conventional hydroelectric plants, resulting in saving significant economic costs and reducing environmental impacts during its implementation. VAHT is a technology under development where hydrofoils play an important role in the performance of the turbine. However, the information available for the specialized design, optimization, and implementation of these systems is somewhat scattered, and is focused on very particular cases; most of them are focused on systems equipped with HAHT [5]. Therefore, this work compared the performance of 5 hydrofoils used in the design of a VAHT, which were subjected to 3 hydrodynamic analyses: i) the quantification of the highest ratio between lift (C_L) and drag (C_D) coefficients; ii) the cavitation analysis considering the environmental conditions that can be experienced in the rivers of Colombia; and, finally, iii) the determination of the pressure coefficient (C_{press}) along the chord length of hydrofoils.

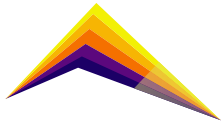

Materials and methods

A literary review focused on the hydrofoils used in the design of vertical axis hydrokinetic turbines (VAHT) was made. This work reports the fluid dynamic analysis of different types of hydrofoils (NACA 0015, NACA 0020, NACA 63018, S 1046, and DU-06-W200). To compare the performance of hydrofoils, they were subjected to 3 following hydrodynamic analyses using the computational fluid dynamics software ANSYS-Fluent.

i). the quantification of the highest ratio between lift (C_L) and drag (C_D) coefficients

The first parameter to compare the performance of the hydrofoils was the highest ratio C_L/C_D for different angles of attack of hydrofoil (α°) between 4° and 10°. The computational domain in C-Topology and the structured mesh used in the CFD simulation are shown in Figure 1. The mesh consisted of a rectangular grid of 25 C of the lend and a semicircle grid of 12.5 C of the radius. C is the chord length of the hydrofoil which was equal to 1 m for the simulation. The hydrofoils were placed at the center of the lower and the upper boundaries. The hydrofoil's leading edge was located 11.5 m from the inlet boundary. A velocity inlet in X-direction equal to 1 m/s was defined in C type boundary and a pressure outlet boundary was imposed at the outlet boundary. Finally, in the hydrofoil and the other boundaries, the wall and the no-slip condition were defined. The steady Reynolds Averaged Navier Stoke equations were used with the *k-w stt* turbulence model for the numerical simulation. A mesh independence test was performed for the simulation, and the number of elements to guarantee independence was greater than 150300. The boundary condition for the simulation was an inlet velocity, the velocity assigned to the fluid conforms to the information found in the literature [6][7], where the average velocity measured in different sections of one of the main rivers of Colombian geography (Magdalena River) is reported. For this first hydrodynamic analysis, all the hydrofoils analyzed have a unit chord length, to make the hydrodynamic analysis independent of the dimensions of the turbine to be designed.

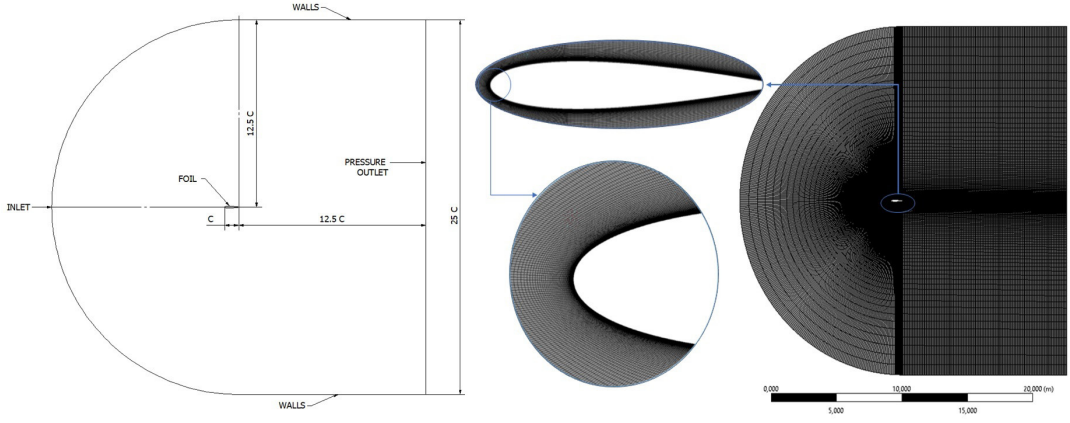

Figure 1. computational domain and mesh used in the CFD simulation

ii). Cavitation analysis based on the environmental conditions that can be experienced in the rivers of Colombia

For cavitation analysis, the hydrofoil must be designed to avoid cavitation phenomena i.e., the formation of water vapor bubbles on the periphery of the hydrofoil, which is undesirable for the good performance of the turbine. These phenomena occur when $|C_{pres}|<\sigma$ [8]; where, C_{pres} is the pressure coefficient along the hydrofoil and is the cavitation number, defined as the following:

$$\sigma=(P_{ref}-P_v)/(0{,}5\rho V^2) \qquad (1)$$

Where, ρ, $P_{ref,}$ and Pv is the water density, the freestream static pressure or the absolute pressure, and the saturation vapor pressure. P_{ref} is defined as $P_{ref}=P_{atm}+\rho gh$, being P_{atm} the atmospheric pressure; g refers to the gravitational acceleration and h is the distance between the hub center and the free water surface. The product ρgh is the so-called gauge pressure.

According to results reported in the highest ratio CL/CD analysis, only two hydrofoils with the highest ratio CL/CD were simulated in a specific case. Where Colombian capital city with lower atmospheric pressure reported in [9] was considered. In turn, $P_{atm}=73327.1\ P_v$ was fixed at 1493.21 Pa for a flow field temperature of $286\ K$ and ρ was fixed at $999.46\ kg/m^3$. Initially σ was set at 60 in this work due to the operating pressure of $83131.8\ Pa$, the blade depth of $1\ m$, and the water velocity of $1.65\ m/s$. To determine the fluid velocity at which cavitation phenomena occur, different simulations were performed, the V of fluid was varying and the cavitation numbers σ were calculated. For cavitation simulation using CFD, the computational domain shown in Figure 1 was used again, however, a transient and multiphase regime was considered, (liquid-vapor) to evaluate the vapor formation around hydrofoils. The turbulence model for this simulation was the k-w stt, and the cavitation model employed was Schnerr-Sauer based on the analyses reported in [10][11]. Table 1 summarizes the velocities and cavitation numbers simulated. The results found in this specific case are important to consider in future designs where the fluid conditions are close to these scenarios.

Table 1. Velocities o fluid and cavitation number simulated

P_{ref} (Pa) 83131.8	V (m/s) 1.65	σ_{min} 60
83131.8	**1.65**	**60**
83131.8	**3.5**	**13.33**
83131.8	**6.2**	**4.18**
83131.8	**7**	**3.33**

iii). The determination of the pressure coefficient () along the chord length of the hydrodynamic profiles

Finally, from the results obtained in the cavitation analysis for the hydrofoils, it was possible to extract the pressure distribution measured by the pressure coefficient C_{pres} along the chord of the hydrofoil. The C_{pres} was calculated through:

$$C_{press}=(Pl-P_{ref})/(0{,}5\rho V^2) \qquad (2)$$

Where is the local pressure reported since CFD simulation results at the points around the hydrofoil.

Results and analysis

i) The quantification of the highest ratio between $C_L/(C_D)$

The results from the CFD simulation referring to the highest ratio C_L/C_D as a function of the **α°** are shown in Figure 2. The highest ratio C_L / C_D is possessed by the profiles called NACA 0015 and S 1046, with great similarity in their hydrodynamic behavior and whose highest ratio C_L / C_D is associated with **α** close to 9 degrees. This is in agreement with the study developed by [12][13], where they designed and manufactured a vertical axis hydrokinetic turbine using symmetrical hydrofoils similar to the NACA 0015 profiles. Additionally, similarities are found in the analyses reported by [14], whose results were obtained in experimental tests performed in wind tunnels.

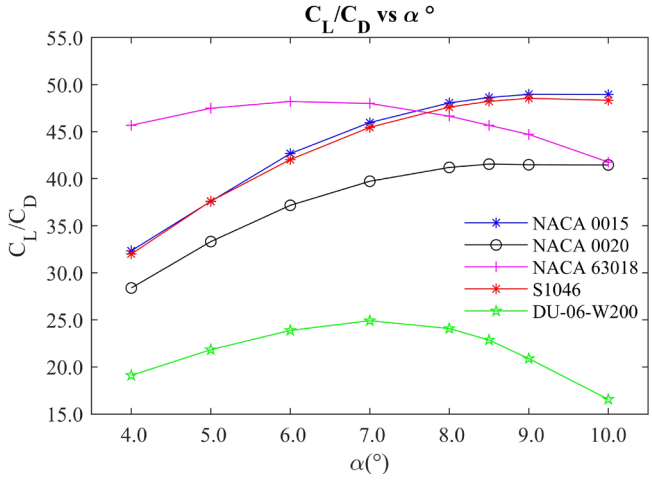

Figure 2. Results CFD simulation ratio CL / CD to (NACA 0015, NACA 63018, S1046 y DU-06-W200).

ii) Cavitation analysis based on the environmental conditions that can be experienced in the rivers of Colombia

Phase (vapor) contours for the NACA 0015 hydrofoil, specifically at a cavitation nnumber $\sigma<4.18$, and $V>6.2\ m/s$ showed cavitation phenomena. The presence of cavitation in hydrofoils coincides with the results of [8][11], where they report cavitation analysis around hydrofoils withσ<4.1. The vapor fraction formed in the NACA 0015 profile occupies a minimal portion compared to the chord length of the profile; on the other hand, in S 1046 hydrofoil there was no observed presence of cavitation phenomena with velocities close to 7 m/s.

iii). The determination of the pressure coefficient (Cpres) along the chord length of the hydrodynamic profiles

The hydrofoil pressure distribution shows the pressure at all points around the lifting surface (hydrofoil). Typically, the graphs of these distributions have negative numbers at the top of the graph, since the C_{press} of the upper curvature of the hydrofoil must be below zero to generate lift and is plotted at the top of the graph [15]. As shown in Figure 3. The results show that the NACA 0015 and S1046 hydrofoils have very similar behavior in the pressure distribution along the chord. The C_{press} lower surface of the hydrofoil should not reach higher magnitudes in the pressure distribution concerning the upper surface, since a downward force would be produced, canceling the lift [16]. NACA 0015 and S 1046 hydrofoils show a great similarity in the pressure distribution along the chord of the compared hydrofoils, but the hydrofoil NACA 0015 obtains a slight advantage when observing that the upper curvature of the hydrodynamic profile reaches much more negative values, especially at the leading edge of the profile and this would generate a better lift.

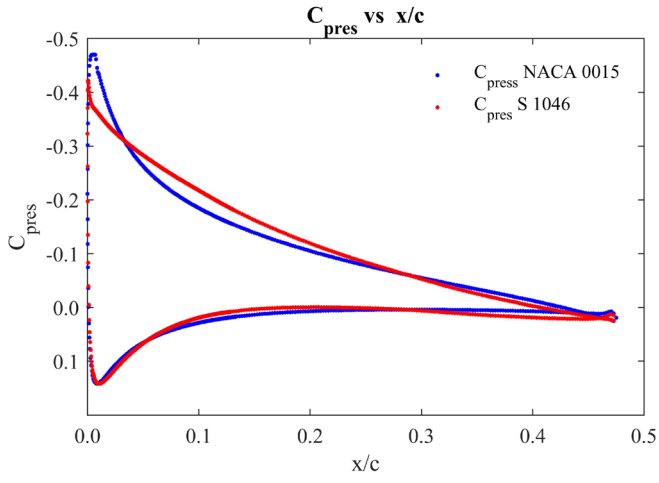

Figure 3. distribution to NACA 0015 and S 1046 hydrofoils.

Conclusions

With the CFD analysis, it is concluded that the highest C_L / C_D ratio was reached by the NACA 0015 hydrofoil at an angle of attack **α** of 9 degrees, also this hydrofoil reaches a higher C_{press} values that favor the lift in a better way concerning the S 1046 hydrofoils, although the NACA 0015 hydrofoil presented cavitation phenomena, forming a tiny vapor bubble, compared to the length of the hydrofoil chord. The presence of cavitation phenomena around the hydrofoils will be conditioned to a greater degree by the reference pressure P_{ref} and to a lesser degree by the velocity assigned to the fluid; reference pressures below $50000\ Pa$ and fluid velocities or relative to the fluid above 7 m/s ensure the presence of cavitation phenomena in the periphery of the hydrofoils analyzed. This study concludes that the hydrofoil NACA 0015 is the best option for designing to design a Gorlov-type VAHT. However, the comparison of the performance of 2 Gorlov-type VAHT with NACA 0015 and S 1046 hydrofoils is left for future research since the differences in hydrodynamic behavior found in this study were minimal.

Acknowledgment

The authors gratefully acknowledge the financial support provided by the second call for R+D+I projects within the framework of the regional agenda of R+D+I for developing the Project “Desarrollo de una turbina hidrocinética tipo propela para la generación de energía eléctrica”. The authors also acknowledge the financial support provided by Universidad de Antioquia (Estrategia de Sostenibilidad 2020-2021. ES84190067).

References

[1] BP, «Statistical Review of World Energy | Energy economics | Home», 2020.

[2] O. US EPA, «Global Greenhouse Gas Emissions Data | US EPA», *Us Epa*, 2021. [En línea]. Disponible en: https://www.epa.gov/ghgemissions/global-greenhouse-gas-emissions-data. [Accedido: 21-may-2021].

[3] E. Chica y A. Rubio-Clemente, «Design of Zero Head Turbines for Power Generation», *Renew. Hydropower Technol.*, jul. 2017, doi: 10.5772/66907.

[4] M. J. Khan, G. Bhuyan, M. T. Iqbal, y J. E. Quaicoe, «Hydrokinetic energy conversion systems and assessment of horizontal and vertical axis turbines for river and tidal applications: A technology status review», *Appl. Energy*, vol. 86, n.º 10, pp. 1823-1835, 2009.

[5] M. Sood y S. K. Singal, «Development of hydrokinetic energy technology: A review», *International Journal of Energy Research*, vol. 43, n.º 11. John Wiley and Sons Ltd, pp. 5552-5571, sep-2019, doi: 10.1002/er.4529.

[6] E. T. Quintero, «Determinación De Caudal, Tiempos De Tránsito, Velocidad Y Coeficiente De Dispersión En El Río Bogotá, Frío Y Magdalena Utilizando Técnicas Nucleares», *Av. Investig. en Ing. - Univ. Libr. Colomb.*, n.º 5, 2006.

[7] IDEAM-CORMAGDALENA, «Estudio ambiental de la Cuenca Magdalena – Cauca y elementos para su ordenamiento territorial», *Estud. Actual. diagnóstico Territ. para Modif. al plan Regul.*, pp. 1-72, 2001.

[8] D. Coiro, U. Maisto, y F. Scherillo, «Horizontal axis tidal current turbine: numerical and experimental investigations», *... Wind Other Mar. ...*, pp. 20-22, 2006.

[9] E. A. Puerto, «Colombia ciudades presión atmosferica | M. en I. Efraín A. Puerto», 2011. [En línea]. Disponible en: https://efrainpuerto.wordpress.com/2011/02/26/f1-2/. [Accedido: 20-jun-2022].

[10] E. Roohi, A. P. Zahiri, y M. Passandideh-Fard, «Numerical simulation of cavitation around a two-dimensional hydrofoil using VOF method and LES turbulence model», *Appl. Math. Model.*, vol. 37, n.º 9, pp. 6469-6488, may 2013, doi: 10.1016/J.APM.2012.09.002.

[11] S. Singh, M. Danish, y K. Saha, «Computational investigation of cavitating flow around two dimensional NACA 4424 and MHKF-240 hydrofoil», *Vibroengineering PROCEDIA*, vol. 29, pp. 159-164, nov. 2019, doi: 10.21595/VP.2019.21121.

[12] R. Keough, V. Mullaley, H. Sinclair, y G. Walsh, «Design, Fabrication and Testing of a Water Current Energy Device», 2014.

[13] I. H. Abbott, A. E. Von Doenhoff, y L. Stivers Jr, «Summary of airfoil data», 1945.

[14] M. Selig, R. Deters, y G. Wiliamson, «Wind Tunnel Testing Airfoils at Low Reynolds Numbers», ene. 2011, doi: 10.2514/6.2011-875.

[15] M. A. Martinez Ordoñez, «Estudio y optimización de una aeronave con fuselaje de ala fija aplicado a vehiculos aéreos no tripulados en la región andina mediante simulación numérica de dinámica de fluidos computacional (CFD)», 2018.

[16] J. John D. Anderson, *Fundamentals of Aerodynamics (in SI units)*, vol. 116, n.º 1176. 2012.

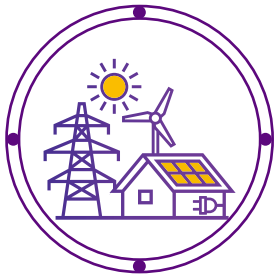

Computational fluid dynamics modelling of an oscillating water column air chamber

Juan David Parra Quintero[1] E-mail: ajuan.parraq@udea.edu.co
Ainhoa Rubio Clemente[1] E-mail: bainhoa.rubioc@udea.edu.co
Edwin Chica Arrieta[1] E-mail: cedwin.chica@udea.edu.co

[1]Grupo de Investigación Energía Alternativa (GEA), Facultad de Ingeniería, Universidad de Antioquia, Calle 70 N° 52-21, Medellín 050010, Colombia.

Abstract

The oscillating water column (OWC) can be a promising option for exploiting the marine power potential in Colombia. Typically, two main stages are identified in the wave energy conversion process using an OWC. In the first stage, an air chamber converts the wave power to pneumatic power and in the secondary stage, a self-rectifying air turbine coupled to an electric generator converts the pneumatic power into electricity. This work aims to determine the hydrodynamic performance of an OWC air chamber on the primary-stage efficiency using a numerical model based on the Reynolds Averaged Navier-Stokes equations and the Volume of Fluid approach for the free surface simulation. The chamber geometry was based on the U-shaped OWC. The chamber maximum efficiency and the mean velocity of the chamber free surface were 66.8% and 0.17 m/s, respectively. Therefore, the optimization of the chamber shape parameters for the wave characteristics is of utmost importance in order to enhance its operating efficiency.

Correspondent author

Keywords: oscillating water column, wave energy, ocean energy, wave energy converter

Introduction

Currently, most countries in the world, including Colombia, aim to supply their domestic energy demand from Non-Conventional Energy Sources (NCES). In this regard, one of the strategies to reduce the vulnerability of the energy sector in the Colombian national energy plan is the search to diversify the electricity generation matrix in the medium and long term [1]. For this purpose, an increase of the complementarity, availability, and reliability of the NCES is required [1]. As a consequence, developing countries are facing challenges related to: i) the development and technological adaptation of devices for the use of NCES; ii) energy generation and efficiency; iii) equity and social development, simultaneously addressing the effects of climate change and sustainable development [2]. Among the NCES types, wave energy stands out, since it uses the movement of waves as a source of energy. To harness this energy, it is necessary to design Wave Energy Converters (WEC), according to the energy availability in the location arranged for the installation, so an Oscillating Water Column (OWC) (considered a WEC) [3]; could be a promising option for harnessing the wave resource. OWC devices have been extensively examined with physical, theoretical, and numerical models. In the literature, it has been found that an OWC onshore allows for greater: resistance to extreme conditions, ease of maintenance, and access to the network [4]. Also, some authors have shown interest in studying the geometry of the resonance chamber under geometrical parameters as a function of wave conditions in the study area. [5]aiming to maximize its available power. The OWC is subjected to two constraints (areas of the chamber and ramp below the chamber. In our country, there is neither a record of the wave spectrum nor large studies about OWC devices for wave resource conditions adapted to the Colombian Pacific and the Caribbean Sea conditions. For this reason, this work is focused on the study and design of an OWC for the Pacific Ocean conditions, the geometry of the chamber is based on the U-shaped OWC [6], considering an inclined novel front ramp prior to wave entry [7]. In line with the above, this work presents the dynamic fluid simulation of the resonant wave chamber of an OWC, which is adapted to the wave conditions of the coastal regions of Colombia; has a low cost; is simple in its manufacture, installation and maintenance; and allows the diversification of the energy matrix and distributed generation in the insular and coastal.

Materials and Methods

An OWC is a device to capture and extracts wave energy. It has the advantage of being a simple structure, easy to be manufactured, without the generation of greenhouse gases or considerable waste during its operation [3]. An OWC consists of a partially submerged structure hollow at the bottom (wave resonant chamber) with an air chamber below sea level. The movement of the wave is translated into pressure on the air inside the chamber, which expands and compresses driving a Wells turbine that in turn drives an electric generator.

In order to design an efficient OWC, it is necessary to optimize it according to the wave characteristics of the installation site. Figure 1a shows a schematic of the wave resonant chamber that will be the subject of the numerical analysis proposed here. The advantages of the proposed geometry are that it is less vulnerable to extreme wave conditions and the front ramp facilitates the wave entry into the chamber and decreases the amount of sediment entering the chamber, which can reduce the interior volume of the water-air interface that facilitates the energy transfer process. In Figure 1b, the two-dimensional (2D) computational domain used for the fluid dynamic analysis of the behavior of the resonant wave chamber in a laboratory scale channel capable of reproducing the wave characteristics of the Colombian Pacific Ocean is illustrated. Numerical simulations were performed in ANSYs Fluent software. The boundary conditions imposed on the computational domain are shown in Figure 1b. To evaluate the performance of the resonant chamber, the water surface elevation (η) is monitored and the chamber efficiency (ε) is determined. In turn, to monitor the elevation, points G1, G2, ..., and G9 are defined. It is widely known that the waves entering the resonant chamber can be characterized under parameters such as the wave height (*H*), the period (*T*), the length (λ), and the amplitude (*A*), as well as the free water surface elevation (η) and the depth (*h*) in which the waves propagate [4]. In the literature, there are analytical expressions relating η to the horizontal distance (*x*) and the time instant (*t*) thanks to the analytical wave theory given by Airy [3] that is described by equation (1).

$$\eta(x,t)=H/2\cos(kx-\omega t) \quad (1)$$

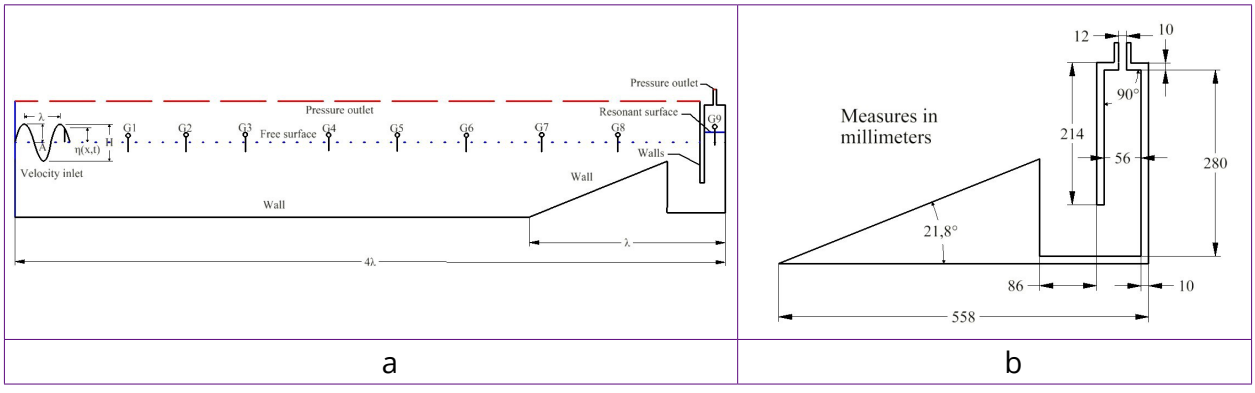

Figure 1. a) Geometry resonant chamber, b) Computational domain for the Colombian Pacific Ocean conditions

Where *k* and *ω* represent the wave number and the angular frequency, respectively. Furthermore, they can be calculated as *2π/λ* and *2π/T*, respectively. Considering the swell conditions of the Colombian Pacific Ocean reported by Portilla et al. [1], the sizing of a laboratory-scale wave channel capable of reproducing the hydrodynamic behavior of the waves was carried out. The following wavefront characteristics were used in the simulation process: *H*=0.02 m, λ=1.47 m and, *h*=0.225 m [1]. *ε* can be evaluated by equation (2) in terms of the ratio between the incident wave power (P_{inc}) and the average pneumatic power obtained at the output of the device (P_{out}), as defined by [3].

$$\varepsilon = P_{out}/P_{inc} \quad (2)$$

P_{inc} during a T is given by equation (3), where E is the total energy per T and C_g is the group velocity given, respectively, by equations (4) and (5).

$$Pin = EC_g \quad (3)$$
$$E = 1/2\ \rho g(H/2)^2 \quad (4)$$
$$C_g = 1/2\ \omega/k\ (1 + 2kh/\sin(2kh)) \quad (5)$$

The average pneumatic power for regular waves can be calculated by equation (6), between an initial and a final time period in the steady state region of the measurements multiplied by the area under the curve of the function defined by the product between the instantaneous pressure drop inside the chamber (ΔP) and the volumetric flow rate, ($Q(t)$). The latter variable is defined for a 2D geometry as $Q(t) = S_{chamber} * V_{fs}$. In this expression, V_{fs} is the free water surface velocity in the vertical direction (m/s) and $S_{chamber}$ is the area of the water plane of the resonant wave chamber that is defined as $b*w$, where b is the length of the chamber and it is equal to 0.056 m, and w is the width of the chamber (in the perpendicular dimension to the wave propagation plane) and is assumed to be 1 since the computational study is in 2D.

$$P_{out} = 1/(T_{end} - T_{ini}) \int (T_{ini})\ (T_{end}) \Delta P\ S_{schamber}\ V_{fs} dt \quad (6)$$

The variable V_{fs} can be calculated through the first time derivative of η inside the resonant chamber using the third order approximation [3], [4]. In addition, this velocity can be calculated using the approximation given by equation (7), as used here.

$$V_{fs} = (d[\ \eta(x,t)\ ])/dt \quad (7)$$

Figure 2a represents the phase contour (where blue and red are air and water, respectively) associated with the simulation, which was analyzed under the laminar regime, unsteady state and, incompressible flow [5]aiming to maximize its available power. The OWC is subjected to two constraints (areas of the chamber and ramp below the chamber.

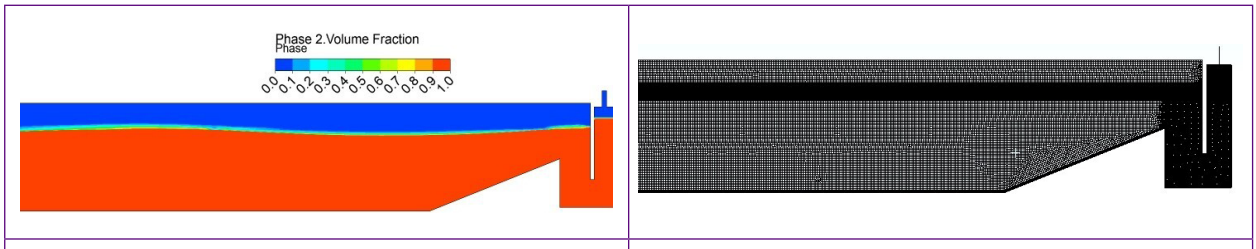

a) b)

Figure 2. a) Phase contour, b) Computational domain mesh.

The Volume of Fluid (VOF) method was used to simulate the free moving interface between the two immiscible fluids water and air [5]aiming to maximize its available power. The OWC is subjected to two constraints (areas of the chamber and ramp below the chamber. The

time-step was set to 0.001 with a maximum number of iterations of 35. Moreover, the convergence criterion of residuals was set to 10^{-6} [5]. In this work, all surface points were assumed with f=0.5 [4]. Regular wave generation was performed at the left side boundary of the channel and it was possible to generate a wavefront by a velocity input using the open channel condition. To set the wave front input directly from the software, a wave height (H) of 0.02 m and a wavelength (λ) of 1.47 m were fixed. Similarly, for the pressure outlet conditions at the top of the channel and at the air outlet in the resonant wave chamber, a relative pressure of 0 Pa was used. The direction of the wave front ranges from $-x$ to $+x$. The no-slip condition was assigned to the bottom of the channel and the walls of the OWC. These boundary conditions have been widely used for the simulation of a wave channel and the walls of a resonant wave chamber. It has been found that taking this condition into account allows capturing of the boundary layer developed between them. Generally, it is used on the bottom and side walls of a numerical wave tank (NWT), chamber and, conduit walls, and points out that the derivative of the volume fraction in time equals zero for the VOF equation [5]aiming to maximize its available power. The OWC is subjected to two constraints (areas of the chamber and ramp below the chamber. The simulation starts (t=0 s) assuming that the fluids are at rest. For the 2D analysis and as an indispensable part of the pneumatic type OWC device to extract and convert the energy of the incident waves, the power take-off (PTO) system adopted here was modeled by using a rectangular hole drilled in the top of the device for the numerical simulations [2]. The mesh was generated using ANSYs Fluent meshing solver and refined mainly on the free water surface area, the channel walls and the resonant wave chamber; locations where a high level of detail and cell-to-cell information are needed for the simulation process. Figure 2b shows the mesh used in the numerical simulations. An independent analysis of the results of the mesh size and time step used for the simulation was performed.

Results and analysis

Figure 3 shows the results of the numerical and analytical free water surface elevation comparison. The analytical solution was obtained using equation (1) [5]aiming to maximize its available power. The OWC is subjected to two constraints (areas of the chamber and ramp below the chamber.

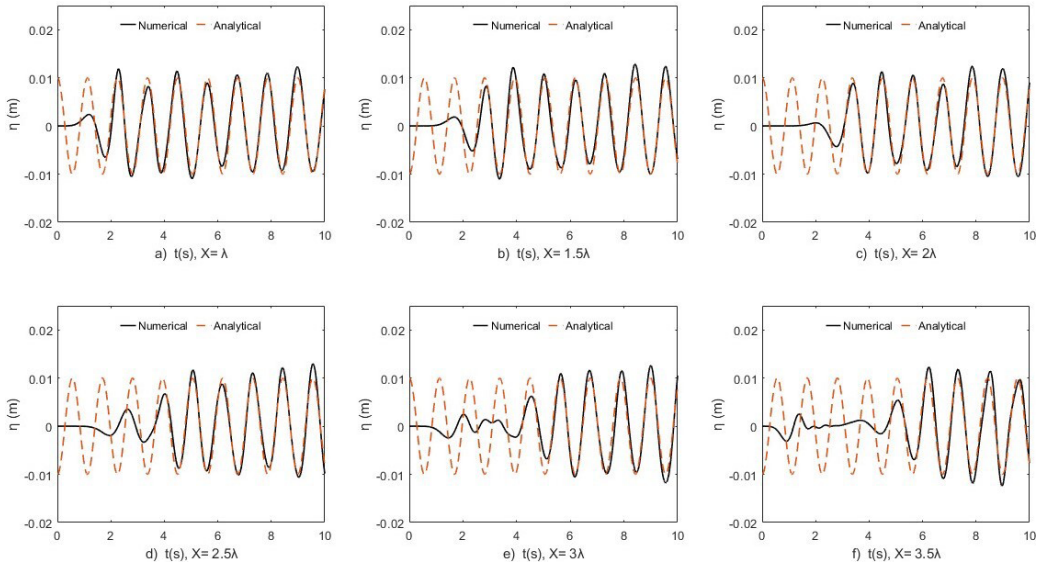

Figure 3. Wave validation was generated between numerical and analytical results for a wave of H=0.02 m. a) X= λ, b) X=1.5λ, c) X=2λ, d) X=2.5λ, e) X=3λ, f) X=3.5λ.

A good degree of correlation between the numerical and analytical results is observed. To verify the wave generation and propagation within the channel, Figure 3 represents the free water surface elevation at various distances from the wave generator using CFD and an analytical solution over time using equation (1). To calculate the wave resonant chamber efficiency, equations (2), (3) and, (6) are used. For this purpose, the velocity of the free water surface (V_{fs}) and the pressure drop inside the chamber (ΔP) were calculated. To obtain the η_{owc}, it is necessary to quantify the incident wave power using equation (3), which was 0.504 W for the defined wave conditions. Similarly, to calculate the pneumatic output power, equation (6) was used, therefore, it was necessary to numerically obtain ΔP and V_{fs} a steady time period defined between 7.61 and 8.7 s, equivalent to a T of 1.09 s. The area under the curve was obtained through numerical methods using a rather small Δt equivalent to 0.001 s. The P_{out} value obtained was 0.337 W. Therefore, ε was 66.8%.

Conclusions

The analysis of the behavior of a resonant wave chamber to profit from wave resource available in the Pacific Ocean of Colombia is presented. From the numerical simulation performed using the VOF method in the CFD software Ansys Fluent, a chamber ε of 66.8% was obtained, which is low efficiency. Therefore, to perform an optimization study of the main geometric factors defining the water resonant chamber is required. Among these parameters, the length of the inner width, the immersion depth and, the angle of inclination of the front wall, as well as the diameter of the air outlet are highlighted. It is important to discern the significance of these factors and their interactions with the process of capturing the energy contained in a wavefront. The response surface or surrogate model methodologies could be

a good option for the sensitivity study of these parameters on their effect on the efficiency of the resonant wave chamber.

Acknowledgment

The authors gratefully acknowledge the financial support provided by the announcement No. 890 de 2020 "Convocatoria para el fortalecimiento de CTeI en Instituciones de Educación de Educación Superior (IES) Públicas 2020 (Contract No. 2022-0452).

References

[1] J. Portilla, A. L. Caicedo, R. Padilla-Hernández, and L. Cavaleri, "Spectral wave conditions in the Colombian Pacific Ocean," *Ocean Model.*, vol. 92, pp. 149–168, 2015, doi: 10.1016/j.ocemod.2015.06.005.

[2] C. Wang and Y. Zhang, "Hydrodynamic performance of an offshore OWC mounted over an immersed horizontal plate : A numerical study," *Energy*, vol. 222, p. 119964, 2021, doi: 10.1016/j.energy.2021.119964.

[3] A. Alfonso *et al.*, "Experimental Investigation of the Hydrodynamic Performance of Land-Fixed Nearshore and Onshore OWC with a Thick Front Wall," pp. 1–26, 2022.

[4] M. M. Samak, H. Elgamal, and A. M. N. Elmekawy, "The contribution of L-shaped front wall in the improvement of the oscillating water column wave energy converter performance," *Energy*, vol. 226, p. 120421, 2021, doi: 10.1016/j.energy.2021.120421.

[5] M. Letzow and Lorenzini, "Numerical analysis of the influence of geometry on a large scale onshore oscillating water column device with associated seabed ramp," *Int. J. Des. Nat. Ecodynamics*, vol. 15, no. 6, pp. 873–884, 2020, doi: 10.18280/ijdne.150613.

[6] P. Boccotti, "Comparison between a U-OWC and a conventional OWC," *Ocean Eng.*, vol. 34, no. 5–6, pp. 799–805, 2007, doi: 10.1016/j.oceaneng.2006.04.005.

[7] T. Vyzikas, S. Deshoulières, M. Barton, O. Giroux, D. Greaves, and D. Simmonds, "Experimental investigation of different geometries of fixed OWC devices," *Renew. Energy*, vol. 104, pp. 248–258, 2017, doi: 10.1016/j.renene.2016.11.061.

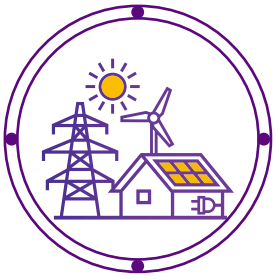

Hydrodynamic characterization of turbomachines focused on pumps as turbines

Daniel Felipe Tobón Espinosa[1] E-mail: dfelipe.tobon@udea.edu.co
Ricardo Moreno Sanchez[2] E-mail: ricardo.moreno@udea.edu.co
Francisco Javier Botero Herrera[3]. E-mail: fboteroh@eafit.edu.co

1, 2 University of Antioquia
3 EAFIT University

Abstract

When we talk about clean and renewable energy generation, hydraulic turbomachines have played a fundamental role in the development of nations. In addition, they have been one of the most widely used renewable energy sources, presenting certain advantages over non-conventional renewable sources. Among these advantages, it can be found that hydraulic turbomachines can deliver their energy in a regulated and controlled manner, thanks to the storage of potential energy in reservoirs.

To estimate the modes of operation, points of best efficiency, hydrodynamic instabilities, and methodologies for harnessing energy from pumps such as turbines, it is necessary to characterize the hydrodynamics of these hydraulic turbomachines in all their modes of operation, using an experimental bench that simulates actual operating conditions.

In this process, the construction of the characteristic curve of four quadrants of a turbomachine is carried out, reviewing its 5 modes: pump mode, brake pump mode, turbine mode, brake turbine mode, and reverse pump mode.

Correspondent author

In addition, thanks to the dynamic sensors installed in the pump volute, it is possible to know the hydrodynamic behavior inside the pump as a turbine, finding its average behavior and frequency response, which is a tool for diagnosis of the condition of the machine.

Keywords: Pumps as a turbine (PAT); Characterization; Hydrodynamics; Spectral analysis.

Introduction

The generation of electrical energy from renewable sources plays a fundamental role in the sustainable development of a country, especially in those countries that have great hydraulic potential, the vast majority of which are paradoxically developing countries[1]; or for countries with a high demand for energy that comes from non-renewable sources such as coal and oil[2].

All the electrical potential from renewable sources can positively affect the development and quality of life of the population[3], especially the population that live in areas of difficult access, which as a general rule are the most vulnerable population of the nations. A solution to this problem is the generation of electrical energy in a localized and non-centralized manner, that is, the generation and distribution of energy on a small scale near the final centers of consumption, using the water sources that are available in the areas, from the use of reversible and easy-to-handle technologies, such as turbine pumps[4]–[7].

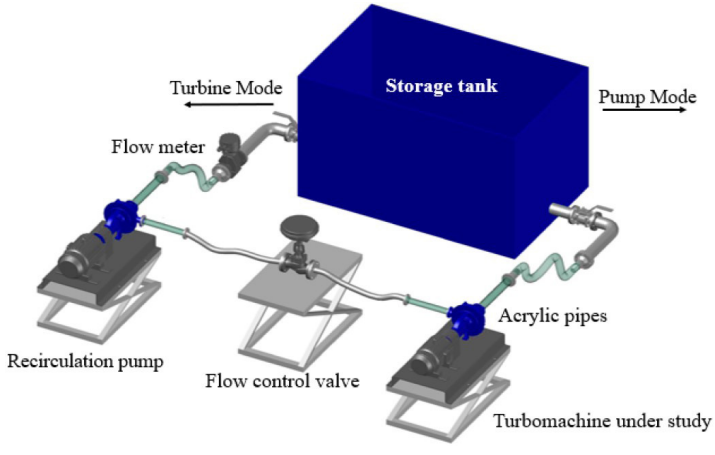

Figure 1. Schematic diagram of the hydraulic test ring.

Although there are advantages when using a pump to work as a turbine, such as its assembly, maintenance, easy access to spare parts, and low initial cost[8], [9], there are also there are some drawbacks when putting them into operation[10]–[12]like electrical submersible pumps (ESP because they were not designed specifically for that purpose. This document presents an experimental hydrodynamic characterization of a centrifugal pump working as a turbine; by constructing the four-quadrant characteristic curve, to find hydraulics instabilities, and to compare the best efficiency point with a no ideal operation point.

Methodology

A commercial stainless-steel ITT-Goulds SSH series pump was used, in particular the 5SH [13], which has a power of 2 HP. This pump was installed in the turbomachinery test bench of the hydraulics laboratory of EAFIT University, which has a second model 8SH recirculation pump. This schematic assembly can be seen in Figure 1. The relevant technical information of the turbomachinery study is presented in Table *1*.

For data acquisition, a digital platform based on LabVIEW® was used with cRIO-type controllers, especially cRIO-9045 and cRIO-9076.

In addition, instruments to measure the main variables such as flow, pressure, torque, dynamic pressure, and temperature acceleration, among others, were used in the characterization. All sensor specifications can also be found in Table *2*.

For the characterization of turbomachines, the international technical standard IEC 60193 is used[14], in which the construction of the four-quadrant characteristic curve is proposed. This curve is constructed using 2 dimensionless numbers, one referring to the flow rate and the other to the rotational speed of the machine, and [14]. From this characteristic curve, the 5 typical forms of operation of a turbomachine can be found, which are pump mode, pump-brake, turbine mode, turbine-brake mode, and pump reverse mode[15], [16], and all the modes of operation can be found in Figure 2.

Table 1. Main technical characteristics of the turbomachine.

Characteristic	Specification
Inlet diameter	0.14764 [m]
Discharge diameter	0.08104 [m]
Number of impeller blades	6 [un]
Rotor speed	1750 [rpm]
Flow rate	0.009 [m3/s]
Dynamic head	10 [mWC]

Table 2: Test ring instrumentation.

Instrument	Output	Range	Span	Linearity
Accelerometer Dytran-3055D6T	±5 [V]	±25 [g]	50 [g]	±1 [%FS]
Dynamic pressure Dytran-2005V	0...5 [V]	0...50 [psi]	50 [psi]	±1 [%FS]
Encoder Omron E6B2-C-CWZ3E	TTL 0...5 [V] pulse	0...6000 [rpm]	6000 [rpm]	-
Optical Tachometer DT2234C+	TTL 0...5 [V] pulse	2.5...99996.5 [rpm]	99994 [rpm]	0.05 [%] +1 digit
GE TransPort PT878	4...20 [mA]	0...0.033 [m3/s]	0.033 [m3/s]	±0.25 [%FS]
PT - Yokogawa-EJA530E	4...20 [mA]	-1...2 [bar]	3 [bar]	±0.055 [%FS]

Results and analysis

To make the characterization curves, it was proposed to maintain a hydraulic load of 4 meters of the water column, through the power supplied by the recirculation pump. It is important to be clear that as the rotational speed of the study turbomachine is increased, the speed of the recirculation pump must be decreased and vice versa to guarantee said stable head. A total of 125 measurements were made, which are presented in Figure 2 b) using the 4-quadrant diagram. It can be evidenced in Figure 2, all the typical operating modes of reversible hydraulic turbomachines, in particular the turbine quadrant. This quadrant is important in the characterization of a pump, hence, the fact that there are data in this quadrant demonstrates the possibility of using the pumps as a turbine.

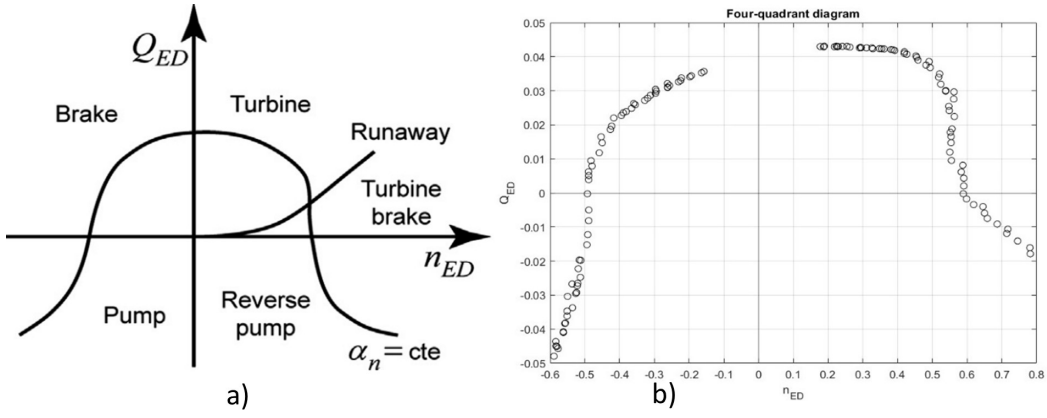

Figure 2. Four-quadrant diagram indicating the operating modes a) theoretical b) experimental.

In Figure 3 a), a frequency analysis of the point of maximum efficiency is carried out. Additionally, the horizontal axis is presented in order, that is, the frequency is divided by the rotation frequency of the turbomachine, thus obtaining the 1X components, which corresponds to something that occurs once every revolution, the 6X that corresponds to a phenomenon that occurs 6 times per revolution, which corresponds to the pitch of the blades.

Due to the different dynamic sensors with which the experimental installation was carried out, it is possible to have the signal for 2 dynamic sensors and 2 accelerometers located tangentially next to each other. This allows us to observe how non-invasive sensors can see the same behavior as invasive sensors. In addition, non-invasive sensors or accelerometers allow us to see other structural and dynamic components that are quite important in the characterization of the pump as a turbine. An example is seen in Figure 3 since the 3X component appears in the accelerometers, a symptom of misalignment [17], which cannot be seen by dynamic sensors that can only provide information on the hydraulic component. Also having a sensor dedicated exclusively to hydraulic dynamic components, the characterizations that go beyond the 4-quadrant characteristic curve can be carried out, as is the case of defining operating points where instabilities or hydrodynamic phenomena occur, as is the case presented in Figure 3. Where nothing different from the main components 1X and 6 X are presented initially in the accelerometers; while the dynamic sensors present components at 0.7X, which presents a sub-synchronous phenomenon, that can be classified as a Rotating Stall [18].

Conclusions or summary

Through an experimental analysis it was possible to generate the characterization of a hydraulic turbomachine in its different modes of operation as a centrifugal pump working as a turbine, corroborating that those centrifugal pumps are reversible machines and that they can be used to generate energy in their mode of operation, turbine.

- Spectral analyzes allow components to be found based on rotation speed or orders that allow identifying operating points or hydrodynamic phenomena of interest, such as the point of maximum efficiency, or the point where a hydrodynamic instability is presented, which can be a rotating stall. This is important for the characterization of the turbomachinery since these points with hydrodynamic phenomena must be avoided, or failing that, the pump as a turbine must operate for the least amount of time possible at said points to avoid damage.
- This type of analysis is not only usable in pumps such as turbines, but it can also be used for any rotating machine, including combustion engines, compressors, gear trains, and, of course, turbines. Therefore, every advance in these non-invasive monitoring techniques can be used on a wide range of industrial machines.

- It is important to continue with the characterization of pumps as turbines to define safe operation zones, types of hydrodynamic phenomena presented, typical generation powers and efficiencies, and mechanical and structural problems that can be generated due to the use of a reversible machine in one mode of operation for which it was not designed.

Acknowledgment

The authors thank the University of Antioquia and the EAFIT University, without the support of these entities the development of the project would not have been possible.

References

[1] K. Goldsmith, *Economic and Financial Analysis of Hydropower Projects*, 6th ed. Trondheim, Norway: Norwegian Institute of Technology, 1993.

[2] E. I. A. EIA, "U.S. Energy Information Administration (EIA)," 2022. https://www.eia.gov/ (accessed Jun. 14, 2022).

[3] A. Zerrahn, W.-P. P. Schill, and C. Kemfert, "On the economics of electrical storage for variable renewable energy sources," *Eur. Econ. Rev.*, vol. 108, pp. 259–279, Sep. 2018, doi: 10.1016/j.euroecorev.2018.07.004.

[4] A. A. Williams, *Pumps As Turbines - a Users Guide*. London: Intermediate Technology Publications, 1995.

[5] S. Rawal and J. T. Kshirsagar, "Numerical Simulation on a Pump Operating in a Turbine Mode," *Twenty-Third Int. Pump Users Symp.*, pp. 21–28, 2007, [Online]. Available: http://turbolab.tamu.edu/proc/pumpproc/P23/ch05-rawal.pdf.

[6] M. Rossi, A. Nigro, G. R. Pisaturo, and M. Renzi, "Technical and economic analysis of Pumps-as-Turbines (PaTs) used in an Italian Water Distribution Network (WDN) for electrical energy production," *Energy Procedia*, vol. 158, pp. 117–122, 2019, doi: 10.1016/j.egypro.2019.01.055.

[7] F. J. Lugauer, J. Kainz, and M. Gaderer, "Techno-Economic Efficiency Analysis of Various Operating Strategies for Micro-Hydro Storage Using a Pump as a Turbine," *Energies*, vol. 14, no. 2, p. 425, 2021, doi: 10.3390/en14020425.

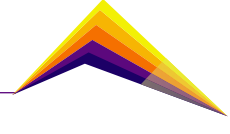

[8] A. Beguin, C. Nicolet, B. Kawkabani, and F. Avellan, "Virtual power plant with pumped storage power plant for renewable energy integration," *Proc. - 2014 Int. Conf. Electr. Mach. ICEM 2014*, pp. 1736–1742, 2014, doi: 10.1109/ICELMACH.2014.6960417.

[9] A. Carravetta, S. Derakhshan Houreh, and H. M. Ramos, *Pumps as Turbines Fundamentals and Applications*. 2018.

[10] Q. Jiang, Y. Heng, X. Liu, W. Zhang, G. Bois, and Q. Si, "A review of design considerations of centrifugal pump capability for handling inlet gas-liquid two-phase flows," *Energies*, vol. 12, no. 6, 2019, doi: 10.3390/en12061078.

[11] Y. Zhang and Y. Wu, "A review of rotating stall in reversible pump turbine," *Proc. Inst. Mech. Eng. Part C J. Mech. Eng. Sci.*, vol. 231, no. 7, pp. 1181–1204, 2017, doi: 10.1177/0954406216640579.

[12] M. Stefanizzi, T. Capurso, G. Balacco, M. Binetti, S. M. Camporeale, and M. Torresi, "Selection, control and techno-economic feasibility of Pumps as Turbines in Water Distribution Networks," *Renew. Energy*, vol. 162, pp. 1292–1306, 2020, doi: 10.1016/j.renene.2020.08.108.

[13] "Goulds pumps," *World Pumps*, vol. 2000, no. 405, p. 36, Jun. 2000, doi: 10.1016/S0262-1762(00)80065-6.

[14] International Electrotechnical Commission, The International Electrotechnical Commission, and International Electrotechnical Commission, *IEC60193 Hydraulic turbines, storage pumps and pump-turbines - Model acceptance tests*, 2nd ed., vol. 3. Geneva, Switzerland: International Electrotechnical Commission, 1999.

[15] H. Bolaños, D. F. Tobon Espinosa, J. A. Pérez Mesa, and F. Botero, *Respuesta Hidráulica y Mecánica en una Bomba Centrifuga de Baja Velocidad Especifica Debida a Inestabilidades de Carga Parcial*, 1st ed. Manizales: Universidad Autónoma de Manizales, 2018.

[16] D. F. Tobon Espinosa, "Estudio numérico y experimental de fenómenos hidrodinámicos que ocurren en bombas centrífugas como turbinas," EAFIT, Medellín, 2016.

[17] B. STANDARD, *BS EN 60994:1993 IEC 994:1991 - Guide for field measurement of vibrations and pulsations in hydraulic machines (turbines, storage pumps, and pump turbines)*, 1st ed. London: British Standard, 1993.

[18] F. Botero *et al.*, "Flow Visualization Approach for Periodically Reversed Flows," *J. Flow Vis. Image Process.*, vol. 19, no. 4, pp. 309–321, 2014, doi: 10.1615/jflowvisimageproc.2014006575.

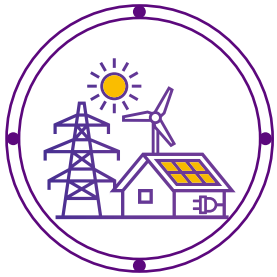

Experimental characterization of hydrokinetic turbines

Fredys Romero-Menco[1] *E-mail: adejesus.romero@udea.edu.co*
Juan David Pineda[1] *E-mail: bjdavid.pineda@udea.edu.co*
Andrés Jahir Chalaca Salas[1] *E-mail: candres.chalaca@udea.edu.co*
Ainhoa Rubio-Clemente[1] *E-mail: dainhoa.rubioc@udea.edu.co*
Edwin Chica[1] *E-mail: eedwin.chica@udea.edu.co*

1. Grupo de Investigación Energía Alternativa (GEA), Facultad de Ingeniería, Universidad de Antioquia UdeA, Calle 70 N° 52-21, Medellín 050010, Colombia.

Abstract

The hydrodynamic performance of propeller horizontal-axis and vertical-axis H-Darrieus hydrokinetic turbines were determined by experimental tests in a circulating water channel. Both turbines have three blades that are located 120° from each other. The propeller hydrokinetic turbine had a diameter of 0.24 m and used an SG6043 foil. The blades of the H-Darrieus hydrokinetic turbine were designed using a NACA 0015 hydrofoil with an angle of attack of -10°. The diameter, height, and chord length for the H-Darrieus turbine were 187.5 mm, 141 mm, and 42.5 mm, respectively. Therefore, the swept area of this turbine was 0.0264 m^2 compared with that of the propeller turbine (0.0452 m^2). In both turbines, the lift force was the predominant driving force. The tangential component of the resultant force of the lift and drag forces provided the torque to generate electrical energy. The experimental results showed a power coefficient (C_p) peak of 0.3076 at a tip speed ratio (λ) of 0.308 for the H-Darrieus turbine. Meanwhile, a C_p of 0.2129 at a λ of 2.952 was obtained for the propeller turbine. The C_p of the H-Darrieus was comparatively higher than that of the propeller hydrokinetic turbine.

Correspondent author

However, the H-Darrieus hydrokinetic turbine had poor starting characteristics and a less stable rotational speed (ω) compared to the propeller turbine. Additionally, the coupling of the turbine with a greater number of electric generators is promoted at higher λ values.

Keywords: propeller turbine, H-Darrieus turbine, power coefficient, renewable energy.

Introduction

Today, there is a worldwide interest in using renewable energy to supply sustainable power generation since the global energy demand is increasing. This fact is due to population and economic growth, especially in emerging market economies. Additionally, there are some challenges in the energy sector, such as fossil fuel depletion and climate change, which demand the use of alternative sources of energy supply. The use of electrical energy is the key to economic growth and the improvement of people living standards. In this regard, providing electricity to communities with less environmental impact is essential [1, 2].

Typical renewable energy sources such as solar, wind, hydro, tidal, ocean, geothermal, and biomass energy, among others, can provide electricity to communities**.** The technologies used to profit from these energy sources have gained increasing attention in the energy market around the world, especially, solar photovoltaic systems and wind turbines [2-4]. Therefore, is important to undertake actions to continue contributing to the development of new technologies for the use of other renewable resources. The potential of unexplored hydro-energy in some countries can be used for electric generation using hydrokinetic technologies, including horizontal-axis (HAHT) and vertical-axis water turbine (VAHT), that capture the energy from the flow of water through hydrodynamic processes. These types of turbines extract energy from natural water currents in oceans, rivers, and channels with a minimum investment in terms of construction [5, 6]. These devices are becoming popular due to their relative simplicity in the rotor design and manufacturing ecologically friendly. However, hydrokinetic turbines are still in their development stage. They usually experience a low power coefficient (C_p) when they are not optimized. In this regard, some studies should be conducted to increase the C_p for their widespread and cost-effective implementation shortly. The C_p value is a measure of the fluid dynamic efficiency. Therefore, different numerically and experimental research have focused on identifying the most suitable technical solutions (rotor design, blade optimization, several rotor shapes, etc.) and operating conditions leading to an increased power extraction [7, 8]. The main aim of this work is to experimentally compare the performance of horizontal- and vertical-axis hydrokinetic turbines to select

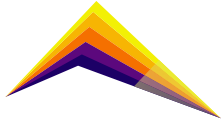

the best one for small-scale hydroelectric power generation in developing countries. The experimental tests are described in detail and the C_p results as a function of the tip speed ratio (λ) are compared.

Material and methods

The characterization of the performance of two different scaled-model hydrokinetic turbines is presented (a HAHT and a VAHT, as illustrated in Figures 1a and 1b, respectively). The HAHT is a propeller hydrokinetic turbine with a 0.24 m diameter rotor (D), a skew angle, and a rake angle equal to 13.3° and -18.06°, respectively. In turn, the VAHT is an H-Darrieus hydrokinetic turbine with a diameter (D), height (H), and chord length (C) equal to 187.5 mm, 141 mm, and 42.5 mm, respectively. The H-Darrieus turbine was designed using a NACA 0015 hydrofoil with an angle of attack of -10°. Meanwhile, the SG6043 foil was used in the propeller turbine. Both turbines have three blades. The models were manufactured in a 3D-printer system.

a) b)

Figure 1. a) Propeller hydrokinetic turbine, b) H-Darrieus hydrokinetic turbine.

The turbine's performance was determined by $C_{P,}$ which is a measure of turbine efficiency. This variable refers to the ratio between the turbine power output and the maximum power available in the free-stream tube of a cross-sectional area (A), and it can be calculated as expressed in Eq. (1). For HAHT, A can be taken as the rotor swept area, which is equal to πR^2; for VAHT, A is calculated by the multiplication of the rotor height (H) and the rotor diameter (D) [6, 7].

$$C_p = T\omega/(1/2\ \rho A V^3) \qquad (1)$$

where T, ρ, and V are the torque, the water density, and the water-free stream velocity. In turn, the tip speed ratio (TSR) is defined as the ratio between the tangential speed of the

blade tip and the upstream flow velocity [5, 7, 9] and calculated by Eq. (2), where R is the turbine radius.

$$TSR=R\omega/V \qquad (2)$$

The turbine performance is typically presented as a plot of C_p *vs.* TSR. The theoretical maximum value of C_p is 0.593 for a single and an open actuator disc. This limit is known as the Betz limit. This efficiency measure is based on the fact that a turbine requires fluid moving through it to generate power. When an extremely high amount of kinetic energy is extracted from the flowing fluid, the turbine would cease to operate [5, 6].
The experiments were conducted in an open hydraulic channel with a width, height, and length equal to 0.31 m, 0.5 m, and 8 m, respectively. Inside the channel, for measuring the water speed, a flow meter (FlowWatch FW450) was used, which had an accuracy of ±0.01 m/s of the velocity. The water recirculated through the canal is driven by an axial flow pump controlled by a 14.9 kW electric motor, producing a water velocity of up to 1 m/s. The water velocity was measured in three different positions in the channel upstream of the rotor and was averaged. Figure 2 presents an overview of the test facility.

T and ω were measured using a sensor of torque (Futek-Model TR605) with an encoder (accuracy of 0.000110 Nm and >10,000 Cpr, respectively). The measurements were saved in real-time employing the intelligent digital display (IHH500 pro), which was connected to the sensor for monitoring its activity. For the measurement of the HAHT, T, and ω, it was necessary to immerse the torque sensor and the data acquisition system in the water current in a submerged water-resistant vessel. For this purpose, a water-resistant vessel that would protect the sensor from the flow of water was constructed, as shown in Figure 1a. For the VAHT, the sensor was attached above the water surface.

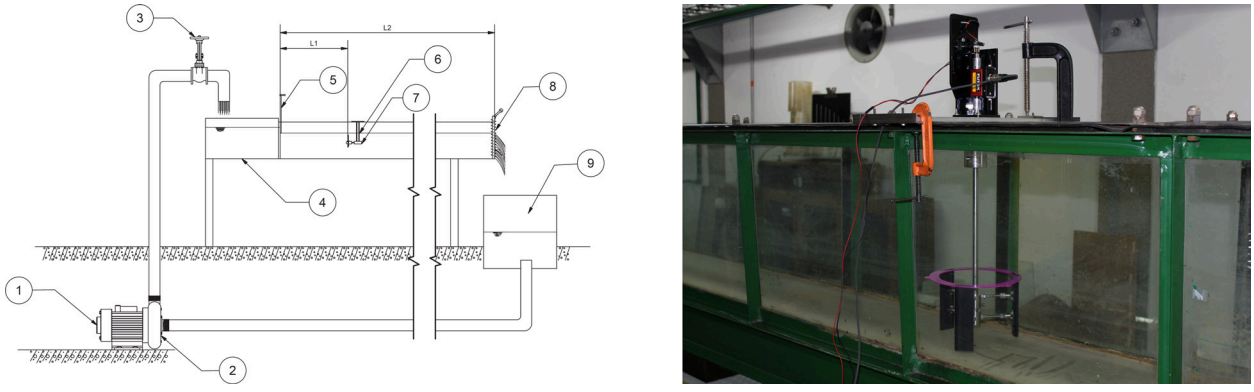

Figure 2. Experimental setup of the recirculating water channel. 1) Motor of 14.9 kW, 2) impeller, 3) water inlet value, 4) channel, 5) gate, 6) model horizontal-axis hydrokinetic turbine, 7) torque sensor, 8) weir assemble, and 9) feed tank.

To measure the torque generated by the turbine at different TSR, a braking system coupled to one end of the torque sensor was used. This system employs a direct current motor and a reverse current braking technique, i.e., an electric motor is used as a brake in the turbine model. It maintains the turbine's model operation at a constant TSR. The technique consists of energizing the DC motor in the opposite direction to the turbine rotation, thus generating torque in the opposite direction (reactive), which reduces the turbine ω. The braking torque is adjusted according to the desired turbine ω, so that the amount of current flowing to the DC motor is regulated by pulse width modulation (PWM). In the developed system, it is achieved using a microcontroller and a power coupling circuit, which has the function of coupling the signal provided by the microcontroller with the power supply of the DC motor. When the turbine ω is required to be decreased (or increased), the microcontroller increases (or decreases) the work cycle of the PWM, subsequently, it increases (or decreases) the energy received by the engine. Consequently, the braking torque also increases (or decreases).

The models of turbines were subjected to a uniform steady flow to be characterized using a non-dimensional power performance curve relating C_P to TSR. For this, the rotors were aligned to be perpendicularly located to the flow direction. The C_p values were calculated using Eq. (1). The free stream velocity of the water was fixed (~ 0.5 m/s) and ω was controlled accordingly to obtain different TSR values. All the results were obtained for the two rotor configurations studied here.

Results and discussion

Figure 3 presents the comparison between the turbine performances from the experiment. The results showed a C_p peak of 0.3076 at a λ of 0.380 for the H-Darrieus turbine; meanwhile, a C_p of 0.2129 at a λ equal to 2.952 was obtained for the propeller turbine. The generators that will be coupled to the turbine produce electrical energy at a certain RPM (usually at high RPM) and because hydrokinetic turbines, particularly the current H-Darrieus turbine, produce power at low RPM, using a gearbox between the turbine and the generator is required to increase the ω from a low-speed of the turbine main shaft to a high-speed shaft connecting with an electrical generator.

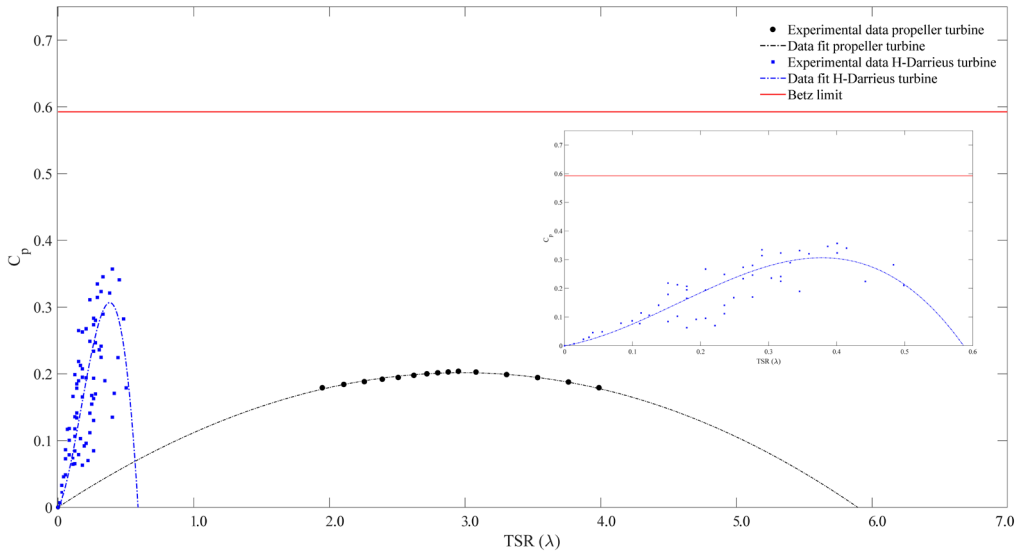

Figure 3. Power coefficient (Cp) vs. tip speed ratio (TSR) values

The H-Darrieus C_p was comparatively higher than that of the propeller hydrokinetic turbine. The H-Darrieus design was simpler than that of the propeller turbine, due to the blade of the latter having a more complex geometry, requiring delicate machining and manufacturing. Therefore, the simple design of the H-Darrieus turbine affects the manufacturing process. In this regard, the total cost can be reduced. With a propeller turbine, the gear and the generator must be placed underwater. In contrast, in a vertical-axis turbine, the generator can be coupled to one end of the shaft, so it can be placed on the top and can reduce the cost of arranging water-sealed technology [5, 6, 9]. Despite the advantages of the H-Darrieus turbine, it presents poor starting characteristics and a less stable ω compared to the propeller turbine. Additionally, the blade of the H-Darrieus turbine does not experience a stable peak load during operation [9]. This variation of force on blades could cause a vibration effect on the turbine, reducing its cycle of life. Therefore, the use of a propeller turbine is recommended for power generation in developing countries.

Conclusions

The performance of two hydrokinetic turbines was studied experimentally in an open hydraulic channel. The results showed that both turbines can contribute to Colombia's future renewable energy supply. The relative difference between the C_p of the H-Darrieus and the propeller turbines is about 44.44%, being the latter with the lower C_p associated. Nevertheless, it has a high ω and a lower T fluctuation, reducing the structural problems in the turbine.

Acknowledgment

The authors thank the second joint call for I+D+i projects within the framework of the I+D→i regional agenda for the financial support provided to the project “Development of a propeller-type hydrokinetic turbine for the generation of electrical energy (In Spanish)”. Additionally, the authors acknowledge the financial support from the University of Antioquia (Sustainability Strategy 2020-2021. ES84190067).

References

[1] Olabi, A. G., & Abdelkareem, M. A. (2022). Renewable energy and climate change. Renewable and Sustainable Energy Reviews, 158, 112111.

[2] Jaiswal, K. K., Chowdhury, C. R., Yadav, D., Verma, R., Dutta, S., Jaiswal, K. S., & SelvaKumar, K. K. (2022). Renewable and sustainable clean energy development and impact on social, economic, and environmental health. Energy Nexus, 100118.

[3] Perez, A., & Garcia-Rendon, J. J. (2021). Integration of non-conventional renewable energy and spot price of electricity: A counterfactual analysis for Colombia. Renewable Energy, 167, 146-161.

[4] Pupo-Roncallo, O., Campillo, J., Ingham, D., Hughes, K., & Pourkashanian, M. (2019). Large-scale integration of renewable energy sources (RES) in the future Colombian energy system. Energy, 186, 115805.

[5] Niebuhr, C. M., Schmidt, S., van Dijk, M., Smith, L., & Neary, V. S. (2022). A review of commercial numerical modeling approaches for axial hydrokinetic turbine wake analysis in channel flow. Renewable and Sustainable Energy Reviews, 158, 112151.

[6] Niebuhr, C. M., Van Dijk, M., Neary, V. S., & Bhagwan, J. N. (2019). A review of hydrokinetic turbines and enhancement techniques for canal installations: Technology, applicability, and potential. Renewable and Sustainable Energy Reviews, 113, 109240.

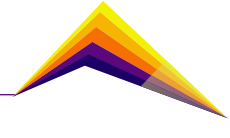

[7] Nunes, M. M., Mendes, R. C., Oliveira, T. F., & Junior, A. C. B. (2019). An experimental study on the diffuser-enhanced propeller hydrokinetic turbines. Renewable energy, 133, 840-848.

[8] Tan, K. W., Kirke, B., & Anyi, M. (2021). Small-scale hydrokinetic turbines for remote community electrification. Energy for Sustainable Development, 63, 41-50.

[9] Yagmur, S., & Kose, F. (2021). Numerical evolution of unsteady wake characteristics of H-type Darrieus Hydrokinetic Turbine for a hydro farm arrangement. Applied Ocean Research, 110, 102582.

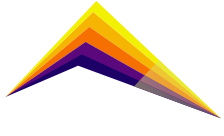

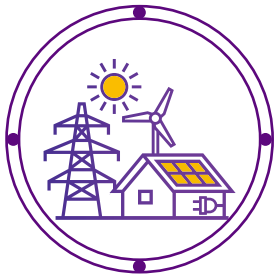

Design and implementation of an on-board laboratory for dual fuel strategies evaluation in real-driving conditions in Colombia

Iván Darío Bedoya Caro
Jairo Luis Durango Padilla
David Zuluaga Castrillón

E-mail: ivan.bedoya@udea.edu.co
E-mail: jairo.durangop@udea.edu.co
E-mail: david.zuluagac@udea.edu.co

Grupo de ciencia y tecnología del gas y uso racional de la energía "GASURE"

Abstract

The road transportation of goods and personnel represents roughly 40% of the gross energy consumption in Colombia, with an average efficiency of 20%, according to UPME (Unidad de Planeación Minero Energética) reports. The combustion engines employed in the vehicle transport sector, use diverse technologies that look to improve efficiency and reduce pollution emissions, however, in Colombia one of the most important issues is the poor access to modern technologies in road transport. Emissions regulation policies and laws in developed countries are moving towards the implementation of real driving tests because of the identified gap between emissions measured under typical driving cycles at laboratory conditions and real driving emissions. In many countries of the Europe Union and the United States, these dynamic tests in a route are obligatory and very important in the homologation process and subsequent commercialization of vehicles. In Colombia, vehicle homologation is based on the results reported by the manufacturers in typical homologation tests made in other countries, which causes an additional gap in emissions calculations, since they have different environmental conditions of operation, different systems of control of emissions, and different types of fuel. Dual fuel operation in

Correspondent author

diesel engines means that a gaseous fuel (typically Natural Gas) is added in the admission or directly injected into the cylinder to replace diesel and reduce carbon dioxide emissions and particulate matter in the exhaust. Although dual fuel operation exhibits possible advantages over typical diesel operation in the Colombian context, the evaluation of real driving conditions is needed to determine the actual effects of this kind of engine combustion mode. This paper reports the methodology followed to design and implement an on-board laboratory for dual fuel strategies evaluation in real-driving conditions in Colombia, additionally, the initial results obtained on emissions and particulate matter for diesel and dual fuel modes operating at several engine speeds are discussed.

Keywords: Emissions, transient, fuel, measurement, dual fuel combustion.

Introduction

The world is facing a shortage of liquid fossils, among them is Diesel, which is vitally important in the transportation of resources and people. Also, diesel engines are one of the main generators of PM (particulate matter) and NOx emissions. For these reasons, alternatives to reduce diesel consumption using no conventional fuels are needed and one of them is dual fuel combustion using Natural Gas injected in the admission port or directly into the cylinder. When dual fuel combustion is used in compression ignition engines operating at transient conditions, Diesel is replaced by up to 50% approximately, but this replacement depends on many factors like compatibility between dual fuel transformation equipment and the diesel engine, atmospheric pressure and temperature, and Natural Gas composition, among others. Dual fuel operation tends to reduce diffusion combustion and PM emissions; however, the ignition delay is increased leading to poorest combustion in the air-Natural Gas mixture, which is ahead of the combustion jet.

Many studies focused on the actual vehicle emissions regulations present problems because the world contamination from the transport sector continues to increase, this is because the type of tests implemented for the vehicle homologation present discrepancies related to the real conditions to which the vehicle is subjected. The implementation of new simulation tools closer to reality like GEM in the United States and VECTO in the EU can throw several important results for the certification of a vehicle like maps of fuel consumption, emissions, maps of transmission, axle efficiency, tire rolling-resistance, and drag coefficient. However, these simulation tools need certain input variables for their appropriate operation, which

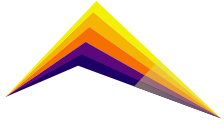

can only be obtained on route tests (Giraldo, M., & Huertas, 2019), (Quirama et al, 2020) and (Sharpe et al, 2019). Also, these parameters, that the simulation test can give, must be verified through on-road testing. The future of the vehicle's homologation is the real-driving tests, where the vehicle is subjected to real operating conditions (Mahesh, et al 2019). Additionally, the effects of energy transition strategies on energy efficiency and emissions should be also determined in real driving conditions.

This paper aims to present the advances in the development and implementation of an on-board laboratory to evaluate dual fuel strategies in the Colombian context at transient conditions. In the author's opinion and best knowledge, although this kind of laboratories are common in developed countries, in Colombia and other developing countries there are not enough reports on compatible diesel engines-dual fuel transformation technologies. Additionally, the experimental facilities needed for a complete analysis of dual fuel operation, involving performance, emissions, and combustion phenomena, using cost-competitive technologies have not been clearly stated in previous research.

Methodology

1. For the vehicle selection and the dual transformation system, one of the most important criteria was the implementation of Common Rail fuel injection in the vehicle engine, and the technological compatibility of the set vehicle engine with the dual system and its operation. The NHR vehicle with the ISUZU 4JH1 engine accomplishes this requirement and has a good representation in the Colombian market. The dual fuel transformation system compatibility with the NHR vehicle was evaluated according to the knowledge and previous projects developed by companies involved in dual fuel retrofit services in Medellin.

2. For the measurement equipment, the more important criteria were enough sampling rate to report information in transient conditions and that they were relatively cheap when compared with higher cost equipment used for vehicle homologation in developed countries (Boulter et al., 2011).

3. For the energy supply equipment, the selection criteria were the power consumption of all equipment and their type of voltage (Delgado et al., 2019).

4. The effect of diesel mode and dual fuel mode on performance, emissions, and combustion parameters will be studied using typical driving cycles like WLTP (Worldwide Harmonized Light Vehicles Test Cycle) and other cycles developed for Medellín running on roller dynamometers. Additionally, real driving tests will be also carried out on Medellin roads, and the results obtained for the two kinds of tests will be compared. Up to the date of writing this paper, only tests running in diesel and dual fuel modes at different engine speeds without load changes have been carried out, the results on emissions and PM are reported in the results section.

Figure 1 shows a conceptual map of the decision-making procedure to design and develop the on-board laboratory, according to the 1-3 step above described.

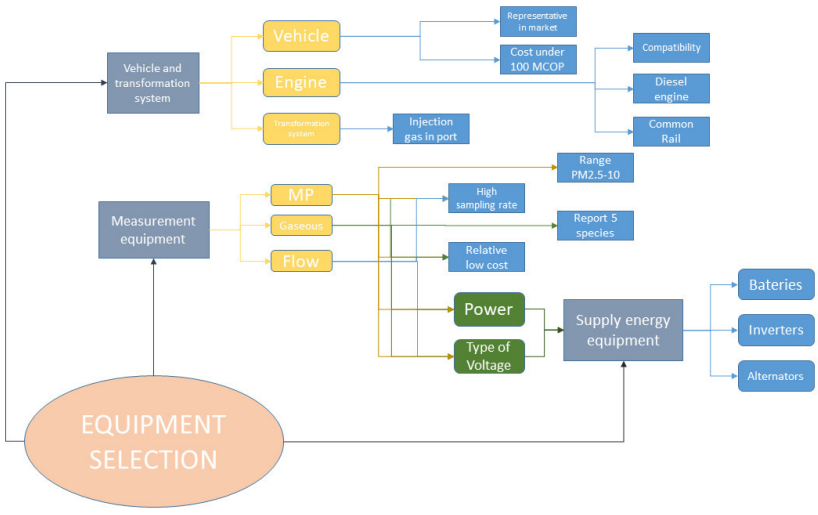

Figure 1. Decision-making diagram for the equipment.

Results and analysis

Table 1-7 show the technical characteristics of the selected equipment:

Table 1. Components of the dual transformation system.

Components of the dual transformation system	Technical description
Engine	Isuzu 4JH1-TC
Dual Fuel transformation technology	Scalmax System

Table 2. Vehicle/ Engine characteristics.

Vehicle/ Engine Characteristics	Value
Vehicle	NHR Chevrolet
Engine	Isuzu 4JH1-TC
Type	Turbo Intercooler
Displacement(cc)	2999
N° cylinders	4 inline
Power (kW@RPM) – ISO CONDITIONS	77@2800
Torque (N.m@RPM) – ISO CONDITIONS	229@1400-3200
Fuel supply	Direct injection Common Rail
Combustible	Diesel
Emissions standard	Euro IV
Oil cooler	Plate on the engine block

Table 3. Liquid flow meter characteristics.

Liquid flow meter characteristics	Value
Designation	TECHNOTON DFM 250
Volumetric flow min/max [l/h]	50/250
Pulses per liter	80
Nominal pressure/maximum of fuel consumption [MPa]	0.2/2.5
Kinematic viscosity min/max [mm^2/s]	1.5/.60
Operating temperature [°C]	-40 - 85

Table 4. Gaseous flow meter characteristics.

Gaseous flow meter characteristics	Value
Designation	Aalborg DPM 77
Volumetric flow min/max for air[smL/min]	501/1000
Maximum pressure drop [psi]	7
Turndown ratio	200 a 1
Average response time [ms]	10
Maximum inlet pressure [PSIG]	120
Temperature of operation [°C]	-10 a 60

Table 5. PM meter characteristics.

PM meter characteristics	Value
Designation	Dekati E-filter with E-diluter system
Dilution factor	8
Dilution pressure [bar]	2
Maximum pressure for the compressor [bar]	10
Flow of compressor	10 lpm - 5 bar
Impactor range diameter [µm]	10, 2.5
Maximum vacuum pressure[bar]	4
Flow range of Efilter [lpm]	10 - 100

Table 6. Gaseous species meter characteristics.

Species gaseous meter characteristics	Value
Designation	Capelec
Time of activation[min]	9
Time of response [s] CO,CO2,HC	5
Time of response [s] oxigeno	28
Temperature of operation[°C]	(-10) – 50
Environmental pressure [mBar]	750 – 1150
RH [%]	0-95
Measured species	CO2, CO, THC, O2, NOX

Table 7. In-cylinder combustion analysis

Equipment/sensors	Technical description
Combustion analyzer	CA-6 BDN Aumotive, 6 input channels for rapid pressure sensing
In-cylinder pressure sensors	Optrand high frequency pressure sensor with modified glow plug, maximum pressure 200 bar (absolute)
Pressure sensor for intake and exhaust ports	Optrand high frequency pressure sensors, maximum pressure 7 bar (absolute)

Figure 2 shows the final array of measurement devices and power supply equipment in the NHR vehicle

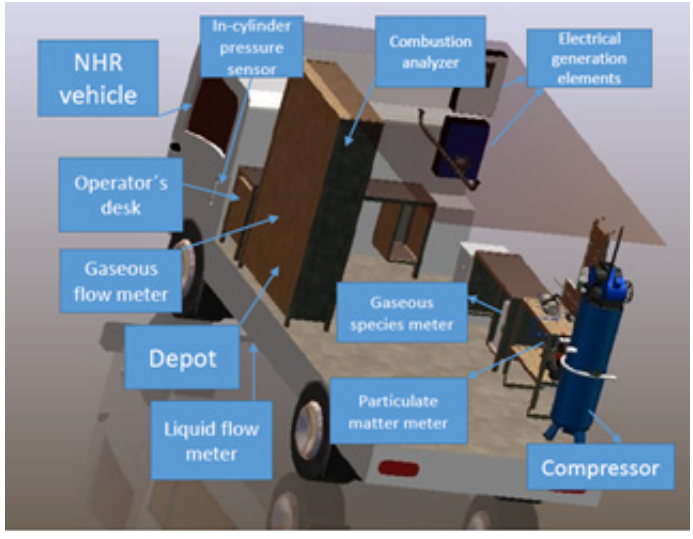

Figure 2. Measurement devices distribution in the on-board laboratory.

Figure 3 shows the emissions results obtained in the stationary tests for several engine speeds running in diesel and dual fuel modes. It is possible to see a decrease of PM in Diesel and dual operation at 2300 rpm compared with 1500 rpm, also there is a decrease of PM when using dual operation at 2300 rpm, while at 1500 rpm the increase of PM is maintained. Particle diameter distribution tends to be slightly lower with dual fuel mode. As for the gaseous species, there is a considerable increase for CO and HC when using dual fuel mode because of the expected delayed combustion and low combustion burning rates at the air-Natural Gas mixture, while CO_2 is reduced due to the reduction of carbon in the fuels, and NOx is reduced because of the lowered combustion temperatures for delayed combustion located in the expansion stroke.

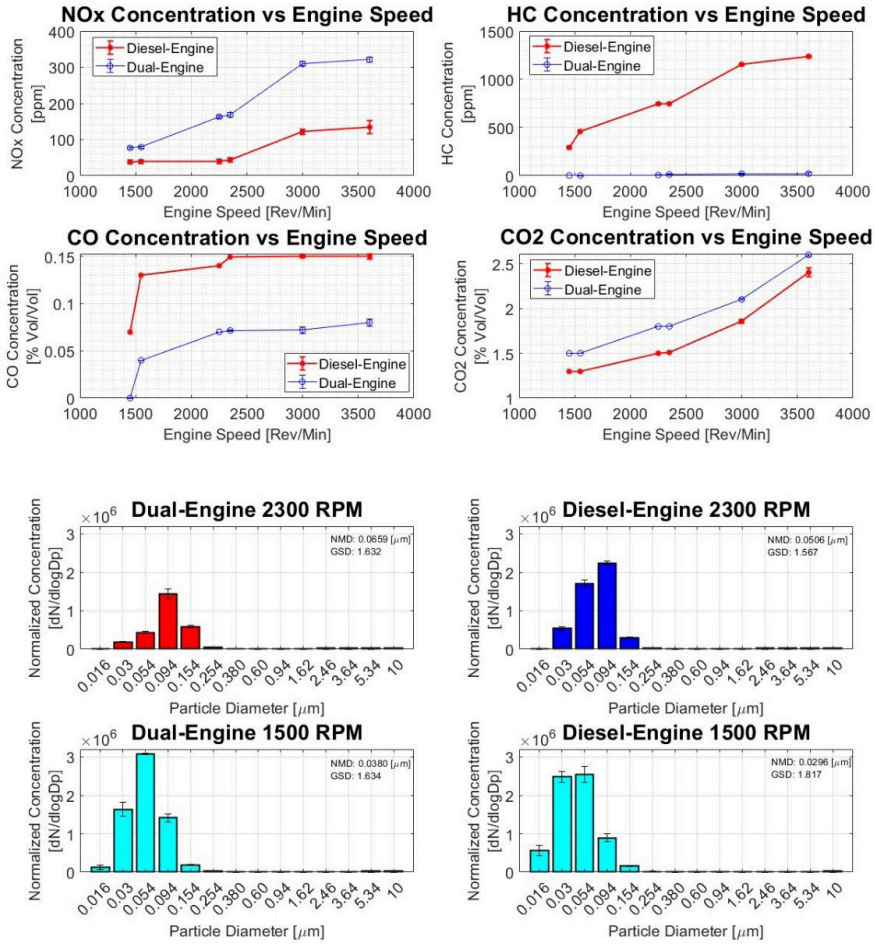

Figure 3. Measurement results with MP measurer (Up) and Gaseous Species measurer (Bottom).

Conclusions

- The emission and fuel consumption variables determination was possible, thanks to the correct installation, synchronization, and set point of the measurement and instrumentation equipment.
- The methodology of the vehicle selection was done taking into account the representative technologies that are marketed in Colombia, also that the measurement and instrumentation equipment was compatible with this technology.
- In dual operation, the addition of natural gas causes an increase in delayed ignition of the fuel, which leads to delayed combustion. Additionally, when the front of the jet flame consumes the of mix air-natural gas that is in the vicinity of

the jet, it produces intermediate species like CO and HC because the mix is usually poor with low combustion velocity, for this reason, there are high concentrations of HC and CO.

- The next test to carry out is the evaluation of performance, emissions, and combustion stability with charge variations on rollers dynamometer implementing dynamic drive cycles (like WLTP) and under real driving conditions.

Acknowledgments

The authors gratefully acknowledge the financial support provided by the Colombia Scientific Program within the framework of the call Ecosistema Científico (Contract No. FP44842- 218-2018).

The authors also acknowledge the technical advice on dual fuel transformation provided by GNV Motor S.A.S. and the technical advice on particle matter measurement provided by Camilo Bernal from GESOLTEC S.A.S.

References

[1] Mahesh, S., Ramadurai, G., & Nagendra, S. S. (2019). On-board measurement of emissions from freight trucks in urban arterials: Effect of operating conditions, emission standards, and truck size. Atmospheric Environment, 212, 75-82.

[2] Giraldo, M., & Huertas, J. I. (2019). Real emissions, driving patterns and fuel consumption of in-use diesel buses operating at high altitudes. Transportation research part D: Transport and environment, 77, 21-36

[3] Quirama, L. F., Giraldo, M., Huertas, J. I., & Jaller, M. (2020). Driving cycles that reproduce driving patterns, energy consumptions and tailpipe emissions. Transportation Research Part D: Transport and Environment, 82, 102294.

[4] Peter Mock, John German (2015), The future of vehicle emissions testing and compliance. International Council on Clean Transportation Europe.

[5] Oscar Delgado, Felipe Rodriguez, and Nikiforos Zacharof (2019), Comparison of Aerodynamic Drag Determination Procedures for HDV CO2 Certification. International Council on Clean Transportation Europe.

[6] Boulter, P., Buekenhoudt, P., Stricker, P., Mäurer, H.-J., Nolte, C., Ost, T., Schulz, W. H., Witz, K.-U., Afflerbach, G., Förster, C., Horn, M., Richter, A., Weissenberger, D., Labro, W., & Oliver, R. (2011). TEDDIE: A new roadworthiness emission test for diesel vehicles involving NO, NO2 and PM measurements, Final Report.

[7] European Parliament and Council. (2019). REGULATION (EU) 2019/1242 OF THE EUROPEAN PARLIAMENT AND OF THE COUNCIL of 20 June 2019 setting CO2 emission performance standards for new heavy-duty vehicles and amending Regulations (EC) No 595/2009 and (EU) 2018/956 of the European Parliament and of the. *Official Journal of the European Union*, *198*(April).

[8] Sharpe, B., Delgado, O., Rodriguez, F., & Miller, J. (2019). *Adapting the Vehicle Energy Consumption Calculation Tool (VECTO) for use in India and other countries*. *September*.

[9] Boulter, P., Buekenhoudt, P., Stricker, P., Mäurer, H.-J., Nolte, C., Ost, T., Schulz, W. H., Witz, K.-U., Afflerbach, G., Förster, C., Horn, M., Richter, A., Weissenberger, D., Labro, W., & Oliver, R. (2011). TEDDIE: A new roadworthiness emission test for diesel vehicles involving NO, NO2 and PM measurements, Final Report.

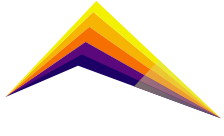

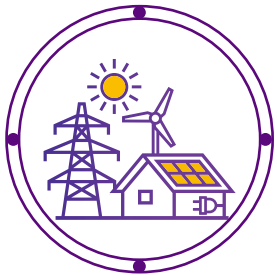

Implementation of a port-fuel injected dual fuel engine in a commercial vehicle and evaluation of diesel substitution for transient operation in Medellín-Colombia.

Jaime Fernando Zapata López *E-mail: jaimef.zapata@udea.edu.co*
Iván Darío Bedoya Caro *E-mail: ivan.bedoya@udea.edu.co*
Felipe Ruiz Zea *E-mail: felipe.ruiz1@udea.edu.co*

Grupo de ciencia y tecnología del gas y uso racional de la energía "GASURE"
Universidad de Antioquia, Medellín, Antioquia, Colombia

Abstract

The necessity to reduce the global greenhouse gas emissions have promoted many research studies about technologies to use alternative fuels in internal combustion engines. In this sense, the use of Natural Gas has an important role in the energy transition process for the transport sector, especially in developing countries where the environmental regulations are not so strict and vehicles with the latest technology are not generally used. On the other hand, diesel vehicles are one of the main sources of polluting emissions and the consequent deterioration of air quality in the cities. In this context, the use of natural gas–diesel dual fuel technology arises as a feasible alternative that allows lower particulate matter *(PM)* and carbon dioxide (CO_2) emissions from diesel engines in urban areas. The dual fuel technology installation does not require major interventions in the diesel engine, however, a correct implementation of this technology needs the adjustment of the diesel and natural gas injection parameters in order to acquire the expected environmental benefits. Diagnostic

Correspondent author

tools like fuels flow meters, gaseous emissions and *PM* measurement equipment, dynamometers for load simulations, and in-cylinder pressure analysis are required to ensure an adequate calibration for dual fuel engine operation. This study describes the transformation process to dual fuel mode operation for a light-duty truck with wide circulation in Colombia utilizing a gas port fuel injection – Diesel direct injection *(PFI-DI)* conversion kit. Results on fuel consumption running on the Worldwide Harmonized Light Vehicles Test Procedure *(WLTP)* driving cycle at Medellín conditions are also reported.

Keywords: Alternative fuels, Dual fuel technology, Fuel consumption and emissions, Real operating conditions, transport sector, Economy decarbonization.

Introduction

The dual fuel strategy is based on the simultaneous use of two fuels in the engine. A primary fuel, Natural Gas *(NG)* in our case, and Diesel fuel which is a secondary or pilot fuel. This strategy is focused on replacing diesel fuel by *NG* as much as possible, while maintaining high-efficiency engine operation and low *PM* and nitrogen oxides *(NO_x)* emissions. However, in dual-fuel engine operation, the combustion process is highly affected by the chemical and physical properties of the gaseous fuel, affecting especially the ignition delay and the combustion duration. In addition, the dual fuel operation usually leads to higher unburned Hydrocarbon *(HC)* and Carbon Monoxide *(CO)* emissions, especially at low loads [1].

In recent years, multiple research studies have produced important technologic advances to use dual fuel *NG* - diesel strategies, the port fuel injection *(PFI)* and the high-pressure direct injection *(HPDI)* the techniques most studied and accepted for *NG* fuel supply in diesel engines. The *PFI-DI* dual fuel concept has been widely studied and is a combination *PFI* of *NG* and direct injection *(DI)* of Diesel fuel. *PFI-DI* concept uses a homogeneous air-natural gas mixture that is formed and admitted in the combustion chamber during the intake stroke, then the homogeneous mixture is compressed and ignited at the end of compression stroke by a pilot injection of diesel fuel [2].

The *PFI-DI* dual fuel systems have great potential for their application in the transport sector in developing countries. There are many dual-fuel conversion kits available commercially which utilize the *PFI* technique for *NG* injection. However, all these technologies use the same method to reach the diesel substitution. For the reduction of diesel quantity to

be injected, the dual fuel engine control unit *(DF ECU)* takes the signals of the original's accelerator pedal position sensor (APP), mass air flow sensor *(MAF)*, diesel fuel pressure sensor *(FPS)*, and produce continuous emulated/modified signals before sending to the conventional diesel *ECU*. Depending on the received signals, the conventional ECU changes in diesel fuel quantity [3].

Several studies have used and evaluated commercial dual-fuel conversion kits. Napolitano et al. performed the dynamic test in a four cylinders Euro V advanced diesel engine equipped with a *PFI NG* system. In this study, the diesel substitution rate, engine performance, and emissions were evaluated through the New European Driving Cycle (NEDC). The main results showed an average Diesel substitution of 32%, the CO_2 emission was reduced about 12% with respect to Diesel mode, and the PM emission were reduced about 40%, while de *HC* emissions were 10 times higher compared to diesel mode [4]. In a later study, Napolitano et al. assessed a methodology for the optimization of Dual Fuel *ECU* calibration to minimize greenhouse gases emissions *(GHG)*. The research showed that an adequate *DF ECU* calibration can produce a reduction of 50% in *HC* emissions compared to a non-optimized *DF ECU* calibration [5]. Both Napolitano's studies were conducted at sea level. According to what was reported in the study, an adequate *DF ECU* calibration requires diagnostic tools like fuels flow meters, gaseous emissions and *PM* measurements equipment, dynamometers for load simulations, and in-cylinder pressure analysis to evaluate the combustion phasing and combustion instabilities. Dual fuel operation is also affected by air intake conditions, however, there is a lack on studies about dual fuel operation for countries located at high altitudes above sea level at transient conditions. This paper reports the dual fuel transformation of a commercial diesel engine, as well as the calibration process and performance at Medellin atmospheric conditions (1500 meters above sea level), focused on Diesel substitution.

Methodology

This study performs an initial experimental evaluation of a commercial technology for dual fuel diesel engine conversion. For that goal, a vehicle Chevrolet NHR – Common rail was selected for the tests due to it is highly representative between light duty trucks in Colombia. This vehicle was adapted for operation in dual fuel mode using a dual fuel *PFI DI* conversion Kit (Brand Bi-gas). Then a natural gas flow meter (Aalborg DPM-77) and a differential flow meter (Technoton DFM 100CD) were installed on the vehicle for NG and Diesel fuel consumption measure, respectively. Fuels consumption tests were carried out on *WLTP* Procedure and performing tests on a chassis dynamometer (Mustang MD-150).

The conversion Bi-gas kit main components used for the vehicle dual fuel adaptation were the following: 1) Two compressed natural gas *(CNG)* cylinders with 50 liters of hydraulic capacity and maximum pressure of 3600 psi each. 2) A pressure regulator from Bi-Gas used to control *CNG* pressure before delivery to NG injectors. 3) *NG* injectors which are the

component that supply the NG into intake manifold. 4) A MAP sensor that is a device for intake air absolute pressure and NG pressure measurement. 5) Two temperature sensors for exhaust gas and NG temperature measurement. 6) The $DF\ ECU$ which is the device for dual fuel system operation control. The $DF\ ECU$ collects input signals from the sensors of the dual fuel system and the original engine sensors and sends output control signals to the actuators components. During the dual fuel operation, the gas injectors will be controlled by $DF\ ECU$ while the diesel injectors shall be controlled by conventional ECU of the diesel engine.

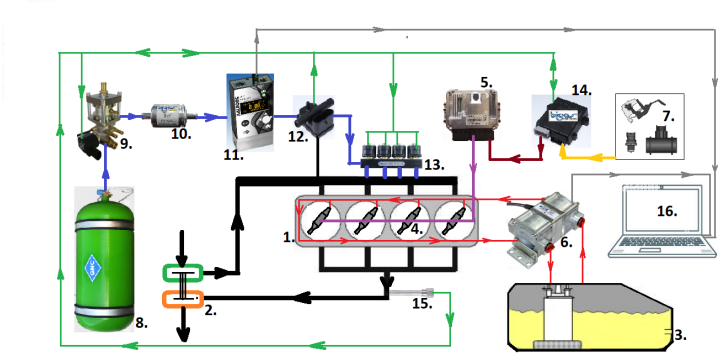

Figure 1. Dual fuel system and fuel consumption measurement - schematic diagram.

The goal of $DF\ ECU$ calibration is finding the best configuration to achieve the maximum substitution rate of diesel fuel maintaining at optimal engine performance with a minimum rate emission as possible. For the reduction of diesel quantity to be injected $DF\ ECU$ use a maps emulation method in which the signals of the originals accelerator pedal position sensor (APP), mass air flow sensor (MAF), rail pressure sensor (RPS) are emulated/modified signals. Depending on the received signal, the conventional ECU changes diesel fuel quantity.

The Bi gas dual system software has two calibration maps. The emulation maps permit to select the signal sensor to be emulated and make specific changes according to the different engine speed and load levels. This emulation process produces a reduction in the amount of diesel injected to the engine.

To adjust the NG flow rate for all engine operating condition (load and speed) the calibration software has a main NG adjustment map. The NG flow rate variation is made through of change the numeric values in a matrix that relates the absolute intake pressure with the engine speed (revolutions per minute). In this way, the system replaces Diesel with the emulation map by NG as a cleaner alternative fuel.

An adequate calibration will must ensure that follows criteria: a similar exhaust gases temperature, no noticeable change in the engine output power and torque, lower amount of PM and NO_x emissions, all this in comparison with conventional Diesel operation.

Results and analysis

A test for determining the average diesel substitution was carried out whit an initial/standard *DF-ECU* calibration. For this test the diesel and natural gas fuel consumption were measured. Additionally, the correct and safe operation of the vehicle operating in dual fuel mode were evaluated. For this preliminary test, *WLTC* was selected. The figure 2. shows the speed profile that was run in the test. The plot shows the vehicle speed in km/h (Y-axis) vs the test time in seconds (X-axis). The overall test duration was 27 minutes.

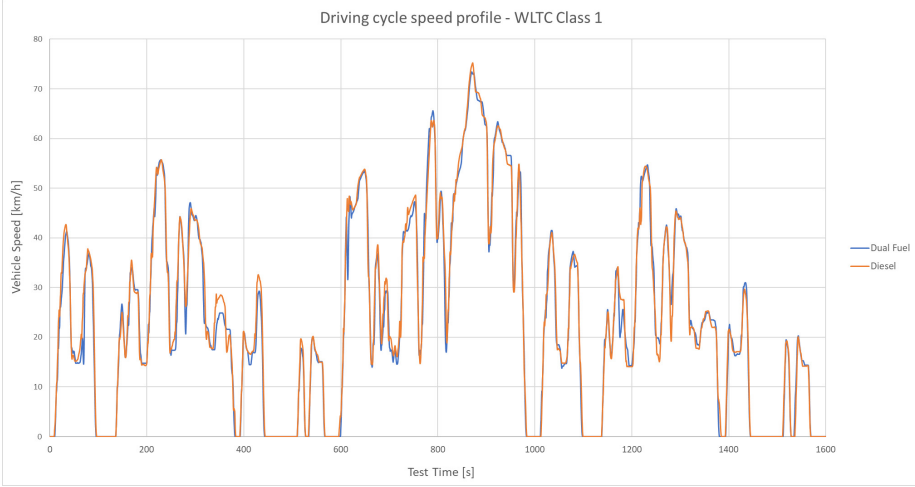

Figure 2. Driving cycle speed profile – WLTC Class 1

The plot shows a high match between dual fuel mode operation (blue lines) and conventional diesel mode operation (orange lines), Which shows that in dual fuel mode the vehicle doesn't lose manageability and the engine performance was similar in comparison to conventional diesel operation mode.

Finally, table 1 shows the diesel and natural gas fuel consumption results for dual fuel and conventional diesel operations. From these results, an overall diesel replacement of 23% was obtained for the entire *WLTC* driving cycle.

Table 1. Fuel consumption data and Diesel replacement during the driving cycles

Research study	Driving Cycle	Conventional Diesel fuel consumption[l]	DF mode Diesel fuel consumption [l]	Height respect to sea level[m]	Diesel fuel replacement [%]
UdeA	WLTC	3.825	2.95	1495	23
Napolitano[4]	NEDC	-	-	17	33

Conclusion

The use of the *PFI-DI* dual conversion kit allows for the use of *NG* in Diesel engines with safe operation, but the system calibration only based on qualitative indicators can lead to lower diesel substitution. Using this form of calibration at Medellín atmospheric conditions, the Diesel substitution for dual fuel mode was 23% at transient operation. An adequate calibration process of this technology requires a high knowledge of the effects of control variables and the substitution ratio on the engine performance and exhaust emissions. Therefore, the implementation of in-cylinder combustion and exhaust emissions analysis to identify the optimal configuration of the system is required, and these targets will be addressed in the near future.

Acknowledgments

The authors gratefully acknowledge the financial support provided by the Colombia Scientific Program within the framework of the call Ecosistema Científico (Contract No. FP44842-218-2018). The authors also acknowledge the technical advice on dual fuel transformation provided by GNV Motor S.A.S. and the technical advice on WLTC driving cycle provided by Institución Universitaria Pascual Bravo.

References

[1] Karim G. A., “Dual-Fuel Diesel engines”, 1er. Ed, New York, Boca Raton-Fl, Taylor & Francis Group, Dual-Fuel Engine Combustion, 2015, pp 153-166

[2] P. Fasching, F. Sprenger, and C. Granitz, “A holistic investigation of natural gas–diesel dual fuel combustion with dual direct injection for passenger car applications,” *Automotive and Engine Technology*, vol. 2, no. 1–4, pp. 79–95, Dec. 2017, doi: 10.1007/s41104-017-0018-4.

[3] D. Stepanenko and Z. Kneba, “ECU calibration for gaseous dual fuel supply system in compression ignition engines,” *Combustion Engines*, vol. 182, no. 3, pp. 33–37, Sep. 2020, doi: 10.19206/ce-2020-306.

[4] P. Napolitano, C. Guido, C. Beatrice, and N. del Giacomo, “Application of a Dual Fuel Diesel-CNG Configuration in a Euro 5 Automotive Diesel Engine,” in *SAE Technical Papers*, Mar. 2017, vol. 2017-March, no. March. doi: 10.4271/2017-01-0769.

[5] P. Napolitano, V. Fraioli, C. Guido, and C. Beatrice, “Assessment of optimized calibrations in minimizing GHG emissions from a Dual Fuel NG/Diesel automotive engine,” *Fuel*, vol. 258, Dec. 2019, doi: 10.1016/j.fuel.2019.115997.

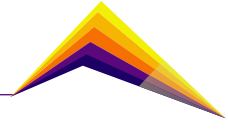

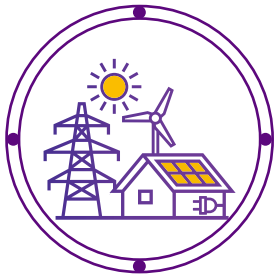

Replication of results: CFD modeling and experimental validation of an alkaline water electrolysis cell for Hydrogen production

P. Hernández[1]
C. Ramirez[2]
A. Carrada[3]

1. Chemical Engineer; MSc; Ph.D., In Silico SE SAS
E-mail: pablo.hernandez@insilicose.com

2. Student of Chemical Engineering, Universidad Nacional de Colombia, In Silico U de A Research Incubator.
E-mail: crramirezm@unal.edu.co

3 Physical Engineer, Universidad Tecnológica de la Mixteca, México, In Silico U de A Research Incubator.
E-mail: carrada1997@gmail.com

Abstract

Due to its absence of an important carbon footprint, the use of hydrogen as a high calorific fuel compared to fossil fuels such as methane is of interest both for the energy matrix and environmentally. However, its use is problematic for two fundamental reasons: (i) its production, mainly by electrochemical processes, and (ii) its storage and transportation. Based on the work of Rodriguez and coworkers [1], this project seeks to replicate the simulation results of the process in the alkaline electrolysis of water towards H_2. In this project, the methodology and results obtained so far are presented and future results are discussed. The replication of simulation results allows training in modern and advanced modeling tools and contributes to a deep understanding of the processes. This way to get new knowledge is extended in research projects that have "*in silico*" methodologies. Taking into account the current global energy situation, the study of the processes of hydrogen generation as an energy vector is fundamental

Correspondent author

and the use of computational tools favors its approach, minimizing the associated experimental costs and allowing the deepening of the applied physicochemical phenomena.

Keywords: Multiphysics modeling, Computational Fluid Dynamics, fuel cells, electrolysis, hydrogen generation, learning by validation.

Introduction

It has been observed that the effects of climate change and factors like the use of fossil fuels increase the generation of greenhouse gases (GHG): It impacts the worldwide environment. To reduce the emission of GHG, solutions that focus on the generation of energy from renewable energy sources have been proposed [2].

Solar Energy is the most interesting renewable energy source because it has no problems of geographical location and the sun is the major clean and free energy source. Photovoltaic technology that involves the use of semiconductors to convert sunlight into electrical energy has become a highly desirable option [3]. But the energy only can be used during the irradiation times. To solve this availability problem one solution is energy accumulation or storage [4, 5].

The storage in chemical fuel form is a useful solution and hydrogen is recognized as a promising clean fuel due to its high specific power (until 142 MJ kg^{-1}) and its zero CO2 emission combustion [5, 6]. The US department of energy has shown that hydrogen generation through water electrolysis is considered the most effective route to use H_2 as an energy carrier[5, 7].

Water electrolysis is divided into alkaline water electrolysis (AWE), proton exchange membrane, and solid oxide electrolysis. AWE is a scalable, flexible, distributed approach to producing pure hydrogen and it is closest to industrial production [7].

Recently, many numerical studies have been published about AWE modeling, studies coupling the model of electrical distribution and computational fluid dynamics (CFD) model. Ye Xia et al. [7] investigate the impact of the structures on the electrochemical and fluid performance of AWE based on the Euler-Euler method and the two-phase flow CFD model considering turbulence. Yu Yang et al. [8] present a scheduling approach to maximize the profitability of AWE coupled with hybrid energy sources, modeling the AWE by CFD and obtaining its polarization curve and efficiency. Zarghami et al. [6] simulate a multiphase flow of a CFD model in an AWE cell and compare the results with the experimental data, particularly the gas fraction and width of the bubble curtain in a cell.

In this work, we are replicating the study made by Rodríguez et al [1]. They have analyzed the fluid dynamics and electrochemical phenomena involved in an electrolysis cell obtaining the changes in gas profiles along the cell, according to current density, electrolyte flow rate, and electrode-diaphragm distance. We propose this replication methodology not only as a "hands-on" exercise to going into Multiphysics Software, but as a tool for a deeper understanding of all process phenomena involved in several technologies.

Methodology

Figure 1 describes the electrolytic cell that is the object of study and the basic characteristics to be considered for the approach of the model.

The model consists of the approach of the electric charge equation, in which a value of reversible electric potential and activation potential in the electrodes, a current density applied to the cathode, and the properties of electric conductivity associated with the electrolyte and the membrane. These electrical conductivities are also a function of the volumetric fraction of gas generated inside the chambers, in this the first multi-physical coupling of the model is observed since the formation of gases is obtained through the simulation of the flow process.

The following considerations are taken into account for the application of this transport model:

- The model is two-dimensional and therefore the electric potential is constant in the direction perpendicular to the flow of transported entities.
- The charge transport in the electrodes is not part of the scope of this study.
- The electrical resistance of the electrodes is negligible with respect to the other elements of the electrolytic cell.

According to Figure 1 (a), the model of the fluid flow in the process considers the flow of the electrolyte throughout the cell. The generation of H_2 and O_2 is described according to Faraday's law, which is the second step of the multi-physical coupling of the problem since the generation of these gases will be a function of the current density inside the reactor chambers. Both in the walls of the chambers and the walls of the membrane, it is considered a non-slip condition. Additionally, to model the flow process, it is considered:

- An Euler – Euler model is used to describe the two phases of the process.
- The movement of gas bubbles in relation to the liquid phase is determined by the balance of viscous buoyancy forces and pressure forces.
- The flow of O_2 and H_2 through the membrane is negligible.

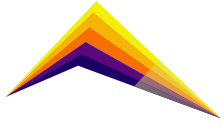

- The electrolytic cell operates with a sufficient electrolyte flow that guarantees the accumulation of gases in the chambers.
- The bubbles have a diameter of less than 1.0 mm, which can be considered the viscous movement of gas bubbles in a fluid medium.

Figure 1 (b) presents the dimensions of the fuel cell, which constitutes the simulation domain of this model.

Table 1 presents the process conditions that are considered for the application of the simulation model. The simulation was carried out using COMSOL Multiphysics

Table 1. Simulation conditions

Symbol	Value	Unit	Description
$\dot{v}_0$	700	ml min^{-1}	Inlet volumetric flow of electrolyte
i	250 – 4000	A m^{-2}	Current density
i_{0C}	21.1 – 93.5	A m^{-2}	Exchange current density at cathode
i_{0A}	1.10 – 9.30	A m^{-2}	Exchange current density at anode
T	303 – 343	K	Temperature
w	22.0 – 42.0	-w%	Electrolyte concentration

The results obtained in this validation and replication exercise are compared with the results reported by the reference authors. This comparison allows not only discussing the considerations raised in previous works but also stablishing study and research questions that broaden the knowledge of the electrolytic production of hydrogen and the associated physicochemical phenomena.

Knowing the porosity of the membrane, which has been reported by Rodríguez et al [1], the implementation of the flow through the membrane in COMSOL Multiphysics requires knowledge of the permeability of this component of the fuel cell. Berg [9] has reported the results of research on the interdependence between the physical characteristics of membranes. According to these results, it is possible to obtain a relationship between the porosity and the permeability of membranes. The equation that describes the Berg model [9] is used as input in the simulation object of this study.

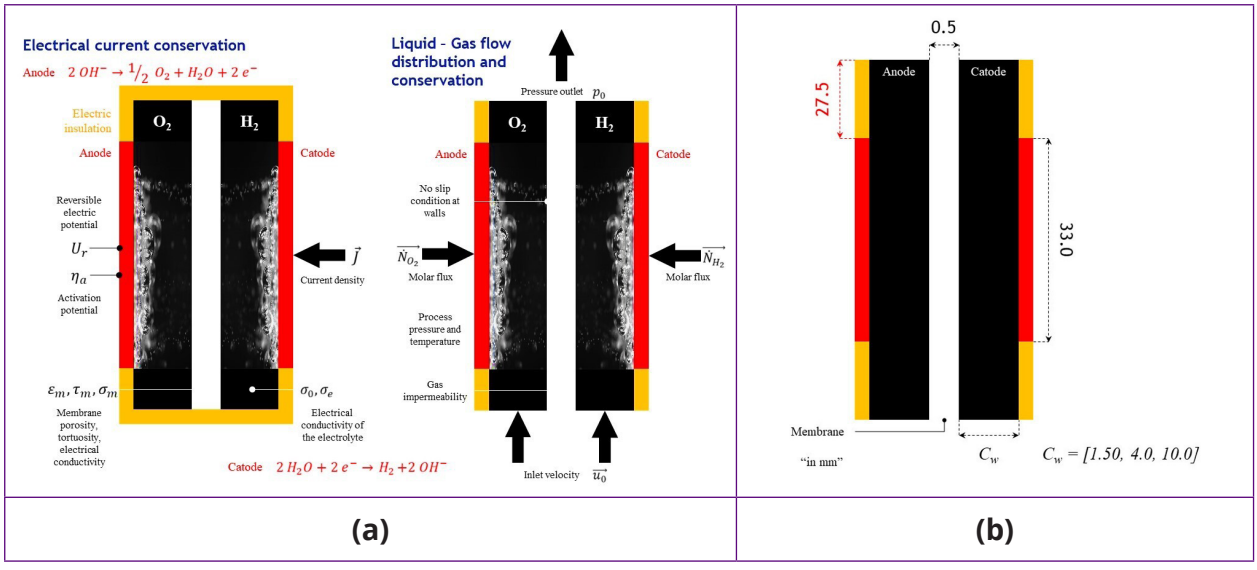

Figure 1. (a). Scheme of the process of water electrolysis and simulation domain for the approach of the model. (b). Geometry for the model of the fuel cell.

For the simulation of the density of the electrolytic solution, Rodríguez et al [1] have proposed the use of the model of Guo et al [10] who, in turn, together with experimental data, propose equations of dependence of the density of KOH solutions with concentration and temperature from the model of Gilliam et al [11]. In this study, all these references have been considered and corrections have been made for certain parameters that previously did not show dependence on the KOH composition and temperature. The results of the analysis of the information and the obtaining of the model used in this study better satisfy the density values determined experimentally by Guo et al [10].

Rodríguez et al [1] have reported the use of a square mesh to discretize the computational domain. In this study, a mesh is discussed and proposed that obeys the consideration of the flow conditions inside the electrolytic chambers, using the concept of laminar boundary layer.

In the area of the domain, where the laminar boundary layer is present, consider a particularly fine mesh, which represents the velocity gradients in this area. The operating conditions considered, in any case, lead to the thickness being always greater than the distance between the membrane and the electrodes. This means that the mesh inside the chambers must be fine for the entire region of the domain. Figure 2 shows the effect of the meshing construction and refining over the simulation result in the case of the velocity field.

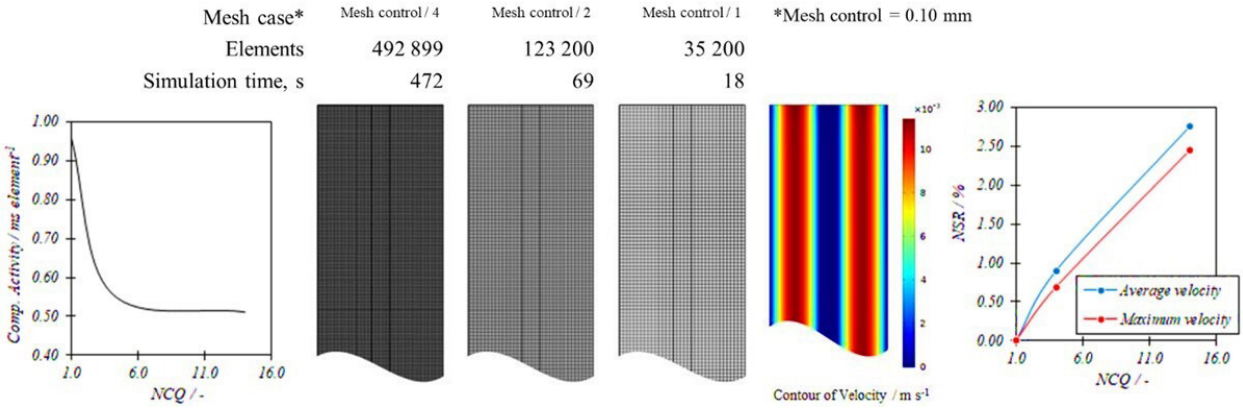

Figure 2. Mesh independency study based on the flow velocity of electrolyte in the chambers. NSR: Normalized Simulation Result (ratio between simulation results for the finest mesh case and other meshes). NCQ: Normalized Cell Quantity (ratio between the quantity of elements in the finest mesh and other meshes).

Conclusions or summary

The results obtained up to this point of the research project have allowed delving into the problem of the electrolysis process for obtaining H_2. The implications, needs, and operating conditions of alkaline electrolytic cells have been understood. Different characteristics and conditions of the process are inferred to have a more profound knowledge of it if necessary, such as (i) the existence of a parameter of freedom in the modeling of membranes, it is obtained from two other physical parameters of the same; (ii) the need to define physicochemical and transport properties that are dependent on both the temperature and the composition of the electrolyte; and, since these properties have been described by different authors, and therefore, it is necessary to make a meticulous selection of their models, which allow the expected experimental results to be obtained from the simulation of the process, (iii) the simplification of the simulation models to reduce the computational cost and facilitate the calculation processes, for example, the suppression of turbulent momentum transport terms in the Navier-Stokes equations.

The use of Multiphysics simulation tools and "in silico" experimentation allows studying the effect of the variation, individual or simultaneous, of the different parameters of the model. Although these models are limited to specific operating conditions, the approach of a robust simulation, which is validated in comparison with experimental data, favors the application of different experiments that propose a general panorama of the processes without incurring the expenses inherent to the laboratory-scale experimentation or physical prototyping in the early stages of technological developments in engineering, particularly in this case, chemical or process engineering.

The result of this replica should be comparable with the results of Rodríguez et al [1] since the same simulation tool is used, that is, COMSOL Multiphysics. However, the model obtained is intended to be extended to the study of additional cases and phenomena such as (i) the analysis of the effect of turbulence on the final process, (ii) the application of models that not only describe the formation zone of bubbles but the rate of their formation, their shape, and size, (iii) the application of chemical kinetic models associated with the electro-hydrolysis reaction of water in an alkaline medium, and (iv) the effect of using another type of electrolytes other than KOH as a reactive medium.

References

[1] Rodríguez, J., Amores, E. CFD Modeling and Experimental Validation of an Alkaline Water Electrolysis Cell for Hydrogen Production. Processes, 2020 (8), 1634.

[2] Martín, D., Ocampo-Martínez, C., Sánchez-Peña, R. Advances in alkaline water electrolyzers: A review. Journal of Energy Storage, 2019 (23): 392.

[3] Kabir, E., Kumar, P., Kumar, S., Adelodun, A. A., Kim, K. Solar energy: Potential and future prospects. Renewable and Sustainable Energy Reviews, 2018 (82) 894.

[4] Takaya, O., Takeuchi, M., Kajikawa, Y. Analysis of trends and emerging technologies in water electrolysis research based on a computational method: a comparison with fuel cell research. Sustainability, 2018 (10.2) 478.

[5] Thakur, A. Ghosh, D., Devi, P., Kim, K-H., Kumar, P. Current progress and challenges in photoelectrode materials for the production of hydrogen. Chemical Engineering Journal, 2020 (397) 125415.

[6] Zarghami, A., Deen, N.G., Vreman, A. W. CFD modeling of multiphase flow in an alkaline water electrolyzer. Chemical Engineering Science, 2020 (227): 115926.

[7] Xia, Y., Gao, M., Yu, J., Si, Y., Chen, L., Mei, S. Numerical Study on Hydrodynamic Characteristics and Electrochemical Performance of Alkaline Water Electrolyzer by Micro-Nano Surface Electrode. *Materials*, 2022 15(14): 4927.

[8] Yang, Y., De La Torre, B. Stewart, K., Lair, L., Phan, N. L., Das, R., Gonzalez, D., Lo, R. C.The scheduling of alkaline water electrolysis for hydrogen production using hybrid energy sources. Energy Conversion and Management, 2022 (257): 115408.

[9] Berg, C. F. Permeability Description by Characteristic Length, Tortuosity, Constriction and Porosity. Transp. Porous Med., 2014 DOI 10.1007/s11242-014-0307-6.

[10] Guo, Y., Xu, H., Guo, F., Zheng, S., Zhang, Y. Density and viscosity of aqueous solution of K2CrO4/KOH mixed electrolytes. Trans. Nonferrous Met. Soc. China, 2010 (20), s32.

[11] Gilliam, R. J., Graydon J. W., Kirk D. W., Thorpe S. J. A review of specific conductivities of potassium hydroxide solutions for various concentrations and temperatures. International Journal of Hydrogen Energy, 2007 (32) 359.

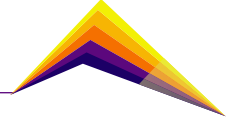

Numerical Analysis of Landfill Biodegradation

Vladimir Buelvas[1] *E-mail: vladimir.buelvas@coc.ufrj.br*
Marcela Mercado-M[2] *E-mail: marcela.mercadom@insilicose.com*

1, 2 Researcher, Semillero In Silico – UdeA, In Silico SE SAS
1 PhD Student, Universidade Federal do Rio de Janeiro
2 CEO, In Silico SE SAS

Abstract

Introduction: In recent years, complete thermo-bio-hydro-mechanical models have been implemented for better landfill design. It is to consider all the variables involved in such a complex model as a landfill. One of the models involved plays an essential role in biodegradation since there is a phase that disappears with time. Many authors have proposed several mathematical models to represent biodegradation. We aim to model and simulate the biodegradation in landfills using a mechanistic approach.

Methods: A mathematical framework for the biodegradation in landfill waste is implemented through the software package COMSOL Multiphysics to numerically solve the governing equations. The biodegradation model has two states and is only considered in the anaerobic part; the model also accounts for the inhibitory effect when it is the non-optimum temperature in the microbial growth. Finally, the model is calibrated with two large-scale laboratory waste biodegradation tests reported in the technical literature. The simulations included six conventional cases carried out in the main landfills in the United States.

Results & Discussion: The results obtained corresponded partially to those reported in the article but showing the same trend which

Correspondent author

is consistent with the chemical process considered. Furthermore, biodegradation models are related to a coupled models with thermal, hydraulic, and mechanical behaviors.

Conclusion: The numerical analysis results show a good fit to the model parameters adjusted to the field data. A better calibration of the parameters used in the mathematical model of biodegradation could be obtained from field data.

Key words: Landfill, waste biodegradation, mathematical model

Introduction

Waste disposal is one of the cheapest and most viable means of disposing of Municipal Solid Waste (MSW). The treatment and subsequent closure of landfills in Colombia are increasing due to failure problems that have occurred in some cities such as Bucaramanga (El Carrasco 2017), Cali (2001) and Bogotá (1998). Settlement estimation is a matter of concern in the management of MSW landfills. Landfill settlement continues over a long period of time, with final settlement that can be as large as 30%-40% of the initial fill height.

A critical phenomenon in the settlements of a sanitary landfill is the biodegradation of the material, which loses properties over time to the disappearing point in most cases. Due to the material biodegradation, by-products are obtained such as the generation of gases and leachate. Consequently, landfills undergo complex processes that involve different physical phenomena: mechanical (settlement, stress, etc.), hydraulic (flow, pressure) and thermal (temperature rise). The degradation model can be explained based on Figure 1 where there is an organic matter that through hydrolysis and acidogenesis is transformed into VFA (Volatile Fatty Acids), once in this stage through acetogenesis processes the product is obtained: methane (CH4) and carbon dioxide (CO2). The generation of methane is also an environmental problem that reinforces the study of biodegradation [1].

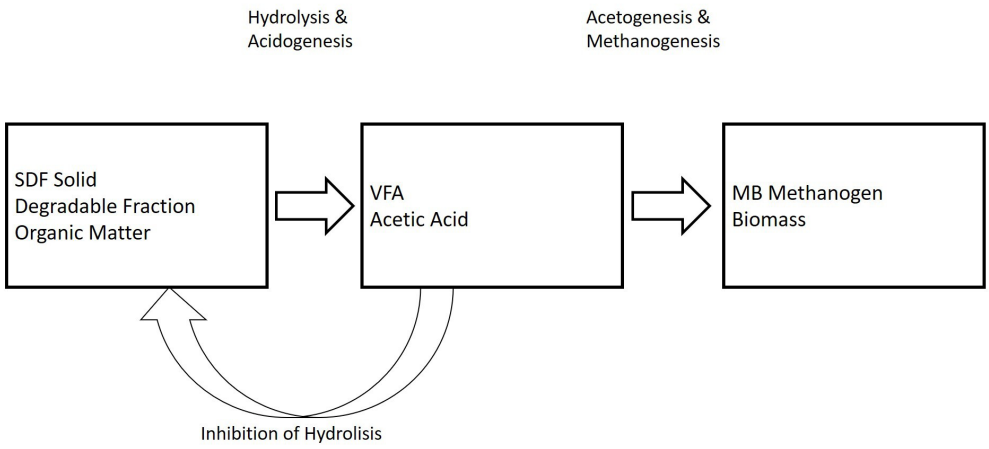

Figure 1. Final chemical process (modified from Hubert et al 2014 [1])

In recent years, many researchers have performed theoretical and numerical analysis in this field [2]–[4]. In most current models, the gas and liquid phases are coupled with effective saturation, and the settling phase and gas phase are directly connected by conservation of gas mass. Biodegradation is usually expressed by first-order kinetics, which does not fit the test results [5]. This paper presents the modeling and simulation of biodegradation in landfills using the mechanistic model of biodegradation proposed in [6], widely used in the technical literature. The analysis is based on the values of the model parameters reported in the literature [7]. In addition, the foundations are laid for future comparison with laboratory measurements to corroborate the theory and calibrate the model parameters.

Methods

The most widely used model for biodegradation in landfills is the McDougall model [6], which was implemented in this study through the COMSOL Multiphysics software. According to the McDougall model, the three main biodegradation mechanisms involved (Figure 1) can be simplified using Eq. 1.

$$Eq.\ 1: \qquad C_6H_{10}O_5\,\square_{162\,g} + H_2O\,\square_{18g} \rightarrow CH_3COOH + 8H_2 + 4CO_2 \rightarrow 3CO_2\,\square_{132g} + 3CH_4\,\square_{48g}$$

The accumulation rate of VFA in $g_{VFA}\ m^{-3}{}_{aqueous}\ day^{-1}$ is expressed mathematically by Eq. 2. Where k_{VFA} is the inhibition factor of the product, c in $g_{VFA}\ m^{-3}{}_{aqueous}$ is the concentration of volatile fatty acids, S is the remaining degradable solid fraction, S_0 is the initial degradable solid fraction, b is the maximum growth of VFA, n is a structural transformation parameter and $\theta_e=(\theta-\theta_r)/(\theta_s-\theta_r)$ is the effective volumetric moisture content, *and* θ, θ_r *and* θ_s respectively the volumetric, residual and saturation moisture contents.

$$Eq.\ 2: \qquad r_g=\theta_E b\ [\ 1-[(S_0-S)/S_0\ ]^n\ ]*e^{-k\_VFA\ (c))}$$

The accumulation of MB (r_j) shown in Eq. 3, represents the methanogenic substrate decreases and the growth of methanogen, which are described by Monod kinetics. Where k_0 is the specific growth rate (day^{-1}), c is the VFA concentration, m is the MB concentration in aqueous phase and k_{MC} is the half-saturation constant ($g_{[VFA]}\ m^{-3}_{[aqueous]}$).

$$Eq.\ 3: \qquad r_j=(k_0\ c)/(kMC+^c)\ m$$

The accumulation rates $r_h=r_j/Y$, and $r_k=k_2\ m$ respectively represent the VFA consumption rate and the MB decay/death rate. VFA consumption rate is associated to the MB growth rate through a substrate yield coefficient Y as shown and k_2 is the constant MB decomposition rate (day^{-1}). Finally, it is possible to establish a system of ordinary differential equations to describe the accumulation rates of VFA (c) and MB (m) through the equations Eq. 4 and Eq. 5 respectively. The rate of change of the degradable solid fraction S can be expressed by Eq. 6.

$$Eq.\ 4: \qquad \partial c/\partial t=[r_g-r_h]$$

$$Eq.\ 5: \qquad \partial m/\partial t=[r_j-r_k]$$

$$Eq.\ 6: \qquad \partial S/\partial t=-\theta\ 162/60\ r_g$$

The model was tested with different combinations of parameter values as shown in Table 1, according to what was reported by Kumar et. al. in [7], and which refers to measurements in different landfills in the USA.

Table 1. Parameter values for different landfill data cases: CAR1, CAR2, MI, TX, AZ and CA

Parameter	Landfill data					
	CAR1	CAR2	MI	TX	AZ	AC
Initial volumetric moisture content (%)	56.3	64.3	27.0	49.0	38.0	42.0
Volumetric residual moisture content (%)	11.0	11.0	7.7	15.0	11.6	16.0
Percentage of degradable solids (%)	55.0	55.0	30.2	11.7	24.0	9.0
Degradable solids density ($kg\ m^{-3}$)	745.0	745.0	882.0	1044.0	955.0	1338.0
Inert solids phase density ($kg\ m^{-3}$)	1735.0	1735.0	895.0	1727.0	1716.0	1660.0
Initial SDF concentration ($kg\ m^{-3}$)	240.6	196.6	93.4	70.1	111.6	57.4
Initial VFA concentration ($g_{[VFA]}\ m^{-3}_{[aqueous]}$)	300.0	300.0	0.0	0.0	8500.0	0.0
Initial MB concentration ($g_{[VFA]}\ m^{-3}_{[aqueous]}$)	1000.0	1000.0	300.0	100.0	1200.0	10.0
Maximum hydrolysis rate ($g_{[VFA]}\ m^{-3}_{[aqueous]}\ day^{-1}$)	18000.0	24000.0	9000.0	2000.0	5200.0	2000.0
Product inhibition factor ($m^3 g^{-1}$)	1×10^{-4}	1×10^{-4}	8.5×10^{-4}	4.2×10^{-4}	1.2×10^{-4}	6.3×10^{-3}
Structural transformation parameter (-)	0.06	0.06	1.00	0.75	1.00	0.70
Maximum specific growth rate for MB (day^{-1})	0.047	0.047	0.128	0.250	0.075	1.00
Methanogen death rate (day^{-1})	0.0040	0.0040	0.0050	0.0005	0.0040	0.0005

Parameter	Landfill data					
	CAR1	CAR2	MI	TX	AZ	AC
Half saturation constant ($g\ m^{-3}$ aq.)	4000	4000	1000	1000	3500	700
Cell to substrate yield coefficient (-)	0.08	0.08	0.30	0.40	0.40	0.30

Results and analysis

According to the simplified chemical process proposed in this article (Figure 1), the depletion of cellulose (SDF) is controlled by the concentrations of VFA and MB, and the moisture content of the residues. Assuming that glucose fermentation involving acidogenesis/acetogenesis is instantaneous, the second stage of anaerobic degradation is methanogenesis involving VFA consumption by MB to produce CH4 and carbon dioxide (CO2). The numerical results for 500s of simulation, presented in Figure 2, show a clear coincidence with what was expected according to the chemical approach. This is evidenced because the Solid Degradable Fraction (S) decreases non-linearly from an initial fraction of solids. For its part, the production of acetic acid occurs until it reaches a maximum peak. Methane production/consumption occurs at a slower rate, also peaking after 200s. The initial solid degradable fraction and VFA are higher in the AZ case, therefore, the MB production is higher in this case, and it is associated with a larger amount of SDF. The opposite happens for the AC case, where the initial SDF and VFA are low compared to the other landfill data studied. This suggests that the different model parameters and initial values considerably affect the results of biodegradation and subsequent MB production.

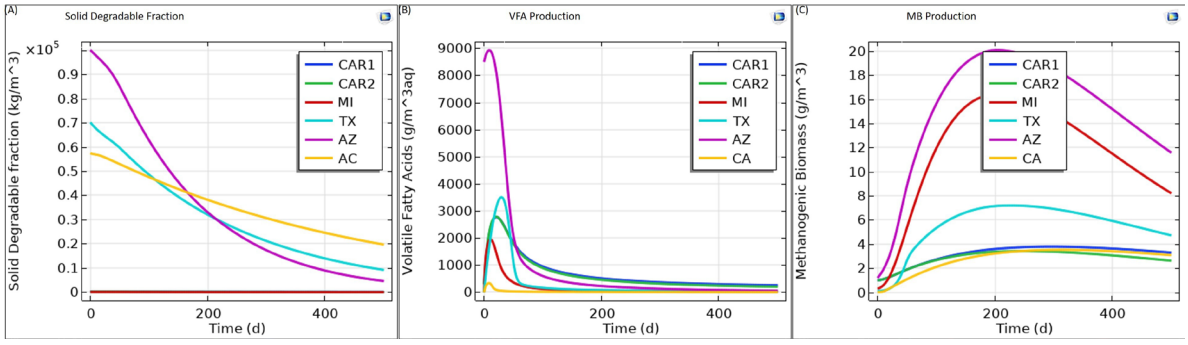

Figure 2. Simulation results. (A) Solid degradable fraction (S), (B) VFA production and (C) MB production for the different study cases. CAR1, CAR2, MI, TX, AZ and CA.

These processes and their respective stages have been replicated through laboratory tests. These measurements have served to calibrate the respective parameters involved in the model. The authors in [6] used experimental values to calibrate the model parameters. The results found in this study partially agree with those of the authors. The curves general trend is quite similar, while the peak values obtained are moderately different, but maintain the

same magnitude order. It is possible to use the experimental data reported by the authors for the calibration of this model.

The model is key to be implemented later with the heat part since it has been shown that the increase in temperature influences the biodegradation process, and heat generation must also be present. The thermal model of heat generation will in turn depends on the biodegradation model to derive the amount of heat generated as a result of substrate depletion and thus to predict temperatures within the fill.

Conclusions

The mechanistic biodegradation model proposed by [6] was successfully implemented in this study. The replication of this model using the parameters reported by [7] calibrated from data for 6 landfills in the USA was not fully possible. It is necessary then to recalibrate the model parameters using the reported experimental data in the same article or even in additional similar references.

The simulation results are highly influenced by the values of model parameters, any value with wrong units or typing error can lead to discrepancies in the exercise of scientific replication. The scientific replication exercise developed in this study was useful to lay the groundwork to expand the analysis by considering additional physics present in landfills: mechanics, thermal and hydraulic.

References:

[1] J. Hubert, X. F. Liu, and F. Collin, "Numerical modeling of the long-term behavior of Municipal Solid Waste in a bioreactor landfill," *Computers and Geotechnics*, vol. 72, pp. 152–170, Feb. 2016, doi: 10.1016/j.compgeo.2015.10.007.

[2] E. Durmusoglu, M Yavuz Corapcioglu, F. Asce, and K. Tuncay, "Landfill Settlement with Decomposition and Gas Generation", doi: 10.1061/ASCE0733-93722005131:91311.

[3] C. H. Hettiarachchi, J. N. Meegoda, J. Tavantzis, and P. Hettiaratchi, "Numerical model to predict settlements coupled with landfill gas pressure in bioreactor landfills," *Journal of Hazardous Materials*, vol. 139, no. 3, pp. 514–522, Jan. 2007, doi: 10.1016/j.jhazmat.2006.02.067.

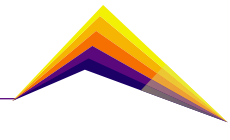

[4] H. Hettiarachchi, J. Meegoda, and P. Hettiaratchi, “Effects of gas and moisture on modeling of bioreactor landfill settlement,” *Waste Management*, vol. 29, no. 3, pp. 1018–1025, Mar. 2009, doi: 10.1016/j.wasman.2008.08.018.

[5] J.-J. Liu, N.-S. Zeng, and W.-X. Xu, “Effects of the Use of Permeable Barrier for Landfill Leachate Treatment,” 2011.

[6] J. McDougall, “A hydro-bio-mechanical model for settlement and other behaviour in landfilled waste,” *Computers and Geotechnics*, vol. 34, no. 4, pp. 229–246, Jul. 2007, doi: 10.1016/j.compgeo.2007.02.004.

[7] G. Kumar, K. R. Reddy, and J. McDougall, “Numerical modeling of coupled biochemical and thermal behavior of municipal solid waste in landfills,” *Computers and Geotechnics*, vol. 128, Dec. 2020, doi: 10.1016/j.compgeo.2020.103836.

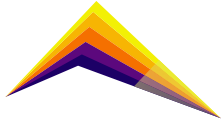

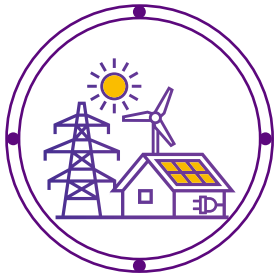

Kinetic model of anaerobic digestion based on the bioenergetics of microorganisms

Hender Albeyro Amaranto Alzate[1,2] *E-mail: hender.amaranto@udea.edu.co*
Darío Naranjo Fernández[3] *E-mail: dario.naranjo@udea.edu.co*

1 MSc Environmental management, Environmental School, University of Antioquia, Colombia.
2 Pollution diagnosis and control group-GDCON, Environmental School, University of Antioquia, Colombia.
3 Ph.D., assistant professor of Environmental school, University of Antioquia, Colombia.

Abstract

Wastewater, carbohydrates, and adequate operating conditions allow the transformation of organic matter into a clean energy source in the form of methane. For this reason, experimental models have sought to simulate possible metabolic pathways to estimate energy efficiencies and yields of anaerobic digestion products. Therefore, the objective of this project is to propose a kinetic model with stoichiometry obtained through a biothermodynamic model for the anaerobic processes of the transformation of organic matter using glucose as the base substrate. An unstructured/unsegregated kinetic model was formulated, continuous in time, simple and with great approximation to the results obtained with commonly used models for biomass, substrate, and methane. Comparing this model focused from the perspective of biochemistry (hydrolysis, acidogenesis, acetogenesis, and methanogenesis) with one from the engineering of unstructured/segregated processes, it is possible to obtain similar results and to elaborate first-order kinetic equations with a lower degree of complexity and greater understanding of the biokinetic phenomena presented in the conversion of organic matter anaerobically. The correlations obtained with the kinetic

Correspondent author

model developed for total biomass, substrate consumption, and methane generation were 0.6818, 0.9702 and 0.9504, respectively. The main contribution is considered to have developed a model that, by using realistic stoichiometry from a biothermodynamic model, allows estimating cell production and energy efficiencies of biological reactions.

Keywords: Anaerobic digestion, biothermodynamic model, non-structured / non-segregated models, unstructured / segregated models.

Introduction

All wastewater generated, regardless of its origin, requires adequate treatment. Both domestic and non-domestic wastewater can be discharged into bodies of water in Colombia if the discharges comply with current environmental regulations and the maximum permissible limits of the required parameters regardless of the treatment carried out. One of the treatments used is anaerobic digestion. This consists of a syntrophic process between various microorganisms that, through different metabolic processes, obtain sufficient energy for their development. Therefore, one of the advantages of anaerobic treatments is the generation of combustible gases in the form of hydrogen and methane for energy use and to contribute to the progressive reduction of the use of fossil fuels. Given this, a high yield in obtaining biogas would imply an adequate treatment of wastewater.

A kinetic model that uses stoichiometric relationships in the formulated equations would allow the understanding of the yields in the organic degradation and the treatment of biological residues. The main contribution is the preliminary analysis of the metabolic routes through a model that allows predicting the behavior of microorganisms and the products generated, knowing initially pH, temperature, and initial concentration of substrate and biomass in a simple and continuous way in time, without the need to run experimental tests.

The objective of this research is the formulation of a kinetic model that includes realistic stoichiometric coefficients in anaerobic digestion, coming from a biothermodynamic model and estimating the yield of methane in the form of energy.

Investigation methodology

For the initial data collection in obtaining hydrogen and methane (in one stage and two stages), tables were prepared with the different combinations of the parameters and the

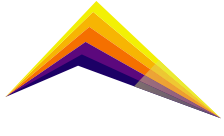

conditions involved in the degradation of organic matter. These tables, therefore, take into account the type of substrate, temperature, pH, hydraulic retention time, type of reactor, performance and number of replicates of the experiments (same conditions carried out by the same author or by another), and finally, the source from which the information was obtained. Additionally, the theoretical value obtained with the biothermodynamic model at the experimentally referenced conditions was also considered.

Specific objectives

- Build a database from a literature review, with the different conditions under which hydrogen and methane have been obtained from organic matter. Normality tests and main effects plots were performed. (Figure 1).

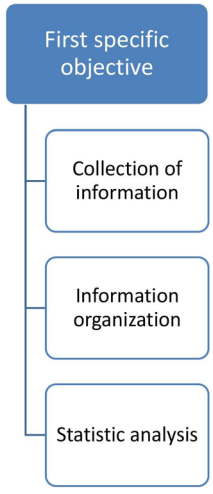

Figure 1. First specific objective diagram.

- Validate a biothermodynamic model based on statistical comparison and data analysis with the literature search. Adjustment of biothermidynamic model and experimental data with energy efficiencies between 0.4 and 0.6 through regression. (Figure 2).

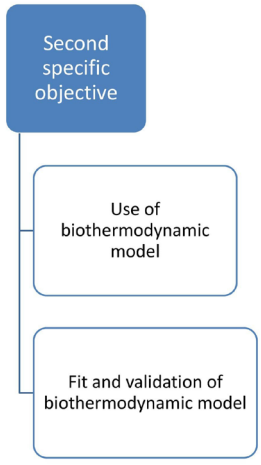

Figure 2. Second specific objective diagram.

- Fit a kinetic model using stoichiometry obtained from a biothermodynamic model to produce methane from the transformation of organic matter using glucose as the base substrate. Model structure in MATLAB software and simultaneous multiple regression with experimental data. (Figure 3).

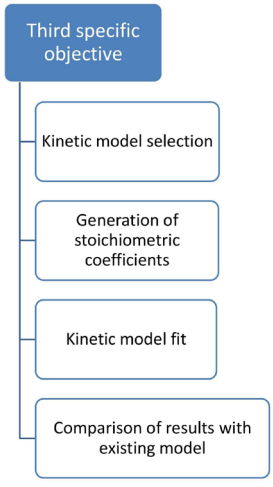

Figure 3. Third specific objective diagram.

Results and analysis

First, a bibliometric analysis for dark fermentation (obtaining only hydrogen and hydrogen that was later used to obtain methane) and anaerobic digestion (obtaining methane in two stages, from an acidogenic reactor and in one stage is the methanogenic reactor) was done. In this first analysis, it was possible to determine how the information was searched in databases of bibliographic references, country of origin, year of publication, and university or institute.

Next, tables were prepared with the operating conditions of each of the references consulted and the yield of hydrogen and methane. The yields were expressed in the units mole hydrogen/mole glucose or mole methane/glucose; for those whose results were presented in other units, the respective conversions were made through the ideal gas equation, stoichiometric ratios if the result was given in COD, and Total Volatile Solids as glucose, starting from the assumption that all organic matter would have been reduced.

Its structure was based on the possible combinations of the factors: substrate, temperature, pH, type of reactor, and hydraulic retention time through the Statgraphics Centurion Version 17.2.00 (64-bit) program. Each of these factors had different levels: substrate with three levels (wastewater, carbohydrates, and solid residues), temperature with two levels (mesophilic, temperatures between 298.15K-313.15K, and thermophilic, temperatures > 323.15K), pH bi-level acidophilic (4 and 6 pH units) and neutrophil (6 to 8 pH units), tri-level reactor CSTR, UASB and Others (previous modified, supplemented or improved reactors), and bi-level hydraulic retention time (stage 1 time ≤ 50 hours and stage 2 time > 50 hours). The strategy consisted of the joint variation of the factors and all possible combinations, to establish interactions between them and the effect on performance. All these factors were expressed as continuous variables, unlike performance, which was expressed as a discrete variable.

Statistical analysis was performed through data normality tests with the Shapiro and Kolmogov tests, box-and-whisker plots, and graphs of main and combined effects such as pH/temperature and their incidence on performance with the RStudio 1.2 program. 5042 years 2009-2020. As for the results obtained for the first specific objective, they were:

The highest yields for obtaining hydrogen would be obtained in CSTR-type reactors and preferably at thermophilic temperature. All hydraulic retention times were below 50 hours. Regarding methane, the best combination is that of neutrophilic pH, mesophilic temperature, improved or supplemented Others reactor, and hydraulic retention time greater than 50 hours with the type of solid waste substrate.

Temperature is a selective factor that affects the growth rate and metabolic pathway of microorganisms; based on the analyzed references, the ones that would behave the best would be the thermophilic bacteria in the degradation of organic matter. Combining this factor with the continuous agitation reactor would generate an effect that would allow the transformation of the molecules into simpler compounds.

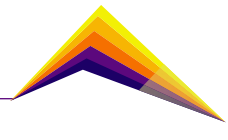

As with temperature, pH is an important factor because it affects the activity of catalytic enzymes (hydrogenase) and metabolic pathways that include oxidation-reduction processes.

Anaerobic digestion, including stages of hydrolysis, acidogenesis, acetogenesis, and methanogenesis, contemplates the activity of microorganisms (acetogenic bacteria and methanogenic archaea) in different periods. This requires periods of latency, growth, stationary, and cell death, according to the necessary and available substrate for each of its metabolic pathways. Therefore, the transformation of the organic matter, when having optimal process conditions, would be a phase that would take at least 50 hours to complete the anaerobic digestion, with different reaction speeds for each of the metabolic stages.

In the second specific objective, the parameters to be taken into consideration were temperature and pH since they are the ones used by the biothermodynamic model to establish the performance in the acidogenic, acetogenic and methanogenic phases. This model does not take into account the type of inoculum, reactor, hydraulic retention time, or the type of substrate since it is assumed that everything is glucose, and depending on the operating conditions of temperature and pH, a maximum yield is established per anaerobic degradation of organic matter. However, the model takes into account the energy (theoretical factor between 0.4 and 0.6) used by microorganisms for their development and growth period, such as cell maintenance; therefore, the estimated yield will be less than the theoretical ideal for hydrogen 4 moles H2/mole glucose, methane in two stages 2 moles CH4/mole glucose, and for methane in one stage 3 moles CH4/mole glucose.

With the tables elaborated in the first specific objective, for each one of the references and at the operating conditions of pH and temperature, a value of the cell energy efficiency parameter and the respective performance for hydrogen and methane were obtained. Subsequently, the experimental yields were compared with the values obtained with the biothermodynamic model and through least squares, the approximation of the model to the experimental results was verified. It was also verified that the average cellular energy use was found between the theoretical reference values.

About obtaining experimental hydrogen, the average yield was well below the minimum calculated by the biothermodynamic model and, therefore, the ideal at average conditions of pH, temperature, and outside the estimated interval for the energy efficiency parameter (ε) that oscillates between 0.4 and 0.6, theoretically. With the analysis carried out for the two stages of hydraulic retention time, it was found that the average yields were similar in order of magnitude for the generation of hydrogen and, therefore, it is related to the degradability of the substrate.

As for obtaining methane in two stages, it was possible to fit the biothermodynamic model to the average pH and temperature conditions found, but the average energy efficiency parameter (ε) was also outside the theoretical range.

For obtaining methane in one stage, the model adequately fitted the experimental data and the value of the epsilon energy parameter was within the theoretical range.

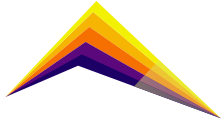

For the energy terms, both the ideal and the realistic stoichiometry predict greater energy production in two stages (obtaining hydrogen and then methane) than in a single stage of obtaining methane, but with the experimental data collected it was not possible to verify this theoretically estimated.

Regarding the development of the models, an unstructured segregated model was taken as a reference, focused on the perspective of process engineering (first-order equations with biodegradable substrate up to biogas and three phases considering products by hydrolysis and volatile fatty acids with three kinetic constants). It is not structured because it does not include the metabolism of microorganisms, but it is segregated because it considered two types of microorganisms: acetogenic bacteria and methanogenic archaea. Although it is an investigation that is not recent, from what was consulted in databases, it was the only one that carried out and published joint data on biomass, substrate consumption, and methane generation (Garcia-Ochoa *et al.* 1999). The model was developed in Excel by the Runge-Kutta method.

From the results obtained in the first two specific objectives, the proper functioning of the biothermodynamic model used was verified (Naranjo-Fernández, 2018). Realistic stoichiometric ratios such as biomass/glucose, biomass/methane, acetate/glucose, methane/acetate, acetogenic bacteria/glucose were extracted from this model. A model similar to that of the authors of the unstructured/segregated model was developed; obtaining adequate adjustments and changing the equation for substrate since in the first half the same as the one presented in the article was used and for the other half of the anaerobic digestion phase the constant of decrease or cell death of the bacteria was included, acetogenic cells and their growth was eliminated, allowing accurate modeling of the experimental data.

On the other hand, three non-structured/non-segregated kinetic models were developed and the first thing that was done was to assume growth of microorganisms in a batch reactor for the anaerobic degradation of glucose until obtaining methane in one stage.

The stoichiometry proposed for the cell stages varies according to the microorganism/substrate system and the operating conditions, such as pH, temperature, and oxidation-reduction potential. It was taken as orientation in the construction of the mass balances for cells, substrate and product, laws of speed, and stoichiometry, what was proposed by references focused from the perspective of biochemical engineering, hydrolysis, acidogenesis, acetogenesis, and methanogenesis (Scott, 2001; Dunn *et al.* 2003).

This system of equations was solved in MATLAB 2021a, license 40903832, by adjusting kinetic parameters and calculating their deviations with the *lsqcurvefit* command, with which systems of differential equations with simultaneous multiple regression are solved and compared with experimental data and for this case, the determination of kinetic parameters that are part of the algorithms proposed for each of the models (Zuluaga *et al.* 2018). Finally, these developed models were compared with others in common use such as the Differential, Logistic and Luedeking-Piret. (Figure 4).

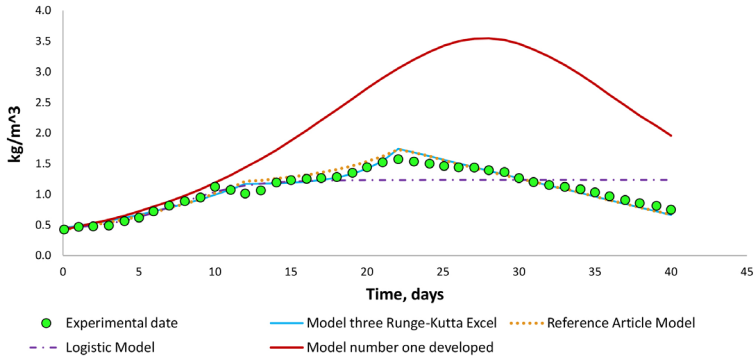

(a) Comparison of models against experimental biomass data.

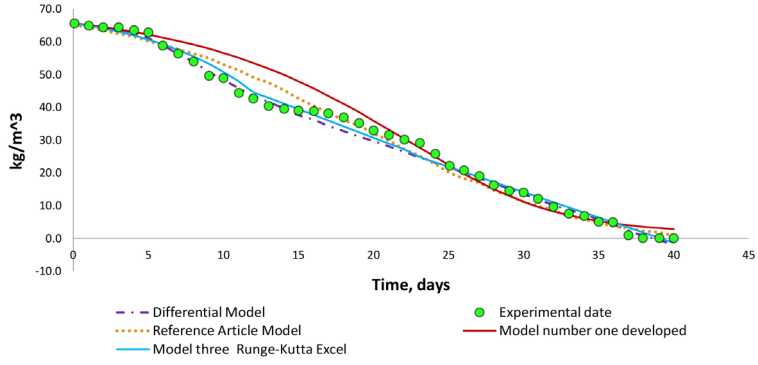

(b) Comparison of models against experimental substrate data.

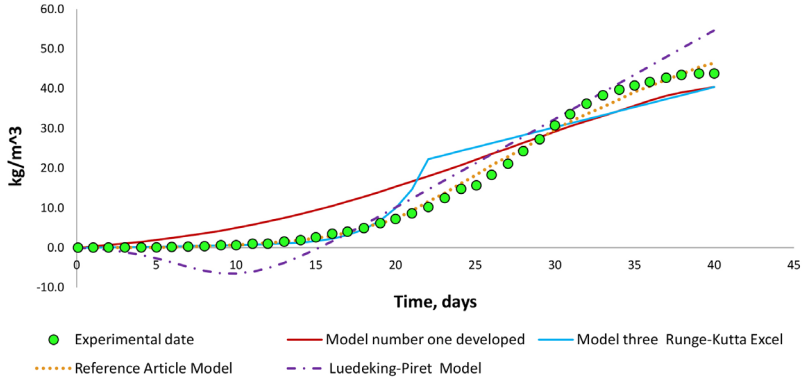

(c) Comparison of models against experimental data for methane.

Figure 4. Comparison of models developed against models in common use and model of the reference article.

General conclusions

- The biothermodynamic model presented an acceptable fit for methane in two stages, but a very good fit for obtaining methane in one stage.
- Hydraulic retention times in dark fermentation are directly related to the type of substrate used and organic degradation, noting that this would work better with agitation and with thermophilic temperature conditions.
- By using coefficients or stoichiometric relationships of the biothermodynamic model, which are realistic approximations and which allow avoiding their adjustment, simple models can be obtained, continuous in time and with good representation for the consumption of substrate and generation of methane, in which these would allow more precise complements for biomass, for more than one substrate such as intermediate products (volatile fatty acids) and mixed cell culture that includes acetogenic bacteria and methanogenic archaea.
- Unstructured/segregated models allow very good adjustments to be obtained for biomass, substrate, and methane, but they are limited by their complexity, since these must be developed for a specific reaction, have a measurement of intermediate products, and establish equations for each one of the variables at different time intervals.

References

[1] Garćia-Ochoa, F., Santos, V. E., Naval, L., Guardiola, E., & López, B. (1999). Kinetic model for anaerobic digestion of livestock manure. *Enzyme and microbial technology*, *25*(1-2), 55-60.

[2] Gouveia, B. F. L., Duarte, E. D. A., Dos Santos, A., & Fernandes, E. C. (2022). Dual-pool, three-phase kinetic model of anaerobic digestion in batch mode.*Heliyon*, e09194.

[3] Naranjo-Fernandez, D. (2018). Análise biotermodinâmica dos processos anaeróbios e fotossintéticos de recuperação de energia (Doctoral dissertation, Universidade de São Paulo).

[4] Scott, H. (2001). Elementos de ingeniería de las reacciones químicas. *Editorial Pearson*.

[5] Dunn, I. J., Heinzle, E., Ingham, J., & Prenosil, J. E. (2003). *Biological reaction engineering*. John Wiley & Sons.

[6] Zuluaga, S., Ibarra, H. N., Dobrosz-Gómez, I., & Gómez, M. Á. (2018). Ajuste de Parámetros Cinéticos y Cálculo de sus Desviaciones usando MATLAB. *Formación universitaria*, *11*(6), 53-62.

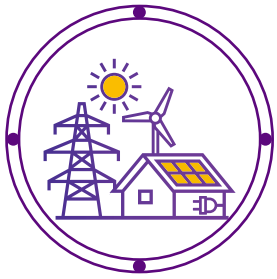

Improving the Stability of Methylammonium Lead Iodide Perovskite by Propionic Acid Doping

Montero-Rama M.P.[1,2]
Ramírez D.[2]
Jaramillo F.[2]
Marsal L.F.[1]

E-mail: mariadelpilar.montero@urv.cat
E-mail: estiben.ramirez@udea.edu.co
E-mail: franklin.jaramillo@udea.edu.co
E-mail: lluis.marsal@urv.cat

[1]Departament d'Enginyeria Electrònica Elèctrica i Automàtica, Universitat Rovira i Virgili, Tarragona, Spain.
[2]Centro de Investigación, Innovación y Desarrollo de Materiales, Universidad de Antioquia, Medellín, Colombia.

Abstract

In a few years, hybrid halide perovskite solar cells (PSCs) have reached a 25.6% power conversion efficiency (PCE) due to their properties such as high carrier mobility, high absorption coefficient, long diffusion length, tuneable bandgap, and low-cost of materials and fabrication. However, because of the solution processing nature and rapid crystal growth of perovskite thin films, several defects can be formed because of the precursor compositions and processing conditions. Additives are common for manufacturing efficient, stable, and hysteresis-free PSCs. Additives can affect perovskite crystallization and film formation, defect passivation in the bulk and/or at the surface and influence the interface tuning of structure and energetics. In this work, the use of propionic acid (CH_3CH_2COOH, PA) to dope methylammonium lead iodide ($MAPbI_3$) perovskite thin films with different PA/$MAPbI_3$ ratios is studied. To conduct this study, several PSCs, using doped and no doped $MAPbI_3$ perovskite thin films, are manufactured and characterized. The carbonyl group

Correspondent author

(−C=O) interacts with Pb ions passivating uncoordinated Pb. At the same time, the hydroxyl group (−OH) forms hydrogen bonds with the methylammonium ion, these hydrogen bonds suppress ion migration in the perovskite film, which will reduce hysteresis and improve the stability of PSCs. In this study, we demonstrated that the PSC fabricated with the $MAPbI_3$ perovskite film doped with a 0.5% wt. of PA results in better power conversion efficiency and fill factor than the devices manufactured without PA. We even, proved that these photovoltaic parameters are more stable over time. In addition, doped and no doped $MAPbI_3$ perovskite thin films were characterized to show how to influence the amount of PA in the optoelectronic and structural properties of these thin films. In summary, we confirmed that the doped $MAPbI_3$ perovskite thin films present a $MAPbI_3$ perovskite crystal formation, a bandgap, an emission peak, and a grain size in agreement with the literature.

Keywords: methylammonium lead iodide perovskite thin-film, additive, propionic acid, defect passivation, stability.

Introduction

Nowadays, Solar energy is one of the most important renewable energies for getting future sustainability.[1] Last years, hybrid halide perovskite solar cells (PSCs) have drawn much attention in research due to their various advantages for photovoltaic (PV) applications.[2], [3] Besides, PCSs record efficiency has reached 25.6%,[4] therefore they are the fastest-advancing solar technology and have become the most promising alternative to replace silicon-based solar cells. However, the issue of perovskite stability which restricts PSC´s outdoor application has not been overcome yet. For this reason, a perovskite stability improvement study has been carried out to manufacture the next generation of photovoltaic devices. Perovskite film degradation may be due to extrinsic factors such as oxygen, temperature, UV light, etc., or intrinsic factors such as applied lighting and electric field, ion migration, etc. Most studies in the literature focus on improving extrinsic stability and most instabilities caused by extrinsic factors can be reduced or avoided by encapsulation.[5] Therefore, we focused on improving intrinsic stability, trying to avoid ion migration. The use of additives is an effective´s pathway for improving the device´s lifetime.[6][7] The interaction of the additives functional groups with the halide perovskite absorber results in defect passivation and ion immobilization improving device performances and stability.[8]

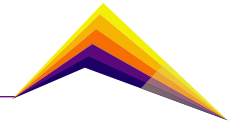

Herein, we investigated how to affect the addition of propionic acid (CH_3CH_2COOH, PA) to the methylammonium lead iodide ($MAPbI_3$) perovskite precursors solutions, with different PA/$MAPbI_3$ ratios, in the PSCs photovoltaic parameters, open-circuit voltage (V_{oc}), short-circuit current density (J_{sc}), fill factor (FF), and power conversion efficiency (PCE), and in the optoelectronic and structural properties of the $MAPbI_3$ perovskite thin films. Hence, several $MAPbI_3$ perovskite precursors solutions were prepared with distinct amounts of PA, and subsequently, various PSCs, employing these solutions, were manufactured. Also, $MAPbI_3$ perovskite precursors solutions were deposited on the top of different substrates (clean glasses) *via* spin-coating. To carry on this study, doped and no doped PSCs were characterized electrically (current to voltage characteristics, *J-V* curve). Besides, the different $MAPbI_3$ perovskite films were characterized by the standard techniques of semiconductor materials.

Materials and Methods

ITO-coated glass substrates were cleaned with neutral soap followed by ultrasonication in DI water, acetone, and isopropanol. Nickel oxide (NiO_x) hole transporting material powder was synthesized by the precipitation method previously reported[9][10] and diluted in DI-water to reach a 23 mg/mL solution. NiO_x layer was deposited in air by spin-coated at 3000 rpm on the top of the pre-treated ITO surface (ultraviolet-ozone (UVO) for 10 min at 100°C). Methylammonium lead iodide ($MAPbI_3$) perovskite absorber layer powder was prepared by modifying the Zhang-reported procedure[11][12]. Following, doped and no doped $MAPbI_3$ perovskite precursors solutions (27% wt. $MAPbI_3$) were prepared. Doped $MAPbI_3$ perovskite precursors solutions (0.3% wt. PA, 0.5% wt. PA, and 1.00% wt. PA) were prepared by adding distinct amounts of (CH_3CH_2COOH, PA). $MAPbI_3$ perovskite layers were deposited, under low humidity (< 20% H.R.) conditions, by spin-coating (4000 rpm) followed by a post-treatment which consist of depositing *via* spin-coated (4000 rpm) a methylammonium chloride (MACl) layer, and subsequently annealed at 100 °C for 10 min. A 12 mg/mL solution of the phenyl-C^{61}-butyric acid methyl ester (PCBM) electron transporting material was prepared in chlorobenzene (CB) and deposited *via* spin-coating at 2000 rpm, and subsequently annealed at 70 °C for 5 min. Rhodamine 101 solution was prepared at 0.5 mg/mL in anhydrous ethanol and deposited by spin coating at 4000 rpm. Finally, the Ag layer (100 nm, 1 A/s, 1×10^{-6} mbar) was deposited by thermal evaporation under a high vacuum. The effective area of the device was 0.14 cm^2. Doped and no doped $MAPbI_3$ perovskite precursors were also deposited on the top of different pre-treated (UVO) clean glasses *via* spin-coating (4000 rpm) and subsequently annealed at 100 °C for 10 min.

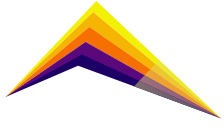

Results and analysis

We performed an extensive stability study of PSC devices. That is, reference $MAPbI_3$ devices and the three doped (0.3%, 0.5%, and 1.00% wt. PA) devices were left in the air (46% R.H., 22 °C) for a prolonged time, and their characteristics were recorded regularly. The evolution of the key parameters of the devices, open-circuit voltage (V_{oc}), short-circuit current density (J_{sc}), fill factor (FF) and power conversion efficiency (PCE) was plotted *vs.* time, and the results are reported in **figure 1**. **Figure 2** shows **a)** the X-Ray diffractograms (XRD), **b)** the absorption (UV-vis) spectra, **c)** photoluminescence emission (PL) spectra, and **d)** atomic force microscopy (AFM) images of the distinct $MAPbI_3$ perovskite precursor solutions deposited over the pre-treated glasses surfaces. In both figures the reference, 0.3%, 0.5% and 1.00% wt. PA is are represented in black, red, blue, and green, respectively.

From **figure 1,** as expected, J_{sc}, FF, V_{oc}, and PCE all show a steady decrease with time for all devices. The devices doped with 0.5% wt. of PA (0.5 PA) show superior FF, PCE, and stability over time to the reference devices. It is due to the carbonyl group (−C=O) interacting with Pb ions passivating uncoordinated Pb, decreasing the non-radiate recombination which results in better FF and PCE. At the same time, the hydroxyl group (−OH) forms hydrogen bonds with the methylammonium ion, which suppresses the ion migration in the $MAPbI_3$ perovskite film, which will improve the stability of PSCs. [13]

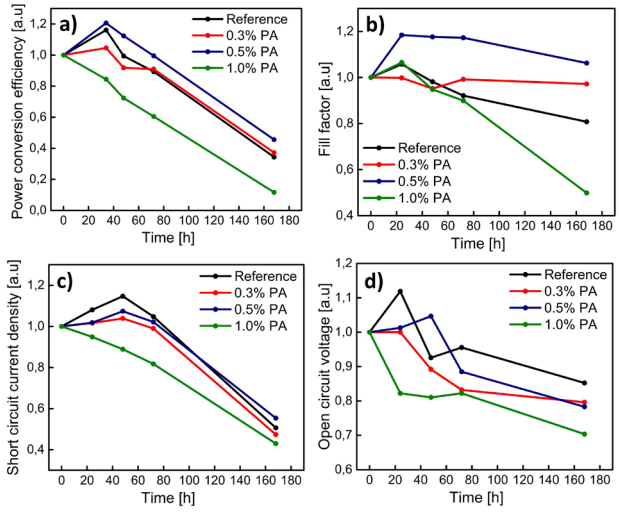

Figure 1. Decomposition study: evolution plots of PCE, FF, Jsc, and Voc vs. time.

As well, as we can see in **figure 2 d)**, 0.5 PA has mayor grains sizes and, therefore, a decrease in the grain boundaries, which reduces the electrical shunt, the probability of charge recombination, and the bulk traps during solar cell operation, with the result, too, in an increase of the FF and the PCE. The PL spectra (**figure 2c**) consist of narrow peaks centered around 770 nm, which corresponds to the band-to-band recombination of electrons in the

conduction band with holes in the valence band. We can observe that the intensity emission for the reference, and doped thin films with 0.3%, and 0.5% wt. of PA are very similar, however for 1.00% wt. PA, the intensity emission, decreases considerably. This decrease is because with increasing PA concentration, the colloid size in the precursor decreases and tends to aggregate into larger particles, leading to reduced nucleation and high non-radiative recombination, which causes a decrease in FF and PCE.[14] In **figure 2b)**, from the onset of absorption (~770 nm) the bandgaps can be estimated (Tauc's plot Method) to be approximately 1.6 eV, which is in agreement with reported surface photovoltage measurements.[15] It is expected that the mean thickness of the quasi-2D perovskite layer increases with the addition of PA, which results in a decrease in the absorbance and therefore in J_{sc}, and V_{oc}. From **figure 2a)**, we can observe, in agreement with the reported literature, the diffraction peaks at 14.0°, 20.0°, 23.5°, 24.5°, 28.2°, 31.7°,35.0°, 40.5° and 43° in the XRD pattern corresponding to (110), (200), (211), (202), (220), (310), (312), (224) and (330) diffraction planes of $MAPbI_3$ perovskite, respectively. These XRD patterns display that the different $MAPbI_3$ perovskite thin films have a tetragonal perovskite phase, which indicates that the tetragonal $MAPbI_3$ perovskite structure is formed. This evidences that the PA presence does not avoid the $MAPbI_3$ perovskite crystal growth.

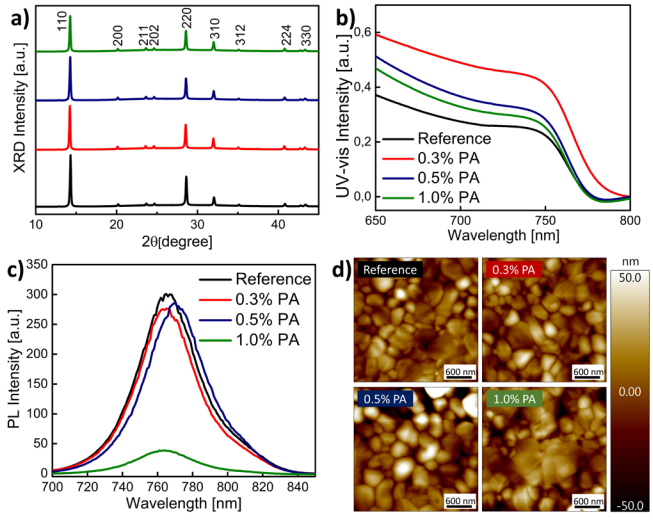

Figure 2. a) XRD diffractogram, **b)** UV-vis absorption and **c)** photoluminescence emission spectra, and **d)** AFM images of the perovskite film with different PA/$MAPbI_3$ ratios.

Conclusions or summary

To conclude, the addition of a 0.5% wt. of PA reduces trap state density in the perovskite films, the non-radiate recombination, and the ion migration resulting in higher FF and PCE and improving the stability of PSCs over time. For future works, we will use this doped thin film with 0.5% wt. of PA to manufacture encapsulated PCSs to achieve devices with major stability over time.

Acknowledgment

The authors acknowledge the financial support of the Ministerio de Universidades of Spain, the NextGenerationEU, and to the Plan de Recuperación, Transformación y Resiliencia, and the Colombia Scientific Program within the framework of the call Ecosistema Científico (Contract FP44842-218-2018).

References:

[1] N. Kannan and D. Vakeesan, "Solar energy for future world: - A review," *Renewable and Sustainable Energy Reviews*, vol. 62, pp. 1092–1105, 2016, doi: 10.1016/j.rser.2016.05.022.

[2] A. Hossain *et al.*, "The hybrid halide perovskite: Synthesis strategies, fabrications, and modern applications," *Ceramics International*, vol. 48, no. 6. Elsevier Ltd, pp. 7325–7343, Mar. 15, 2022. doi: 10.1016/j.ceramint.2021.11.313.

[3] D. Saikia, A. Betal, J. Bera, and S. Sahu, "Progress and challenges of halide perovskite-based solar cell- a brief review," *Materials Science in Semiconductor Processing*, vol. 150, p. 106953, Nov. 2022, doi: 10.1016/j.mssp.2022.106953.

[4] "Best Research-Cell Efficiency Chart, in: NREL, 2021".

[5] J. Li *et al.*, "Encapsulation of perovskite solar cells for enhanced stability: Structures, materials and characterization," *Journal of Power Sources*, vol. 485. Elsevier B.V., Feb. 15, 2021. doi: 10.1016/j.jpowsour.2020.229313.

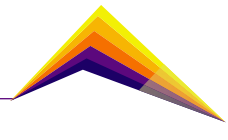

[6] S. Liu *et al.*, "A Review on Additives for Halide Perovskite Solar Cells," *Advanced Energy Materials*, vol. 10, no. 13. Wiley-VCH Verlag, Apr. 01, 2020. doi: 10.1002/aenm.201902492.

[7] C. Pereyra, H. Xie, and M. Lira-Cantu, "Additive engineering for stable halide perovskite solar cells," *Journal of Energy Chemistry*, vol. 60. Elsevier B.V., pp. 599–634, Sep. 01, 2021. doi: 10.1016/j.jechem.2021.01.037.

[8] J. Xie *et al.*, "Identifying the functional groups effect on passivating perovskite solar cells," *Science Bulletin*, vol. 65, no. 20, pp. 1726–1734, Oct. 2020, doi: 10.1016/j.scib.2020.05.031.

[9] J. Ciro, R. Betancur, S. Mesa, and F. Jaramillo, "High performance perovskite solar cells fabricated under high relative humidity conditions," *Solar Energy Materials and Solar Cells*, vol. 163, pp. 38–42, Apr. 2017, doi: 10.1016/j.solmat.2017.01.004.

[10] J. Ciro *et al.*, "Self-Functionalization behind a Solution-Processed NiOx Film Used As Hole Transporting Layer for Efficient Perovskite Solar Cells," *ACS Applied Materials and Interfaces*, vol. 9, no. 14, pp. 12348–12354, Apr. 2017, doi: 10.1021/acsami.6b15975.

[11] Y. Zhang, S. G. Kim, D. K. Lee, and N. G. Park, "CH3NH3PbI3 and HC(NH2)2PbI3 Powders Synthesized from Low-Grade PbI2: Single Precursor for High-Efficiency Perovskite Solar Cells," *ChemSusChem*, vol. 11, no. 11, pp. 1813–1823, Jun. 2018, doi: 10.1002/cssc.201800610.

[12] M. Vásquez-Montoya, J. F. Montoya, D. Ramirez, and F. Jaramillo, "Understanding the precursor chemistry for one-step deposition of mixed cation perovskite solar cells by methylamine route," *Journal of Energy Chemistry*, vol. 57, pp. 386–391, 2021, doi: 10.1016/j.jechem.2020.08.059.

[13] X. Li *et al.*, "Defect Passivation Effect of Chemical Groups on Perovskite Solar Cells," *ACS Applied Materials and Interfaces*. American Chemical Society, 2021. doi: 10.1021/acsami.1c08539.

[14] L. Meng *et al.*, "Improved perovskite solar cell efficiency by tuning the colloidal size and free ion concentration in precursor solution using formic acid additive," *Journal of Energy Chemistry*, vol. 41, pp. 43–51, Feb. 2020, doi: 10.1016/j.jechem.2019.04.019.

[15] I. Levine, G. Hodes, H. J. Snaith, and P. K. Nayak, "How to Avoid Artifacts in Surface Photovoltage Measurements: A Case Study with Halide Perovskites," *The Journal of Physical Chemistry Letters*, vol. 8, no. 13, pp. 2941–2943, Jul. 2017, doi: 10.1021/acs.jpclett.7b01332.

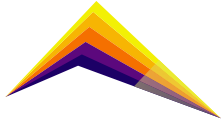

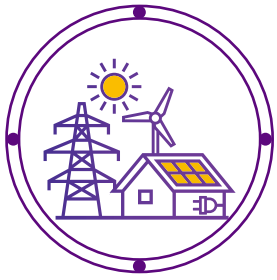

Representative evaluation methodology of graphene transfer processes applied to inverted perovskite solar cell

Kevin Ballestas[1] E-mail: kevin.ballestas@udea.edu.co
Juan D. Zapata[2] E-mail: estiben.ramirez@udea.edu.co
Daniel Ramírez[3] E-mail: juan.zapata@udea.edu.co

[1] Materials engineering student, [3]Ing., PhD., Centro de Investigación, Innovación y Desarrollo de Materiales - CIDEMAT, Facultad de Ingeniería, Universidad de Antioquia
[2] Ing., MSc., PhD., Facultad de Ingeniería, Universidad de Antioquia

Correspondent author

Abstract

The most common source of graphene for energy applications is a material grown via CVD on copper foils. For this, there are several transfer methods reported in the literature that take graphene from the copper foils and move it to a target substrate. The transferred graphene does not always maintain the high quality that it had from the CVD process since transferring it might generate defects such as wrinkles, cracks, etc. Moreover, the quality of the transferred graphene varies depending on the zone of the target substrate that is being analyzed. This makes obtaining a representative evaluation of the transfer process somewhat challenging, which might, to the best of our knowledge, justify the lack of a well-defined strategy for this evaluation. Here we present a simple methodology for a systematic and representative study of the quality of the transferred graphene using image analysis with MATLAB, Raman spectroscopy, and a transfer parameter defined by the authors. For this, polydimethylsiloxane (PDMS), thermal release tape (TRT), and PMMA-assisted transfer methods are applied to transfer graphene onto Si/SiO_2 substrates and a comparison of the quality obtained

with each method is done by using the proposed methodology. This methodology can be implemented in specific energy applications, such as in perovskite solar cells. Particularly, thanks to its work function, graphene can be transferred onto a [6,6]-phenyl-C61-butyric acid methyl ester (PCBM) layer of an inverted $MAPbI_3$ solar cell. This can be done by using PDMS of TRT-assisted methods, and the selection of the best-suited methods for this can be done by taking into consideration the evaluation methodology shown here.

Keywords: monolayer graphene, transfer method, transfer analysis, perovskite solar cell.

Introduction

Since its discovery in 2004 [4], graphene has been extensively studied. Thus, many of its properties that have been reported [5]–[7] have made this material suitable for applications in several fields, such as high-speed electronics, transistors, supercapacitors, and solar cells [8]. Typically, graphene was obtained by mechanical exfoliation of graphite flakes (*top-down* process), but an alternative *bottom-up* method based on chemical vapor deposition (CVD) introduced in 2006 [9] has made great advances over the years and allowed graphene to be commercially available mainly in the form of MLG or FLG grown on metal substrates (mainly copper). For this reason, in many scenarios where graphene is going to be used a transfer process that allows to move it from the metal substrate where it has been grown to a target substrate is required. This transfer processes make use of a carrier substrate, generally, of polymeric nature, that helps move the material to the target substrate. Many transfer processes have been reported in the literature [1], but little attention has been paid to the quality of the graphene once it is on the target substrate, i.e., its coverage, the presence of residues from the carrier substrate and defects, etc. Here, a simple methodology to evaluate the quality of the transfer process of graphene is presented. By using image analysis with MATLAB and Raman spectroscopy, some quantitative transfer parameters that allow direct comparison between different transfer methods are defined. With this methodology, defects introduced to graphene by the transfer process can be identified and the coverage obtained during the transfer process can be quantified.

To show this, a direct comparison between polydimethylsiloxane (PDMS), thermal release tape (TRT) and PMMA-assisted transfer methods is made, showing that better results are obtained with the TRT-assisted transfer method.

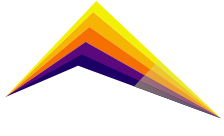

Methodology

PDMS and TRT transfer method.

Graphene on Cu foil (purchased from 2D semiconductors) is put on direct contact with the carrier substrate and a pressure of 0.2 MPa is applied for 30 minutes using a known load and controlling the area of application with a glass substrate with customized dimensions (the carrier substrate adheres to the graphene/copper system). The carrier/graphene/copper system is taken to an etching solution (1 M ammonium persulfate solution) in such a way that the copper is in contact with the solution and the foil is floating on the solution (see Figure 1). After 3 hours, the copper foil is completely diluted by the solution. The carrier/graphene system is taken out from the solution and rinsed with deionized (DI) water and dried with a nitrogen flow. The system is then put in contact with the target substrate (Si/SiO_2) in such a way that the graphene contacts the substrate. A 0.5 MPa pressure is applied for 1 hour and the carrier/graphene/target system is heated to 100 °C in a hot plate for 6 minutes. Finally, the carrier substrate is mechanically removed.

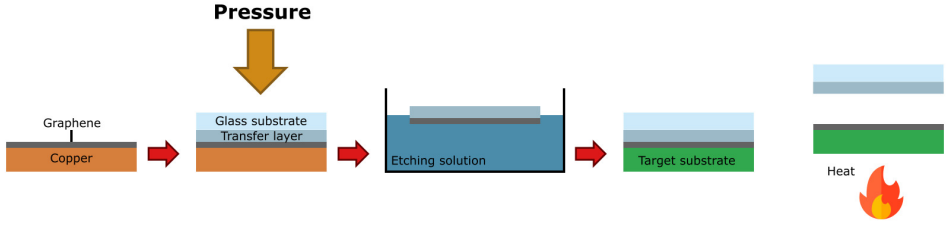

Figure 1. Representation of PDMS and TRT assisted graphene transfer methods.

PMMA transfer method.

Shortly, a thin layer of PMMA was spin coated on top of a copper foil with CVD-grown graphene on it. This was done at 3000 rpm, 1000 rpm/s during 60 seconds by using a solution of PMMA in anisol. Thereafter, an etching process with a 1 M ammonium persulfate solution was done in the same way than the PDMS and TRT transfer method. This leaves a system of PMMA/graphene that was carefully rinsed with DI water and the carrier/graphene system was scooped up with the target substrate (Si/SiO_2). Then the PMMA/graphene/target system is heated at 100 °C for 1 hour in a hot plate. Subsequentially, the system is submerged in a CB solution at 100 °C for 1 hour to remove the PMMA layer. Finally, the graphene/target system is rinsed with isopropanol and dried with a dry air flow.

Characterization.

Micro Raman spectroscopy measurements were done with a Horiba Yvon equipment, with 632.81 nm laser. Optical microscopy images were taken with a Leice DM750P microscope.

Scanning Electron Microscopy (SEM) images were taken with a JEOL-JSM 6490LV equipment. ATR-FTIR were made with NICOLET 6700 equipment.

Image analysis.

Analysis of the optical microscopy images was performed with a code made by the authors in MATLAB using predefined functions in the *Image Processing and Computer Vision* toolbox. Shortly, the code is able to obtain the graphene *coverage*. The code also counts the number of *individual zones* in the image that are covered with graphene and uses it to calculate two representative transfer parameters: *uniformity* (the fewer individual areas covered the higher the uniformity) and *quality* (representative of the overall quality of the transferred graphene regarding coverage and uniformity). The formulas used for these two parameters correspond to Equation 1 and 2.

$$uniformity = \frac{1}{(individual\ zones)^{0.25}} * 100 uniformity = \frac{1}{(individual\ zones)^{0.25}} * 100 \quad \text{Equation 1}$$

$$quality = \frac{coverage * uniformity}{100} quality = \frac{coverage * uniformity}{100} \quad \text{Equation 2}$$

Results and analysis

Characterization of graphene on copper foil

To have a reference point, quality of the initial CVD-grown graphene on copper foil was evaluated with SEM and Raman spectroscopy. Figure 2a shows that the initial coverage of the graphene on the foil is very good (graphene corresponds to the darker areas). This was corroborated with more images, and it was seen that the initial coverage in the foil was greater than 90 %, indicating that the maximum coverage that could be obtained with a transfer must be around that value. There are some parts of the copper foil that were oxidized (white dots in Figure 2a), but their presence is not significant. Raman spectra were taken in different zones of the copper foil to have a better idea of the quality of the graphene (see Figure 2b). In general, in the zones with no oxidized copper, the quality of the monolayer graphene (indicated by I_{2D}/I_G ratios relatively close to 2 and the FWHM values of the 2D band between 30 and 50 cm^{-1} in Figure 2b) is good, and the lack of D band in the spectra indicates that there are no vacancies (or at least very few) in the graphene hexagonal structure. Nonetheless, in the oxidized zones there is a significant D band and the values of I_{2D}/I_G and the FWHM of the 2D band indicate that the graphene is bilayer, which might be caused by mechanical deformation caused by changes in density when copper oxide is formed. However, the oxidized zones are very few and, in general, the quality of the initial graphene is good, indicating that the appearance of the D band or other changes in the spectrum related to defects in the graphene must be induced by the used transfer process.

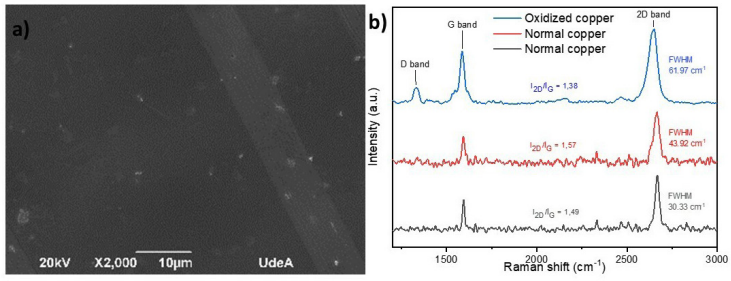

Figure 2. a) SEM image of graphene of Cu foil (darker zones correspond to graphene), b) Raman spectrums taken in different zones of CVD-grown graphene on copper foil.

Transferred graphene on Si/SiO2 substrate

Representative images of transferred graphene using each methods are shown in Figure 3. Apparently, graphene transferred with PMMA (Figure 3c) shows more residues that have a river-like appearance. However, the image analysis with MATLAB (done with 40 images of each transfer method) gives a more representative result in this regard, since it is also able to quantify the residues in the images. Figure 4 shows the transfer parameters calculated with the MATLAB code (average values). This indicates that the transfer method with the best coverage and quality is the one with TRT, since it also shows the least residues. The lower intensities obtained for D peaks in the Raman spectra of graphene transferred with TRT (see Figure 5b) also indicate that this transfer method introduces the least number of defects in the crystal graphene's structure. It is also interesting to note that in the spectra taken in zones with residues, in both TRT and PDMS transfer methods, the intensity of the D band increases, and the I2D/IG ratio approaches a value of 1, indicating that the residues left by the carrier substrates generate vacancies in graphene structures and tend to fold the MLG that is being transferred, making it turn to two-layer graphene.

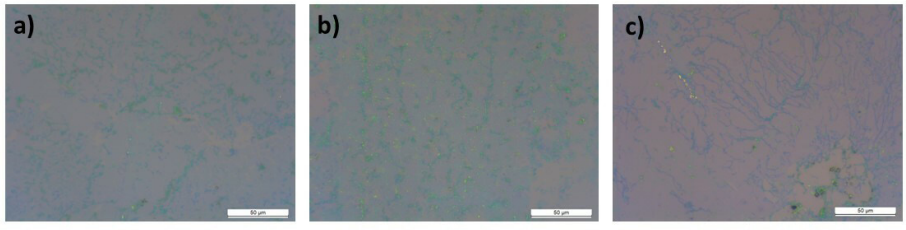

Figure 3. Optical microscopy images of graphene on Si/SiO2 substrate transferred with a) PDMS, b) TRT, c) PMMA.

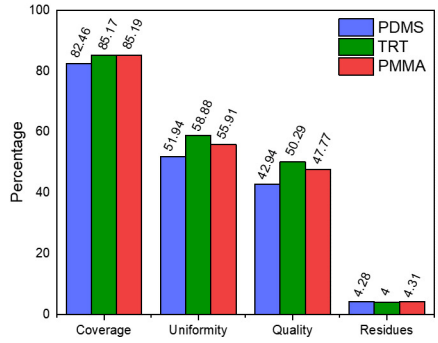

Figure 4. Transfer parameters calculated for each transfer method.

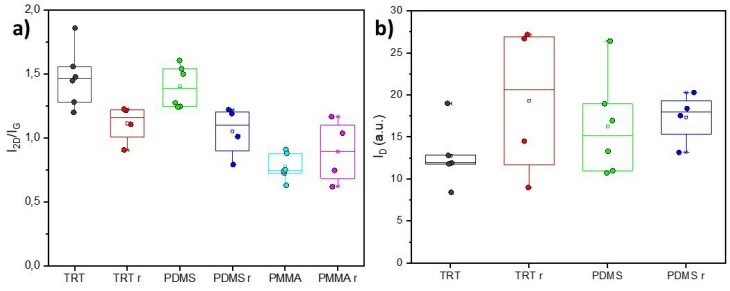

Figure 5. a) Comparison of I2D/IG ratios in different spectrums for different transfer methods, b) comparison of intensities of D peaks in TRT- and PDMS-assisted transfer methods (suffix r indicates that the spectrums were taken in a zone with residue).

Conclusions

The methodology presented in this works allows a direct comparison of the quality of the transferred graphene onto Si/SiO_2 substrates via different transfer methods. However, this methodology can be used to graphene being transferred to other target substrates. For this, several transfer parameters defined by the authors are used to effectively quantify features of the transferred graphene, such as its coverage and uniformity.

In the case of the methods being compared in this work, the methodology clearly indicated that the best result (regarding coverage, uniformity, residues, and vacancies in the carbon structure of graphene) are obtained with the TRT-assisted method. This indicates that, regarding the quality of the transferred graphene, this transfer method might be the most suitable one for transferring graphene onto PCBM for the fabrication of inverted perovskite solar cells. Nonetheless, further evaluations must be done to corroborate the feasibility of this method.

Ackowledgments

The authors thank Minciencias for the financial support of the project “Generación de hidrógeno de bajo impacto ambiental mediante el aprovechamiento de energías renovables, para su posterior uso como combustible limpio en sistemas de transporte” under the contract 177-2021.

References

[1] L. P. Ma, W. Ren, and H. M. Cheng, “Transfer Methods of Graphene from Metal Substrates: A Review,” *Small Methods*, vol. 3, no. 7, pp. 1–13, 2019, doi: 10.1002/smtd.201900049.

[2] Y. Chen, X. L. Gong, and J. G. Gai, “Progress and Challenges in Transfer of Large-Area Graphene Films,” *Adv. Sci.*, vol. 3, no. 8, pp. 1–15, 2016, doi: 10.1002/advs.201500343.

[3] M. V. Khenkin *et al.*, “Consensus statement for stability assessment and reporting for perovskite photovoltaics based on ISOS procedures,” *Nat. Energy*, vol. 5, no. 1, pp. 35–49, 2020, doi: 10.1038/s41560-019-0529-5.

[4] K. S. Novoselov *et al.*, “Electric Field Effect in Atomically Thin Carbon Films,” *Science (80-.).*, vol. 306, no. 5696, pp. 666–669, 2004, doi: 10.1126/science.1102896.

[5] K. S. Novoselov *et al.*, “Two-dimensional gas of massless Dirac fermions in graphene,” *Nature*, vol. 438, no. 7065, pp. 197–200, 2005, doi: 10.1038/nature04233.

[6] H. I. Rasool, C. Ophus, W. S. Klug, A. Zettl, and J. K. Gimzewski, “Measurement of the intrinsic strength of crystalline and polycrystalline graphene,” *Nat. Commun.*, vol. 4, pp. 1–7, 2013, doi: 10.1038/ncomms3811.

[7] P. Zhang *et al.*, “Fracture toughness of graphene,” *Nat. Commun.*, vol. 5, pp. 1–7, 2014, doi: 10.1038/ncomms4782.

[8] E. P. Randviir, D. A. C. Brownson, and C. E. Banks, “A decade of graphene research: Production, applications and outlook,” *Mater. Today*, vol. 17, no. 9, pp. 426–432, 2014, doi: 10.1016/j.mattod.2014.06.001.

[9] P. R. Somani, S. P. Somani, and M. Umeno, “Planer nano-graphenes from camphor by CVD,” *Chem. Phys. Lett.*, vol. 430, no. 1–3, pp. 56–59, Oct. 2006, doi: 10.1016/j.cplett.2006.06.081.

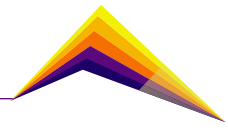

Hybrid perovskite $(Cs_{1-x}DMA_x)Pb(Br_{1-x}I_x)_3$ solar cells with improved stability

Juan J. Patiño — E-mail: juan.patino11@udea.edu.co
Juan F. Montoya — E-mail: felipe.montoya@udea.edu.co
Edwin Ramírez — E-mail: ramirezp.edwin@gmail.com
Franklin Jaramill — E-mail: franklin.jaramillo@udea.edu.co
Daniel Ramírez — E-mail: estiben.ramirez@udea.edu.co

Centro de Investigación, Innovación y Desarrollo de Materiales – CIDEMAT, Facultad de Ingeniería, Universidad de Antioquia

Abstract

Inorganic perovskites have attracted the interest of the scientific community because they have improved stability when compared with their hybrid counterparts used in Solar Energy. However, increasing the inorganic component of this material makes it necessary to considerably increase the annealing temperatures during its crystallization, therefore, it opens a possibility of research in perovskites with high inorganic content and relatively low annealing temperatures. Inorganic perovskites with DMA in their composition generate coordination between cations and anions that allows a decrease in annealing temperatures, in addition to a suitable morphology and properties that lead to promising devices. Since, the final properties are very different from those obtained with traditional perovskites such as $MAPbI_3$, it is necessary to deposit layers with adequate thickness for good light absorption and correct charge generation. Therefore, this work studied the conditions to obtain a pure inorganic phase with relatively small amounts of DMA, adequate thickness, good absorption, homogeneous morphology, and optoelectronic properties comparable to the reference $MAPbI_3$. We found that layers with thicknesses above 300 nm led

Correspondent author

to the best conditions, which are varied by changing the precursor concentration and the spin-coating deposition parameters. By using this thickness, maximum efficiency of 7.93% is obtained, in addition to a pure phase, adequate morphology and, excellent stability at the conditions studied yielding higher stability that the reference after twelve days of testing.

Keywords: Solar energy, renewable energy, hybrid perovskite, inorganic perovskite.

Introduction

One of the most challenging issues facing humanity today is the reduction of pollution generated by the energy industry. To meet this challenge, strategies have been developed to reduce greenhouse gases and contribute to the energy transition. Photovoltaic solar energy (PV) provides a solution to this problem, by using semiconductor materials in contact with sunlight it is possible to transform the photons into electrons and produce energy (photoelectric effect) [1].

Historically, silicon has been the most widely used semiconductor to develop this technology because its raw material is abundant, and it has high stability that allows long operation times. However, its purification process requires a lot of energy, which involves the application of high temperatures, increasing the cost. To overcome this, new materials such as hybrid perovskites (Pvkt), have been investigated. The use of these materials represents several advantages over other semiconductors because they are processed, using solution precursors, by simple and scalable methods such as spin-coating. Additionally, they have a high absorption coefficient that facilitates the production of thin, light and, even flexible devices [2]. Hybrid compositions, such as MAPbI3 is the most investigated, due to their versatility; however, this material degrades very easily in contact with water or humid conditions. This is largely due to the organic component in the structure, which destabilizes the material.

By reducing the organic component, the resistance to general conditions such as temperature, illumination and humidity can be improved. Recent reports have shown that Cs+ is the best-conditioned cation to synthesize this structure and replace the commonly used MA+. This is because the optoelectronic properties are adequate to meet the requirements needed in the perovskite family [3].

In this work, a composition with a significant decrease in the organic component of the perovskite structure ((Cs1-xDMAx)Pb(Br1-xIx)3) was studied. A pure phase of this material

with morphology suitable for device fabrication was achieved. Additionally, we demonstrated with XRD analysis that the stability of this composition is considerably higher than that of the MAPbI3 sample. Furthermore, this perovskite was integrated in an optoelectronic device obtaining a photovoltaic conversion efficiency (PCE) of 7.93%.

Methodology

$DMAPbI_3$ synthesis: This phase is synthesized by the decomposition of DMF in the presence of an acid rich environment (HI), subsequently mixed with lead precursor (PbI_2). The reaction mechanism is shown in Equation 1, where DMF upon decomposition and mixing with the acid iodide produces DMAI. Finally, the DMAI when mixed with lead, forms the $DMAPbI_3$ phase. The mixture contained a 1:1 ratio of HI and DMF, and PbI_2 with a 1M concentration was added, the solvent was slowly evaporated in a rotoevaporator for 6 h at 110°C, and faint yellow powders were collected.

$$HCON(CH_3)_2 + HI + H_2O \rightarrow (CH_3)_2NH_2I(DMAI) + HCOOH \quad \textbf{Equation 1}$$

Synthesis of precursor $((Cs_{1-x}DMA_x)Pb(Br_{1-x}I_x)_3$: The precursor of this perovskite is synthesized using the phase $DMAPbI_3$ above and mixing it with $PbBr_2$ and CsI in DMF:DMSO 1:1.4. For this, different molar ratios between the components were used to arrive at the purest possible phase. The ratios used were 1:1:2, 1.36:0.74:2 and 0.3:0.7:0.7, leading to the phases $Cs_{1-x}DMA_xPb_{0.66}Br_{1.66}I_{0.66}$, $Cs_{0.45}DMA_{0.66}Pb_{0.7}Br_{0.49}I_2$ and $(Cs_{1-x}DMA_x)Pb(Br_{1-x}I_x)_3$.

Solar cell fabrication: The solar cell was fabricated by spin coating, where ITO was coated layer by layer at different conditions. Initially, $SnCl_2$ dissolved in isopropanol was deposited at a speed of 3000 rpm using the static method. Then, it was annealed at 180 °C for 1 h to obtain SnO_2 used as ETL. Then, another layer of SnO_2 was deposited by chemical bath synthesis (CBD) to fill the imperfections and improve the surface morphology of the ETL. Then, perovskite was deposited under different spin-coating conditions, as shown in Table 1. After that, Spiro-OMeOTAD doped with Co and Li is deposited to form the HTL of the solar cell by dynamic spin-coating at 4000 rpm. Finally, 100-nm gold is thermally evaporated as an electrode (Figure 1).

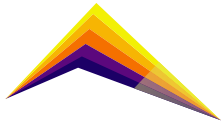

Table 1. Sample deposition parameters.

Concentration (M)	Speed/ Acceleration 1	Speed / Acceleration 2	Layer thickness (nm)
1	1000/1000	1000/1000	175
1	1000/1000	2500/2500	145
1,3	1000/1000	1000/1000	310
1,3	1000/1000	1500/1500	290
1,3	1000/1000	2500/2500	210

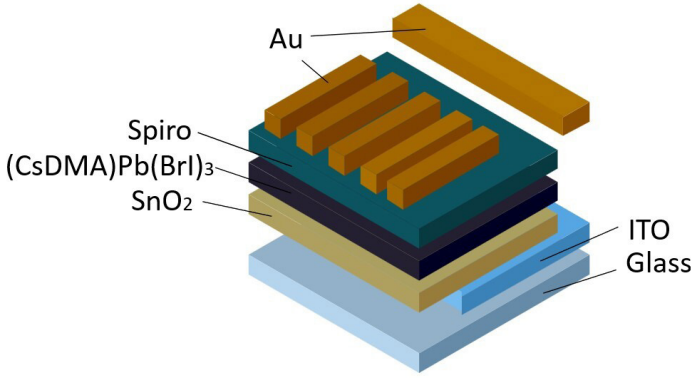

Figure 1. Diagram of integrated solar cell.

Results and analysis

Different molar ratios such as 1:1:2, 1.36:0.74:2 and 0.3:0.7:0.7, leading to the phases $Cs_{1-x}DMA_xPb_{0.66}Br_{1.66}I_{0.66}$, $Cs_{0.45}DMA_{0.66}Pb_{0.7}Br_{0.49}I_2$ and $(Cs_{1-x}DMA_x)Pb(Br_{1-x}I_x)_3$ were evaluated. These ratios provide different properties to the final structure, where it is expected that the purity of the phase depends on the number of cations and anions that are added during the synthesis of the precursor. It was found that the phases obtained using composition $Cs_{1-x}DMA_xPb_{0.66}Br_{1.66}I_{0.66}$ and $Cs_{0.45}DMA_{0.66}Pb_{0.7}Br_{0.49}I_2$ present high inter-phase mixing with a reduction in the purity of the final structure, however, the $(Cs_{1-x}DMA_x)Pb(Br_{1-x}I_x)_3$ phase is much purer with the appearance of characteristic peaks in the XRD at 14.35° and 29.3°(Figure 2a) [4]. Moreover, in the photoluminescence (PL) spectra, it is found that the composition producing phase mixture has different emissions, indicating active phases with different band-gap. The band gap smaller than 1.8 eV belongs to iodine-rich phases with low emissions, appearing

around 10° in the XRD, and the band gap higher than 2.2 eV to bromine-rich phases (Figure 2b), with the appearance in the XRD between both characteristic peaks.

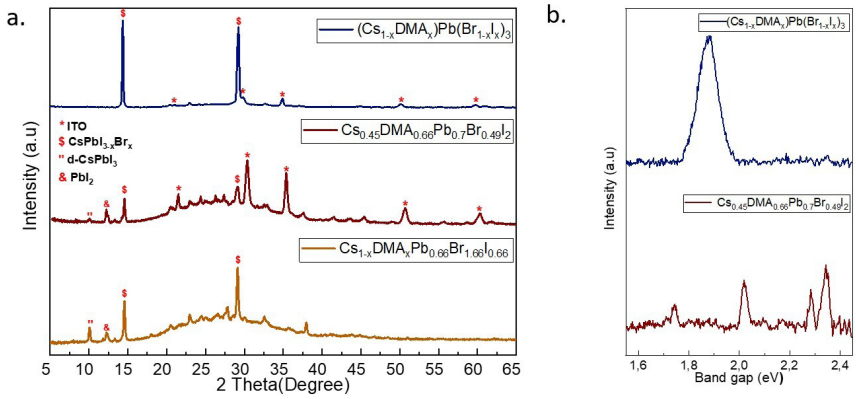

Figure 2. a) XRD spectra and b) PL spectra of perovskites with different molar ratios constituent ions.

It it was found that the $(Cs_{1-x}DMA_x)Pb(Br_{1-x}I_x)_3$ phase is more suitable, therefore, deposition by spin coating was optimized to obtain films with suitable thicknesses (as indicated in Table 1). This is crucial since obtaining thicknesses large enough to allow high absorption can lead to improvement in the final efficiency of the device. To confirm this, the optical characterization of these layers is performed, observing in the PL an increase in the intensity of the emission peak at higher values of the layer thickness (Figure 3a) , with higher absorption in the UV-Vis spectrum (Figure 3b). Meaning that the charges at higher thicknesses are generated at a higher rate, producing a better optical behavior [5]the cubic perovskite α-phase is thermodynamically stable only at >330 °C and the low-temperature perovskite γ-phase is metastable and highly susceptible to non-perovskite δ-phase conversion in moisture. Many methods have been reported which show that the incorporation of acid (aqueous HI.

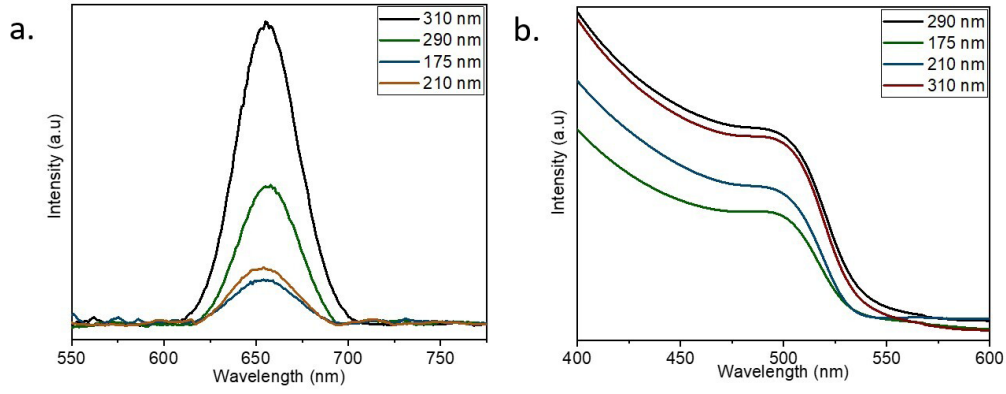

Figure 3. Perovskite layer with different thicknesses a) PL, and b) UV-Vis spectra

To correlate the variables studied here with the optoelectronic properties of the device, the solar cells described in the methodology are built with $MAPbI_3$ as the reference perovskite (Figure 4). We observed that on average the photovoltaic parameters closer to the reference

correspond to the layers with greater thickness, this is due to a better absorption of light by increasing the thickness, since this perovskite has a lower absorption coefficient than $MAPbI_3$. Therefore, the thickness must be increased to provide a charge production comparable to that of $MAPbI_3$.

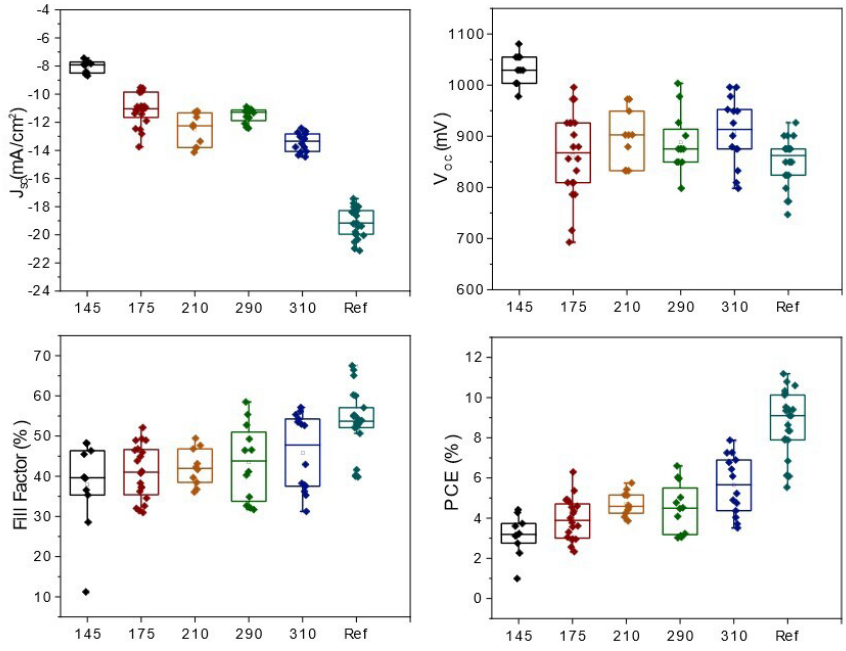

Figure 4. Optoelectronic properties of solar cells with different deposition conditions.

Finally, the stability of the $(Cs_{1-x}DMA_x)Pb(Br_{1-x}I_x)_3$ perovskite was studied by comparing it with that of $MAPbI_3$, where we observed that the time evolution of the PbI_2 peak in the XRD spectra is significantly higher in $MAPbI_3$ than in $(Cs_{1-x}DMA_x)Pb(Br_{1-x}I_x)_3$ (Figure 5). This indicates that the degradation rate at the conditions under study of $MAPbI_3$ perovskite is higher than in $(Cs_{1-x}DMA_x)Pb(Br_{1-x}I_x)_3$ perovskite. This figure shows that at 12 days, the $MAPbI_3$ perovskite is already considerably damaged when returning to its main precursor, however, the $(Cs_{1-x}DMA_x)Pb(Br_{1-x}I_x)_3$ has not yet started to degrade.

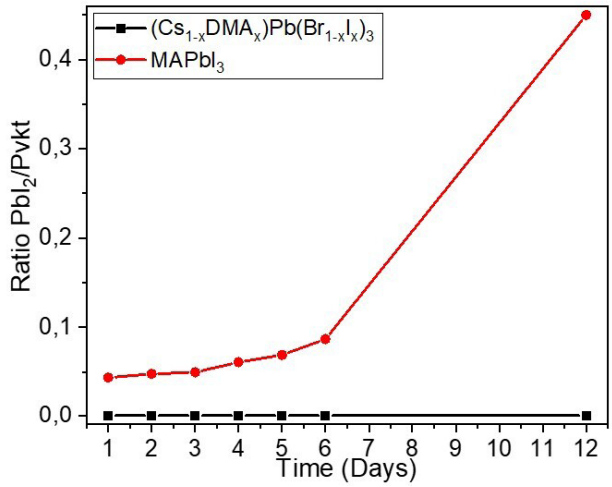

Figure 5. Comparative plot of the PbI_2/Pvkt ratio in the perovskite $(Cs_{1-x}DMA_x)Pb(Br_{1-x}I_x)_3$ and the reference. Study carried out at 30-40% relative humidity.

Conclusions

Inorganic perovskites that eliminate a large part of the organic component in their composition present extremely interesting properties, which solve essential problems of stability of this family of semiconductors. For this work, it is concluded that the most important variables to control are the thickness of the layer, the morphology and phase obtained. This is because the optical properties such as band-gap and absorption coefficient are very different from those of traditional perovskites, which makes it necessary to find the appropriate parameters to deposit a good layer with the required purity for the integration in optoelectronic devices. In this work, the conditions for the deposition of $(Cs_{1-x}DMA_x)Pb(Br_{1-x}I_x)_3$ perovskite layers of 300 nm were found. Our experimental procedure led to a pure phase material with adequate thickness and optical absorption properties which enabled the fabrication of solar cell that reach an average PCE of around 80% of the reference device.

Acknowledgments:

The authors thank Minciencias by the financial support of the project “Generación de hidrógeno de bajo impacto ambiental mediante el aprovechamiento de energías renovables, para su posterior uso como combustible limpio en sistemas de transporte” under the contract 177-2021.

References

[1] M. Kumar, "Social, Economic, and Environmental Impacts of Renewable Energy Resources," *Wind Sol. Hybrid Renew. Energy Syst. [Working Title]*, pp. 1–11, 2020, doi: 10.5772/intechopen.89494.

[2] X. Li, P. Li, Z. Wu, D. Luo, H.-Y. Yu, and Z.-H. Lu, "Review and perspective of materials for flexible solar cells," *Mater. Reports Energy*, vol. 1, no. 1, p. 100001, 2021, doi: 10.1016/j.matre.2020.09.001.

[3] M. Kulbak, D. Cahen, and G. Hodes, "How Important Is the Organic Part of Lead Halide Perovskite Photovoltaic Cells? Efficient CsPbBr3 Cells," *J. Phys. Chem. Lett.*, vol. 6, no. 13, pp. 2452–2456, 2015, doi: 10.1021/acs.jpclett.5b00968.

[4] H. Wang, H. Liu, Z. Dong, W. Li, L. Zhu, and H. Chen, "Composition manipulation boosts the efficiency of carbon-based CsPbI3 perovskite solar cells to beyond 14%," *Nano Energy*, vol. 84, no. January, p. 105881, 2021, doi: 10.1016/j.nanoen.2021.105881.

[5] A. R. Marshall *et al.*, "Dimethylammonium: An A-Site Cation for Modifying CsPbI3," *Sol. RRL*, vol. 5, no. 1, 2021, doi: 10.1002/solr.202000599.

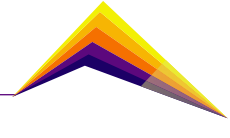

INFRASTRUCTURE

Insights and research in materials used to decrease noise pollution: developments for Colombia

Jeiser Rendón[1]
Carlos H. C. Giraldo[2]
Henry A. Colorado[1]

Email: jeiser.rendon@udea.edu.co

[1]CCComposites Laboratory, Universidad de Antioquia UdeA, Medellín, Colombia.
[2]Department of Nuclear Engineering, Missouri University of Science and Technology, Rolla, MO 65409, USA.

Abstract

Noise pollution is related to elements that are not only linked to the noise source, but also external factors. This is the case for reflective surfaces in urban canyons, where, due to the characteristics of the highly reflective materials that are usually used, long reverberation fields are generated that increase the noise pollution present. This causes detriment of urban environments and therefore of the population that inhabits them. The following research looks for ways to mitigate noise in this type of environment with materials that manage to absorb the noise that impacts against a facade. But at the same time, they manage to be functional on an outdoor surface, to have additional uses more than the noise pollution itself, such as structural applications or solid waste management. Four binders were used to be tested in this goal: concrete mix, mortar mix, vinyl spackling, and epoxy resin, in which, all of them, in combination with rice husk nanoparticles (RH NPs), could have good sound absorption conditions. The rice husk is not only known for its benefits to absorb sound, upon the mix with other binders but also is known as one of the main agricultural wastes worldwide. Different samples were mixed in mass proportions Binder/RH NPs of 100/0, 80/20, 60/40,

Correspondent author

40/60, 20/80, 0/100. Subsequently, measurements of the acoustic absorption coefficient were made in an impedance tube under the ISO 10534-1 standard. Characteristics on the surface of the samples were analyzed identifying cracks, wear, or any damage in the structure, that account for the structural material response in the facade. The results obtained show that these four binders present a growing trend of sound absorption as the proportion of RH NPs increases in their mixture. However, it is possible to appreciate different conditions on the surface of the samples that would be important to study further by subjecting the samples to outdoor conditions such as humidity and UV radiation and then performing compressive strength tests.

Keywords: Noise pollution; Urban canyons; Sound absorbing composites; Rice husk nanoparticles.

Introduction

Environmental noise is currently one of the main pollutants in urban environments. Many diseases and problems are generated in urban areas due to this pollutant [1]. Some diseases are easily related to noise such as tinnitus, hearing loss, or hyperacusis. But others seem not to be derived from this contaminant. This is the case of diabetes, preeclampsia, strokes, respiratory and cardiac arrhythmias, and can even accelerate the onset of mental problems [2]. In addition, there are also many problems associated with noise such as alterations in cognitive capacity, sleep interruptions, mood changes, stress, fatigue, and so on [3], [4].

Noise pollution has several causes, and this pollutant is commonly related to the different sources of noise that exist in urban environments. Among those are cars, aircraft, trains, sound amplification systems, machinery, construction works, industrial processes, ventilation systems, and pedestrians, among others [5]. But other elements are part of the increase in this type of pollution, such as reflections on urban surfaces. This type of phenomenon occurs in urban canyons where the parallelism between buildings on both sides of the roads causes constant reflections of the noise pollution generated by the sources from one building to another [6]. In this way, the energy generated by the noise tends to increase and remain longer. Urban surfaces covered with stone, glass, metal, concrete, asphalt, and other highly reflective stone materials generate long reverberation fields that harm these spaces for those who are in them, as is the case of pedestrians [7].

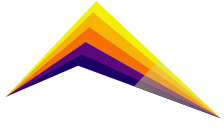

The following work seeks, using acoustically absorbent compounds, to mitigate the pollution generated by noise. However, this type of compound must fulfill a dual purpose of absorbing sound and at the same time resisting weather conditions. For this, different materials are investigated that, based on their ability to absorb sound waves and their resistance to outdoor conditions, can fulfill this double objective. For this, binders that can be commonly found in a facade were used, which in combination with RH NPs manage to have a good sound absorption coefficient and at the same time can resist external conditions.

Methodology

First, the rice husk (Homebrew Ohio Rice Hulls Brown) was ground to obtain the nanoparticles. This was done in a ball mill for 12 hours. Then, the samples were analyzed in a dynamic light scattering to corroborate the presence of nanoparticles (particles below 500 nm). Next, the powder from this grinding was mixed with the four binders: Concrete Mix “Quikrete” (Mix according to ASTM C287), Mortar Mix “Quikrete” (Mix according to ASTM C270 for type-N mortar), Vinyl Spackling “DAP” (Indoor/Outdoor) and epoxy resin “Clear Casting and Coating HXDZFX”.

To blend the samples according to their mass, a balance was used where each of the compounds to be mixed was weighed in the proportions of 100/0, 80/20, 60/40, 40/60, 20/80, and 0/100. After that, they were mixed with distilled water, except for the resin, to obtain a compound to pour into the molds (cylinders with a diameter of 4 cm and a height of 2 cm). The samples were then left to dry in the open air for 24 hours with a relative humidity inside the laboratory of 45% +/- 5%. They were then placed in an oven at 90 degrees centigrade, except for the resin, until complete drying.

The epoxy resin was mixed in the absence of water since both the resin and the catalyst were liquid and allowed easy mixing with the RH NPs. In addition, the drying of this compound was carried out completely for 24 hours in the open air and did not require an oven.

Finally, the samples were measured in the impedance tube see Figure 1. The measurements were made using the standing wave method according to standard. In this way, it was possible to obtain the sound absorption coefficient of the different samples

Results and analysis

Dynamic light scattering analyses show the presence of nanoparticles in percentage intensities of 3.16% in each of the samples analyzed after grinding for 12 hours. When mixing the RH NPs with the binders, it was possible to obtain a by-product with an appropriate consistency to put in the molds, requiring a longer mixing time for the epoxy resin. After demolding the samples and drying them in the open air, the samples (except the epoxy resin) required approximately 3 hours in the oven at 90ºC for complete drying.

The measurements made in the impedance tube show that the manufactured samples manage to increase their acoustic absorption by up to 21% (see Table 01), the change in the sound absorption coefficient that remained positive, gradual, and constant for all the compounds except for the concrete that went from a sound absorption coefficient of 0.28 in the 100/0 mix to 0.27 in the 80/20 mix. An average acoustic absorption coefficient can be seen that went from 0.25 in the 100/0 mix to 0.46 in the 80/20 mix. Likewise, more abrupt changes are observed between the mortar mixtures from 100/0 to 80/20 with a change difference of 0.15 and the resin mixture from 60/40 to 20/80 with a change difference of 0. 13.

It is important to consider the homogeneity of the different surfaces in the manufactured samples. Cracks and wear are evident in several of the different mixtures, see Figure 2, this type of damage on the surface of the samples increased with the greater amounts of RH NPs added to the mixtures, which means that several of these compounds may not be conducive to being placed on a facade. For this reason, it is important to contrast Table 1 with Figure 2. In this sense, the facade materials that best manage to mix with the RH NPs are vinyl spackling and epoxy resin (both compounds exhibit few cracks or wear).

Regarding the result of the measurements carried out in the impedance tube Figure 1. The 125 Hz band presents similar conditions in all the samples and measurements including high sound-absorbing materials. This supposes a bias of the measurements derived from a fault in the impedance tube for this band that requires a deeper analysis. Therefore, this band (125 Hz) was not considered for the averages of the acoustic absorption coefficient.

To compare results with reported investigations, other works are mentioned, such as the one carried out by Sekunowo et al in 2020. In this work, calcined rice husk nanoparticles are combined with epoxy resin. The results show averages in the acoustic absorption coefficient of up to 0.8 in the bands of 1,2,3,4,5 and 6 KHz in wt combinations of 10% NPs, 60% Epoxy Resin, and 30% Hardener [8]. Another investigation carried out by Adnan et al in 2020 shows how acoustic absorption coefficients of 0.99 can be achieved in the 250 Hz frequency band for compounds that mix 20% of Palm Oil Fuel Ash in substitution of sand for the Mortar Mix [9].

Conclusions or summary

It was observed that the best compound was the one that mixed epoxy resin and rice husk nanoparticles in a ratio of 20/80. This compound manages to have an average absorption coefficient between 125 Hz and 5000 Hz of 0.4, presenting an absorption peak of 0.65 in the 5 KHz band. If this mixture is compared with the initial 100/0 without rice husk nanoparticles, it is possible to appreciate a percentage increase in the average sound absorption coefficient of 167% between the 500 Hz and 5 KHz bands.

Other studies that involve subjecting these samples to moisture and ultraviolet radiation should be considered. Thus, it will be possible to know with greater certainty the virtues of this compound in the facades. It is also important to consider other drying temperatures (other than 90 degrees Celsius) to know if the drying is related to the appearance of cracks and wear on the surface of the samples.

References

[1] B. Berglund, T. Lindvall, and D. H. Schwela, «New Who Guidelines for Community Noise», *Noise & Vibration Worldwide*, vol. 31, n.º 4, pp. 24-29, abr. 2000, doi: 10.1260/0957456001497535.

[2] J. Rendón, D. M. Murillo Gómez, and H. A. Colorado, «Useful tools for integrating noise maps about noises other than those of transport, infrastructures, and industrial plants in developing countries: Casework of the Aburra Valley, Colombia», *Journal of Environmental Management*, vol. 313, p. 114953, jul. 2022, doi: 10.1016/j.jenvman.2022.114953.

[3] H. A. Colorado, L. Saldarriaga, J. Rendón, and M. A. Correa-Ochoa, «Polymer composite material fabricated from recycled polyethylene terephthalate (PET) with polyurethane binder for potential noise control applications», *J Mater Cycles Waste Manag*, vol. 24, n.º 2, pp. 466-476, mar. 2022, doi: 10.1007/s10163-021-01330-4.

[4] R. K. Jazani, M. Saremi, T. Rezapour, A. Kavousi, and H. Shirzad, «Influence of traffic-related noise and air pollution on self-reported fatigue», *International Journal of Occupational Safety and Ergonomics*, vol. 21, n.º 2, pp. 193-200, abr. 2015, doi: 10.1080/10803548.2015.1029288.

[5] E. Badino, R. Manca, L. Shtrepi, C. Calleri, and A. Astolfi, «Effect of façade shape and acoustic cladding on reduction of leisure noise levels in a street canyon», *Building and Environment*, vol. 157, pp. 242-256, jun. 2019, doi: 10.1016/j.buildenv.2019.04.039.

[6] A. Can, N. Fortin, and J. Picaut, «Accounting for the effect of diffuse reflections and fittings within street canyons, on the sound propagation predicted by ray tracing codes», *Applied Acoustics*, vol. 96, pp. 83-93, sep. 2015, doi: 10.1016/j.apacoust.2015.03.013.

[7] H. S. Jang, S. C. Lee, J. Y. Jeon, and J. Kang, «Evaluation of road traffic noise abatement by vegetation treatment in a 1:10 urban scale model», *The Journal of the Acoustical Society of America*, vol. 138, n.º 6, pp. 3884-3895, dic. 2015, doi: 10.1121/1.4937769.

[8] Sekunowo, O.I., Bolasodun, B.O., Oyedepo, C.P., and Oluwole, J.Y., «Noise Pollution Mitigation Study of Rice Husk-Ash Nanoparticle Reinforced Epoxy Resin Composites», *Journal of Engineering Research,* vol. 25, n.º 1, pp. 29-38, 2020.

[9] S. H. Adnan *et al.*, «Sound absorption of lightweight brick containing expanded polystyrene beads and palm oil fuel ash», *IOP Conf. Ser.: Earth Environ. Sci.*, vol. 476, n.º 1, p. 012026, abr. 2020, doi: 10.1088/1755-1315/476/1/012026.

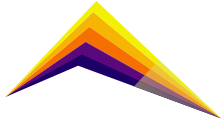

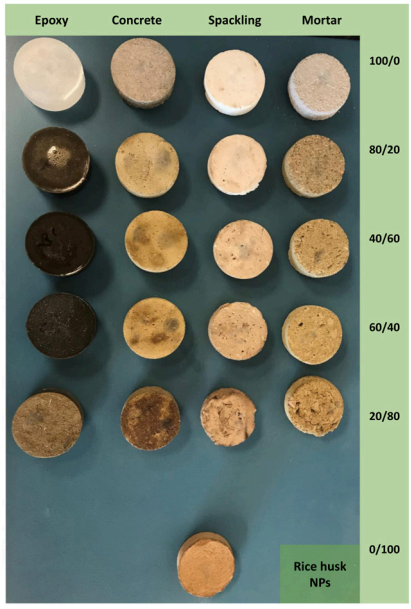

Figure 1. Impedance tube parts.

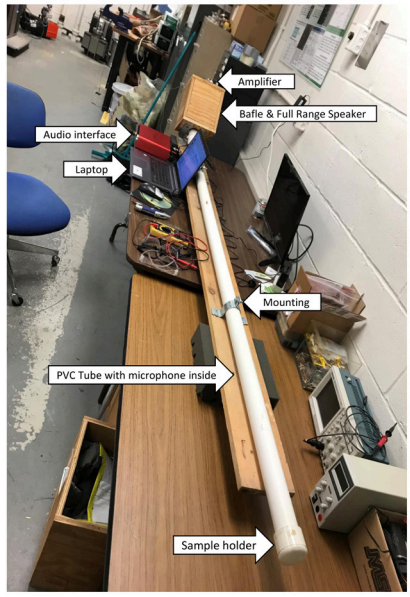

Figure 2. Experiment design of samples analyzed in the impedance tube. From left to right (Epoxy Resin, Concrete Mix, Vinyl Spackling, Mortar Mix). From top to bottom Composite/Rice Husk NPs (100/0, 80/20, 40/60, 60/40, 20/80, 0/100).

Table 1. Average sound absorption coefficient without 125 Hz band. Mortar Mix (M.M), Vinyl Spackling (V.S.), Concrete Mix (C.M.), and Epoxy Resin (E.R.).

Binder/RH NPs	M.M.	V.S.	C.M.	E.R.
0/100	0.194321196	0.27399906	0.28037818	0.18972408
80/20	0.338252799	0.3248794	0.27430583	0.22273658
60/40	0.370166503	0.32953486	0.33202627	0.23279424
40/60	0.422647695	0.40551438	0.39710952	0.26262751
20/80	0.485599471	0.45785742	0.49419635	0.38928149
0/100	0.51531598	0.51531598	0.51531598	0.51531598

Hybrid dust of construction and demolition waste in the compressive strength of hydraulic concrete mixtures

L. Carolina Hernández G. *Email: carolina.hernandez8@udea.edu.co*
Henry A. Colorado L. *Email: henry.colorado@udea.edu.co*

Universidad de Antioquia, Facultad de Ingeniería. Bloque 20, Calle 67 No. 53 - 108, Medellín, Colombia.

Abstract

The use of recycled aggregates in the production of concrete brings with it interesting challenges due to its high absorption, cracking, porosity and variability in chemical composition. This work describes the mechanical behavior of a mixture of hydraulic cement and recycled aggregates through compression tests of concrete cylinders, prepared in the laboratory and compacted with a vibrating table. The blends were made using gravel and sand that were manufactured from a recycling plant for Construction and Demolition Waste CDW, sands that result from the crushing and spraying of bricks and clay ceramics, and the hybrid dust that results from the spraying of CDW waste. The experimental model contemplates several dosages of the mixture replacing cement with the hybrid powder, so that the appropriate dosage is interpolated to guarantee the greatest resistance. The results indicate that the hybrid powder of CDW, consisting of silica, calcite and 40% amorphous, behaves as a supplementary cementitious material that could replace 20% of the cement content, in a conventional hydraulic concrete. Studies indicate that brick dust has a higher activity than concrete waste dust, because brick is a ceramic made of clays that are thermally activated

Correspondent author

after firing. This work characterized both ceramic powder and hybrid powder, understanding as a hybrid the mixture of various wastes such as concrete, bricks, masonry and glass. Similarities were found in the amount of amorphous, which facilitated the development of resistances, despite the reduction of cement in some mixtures. The current research is part of local efforts for improving materials and processes towards circular economy and sustainable goals.

Key words: demolition and construction waste, powder, aggregates, recycling

Introduction

Some of the biggest challenges of the construction sector is to improve the efficiency of raw materials, and to reduce the volumes of resource exploitation and the production of waste. The techniques of implementing the recycling of demolition and construction waste (CDW) are growing with the state policies and government support [1]. Although there are numerous investigations that point to the transformation and reuse of CDW ([2], [3]), the imbalance between demand and supply in the market, the lack of supervision and regulation, and the inferior quality of the products, put barriers to the flow of the circular economy in these materials [4].

Despite all the difficulties, the applications of recycled debris aggregates in concrete are limited because they increase the porosity of the mixture, have high absorption, which reduces fluidity and resistance[5]. However, it is known that some residues are thermally activated, such as bricks [6]. This paper describes the mechanical behavior of a concrete made with hydraulic cement and recycled aggregates through compression cylinder tests. In this case, gravels that were crushed from CDW, manufactured sands from CDW, sands that result from the crushing and spraying of bricks and clay ceramics, and the hybrid dust that results from concrete, bricks, masonry, and glass are used. Several dosages of cement replacement by hybrid powder are carried out, so that the appropriate dosage is sought to guarantee the greatest resistance. This is a local effort towards increasing the circularly of materials and sustainability of processes particularly in large scale solid wastes, that includes CDW [7], hazardous waste [8], aggregates [9], organic waste [10], and rubber tires [11]–[13].

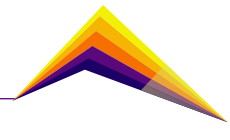

Materials and Methods

The materials included natural sand (N-S), processed sand from CDW (S-CDW), gravel of maximum size of 1" crushed from CDW (G-CDW), Brick Sand (A-L), hybrid powder CDW, passes Sieve No. 80 (PH), hydraulic cement, water, and plasticizing additive. After performing the physical characterization of all aggregates (see Table The granulometric curve is then adjusted to ensure the highest density of vibro-compressed concrete, without using the traditional methods of emptying, compaction and vibrating of conventional concrete.

Table 1), granulometry is performed by Sieving with washing to adjust the mixture according to the Fuller-Thompson curve to establish the optimal dosage of aggregates. The granulometric curve is then adjusted to ensure the highest density of vibro-compressed concrete, without using the traditional methods of emptying, compaction and vibrating of conventional concrete.

Table 1. Characterization of the physical properties of aggregates

Sample	S-CDW	B-S	N-S	G-CDW
Absorption	10.67%	9.52%	2.71%	9.77%
Bulk Density	2.308 gr/cm³	2.451 gr/cm³	2.528 gr/cm³	2.332 gr/cm³
Loose unit mass	1.517 gr/cm³	1.472 gr/cm²	1.268 gr/cm³	1.571 gr/cm³
% Empty	49%	51%	86%	30%

The chemical characterization and mineralogical composition of the hybrid powder and manufactured sand of the brick waste is carried out through the use of an analytical method of X-ray diffraction (DRX) in a Malven-PANalytical Diffractometer Empyean Model 2012 and X-ray fluorescence (XRF) with a Thermo ARL Optim'X WDXRF equipment. 215 cylindrical samples of 3 in diameter with different proportions of DRC hybrid powder were prepared, according to the ASTM-C172M-17 test standard [14]. The compaction method used was done with vibrating Table [15]. Samples were covered with plastic for the first 24 hours and then cured by immersion in water at 23°C until the age of the compression test, in accordance with the ASTM-C192M-19 standard [16]. Samples were failed at 7 days, others at 14 days and others at 28 days of age, at simple compression according to the test standard.

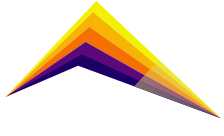

Table 2. Dosage of aggregates in the mixture (percentage by weight)

Material	S-CDW	S-N	B-S	G- CDW
Dosage	22%	24%	3%	51%
Sand	45%	48%	7%	

Table 3. Phase quantification of hybrid powder HP

No.	Name	Chemical formula	Composition (%)
1	Rutile	TiO2	Not applicable
2	Quartz low	SiO2	37.1
3	Calcite	CaCO3	15.6
4	Microcline	AlKO8Si3	1.3
5	Lizardite 1T	H4Mg3O9Si2	5.4
6	Amorphous material		40.6

Results and analysis

The results of the tests that were carried out in X-ray diffractometer (XRD) record that the sample 'hybrid powder RDC' presents 40.6 of amorphous material, with the phases summarized in Table 3. While of the brick sand (S-B) it registers 43% of amorphous, in a different distribution of phases, as shown in Table 4.

Table 4. Quantification of phases of brick sand B-S

No.	Name	Chemical formula	Composition (%)
1	Quartz low	SiO_2	43
2	Plagioclasa	$(Ca)Al_1Si_3O_8$	5
3	Calcite	$CaCO_3$	2
4	Hematita	Fe_2O3	3
5	Tridimita	$AlKO_8Si_3$	2
6	Caolinita	$H_4Mg_3O_9Si_2$	3
7	Amorphous material		43

With the X-ray fluorescence (XRF), the chemical composition for the CDW hybrid dust sample has been obtained and presented in Table 5.

Table 5. XRF chemical composition analysis of CDW hybrid powder

Oxide	%p/p	Oxide	%p/p	Oxide	%p/p
SiO2	46.81	P2O5	0.404	ZnO	0.0230
CaO	19.64	Na2O	0.197	CuO	0.0168
Al2O3	14.10	ZrO2	0.0923	WO3	0.0116
Fe2O3	3.980	BaO	0.0643	NiO	0.0110
SO3	1.080	SrO	0.0505	PbO	0.0088
MgO	0.835	MnO	0.0479	CeO2	0.0063
K2O	0.815	V2O5	0.0275	Nb2O5	0.0015
TiO2	0.795	Cr2O3	0.0254	-	-

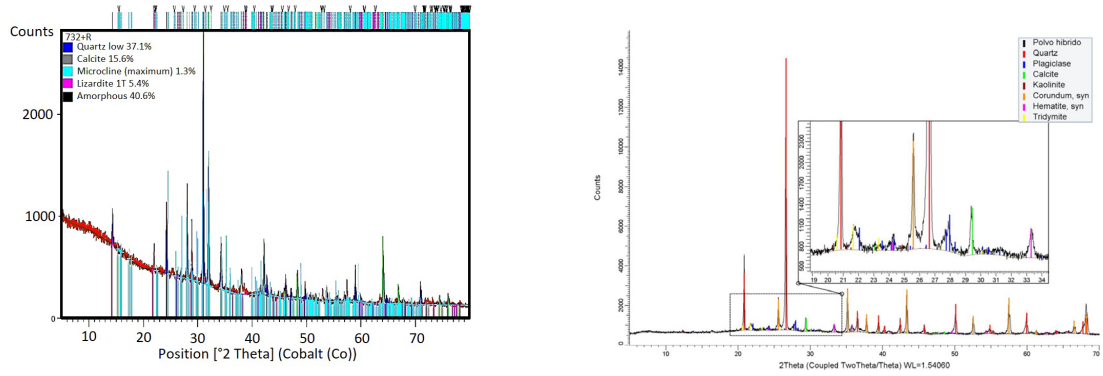

Figure 1. XRD patterns of hybrid powder and brick dust

On the other hand, the compression tests of the mixtures indicate that a development of resistances ranging from 1000 psi at 3 days of age, to 4000 psi at 28 days.

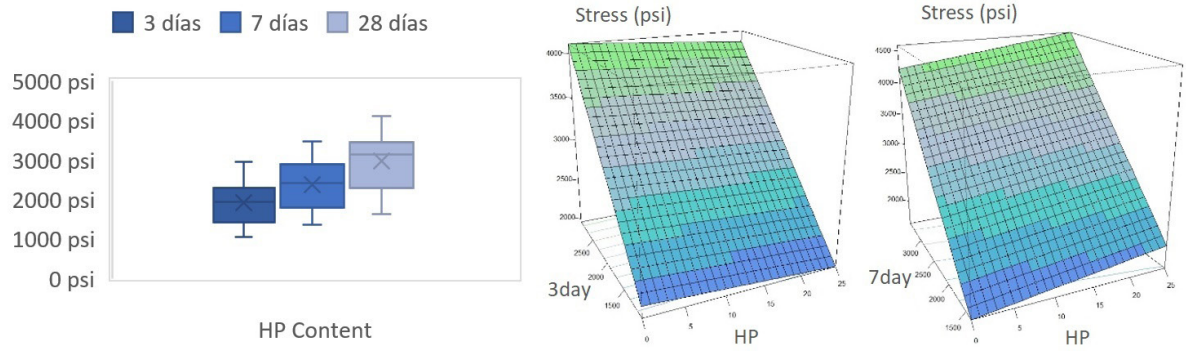

Figure 2. Development of resistances in the time of maturity of the concrete

Performing Anova to the previous results, it is observed that the dosage of hybrid powder significantly affects the compressive strength, see Table 6.

Table 6. Anova of the linear model of correlation between PH content and resistance

	Df	Sum Sq	Mean Sq	F value	Pr (>F)
HP	1.0	2868723	2868723	28.305	0.00003306***
3day	1.0	6708833	6708833	66.195	8.974E-08***
7day	1.0	2079922	2079922	20.522	0.0002039***
Residuals	20.0	2026984	101349		

Correlating the HP hybrid powder content, with the resistance recorded at 3 days of age, it is observed that the response surface is positive and increasing, almost linear. In relation to the optimal content of hybrid powder in the hydraulic concrete mixture, the means of the test results at 28 days of age are correlated, resulting in a parabolic function, which indicates a maximum value of 9.8% ≈10%.

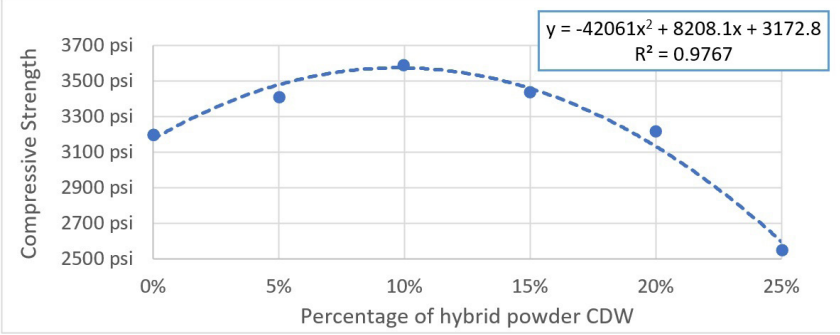

Figure 3. Compressive strength of mixtures replacing different percentages of cement with hybrid powder

Summary

The chemical characterization indicates that the percentage of amorphous brick waste dust is similar to that of CDW hybrid powder, facilitating the production process in the recycled aggregates plant. Recycled aggregates have higher absorption percentages than natural aggregates, so they should be used in low-fluid mixtures with super plasticizing additives. The dosage used is for a concrete of 3000 psi, which has in addition to the proportion of aggregates of Table 2, 300 kg of cement for a cubic meter of mixture. With the replacement of 10%, that is, with 30 Kg of hybrid powder and 270 Kg of cement, an average resistance of 3583 psi was recorded, that is, with a replacement of 20% of the cement the same resistance of the mixture without hybrid powder would be achieved. This in terms of dosage, is equivalent to 58 Kg of cement less for each cubic meter of concrete, which would be replaced by 58 Kg of the hybrid powder. This represents savings not only in the production of hybrid powder but also in the manufacture of concrete. Certainly, the implementation of these results contributes to reduce pollution and improve sustainability of materials and processes.

References:

[1] T. B. Christensen, "Closing the material loops for construction and demolition waste: The circular economy on the island Bornholm, Denmark," *Resources, Conservation & Recycling Advances*, vol. 15, p. 200104, Nov. 2022, doi: 10.1016/j.rcradv.2022.200104.

[2] F. de Andrade Salgado and F. de Andrade Silva, "Recycled aggregates from construction and demolition waste towards an application on structural concrete: A review," *Journal of Building Engineering*, vol. 52. Elsevier Ltd, Jul. 15, 2022. doi: 10.1016/j.jobe.2022.104452.

[3] Q. Zeng *et al.*, "Total recycling of low-quality urban-fringe construction and demolition waste towards the development of sustainable cement-free pervious concrete: The proof of concept," *J Clean Prod*, vol. 352, Jun. 2022, doi: 10.1016/j.jclepro.2022.131464.

[4] A. Luciano, L. Cutaia, P. Altamura, and E. Penalvo, "Critical issues hindering a widespread construction and demolition waste (CDW) recycling practice in EU countries and actions to undertake: The stakeholder's perspective," *Sustain Chem Pharm*, vol. 29, p. 100745, Oct. 2022, doi: 10.1016/j.scp.2022.100745.

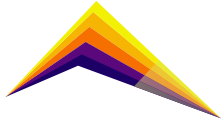

[5] E. Garzón, S. Martínez-Martínez, L. Pérez-Villarrejo, and P. J. Sánchez-Soto, "Assessment of construction and demolition wastes (CDWs) as raw materials for the manufacture of low-strength concrete and bases and sub-bases of roads," *Mater Lett*, vol. 320, Aug. 2022, doi: 10.1016/j.matlet.2022.132343.

[6] K. Lazaar, W. Hajjaji, B. Moussi, F. Rocha, J. Labrincha, and F. Jamoussi, "Metakaolin and demolition wastes in eco-based sand consolidated concrete," *Boletin de la Sociedad Espanola de Ceramica y Vidrio*, 2020, doi: 10.1016/j.bsecv.2020.02.004.

[7] H. A. Colorado, A. Muñoz, and S. Neves Monteiro, "Circular Economy of Construction and Demolition Waste: A Case Study of Colombia," *Sustainability*, vol. 14, no. 12, p. 7225, Jun. 2022, doi: 10.3390/su14127225.

[8] E. Ordoñez, S. Neves Monteiro, and H. A. Colorado, "Valorization of a hazardous waste with 3D-printing: Combination of kaolin clay and electric arc furnace dust from the steel making industry," *Mater Des*, vol. 217, May 2022, doi: 10.1016/j.matdes.2022.110617.

[9] G. Agudelo, C. A. Palacio, S. Neves Monteiro, and H. A. Colorado, "Foundry Sand Waste and Residual Aggregate Evaluated as Pozzolans for Concrete," *Sustainability*, vol. 14, no. 15, p. 9055, Jul. 2022, doi: 10.3390/su14159055.

[10] J. E. Jiménez, C. M. Fontes Vieira, and H. A. Colorado, "Composite Soil Made of Rubber Fibers from Waste Tires, Blended Sugar Cane Molasses, and Kaolin Clay," *Sustainability (Switzerland)*, vol. 14, no. 4, Feb. 2022, doi: 10.3390/su14042239.

[11] C. F. Revelo Huertas, C. M. F. Vieira, and H. A. Colorado, "A hybrid composite for structural applications made of rubber waste tires and calcium phosphate cement," *Int J Appl Ceram Technol*, vol. 18, no. 4, pp. 1342–1353, Jul. 2021, doi: 10.1111/ijac.13747.

[12] G. Agudelo, S. Cifuentes, and H. A. Colorado, "Ground tire rubber and bitumen with wax and its application in a real highway," *J Clean Prod*, vol. 228, pp. 1048–1061, Aug. 2019, doi: 10.1016/j.jclepro.2019.04.353.

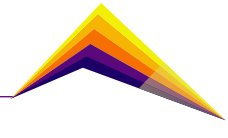

[13] C. F. Revelo, M. Correa, C. Aguilar, and H. A. Colorado, “Composite materials made of waste tires and polyurethane resin: A case study of flexible tiles successfully applied in industry,” *Case Studies in Construction Materials*, vol. 15, Dec. 2021, doi: 10.1016/j.cscm.2021.e00681.

[14] ASTM International, *C172/C172M − 17 Standard Practice for Sampling Freshly Mixed Concrete*. 2017, pp. 1–3. doi: 10.1520/C0172_C0172M-17.

[15] ASTM International, *C1176/C1176M -20 Standard Practice for Making Roller-Compacted Concrete in Cylinder Molds Using a Vibrating Table*. 2020, pp. 1–5. doi: 10.1520/C1176_C1176M-20.

[16] ASTM International, *C192/C192M-19 Standard Practice for Making and Curing Concrete Test Specimens in the Laboratory*. 2019, pp. 1–8. doi: 10.1520/C0192_C0192M-19.

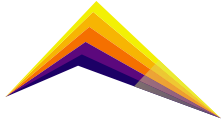

Vulnerability assessment by geographic information systems in buildings of the historic center of Tunja

Hernandez- Carrillo Carlos Gabriel *Email: jeiser.rendon@udea.edu.co*
Alarcon, Juan José *Email: juan.tarazona@uptc.edu.co*
Gutierrez- Junco, Oscar Javier *Email: oscarjavier.gutierrez@uptc.edu.co*

Rsearchers, Universidad Pedagógica y Tecnológica de Colombia

Abstract

The phenomena of globalization and urban inclusion have repercussions on the restructuring of cities. Therefore, urban recovery policies must be formulated to preserve the historical and architectural heritage. Recently, the notion of vulnerability has been promoted as a dimension of the social development of the territory that seeks to mitigate the risks generated by the various socioeconomic activities integrated in the changing environment and the affectation of performance, stability of structures and risk mitigation. Therefore, this research analyzes the phenomena of vulnerability in the buildings that make up the historic center of Tunja, by means of geographic information systems. Likewise, this evaluation allowed the analysis of the affectation of these buildings, together with the understanding of the causes, types, and severity of the damages, illustrated through the geospatial distributions of variables related to the components of the building, which allows capturing the variability, capacity and use derived from the state and vulnerability of the heritage that integrates the historic center of Tunja.

Correspondent author

Keywords: Vulnerability, Geographic Information Systems, Historic Center, Tunja, Building, Risk.

Introducción

The city of Tunja, located in the Andes Mountains and the heart of the Cundinamarca-Boyacá highlands, is the capital of the department of Boyacá and is home to a historic center enriched by an extensive cultural and architectural heritage. This spectrum of historical infrastructure and monumental ensembles reflect and represent great events of Colombian history along with the accumulated heritage of an active and dynamic community that constituted as the largest concentration of demographic and commercial activity, the result of its formation as an urban center since pre-Hispanic times. Therefore, due to its historical and patrimonial importance, efforts must be made to preserve, defend, watch over, incorporate and transmit the values inherited by a living cultural nucleus and socially organized communities that guarantee the historical patrimonial legacy, by safeguarding its protection and conservation in its diverse manifestations and tending to disappear, as a result of the new socioeconomic activities present today[1]however, remains an on-going challenge, as information is often expressed in different data representations and stored in disparate locations and formats. There have been a limited number of studies that have examined the relationship among physical objects, schedule, and quality management information related to the process of inspection as well as the difficulties associated with enabling real-time monitoring and control of quality. In addressing this issue, a design science research approach is used to develop and apply an Industrial Foundation Classes-based Inspection Process Model (IFC-IPM [2].

For the above reasons, this research analyzed characteristics related to vulnerability phenomena in the buildings that make up the historic center of Tunja. This by means of geographic information systems and integration of previously validated qualitative indicators of quality, from its collection, acquisition, compilation, and derivation of the state and vulnerability of the heritage that integrates the historic center of Tunja, the resulting data are concatenated through the use of Geographic Information Systems (GIS) along with the formulation of a methodology that allows generating reliability, credibility and quality of content that allows its impact on decisions aimed at sustainable conservation of heritage.

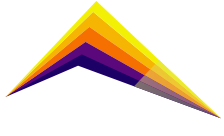

Methodology

General procedure to establish vulnerability characteristics in buildings in the historic center of Tunja.

Figure 1 illustrates the methodological process for establishing the vulnerability of buildings in the historic center of Tunja.

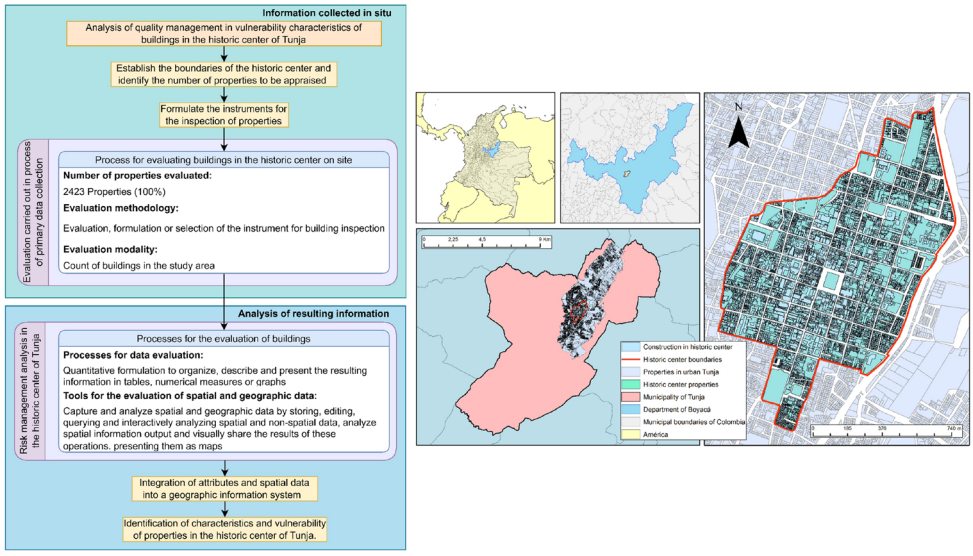

Figure 1. Schematic diagram of the methodology implemented.

Resolution 0428 of 2012, "Special Management and Protection Plan for the Historic Center of the City of Tunja" [3] establishes the study area as the area that integrates the historic center of Tunja, without considering its zone of influence. This area has an extension of 1,124,132.21 m² and a total of 2423 properties.

Form for inspection of building vulnerability

Using the inspection and scoring methodology, formulated by the Association of Earthquake Engineering (AIS) through the "*Single form for inspection of buildings after an earthquake*"[4]. Identified Potential structural deficiencies and characterized by attributing numerical values to each significant component of the building. Based on the above, the methodology based on damage states (obtained through demand versus capacity ratios in terms of stiffness, strength and energy dissipation), is expressed in the standardization of its percentage, according to the qualitative assessment shown in Table 1.

Table 2. Percentage of damage assessment in buildings

Habitability rating (color)	Damage type	Damage range (%)	Description
Habitable (Green)	None	0	No damage
Habitable (Green)	Slight	0-10	Minor localized damage to some elements that does not always require repair.
Restricted Use (Yellow)	Moderate	10-30	Minor localized damage to many elements that must be repaired.
Not habitable (Orange)	Heavy	30-60	Extensive damage requiring major repairs.
Danger of collapse (Red)	Severe	60-10	Severe widespread damage may mean demolition of the structure.
Collapsed	Total Collapse	100	Total destruction or collapse.

Results and analysis

Figure 2 illustrates the habitability assessment according to the AIS methodology proposed and evaluated in the historic center of Tunja. This was formulated based on detailed knowledge of the geometric and structural characteristics of the buildings [5]. Therefore, the spatial distribution of buildings with different structural systems is evidenced in the architectural heterogeneity, commercial and damage-related information described in urban environments, and vulnerability phenomena through the use of Geographic Information Systems (GIS)[6].In addition, some risks can be anticipated and their identification allows the assignment of changes in scope, requiring different types of response, integrated in an urban planning proposal according to the appropriate identification.

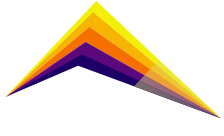

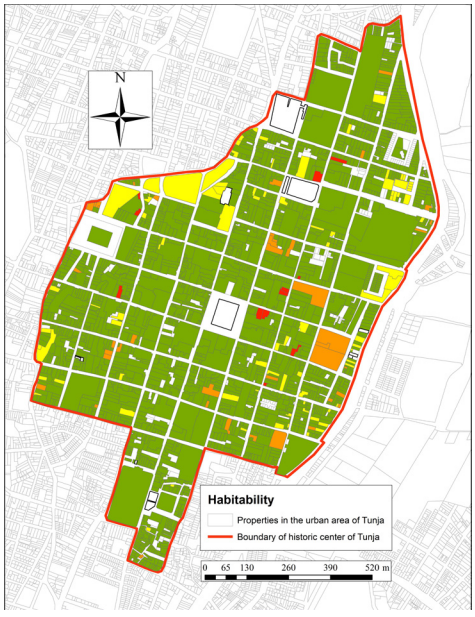

a)

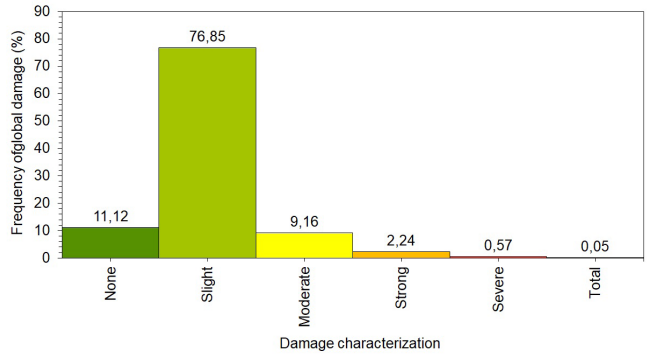

b)

Figure 2. Classification of damage in the historic center of Tunja. a). Global frequency of damage to buildings in the historic center of Tunja. b). Global frequency of damage to buildings in the historic center of Tunja.

Therefore, through analytical support, a sustained evaluation and response and control strategies, the areas of greatest damage are identified, integrated by the spatial location of the damage concentration and its relationship with the residential areas on the eastern side of the historic center with a larger vulnerable population [7]. Likewise, the buildings in danger of collapse represent a latent risk and these are distributed in areas near the central square (Bolivar), which adds to the impact of a larger population.

In addition, the quality of the construction materials and their structural system is fundamental to provide the resistance of the elements that compose the building. Therefore, the evaluation of these properties indicates a susceptibility to seismic events or those that imply the reduction of the mechanical resistance of the material. Therefore, the use of unreinforced masonry predominates in the residences located in the southeastern area of the city with the greatest damage identified. This evaluation is shown in Figure 3.

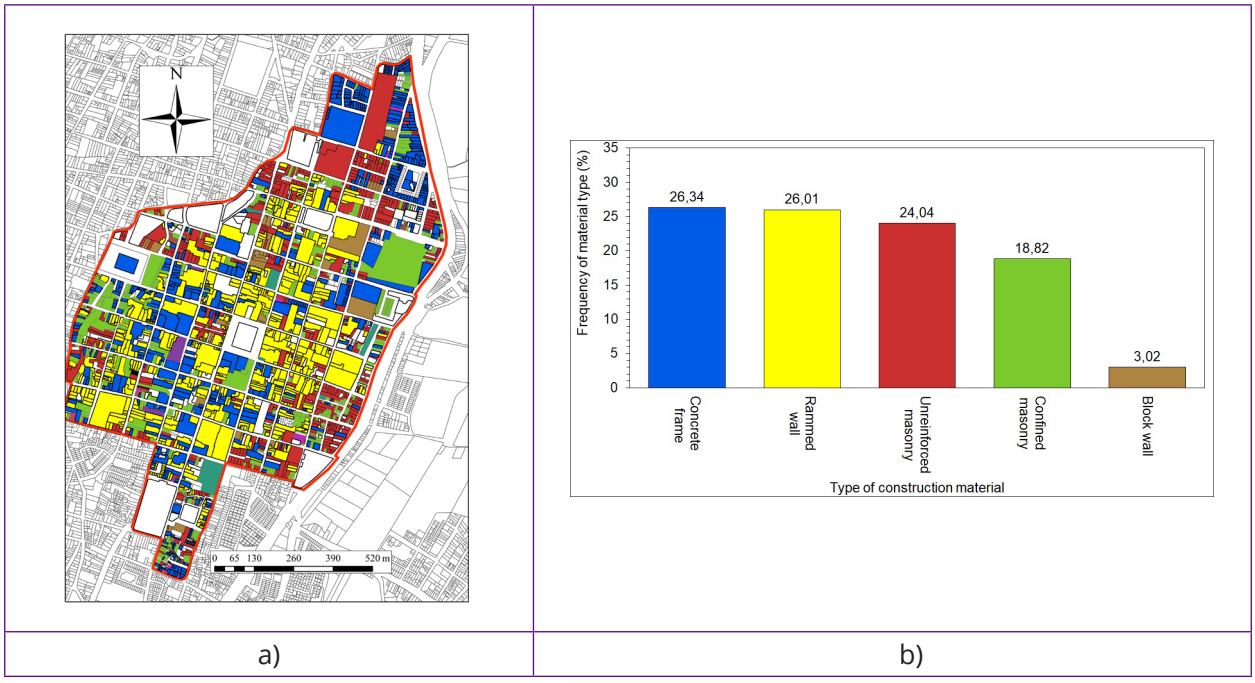

a) b)

Figure 3. Type of materials and structural system of the buildings in the historic center. a) GIS of these attributes. b) Majority frequencies according to number of buildings.

On the other hand, the materials and structural systems of clay wall or block together with unreinforced masonry make up 50% of the buildings in the historic center, consistent with the type of heritage buildings, which in the majority of these types of materials are used for one and two-story houses. In view of the above, the susceptibility to phenomena involving the integrity and wear of these buildings is greater, especially if the proposed use is residential, due to the low investment in maintenance.

Evaluation of densities or zone of influence of damage in the historic center of Tunja

Figure 4 illustrates the conformation of the Kernel densities, which show zones with different strong, severe and total damage. In addition, these are correlated with the habitability and the construction materials that compose the structural systems in residential buildings in the zone of highest structural and social vulnerability. These are related to masonry materials and masonry walls. Although the type of buildings with these characteristics is numerically lower, the risk is higher, since the southeast zone concentrates the largest number of areas of residential and commercial use. Therefore, risk management can be the basis for planning that integrates quality management systems [6].

Figure 4. Densities or zones of influence of damage and habitability in the historic center of Tunja.

Conclusions

Thanks to the implementation of tools to identify the physical conditions of the properties, it is possible to reinforce the management and application of information technologies through geographic information systems applied to the heterogeneous environment of the historic center, which is composed of a diverse and enriched historical and architectural heritage for its preservation. The evaluation of vulnerability and risk in buildings in the historic center of Tunja allows the support of strategic planning decisions that incorporate adaptation actions in the face of the diverse changes in the urban environment.

References

[1] L. Ding, et al, “An IFC-inspection process model for infrastructure projects: Enabling real-time quality monitoring and control,” Aut Const, vol. 84, pp. 96–110, 2017.

[2] H. Senaratne, et al, “A review of volunteered geographic information quality assessment methods,” Int. J. Geogr. Inf. Sci., vol. 31, no. 1, pp. 139–167, 2017.

[3] Ministerio de Cultura, Resolución 0428 del 27 de Marzo de 2012. República de Colombia, 2012, p. 37.

[4] Asociación Colombiana de Ingeniería Sísmica – AIS, Guía técnica para inspección de edificaciones después de un sismo. Bogotá D.C: Alcaldia Mayor de Bogotá, 2002.

[5] A. Costanzo et al., “The Combined Use of Airborne Remote Sensing Techniques within a GIS Environment for the Seismic Vulnerability Assessment of Urban Areas : An Operational Application,” MDPI, vol. 8, no. 146, p. 22, 2016.

[6] E. Osipova and P. E. Eriksson, “Balancing control and flexibility in joint risk management: Lessons learned from two construction projects,” Int. J. Proj. Manag., vol. 31, no. 3, pp. 391–399, 2013.

[7] S. M. E. Sepasgozar, et al , Delay causes and emerging digital tools: A novel model of delay analysis, including integrated project delivery and PMBOK, vol. 9, no. 9. 2019.

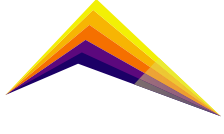

Analysis of the geographic coverage of urban green areas and its relationship with the socioeconomic conditions of the population in Tunja, Boyacá

Alarcón, Juan José *E-mail: juan.tarazona@uptc.edu.co*
Hernández Carrillo, Carlos Gabriel *E-mail: carlosgabriel.hernandez@uptc.edu.co*
Sarmiento Rojas, Jorge Andrés *E-mail: jorge.sarmiento02@uptc.edu.co*

Research, Universidad Pedagógica y Tecnológica de Colombia

Abstract

Colombian cities like Tunja have experienced accelerated urban development in recent decades. This leads to require different formulations that support government politics for harmony between socioeconomic variables, urban planning and the environment in coherence with the objectives of sustainable development. However, at present there are deficiencies in implementing ideas in the set of land-use planning policies, which have been insufficient and historically have focused on the construction of physical infrastructure, urban facilities and elements centered on short-term solutions to supply of first-order needs. Therefore, the evaluation of urban services is relevant for the diagnosis and constitution of green areas, together with the evaluation of socioeconomic variables, through institutional open data and their integration in geographic information systems for proximity and coverage analysis of the current green areas and their relationship with the socioeconomic conditions of the potential population that accesses those spaces. As result, it was established that green areas in Tunja are not homogeneously distributed.

Correspondent author

For that reason, there are areas with null coverage, which relates to the vulnerable population and reduced economic resources. Consequently, this research supports the public policy approach to improve socioeconomic and environmental development in a harmonious and equitable manner.

Key words: Human geography, Urban planning, Urban population, Tunja

Introduction

The concept of green areas includes ecological, economic and social sustainability variables, allowing these elements to be considered as inclusive spaces with diverse population uses [1]. Medrano y Quintero [2] demonstrated that the adequate planning of these spaces generates social, environmental and economic benefits, including: air quality improvements, urban heat island reduction, carbon sequestration increase, public health improvements, interpersonal ties creation and population social identity strengthening . Despite these benefits, planning policies in Latin American cities often focus on physical infrastructure construction or industrial complexes [3]. In addition, population dynamics have caused an accelerated cities densification. Alarcón et al [4] described the land evolution within the urban area of Tunja and the influence of social, political and economic events that motivated the infrastructure construction. In terms of indicators, Tunja has a low coverage, where the green area per inhabitant is 1.34 m2, which is low compared to the national parameter of 15 m2 per inhabitant [4]. In addition to the disorderly growth, the poor planning and execution of public policies have caused the relationship between the number of inhabitants and green areas to show a decreasing trend.

The first approach to the construction of these policies consists of identifying the areas where the population has less access to certain elements of urban infrastructure. By mapping those elements, it is possible to efficiently manage land use, the road network and high-impact property aspects [5]–[8].

The facilities general condition is that their distribution should be equitable and homogeneously distributed to the population [9]. Therefore, the study has two objectives: first, to identify whether there is a green areas homogeneous coverage within the urban area and second is to characterize the population socioeconomic conditions with access to those spaces.

Methodology

The research has a methodology composed by 3 stages. The first stage comprises the digitization of green areas based on the principle of minimum considerable area. The second comprises the application of geographic processing algorithms that analyze the accessibility to areas of interest represented by isochrones. Finally, the third stage comprises the production of digital cartography and reports according to the need. The last stage comprises the areas of interest analysis and the export of maps. The methodological scheme is presented in Figure 1.

Among the techniques and inputs, zoning was carried out using an orthomosaic of the year 2021. The accessibility criterion used corresponds to that proposed by Boone et al [10], who concluded that the average distance a person travels to a park is 400 meters.

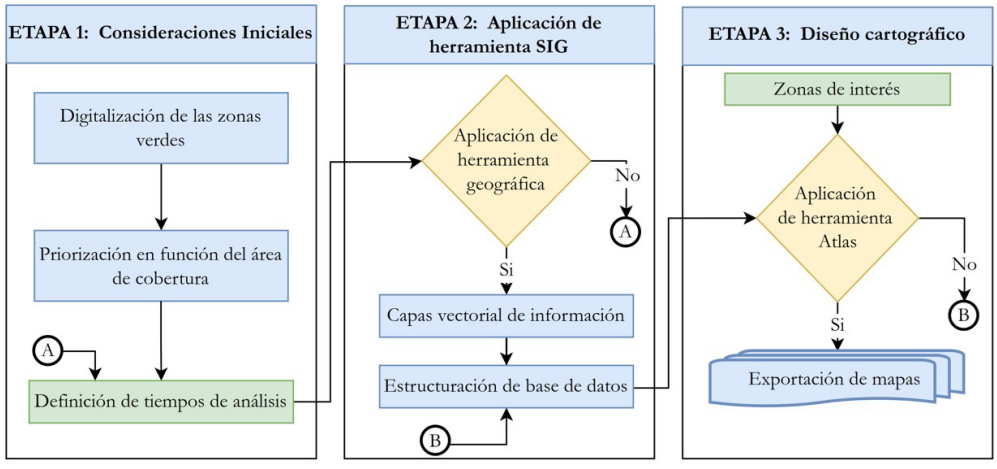

Figure 1. Proposed methodological scheme.

Results and analysis

In order to identify the concentration areas , the urban division proposed by the National Administrative Department of Statistics (DANE) was adopted, which divides Tunja into 24 zones, as shown in Figure 2.

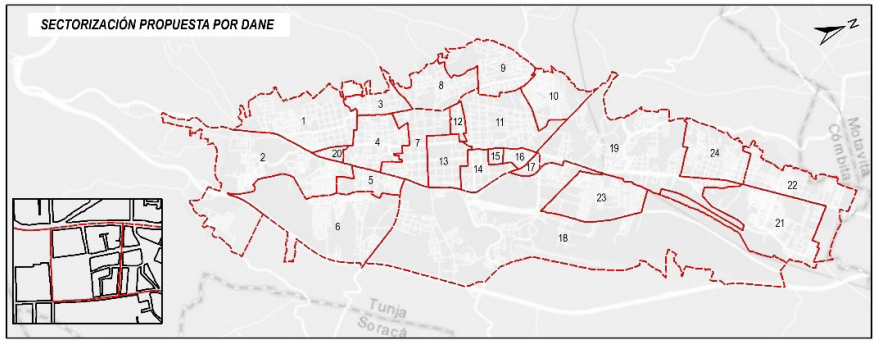

Figure 2. Schematic sectorization of the city.

Figure 3 shows the spatial distribution of green areas and their coverage according to a 400 m radius. The isochrones represent the coverage distribution of those elements for a distance of 200 m and 400 m respectively. It is possible to identify certain areas of the city that lack green coverage. These areas are located on the urban expansion corridor or in marginal areas of the city.

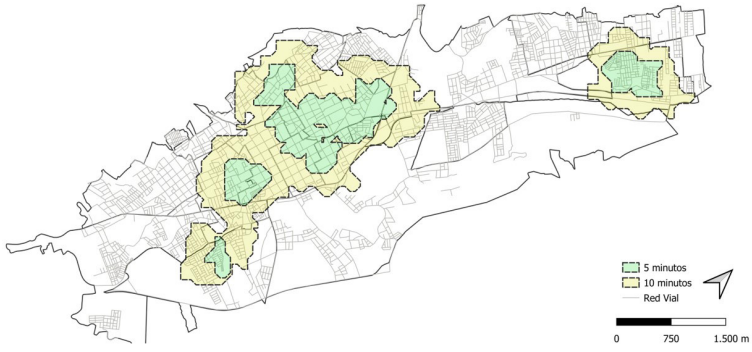

Figure 3. Representation of green area coverage.

Based on the proposed distribution, the sectors with the largest number of parks are 6, 10, 19, 21 and 23. At the same time, the sectors without parks are sectors 5, 7, 13, 15 and 20. Sectors 5, 13 and 15 do not have park areas; they are located in the center of the city and are characterized by steep slopes, few unbuilt polygons and a high concentration of urban facilities for non-recreational activities. Among the neighborhoods that are part of these

sectors are: Balcones del Norte, Ciudadela Comfaboy, El Dorado, El Rodeo, Fuente Higueras, La Esmeralda, La Colina, Montecarlo, Olímpica, Pinar del Río, Portales de Terranova, San José and Santa Teresa.

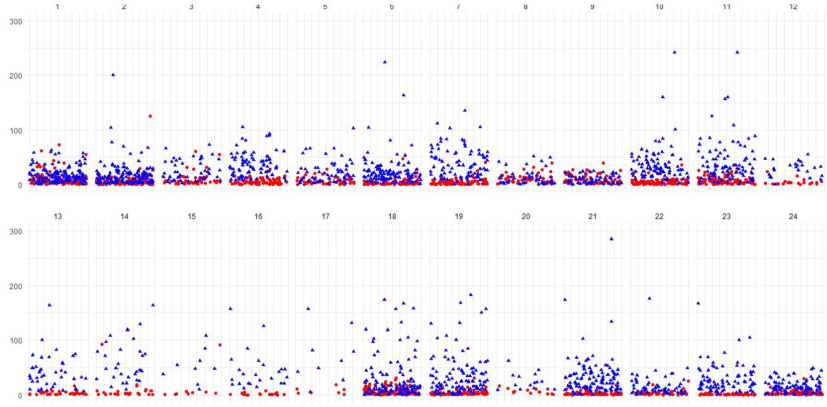

(a)

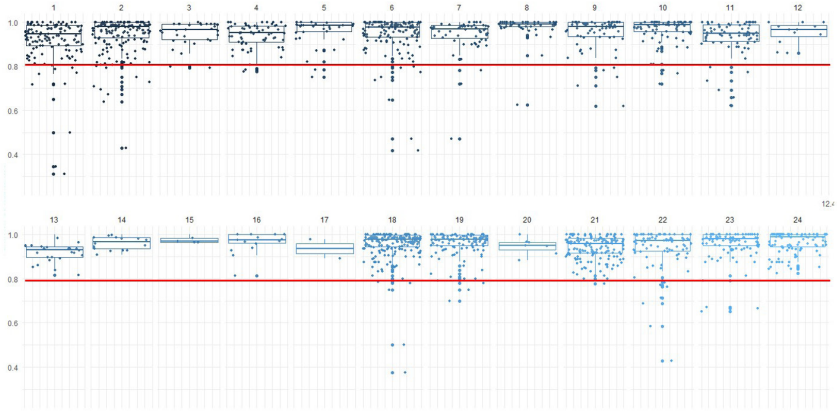

(b)

Figure 4. Distribution of people with professional educational level.

Graph 4.a shows the number of people with no education (in red) and those with university degrees (in blue). It can be seen that sectors 1, 2 and 3 have the highest uneducated population; these areas are located in the southwestern part of the city. In Figure 4.b in terms of service coverage, sectors 1, 2, 6, 7, 8 and 18 have the lowest coverage of comprehensive services. The above allows inferring that there is no direct relationship between the population's socioeconomic conditions with the green areas accessibility conditions.

Conclusions

The spatial distribution of urban facilities in Tunja is not homogeneous, contradicting its fundamental principle. This should be the basis for decision making and the creation of plans that allow decentralization and increased coverage in less favored areas. The results obtained allow the identification of zones without green area coverage and their relationship with sociodemographic variables of their population.

The use of GIS proves to be a tool that facilitates the analysis of population dynamics within a city, since through them, it is possible to simultaneously compare a set of data from different variables and time periods. Open access data is an opportunity to progress in studies of this type, since its easy acquisition and management reduces time and costs that can be invested in the decision-making stage.

References:

[1] R. Flores Xolocotzi and M. González Guillén, "Consideraciones sociales en el diseño y planificación de parques urbanos," *Econ. Soc. y Territ.*, vol. 7, no. 24, pp. 913–951, 2007, doi: 10.22136/est002007242.

[2] L. Medrano Álvarez and J. R. Quintero González, "Experiencias De Valoración De Los Parques Urbanos En Las Ciudades. Contextos Regionales, Prospectiva Para Colombia," *AREA*, vol. 27, no. 1, p. 4, 2021, [Online]. Available: https://publicacionescientificas.fadu.uba.ar/ index.php/area/article/view/1819/1963.

[3] G. E. Flores Juca and J. G. Chica Carmona, "La pérdida de las áreas verdes privadas como consecuencia de la construcción irregular. El caso de Cuenca-Ecuador," *Estud. Sobre Arte Actual*, vol. 4, p. 10, 2016, [Online]. Available: https://dialnet.unirioja.es/servlet/articulo?codigo=5634812.

[4] J. Ruiz, E. Parra, and D. López, "Una visión geográfica de los parques urbanos de la ciudad de Tunja, Boyacá, Colombia," *Perspect. Geográfica*, vol. 20, no. 2, pp. 245–268, 2015, [Online]. Available: http://www.scielo.org.co/pdf/pgeo/v20n2/v20n2a02.pdf.

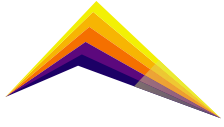

[5] G. Brown, “Mapping spatial attributes in survey research for natural resource management: Methods and applications,” *Soc. Nat. Resour.*, vol. 18, no. 1, pp. 17–39, 2005, doi: 10.1080/08941920590881853.

[6] G. Brown, “A method for assessing highway qualities to integrate values in highway planning,” *J. Transp. Geogr.*, vol. 11, no. 4, pp. 271–283, 2003, doi: 10.1016/S0966-6923(03)00004-8.

[7] G. Brown, “Mapping landscape values and development preferences: a method for tourism and residential development planning,” *Tourism*, vol. 113, no. November 2012, pp. 101–113, 2006, doi: 10.1002/jtr.

[8] B. Y. G. Brown and L. Alessa, “A GIS – based Inductive Study of Wilderness Values,” *Int. J. Wilderness*, vol. 11, no. 1, pp. 1–5, 2005.

[9] G. Speller and N. Ravenscroft, “Facilitating and evaluating public participation in urban parks management,” *Local Environ. Int. J. justice Sustain.*, vol. 10, no. 1, pp. 41–56, 2005, doi: 10.1080/1354983042000309300.

[10] C. G. Boone, G. L. Buckley, J. M. Grove, and C. Sister, “Parks and People: An Environmental Justice Inquiry in Baltimore, Maryland,” *Ann. Assoc. Am. Geogr.*, vol. 99, no. 4, pp. 767–787, 2009, [Online]. Available: http://eds.b.ebscohost.com.libproxy.smith.edu:2048/eds/pdfviewer/pdfviewer?sid=9d889308-036e-4fd7-a1e1-3324503d4446%40sessionmgr114&vid=7&hid=116.

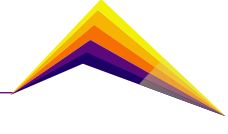

Application of isothermal heat treatments in AISI A2 tool steel to improve life of cold working tools

Jheison Tobón-Aguirre
Claudia Serna-Giraldo
Oscar Rios-Diez

E-mail: jheison.tobon@udea.edu.co
E-mail: claudia.serna@udea.edu.co
E-mail: eduardo.rios@udea.edu.co

Gipimme, Facultad de Ingeniería, Universidad de Antioquia, Medellín, Colombia.

Abstract

Cold work tool steels are characterized by their high resistance to abrasive and adhesive wear which allow them to perform well when they are used as tooling in carbon steel cold forming applications [1]. When the conformation process involves impact loads, as in stamping and impact cold forming, tool life decreases due to the generation and propagation of cracks on their cutting edges [2]. This is attributed to the limited toughness of cold work tool steels subjected to conventional quenching and tempering heat treatments (Q&T) [3]. As an alternative to the conventional Q&T heat treatment, isothermal heat treatments such as austempering and Quenching & Partitioning (Q&P) were proposed, which allow having multiphase microstructures composed of bainite, martensite, austenite, and carbides, which can improve the impact resistance of the tooling, furthermore, wear resistance levels like those obtained with Q&T [4-9]. For this reason, samples of AISI A2 tool steel were subjected to austempering and Q&P heat treatments. The results confirm that the formation of martensite, during the quenching step, reduces the bainite transformation times, because this martensite acts as a preferential nucleation site, and thus showed a reduction of bainite transformation times in the Q&P samples, compared with austempered samples. Also, the mechanical behavior was compared with samples of the same steel subjected to the Q&T cycle. The

Correspondent author

application of the isothermal route in AISI A2 tool steel favored to have significative improvements in impact resistance without a detriment in mechanical resistance compared with samples subjected to Q&T heat treatment.

Key words: Tool Steels, Bainite, Austempering, Quenching & Partitioning.

Introduction

The hardened microstructure, subjected to Q&T, of AISI A2 steel is mainly martensitic with lower quantities of retained austenite and a great quantity of carbides distributed throughout the material. This microstructure makes them ideal for applications with high abrasive and adhesive wear, providing them with superior performance compared with low alloy steels or other tool steels families [1]. Cold deformation processes in which the deformation is generated by impact loads, require tools that have good wear resistance and furthermore high impact resistance. This combination of properties is difficult to obtain with tool steels due to a great quantity of carbide-forming alloying elements. In the search for alternatives to improve the impact properties of these materials, bainitic microstructures could be an alternative. This option has been extensively studied in low-alloy steels [6], while in steels with high amount of alloying elements, such as tool steels, the studies are more restricted due to the carbides that precipitate and grow during isothermal holding. These carbides make more difficult to evidence improvements in impact properties [10]. The low rate of nucleation of bainite is another limitation to overcome in the application of isothermal heat treatments hence, the use of Q&P heat treatment is proposed. In this two-step isothermal heat treatment, the reduction of bainite transformation times is achieved, through the generation of preferential nucleation sites for bainite (austenite-martensite boundaries). With Q&P heat treatments bainite nucleation has been observed on the limits of martensite previously formed during the quenching stage, favoring the increase in nucleation sites, and therefore allowing the reduction of bainite transformation times [6].

Methodology

The heat treatments were carried out using commercial A2 steel of Uddeholm brand [2], the chemical composition was measured by Optical Emission Spectometry (OES) showed in table 1.

Table 1. Chemical composition and hardness of AISI A2 steel (Rigor)

Steel	Equivalent standards	Hardness	Chemical Composition					
			%C	**%Si**	**%Mn**	**%Cr**	**%Mo**	**%V**
AISI A2	BA2, F 5227	215 HB	1.0	0.3	0.6	5.3	1.1	0.2

Table 2 shows the conditions for the three types of heat treatments applied in this work. Conventional oil Q&T heat treatment was made for the purpose of comparison to an austempering heat treatment and two Q&P heat treatments, in which the quenching temperature was modified to vary the initial amount of martensite in the microstructure, allowing to determinate the influence of this parameter on the bainite transformation kinetics and the mechanical properties of the steel.

Table 2. Heat treatments conditions applied to AISI A2 steel

Heat treatment	T(°C) Austenitization	Austenitization time (min)	Quenching T(°C)	Quenching time (min)	T(°C) Isothermal holding	Isothermal time (min)
Q&T	950	45	N/A	N/A	N/A	N/A
Aust					300	180
Q&P-1			170	5		180
Q&P-2			150			180

The austenitization was performed in a controlled atmosphere furnace to minimize the decarburization of the surface, the holding time was 45 minutes. For isothermal holding time, sodium nitrite and potassium nitrate salt baths were used in a 50-50 ratio at 170°C and it was 70-30 ratio at 150°C, to guarantee their fusion. Dilatometry tests were carried out in a high-resolution dilatometer BAHR 805A. These tests allow to determine: 1) Critic temperatures Ac1, Ac3 and Ms according to different standard methods: [11] to Ms, [12] to Ac1, and [13] to Ac3, 2) Martensite formed during quenching, and 3) Advance of the bainitic transformation. A microstructural characterization allowed to determine the phases that are present, its distribution and quantities obtained by the heat treatments applied. The techniques used were: Optical microscopy (OM), by chemical etching with Nital 2%, Beraha and sodium metabisulfite it allowed quantify martensite and carbides phases by manual

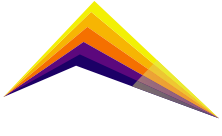

point count method ASTM E562 [14], Scanning electron microscopy (SEM), X-Ray diffraction (XRD) which allowed to quantify austenite present in each sample, according with ASTM E975-13 standard [15]. Charpy test was executed according to ASTM E-23 standard [16] with unnotched specimens and tensile test was performed according to ASTM E-8 standard [17] in an INSTRON 5984 machine with maximum capacity of 150 KN. All samples for dilatometry and mechanical tests were performed in triplicate.

Results and analysis

Dilatometry

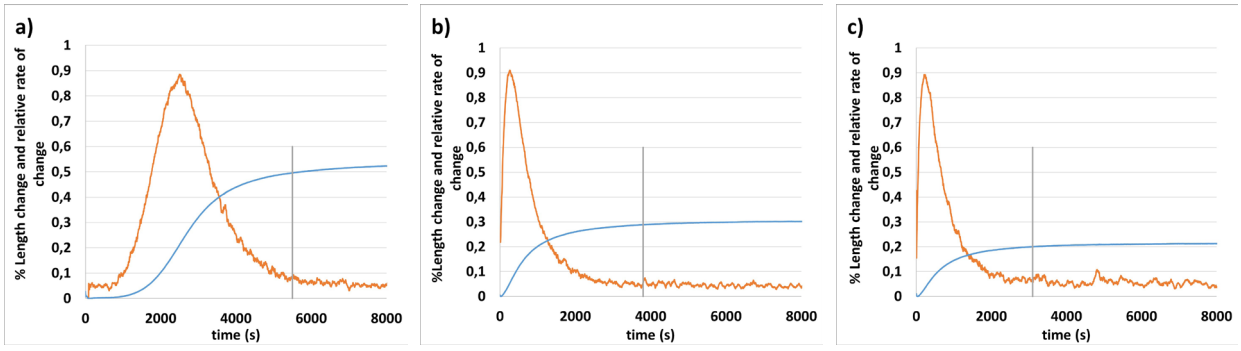

Figure 1. Relative change in length (RCL) curves as a function of Temperature and time by different heat treatments: a) Austempering, b) Q&P-1, c) Q&P-2

Figure 1 shows the graphics of bainite transformation kinetics for the three different isothermal heat treatments applied to AISI A2 tool steel. The literature reports a total bainite transformation between 90% and 94% of the total time [18]. In this work, the total transformation time is the time when the bainite formation reaches 94% of the complete reaction. It is possible to identify that the incubation time is 1000 seconds in austempered condition, while in Q&P condition this time is zero. Also, in Q&P heat treatments the total time of transformation is reduced from 5500 seconds in austempering to 3800 seconds in Q&P-1 and 3100 seconds in Q&P-2. A large amount of the reduction in the total transformation time is due to the elimination of the incubation period observed in austempering, which shows that martensite previously formed during quenching is a preferred nucleation site for bainite, even above the austenitic grain boundary [4].

Microstructural characterization

Figure 2 shows the microstructure of the isothermal heat treatments whose compositions are summarized in Table 3. Samples subjected to austempering and Q&P-1 have more bainite phase compared with Q&P-2 due to the amount of martensite that is formed in the

quenching stage. The phases proportion, the phases morphology and the low quantity of carbides observed in the Q&P-1 condition, are the main cause of significant improvements in the impact resistance of these samples as shown in table 4.

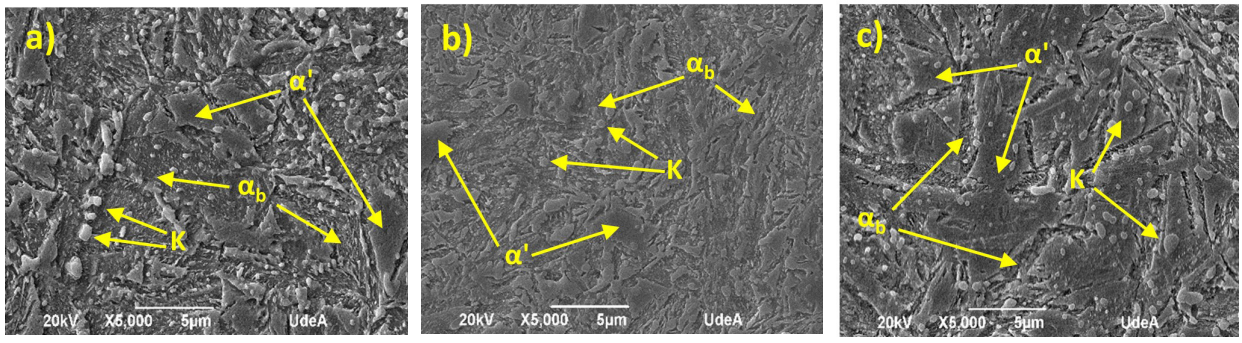

Figure 2. SEM micrographs for the isothermal heat treatments: a) Austempering, b) Q&P-1, c) Q&P-2. (K: carbides, αb: bainite, α': martensite)

Table 3. Phases quantification

Sample	Martensite of quenching by dilatometry	Total martensite by OM	Carbides by OM	Retained austenite by XRD	Bainite (by difference)
Q&T	N/A	79%	9%	12%	N/A
Aust	N/A	12%	10%	22%	56%
Q&P-1	12%	22%	5%	17%	55%
Q&P-2	26%	35%	9%	23%	32%

Mechanical properties

The tensile, Charpy V-notched impact energy and hardness tests were conducted at room temperature in samples heat-treated under the conditions just described, and results thus obtained are summarized in Table 4. The better tensile properties of austempered and Q&P conditions, against Q&T heat treatment, are related with the complex nature of their microstructures that include through the thickness of the sample different amounts of structural components with antagonistic properties like bainite, fresh martensite and tempering, retained austenite and carbides. On the other hand, that superior impact energy in austempered and Q&P1 can be explained in several factors: (1) a matrix composed smaller plates and therefore smaller (crystallographic) packets; (2) a milder matrix in terms of strength (smaller mismatch of properties between the matrix (bainite) and the second phase (retained austenite)), (3) low volume fraction of fresh martensite, and, (4) retained austenite size and its mechanical stability. The presence of mechanically stable retained austenite at the tip of growing cracks can induce a crack tip blunting effect due to its higher ductility

(compared to ferrite). Furthermore, since the stress concentration at the crack tip is very high, the transformation of austenite into martensite will be induced. This transformation phase will require some energy and the total work of fracture would be consequently increased. The low impact energy in the Q&P-2 sample can be explained by morphology and quantity of retained austenite. The appearance of large "blocky" regions of austenite in the Q&P-2 condition (see figure 2c) acts to the detriment of the mechanical properties of steel. This austenite is mechanically unstable and will transform to brittle, untempered martensite if subjected to moderate stresses [19]. The high hardness and brittleness of the martensite will cause a decrease in the impact energy of the steel. However, if austenite appears as a film covering the bainite phase, as in the case of Q&P-1 condition, it requires much higher strains in order to transform to martensite. In this case the austenite is mechanically stable and acts as a dislocation trap, leading to further strengthening of the material without compromising its toughness [19]. Finally, the similar total elongation, related with the same volume fraction of retained austenite in the microstructure in all conditions, will enhance even further the total elongation by TRIP effect. In the bainitic structures the ductility is controlled by the volume fraction of retained austenite, which is also capable of enhancing the ductility by its ability to transform into martensite by the TRIP effect. The transformation implies relaxation of the local stress concentration and extra strain hardening by means of two sources: (a) progressive increase in the volume fraction of the hard phase and (b) additional plastic deformation due to transformation strains.

Table 4. Mechanical tests results

Average mechanical properties					
Sample	**Impact energy (J)**	**UTS (MPa)**	**YS (MPa)**	**Elongation (%)**	**Hardness (HRC)**
Q&T	32±2	1874±10	1622±15	10±1	60±1
Aust	102±3	1908±18	1729±15	12±1	50±1
Q&P-1	122±2	1995±13	1883±15	12±1	51±1
Q&P-2	39±10	2003±22	2003±20	10±1	54±1

Conclusion

According to this work, the mechanical properties: strength and ductility, in A2 tool steel, with matrix of bainitic structure, because of the application of low-temperature isothermal treatments (austempered and Q&P), are governed by several factors. Within which, the phases fraction volume and its morphology play a preponderant role. Therefore, the volume fraction and morphology of retained austenite is the most important structural parameter to control, from the chemical composition of the alloy and the isothermal transformation conditions. Heat treatment variables are vital to facilitate the refinement of the structure and thus increase the levels of strength and hardness. Finally, the formation of martensite during quenching step allowed to reduce the bainite transformation times, which confirms this martensite as a preferred nucleation site for bainite. Due to the carbon enrichment of the parent austenite during partitioning, martensite can also affect other characteristics of the microstructure resulting from the bainite transformation. That issue is the reason why martensite should stay in an optimal amount, enough to accelerate bainite transformation but not too much to affect the impact properties of the steel.

References

[1] Roberts G, Krauss G, and Kennedy R. (1998). Tool Steels 5th edition. ASM Handbook. ASM International. 121.

[2] Uddeholm. (2017). Steel for cold working tooling 14th edition. Uddeholm AB. https://www.uddeholm.com/app/uploads/sites/54/2018/05/Tech-Uddeholm-Cold-work-EN.pdf

[3] Vatavuk, J., Totten, G. E., Nucci, J. E., (2016). Comparative Impact Behavior of High-C Steel After Conventional Quenching, Tempering, and Austempering, Materials Performance and Characterization, 5(1).

[4] Santigopal S., Pinaki B., Sushil G. (2016). Formation of Bainite Below the Ms Temperature: Kinetics and Crystallography, Acta Materialia 105. P 390-403.

[5] Speer J.G. (2012). “Phase Transformation in quenched and partitioning steels” in: Phase transformation in steels vol 2. Cap 9. Woodhead Publishing Limited, p 247-270.

[6] Lan H.F, Du L.X, Li Q, Qiu C.L, Li J.P, Misra R.D.K. (2017). Improvement of strength toughness combination in austempered low carbon bainite steel. Journal of alloys and compounds 710. 702-710.

[7] Hui G, Xianying F, Aimin Z, Qiang L, Jun M. (2019). Influence of prior martensite on bainite transformation, microstructures, and mechanical properties in ultra-fine bainitic steel. Materials 12.

[8] Chen S, Wang G, Liu C, Wang C, Zhao X, Xu W. (2017). Correlation of isothermal bainite transformation and austenite stability in quenching and partitioning steels. Journal of Iron Steel Research International 24, p. 1095-1103.

[9] Zhou L, Tang G, Ma X, Wang L, Zhang X. (2018). Relationship between microstructure and mechanical properties of M50 ultra-high strength steel via quenching-partitioning-tempering process. Materials Characterization 146; 258-266.

[10] Krauss G. (2005) Steels: Processing, structure, and performance. ASM International. p 87-100.

[11] T. Sourmail, V. Smanio, (2013). Determination of Ms temperature: methods, meaning and influence of 'slow start' phenomenon, Mater. Sci. Technol., 29 (7) 883–888.

[12] F. Caballero, C. Capdevila, C. Garcia De Andrés, (2001). Modelling of kinetics of austenite formation in steels with different initial microstructures ISIJ Int., 41 (10) 1093–1102.

[13] C. Garcia De Andres, F. Caballero, C. Capdevila, L. Alvarez, (2002). Application of Dilatometric Analysis to the Study of Solid-solid Phase Transformations in Steels. Invited Review, Mater. Charact., 48 101–111.

[14] ASTM International, (2001). "Método estándar para determinar fracción volumen por conteo de puntos manual de manera sistemática ASTM E562-01" Astm.

[15] ASTM International, (2013). "Standard Practice for X-Ray Determination of Retained Austenite in Steel with Near Random Crystallographic Orientation ASTM E975-13" Astm.

[16] ASTM International, (2012). "Método de medición estándar para prueba de impacto de barra entallada en materiales metálicos ASTM E-23-12c".

[17] ASTM International, (2011). "Ensayo de tracción bajo la Norma ASTM E8" Astm, pp. 46–57.

[18] D. San-Martin, M. Kuntz, F. Caballero, C. García, (2021). A new systematic approach based on dilatometric analysis to track bainite transformation kinetics and the influence of the prior austenite grain size. Metals, 11, 324.

[19] Bhadeshia, H.K.D.H, (2015). Bainite in Steels. Transformations, Microstructure and Properties, 3rd ed. Institute of Materials, Minerals and Mining: London, UK.

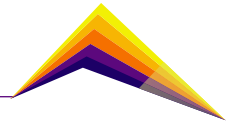

Carbo-austempering of high silicon steels: an innovative alternative for surface heat treatment

Oscar Ríos-Diez[1]
Claudia Serna-Giraldo[1]
Ricardo Aristizabal-Sierra[1]
Carlos García-Mateo[2]

Email:eduardo.rios@udea.edu.co

1 Gipimme, Department of Materials Engineering, Engineering Faculty, Universidad de Antioquia, Calle 67 No. 53- 108, Bloque 18, Oficina 240, Medellín, Colombia.
2 MATERALIA Research Group, Department of Physical Metallurgy, National Center for Metallurgical Research (CENIM-CSIC), Avenida Gregorio Del Amo, 8, Madrid, 28040, Spain

Abstract

In this work, a high silicon low carbon cast steel was fabricated and subjected to carburization. After that, the steel was austempered using different austenitization and austempering conditions to obtain carbo-austempered cast steels. The microstructure and mechanical properties of the steels were compared with those obtained by the traditional carburization, followed by a quenching and tempering (Q&T) process. The results showed that carbo-austempering of high silicon steels gives better mechanical properties than carburization followed by Q&T. Also, the mechanical properties, fatigue life, and wear resistance of the carbo-austempered steels vary as a function of the heat treatment parameters, austenitization, and isothermal holding temperatures, which can be linked to the microstructural differences that arise from changing the heat treatment temperatures.

Key words: carbo-austempered, heat treatment, nanobainitic steels.

Correspondent author

Introduction

Carbo-austempering is an innovative way for the surface treatment of steels [1]. The process consists on carburization followed by isothermal transformation at a temperature above the martensite starting temperature (Ms) of the carburized surface. The microstructure of carbo-austempered steels consists of bainitic ferrite (α_b), carbides, fresh martensite (α'), and/or retained austenite (γ_{ret}) in the surface, whereas a low carbon tempered martensite (α'_T) -low carbon α'_T and γ_{ret} – is produced in the core. It should be noted that the carbo-austempered treatment arises as an alternative to the traditional carburized-Q&T cycle (carburization, quenching, and tempering). In the use of bainitic microstructures for the superficial strengthening of steels, studies have been registered since 2002. Hayrynen et al. [1,] presented several studies, where they examined steels heat treated by carbo-austempering, which presented higher strength and toughness than martensitic commercial steels when they were treated isothermally at bainitic transformation temperatures. Zhang et al. [2] found a residual compressive stress of ~196MPa on the top case of nanobainitic carburized steels. The microstructures exhibited better wear and fatigue resistance than the traditional Q&T steel [3]. Currently, some companies have successfully applied the carbo-austempering process to the manufacturing of gears that work under hard impact and low lubrication conditions, such as those required for mining, railway, and automotive industry [1, 3]. The aim of the present investigation was to study the production of carbo-austempered cast-steels with different microstructure combinations, in the case and core, to comprehend the effect of these parameters on the tensile, impact, wear, and fatigue properties.

Materials and Methods

The steel for this research was fabricated in an induction furnace at the Universidad de Antioquia's foundry laboratory in Medellin, Colombia. The as-cast steel was austenitized at 1150°C for 48 hours in a vacuum environment. The chemical composition of the steel was Fe-0.29C-1.87Si-0.55M-0.92Ct (wt. %) (OES, Bruker Q8 Magellan). Tensile, impact toughness (V-notch), wear and fatigue samples were cut and machined, according to [4, 5], respectively. The machined specimens were carburized at 920°C in a gas-carburizing furnace for at total time of 4 h. The C content on the surface after the carburizing treatment was 0.76 wt% and the carburized layer was 1.6mm depth. The carburized steel was austenitized at (Tγ) 830°C and 900°C, for 15 min. After that, the steels were isothermally transformed at (T_{iso}) 250°C – 8 h and 300°C – 4 h, and finally they were cooled in water. Group samples were heat treated using the typical industrial cycle of carburization followed by quenching -from 900°C to room temperature in oil- and tempering -at 250°C for 120min- for comparison purposes. Samples prepared by standard metallographic techniques ASTM E3 [6] were observed by SEM -scanning electron microscope (JEOL-JSM 6490LV). SEM micrographs were used to measure the thickness of the bainitic ferrite plates and retained austenite thin films as explained in

[7]. X-ray diffraction (-XRD- Panalytical Empyrean 2012) was performed using Co K radiation at 40 kV/100 mA, rate of 0.06°min^{-1}, and scanning in the 2θ range from 30° to 110°. The XRD information was used to calculate the volume fraction of austenite, and its C concentration [8]. Ultimate tensile strength (UTS), yield strength (YS) and total elongation were determined in an INSTRON 5984 machine with 150kN loading capacity at 3s^{-1}. Round sub-size specimens with a gauge diameter of 6mm were used to conduct the tensile testing. A Karl Frank GMBH - 300J Charpy testing machine was used to measure the impact toughness of V-notch 10x10x55mm samples at room temperature. Finally, the effect of the austenitizing and isothermal temperatures was studied by rotating-bending fatigue and rolling-sliding testing. Ref. [9] contains information about the test conditions that were chosen in detail.

Results and analysis

Figure 1 shows that the microstructure is composed of interlinked nanometric plates of α_b and γ_{ret}. The γ_{ret} was present as films between the α_b subunits and as blocks. The information from the microstructural characterization of the surface and core of the carbo-austempered steel, presented in Table 1, shows that a higher austenitization temperature (T_γ) has little or no influence on the microstructure and hardness of the surface; on the other hand, increasing the isothermal temperature results in a lower fraction of α_b, a larger fraction of γ_{ret} and coarser microstructure. All these characteristics are consistent with the theory of bainitic transformation [10]. The C concentration in the austenite (C_γ) is higher for samples austempered at higher temperature, which can be explained by the lower presence of dislocations acting as traps for carbon atoms in the α_b obtained at higher temperatures [11], therefore, more carbon can diffuse towards the γ. Also, the structure of the core reveals a mixture of $\alpha + \alpha_b + \gamma_{ret} + \alpha'_T$, in varying proportions according to the T_γ and T_{iso} temperatures. An important aspect is the morphology of the bainitic structure obtained in the core, which is much coarser compared to the surface, with α_b plates and γ_{ret} sheets being in the submicrometer size range. When the carburized steel was austenitized at 900°C, the γ was the only phase present. During the cooling and/or isothermal transformation stage, this was transformed into α_b or α', in addition, to achieving stabilization as γ_{ret}. When the austenitization of the carburized steel was carried out at a temperature of 830°C, it was favored the presence of proeutectoid ferrite (α). Under these conditions, due to the low carbon solubility of the α, the excess carbon atoms are rejected and accommodated in the adjacent austenitic regions, which favors a higher level of chemical stability in the γ before cooling to T_{iso} (increased levels of hardenability). One of the significant results of applying this processing sequence was the decrease in the transformation to α' and the increase of the fraction of α_b in the core, in addition, to promoting the stability of γ_{ret} at room temperature. Finally, the samples subjected to the conventional carburization followed by Q&T exhibited a microstructure of α'_T and some γ_{ret} (Figure 1(i)).

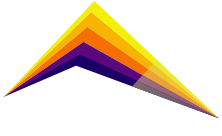

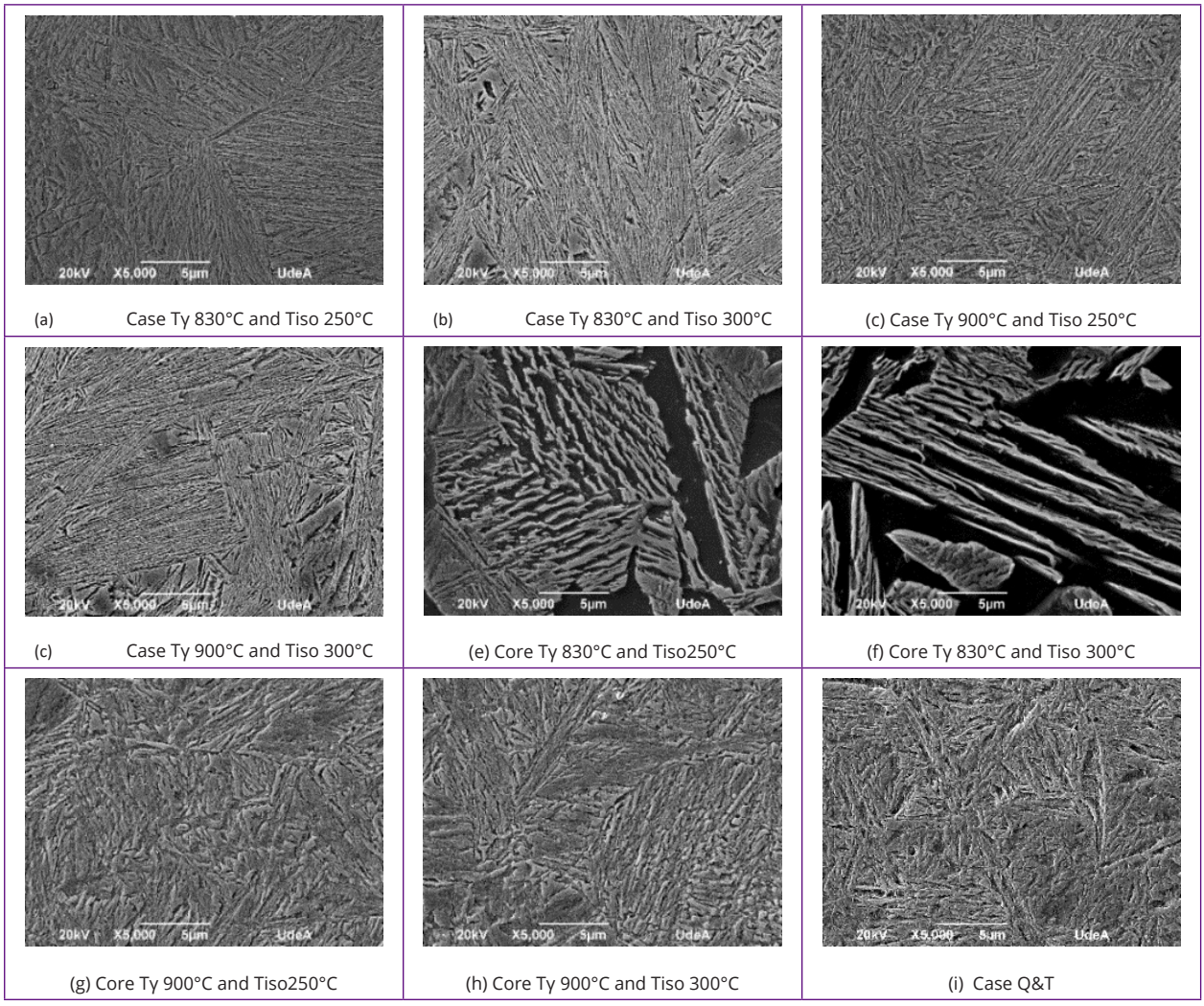

Figure 1. SE-SEM images showing the microstructure of the carbo-austempered and Q&T cast steels at the case and core.

Table 1. Results of the microstructural characterization of carboaustempered steels.

	ISOTHERMALLY TREATED SAMPLES				Q&T SAMPLES
	Heat treatment conditions (°C/min)				
	Austenitization	900/15		830/15	900/15
	Isothermal	250/480	300/240	250/480	300/240	NA
	Plate Thickness (nm)					
Case	Bainitic Ferrite	57±6	95±18	55±6	103±18	-
Case	Retained Austenite	43±6	71±10	44±9	64±11	-
Case	***Volume Fraction (Vol %)***					
Case	Bainitic Ferrite	84±3	82±3	85±3	86±3	-
Case	Martensite	-	-	-	-	87±3
Case	Retained Austenite	14.5±3	16.7±3	13.3±3	14.9±3	12±3
Case	***Carbon content (wt. %)***					
Case	Retained Austenite	1.03 ± 0.12	1.24 ± 0.12	1.20 ± 0.12	1.33 ± 0.12	0.95 ± 0.12
Case	***Hardness Vickers 10Kg***					
Case	HV10	579±4	513±5	576±6	510±10	632±10
Core	***Plate Thickness (nm)***					
Core	Bainitic Ferrite	167 ± 13	251 ± 13	136 ± 15	171 ± 16	NA
Core	Retained Austenite	145 ± 14	196 ± 15	91 ± 14	142 ± 10	NA
Core	***Volume Fraction (Vol %)***					
Core	Bainitic Ferrite	25.5	34.5	25.3	58.5	NA
Core	Martensite	70	56	36	-	94.5
Core	Proeutectoid Ferrite	-	-	32.3 ± 3	33 ± 3	NA
Core	Retained Austenite	4.5 ± 3	9.5 ± 3	6.7 ± 3	8.5 ± 3	5.5 ± 3
Core	***Carbon content (wt. %)***					
Core	Retained Austenite	1.54 ± 0.12	1.67 ± 0.12	1.63 ± 0.12	0.79 ± 0.12	1.37 0.12
Core	***Hardness Vickers 10Kg***					
Core	HV10	490±9	440±7	380±6	340±8	527±9

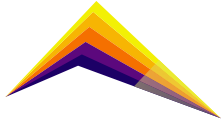

Regarding the mechanical properties, carbo-austempering provided a better performance compared to the conventional carburized-Q&T steel (see Table 2). UTS and YS were higher, and ductility and toughness were lower as the isothermal transformation temperature decreases, which can be linked to a finer microstructure and a higher fraction of α'_T through the section of the samples. The data in Table 2 also shows that lowering the austenitization temperature improves ductility and impact toughness, which can be associated to the multiphasic microstructure of the core, that contains proeutectoid ferrite [9, 10].

Table 2. Mechanical properties in carbo-austempered steel.

	ISOTHERMALLY TREATED SAMPLES				**Q&T SAMPLES**
Heat treatment conditions (°C/min)					
Austenitization	*900/15*		*830/15*		*900/15*
Isothermal	*250/480*	*300/240*	*250/480*	*300/240*	*NA*
YS (MPa)	1220 ± 7	1025 ± 26	1289 ± 5	1106 ± 11	846 ± 13
UTS (MPa)	1310 ± 16	1110 ± 17	1390 ± 26	1179 ± 25	911 ± 15
Total Elongation (%)	8.0 ± 0.4	8.5 ± 0.4	9.0 ± 0.2	10 ± 0.2	6.0 ± 0.5
V-Notch (J)	6 ± 0.4	8 ± 0.8	9 ± 0.3	12 ± 0.4	4 ± 0.5
Specific Wear, K ($mm^3/N.m)x10^{-7}$	12.407	13.472	11.578	14.402	15.933
Cycles to failure, N_f	2.68E+5 ± 8.0E+3	1.73E+5 ± 1.4E+4	2.46E+5 ± 1.2E+4	1.93E+5 ± 9.0E+3	1.49E+5 ± 1.0E+4

As for the wear resistance and fatigue life, carbo-austempered samples also performed better than the traditional carburized Q&T samples. This result may be associated with a higher compressive residual stress at the surface [9], and an improved crack tip blunting effect. Also, the more complex and miss-oriented microstructure of carbo-austempered samples can add a more tortuous path for crack growing, which delays crack propagation. Finally, nanobainitic carbo-austempered steels performed better at lower austempering temperatures, which was also linked to an increase in the microstructural barriers to stage I crack propagation and a shorter dislocation glide path.

Conclusions

Carbo-austempering of high silicon cast steels gives better mechanical properties, fatigue, and wear performance than the traditional carburization Q&T process. The results are associated with the combination of bainitic and multiphasic microstructures (mixture of proeutectoid ferrite, bainitic ferrite, martensite and retained austenite), whose fractions vary depending on the heat treatment conditions. The results indicate that this technology can be used for the fabrication of components with complex geometries that can be more easily fabricated by casting than by plastic deformation, which can be a way of enhancing the potential applications of the nanobainitic steels.

References

[1] Hayrynen, K., Brandenberg, K., Keough, J. (2008) Carbo-Austempering™ - A New Wrinkle? Technical Report, Applied Process - Livonia, Michigan, USA.

[2] Zhang, F., Wang, T., Zhang, P., Lv, B., Zhang, M., Zheng, Z. (2008) Scr. Mater. (59:3) 294–296.

[3] Zhang, F., Yang, Z. (2019) Engineering. (5:2) 319–328.

[4] ASTM International (2016) E8 / E8M-16a. West Conshohocken, PA, www.astm.org

[5] ASTM International (2016) E23-16b. West Conshohocken, PA, www.astm.org

[6] ASTM E3-11(2017.) West Conshohocken, PA.

[7] García-Mateo, C., Jiménez, J., López-Ezquerra, B., Rementeria, R., Morales-Rivas, L., Kuntz, M., Caballero, F. (2016). Mater. Charact. (122) 83–89.

[8] Dyson, D., Holmes. B. (1970) J. Iron Steel Inst. (208) 469-474.

[9] Oscar, R-D. (2020) Memoria para optar al grado de Doctor -Universidad de Antioquia. 120 pp.

[10] Bhadeshia, H. (2015) Bainite in Steels, 3rd ed. Maney Publishing: Leeds, UK.

[11] Santofimia, M. (2007) Memoria para optar al grado de Doctor - Universidad Complutense de Madrid. 223pp.

Austenite formation in ductile iron alloyed with copper and nickel

Harold D Machado *E-mail: harold.machado@udea.edu.co*
Mateo Montoya Mejía *E-mail: mateo.montoya@udea.edu.co*
Ricardo Aristizábal Sierra *E-mail: ricardo.aristizabal@udea.edu.co*

Gipimme; Engineering Faculty, Universidad de Antioquia, Medellin.

Abstract

In this investigation, the effect of the microsegregation in the formation of austenite in the intercritical interval was studied. For this, high-resolution dilatometry was used to monitor the formation of austenite and an electron probe micro-analyzer (EPMA) was used to quantify the microsegregation present in the matrix. The results showed local differences in the transformation of austenite within the ductile iron matrix associated with the microsegregation of silicon, manganese, copper and nickel, which affect the volume fraction and distribution of the austenite during the intercritical austenitization step of the heat treatment.

Key words: Intercritical austenitizing, austenite formation, intercritically austempered ductile iron.

Correspondent author

Introduction

Ductile iron is an alloy frequently subject to heat treatment in order to tune its mechanical properties. Austenitization is a critical step on most ductile iron heat treatments and it becomes critical when the alloy has to be subjected to intercritical austenitization. This is especially true for the fabrication of intercritically austempered ductile iron -IADI-, which has a good combination of ultimate tensile strength and ductility, which is suitable for the fabrication of power transmission parts in different industries such as the automotive industry. The mechanical properties of these materials depend highly on the intercritical austenitizing step of the heat treatment, which makes the study of the formation of the austenite paramount for the further development of this kind of alloys. At the same time, austenite formation in ductile iron can be affected by microsegregation of the alloying elements during the solidification process [1]. With the purpose of making ductile cast irons with good mechanical resistance and ductility, studies and mathematical modeling have been carried out to understand the kinetics of the transformation in the intercritical interval [2,3]. Research such as that of Nastac and Stefanescu propose a model to calculate the distribution of Mn, Mo, Cu, and Si in ductile cast iron, considering the diffusion in liquid and solid states [2]. B.Y. Lin, et al. studied the effect of the segregation of elements such as Mn, Cu, Ni, and Mo on the phase transformations of a nodular iron during austempering, for which they modified the solidification modulus of the specimens and measured the variation of the alloying elements with EPMA [3].

Even so, there is limited information on the formation of austenite for ductile irons in the intercritical range and the effect of microsegregation during austenitization, the study of which is the purpose of this work.

Methodology

The chemical composition of the ductile iron used in the present study were 3.45%C, 2.66%Si, 0.18%Mn, 0.9%Ni, 0.6%Cu, 0.042% Mg and 4.34% CE. Step blocks having 16 mm and, 48 mm wall thicknesses were cast into green sand molds, specimens of the alloy were annealed to obtain fully ferritic and fully pearlitic microstructures shown in the figure 1.

The heat treatments were as follow: 1) Ferritic annealing: Austenitization at 920 °C and cooled at 730 for 5 hours. 2) Pearlitic annealing Austenitization at 920°C and cooled at 460°C for 1 hour. Samples were taken from equivalent points of the castings at each thickness, so they can be compared to each other.

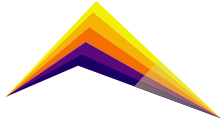

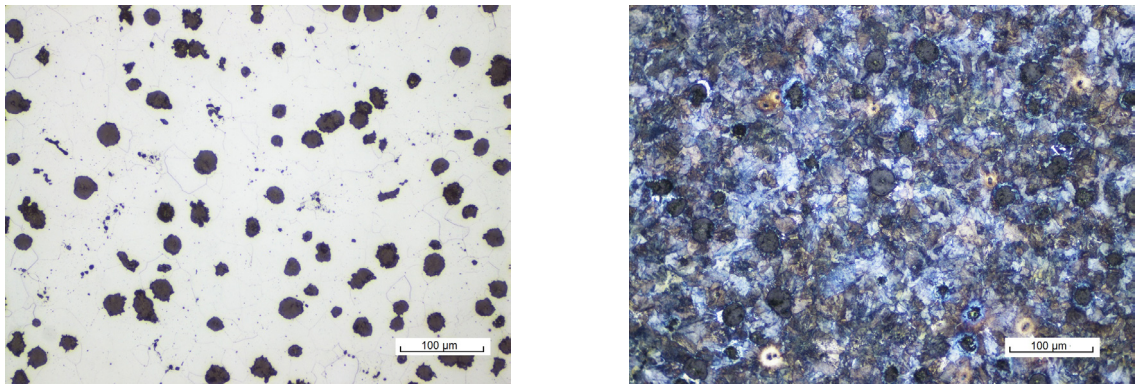

a) b)

Figure 1. Starting microstructures: a) Ferritic matrix and b) pearlitic matrix.

Microstructure was examined in samples prepared by standard metallographic techniques using optical microscopy. Nodularity was above 90% and nodule count range between 300 and 320 nodules/mm^{2}according to ASTM 247. Also, electron probe micro-analyzer (EPMA) was used to quantify the microsegregation of Si, Mn, Cu and Ni in a 500µm x 500µm area. The analysis was performed every 1µm, X-ray line profiles between three neighbor graphite nodules were taken and the maximum and minimum molar fractions of each element were calculated. After the test, Matlab® was used to process the data and obtain compositional maps. Besides, using equations developed by Gerval and Lacaze [4], maps of variation of the initial austenite formation temperature for ductile irons were obtained based on microsegregation, the equations vary depending on the type of starting matrix.

Austenite formation was monitored in Bahr 805A high-resolution dilatometry using cylindrical specimens 10 mm long and 4 mm diameter. The analysis was performed in a high-vacuum environment at a heating rate of 0.18 °C/s. Specimens were heated to 1000°C. High resolution dilatometric analysis allowed to obtain the initial austenite formation temperature (T_{Low}) and, end of austenite formation temperature (T_{End}).

Results and analysis

Figure 2 shows the dilatometry results for the evaluated matrices. The start of the austenite formation in the ferritic matrix occurs at higher temperatures than in the pearlitic matrix, the difference is because the nucleation of austenite occurs much faster in the pearlite colonies where the available carbon is higher than in ferritic matrices, where nucleation occurs at the grain boundaries of the ferrite and the available carbon is lower, depending on the austenitization temperature and the carbon diffusion of the graphite nodules towards the matrix. Table 2 shows the results of the dilatometry for the different types of matrix and

thicknesses. Results showed that the end temperature of the austenite formation is very different for the two matrices, if we take into account that for the ferritic matrices it is around 885 °C and for the pearlitic matrices it is ± 850 °C, the difference between the temperatures of completion is mainly due to the diffusion of carbon, as mentioned above in ferritic matrices the transformation to these temperatures depends mainly on carbon diffusion and in this case there is carbon available only from the graphite nodules. On the other hand, the average carbon path is smaller in pearlitic matrices, therefore the transformation will occur in pearlitic matrices at a lower temperature and end at a lower temperature. Regarding nodule count, there is an effect on the rate of the transformation, the smallest casting thickness gives a higher transformation temperature [5].

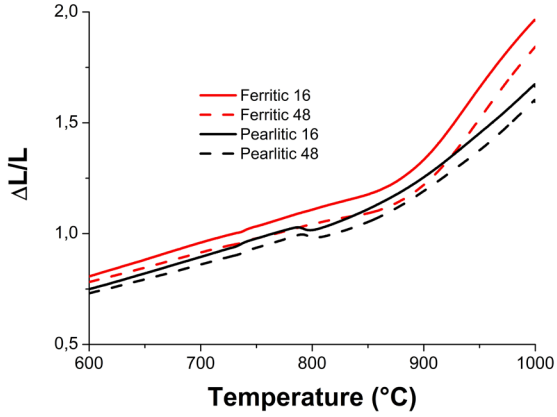

Figure 2. Dilatometric results

Table 1. Dilatometric results

Matrix	Thinckness (mm)	Nod/mm²	T_{low} (°C)	T_{end} (°C)
Ferritic	16	320	797	880
	48	241	801	887
Pearlitic	16	295	780	845
	48	254	782	848

Figure 3 shows the compositional maps for the Ni-Cu alloy for both ferritic and pearlitic starting matrices. In all cases, the segregation of the elements of interest is similar to what has been reported by other authors [2,3]. Manganese is segregated to the intermediate zones between the graphite nodules. In contrast, silicon, copper, and nickel are segregated towards the zones close to the primary graphite contours, with copper having greater microsegregation around the graphite when there is no nickel in the matrix. In addition, microsegregation increased with thickness, or what is the same when the count of nodules decreased.

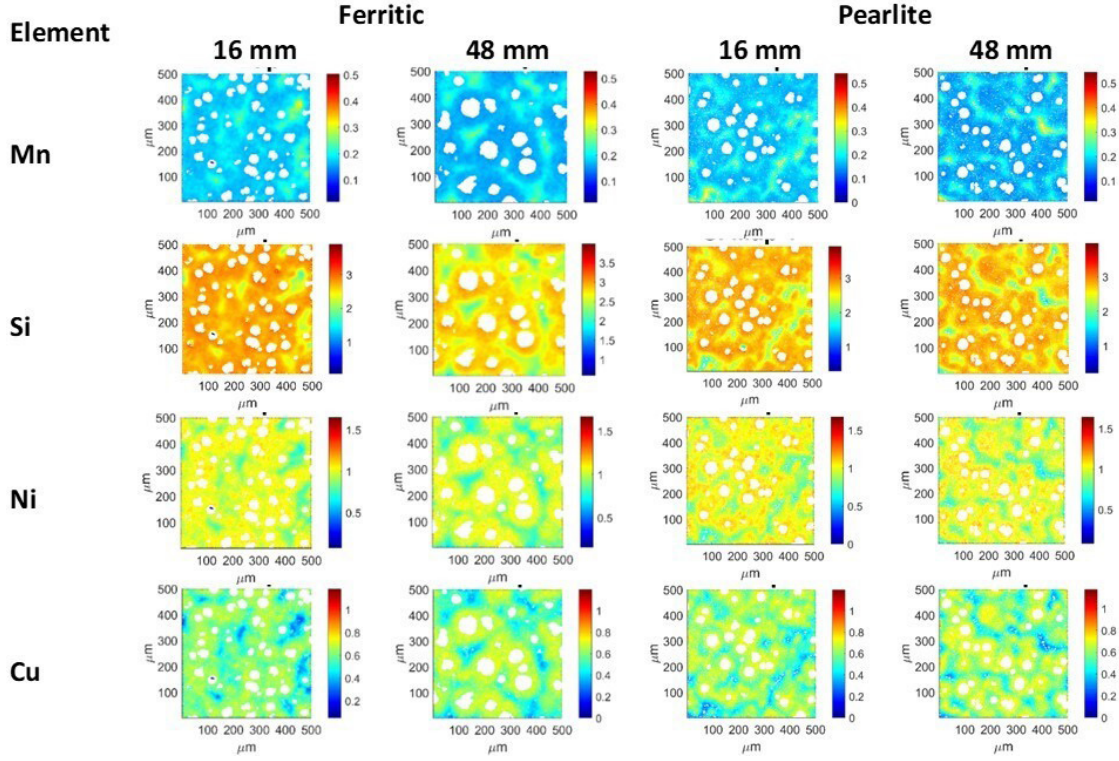

Figure 3. Compositional maps obtained by EPMA for ferritic and pearlitic matrix for ductile iron.

The importance of analyzing microsegregation comes from the effect that the chemical composition has on the critical temperatures of austenite formation, which will be affected locally in the matrix, producing zones where the transformation begins at lower temperatures than in others. Therefore, when austenitizing in the intercritical range, some regions of the matrix will form austenite and others will need a higher temperature to start the transformation. Using equations from the study conducted by Gerval et al [4], the austenitic transformation onset temperature (T_{low}) maps were plotted in the areas analyzed by EPMA. The results of figure 4 show that the zones close to the primary graphite nodules have higher T_{low} than the zones further away. This result indicates that in the zones farthest from the

primary graphite, austenite will form more easily during intercritical austenitization, and depending on the selected intercritical austenitization temperature, there will be areas close to the nodules that will not be austenitized, even under prolonged holding times.

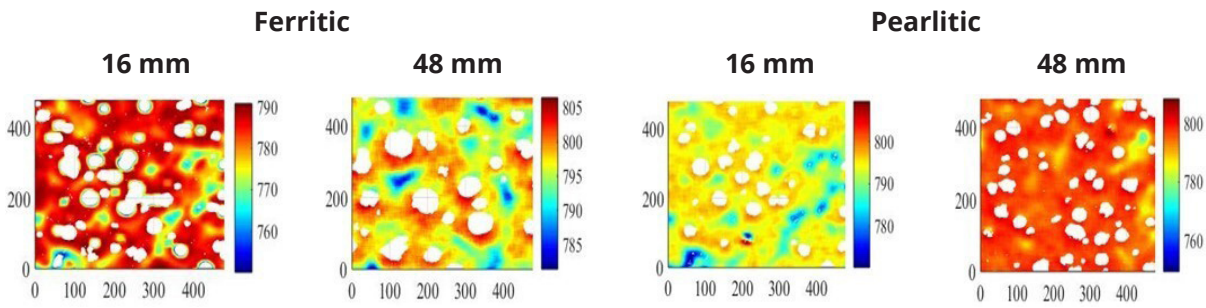

Figure 4. Austenitic transformation starts temperature maps for ferritic and pearlitic matrices.

Table 4. Austenite formation initiation temperatures

Temperature (°c)	Ferritic		Pearlite	
	Thinkness (mm)		Thinkness (mm)	
	16	48	16	48
T_{low}^{min}	781	785	770	772
T_{low}^{max}	801	805	789	791

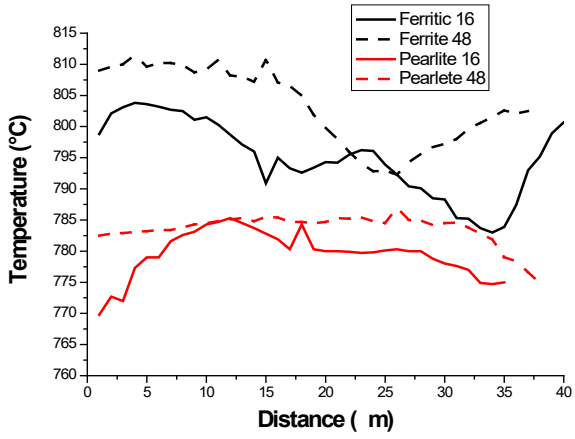

Figure 5. Variation of the beginnin of the austenite formation temperature between two primary graphite nodules.

Figure 5 and table 4 show the variation of the beginning of the austenite formation temperature between two primary graphites, the analysis shows that: 1) the difference between T_{low}^{min} and T_{low}^{max} in the evaluated matrices varies from 14°C to 30°C and that in most cases this difference increases as the nodule count decreases, (2) T_{low} for the pearlitic matrix samples is lower than for the ferritic matrix, in values that can vary from 11°C to 36°C and (3) the T_{low} gradients are greater in the unalloyed ductile iron than in the alloyed ones.

When comparing the results of the determination of T_{low} by dilatometry with the calculations using microsegregation data, it is observed that the results are similar, and again it is found that T_{low} is lower when treatment with a pearlitic matrix is started. It has been argued that the nucleation of austenite occurs faster when there is a greater amount of carbon, considering that the average path of the carbon is smaller [6]. The higher austenite formation initiation temperatures reported in the temperature maps and in Figure 4 for the ferritic samples may also help explaining why the intercritical interval is greater, having transformation initiation temperatures in some areas around 840°C, requiring a higher temperature for the austenite grain to start and grow.

Conclusions

The start and end temperatures of austenite formation under continuous heating conditions depend on the initial matrix, these temperatures are higher for a ferritic matrix, which is caused by the lower amount of carbon in the matrix and the lower number of nucleation sites compared to pearlitic matrices. The nodule count influences the degree of microsegregation of ductile cast irons, the higher the nodule count, the lower the microsegregation, which affects the temperature of austenite formation locally in the matrix and has an impact on the rate of formation of austenite in the intercritical interval and in the carbon diffusion distance. A lower nodule count slows down the formation of austenite.

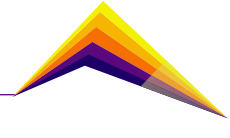

References

[1] Druschitz, A. P, Ostrander, R. W., and Aristizabal, R. (2014). "The science of intercritically austempered ductile iron (IADI)," AFS Transactions., paper 14-070, 279-286.

[2] Nastac, L and Stefanescu, D. M., (1993). "Modeling of Microsegregation in Ductile Iron Modeling of Microsegregation in Cast Iron," *AFS Trans.*, vol. 101, 1–14.

[3] Lin, Y. L, Chen, E. T., (1998) "The Effect of Segregation on the Austemper Transformation of Ductile Irons,". Journal of Materials Engineering and Performance, 407–419,

[4] Gerval, V and Lacaze, L,. (2000) "Critical Temperature Range in Spheroidal Graphite Cast Irons Valérie," *ISIJ Int.*, vol. 40, no. 4, 356–392.

[5] Machado, H. D., Aristizabal-Sierra, R., Garcia-Mateo, C. and Toda-Caraballo, I., (2020). "Effect of the Starting Microstructure in the Formation of Austenite at the Intercritical Range in Ductile Iron Alloyed with Nickel and Copper," *Int. J. Met.*, vol. 14, no. 3, 836–845.

[6] Caballero, F. G., Capdevila, C. and C. G. De Andrés, (2001). "Mathematical Modeling of Iron and Steel Making Processes. Modelling of Kinetics of Austenite Formation in Steels with Different Initial Microstructures.," *ISIJ Int.*, vol. 41, no. 10, 1093–1102.

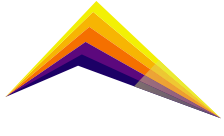

Nanobainitic cast steels: Scientific advances for the industrial sector

Mateo Montoya-Mejia *E-mail: mateo.montoyam@udea.edu.co*
Andrés Felipe Santacruz-Londoño
Oscar Eduardo Ríos-Diez
Ricardo Aristizábal-Sierra

Gipimme, Department of Materials Engineering, Engineering Faculty, Universidad de Antioquia, Calle 67 No. 53- 108, Bloque 18, Oficina 240, Medellín, Colombia

*

Abstract

Nanobainitic steels are materials that exhibit high mechanical strength, good ductility, and toughness, these characteristics make them attractive for agricultural, mining, railway, and military applications, among others. The microstructure of nanobainitic steels is obtained by a low-temperature isothermal heat treatment called austempering. In the last years, thestudy of nanobainitic steels with high silicon and carbon concentration has been attractive for the industrial sector, since the high silicon concentration inhibits the precipitation of carbides during the bainitic reaction increasing the mechanical properties. The development of these steels has been focused on the production of wrought steels and there is very little information related to nanobainitic cast steels. For this work, a cast steelwith chemical composition of ~0.7 C, 2.0 Si and ~1.0 Mn (wt %) was fabricated. The steel was austempered at two temperatures and it was microstructural characterized using optical microscopy, scanning electron microscopy, and X-ray diffraction. Hardness, tensile properties and impact toughness were evaluated in order to contribute to the future implementation in the industrial sector. The mechanical performance of the isothermally treated material is comparable, yet lower, to those observed in wrought steels. In

Correspondent author

general, it was observed that thanks to the high carbon and silicon contents, it is possible to obtain nanometric microstructures at relatively high transformation temperatures, which allows short processing times. The yield strength and impact toughness values obtained were similar to those reported in wrought steel. Moreover, the ultimate tensile strength and ductility values are lower, this behavior is attributed to the distribution of non-metallic inclusions, microsegregation and microdefects. The results indicate that the microstructural concept of nanobainitic steels can be transferred to cast steels with similar results.

Keywords: Nanobainitic Steel, High Silicon Steel, Austempering Isothermal transformation, Bainitic transformation.

Introduction

Nanoscale bainite is an outstanding microstructure that exhibits a very promising combination of mechanical properties [1]. This microstructure is obtained by austempering heat treatment, which consists of austenitization followed by quenching in a salt bath at a temperature between the bainite start (Bs) and the martensite start (Ms) temperatures. The high silicon concentration inhibits the precipitation of carbides during the bainitic reaction. The final microstructure is a mixture of bainitic ferrite plates and retained austenite, the later in two morphologies, thin films of C-enriched retained austenite and block austenite [2]. This microstructure confers to steels high ultimate tensile strengths (UTS) above 2.0 GPa, high yield strength (YS) above 1.5 GPa, total elongation between 5- 20%, and fracture toughness 45-90 $MPa/m^{1/2}$.

During the last couple of decades, the majority of the research on the development of nanoscale bainitic microstructures in steels has been focused on wrought materials and very scarce information related to cast steels is available [3-8].

This paper presents a summary of developing nanobainitic microstructures in cast steels using data obtained at the Universidad de Antioquia casting laboratory by the group Gipimme [9] and compares the results with some information available in the literature fornanobaintic wrought steels.

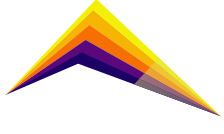

Materials and Methods

A cast steel with a chemical composition of ~0.7 C, 2.0 Si y ~1.0 Mn (wt %) was fabricated using a 50 Kw induction furnace. After melting, it was deoxidized with 0.1% Al and poured at ~1610°C into chemical bonded silica sand molds. The as-cast steel was homogenized at 1100°C for 48 h in a vacuum. Samples for tensile testing, impact toughness and hardness, were thermally processed as follows: Austenization temperature was defined at 900°C holding for 45 minutes and the isothermal transformation temperatures (T_{iso}) and times were defined as 250°C-4 h and 300°C-2 h. The austenitizing treatment was performed in anelectric furnace in a vacuum environment to avoid decarburization problems. The isothermal transformation was carried out in a salt bath (50% $NaNO_2$ + 50% KNO_3) and finalcooling at room temperature was done in water.

To carry out the microstructural characterization, samples were polished following conventional metallographic techniques and etching with 2% Nital solution to reveal the structure. The microstructure and the thicknesses of the ferrite bainite plate (α_b) and the retained austenite thin film (γ_{film}) was analyzed using a JEOL-JSM 6490LV scanning electron microscope (SEM). X-ray diffraction (XRD) analysis in a Panalytical Empyrean 201 the austenite (γ) volume fraction and C content. Scanning was performed in the 2θ range from 30° to 110° at a rate of 0.06°min^{-1}. Carbon austenite content (C_γ) was estimated using the equation of Dyson and Holmes [10].

Tensile test was carried out at room temperature using an INSTRON 5984 machine with 150 KN load capacity at 3s^{-1} in 6 mm thick rectangular sub-size specimens. An extensometer was used for strain measurement. Impact toughness was evaluated using a Karl Frank GMBH-300J Charpy testing machine at room temperature. Rockwell C Hardness measurements were made using a Harterprufer-Swiss MAX 300 hardness testing machine. At least three specimens were tested mechanical property.

Results and analysis

Microstructural characterization results are presented in Table 1 and Figure 1. The microstructure consists of a ferrite bainite and austenite, in two different morphologies: as a blocks and thin films. No cementite or martensite was detected, the absence of the former is linked to the high silicon content of the alloy, which delays carbide precipitation during austempering, as for the later (the no presence of martensite), it indicates that the remaining austenite was carbon enriched to an extent that avoided its transformation upon cooling to room temperature.

As expected, low T_{iso} promotes the refinement of the microstructure, lower volume fractionof γ and a higher volume fraction of α_b. On the other hand, high T_{iso} coarses the microstructure, increase volume fraction of γ, and decreases the volume fraction of α_b. All these characteristics are consistent with the theory of bainitic transformation [6]. On the other hand, according to the bainitic transformation theory, higher austenite carbon enrichment is expected at 250°C, however, carbon concentration in austenite (C_γ) is higherfor samples treated at 300°C, which can be explained by the lower presence of dislocationsacting as traps for carbon atoms in the αb obtained at higher temperatures [11], therefore,more carbon can diffuse into the γ. The tetragonality (c/a ratio) of bainite ferrite decreasesslightly from 250 to 300°C, researches has reported a tetragonal crystalline structure in bainitic ferrite which is associated with the solid solution carbon content of the ferrite [12].

Table 1. Microstructural characterization isothermal transformation.

Tiso(°C)	$t\alpha_b$ (nm)	$t_{\gamma ret}$ (nm)	$V\alpha_b$ (%)	$V_{\gamma ret}$ (%)	C_γ % (p/p)	Tetragonality (c/a)
250	58 ± 6	44 ± 6	91.2 ± 3	10±3	1.3±0.12	1.0088
300	98 ± 8	70 ± 10	83.3 ± 3	18±3	1.5±0.12	1.0083

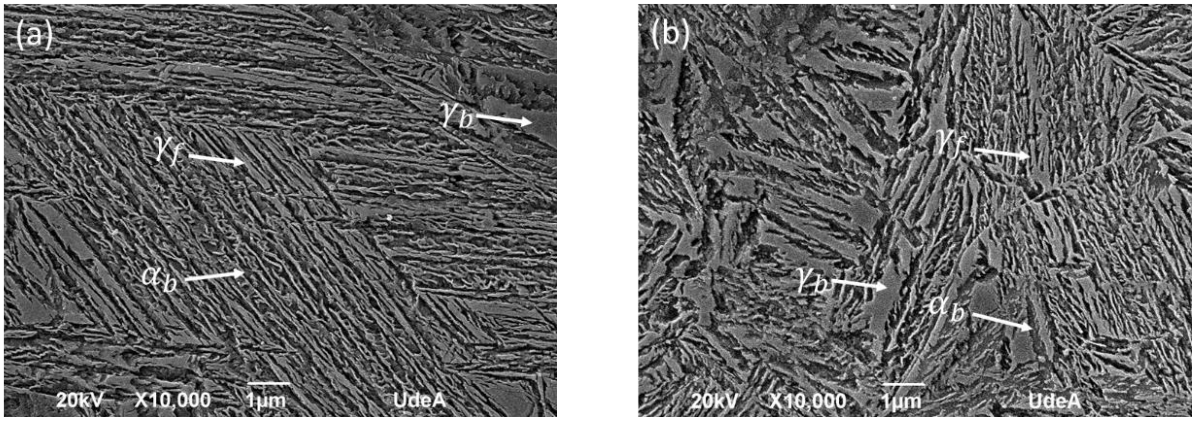

Figure 1. Secondary electron SEM images of the microstructure treated isothermally at: (a) 250°C-4h, and (b) 300°C-2h. Where γf is austenite films, γb is austenite blocks and αb is bainitic ferrite.

Mechanical proprieties are present in Table 2. The results at both T_{iso} are expected in concordance with the microstructural analysis. In the case of hardness, the volume fraction of α_b and its thickness is considered the most influential factors, at T_{iso} 250°C it is observed a higher volume fraction and smaller thickness of α_b, so it is expected higher hardness in this condition, this behavior is directly linked to dislocation density in the microstructure and C content of the bainitic ferrite. the strength is mainly decided by the fraction, carbon content, and thickness of the ferrite bainite laths. Besides, ductility is principally decided by the structure of the ab lath and the quality and morphology of the carbon-enriched austenite. At 250°C, ferrite bainite laths become finer and closer and the amount of retained austenite decreases; this gives rise to higher strength and hardness but lower ductility. As the transformation temperature increases to 300°C, the diffusion ability of carbon atoms increases and the degree of supercooling of the bainitic transformation decreases. All these will reduce the amount of ferrite bainite, widen the laths, increase the amount of retained austenite, lower the strength and hardness, and increase the ductility. On the other hand, total elongation (TE) and impact toughness (IT) decrease whit volume fraction and thickness of $\alpha_b$and increase with the volume fraction of γ, these properties are directly related with the ductility of the alloy. The higher ductility was found at T_{iso} 300°C and this can be relatedto the higher volume fraction of austenite which improves the strain-hardening capability of the microstructure by a TRIP effect.

Table 2. Mechanical characterization for isothermal transformation.

Tiso (ºC)	Hardness (HRC)	UTS (MPa)	YS (MPa)	TE (%)	IT (J)
250	55.2 ± 0.7	1897 ± 83	1807 ± 47	3 ± 1	9.8 ± 1.7
300	51.5 ± 0.3	1749 ± 6	1629 ± 12	9 ± 3	17.4 ± 2.1

It is important to notice that the individual mechanical properties of each phase have a direct influence on the final mechanical performance of the material. This is especially true for the strain hardening response. As shown in Table 1 the carbon content in the austenite is higher at 300 °C than at 250°C. On the other hand, the bainitic ferrite is coarser and less dislocated as the austempering temperature increases, thus α_b should have lower strength at 300 °C than at 250 °C As a consequence, there is a lower strength mismatch between the phases at 300 °C, which enhances the composite-like nature of the microstructure and gives higher elongation and strain hardening.

Finally, yield strength of the nanobainitic cast steels are comparable with those obtained in wrought steels [13], yet ductility and UTS are lower. The differences may arrive from different factors, which include: 1) a higher microsegregation in cast steels, which may givea less homogeneous microstructure, 2) the higher number of defects such as pores and micro-

shrinkages in cast steels and 3) the morphology and distribution of non-metallic inclusions. The study of these factors is beyond the scope of this paper, and they can be the subject of future research.

Conclusions or summary

This work shows how it has been possible to process cast steel by isothermal transformation to obtain nano-bainitic microstructure which exhibits good mechanical properties comparable with those reported for nanobainitic wrought steels. To obtain the desired microstructure, it is necessary a correct selection of chemical compositions and isothermal transformation conditions. It was possible to explain the microstructure-mechanical properties relationship of the cast steel under study. This work shows that the future implementation of nanobainitic cast steel in the industrial sector is a plausible possibility, but there are still some challenges to overcome.

References

[1] Folgarait, P. (2006) "Bainitic steels for new rail materials." Publications Office of the EU: Luxemburg.

[2] Bhadeshia, H. (2015) Bainite in Steels: Theory and Practice; Maney Publishing: Leeds, UK.

[3] Voigt, R. (1985) "Development of Austempered High Silicon Cast Steels." AFS Trans.

[4] Son, J. (2010). "Effects of austempering conditions on the microstructures and mechanical properties in Fe-0.9%C-2.3%Si-0.3%Mn Steel". Met. Mater. Int.

[5] Tenaglia, N. E. (2018) "Assessment of the austemperability of high-silicon cast steels through Jominy hardenability tests". Mater. Sci. Technol transformation in a high-silicon cast steel". Mater. Sci. Technol

[7] Basso, A.D (2020) " Effect of the Microsegregation on Martensitic and Bainitic Reactions in a High Carbon-High Silicon Cast Steel ".Metals

[8] Cornide, J. (2013). “An assessment of the contributing factors to the nanoscale structural refinement of advanced bainitic steels”. J. Alloy. Compd.

[9] Santacruz-Londoño, A. (2020). “Microstructural and mechanical characterization of a nanostructured bainitic cast Steel”. Metals (Basel).

[10] Garcia-Mateo, C. (2012). “On measurement of carbon content in retained austenitein a nanostructured bainitic steel”. J. Mater. Sci.

[11] Santajuana, M.A (2018) “Low-temperature bainite: A thermal stability study”. Met. Mater. Trans.

[12] Garcia-Mateo, C. (2015) “Low-temperature bainitic ferrite: Evidence of carbon super-saturation and tetragonality.” Acta Mater.

[13] García-Mateo, C.(2005) “The Role of Retained Austenite on Tensile Properties of Steels with Bainitic Microstructures”. Mater. Trans.

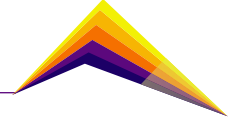

Evaluation of the anticorrosive properties of a paint using *Buddleja incana* extract as a corrosion inhibitor

Paucar K.[1] E-mail: kpaucar@uni.edu.pe
Tufinio K.[2] E-mail: ktufiniom@uni.pe
Vergara A.[3] E-mail: avergara@uni.edu.pe
Ames H.[4] E-mail: hamesc@uni.pe
Pizarro P.[5] E-mail: ppizarro@uni.edu.pe
Orcón B.[6] E-mail: borcon@uni.edu.pe
Cruz M.[7] E-mail: mcruzt@uni.edu.pe
La Rosa A.[8] E-mail: toro@uni.edu.pe

[1,2,3,4,5,6] Corrosion and Materials Laboratory. FIQT. National University of Engineering.
[7] Corrosion and Degradation of Materials Laboratory. FIGMM. National University of Engineering.
[8] Applied Electrochemistry Research Laboratory. FC. National University of Engineering.

Abstract

In this investigation, the anticorrosive evaluation of steel was carried out using paint that contains a natural inhibitor against corrosion obtained from the ethanolic extract of *Buddleja incana*, a native plant from Peru. The plant was characterized photochemically. The corrosion inhibition efficiency of the ethanolic extract in saline solution 3.5 wt.% NaCl on steel was determined at different inhibitor concentrations: 125, 250, 500 and 750 ppm using polarization curves. The highest inhibition efficiency, 76%, was reached at 500 ppm. The inhibitor extract was used in an epoxy paint to evaluate its anticorrosive properties on steel. The steel plates were painted with an epoxy paint in the absence of the inhibitor and with different concentrations of the inhibitor: 1%, 2% and 4 wt.%. The anticorrosive properties of the paint were evaluated using the neutral salt spray test (ASTM B117) and the REAP (Rapid Electrochemical

Correspondent author

Assessment of Paint) test. The salt spray test was performed at 250 h and 500 h of exposure and the Degree of Oxidation (ASTM D610), Degree of Blistering (ASTM D714) and Failure at scribe (ASTM D1654) were evaluated. The REAP test was performed in a 0.5M NaCl solution and in polarization conditions of -1.05V for 2h 30min. In the salt spray test at 250 h of exposure, the samples tested in the absence and presence of the inhibitor extract did not show significant differences in the degree of blistering, oxidation and failure at scribe. At 500 h of exposure, the steel plates painted with inhibitor presented similar behavior in the Degree of Blistering and Oxidation. In relation to the failure at scribe, the plates painted with inhibitor at different concentrations showed less deterioration compared to the one without inhibitor. As the concentration of the inhibitor increases, a better protection is observed, although with a decrease in adherence, due to the formation of blisters. The least deterioration at the incision was reported by the sample with 4 wt.%. The REAP tests allowed to establish that the protection current density of the steel plates with the paint with inhibitor at 4 wt.% is lower than the blank and the concentrations of 1% and 2 wt.%. The order of lowest current density is as follows: Inhibitor 4 wt.% (1.01mA/cm^2) < Inhibitor 2 wt.% (1.42mA/cm^2) < Inhibitor 1 wt.% (1.94mA/cm^2) < Blank (2.19mA/cm^2). The neutral salt spray results correlated with those shown with the REAP test.

Key words: *Buddleja incana*, neutral salt spray, REAP.

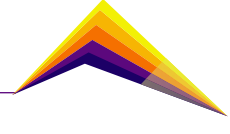

Introduction

The saline environment is a corrosive environment for carbon steel and other metals because it contains salts that, by rapid hydrolyzing, allow the transport of ions that attack the metal corroding it. One of the most common and least expensive ways to protect them is by means of paints that allow the metal to be separated from the corrosive medium. Among the main sectors that demand the use of paints, there is the construction sector with 22%[1]. The electrochemical measurements carried out have shown that alkyd paints have low protection against corrosion, while epoxy and vinyl paints have shown high protection[2]. To prevent any attack due to the permeability of the paint or the presence of imperfections such as small scratches that allow the diffusion of corrosive agents, it is better to add an inhibitor. Among the known pigments that act as inhibitors and that contain lead, are: minium lead Pb_3O_4-red, calcium plumbate Ca $(PbO_3)_2$-orange, lead is known to be toxic and can cause anemia and intellectual deficit in children; those known to contain chromate, are: zinc chromate $ZnCrO_4$ –yellow, calcium chromate $CaCrO_4$ -yellow, barium chromate $BaCrO_4$ –yellow[3], these contain Cr^{+6} ion which is very toxic to health and harms aquatic species. Although tannates have been synthesized from the tannin plant to obtain a pigment that acts as an inhibitor and at the same time is friendly to the environment[4], the synthesis is more expensive due to the reagents that are needed, as well as the equipment to be used and energy required. The plant that was used in this research was the species *Buddleja incana*, studies carried out for photoprotective effects with the extract of its aerial parts, were used to make sun creams due to the presence of flavonoids[5]. *Buddleja globosa* (matico), from Ecuador, phenylethanoid, flavone, flavonol, flavonova and quercetin[6] were observed. Other studies of optimization of conditions for the best extraction of *Buddleja Officinalis* showed the content of luteolin, glucoside, apigenin, acacetin, among others[7]. Therefore, in this work it is desired to test the inhibitory effect of the *Buddleja incana* extract in saline solution and later its addition in an epoxy paint whose protective properties were evaluated in the neutral salt spray and REAP tests.

Methodology

Preparation of plant extract and Phytochemical characterization

The *Buddleja incana* plant known as Quishuar was collected in Lima, Oyon District. The leaves were cleaned and dried under the shade for 3 weeks then were crashed into powder and stored in bottles for their use. 200 g of the plant powder was taken in 100 mL of ethanol at 30°C for 3 days, between immersion and ultrasound. Vacuum filtration was used to separate the liquid extract from the solid. The liquid extract was dried for later use. The phytochemical characterization was carried out following the procedure described by Lock[8].

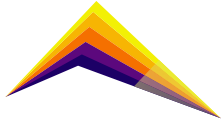

Preparation of the steel samples

The nominal composition of the carbon steel used was: C 0.17%, Si 0.17%, Mn 0.13%, S 0.009%, F 0.017%, Al 0.001%, N 0.0043%, Cr 0.32%, Ni 0.015% and Cu 0.014% and the remainder Fe. For electrochemical measurements, samples of 2.5x5.0x0.2 cm. were wet sanded through successive grades of silicon carbide abrasive papers from P80 to P1000. For salt spray and REAP tests, samples of 10.0 x 15.0 x 0.2 cm were wet sanded with silicon carbide abrasive paper of P80.

Preparation of the solutions for electrochemical measurements

The *Buddleja incana* dry extract was weighed and then diluted in ethanol using a stirrer. These ethanolic solution was added to 3.5 wt.% NaCl solution and stirred for 1h at 30°C. Thus, inhibitor concentrations were obtained in saline solution from 125 to 750 ppm.

Paint preparation with the extract inhibitor

An epoxy-polyamide resin was used in the preparation of the paint. The volume ratio of base paint (A) to hardener (B) was 4:1. The paint was mixed according to its formulation and an amount of *Buddleja incana* extract was added at 1%, 2% and 4 wt.%. It was applied using a brush. A dry film thickness of 3 mils was achieved.

Electrochemical measurements

A Gamry computer-controlled potentiostat (Reference 3000) connected to a three-electrode cell at room temperature, was used for the electrochemical measurements. The working electrode (WE) was the sample with an immersed area of 1 cm^2 and saturated Calomel electrode (SCE) and graphite were used as reference and counter electrode respectively. Measurements were performed three times to ensure reproducibility of the results. The Open Circuit Potential (OCP) measurements were performed for 1 hour. Tafel curves were obtained at a scan rate 0.166 mV/s and ± 250mV with respect to the open circuit potential (OCP). The corrosion inhibition efficiency was calculated using the following relationships[9]:

Where I^{o}_{corr} and I^{corr}_{inh} are the corrosion density currents in the absence and presence of inhibitor respectively.

Neutral salt spray (Fog) test

This test was performed in a BASS Equipment chamber. The test conditions were those indicated in the ASTM B117 Standard and the samples were run in triplicate. The time of exposure was 250 and 500 h. At the end of the test, the samples were evaluated according to ASTM D610, ASTM D 714 and ASTM D 1654.

Rapid Electrochemical Assessment of Paint (REAP) test

REAP test was performed using a Gamry Interface 1010B potentiostat in a three-electrode cell at room temperature. An incision using a scalpel was made inside the immersed area of 5cm^2 in 0.5M NaCl. The OCP was measured for 300 s, the impedance was measured from 0.1 MHz to 0.01 Hz. The potentiostatic test was performed at E = -1.05 V for 2.5 h; I limit = 1000 mA/cm^2. Intervals of polarisation of ±15 mV around the corrosion potential at a scan rate 0.166mV/s. were used in RPL measurements.

Results and analysis

Phytochemical characterization

It was possible to establish the presence of phenolic components, tannins, saponins, triterpenoids and alkaloids.

Electrochemical measurements

Table 1 shows the electrochemical data obtained from polarization curves. The extract acts as a mixed inhibitor[10]. At 500 ppm, the inhibition efficiency was 76%, a value slightly lower than that the observed for zinc chromate $ZnCrO_4$[11]. The presence of metabolites in the extract inhibitor can donate e^- from the free pairs present in their bonds and heteroatoms can have been protecting the steel.

Table 1. Polarization data of steel tests in 3.5 wt.% NaCl at different concentrations of extract inhibitor.

Concentration (ppm)	E_{corr} (V)	I_{corr} (µA/cm^2)	Tafel slope (mV/decade)		Inhibitor Efficiency (%)	Covered surface (θ)
			ba	bc		
Blanck	-59.6	4.63	121.1	232.1	-	-
125	-51.5	1.16	82.20	143.70	74.95	0.75
250	13.7	1.73	56.20	232.30	62.63	0.63
500	-29.6	1.09	55.00	170.20	76.46	0.76
750	-19.6	2.42	61.10	297.20	47.73	0.48

Neutral salt spray (Fog) test

The results obtained from painted steel in the absence and presence of inhibitor at different concentrations and time exposition is shown in table 2. At 250 h no difference was observed between the painted samples. At 500 h no difference was observed between the painted samples in Degree of Oxidation and Blisters. Considering the failure at scribe, the sample painted with 4 wt.% of the inhibitor presented less rust.

Table 2. Evaluation of painted steel samples for 250 and 500 h.

Samples painted, w/w %	Degree of Oxidation ASTM D610		Degree of Blistering ASTM D714		Failure at Scribe ASTM D 1654	
	250h	500h	250h	500h	250h	500h
Blank	10	10	10	10	9	8
1	10	10	10	10	9	9
2	10	10	10	10	9	9
4	10	10	10	10	9	9

REAP test

Figure 1 shows the current density to protect the painted samples. All samples with different concentrations of inhibitor need a lower current density for steel protection, in the following order: 4 wt.% (1.01mA/cm^2) < 2 wt.% (1.42mA/cm^2) < 1 wt.% (1.94mA /cm^2) < Blank (2.19mA/cm^2). The number of coulombs passing through the surface is lower in samples painted with the inhibitor than without the inhibitor (blank). The 4 wt.% inhibitor may have formed a kind of film on the metal surface that prevents the continuous release of ions from the steel, thus protecting the carbon steel.

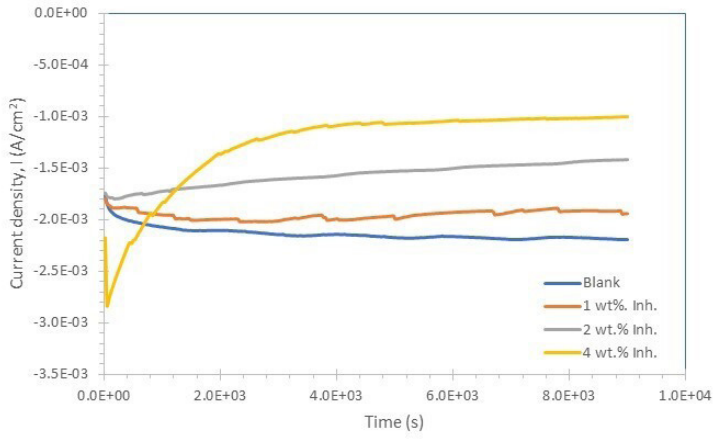

Figure 1. Current density, REAP, on the painted samples.

Conclusions

1. The phytochemical characterization found the following metabolites: phenolic components, tannins, saponins, triterpenoids and alkaloids.
2. In the Tafel tests, the maximum inhibition efficiency was reached at a concentration of 500 ppm with an inhibition efficiency of 76.46%. The inhibitor is of the mixed type.
3. At 500 h, the greatest failure at scribe was observed in the order Blank > 1 wt.% > 2 wt.% > 4 wt.%, although with a loss of adherence in this last concentration.
4. The REAP test evidenced the improvement in the protection of the inhibitor, 1.01mA/cm^2. The REAP results correlated with the results obtained in neutral salt spray.

Acknowledgment

The authors are grateful to Pro Ciencia – CONCYTEC (Grant 155 - 2017 – FONDECYT) for the monetary support for the purchase of equipment and materials and to the *VRI* of UNI.

References

[1] SNI (Sociedad Nacional de Industrias). (2016). Fabricación de pinturas, barnices y lacas. Instituto de estudios económicos y sociales (5) 6.

[2] Vera, R., Gomez, H., Layana, G. and Coñajagua, C. and Olguin, A. (1999). "Evaluación de pinturas mediante métodos electroquímicos y ensayos acelerados de corrosión". Información tecnológica. 10(2), 215-220.

[3] Shymala, M. (2013). Plant extract as corrosion inhibitors. Saarbrücken, Alemania: LAP LAMBERT.

[4] Hadzich Girolla, A. (2016). Síntesis y caracterización del tanato de zinc a partir del polvo de Tara (caesalpinia spinosa) y óxido de zinc como pigmento anticorrosivo para pinturas industriales. Obtenido de PUCP: http://tesis.pucp.edu.pe/repositorio/handle/123456789/7015.

[5] Panimboza, L., & Lida, V. (2015). Estudio de la actividad fotoprotectora de la Buddleja incana, en fototippos de piel III para la elaboración de protector solar. Rìobamba-Ecuador: Escuela superior politécnica de Chimborazo.

[6] Goity Vivar, L. E. (2007). Estudio químico y farmacológico de un extracto activo de Buddleja Globosa Hope, Matico y diseño de la metodología analítica. Santiago de Chile: Univ. de Chile.

[7] Guoyong , X., Ran, L., Han, Y., Zhu, Y., Wu, G., and Qin, M. (2017). Optimization of the Extraction Conditions for *Buddleja officinalis* Maxim. Using Response Surface Methodology and Exploration of the Optimum Harvest Time. Molecules, 22(11), 1877.

[8] Lock, O. (1994). Investigación fitoquimica. Métodos en el estudio de productos naturales. Segunda edición. Fondo editorial de la PUCP. Lima-Perú.

[9] Singh, A., and Lin, Y. (2014). Gingko biloba fruit extract as an eco-friendly corrosion inhibitor for J55 steel in CO2 saturated 3.5% NaCl solution. JIEC, 24, 219-228.

[10] Pradityana, A., Sulistijono, Shahab, A., Noerochim, L., and Susanti, D. (2016). Inhibition of corrosion of carbon steel in 3.5% NaCl solution by Myrmecodia Pendans extract. Hindawi, 1-6.

[11] Bethencourt, M., Botana, F., Marcos, M., Osuna, R., and Sanchez-Amaya, J. (2003). Inhibitor properties of "green" pigments for paints. Progress in Organic Coatings 46,280–287.

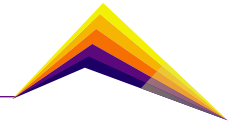

Analysis of mechanical energy transfer and dissipation in natural rubber – recycled EPDM compounds with potential use in piezoelectric tile contact surfaces

Fabián Andrés Giraldo Agudelo[1] *E-mail: fandres.giraldo@udea.edu.co*
Valentina Arenas Arevalo[2] *E-mail: valentina.arenasa@udea.edu.co*
Kelly Geraldine Rivera Botia[2] *E-mail: geraldine.rivera@udea.edu.co*
Diego Hernán Giraldo Vásquez[3]. *E-mail: dhernan.giraldo@udea.edu.co*

[1] Student, Master's Program in Materials Engineering, Universidad de Antioquia
[2] Student, Materials Engineering Program, Universidad de Antioquia
[3] Associate professor, Department of Metallurgical and Materials Engineering, Universidad de Antioquia

Abstract

In recent years, unexplored ways to obtain energy from clean sources are being studied. Piezoelectric tiles have been developed to transform mechanical energy from daily activities, such as walking and vehicle traffic, into usable electrical energy. In this work, the technical feasibility of using a compound of natural rubber (NR) with ethylene propylene diene monomer (EPDM) recycled ground rubber as contact surfaces for piezoelectric tiles was studied. The influence of recycled EPDM (EPDM-R) content on the mechanical properties and viscoelastic behavior of the compound was evaluated. The way in which mechanical energy is transferred and dissipated through the material obtained to the piezoelectric component was also studied. NR-based compounds with 0 phr, 10 phr, 30 phr and 50 phr of ground EPDM-R with particles having an average size of 1.7 millimeters were

Correspondent author

prepared by using an open roller mill. Each compound was analyzed in a moving die rheometer (MDR) at 160 °C according to ASTM D5289 standard, evaluating the storage modulus (S') related to mechanical energy transfer and the loss modulus (S") related to mechanical energy dissipation. The vulcanization time in which the ratio between S' and S" allowed to transfer the greatest amount of mechanical energy without neglecting the damping capacity to provide comfort was also found. Cyclic and transient uniaxial compression tests were carried out under loading and deformation-controlled conditions. Finally, the voltage at the output of a piezoelectric element located on the underside of vulcanized cylindrical specimens subjected to impact was measured. It was found that the compound with 30 phr of recycled post-consumer EPDM particles is technically feasible to be used in piezoelectric tiles.

Key words: NR and EPDM-R blends, recycled EPDM rubber, energy efficiency, piezoelectric tiles, mechanical energy transfer and dissipation.

Introduction

The implementation of renewable and environmentally friendly sources such as wind, solar, tidal, hydraulic energy, among others, has been sought, seeking to meet the energy needs for man-made activities [1]. This is how unconventional low-generation sources have been proposed, such as piezoelectric tiles that obtain electrical energy from the use of the mechanical energy of people walking [2], [3].

Nowadays, the high cost and the need to improve the energy efficiency are diminishing the demand for piezoelectric tiles. It has been reported the improvement in the generation and storage systems of the electrical energy, aiming to reduce costs and increase the performance of these devices [4], [5]. The role that the material of the exposed surface may have on the energy efficiency of piezoelectric tiles has not been reported yet. It is also necessary to study the viscoelastic behavior of polymeric materials used in piezoelectric tile surfaces seeking to increase the delivery of mechanical energy to the piezoelectric sensors by having a high storage modulus and simultaneously offer the sensation of comfort when walking.

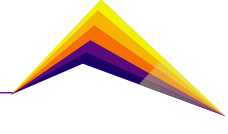

In this work, a circular economy case study is addressed. Since NR compounds with post-consumer EPDM from parts of the Medellin Metro trains are evaluated in a way that the compound obtained can be potentially used in the manufacture of piezoelectric tiles surfaces that can be installed in this mass transportation system. The influence of the EPDM-R content on the mechanical properties and the viscoelastic behavior inherent to the rubbers was studied.

Materials and Methods

NR/ EPDM-R rubber compounds were prepared in an open roller mill following the formulation shown in Table 1. For each compound, the complete vulcanization time t100, and the value of tan at t100 were measured by MDR at 160 °C. Three cylindrical specimens of 29 mm diameter and 12.5 mm height of each compound were vulcanized at 160 °C, using a time of 11/3 times the t100 obtained by MDR, and considering the effect of the thickness of the cylinder on the heat transfer [7].

Table 1. Ingredients used in the formulation, phr (parts per hundred of rubber by mass).

Ingredient	phr
NR SSR	100
R-EPDM	0, 10, 30, 50
Zinc oxide	5
Sulphur	2.25
Stearic acid	2
Accelerator, TBBS	0.7
Carbon black, N550	35

NR ADS= natural rubber air-dried sheets, TBBS = N-Tertiarybutyl -2- benzothiazole sulfonnamide, R-EPDM= recycled ethylene-propylene-diene rubber.

The Shore A hardness of the vulcanized cylinders was measured using a CEAST durometer. Static uniaxial compression tests were carried out by applying three consecutive cycles of loading and unloading, in such a way that in the third cycle the elastic modulus was measured, using a jaw speed of 12 mm/min and applying a maximum deformation of 25%, according to the method B of the standard ASTM D575 [8]. Transient tests were carried out applying a maximum stress of 0.8 MPa during 13 cycles of loading and unloading in compression. During transient tests a jag speed of 180 mm/min was applied both in the loading phase and in the unloading phase, using a time between cycles of 30 seconds, recording the data in cycles 3 and 13 seeking to determine the change in energy dissipation and the compressive modulus

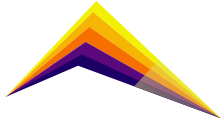

as a result of the applied loads. The dimensions of the specimens were measured before and after the compression tests to verify that the tests were carried out in the viscoelastic regime of the compounds.

Finally, the transfer and dissipation of the mechanical energy of the evaluated compounds were evaluated using an experimental setup. A steel bar with a diameter of 9.5 mm, a length of 10 cm and a weight of 59 grams was dropped 47 cm vertically from rest inside a transparent PVC tube, until the cylinder impacted the specimen surface. A piezoelectric sensor connected to a UniT oscilloscope was placed under the cylindrical specimen, with which the voltage signals, produced by the piezoelectric sensor, were measured when it was mechanically excited by the first and second impact of the bar on the surface of the specimen. The base-peak potential difference produced by the first impact was measured as an indication of mechanical energy transfer. The time elapsed between the signal produced by the first impact and that produced by the second impact was also measured, as an indication of the dissipation of mechanical energy that occurred as a rebound effect. Three cylindrical specimens of each compound were evaluated, subjecting each specimen to 7 periodic launches with a time of 3 minutes between each launch. The data of voltages and times were analyzed to identify the effect of the content of recycled EPDM on the transfer and dissipation of energy.

Results

Moving die rheometry

The NR/EPDM-R compounds with 0, 10, 30 and 50 phr of recycled ground particles presented a decrease in t100 with the increase in the content of EPDM-R, obtaining 9.68 ± 0.42, 9 .01 ± 0.12, 8.68 ± 0.31 and 8.48 ± 0.19 minutes, respectively. The damping capacity is related with the tanδ value when the compound reaches the maximum degree of vulcanization. It was found at 160 °C that tanδ increased with the increase in EPDM-R content, reaching values of 0.046 ± 0.007, 0.057 ± 0.010, 0.074 ± 0.004 and 0.094 ± 0.005 for the compounds with 0, 10, 30 and 50 phr of EPDM-R, respectively. The results indicate that the addition of EPDM-R decreases the energy expenditure required for vulcanization and increases the damping capacity related to walking comfort, evidencing the technical feasibility of using EPDM-R in piezoelectric tiles.

Shore A hardness and stiffness under uniaxial compression

Figure 1 shows the results obtained from the measurements of Shore A hardness and secant modulus at 20% strain under uniaxial compression. All the stress-strain curves obtained during the compression tests showed the typical behavior of rubbers subjected to compressive stresses with low levels of deformation.

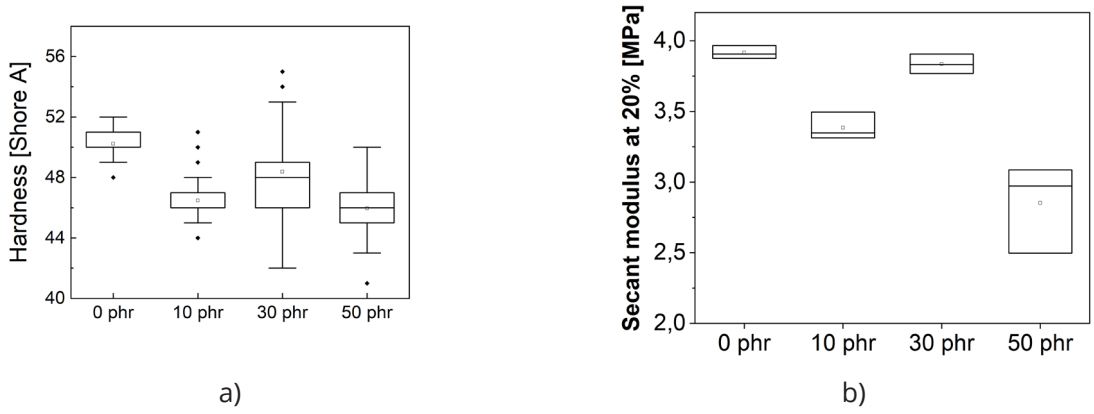

Figure 1. a) Hardness and b) Secant modulus at 20% strain of the studied compounds.

A Tukey test with a significance level of 95% showed that no statistically significant differences were found between the compound without recycled rubber and the compound with 30 phr of EPDM-R.While the compound with 50 phr exhibited the lowest uniaxial compression stiffness among the materials studied and the highest variability in hardness. The compressive stiffness results indicate that the compound with 30 phr is potentially useful for fabricating the contact surface of the tiles.

Cyclic load-unload tests under uniaxial compression

Figure 2.a shows a typical curve obtained for cycles 3 and 13 of charge-discharge. The observed behavior is convenient in contact surfaces of piezoelectric tiles because when this stiffening occurs between cycles, the energy dissipated in the deformation process of the rubber compound exhibited low variation. However, it is advisable to evaluate the behavior of the mixtures by applying a greater number of charge-discharge cycles. Figure 2.b shows the results of the hysteresis calculated for cycles 3 and 13 of the load-unload tests under uniaxial compression. An increase in hysteresis was found as the EPDM-R content increased, confirming the behavior of tanδ at t100 observed by MDR at 160 °C.

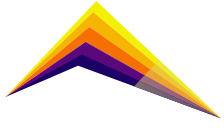

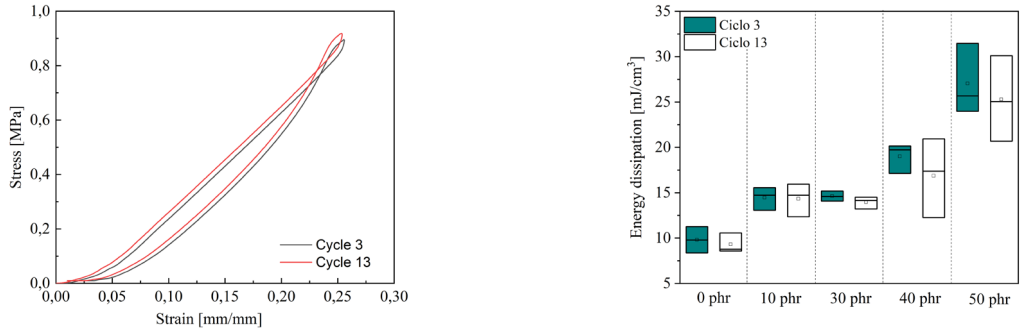

a) b)

Figure 2. a) Load-unload curves of the compound with 10 phr of EPDM-R. b) Energy dissipation (mJ/cm^3) in uniaxial compression.

Rebound test

A Tukey test with a significance level of 95% showed significant differences when comparing the rebound between the mixtures studied, achieving output voltages between 8 and 13 volts in all tests. The rebound time tended to decrease on average with the increase in EPDM-R content from 0 to 50 phr, but no statistically significant difference was found between the mixtures with 0 and 10 phr of EPDM-R. These results indicate that as the content of EPDM-R increases, there is a greater dissipation of energy within the material, which explains why the rebound is less, but without showing any significant effect on the voltage at the output of the piezoelectric element.

Conclusions

The mixture of a natural widely traded biopolymer such as NR mixed with 30 phr with an industrial waste such as EPDM-R, offers the best balance between circular economy objectives and the transfer of mechanical energy using waste that required less grinding energy than the particle sizes reported in the literature. For future studies, it is recommended to analyze compositions between 30 phr and 50 phr to assess the possibility of including a higher content of EPDM-R without a significant decrease in the voltage at the piezoelectric output.

Acknowledgments

The authors wish to thank the CODI of the University of Antioquia for financing this work with resources from the PRG2020-34225 project.

References

[1] P. G. Technologies, Renewable Energy Systems and Distributed Generation. 2019. doi: 10.1109/ess.2019.8764222.

[2] J. Cifuentes, «Baldosas piezoeléctricas para alimentar sistemas de iluminación de bajo consumo energético», 2013, doi: 10.1190/segam2013-0137.1.

[3] E. Ojeda, «Diseño de instalación de baldosas piezoeléctricas para iluminar multicancha en la sede Viña del Mar», 2019.

[4] M. R. Sarker, S. Julai, M. F. M. Sabri, S. M. Said, M. M. Islam, y M. Tahir, «Review of piezoelectric energy harvesting system and application of optimization techniques to enhance the performance of the harvesting system», Sensors Actuators, A Phys., vol. 300, p. 111634, 2019, doi: 10.1016/j.sna.2019.111634.

[5] S. Nandan y R. Trivedi, «Design and Fabrication of Mechanical Footstep Power Generator», SSRN Electron. J., 2020, doi: 10.2139/ssrn.3555638.

[6] H. Nabil y H. Ismail, «Blending of Natural Rubber/Recycled Ethylene-Propylene-diene Rubber: Promoting the Interfacial Adhesion Between Phases by Natural Rubber Latex», Int. J. Polym. Anal. Charact., vol. 19, n.o 2, pp. 159-174, 2014, doi: 10.1080/1023666X.2014.873597.

[7] M. Guzmán, D. Giraldo, y R. Sánchez, «Rheometric, transient, and cyclic tests to assess the viscoelastic behavior of natural rubber-based compounds used for rubber bearings», Mater. Today Commun., vol. 22, n.o March 2019, p. 100815, mar. 2020, doi: 10.1016/j.mtcomm.2019.100815.

[8] ASTM D575-91, «Standard Test Methods for Rubber Properties in Compression», ASTM, vol. 91, n.o Reapproved 2012, pp. 2012-2015, 2014, doi: 10.1520/D0575-91R18.2.

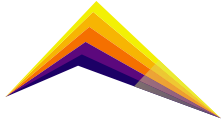

Evaluation of the erosion behavior of UNS C52400 bronze for potential application in 1 KW hydrokinetic turbine blades

Daniel Ramírez
Marcelo Rojas

E-mail: daugusto.ramirez@udea.edu.co

Universidad de Antioquia

Abstract

Currently, technological advances applied to the production of sustainable electrical energy have brought the development and implementation of various technologies such as hydrokinetic turbines. This type of turbines are used in rivers of medium flow and medium fall water in remote regions called non-interconnected zones. This has become the object of study and development of materials that can be used in the manufacture of components for this equipment in search of clean energy production. Phosphor bronzes have good wear resistance properties and for this reason UNS C52400 bronze refined with Zr has been considered for its study and evaluation against erosion wear phenomena for its potential application in the manufacture of hydrokinetic turbine blades. Therefore, the design and fabrication of a phosphor bronze alloy has been carried out to carry out erosion tests by sediment in Rotatory Disk Apparatus (RDA), using bronze samples as-cast, water with pH=10 and pH=4 at room temperature, an exposure time of 18 hours and in the presence of silica sand with a size between 0.5 and 2mm in diameter, inside a system rotating at 1250 RPM to simulate real operating conditions at laboratory level. Mass loss was measured and evidence of wear

Correspondent author

was sought by obtaining stereoscopic, optical microscopic and SEM images. With the evidence obtained, it was determined that the pH of the water is a very influential factor in the behavior of the material in the face of erosion phenomena, showing that at pH=10 there is a greater loss of material with respect to the medium with pH=4, making comparisons of Mean Depth Erosion (MDE). The results obtained allowed to know the behavior of the material under the test conditions used, and in this way to predict the performance of the bronze UNS C52400 in operation according to the characteristics of the water resource in which this hydrokinetic turbine technology is to be implemented.

Key words: hydrokinetic turbines, blades, erosion, phosphor bronze, RDA, MDE.

Introduction

The energy provided by the flow of a river is considered clean and constant, and to implement technologies with these characteristics it is important to identify the advantages of minimizing the need to build a civil infrastructure as traditionally done in the assembly of large hydroelectric dams. Due to this, a series of submersible turbines have been developed in riverbeds called hydrokinetic turbines, whose main purpose is to generate electricity to supply populations far from urban areas and the electrical interconnection system, also called non-interconnected zones (ZNI). These activities involve the transport of particulate material from the sludge as it is naturally found in riverbeds or from other activities such as mining. The mechanical action of the particles and the chemical attack result in an increase in the frequency and types of failure of critical turbine components, such as blades [1], [2].

It has been identified that one of the most aggressive wear phenomena for this type of applications is erosion. This phenomenon is a form of wear caused by the impacts of solid or liquid particles on a solid surface. In general, erosion by solid particles depends on the material exposed to the fluid and the properties of the particles carried by the fluid. In turn, it is determined by the relative velocity and the angle of impact of the particles, so it is a dynamic process because the particle-surface interaction times are very short. Therefore, there is still no precise model that can fully explain this wear phenomenon. In general, the existing models represent only the experimental results, from which they were constructed [3], [4].

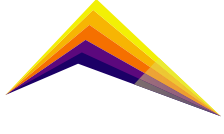

For the study of the behavior of a certain material under erosive wear, an equipment called RDA is usually used, where experimental tests are carried out thanks to a flow of water with the presence of sediments. The main objective is to subject the material to conditions similar to those it would be exposed to in a riverbed. Figure 1 shows a scheme detailing the main parts that make up the RDA.

The selection of materials for the construction of a turbine is an important decision to achieve the sustainable implementation of the technology, traditionally materials such as martensitic stainless steels, bronzes or aluminum have been used for the manufacture of blades. These materials, due to their microstructural characteristics, confer them high resistance to wear phenomena such as erosion or it is evidenced that the formation of secondary phases increases the hardness of the material, thus favoring its resistance to phenomena such as erosion and decreasing mass loss [7].

Phosphor bronzes are copper, tin and, phosphorus alloys characterized by high hardness, good wear resistance, good toughness, good properties in bearing applications and good corrosion resistance. The addition of tin increases the corrosion resistance and mechanical strength of the alloy. Phosphorus increases the wear resistance and stiffness of the alloy, that is designated as UNS C50100 to C54200 [8].

Methodology

The material chosen to evaluate its erosive wear behavior is a UNS S52400 bronze casting inoculated with zirconium and for the experimental section samples should be obtained as presented in Figure 2 under ASTM A48 standard with 26 mm diameter and 7 mm thickness. This design was adapted using software such as SolidWorks and SolidCast to obtain the prediction of healthy parts for the casting of bars as shown in Figure 3. These simulated designs were used for the 3D prototyping of the casting models. Successively, these models were used in the manufacture of the casting molds to obtain the cast metal bars.

These samples were extracted from the bars by MDE cutting and subsequently prepared superficially based on the ASTM E3-11 standard and their roughness was analyzed using a Taylor Hobson Surtonic S-128 portable profilometer using ASTM D7127-17 [103] and ISO 4287-97 standards. Wear resistance was performed by evaluating the mass loss and the MDE measurement attributed to the effect of the tests on the RDA. The equipment was configured to simulate the operation of a 1KW hydrokinetic turbine, where a speed of 1250 RPM was used at pH=4 and pH=10 for water, a sediment size between 0.5 and 2 mm in diameter and a wear exposure time of 18 hours in 3-hour intervals for measurements. The parameters for the tests were selected according to the ASTM G32 standard and the studies carried out by different authors such as Neopan, Ramírez and Usma, which can be seen in Table 1.

Results and analysis

The erosion tests were carried out in an RDA, the assembly of the bronze samples in the equipment can be seen in figure 4. The MDE presented in Table 1 corresponds to the height in μm of material that has been detached due to the erosion phenomenon and is attributed to the presence of silica sand as abrasive material. It was observed that at pH=4 the bronze presents a MDE of 542.9 μm and at pH=10 it presents a MDE of 961.9 μm. Due to this, it was identified that one of the variables that plays a more vital role is the pH of the water. At different pH conditions, this material can form passive oxide layers of different composition, or can present itself in the form of an ion on its surface as indicated by the Pourbaix diagrams. When experimentally subjected to a basic medium, in this case pH=10, and depending on the potential formed in the system, there will be a tendency to the formation of cuprite (low potentials) or tenorite (higher potentials). In both cases a passive layer, that protects the material from oxidation, is formed, but under the erosion conditions presented, the layers facilitate the detachment of material. Figure 5 shows a comparative diagram of MDE for both water pH and erosion tests.

Figure 6 shows micrographs of the bronze refined with zirconium, showing a dendritic growth of the primary phase, in addition to the micro-segregation of tin, due to the fact that the last regions that solidify have a higher tin content (white color), the regions with lower amount of tin are found in the center of the dendritic arms (brown color) and faceted particles that presumably correspond to ZrC, in addition, the presence of a phase (gray color) can be seen in the interdendritic region that corresponds to the delta phase.

Figure 7a and 7b show stereoscopic and SEM images of the bronze samples subjected to erosion tests at pH=10 and pH=4, respectively. Zone 2, defined in the stereoscope images, denotes the direction of the flow during the 18 hours of testing. The SEM images were taken at 1000X, where the surface deformation produced by the interaction of the particles on the surface of the metal can be identified. A more accentuated wear on the sample evaluated at pH=10 can be observed. The basic medium gave a MDE of 13.7% and average roughness of 0.281 μm, while the acid medium yields a MDE of 7.8% and average roughness of 0.292 μm, which shows that the loss of material is lower in the acid medium.

Conclusions or summary

The pH of the medium is a particularly influential factor. At pH=10, the bronze presents a MDE of 542.9 μm and at pH=4, it was 961.9 μm due to instability of the passive layer of the bronze that allows material detachment in a basic environment.

The refined bronze shows a better erosion wear behavior in a medium with pH=4 according to the methodology used, presenting lower average values of MDE compared with what is evidenced in a medium with pH=10.

References

[1] H. Dubrovsky, G. Nadal, N. Di Sbroiavacca, and R. Contreras, "Rol y perspectivas del gas natural en la transformación energética de América Latina CEPAL," 2019.

[2] S. Chitrakar, H. P. Neopane, and O. G. Dahlhaug, "Study of the simultaneous effects of secondary flow and sediment erosion in Francis turbines," Renew. Energy, vol. 97, pp. 881–891, 2016, doi: 10.1016/j.renene.2016.06.007.

[3] M. K. Padhy and R. P. Saini, "A review on silt erosion in hydro turbines," Renew. Sustain. Energy Rev., vol. 12, no. 7, pp. 1974–1987, 2008, doi: 10.1016/j.rser.2007.01.025.

[4] H. P. Neopane, "Sediment erosion in hydro turbines," 2010.

[5] V. Javaheri, D. Porter, and V. T. Kuokkala, "Slurry erosion of steel – Review of tests, mechanisms and materials," Wear, vol. 408–409, no. May, pp. 248–273, 2018, doi: 10.1016/j.wear.2018.05.010.

[6] A. Usma, "Comportamiento de diversos materiales usados en la fabricación de álabes de turbinas hidrocinéticas ante los efectos combinados de erosión/corrosión/cavitación bajo diferentes condiciones hidráulicas," Universidad de Antioquia, 2019.

[7] R. H. Richman and W. P. McNaughton, "Correlation of cavitation erosion behavior with mechanical properties of metals," Wear, vol. 140, no. 1, pp. 63–82, 1990, doi: 10.1016/0043-1648(90)90122-Q.

[8] Copper Development Association Inc., "Phosphor Bronze," 2013. https://www.copper.org/resources/properties/microstructure/phos_bronze.html.

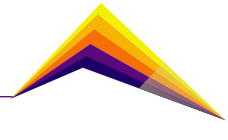

Table 1. Erosion and cavitation test results in RDA.

	pH water	Exposure time (h)	Mass before (g)	Mass after (g)	Mass loss (mg)	MDE (μm)	Average wear rate
Erosion	4	18	24,69680	22,25680	2439,99750	542,91856	0,09470
	10		25,43526	21,13553	4299,72100	961,99131	0,16861

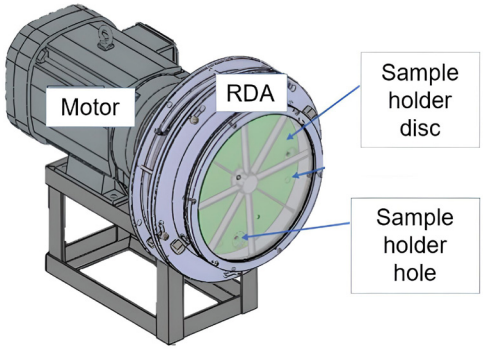

Figure 1. Components of the RDA [6].

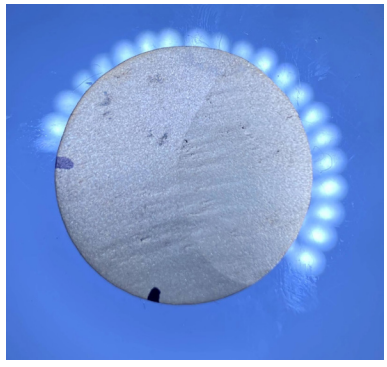

Figure 2. Bronze sample for experimental tests.

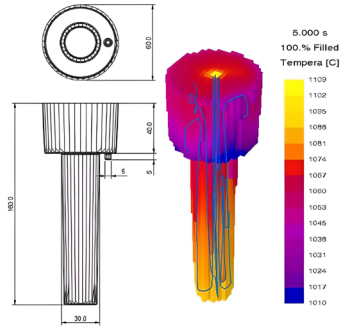

Figure 3. CAD design of the casting system.

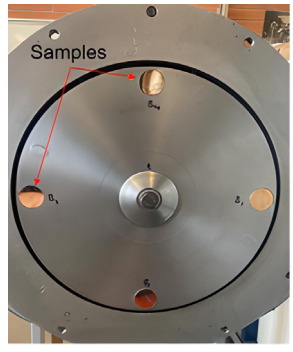

Figure 4. RDA enabled for erosion testing.

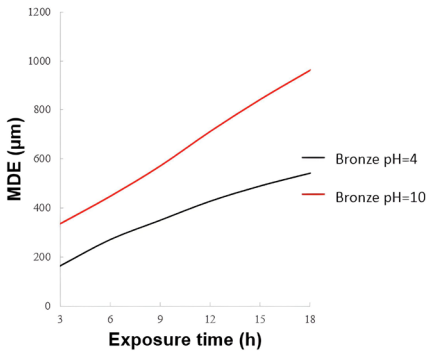

Figure 5. Average MDE of the erosion tests.

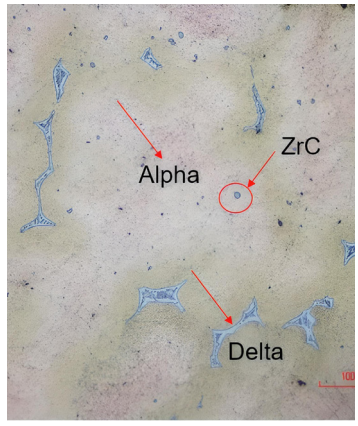

Figure 6. Micrograph of bronze sample refined with zirconium 200x.

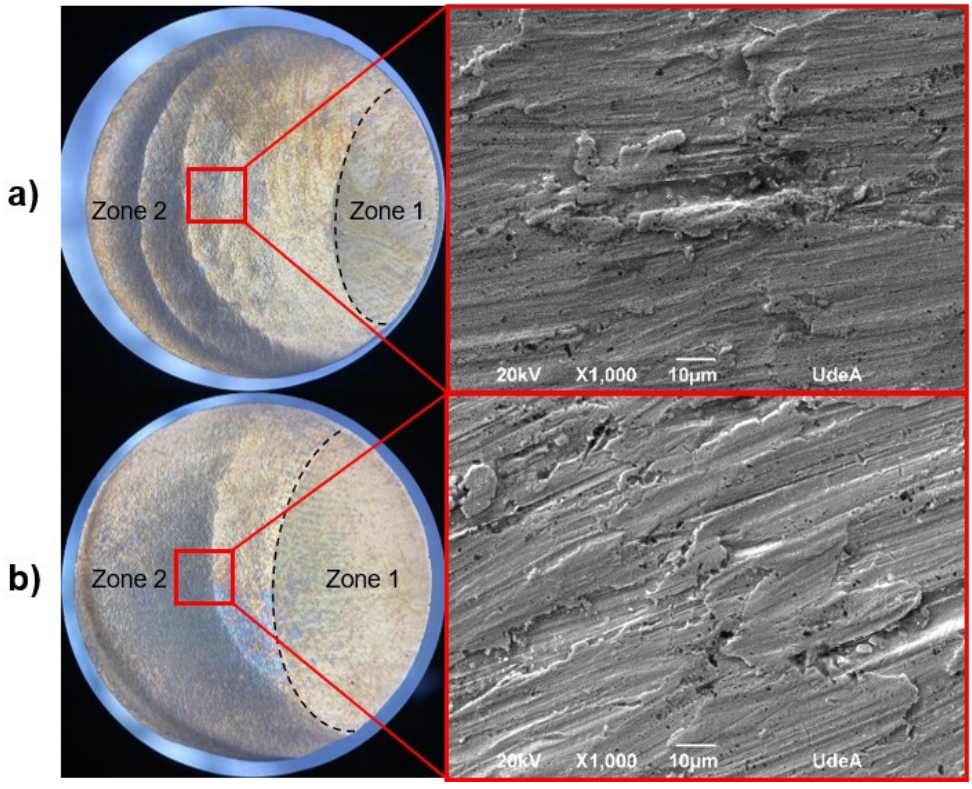

Figure 7. Stereoscope and SEM images of erosion weathering in a) water with pH=10 and b) water with pH=4.

Thermally sprayed hydroxyapatite-based coatings: advantages and challenges

John Henao[1] *E-mail: john.henao@ciateq.mx*
Astrid Giraldo-Betancurt[2] *E-mail: agiraldo@cinvestav.mx*
Carlos Poblano-Salas[3] *E-mail: carlos.poblano@ciateq.mx*

[1]PhD., CONACYT-Centro de Tecnología Avanzada A.C (CIATEQ), Unidad Querétaro, México
[2]PhD., CONACYT-CINVESTAV-IPN, Unidad Querétaro, México
()[3]PhD., Centro de Tecnología Avanzada A.C (CIATEQ), Unidad Querétaro, México

Abstract

Thermal spraying has been employed for over a century in the development of industrial, decorative, and biomedical coating applications. Since the seventies, hydroxyapatite coatings were developed as an option to increase metallic implant osseointegration in human bone. Many clinical trials have demonstrated that thermal sprayed hydroxyapatite coatings can achieve a good mechanical and chemical bone bonding in orthopedic implants. Nevertheless, in the last two decades, the development of new biomaterials and different thermal spraying techniques have opened new spraying and material combinations that are focused on achieving better mechanical response and multifunctionality. Nowadays, thermal spraying is still one of the most accepted techniques within the biomedical industry for the treatment of metallic biomedical implants to provide them with bioactive and multifunctional properties. This work is a summary about the past and present of hydroxyapatite-based coatings obtained by thermal spraying.

Correspondent author

Keywords: Hydroxyapatite, Thermal Spraying, Biomedical Applications.

Introduction

Hydroxyapatite (HA) is a bio-ceramic constituent of human bones and teeth, possessing significant biocompatibility and bioactivity. Its chemical formula is $Ca_{10}(PO_4)_6(OH)_2$, which is similar to the natural apatite present in the human bone. The elemental distribution of HA consists of 40 % Ca, 18.5 % P and 3.38 % OH by weight with a ratio Ca/P of 1.67. The unit cell of HA is constituted by a hexagonal crystal structure and space group □63/□. Since HA can mimic the mineral component of the human bone, this material has been prepared in various forms and has been extensively studied for orthopedics, dental, and craniofacial applications. It is worth pointing out that dense hydroxyapatite does not have the mechanical strength, especially fracture toughness, to allow its use in long-term load-bearing applications in the human body [1].

It is a common praxis the use of metallic biomaterials for orthopedic, cranial, and maxillofacial applications, and the clinical experience has proved that this type of metallic biomaterials can work well to improve the lives of several patients along the years. Several metallic biomaterials are currently known such as titanium, Ti6Al4V alloy, stainless steel, and cobalt based alloys; the advantage of these metallic alloys is their mechanical strength, which allows their use for load bearing applications, including hip, knee, and dental implants [2].

However, after prolonged use, there is clinical evidence that metallic implants can show some weakening in their bone bonding capacity as well as the release of toxic ions towards the physiological fluids, establishing, in some scenarios, a risk for the health of the patients. Since metallic biomaterials are prone to experience corrosion in body fluids and have limited bioactivity, the biomedical industry has put efforts to improve the physical and chemical properties of the implants; for instance, working on the enhancement of biocompatibility, the control of ion release, and promotion of osseointegration [3]. Osseointegration is often promoted by bioactive materials such as HA. Bioactive materials are those that can stimulate a biological response from the body such as mineralization and adhesion of a surface to body tissues. Bioactive materials are classified as osteoconductive and osteoproductive. An osteoconductive material favors the formation of a bond between its surface and the hard tissue (bone) and can stimulate bone growth. HA and tri-calcium phosphate ceramics are included among the bioceramics with osteoconductive ability. On the other hand, osteoproductive biomaterials are those that can stimulate the growth of new bone on their surface. Bioactive glasses are one of the biomaterials that possess osteoproductive properties, receiving a lot of attention towards the development of composite materials with applications requiring bone repair [4]. In this manner, based on the properties of bioactive materials, many investigations have been performed in the last three decades on the use

of ceramic bioactive materials to provide osteoconductive and osteoproductive properties to metallic implants [5, 6]. The deposition of bioceramic coatings on metallic implants is a procedure that has been studied by using different methods such as dip-coating, electrochemical deposition, electrophoretical deposition, and thermal spray [7].

The fundamental requirement of a permanent bone implant is the achievement of a strong bonding with the surrounding host bone, which ensures a good mechanical anchorage of the implant and reduces the risk of osteolysis. In this sense, despite the different deposition methods reported in the literature, thermally sprayed HA-based coatings have shown a high rate of success in orthopedics implants under in-vivo evaluations and clinical tests [8, 9]. In fact, nowadays, large multinational companies in the biomedical industry offer thermally sprayed HA coatings among their technological options of commercial orthopedic and dental devices.

HA-based coatings by thermal spraying

Thermal spraying is a category of coating processes that apply a feedstock material as a spray of finely divided molten and/or semi-molten droplets, or heated solid particles, to produce a coating by the successive impact of these droplets and particles on the surface of a part or device. Thermal spraying is known by its ability to deposit coatings of various materials such as metals, ceramics, cermets, and polymers in coating thicknesses comprising 0.05 to 1 mm. One can say that almost any powdered material can be deposited by thermal spraying as long as it can melt before and at the impact or becomes plastic upon the impact on the substrate surface [10]. The coating obtained does not promote substrate melting, which is a significant signature of thermal spraying when compared to many other coating processes, making it a good option for the biomedical industry.

There is a family of thermal spraying processes, all working under the same operation principle based on the acceleration, heating, and impact of a material in a molten, semi-molten, or solid state on the surface of a part. These processes are usually classified according to the source of energy that they employ, which can be chemical, electrical, or kinetic. Chemical-based processes are those involving the combustion of gases to produce a flame which has the target of melting the material to form the coating. These processes include flame spray (FS), high velocity oxygen fuel spray (HVOF), high velocity air-fuel spray (HVAF), and the detonation gun (D-GUN) spray process. Alternatively, the processes based on electrical energy are those that generates an electric arc between two electrodes to heat a gas stream injected into a gun. Plasma spraying (PS) and Arc-Spraying (AS) are two well-known processes. Finally, the low-temperature high-kinetic energy-based processes, known as cold spraying (CS) or kinetic spraying deposition, are an attractive option to process ductile metal/alloys and some ceramics with the advantage of avoiding undesirable high-temperature transformations in this type of materials. Usually, materials processed by CS impact on the substrate surface in solid state and the formation of the coating is promoted by the plastic deformation of the interacting surfaces [11]. Among the above-mentioned family of thermal spraying processes,

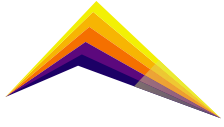

PS is the preferred spraying technique for the fabrication of HA-based coatings in most of the implants in the current market. This confidence has been gained along many years of research and successful clinical trials around world.

The PS technique involves a high electrical energy source employed to create a plasma jet, which provides enough thermal energy to the HA particles to melt and propel them onto the surface of the metallic implant. In PS, the arc gases, known as plasma forming gases, are mainly Ar, He, N_2 and H_2. Depending on the different processes, the temperature ranges from 10,000 to 15,000 °C. Thus, due to this wide range of temperatures, HA and any type of oxides and ceramic materials can be deposited by PS [10, 11]. Interestingly, in the last decades, some clinical trials have mentioned that the benefits of plasma sprayed HA coatings can be lost after some years of use, which have been associated with a high rate of dissolution of the coating in body fluids [12]. This fact has been taken as a limitation associated with the PS process which favors the decomposition and phase changes of the HA powder at high temperature. Less stable phases of HA can be formed during the deposition of HA by PS, including amorphous calcium phosphate, β-tricalcium phosphate, tetracalcium phospahate, α-tricalcium phosphate and calcium oxide.

Similarly, the scientific community have focused efforts on developing new alternatives for the fabrication of HA-based coatings. Combustion-based thermal spraying has risen as a promising alternative for the development of HA coatings. FS and HVOF processes concentrate most of the academic research in the last decade for the development of HA coatings [13, 14]. For instance, the published results [14] on the fabrication of HA coatings by HVOF suggest that a reduced number of metastable phases, compared to those obtained by PS, are formed by employing this technique. This fact is associated with the less pronounced thermal gradient experienced by the HA particles upon impact in the HVOF process than that observed in PS. Along with the biological response of HA-based coatings, studies on the mechanical properties and fracture toughness of such coatings have also been of a great importance, in particular, to get the best possible performance for load bearing orthopedic applications. Some efforts have been performed at Mexico´s National Thermal Spray Laboratory (CENAPROT) on the development of HA-graded coatings [14, 15]. Graded coatings are multilayered deposits which combine at least two different materials. The properties of the two materials are combined to achieve a better adhesion and fracture toughness. For instance, HA-TiO_2 graded coatings have shown a better mechanical response after several days of immersion in simulated body fluids [15]. Further in-vitro studies have also demonstrated the ability of HA-TiO_2 graded coatings to promote the formation of apatite on its surface. Other coating alternatives developed by CENAPROT´s research team have been the introduction of different ceramic materials not only to achieve a better mechanical coating behavior but also to provide multifunctional properties such as osteogenesis and antibacterial response [16]. For instance, HVOF HA-graphene oxide sprayed coatings are promising candidates to replace pure HA, in particular, for applications involving patients with pre-existent comorbidities. Preliminary studies have shown that the combination of HA and graphene oxide is biocompatible, osteoconductive, and antibacterial [16 17]. Nevertheless, there is still some work ahead for optimizing this type of coatings by thermal spraying, especially, due to the dissimilar densities and degradation that can be experienced

by the high temperatures of some thermal spraying process. Other multifunctional coatings developed for biomedical applications by thermal spray include HA-piezoelectric compounds, which are mostly intended to stimulate bone remodeling through the activation of cellular processes [18]. This topic is currently one of the most interesting developments associated with HA-based coatings by thermal spray, since there are several fronts to explore, such as the use of lead-free high-performance piezoelectric compounds and all the optimization involved with the deposition of the coatings by thermal spray process such as PS and HVOF.

Other research groups around the world have also continued the development of HA coatings by PS. As mentioned above, the new alternatives proposed are focused on improving mechanical behavior and multifunctionality (for instance, HA reinforced with graphene nanoplatelets). Some reports [19] have suggested that graphene nanoplatelets can result in the reduction of porosity, dispersion strengthening, and enhanced toughness. Other approaches include the fabrication of HA-bioactive glass composite coatings by PS [20, 21]. The advantage of using bioactive glasses in the coatings their ability to provide properties of osteoproduction and osteoconduction to the coating.

As mentioned above, some of the main challenges in the fabrication of HA-based coatings by thermal spraying are the high temperatures and thermal gradients involved in such processes, which promotes the precipitation of undesired phases. Related to this issue, in the last decade, some research groups have explored the cold spraying process as an alternative method for the deposition of HA-based coatings. Interestingly, it is well-known that ductility is one of the requirements for the deposition of materials by cold spraying. However, HA is a bioceramic material that lacks of ductility under the operation conditions of the cold spraying process. Some of the explored alternatives to obtain HA coating by cold spraying are the use of a rough bond coat layers, agglomerated sub-micrometric particles as raw materials, and powder mixtures including a ductile phase [22-24]. This topic is still in the frontiers of science; however, there are some efforts to understand the deposition mechanisms of bioceramic materials by cold spray in order to produce high quality coatings that can compete with, and even replace, the commercial PS HA-based coatings. Some of these known efforts are carried out nowadays by the CNRS in France and CONACYT in Mexico through basic science funded projects.

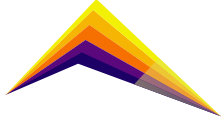

Summary

Hydroxyapatite coatings are widely applicable in biomedical implants such as hip, knee, cranial, maxillofacial, or dental devices. Thermal sprayed HA coatings indeed are designed to reduce the time of the healing process, when metal-based implants are employed, by aiding to the formation of newly bone in patients. Conventional thermal spraying techniques such as PS are mostly accepted in commercial devices due to their proved clinical outcomes. However, new alternatives have arisen in the last decade due to the need of improving mechanical and multifunctional behavior of this type of coatings. For instance, HA-composite coatings are also being functionalized to offer additional properties of osteoinduction, osteoproduction, antibacterial, and even therapeutic performance. There is still a lot of work to come exploring new materials combinations such as bioactive glasses, graphene, polymers, piezoelectric, pyroelectric, and other oxides for developing a new generation of multifunctional coatings for biomedical applications based on HA by thermal spray. In this sense, recent efforts are also focused on exploring other thermal spraying techniques such as cold spray.

Acknowledgment

The authors acknowledge the support of Mexico´s National Council of Science and Technology (CONACYT) through the “Investigadores por México” program, projects 848 and 881, and to the “Paradigmas y Controversias 2022” frontiers of science research fund, project 320126.

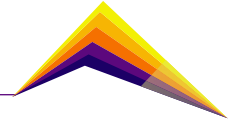

References

[1] Tavoni, M., Dapporto, M., Tampieri, A., & Sprio, S. (2021). Bioactive calcium phosphate-based composites for bone regeneration. *Journal of Composites Science*, *5*(9), 227.

[2] Davis, R., Singh, A., Jackson, M. J., Coelho, R. T., Prakash, D., Charalambous, C. P., ... & Lawrence, A. A. (2022). A comprehensive review on metallic implant biomaterials and their subtractive manufacturing. *The International Journal of Advanced Manufacturing Technology*, 1-58.

[3] Eliaz, N. (2019). Corrosion of metallic biomaterials: A review. *Materials*, *12*(3), 407.

[4] Cao, W., & Hench, L. L. (1996). Bioactive materials. *Ceramics international*, *22*(6), 493-507.

[5] Kokubo, T., Kim, H. M., & Kawashita, M. (2003). Novel bioactive materials with different mechanical properties. *Biomaterials*, *24*(13), 2161-2175.

[6] Mazzoni, E., Iaquinta, M. R., Lanzillotti, C., Mazziotta, C., Maritati, M., Montesi, M., ... & Martini, F. (2021). Bioactive materials for soft tissue repair. *Frontiers in bioengineering and biotechnology*, *9*, 613787.

[7] Hussain, M., Askari Rizvi, S. H., Abbas, N., Sajjad, U., Shad, M. R., Badshah, M. A., & Malik, A. I. (2021). Recent developments in coatings for orthopedic metallic implants. *Coatings*, *11*(7), 791.

[8] Lee, J. J., Rouhfar, L., & Beirne, O. R. (2000). Survival of hydroxyapatite-coated implants: a meta-analytic review. *Journal of Oral and Maxillofacial Surgery*, *58*(12), 1372-1379.

[9] Zhou, W., Liu, Z., Xu, S., Hao, P., Xu, F., & Sun, A. (2011). Long-term survivability of hydroxyapatite-coated implants: a meta-analysis. *Oral Surgery*, *4*(1), 2-7.

[10] Fauchais, P. L., Heberlein, J. V., & Boulos, M. I. (2014). *Thermal spray fundamentals: from powder to part*. Springer Science & Business Media.

[11] Henao, J., Poblano-Salas, C. A., Vargas, F., Giraldo-Betancur, A. L., Corona-Castuera, J., & Sotelo-Mazón, O. (2021). Principles and applications of thermal spray coatings. In *Advanced Surface Coating Techniques for Modern Industrial Applications* (pp. 31-70). IGI Global.

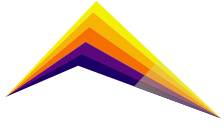

[12] Heimann, R. B. (2021). Functional plasma-sprayed hydroxylapatite coatings for medical application: Clinical performance requirements and key property enhancement. *Journal of Vacuum Science & Technology A: Vacuum, Surfaces, and Films*, *39*(5), 050801.

[13] Bhadang, K. A., Holding, C. A., Thissen, H., McLean, K. M., Forsythe, J. S., & Haynes, D. R. (2010). Biological responses of human osteoblasts and osteoclasts to flame-sprayed coatings of hydroxyapatite and fluorapatite blends. *Acta biomaterialia*, *6*(4), 1575-1583.

[14] Henao, J., Sotelo-Mazon, O., Giraldo-Betancur, A. L., Hincapie-Bedoya, J., Espinosa-Arbelaez, D. G., Poblano-Salas, C., ... & Martinez-Gomez, L. (2020). Study of HVOF-sprayed hydroxyapatite/titania graded coatings under in-vitro conditions. *Journal of Materials Research and Technology*, *9*(6), 14002-14016.

[15] Henao, J., Cruz-Bautista, M., Hincapie-Bedoya, J., Ortega-Bautista, B., Corona-Castuera, J., Giraldo-Betancur, A. L., ... & Poblano-Salas, C. A. (2018). HVOF hydroxyapatite/titania-graded coatings: microstructural, mechanical, and in vitro characterization. *Journal of Thermal Spray Technology*, *27*(8), 1302-1321.

[16] Martinez, G., Henao, J., Mandujano-González, V., Giraldo-Betancur, A., Forero-Sossa, P. A., Corona-Castuera, J., ... & Poblano-Salas, C. (2022). Exploring hydroxyapatite/graphene oxide/zinc oxide composite powders for the preparation of bioactive-antibacterial coatings by HVOF. *Applied Physics A*, *128*(9), 1-13.

[17] Fu, X. K., Cao, H. B., An, Y. L., Zhou, H. D., Shi, Y. P., Hou, G. L., & Ha, W. (2022). Bioinspired Hydroxyapatite Coating Infiltrated with a Graphene Oxide Hybrid Supramolecular Hydrogel Orchestrates Antibacterial and Self-Lubricating Performance. *ACS Applied Materials & Interfaces*, *14*(28), 31702-31714.

[18] Senthilkumar, G., Kaliaraj, G. S., Vignesh, P., Vishwak, R. S., Joy, T. N., & Hemanandh, J. (2021). Hydroxyapatite–barium/strontium titanate composite coatings for better mechanical, corrosion and biological performance. *Materials Today: Proceedings*, *44*, 3618-3621.

[19] Singh, S., Pandey, K. K., Islam, A., & Keshri, A. K. (2020). Corrosion behaviour of plasma sprayed graphene nanoplatelets reinforced hydroxyapatite composite coatings in simulated body fluid. *Ceramics International*, *46*(9), 13539-13548.

[20] Müller, V., & Djurado, E. (2022). Microstructural designed S58 bioactive glass/hydroxyapatite composites for enhancing osteointegration of Ti6Al4V-based implants. *Ceramics International*.

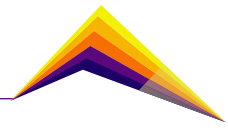

[21] Henao, J., Poblano-Salas, C., Monsalve, M., Corona-Castuera, J., & Barceinas-Sanchez, O. (2019). Bio-active glass coatings manufactured by thermal spray: A status report. *Journal of Materials Research and Technology*, *8*(5), 4965-4984.

[22] Vilardell, A. M., Cinca, N., Garcia-Giralt, N., Dosta, S., Cano, I. G., Nogués, X., & Guilemany, J. M. (2020). In-vitro comparison of hydroxyapatite coatings obtained by cold spray and conventional thermal spray technologies. *Materials Science and Engineering: C*, *107*, 110306.

[23] Tang, J., Zhao, Z., Liu, H., Cui, X., Wang, J., & Xiong, T. (2019). A novel bioactive Ta/hydroxyapatite composite coating fabricated by cold spraying. *Materials Letters*, *250*, 197-201.

[24] Guillem-Marti, J., Cinca, N., Punset, M., Cano, I. G., Gil, F. J., Guilemany, J. M., & Dosta, S. (2019). Porous titanium-hydroxyapatite composite coating obtained on titanium by cold gas spray with high bond strength for biomedical applications. *Colloids and Surfaces B: Biointerfaces*, *180*, 245-253.

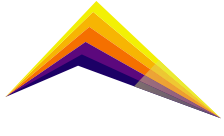

Aglomeration of al_2o_3 nanometric and submicrometric particles by spray drying for their use as feedstock in thermal spraying coatings

Edwin Cadavid[1] — E-mail: edwin.cadavid@udea.edu.co
Geraldin Estrada[2] — E-mail: geraldin.estradaz@gmail.com
María Esperanza López[3] — E-mail: esperanza.lopez@udea.edu.co
Fabio Vargas Galvis[4] — E-mail: fabio.vargas@udea.edu.co

[1]Materials engineer, Ph.D. in Materials Engineering Candidate, Grupo de Investigaciones de Materiales y Recubrimientos Cerámicos (GIMACYR) - Grupo de Investigaciones Pirometalúrgicas y de Materiales (GIPIMME) - Universidad de Antioquia. Medellín-Colombia
[2]Materials engineer, Universidad de Antioquia. Medellín-Colombia
[3]Ph.D. in Materials Science, Engineering and Technology, Grupo de Investigaciones de Materiales y Recubrimientos Cerámicos (GIMACYR) - Grupo de Investigaciones Pirometalúrgicas y de Materiales (GIPIMME) - Universidad de Antioquia. Medellín-Colombia
[4]Ph.D. in Materials Science and Engineering, Grupo de Investigaciones de Materiales y Recubrimientos Cerámicos (GIMACYR) - Grupo de Investigaciones Pirometalúrgicas y de Materiales (GIPIMME), Universidad de Antioquia. Medellín-Colombia

Abstract

This study is focused on the optimization of the spray-drying parameters for the agglomeration of both, nanometric and submicrometric Al_2O_3 particles, for their use as feedstock material to manufacture thermally sprayed coatings. Initially, for an aqueous suspension made of submicrometric alumina particles named MA (d_{10} = 0.8 **µm** to d_{90} = 2.0 µm), and based of a factorial experimental design with three factors and two levels, it was evaluated the effect of: *i)* The solids percentage in the aqueous suspension, *ii)* the feed flow rate and *iii)* the hot air rate used to evaporate the water in the suspension; on the agglomeration efficiency and the morphology of the obtained agglomerated. The agglomeration efficiency was calculated as the weight percentage of granulated particles with respect to the weight

Correspondent author

of solids in the sprayed slurry, while the morphology was analyzed by scanning electron microscopy (SEM). The agglomeration results for the MA suspension indicated that the highest efficiency was achieved with a solid percentage in the aqueous suspension of 30 wt. % (10 vol. %), a feed rate of 3.1 ml/min and a hot air rate of 5.5 m^3/min at a temperature of 220 ^oC, obtaining spherical agglomerates. Nevertheless, different morphologies of agglomerate were obtained based on the others experimental runs, such as hollow spheres. Subsequently, these parameters were replicated in an aqueous suspension of alumina nanoparticles (d_{50}=80 nm) called NA (Nanometric Alumina), from which the granulates obtained had a spherical morphology, made up of primary and secondary agglomerates, whose size distributions correspond to a d_{10} = 5 **µm** to d_{90} = 11 µm and d_{10} = 30 **µm** to d_{90} = 44 µm respectively. The total granulation efficiency was of 80%, of which 90% have a suitable range size to be used as raw material in the production of coatings by means of thermal spraying.

Key words: Spray drying, agglomeration efficiency, granules morphology, nanometric and micrometric alumina particles.

Introduction

Ceramic coatings thermally sprayed from nanometric and submicrometric agglomerated particles are being widely used to protect metallic substrates thanks to their good performances in demanding mechanical, tribological and thermal conditions [1], [2]. The agglomerated powders commercially available for manufacturing ceramic thermally sprayed coatings are processed mainly by spray drying process [3], because this technique allows to obtain size particles between 10 and 110 µm which is an ideal size distribution for an adequate flux in feeder systems for thermal spraying processes [1], [4], [5].

In the spray-drying process, an aqueous suspension is atomized through a nozzle, which allows control of the size, distribution, trajectory, and speed of the drops, which are exposed to a flow of hot air in the drying chamber. Due to the interactions occurring between the particles in the drying chamber (collision, electrostatic and the added agglutinating effects), the formation of granules with different morphologies and size distributions is achieved. [6]–[10].

Considering the above, this study intends to understand the effect of variables related to the aqueous suspension and the spray-drying equipment, on the agglomerates obtained that have the appropriate size and shape to be used as raw material in the production of coatings by thermal spraying.

Materials and Methods

Two alumina powders named MA (submicrometric Alumina) and NA (Nanometric Alumina) with size distribution d10= 0.8 - d90=2 µm for MA and d50=80 nm for NA, were used in this investigation. The spray-drying processes were carried out in a Toption TP-S15 equipment.
The experimental methodology was divided into three phases: *i)* Evaluation of the effect of the feeding rate, solid concentration in the suspension and flow of hot air used to dry the MA suspension, on the granulation efficiency, by means of an experimental design (2^3), which factors and experimental domain are shown in Table 1. An inlet temperature of 220 °C, to avoid PVA degradation, a nozzle diameter of 1 mm, and a suspension atomization pressure of 0.2 MPa, were left as fixed parameters; then *ii)* the results obtained in the previous step were replicated for a NA suspension and finally, *iii)* the characterization of the agglomerates obtained in *i)* and *ii),* which was carried out by means of image analysis. The images were acquired by scanning electron microscopy (SEM) using a Jeol JSM-6490LV equipment. Moreover, the agglomerates obtained in phase *ii)* were classified according to their size using sieves of the Tyler series number 200 (75 µm) and 500 (25 µm).

Table 1. Factors and experimental domain.

Factors	Level		Test number							
	(-)	(+)	1	2	3	4	5	6	7	8
A: Suspension feed rate [ml/min]	3.1	5.8	+	+	+	-	-	-	-	+
S: Solid concentration in the aqueous suspension [wt. %]	15	30	+	+	-	-	+	+	-	-
V: Hot air ventilation rate [m3/min]	3.9	5.5	+	-	-	+	+	-	-	+

Suspensions with two solid concentrations were prepared from the components shown in Table 2, using an aqueous solution with 2 wt. % PVA.

Table 2. Components of MA suspensions.

Solid concentration [wt.%]	Deflocculant [wt.%]	PVA Solution [wt.%]
15 (5 Vol.%)	0.25	84.75
30 (10 Vol.%)	0.50	69.50

Results and analysis

Spray drying of MA particles

Granulation efficiency

Figure 1 presents the results of the granulation efficiency for de MA suspension. Test 5 (A=3.1 ml/min; S=30 %; V=5.5 m^3/min) presents the highest efficiency with a granulation between 40 and 45 wt.% of the material fed. This was due to the higher solid percentage in the suspension and hot air flow along with a lower fed rate of the suspension, which facilitates the drying and consequent agglomeration of the material. On the other hand, test 3 (A=5.8 ml/min; S=15 %; V= 3.9 m^3/min) showed the lowest efficiency, only 25 wt.% of the material fed was granulated due the atomized droplets did not dry completely.

Agglomerate morphology

Figure 2 shows the agglomerates obtained for tests 3 and 5. The morphology of the particles obtained in test 3 was irregular, hollow and with thin walls, see Figure 2a. This occurs when the internal pressure of the agglomerate causes the expansion of the drop at the same time that the solids inside move towards its surface, eventually, the liquid phase evaporate causing a collapse of the granules due to the release of the internal pressure [11]. It can be seen in Figure 2b (test 5) that the amount of particles in each of the drops was greater than in test 3, permitting the formation of granules with a greater wall thickness, reducing the internal gases escape generated by the evaporation of the liquid phase, increasing the pressure difference between the interior of the agglomerate and the atmosphere, causing that a part of the granule breaks allowing the gases to escape, producing apple shape agglomerated particles [5], [12].

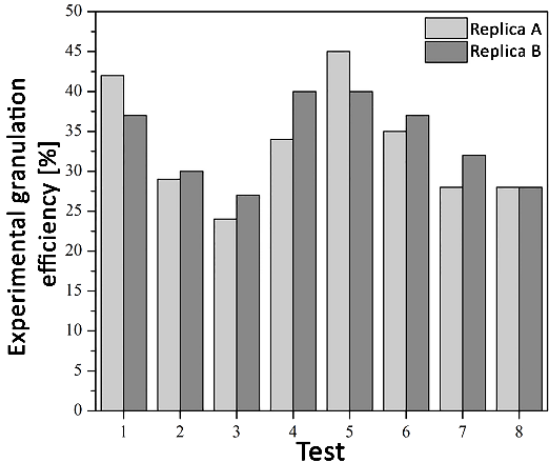

Figure 1. Experimental granulation efficiency.

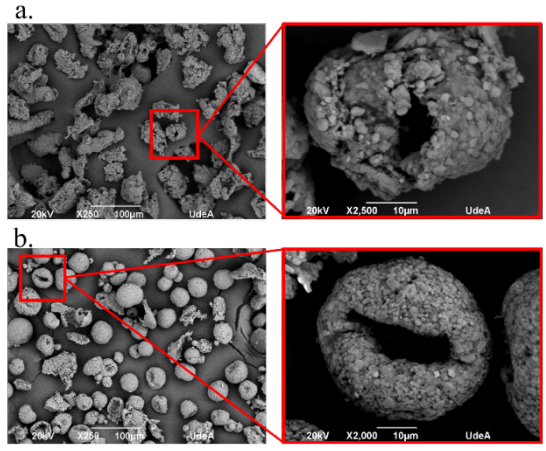

Figure 2. Micrographs for the granules obtained, with their respective magnification. a) Test 3. and b) Test 5.

The granules with spherical shape, as obtained in the test 5, allow a better flow when they are used as raw material in thermal spraying equipment.

Spray drying of NA particles.

Granulation efficiency and size classification

Based on the granulation results of the MA particles, a suspension was prepared with 30 wt. % NA (10 vol. %) and the components shown in Table 2 for this solids concentration. The suspension was spray dried using the test 5 parameters (A=3.1 ml/min; S=30 %; V= 5.5 m^3/min). A granulation efficiency of 80% was obtained with a material loss of 20 % that was dry but not agglomerated. The results of the granules size distribution determined by sieving are presented in Table 3.

Morphology and size efficiency

The morphology and size distribution of the granules of the sieve fractions smaller than 75 µm were evaluated by SEM images and image analysis; the results are presented in Figure 3 and Table 4, respectively.

Table 3. Size classification of agglomerates made from NA

Sieve fraction	Agglomerated particles [wt.%]
+200 (>75 µm)	10
-200 +500 (75 – 25 µm)	30
-500 (<25 µm)	60

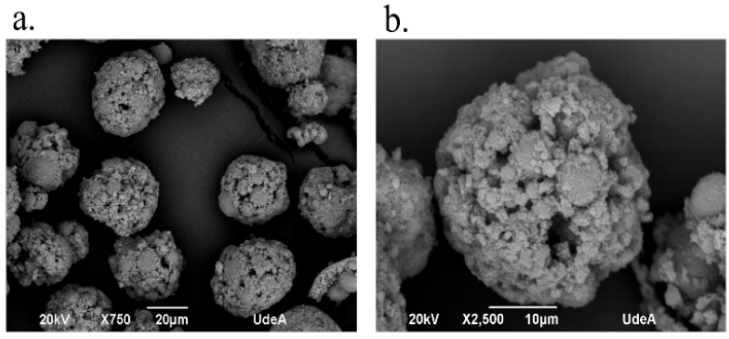

Figure 3. Granules obtained by spray drying of the NA suspension
a) Size fraction -200 +500 and b) a zoom in for a single particle.

Table 4. Granules size distribution.

Nominal size	Tyler mesh size	
	-200 +500	-500
d10 [µm]	30	5
d90 [µm]	44	11

It can be seen in Figure 3 that the agglomerated nanoparticles have a spherical morphology, in addition, when zooming in, it is to be noted that the agglomerates are made up of smaller granules (primary agglomerates) whose diameters is between 5 and 10 µm, Figure 3b. That means the granules obtained (secondary agglomerates) are made up by a conglomerate of the primary agglomerates.

The granules obtained are within an appropriate range to be used as raw material in the thermal spraying process (between 5 and 75 µm); the material in this size range is equivalent to 90% by weight of the agglomerated material, which corresponds to 80% by weight of the atomized nanoparticles, therefore, the overall efficiency for the desired particle size was 72%.

Conclusions

It was determined that the increase in the percentage of solids in the suspension, the decrease in the rate of atomized suspension, and the increase in the flow of hot air supplied to evaporate the liquid phase of the suspensions increases the efficiency in granulation and sphericity of the granules. A low suspension feed rate allows the atomized droplets to take better advantage of the thermal energy delivered to them by the hot air flow to achieve complete drying, which improves granulation.

Granules with a spherical morphology were obtained from a NA suspension with 30 wt.% of solids (10% by volume) that were fed and atomized with a 3.1 ml/min rate and dried with a current of hot air with a 5.5 m^3/min flux. 80 wt.% of the NA present in the atomized suspension were agglomerate and 72 wt.% of the granules obtained had a range of size consistent with that required to be used as raw material for thermally sprayed coatings.

Acknowledgment

To the National Financing Fund for Science, Technology and Innovation “FRANCISCO JOSÉ DE CALDAS” COLCIENCIAS for the scholarship for doctoral studies assigned to the student Edwin Cadavid through convocation No. 727.

References

[1] P. L. Fauchais, J. V. R. Heberlein, and M. I. Boulos. (2014). “*Thermal Spray Fundamentals From Powder to Part*”. Boston, MA: Springer US.

[2] L. Pawlowski. (2008). "Finely grained nanometric and submicrometric coatings by thermal spraying: A review," *Surf. Coatings Technol.*, vol. 202, no. 18, pp. 4318–4328.

[3] J. A. Árias *et al.* (2019). "Pelletisation by tumbling as an alternative method of agglomerating nanometric particles for use as feedstock in bi-modal structured flame-sprayed ceramic coatings," *Ceram. Int.*, vol. 45, no. 16, pp. 20936–20944.

[4] J. R. Davis. (2004). "Handbook of thermal spray technology", ASM Intern. USA.

[5] H. Herman. (1991). "Powders for Thermal Spray Technology," *KONA Powder Part. J.*, vol. 9, no. 9, pp. 187–199.

[6] L.-H. Tian, C.-X. Li, C.-J. Li, and G.-J. Yang. (2012). "Effect of dispersed TiC content on the microstructure and thermal expansion behavior of shrouded-plasma-sprayed FeAl/TiC composite coatings," *J. Therm. Spray Technol.*, vol. 21, no. 3–4, pp. 689–694.

[7] R. Mondragón, J. E. Julia, A. Barba, and J. C. Jarque. (2013). "El proceso de secado por atomización: Formación de gránulos y cinética de secado de gotas," *Bol. la Soc. Esp. Ceram. y Vidr.*, vol. 52, no. 4, pp. 159–168.

[8] M. Vicent, E. Sánchez, A. Moreno, and R. Moreno. (2012). "Preparation of high solids content nano-titania suspensions to obtain spray-dried nanostructured powders for atmospheric plasma spraying," *J. Eur. Ceram. Soc.*, vol. 32, no. 1, pp. 185–194.

[9] S. R. Candane, C. Balaji, and S. P. Venkateshan. (2007). "Ablation and aero-thermodynamic studies on thermal protection systems of sharp-nosed re-entry vehicles," *J. Heat Transfer*, vol. 129, no. 7, pp. 912–916, 2007.

[10] L. Pawlowski. (2008). "The Science and Engineering of Thermal Spray Coatings". Ecole Nationale Sup´erieure de Chimie de Lille,Villeneuve d'Ascq, France. John Wiley & Sons Ltd. 2nd ed.

[11] G. Bertrand, C. Filiatre, H. Mahdjoub, A. Foissy, and C. Coddet. (2003). "Influence of slurry characteristics on the morphology of spray-dried alumina powders," *J. Eur. Ceram. Soc.*, vol. 23, no. 2, pp. 263–271, 2003.

[12] R. V. Tonon, C. Brabet, and M. D. Hubinger. (2008). "Influence of process conditions on the physicochemical properties of açai (Euterpe oleraceae Mart.) powder produced by spray drying," *J. Food Eng.*, vol. 88, no. 3, pp. 411–418.

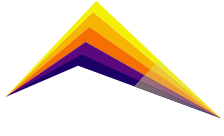

Flame spraying as alternative for sintering spray dried AT-13 granules

Juan David Holguín[1] E-mail: david.holguin@udea.edu.co
Francy Milena Hurtado[2] E-mail: francy.hurtado@udea.edu.co
María Esperanza López[3] E-mail: esperanza.lopez@udea.edu.co
Fabio Vargas Galvis[4] E-mail: fabio.vargas@udea.edu.co

[1]Eng., Universidad de Antioquia
[2]MSC., Universidad de Antioquia
[3,4] Ph.D. Universidad de Antioquia

Abstract

This paper analizes the results of the sintering process performed by flame spraying on agglomerated Al_2O_3-13 wt.% TiO_2 (AT-13) nanoparticles. Al_2O_3 and TiO_2 nanoparticles were blended and subsequently agglomerated by spray drying obtaining granules with both spherical and raspberry shapes with a particle size distribution between 8.9 – 16.2 µm and 14.8 – 40.0 µm respectively. The granules of nanoparticles agglomerated were sprayed using three flames: neutral, oxidizing, and highly oxidizing (super-oxidizing), in order to provide them different thermal treatment for their sintering. The sintering level reached on the particles was determined analyzing their transformation from raspberry shape to spherical particles. The results of the sintering process showed two clearly defined trends, the first of them was the effect of the flame type and the second one the effect of the size of the granules, on the sintering level reached by the agglomerated nanoparticles. The particles treated using the oxidizing and super-oxidizing flames reached a higher sintering level than those treated with the neutral one, then, a higher spheroidization of particles with raspberry shape was reached along these flames, being more effective the sintering in the oxidizing flame. Although the neutral flame reaches the highest localized temperature, in oxidizing and super-oxidizing flames the length of the primary zone,

Correspondent author

which is the highest energy zone in the combustion flames, is longer, which allows a higher residence time of the sprayed particles in this highly energetic zone. The oxidizing flame has the best trade-off threshold between the localized maximum temperature and the length of the primary zone. On the other hand, the smaller particles reached better sintering (with melting risk), than larger ones, owing to the higher heating achieved in small ceramic particles exposed to a short time heat treatment.

Keywords: alumina-titania nanoparticles, spray drying agglomeration, flame spraying sintering.

Introduction

In the last two decades, it has been shown that when ceramic agglomerated nanoparticles are thermally sprayed in order to manufacture coatings, bimodal structures are usually obtained. The nanoparticles retained in the bimodal structure of the coatings substantially improves their adhesion, fracture toughness, wear and thermal shock resistances [1]–[3]. However, the use of nanometric powders is subject to flow problems, associated with electrostatic forces in particles with a high surface area. The excessive electrostatic forces acting on nanoparticles make them highly cohesive and can cause clogging of the ducts that transport them, promoting irregular flows in feed systems for thermal spraying [4], [5], and reducing the added value of using nanoscale powders. For this reason, nanoparticles are sprayed both as liquid suspensions or as micrometric granules of agglomerated nanoparticles. Micrometric granules can be sprayed using conventional powders feedstock feeders [6].

Spray drying process is conventionally used at both industrial and research levels for the agglomeration of nanometric particles for their use in thermal spraying [7]. Although this is a versatile technique, it can have some disadvantages in terms of high energy and liquid consumption, associated with the need to eliminate the dispersing phase that contains the nanometric particles. The granules obtained must be sintered in order to improve the cohesion among the nanoparticles that make them up, requiring a subsequent sintering process with a high energy consumption [8]. The global trend towards sustainable development requires the implementation of a technique that uses less water and energy to agglomerate nano or

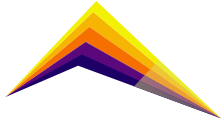

submicrometer particles obtaining granules with a size distribution between 5 and 75 µm [5]. An alternative technique that meets these requirements is used by the GIMACYR group at the University of Antioquia, using a rotary drum pelletizer, in which the agglomeration occurs by the addition of small amounts of an aqueous binder solution and the interaction among the particles as they move along the rotary drum wall, promoting the growth and consolidation of granules, which preserve the spherical morphology, propitiated by the effects of impact and friction, associated with the relative movement between particles. In previous works, an aqueous solution with 2.3 wt.% of PVA commercial grade has been used as a binder [5]. However, it was wanted to evaluate the effect of others binder solutions such as PVA 3% reactive grade and Maltodextrin pharmaceutical grade at 37 wt.% with a viscosity of 20 cSt, to evaluate the yield in terms of granulation with size between 5 – 75 µm. The methodology used and the results obtained are presented below.

Methodology

The alumina and titania nanoparticles (US Research Nanomaterials Inc), with d_{50} particle sizes of 80 and 18 nm respectively, were agglomerated by a spray drying process to obtain AT-13 granules with $d_{10} > 5\mu m$ and $d_{90} < 75\mu m$.

Previously to the spray drying process, the nanoparticles were mechanically blended using a rotating drum at 60 rpm for one hour, to obtain a homogeneous distribution of titania nanoparticles on the alumina ones. Subsequently, it was prepared an aqueous slurry with 2 wt.% of polyvinyl alcohol as the binder, 0.33 wt.% of polyacrylic dispersant, and 20 wt.% (6.6 vol.%) of the mixed AT-13 nanoparticles, which were mechanically stirred and pumped at the flow rate of 7.0 ml/min to the drying chamber of a Toption TP S-15™ spray dryer, operating at 220 °C.

The granules obtained were sieved using an ASTM E11 mesh number 200 and then, the agglomerates with sizes lower than 75 µm were sprayed in three oxyacetylene flames to sinter them. In order to produce the neutral, oxidizing, and highly oxidizing (super-oxidizing) flames, 22 l/min of acetylene was mixed with 37, 55, and 70 l/min of oxygen respectively. Each of these three flames was used to heat and spray a flow rate of 3.6 g/min of the agglomerated nanoparticles, which were subsequently collected on a filter located 1 m in front of the nozzle of the Eutectic Castolin Terodyn 2000™ torch used to spray them.
The morphology of granules, before and after the sintering process, was analyzed by Scanning Electron Microscopy-SEM, using a JEOL JSM-6490LV equipment, and their size distribution, as well as the percentage of agglomerates corresponding to each shape, were determined using the Image-J software. The results obtained are shown below.

Results and analysis

The results of the morphological analyses indicate that before sintering the granules of nanoparticles agglomerated by spray drying showed two different shapes. The first one corresponds to spherical particles with size distribution ($d_{90} - d_{10}$) is 8.9 – 16.2 µm, representing the ≈23.3% in the number of all granules, named as primary agglomerates for the purpose of this study. The second one corresponds to raspberry shape granules, which are formed by spheres of primary agglomerates, here they are named secondary agglomerates, their size distribution is 14.8 – 40.0 µm and represents ≈76.7% in the number of all granules, as is shown in Figure 1 a).

The granules heat treated in the neutral flame did not show major changes in their morphology regarding before treatment, the number percentage of primary agglomerates as sphere shape is ≈25.2%, while raspberries shape is ≈74.8%. The granule size distribution for the sphere shape is 8.8 – 43.2 µm and for raspberry shape is 20.3 – 76.4 µm, see Figure 1 b).

On the other hand, the granules sprayed along the oxidizing flame experienced a high level of spheres, allowing them to reach a number percentage ≈ of 66%, while that for raspberry shape is only ≈34%. The granule size distribution for the spheres is 25.4 – 47.6 µm, while for the raspberries is 20.2 – 58.7 µm. Figure 1 c).

Finally, the number percentage of spheres obtained in the super-oxidizing flame experienced a decrease since it was treated in the oxidizing flame, ≈66% vs ≈53%, consequently, the raspberry shape is ≈47%. The granule size distribution for the spheres and raspberries is 24.8 – 48.8 µm and 19.1 – 49.5 µm respectively, see Figure 1 d).

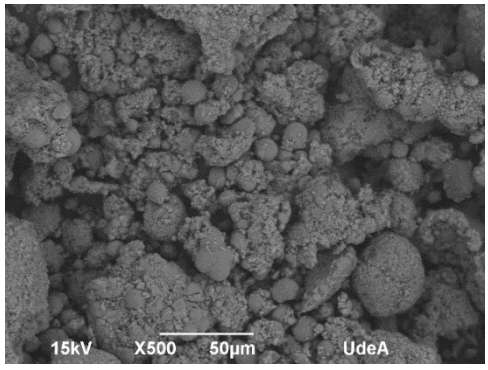

a)

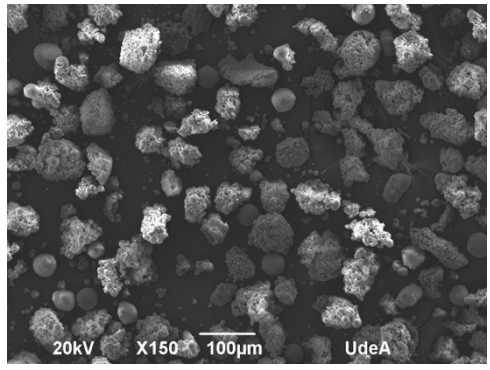

b)

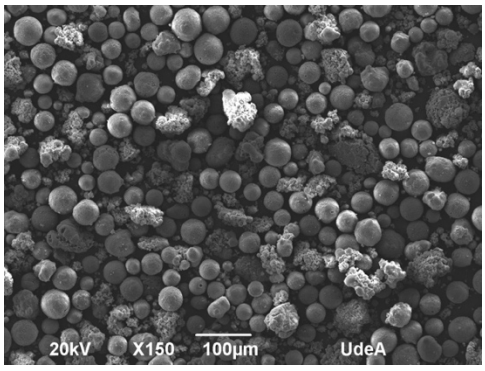

c)

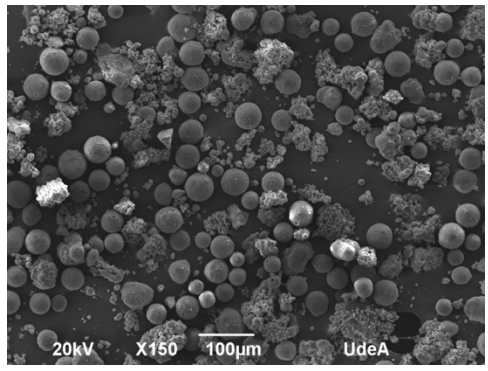

d)

Figure 1. Morphology of AT-13 spray dried granules. a) Without in flame treatment. b) Treated in a neutral flame. c) Treated in an oxidizing flame. d) Treated in a super-oxidizing flame.

Consequently, it is possible to indicate that the larger granules heat treated in the neutral flame did not reach sufficient energy for their softening by partial or total melting, and therefore, based on the percentage in the number of raspberries transformed into spheres, it was not possible to establish whether they reached any degree of sintering.

On the other hand, the transformation from raspberry shape to spheres experienced by the granules heat treated along the oxidizing and super-oxidizing flames evidences their softening, and then, the sintering produced among the nanoparticles that make them up. The higher transformation from raspberries to spheres in granules treated by the oxidizing flame is due to the best trade-off threshold between the maximal temperature reached by this flame and the length of its primary zone, which are 3080 °C and 7.6 cm [10].

Figure 2 shows the sintering level produced among particles treated by the different flames. It is evident that as the granules are smaller, the sintering among the agglomerated particles is higher, producing the coarsening from nanoparticles to submicrometer ones. Additionally, it was established that the smallest particles treated with the super-oxidizing flame were able to melt. Despite the maximal temperature of this flame is the lowest (2980 °C [10]) of the three used, its length is the greatest (8.5 cm [10]), indicating that, for the nanoparticles agglomerated, the maximal temperature reached by the three flames is enough to melt them and, consequently, to sinter them, but the driven parameter to sinter them is the length of the primary zone.

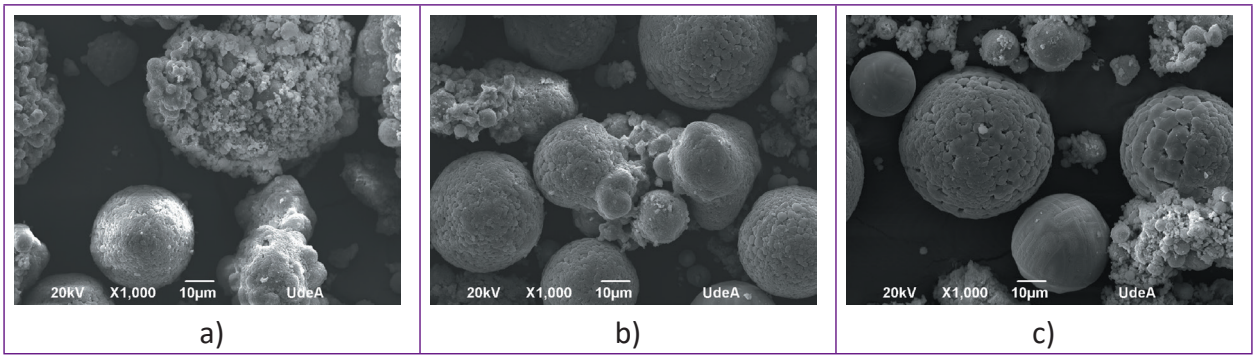

a) b) c)

Figure 2. Sintering level achieved by the agglomerated nanoparticles in different flames. a) Neutral flame. b) Oxidizing flame. c) Super-oxidizing flame.

Conclusions

Alumina and titania nanoparticles were blended and spray dried to obtain AT-13 granules, which were sieved to, subsequently, thermally spray them along three different flames, corresponding to a -75 µm fraction. The neutral, oxidizing, and super-oxidizing flames were used to heat the granules to evaluate the capability of the flames type to sinter granules of different sizes. The results obtained allow us to conclude the following:

The neutral flame reaches a maximal temperature (3170 °C), which is sufficient for sintering the nanoparticles that make up the granules, but the length of its primary zone may not be enough to sinter the larger raspberry-shaped granules.

In contrast, the super-oxidizing flame has the lowest temperature of all those studied, it has the longest primary zone length though. It allows a longer residence time for the granules in the most energetic zone of the flame and, consequently, the smaller granules reach the melting point of alumina and titania nanoparticles.

The granules thermally treated in the oxidizing flame achieved the best trade-off threshold between the maximum temperature of the flame and the length of its primary zone, and the growth of the nanoparticles that make up these granules was evidenced.

Acknowledgments

The authors would like to thank Minciencias for the support given to project 70395, which is part of the program 111885270260, contract Fiduprevisora-Unalmed 80740-167-2021.

References

[1] P. L. Fauchais, J. V. R. Heberlein, and M. I. Boulos, *Thermal spray fundamentals: from powder to part*. Springer Science & Business Media, 2014. https://doi.org/10.1007/978-0-387-68991-3.

[2] L. Pawlowski, "Finely grained nanometric and submicrometric coatings by thermal spraying: A review," *Surf. Coatings Technol.*, vol. 202, no. 18, pp. 4318–4328, Jun. 2008, doi: 10.1016/J.SURFCOAT.2008.04.004.

[3] R. S. Lima and B. R. Marple, "Thermal Spray Coatings Engineered from Nanostructured Ceramic Agglomerated Powders for Structural, Thermal Barrier and Biomedical Applications: A Review," *J. Therm. Spray Technol.*, vol. 16, no. 1, pp. 40–63, 2007, doi: 10.1007/s11666-006-9010-7.

[4] L. Wang, Y. Wang, X. G. Sun, J. Q. He, Z. Y. Pan, and C. H. Wang, "Microstructure and indentation mechanical properties of plasma sprayed nano-bimodal and conventional ZrO2–8wt%Y2O3 thermal barrier coatings," *Vacuum*, vol. 86, no. 8, pp. 1174–1185, Feb. 2012, doi: 10.1016/J.VACUUM.2011.10.029.

[5] H. N. Ch'ng and J. Pan, "Sintering of particles of different sizes," *Acta Mater.*, vol. 55, no. 3, pp. 813–824, Feb. 2007, doi: 10.1016/J.ACTAMAT.2006.07.015.

[6] N. Gupta and B. Basu, "Hot pressing and spark plasma sintering techniques of intermetallic matrix composites," *Intermet. Matrix Compos.*, pp. 243–302, Jan. 2018, doi: 10.1016/B978-0-85709-346-2.00010-8.

[7] M. Vicent, E. Bannier, R. Moreno, M. D. Salvador, and E. Sánchez, "Atmospheric plasma spraying coatings from alumina–titania feedstock comprising bimodal particle size distributions," *J. Eur. Ceram. Soc.*, vol. 33, no. 15–16, pp. 3313–3324, Dec. 2013, doi: 10.1016/J.JEURCERAMSOC.2013.05.009.

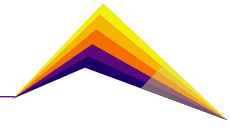

[8] B. K. Kim, D. W. Lee, and C. J. Choi, “Plasma densification of agglomerated Cr2O3 powder for thermal spray coating,” *http://dx.doi.org/10.1179/003258901666347*, vol. 44, no. 3, pp. 274–278, 2013, doi: 10.1179/003258901666347.

[9] P. Fauchais, G. Montavon, R. S. Lima, and B. R. Marple, “Engineering a new class of thermal spray nano-based microstructures from agglomerated nanostructured particles, suspensions and solutions: an invited review,” *J. Phys. D. Appl. Phys.*, vol. 44, no. 9, p. 093001, Feb. 2011, doi: 10.1088/0022-3727/44/9/093001.

[10] E. Cadavid Iglesias, C. Parra Velásquez, and F. Vargas Galvis, “ESTUDIO DE LLAMAS OXIACETILÉNICAS USADAS EN LA PROYECCIÓN TÉRMICA,” *Rev. Colomb. Mater.*, no. 9, pp. 15–26, Dec. 2016, Accessed: Feb. 24, 2021. [Online]. Available: https://revistas.udea.edu.co/index.php/materiales/article/view/326490

[11] J. Henao, C. A. Poblano-Salas, F. Vargas, A. L. Giraldo-Betancur, J. Corona-Castuera, and O. Sotelo-Mazón, “Principles and Applications of Thermal Spray Coatings,” *https://services.igi-global.com/resolvedoi/resolve.aspx?doi=10.4018/978-1-7998-4870-7.ch002*, pp. 31–70, Jan. 1AD, doi: 10.4018/978-1-7998-4870-7.CH002.

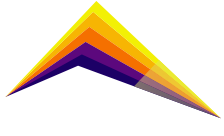

Effect of the binder type on the yield of 3-YSZ nanoparticles pelletized to their use as feedstock in thermally sprayed coatings

Róbin Nilson Muñoz[1] Email: robin.munoz@udea.edu.co
Santiago Marín[2] Email: santiago.marinz@udea.edu.co
Nicolás Puentes[3] Email: nsebastian.puentes@udea.edu.co
Jhoman Arias[4] Email: jhoman.arias@udea.edu.co
Fabio Vargas Galvis[5] Email: fabio.vargas@udea.edu.co

[1]Eng., Universidad de Antioquia
[2,3]Materials Engineering Student
[4]MSc Universidad de Antioquia,
[5]Ph.D. Universidad de Antioquia

Abstract

The present paper shows the effect of binder type on the effectiveness of the agglomeration of 3 mol % yttria stabilized zirconia (3-YSZ) nanoparticles by means of the rotary drum pelletizing process for its potential use as raw material in thermally sprayed coatings. Three aqueous binders were evaluated: *i)* PVA 2.3 wt.% (commercial type Polyvinyl Alcohol), *ii)* PVA 3 wt.% (reagent grade, 99+% hydrolyzed) and *iii)* Maltodextrin 37 wt.% (pharmaceutical grade). These aqueous solutions were prepared considering that their viscosity must be ≈20 cSt in order to be used in the nanoparticle pelletizer. The wettability between each aqueous binders and a pellet 10 mm in diameter and ≈6 mm in thickness manufactured from compacted nanoparticles, was determined from the contact angle between them. The yield of the agglomeration process was established from the percentage of granules with particle sizes between 25 µm and 75 µm (corresponding to sieves fraction -200 +500), regarding nanoparticles fed to the pelletizer. Results indicate that the yield obtained by the granulation

Correspondent author

using as binder the 37 wt.% Maltodextrin solution is slightly lower than those obtained for the two PVA solutions. Nevertheless, yields obtained by granulations performed with PVA aqueous solutions are still low and then, it is necessary to increase the performance of the agglomeration process with these binders.

Keywords: Pelletizing of nanoparticles, aqueous binder solutions, agglomerates.

Introduction

In the last two decades, it has been shown that when ceramic agglomerated nanoparticles are thermally sprayed in order to manufacture coatings, bimodal structures are usually obtained. The nanoparticles retained in the bimodal structure of the coatings substantially improves their adhesion, fracture toughness, wear and thermal shock resistances [1]–[3]. However, the use of nanometric powders is subject to flow problems, associated with electrostatic forces in particles with a high surface area. The excessive electrostatic forces acting on nanoparticles make them highly cohesive and can cause clogging of the ducts that transport them, promoting irregular flows in feed systems for thermal spraying [4], [5], and reducing the added value of using nanoscale powders. For this reason, nanoparticles are sprayed both as liquid suspensions or as micrometric granules of agglomerated nanoparticles. Micrometric granules can be sprayed using conventional powders feedstock feeders [6].

Spray drying process is conventionally used at both industrial and research levels for the agglomeration of nanometric particles for their use in thermal spraying [7]. Although this is a versatile technique, it can have some disadvantages in terms of high energy and liquid consumption, associated with the need to eliminate the dispersing phase that contains the nanometric particles. The granules obtained must be sintered in order to improve the cohesion among the nanoparticles that make them up, requiring a subsequent sintering process with a high energy consumption [8]. The global trend towards sustainable development requires the implementation of a technique that uses less water and energy to agglomerate nano or submicrometer particles obtaining granules with a size distribution between 5 and 75 µm [5]. An alternative technique that meets these requirements is used by the GIMACYR group at the University of Antioquia, using a rotary drum pelletizer, in which the agglomeration occurs by the addition of small amounts of an aqueous binder solution and the interaction among the particles as they move along the rotary drum wall, promoting the growth and consolidation of granules, which preserve the spherical morphology, propitiated by the effects of impact and friction, associated with the relative movement between particles. In previous works, an aqueous solution with 2.3 wt.% of PVA commercial grade has been used

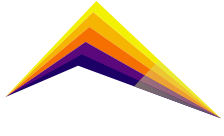

as a binder [5]. However, it was wanted to evaluate the effect of others binder solutions such as PVA 3% reactive grade and Maltodextrin pharmaceutical grade at 37 wt.% with a viscosity of 20 cSt, to evaluate the yield in terms of granulation with size between 5 – 75 μm. The methodology used and the results obtained are presented below.

Methodology

Nanoparticles of 3 mol % yttria stabilized zirconia (3-YSZ), US Research Nanomaterials, Inc, with d_{50} ≈ 40nm were selected to the agglomeration process. Additionally, polyvinyl alcohol (PVA) commercial grade acquired locally (Antioqueña de Químicos), PVA 99+% hydrolyzed reagent grade (Sigma Aldrich, USA) and Maltodextrin pharmaceutical grade (Mckenna Group S.A.S, Colombia), were diluted in deionized water type II using constant magnet stirring at 800 rpm, to use as binder solutions. Owing to the low solubility of PVA at room temperature the aqueous solution was heated up to 70 °C until PVA powders were completely solubilized. In a paper previously published, it is indicated that the cinematic viscosity of binder solution fed into the pelletizer nozzle must be ≈20 cSt for the formation of a mist capable of agglomerating nanoparticles to obtain micrometric size granules [5]. Preliminary tests were carried out to determine the quantity of PVA commercial and reagent grades as well as Maltodextrin, required to obtain the aqueous solution with cinematic viscosity ≈20 cSt. The cinematic viscosity was measured by a Ford Cup #3 (BYK) according to ASTM D1200-10 standard [9].

For its part, wettability of each binder solution on the nanoparticles to be agglomerated, was determined from the contact angle measured dropping a drop of binder on the surface of a pressed nanoparticles pellet 10 mm in diameter and ≈6 mm height. The interface between the pellet and the drop of each binder solution was analyzed with a stereographic microscope and the contact angle was measured from images shot with this equipment using Image-J software.

The liquid-to-solid ratio (L/S) was determined by an empirical method developed by GIMACYR group, forming a large spherical pellet (≈12 mm in diameter) by manual kneading of nanoparticles. In order to obtain the spherical pellet 2.5 g of raw powder, it is weighed and then, the binder aqueous solution is added progressively until obtaining a paste with an adequate plasticity to retain the agglomerate shape after its manual kneading.
The parameters used to agglomerate the 3-YSZ nanoparticles by rotary drum pelletisation method are shown in Table 1.

Table 1. Parameters for granulating process of 3-YSZ nanoparticles using the three binder solutions.

Weight of powder fed (g)	30
Binder volume (mL)	7
Binder flow (mL/min)	2
Drum inclination Angle (°)	88
Drum rotation speed (RPM)	75
Agglomeration Time (s)	120

The nanoparticles used to manufacture both pressed and granulated pellets in the rotary drum, were previously dried at 110 °C for 2 hours.

After the agglomeration process, the granules were dried out at room temperature for about 3 days, then sieved using number 200 and 500 sieves which specifications are established by ASTM E11, in order to calculate the percentage of granules with particle sizes between 25 µm and 75 µm regarding nanoparticles fed to the pelletizer. This represents the yield of the agglomeration process.

Finally, the morphological characterization of both the starting nanometric powders and the granules of agglomerated nanoparticles was performed by means of scanning electron microscopy (SEM) images using a JEOL JSM-6490LV equipment.

Results and analysis

Representative images were used to measure the contact angle between the nanoparticles pellets and each one of binders solution, which are shown in Figure 1.

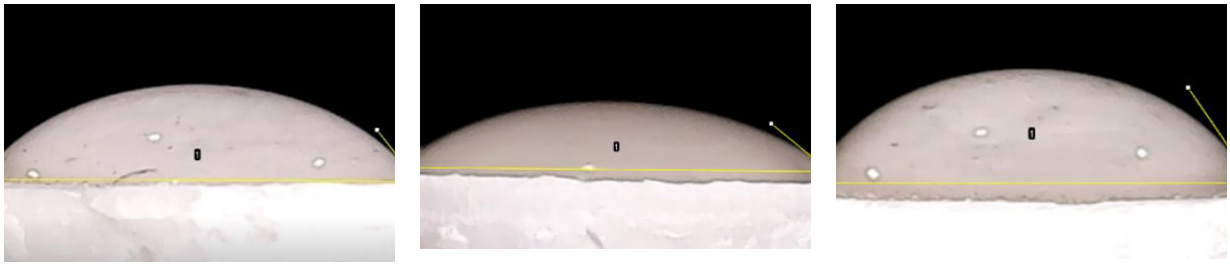

a) b) c)

Figure 1. Contact angle between the pellet of 3-YSZ nanoparticles and the drops of each binder. a) Commercial grade PVA- 2.3 wt.%. b) Reagent grade PVA - 3.0 wt.%. c) Pharmaceutical grade Maltodextrin 37 wt.%.

The angles measured for the aqueous binder solutions with 2.3 wt.% PVA commercial grade and with 3.0 wt.% PVA reagent grade are 49.8º ± 3.0º and 45.2º ± 2.0º, respectively. Furthermore, for the binder solution with 37 wt.% Maltodextrin pharmaceutical grade is 59.0º ± 4.2º. The above indicates that the aqueous solution with 3.0 wt.% PVA reagent grade has a greater capacity to wet the nanoparticles of the pellet manufactured by pressing, while the Maltodextrin solution has the lowest wettability.

On the other hand, the results of the granules size distribution are shown in Table 2.

Table 2. Granules size distribution obtained for different aqueous binder solutions.

Aqueous binder solution	Granules in each fraction size [%]			
	+75 μm	-75 +25 μm	-25 μm	Losses of process
2.3 wt.% PVA commercial grade	29.5	19.8	28.0	22.7
3.0 PVA wt.% reagent grade	15.6	19.8	54.3	10.3
37wt.% Maltodextrin	9.8	17.1	65.6	7.5

The results shown in the previous table indicate that the yield (% of the fraction -200 +500) of the agglomeration carried out with the PVA binders is similar (≈20%), while that of the agglomeration carried out with Maltodextrin is slightly lower.

For its part, the morphology of the 3-YSZ nanoparticles, as well as that of granules obtained using the three aqueous binder solutions are shown in Figure 2.

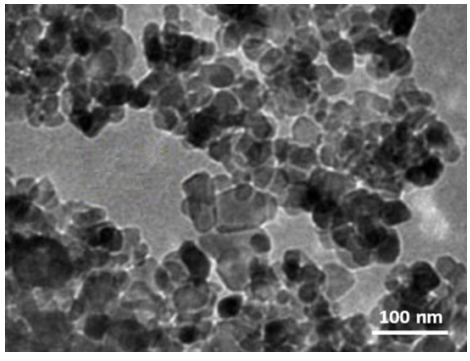

a)

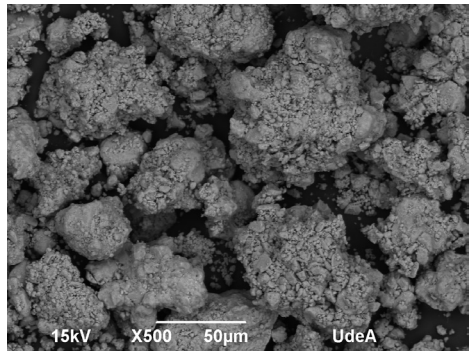

b)

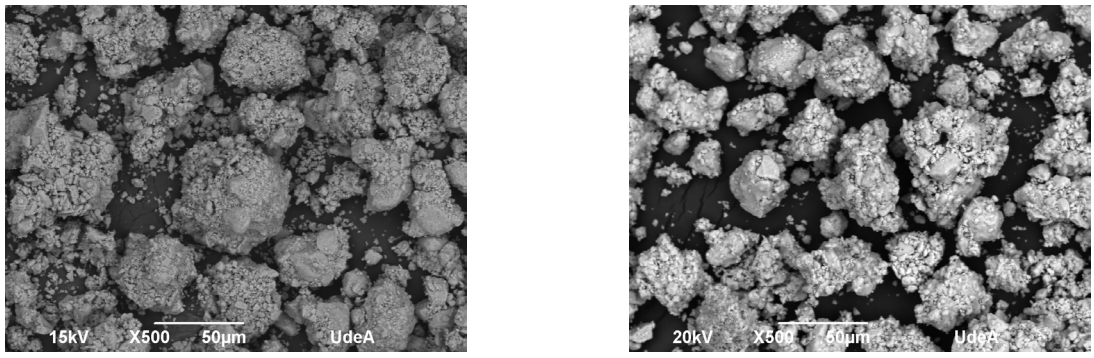

c) d)

Figure 2. Morphology of nanoparticles before and after agglomeration process. a) TEM Image of 3-YSZ nanoparticles [10]. Granules obtained with b) PVA 2.3 wt.% commercial grade. c) PVA 3.0 wt.% reagent grade. d) Maltodextrin 37 wt.%.

The results of the morphological analyses show that the granules obtained with the PVA binder solutions are more spherical than those manufactured with the Maltodextrin binder and are primary made up of agglomerates that are also spherical, while the primary granules obtained with Maltodextrin binder solution have a prismatic shape.

Conclusions

According to the results of this work can be concluded that agglomeration of 3-YSZ nanoparticles using aqueous solutions of PVA (commercial and reagent grade) presents a similar yield with spherical shape of granules, while Maltodextrin granules achieved a slightly lower yield and predominantly prismatic shape. The lower yield and the prismatic granules obtained with Maltodextrin binder are related to the lower capacity of this solution to wet the 3-YSZ nanoparticles.

Acknowledgment

The authors would like to thank Minciencias for the support given to project 70395, which is part of the program 111885270260, contract Fiduprevisora-Unalmed 80740-167-2021

References

[1] P. Bansal, N. P. Padture, and A. Vasiliev, "Improved interfacial mechanical properties of Al2O3-13wt% TiO2 plasma-sprayed coatings derived from nanocrystalline powders," *Acta Mater.*, vol. 51, 2003.

[2] G. Di Girolamo, F. Marra, C. Blasi, E. Serra, and T. Valente, "Microstructure, mechanical properties and thermal shock resistance of plasma sprayed nanostructured zirconia coatings," *Ceram. Int.*, vol. 37, no. 7, pp. 2711–2717, Sep. 2011, doi: 10.1016/J.CERAMINT.2011.04.024.

[3] G. Skandan, R. Yao, B. H. Kear, Y. Qiao, L. Liu, and T. E. Fischer, "Multimodal powders: a new class of feedstock material for thermal spraying of hard coatings," *Scr. Mater.*, vol. 44, no. 8–9, pp. 1699–1702, May 2001, doi: 10.1016/S1359-6462(01)00866-1.

[4] P. Fauchais, G. Montavon, and G. Bertrand, "From powders to thermally sprayed coatings," *J. Therm. Spray Technol.*, vol. 19, no. 1–2, pp. 56–80, Jan. 2010, doi: 10.1007/S11666-009-9435-X/FIGURES/21.

[5] J. A. Árias *et al.*, "Pelletisation by tumbling as an alternative method of agglomerating nanometric particles for use as feedstock in bi-modal structured flame-sprayed ceramic coatings," *Ceram. Int.*, vol. 45, no. 16, pp. 20936–20944, 2019, doi: 10.1016/j.ceramint.2019.07.083.

[6] P. L. Fauchais, J. V. R. Heberlein, and M. I. Boulos, *Thermal spray fundamentals: from powder to part*. Springer Science & Business Media, 2014.

[7] A. B. D. Nandiyanto and K. Okuyama, "Progress in developing spray-drying methods for the production of controlled morphology particles: From the nanometer to submicrometer size ranges," *Adv. powder Technol.*, vol. 22, no. 1, pp. 1–19, 2011.

[8] L. Pawlowski, *The Science and Engineering of Thermal Spray Coatings: Second Edition*, SECOND EDI. 2008.

[9] W. Conshohocken, "Standard Test Method for Viscosity by Ford Viscosity Cup 1," October, vol. 06, no. Reapproved, pp. 94–96, 1999, doi: 10.1520/D1200-10.2.

[10] "Zirconia-Yttria Nanopowder / Nanoparticles (ZrO2-3Y, 99.9%, 40 nm, metal basis)." https://www.us-nano.com/inc/sdetail/357 (accessed Aug. 01, 2022).

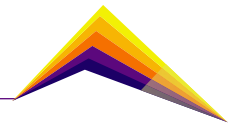

Characterization of YSZ powders obtained by ball mill grinding with possible application for TBCs thermal barrier systems

Jhonatan Román Román[1] *E-mail: jromanr@unal.edu.co*
Maria Estéfany Bedoya[2] *E-mail: maebedoyave@unal.edu.co*
Juan Camilo Nanclares Cárdenas[3] *E-mail: jcnanclaresc@unal.edu.co*
Alejandro Toro Betancur[4] *E-mail: aotoro@unal.edu.co*
Lina Chica[5] *E-mail: lmchica@udemedellin.edu.co*

[1, 2, 3, 4] *Universidad Nacional de Colombia. Sede Medellín*
[5] *Universidad de Medellín*

Abstract

Thermal barrier coatings (TBCs) are widely used to increase the service life of parts subjected to thermomechanical stresses in the hot gas path of thermoelectric generation plants. These coatings are generally composed of two layers, a bond coating (BC) and a top coating (TC). Yttria stabilized zirconia (YSZ) powders are commonly used as TC and can be applied by atmospheric plasma spray (APS), atmospheric plasma suspension (SPS) or Electron Beam – Physical Vapor Deposition (EB-PVD). In this work, ball mill grinding of YSZ powder was carried out with the aim of obtaining a product with suitable attributes for later application as TC in TBCs. The characterization focused on density, size, and shape of the powder particles since it has been shown that they affect the most the microstructure and properties of the coatings. The YSZ powders obtained by conventional grinding in a zirconia ball mill were classified with the 200 (74 µm) and 635 (20 µm) meshes of the Tyler series.

Correspondent author

The properties of interest were shape, microstructure, and particle size distribution (PSD). X-ray diffraction (XRD) was carried out to identify possible phase transformations due to the milling process, with a special interest in the presence of monoclinic phase, since during the thermal cycling it can be induced TBC´s failure due to volume changes at the industrial operating temperature range. Particle shape analysis was carried out by scanning electron microscopy (SEM) and the PSD was determined by laser diffraction.

The XRD analysis showed that grinding did not induce phase changes in the material, hence the microstructure of the powder particles was composed of tetragonal and cubic phases. It was also determined that grinding increased the percentage of particles smaller than 74 µm from 56.25% to 94.15%, and those smaller than 20 µm from 0% to 7.58% with respect to the total mass; this was corroborated by SEM analysis.

Keywords: YSZ, thermal barrier coatings, ball milling

Introduction

Market pressures, global competition and environmental requirements on industries that use turbines for power generation or transportation demand greater performance from thermal barriers that must be manufactured at a lower cost [1] [2]. In a thermal barrier coating, very strong control over the adherence to the substrate is expected [3], and also the thermo-mechanical properties that fundamentally depend on the microstructure of the material [4]. An essential process for the control of such microstructure is associated with the preparation of the coating material. YSZ is a ceramic in which the cubic crystalline structure of zirconium dioxide is stabilized at room temperature by adding yttrium oxide, of which composition is usually 8-10 mol% [5]. Coating with YSZ powders has shown to be efficient in delaying the aging of parts subjected to wear in extreme conditions without modifying the structure of the engine [6] [7] [8], thanks to its superior thermal insulation potential and its resistance to high temperatures [9]. Tao Wang et al. [10] suggested that applying YZS can modify the service life due to bonding caused by the material at elevated temperatures. The milling of YSZ is a challenge that seeks to be solved to produce optimal Colombian raw materials for coatings, the final powder must have specific characteristics for its correct application, among them, one of the most important is the final particle size, which should not exceed 20 µm [11]. There are two methods to produce fine ceramic powders: milling or breaking-

down and building-up [12]. In the case of physical methods, grinding cycles must be carried out, in which the material fractures and reaches the desired size [13] [14]. However, this process is not easy to achieve in YSZ due to the hardness and the lack of knowledge about the conditions to optimize the fracturing process [15]. For this, variables such as type of mill, grinding time, frequency, and amount of material fed, among others, must be considered [16]. During the grinding of YSZ powders, the stress transmission due to the grinding itself occurs differently when analyzing the behavior of a particle and the particles in a ceramic matrix [17]. If the case of the ceramic matrix is analyzed, it encloses the YSZ particles and acts as an elastic medium that transfers the stresses between the particles that are not in direct contact. On a microscale, stress transfer can only occur due to direct particle-particle type contacts, which implies that at this scale, complex stress states are generated that include compressive, shear and possibly tensile stresses. Because of the shear stress that can be generated on a micro scale, the transformation from tetragonal to a monoclinic phase of the YSZ particles is induced [18] [19] [20]. In this work, ball mill grinding of YSZ powder was carried out to obtain a product with suitable attributes for later application as TC in TBCs. The characterization focused on the density, size, and shape of the powder particles, since it has been shown that they affect the microstructure the most and the properties of the coatings. Also, XRDs were performed to identify the phases' behavior due to the YSZ milling processes, focusing on the presence of the monoclinic phase.

Materials and Methods

An experimental set of tests was carried out. A batch 500 cm^3 zirconia ball mill (See Figure 1) was designed and built to reduce the particle size under dry milling conditions. Conventional ball milling was used to avoid phase transformations due compression and abrasion mechanism at high shear rates. The filling level of the mill was set under 50%. Optimal milling conditions were founded at 170 rpm with feeding on 180 g and size ball diameters setting between 1.4mm to 8 mm, time milling setting was on 6 hours. After milling, a sieving process was used to classified particles between Tyler 200 mesh (74 μm) and 635mesh (20 μm) as size distribution required to produce YSZ APS coatings. Milling feeding and product (particles under 625 mesh) were characterized physically and mineralogically. The characterization was focused on mineral composition, size distribution and particle morphology. The powders morphological characterization was achieved using the scanning electron microscope SEM Carl Zeiss EVO MA10. Particle size distribution was measure using a Malvern MasterSizer 2000 with a Hydro 2000MU accessory. Microstructural characterization was made by XRD employing a Panalytical EMPYREAN with Bragg Brentano geometry Cu-kα (λ=1.5406 Å). Phase quantification was made with Rietveld method using Xpert High Score Plus software. Goodness of fit under 3 was the minimum value to accept the analysis.

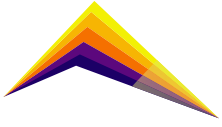

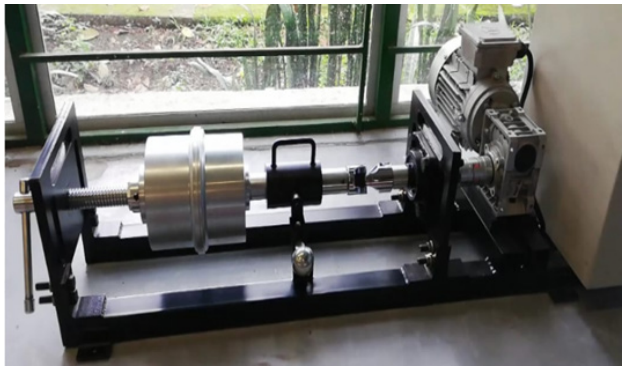

Specifications	
Power	0.5 HP
Electric current	2.5 A
Angular velocity	100 to 1700 rpm

Figure 1. Conventional ball mill

Results and analysis

Figure 2 shows the particle size distribution of the material fed and its morphology. The particle sizes of the distribution are between 26 μm and 182 μm. Furthermore, 90% of the dust has a size that is below 106,411 μm () and only 10% is below 46,077 μm (). Figure 3 shows the SEM images of the YSZ powder after being milled, the powder with a particle size retained at 635 mesh, and the powder passing through 635 mesh after milling. It is noted that the particles obtained have a sharp-edged and blocky structure, which is similar to the morphology of the initial powder. Table 1 shows the values of $\bar{D}_{10}$, $\bar{D}_{50}$ and $\bar{D}_{90}$ taken after the grinding process.

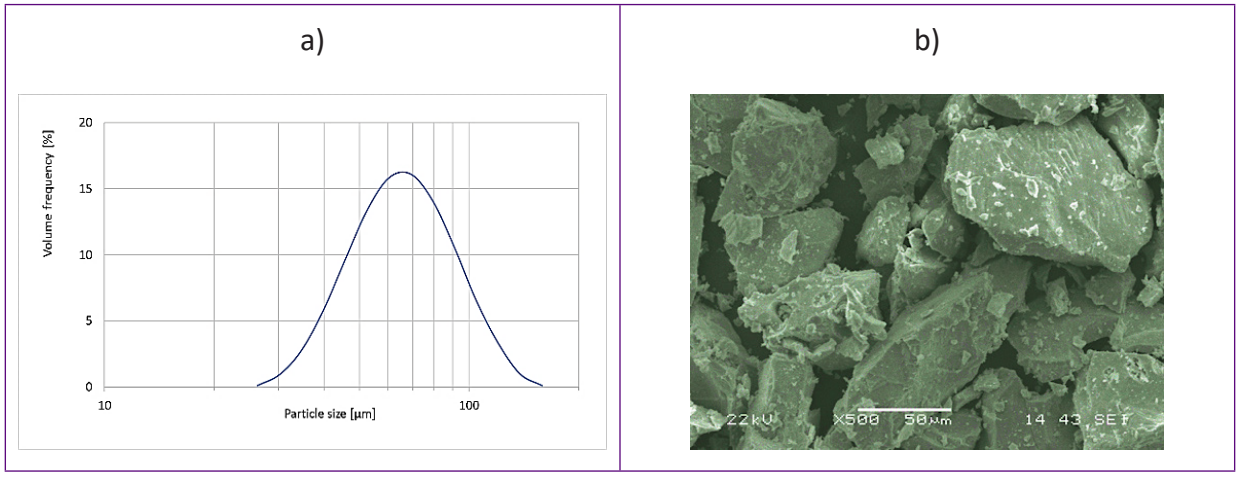

Figure 2. A particle size distribution and SEM for milling feeding

When comparing the data of the powder after grinding without classifying with feed, it is important to note that the greatest change occurs in the, which goes from 46 to 25 µm. In addition, a change in is also evident. It should be considered that the grinding products exhibit a bimodal particle size distribution, which implies that after the grinding process there is a large presence of both coarse and fine particles.

Figure 4 shows the results of the XRD patterns of the initial powder and the resulting powders. When comparing the ground powder and the coarse fraction (retained in the 635 mesh), it is evident that grinding does not promote the transition from the tetragonal and cubic phases to the monoclinic phase. This is evident since the peaks at 2θ~28° and 2θ~31° do not appear. Similarly, when reviewing the XRD patterns of the fine fraction resulting from grinding, with the powder fed, it is also concluded that the transition from phases to monoclinic is not promoted. In general, it is stated that the microstructure of the powder is composed of a solid solution of the cubic and tetragonal phases. It is important to emphasize that, according to the patterns obtained, there is a transition from the tetragonal to the cubic phase in the coarse fraction, since the peak at 2θ~73.7° becomes more pronounced.

Table 1. Particle size distribution of YSZ powders after milling

Mill product	$\bar{D}_{10}$	$\bar{D}_{50}$	$\bar{D}_{90}$
Raw mil product	25.302	59.157	106.748
Coarse (+ 635 mesh)	38.411	65.786	109.987
Fine (- 635 mesh)	3.769	16.694	31.267

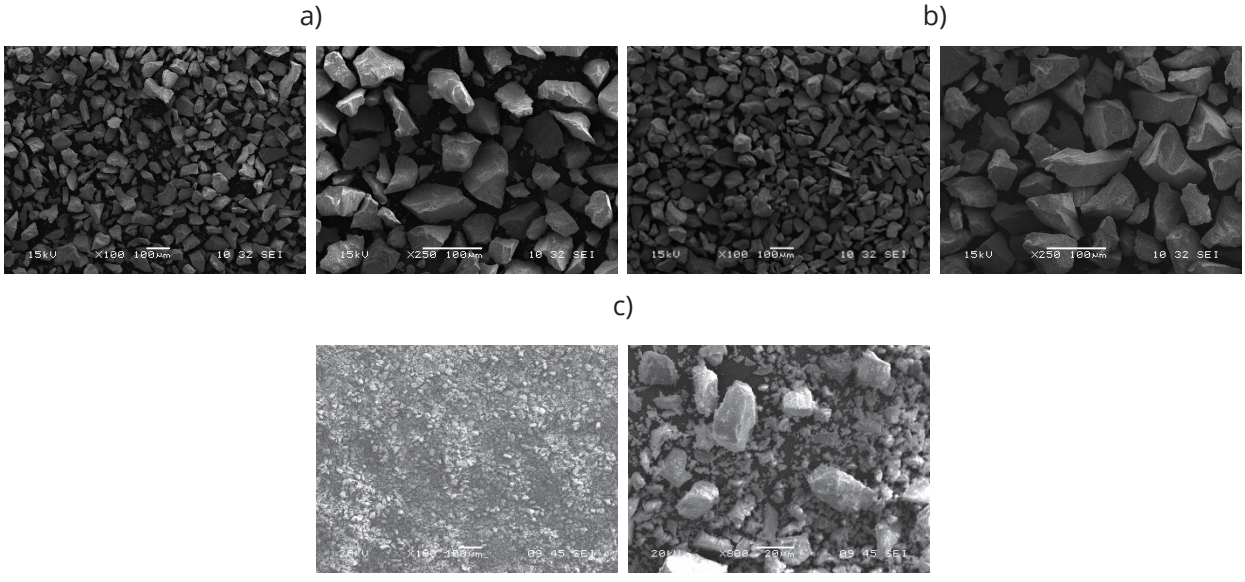

Figure 3. SEM images of YSZ powders a) raw milled b) + 635 mesh, c) -635 mesh

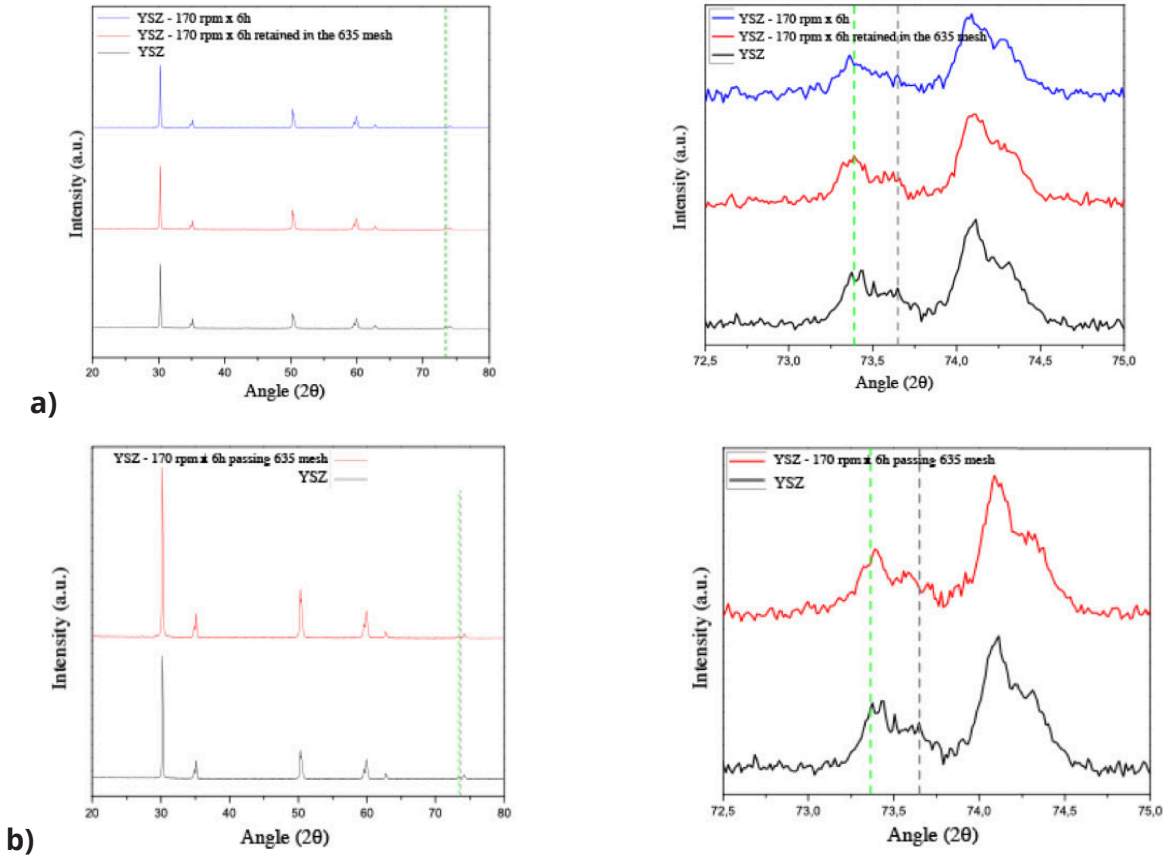

Figure 4. XRD results for YSZ powders
a) feed powder vs coarse product b) feed powder vs passing 635 mesh.

Conclusions

Ball milling is a complex process and involves optimizing several variables to achieve a desired phase or microstructure. Grinding is a safe method for the modification of the size of YSZ powder particles since the promotion of the phase transformation to monoclinic does not occur. Because of the high-energy impact resulting from the ball's collision with the powder, the shape of the generated particles inherits the angular and blocky shape, characteristic of the fed powder. As a consequence of the obtained results, it is concluded that the powder obtained has potential use as a material for CT in TBCs, since its macrostructural and particle size characteristics are similar to those of some commercial powders. YSZ powders obtained from milling are a suitable alternative to commercial powder for Colombian industry. Raw YSZ powders for milling are easily available and they have less cost. The use of these powders allows the implementation of thermal projection processes and related processes in the country to accelerate industrial development.

References

[1] X. Li et al., “Oxidation and hot corrosion behaviors of MAX-phase Ti3SiC2, Ti2AlC, Cr2AlC”, Ceramics International, 2022.

[2] S. Singh, K. Goyal, R. Bhatia, “A review on protection of boiler tube steels with TBC from hot corrosion”, Materials Today: Proceedings, vol. 56, pp. 379–383, 2022.

[3] L. Baiamonte et al., “Thermal sprayed coatings for hot corrosion protection of exhaust valves in naval diesel engines”, Surface and Coatings Technology, vol. 295, pp. 78–87, 2016.

[4] Á. J. Villavieja Urzainqui, «Circonia estabilizada con itria; obtención y caracterización», Tesis doctoral, Universidad de Málaga, Málaga, 2015.

[5] A. Islam, A. Sharma, P. Singh, N. Pandit y A. K. Keshri, “Plasma-sprayed CeO2 overlay on YSZ thermal barrier coating: Solution for resisting molten CMAS infiltration”, Ceramics International, vol. 48, n.º 10, pp. 14587–14595, 2022.

[6] L. Bai, S. Wan, G. Yi y H. Sun, “Exploring the influences of the counterpart materials on friction and wear behaviors of atmospheric plasma-sprayed YSZ coating”, Ceramics International, 2022

[7] A. Rabieifar, M. R. Afshar, H. Najafi y S. Nategh, “Investigation of microstructural changes of Pt-Al-7% YSZ coating during high-temperature hot corrosion and its effect on tensile properties of coated Rene-80 superalloy at 950 °C”, Surface and Coatings Technology, p. 128461, 2022.

[8] P. G. Lashmi, N. Balaji, S. Senthil Kumar y S. T. Aruna, “Hot corrosion properties of plasma sprayed La2Ce2O7/YSZ vis-à-vis La2Ce2O7/ cluster paired zirconia thermal barrier coatings”, Surface and Coatings Technology, vol. 409, p. 126902

[9] S. T. Vagge, A. B. Pahurkar y S. B. Ghogare, “Synthesis and processing of thermal barrier coatings with the use of YSZ, LTA and LTA/YSZ”, Materials Today: Proceedings, vol. 48, pp. 1680–1689, 2022.

[10] T. Wang, L. Zhu, H. Wang, Y. Li y J. Xie, “Tribological property and thermal shock resistance of NiCoCrAlY coated YSZ composite coatings prepared by different laser additive manufacturing scanning speeds”, Materials Today Communications, vol. 31, 2022

[11] A. Patidar, A. K. Mandal, A. K. Chaudhary y V. Jain, “Surface

roughness of sintered yttria stabilised zirconia (YSZ) using high speed moderate depth super-abrasive grinding", Materials Today: Proceedings, vol. 44, pp. 2705–2709, 2021

[12] S. C. Chelgani, M. Parian, P. S. Parapari, Y. Ghorbani y J. Rosenkranz, "A comparative study on the effects of dry and wet grinding on mineral flotation separation–a review", Journal of Materials Research and Technology, vol. 8, n.º 5, pp. 5004–5011, 2019

[13] M. Peltoniemi, R. Kallio, A. Tanhua, S. Luukkanen y P. Perämäki, "Mineralogical and surface chemical characterization of flotation feed and products after wet and dry grinding", Minerals Engineering, vol. 156, p. 106500, 2020.

[14] P. Prziwara y A. Kwade, "Grinding aid additives for dry fine grinding processes – Part II: Continuous and industrial grinding", Powder Technology, vol. 394, pp. 207–213, 2021.

[15] A. Choudhary y S. Paul, "The wear mechanisms of diamond grits in grinding of alumina and yttria-stabilized zirconia under different cooling-lubrication schemes", Wear, vol. 454-455, p. 203315, 2020

[16] T. Wang et al., "Assessing load in ball mill using instrumented grinding media", Minerals Engineering, vol. 173, p. 107198, 2021.

[17] S. Lamnini, Z. Fogarassy, Z. E. Horváth, S. Tóth, K. Balázsi y C. Balázsi, "The role of the attrition milling on the grain size and distribution of the carbon nanotubes in YSZ powders", Boletín de la Sociedad Española de Cerámica y Vidrio, vol. 58, n.º 3, pp. 126–133, 2019

[18] R. Ali et al., "Tribological performance and phase transition of MAX-phase/YSZ abradable seal coating produced by air plasma spraying", Ceramics International, vol. 48, n.º 3, pp. 4188–4199, 2022.

[19] G. Lyu et al., "Sintering behavior and phase transformation of YSZ-LZ composite coatings", Ceramics International, vol. 46, n.º 2, pp. 1307–1313, 2020.

[20] X. Y. Liu, J. W. Che, H. Yi y G. Y. Liang, "Influence of powder states on the composition and phase stability of LZ/YSZ composite thermal barrier coatings", Ceramics International, vol. 44, n.º 16, pp. 20291–20298, 2018.

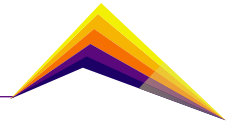

Arc sprayed coatings on infrastructure elements to protect them from corrosion and abrasion

Carlos Andrés Zuñiga Gañan *E-mail: jefetermorociado@soldinsas.com*

Soldaduras Industriales

Abstract

Despite the fact that the development of thermal spraying applications in the infrastructure sector has not been very relevant, there is a sector that, if it has evolved, is that of applications in boiler tubes, which is why this work is focused on the solution that occurred due to the problem of wear due to corrosion and erosion presented by the internal pipe of the 2011 boiler of the generation company TERMOTASAJERO S.A. ESP. phenomenon caused by the impact of the ash flow at high speed and by the constant changes in temperature.

Infrastructure is the set of works, structures, and other capital goods that an economy has. In this way, elements such as roads, railways, irrigation systems, sewage systems, houses, dams, schools, and electrical distribution networks will be included.

With the Arc spray process, high-voltage masts have been internally coated with aluminum and zinc alloy wire, zn-coated gas cylinders, containers coated with Zn, Zn-Aluminum or Aluminum, digesters and boiler tubes with iron alloys and nickel alloys. They have also used paints on the thermal pray, to give a presentation and more protection.

In the flame spraying process, the wire used as raw material melts into an oxygen-fuel flame. The fuel can be acetylene, propane, or

Correspondent author

hydrogen. The wire is fed concentrically into the flame, where it is melted and atomized by the addition of compressed air which also drives the molten material toward the surface of the workpiece. In the electric arc process, two metallic wires are used, preferably of the same composition, which is electrically charged with opposite polarity and are fed towards the arc gun at adapted and controlled speeds. When the wires meet at the point of contact, an arc is created that continuously melts the ends. A stream of compressed air is used to atomize the already molten material and accelerate it over the work surface to form the coating.

The presentation of this work is intended to be a model for the execution of other infrastructure works, since the methodology or application parameters as ampere, voltage, and pressure as well as the selection of abrasive material for surface preparation, material for making the coating, knowledge of substrate and wear mechanism, could be similar to those for other components whose useful life is to be extended, protecting it from corrosion and abrasion.

Keywords: Therma spray, Arc spray, corrosion, abrasion

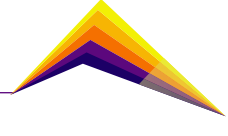

Introduction

Thermal Spray

why to do Thermal Spray

The more developed the infrastructure in a country, the greater its productive capacity must also be. First world countries are a clear example of this development and are a benchmark for emerging economies like Colombia. In some elements of the infrastructure, we can find a phenomenon that impacts the economy from the point of view of maintenance costs, and that is corrosion, is one part of this problem that has already been solved in Europe and the United States with thermal spray processes. sprayed mainly arc spray and flame Spray. High voltage masts, as well as bridges and structures among other elements, have been protected against corrosion with these two methods [1][2][3][4].

The challenge now for the region is to take advantage of these experiences and adapt successful applications to the local environment. All in search of productivity.

These applications could be said to be null in the country, but they could increase in the coming years due to the growth that has taken place in infrastructure, for which it is necessary for new companies to emerge or for companies dedicated to corrosion protection to adapt this technology and in this way, they increase their portfolio to meet the demand to come.

Principle of the thermal spraying process

It is also known as Metallizing. It is a process of coating consisting of the spraying of metallic or ceramic particles, either molten or in the state plastic on a workpiece called a substrate, previously prepared to provide a surface with specific characteristics to satisfactorily comply with the operating conditions of the process. The Figure 1 is a diagram showing the principle of thermal spray. The coating feedstock material is melted by a heat source. This liquid or molten material is then propelled by process gases and sprayed, where it solidifies and forms a solid layer. The individual aspect of a thermal sprayed coating follows [5].

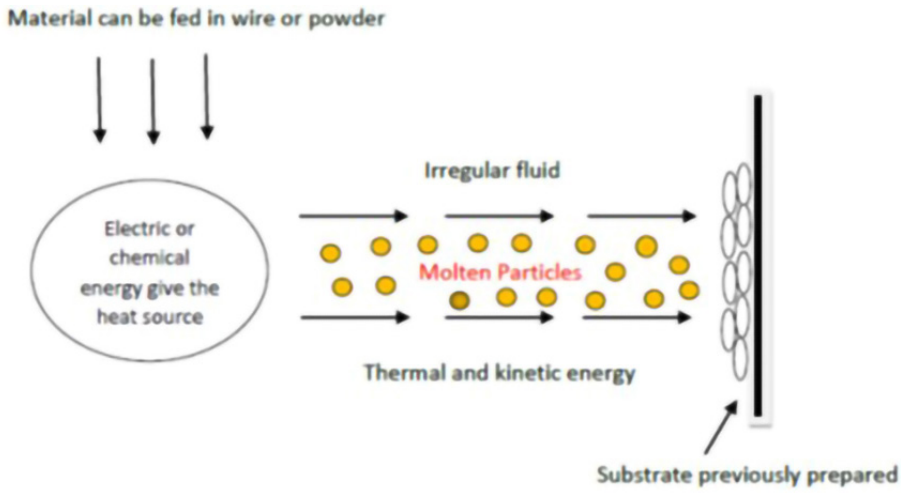

Figure 1. Principle of thermal spraying.

Substrate material

Suitable substrate materials are those that can withstand blasting procedures to roughen the surface. Because the adhesion of the coating to the substrate consists of mechanical bonding, careful cleaning, and treatment of the surface to be coated is extremely important. After the removal of surface impurities by chemical or mechanical methods, the surface is usually roughened using a blasting procedure. This activates the surface by increasing the area to be bonding of the sprayed particles. The liquid or molten coating particles impact the surface at high speed. This causes the particles to deform and spread like "pancakes" on the substrate. Heat from the hot particles is transferred to the cooler substrate. This procedure is represented schematically in Figures 1 and 2.

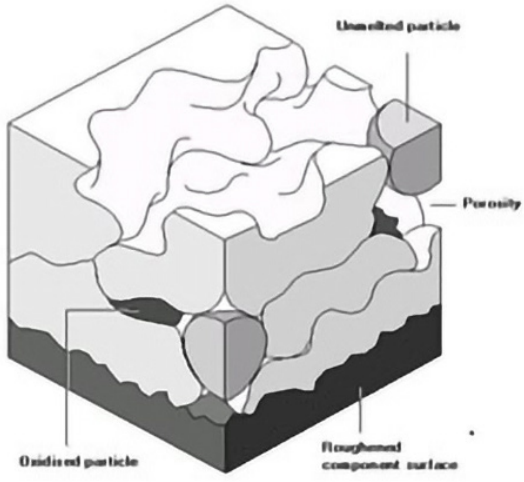

Figure 2. Schematic diagram of a thermal sprayed coating. Oerlikon Metco An Introduction to Thermal Spray – Issue 6 – July 2016

Coating Material

Any material that does not decompose when melted can be used as a thermal spray coating material. According to the thermal spray process, the coating material can be in wire or powder form. Choosing a coating material that is suitable for a specific application requires special knowledge about the service environment as well as knowledge about the materials. Apart from the physical characteristics, such as coefficient of expansion, density, heat conductivity, and melting point, additional factors, such as particle shape, particle size distribution and manufacturing process of powder material will influence coating.

Thermal spray coating processes

According to the energy source, Figure 3 shows the four most common processes in Colombia, where arc spray is the most popular.

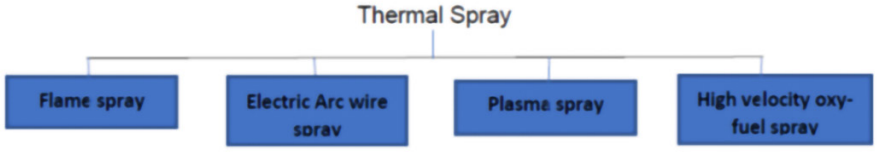

Figure 3. Schematic diagram of four spray processes.

Electric Arc Wire Spray

In the arc spray, the weight of the coating deposited per unit of time is directly related to the amperage output, density, and melting point of the material. Figure 4 shows the schematic diagram of the process.

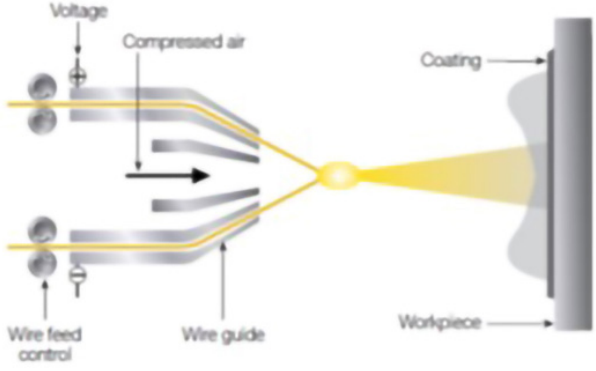

Figure 4. Schematic diagram of the electrical arc wire process. Oerlikon Metco Issue 6 – July 2016

Experimental procedure

In the schematic of figure 5 are shown the steps to make the thermal spraying coating.

Figure 5. Schematic diagram of experimental steps of arc spray process.

Materials suppliers

We used a cored wire, commercial reference PMET 292 specifically designed for arc spray systems. It produces a nano- structured, hard, and corrosion- resistant coating, with a service environment up to 1700 F. Is used in a wide variety of highwear applications, including boiler tubes, fans and ant-skid surfacing applications. The chemical composition of the core wire used to spray the coating is shown in table 1 (in weight percentages)

Table 1. Wire chemical Composition. Information supplied by the manufacturer.

C	Nb	Cr	B	Mn	W	Si	Mo	Fe
1.4 %	7 %	16%	4.5%	0.5 %	8%	0.5%	3.2	Balance

Substrate material was boiler tube ASTM A192 Grade B7, its Chemical Composition is shown in Table 2.

Table 2. Chemical composition boiler tube ASTM 192 from Data Sheet company.

ASTM A192 (wt.%)					
C	Mn	P	S	Si	Fe
0.06% -0.18%	0.27% - 0.63%	0.035%	0.035%	0.25%	Balance

Surface preparation

The preparation was in situ and the portable equip for this process was taken to the site. This is one of the most important steps to make in thermal spraying applications because having the activation in the surface is essential to ensure the union coating. G25 aluminum oxide angular abrasive was used in the process. This was projected at 15 cm from the substrate and the work pressure was 0.5 Mpa. At the end of the process, a roughness Ra between 3.5 to 4 µm was obtained. It was tested with a TIME 3100 digital roughness tester.

Arc spray parameters

Before of making the application, it was necessary to search for information of parameters in data sheet of equips and in datasheet of materials. Each of the parameters has a relevant effect on the success of the application; Arc sprays equipment, wire material, abrasive blasting material, amperage, voltage, air pressure, and spraying distance. The table 3 shows the parameters used in the spraying process.

Table 3. Application parameters.

Diameter	Amperage	Voltage	Air pressure	Standoff
1.6 mm	180 -200	29 -30	0.45 Mpa	15 -20 cm

Coating application

For the execution of the work, the Arc Tafa Spray thermal spray system from Ferresolda Company was used. The application was made in Termotasajero Coal Fired power plant in San Cayetano, North Santander Colombia. Figure 6 shows Arc thermal spraying.

Figure 6. Courtesy of Ferresolda

The spraying of the coating was carried out 15cm from the substrate at a deposition rate of 9.9 kg/ hr. On the thermally sprayed layer, no machining or pore-filling work was carried out with sealant or paint.

Job site testing

Once the process was finished, the power plant began operation and the pipe began to suffer the effects of fireside corrosion fatigue, fly ash erosion, waterwall fireside corrosion, thermal fatigue, Erosion corrosion, falling slag erosion, soot blower erosion, short-term/ long-term overheating, chemical cleaning damage, pitting corrosion.

Results and analysis

According to the application parameters, the particulate material reached a speed between 100 to 150 m/s [5]. The application was completed until that 16.9 m2 were coated and an average thickness of 1 mm (Elcometer) was reached on the surface of the pipe. Also, the final roughness Ra was between 1.5 to 2.5 µm and the hardness was between 60 and 65 Rc (Portable Hardness tester UCI Method).

The Figure 7 shows some boiler pipes after 1 year of operation.

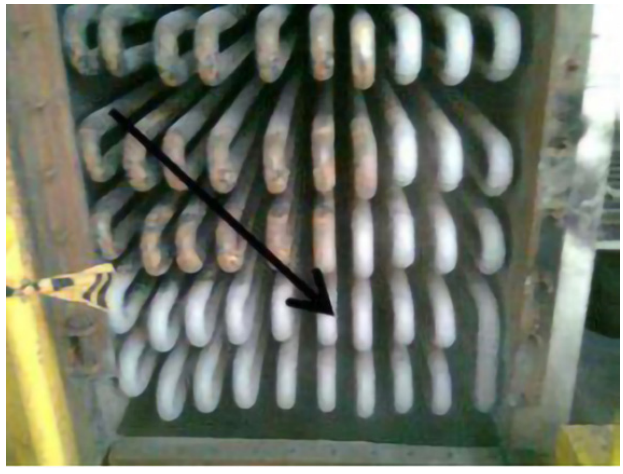

Figure 7. Boiler pipes after one year of operation. Courtesy of Ferresolda

An inspection was conducted after one year, in which it was evidenced that the metallic areas were in perfect condition, in this way the following inspections were carried out year after year and a useful life of at least 5 years could be guaranteed.

Conclusions or summary

Thermal spraying is a widely available and widespread technique for power generation boiler tube applications.

Before making the selection of the coating material, the type of boiler and characteristics of the fluids that attack the tubes to be coated must be known.

Standardization of operating parameters is key to the success of any Arc Spray application. The thermal spray to boiler tubes can help with the efficiency in the transformation of Thermal energy into electrical energy.

By extending the useful life of the boiler tubes, replacement and interruption costs are reduced, thus avoiding lost income for the company.

References

[1] Armor Thane. (2021). Corrosión protection coatings against rust, Chemical, environment. https://www.armorthane.com

[2] OERLIKON METCO (2002). Corrosion Coating of Win track High-Voltage Masts. https://www.oerlikon.com

[3] OERLIKON METCO (2018). Corrosion Protection for Shipping Containers. https://www.oerlikon.com

[4] SULZER METCO (2010). Corrosion protection under insulation. https://www.oerlikon.com

[5] OERLIKON METCO. Issue 6 – July (2016). Introduction An Introduction to Thermal Spray.

Axisymmetric modeling and CFD simulation of cold projection for ceramic particles of HAp (Hydroxyapatite)

Esaú M. Rodríguez[1]
John Henao[2]
Jonathan S. Unda[3]
Carlos A. Poblano[1]
Astrid L. Giraldo[3]

E-mail: m12200846@pachuca.tecnm.mx
E-mail: john.henao@ciateq.mx
E-mail: ualj991228@gs.utm.mx
E-mail: carlos.poblano@ciateq.mx
E-mail: agiraldo@cinvestav.mx

1.CIATEQ Unidad Querétaro
2. CONACYT-CIATEQ Unidad Querétaro
3. CONACYT- Cinvestav, Campus Juriquilla, Querétaro.

Abstract

According to the information collected from open access scientific articles concerning the deposition of hydroxyapatite (HAp) coatings by the cold spray technique, a finite element analysis and simulation study was carried out using the ANSYS-Fluent software. This work is aimed at establishing a numerical panorama that allows adjusting and improving the necessary conditions for the deposition of HAp particles by cold spray. The present study contributes to the state of the art of the cold spray process for ceramic materials and intends to discuss not only the in-flight trajectory of the particles within the gas stream but also the effects of processing gas conditions (gas pressure and temperature) on the main output variables of the process (gas velocity and temperature and particle velocity and temperature). Some results of this work could be not only applicable to HAp, but also to other ceramic materials with different chemical structures. Overall, experimental and simulation results in the present work can allow to get a better understanding of cold sprayed ceramic particles. The energy efficiency as well as the reduction of chemically polluting by-products that the cold spray method has

Correspondent author

over other types of coating methods, represents an environmental benefit and makes this technique a potential candidate for the deposition of bio-ceramic coatings for the biomedical industry. Particularly, in this work, a detailed study to determine both physical and mechanical influence of the main processing parameters that are present in the cold spray process was carried out; these include temperature, pressure, speed and morphology of the particles and, at the same time, it explores the design and analysis of the model and meshing of the nozzle used in the cold spray process. The analysis of computational fluid dynamics (CFD) is a powerful tool to get a better comprehension of some processes such as cold spray and can allow to find out parameter interactions that can drive to predict processing conditions resulting in the deposition of coatings with medium to high deposition efficiency and adhesion.

Keywords: Computational Fluid Dynamic, Hydroxyapatite, Coatings, Low Pressure cold gas spray, Ceramic particle impact.

Introduction

The use of HAp as bioactive material comes from the 1960's and has been a topic of research throughout the world since this material can be used for many different applications in the biomedical field such as including the osseointegration of implants in the human body. For instance, HAp coatings are common in cementless hip implants and are often fabricated by plasma spray. In the last two decades, the cold spray process has been the focus of attention for the relatively low processing temperatures with respect to conventional thermal spray processes and, as a result, various authors have been interested in studying the feasibility of preparing HAp coatings by means of cold spray looking for better performance in biological environments. However, due to the fragility of ceramics, the deposition of thick coatings has been quite difficult and still new techniques for the deposition of this coating continue to be explored. Some techniques such as physical vapor deposition generate good adherence and homogeneity, but it requires vacuum conditions and long operation times [1]. Some experience with spherical HAp powders by cold spray shows that spherical morphology tends to easily lose its sphericity and multiple fracture can occur. A study conducted by Vilardell, A. et al states that spraying HAp particles by cold spray does not provide either adequate deposition or coating conformation under certain experimental conditions. One of the solutions found out in the literature for the deposition of HAp powder by cold spray is the used of rough substrates, which increases the deposition efficiency. This fact is mainly

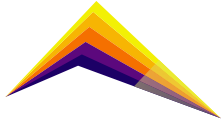

associated with a mechanical anchorage factor that helps to retain ceramic fragments obtained upon impact. On the other hand, at very high shock pressures, thick coatings with low adhesion and fracture toughness are often obtained, which is attributed to the lack of plastic deformation of ceramics. Thus, there is a consensus that the low-pressure cold spray system is still promising for the formation of HAp coatings highly homogeneous [2].

It should be noted that the mechanical properties of cold sprayed coatings are due to the influence of the shearing of the substrate surface and the intertwining of the particles with the substrate and among themselves. Numerical analysis and mathematical models representing the dynamics of the gas and thermo-kinetics of the particles in the cold spray process can helps to identify the physical factors that dictate fluid and particle velocity and thermal interaction. If a CFD analysis is carried out correctly, it will allow to accurately predict the relationships within multiple parameters and it that can be useful to understand the formation of coatings, in particular, when some experimental variables are hardly measurable with available experimental tools [3]. According to **M. Hasniyati et al**, to optimize the cold spray process for the deposition of HAp coatings there are four relevant factors to account: The stand-off distance between the nozzle exit and the substrate surface, the substrate roughness and temperature, and the number of sprays or passes [4]. For completing this series of parameters, one can also mention the particle morphology, gas pressure and temperature, and the geometrical design of the De-Laval nozzle.

On the other hand, several studies have reported models and conditions for the deposition of metallic coatings; these models relate the impact velocity and the minimum velocity that induces plastic deformation and from which deposition efficiency increases. This velocity is known as the critical velocity and for metals critical velocity values are reported in the range from 200 m/s to 1100 m/s depending on the type of metal. However, the deposition of ceramic materials such as HAp on metallic substrates such as titanium still is not well described with the current models, since most of them are based on plastic behavior and does not include the fragile behavior of ceramics under high velocity impact conditions. One of the scopes of current researchers is the study of the impact velocities and temperatures at which the particles are deposited, since this kind of information can help to develop new models that can be used to predict optimal conditions [5]. A study of fluid dynamics using CFD can allow exploring different nozzle geometries and flow conditions to be compared under a variety of parameters combinations. Regarding nozzles in cold spray, it is worth mentioning that the geometric design of the nozzle plays a fundamental role in the process since it is the channel that conducts the gas in the process [6]. De-Laval commercial nozzles are regularly designed with a convergent-divergent section that accelerates the particles reaching supersonic speeds. With the introduction of 3D printing in their manufacturing, cost and manufacturability have been substantially improved. Figure 1 shows a schematic representation of the cold spray process; one can observe that the processing gas is fed from a high pressure reservoir and conducted through and electric heating to increase its temperature. Meanwhile, a feeder is in charge of introducing the particles into a mixing chamber and then to the De-Laval nozzle [7].

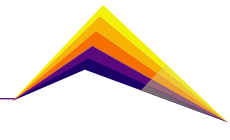

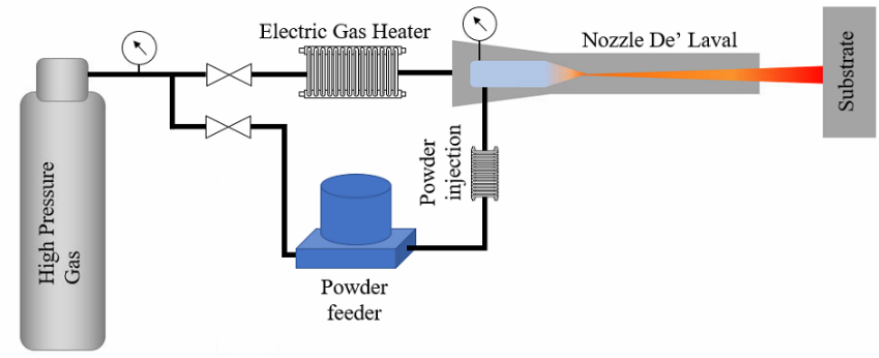

Figure 1. Diagram of the Cold Projection Process image extracted from.

Although there are previous studies about the formation of HAp coatings, there is still an open window to explore parameters interactions to get a better comprehension of the process for HAp particles deposition. In this work, finite element analysis and simulation was employed to analyze gas dynamics under real operation conditions of the cold spray process. Processing conditions were selected from previous experimental works. In addition, particle kinetics and thermal behavior in-flight were studied through axisymmetric modeling and CFD simulation in order to analyze physical properties and mechanical properties related to the formation of HAp coatings in the cold spray process.

Methodology

To model the fluid dynamics of the gas, the ANSYS software 2022 R2 version was used. Through CFD analysis, the speed and temperature curves were studied along the entire axisymmetric line from the mixing chamber to the impact with the substrate. Comparing it with the data found in the bibliographic search of experimentation with the cold spray process in the formation of HAp coatings. Based on previous works, nitrogen gas was employed and it was considered as an ideal gas.

Generation of the CAD model

The CS-2000 nozzle was modeled in the present study. Figure 2 shows a geometry in a continuous line that corresponds to the walls of the nozzle and in line of axis, an axis (axis of symmetry) is shown, so this schematic representation is a model for an asymmetric study. From another perspective, to obtain the complete solid, an extruded revolution solid could be made, taking the mentioned axis as reference. The purpose of the asymmetric study is to simplify the analysis and allows to get a simulation with reasonable results in less computational times compared with a 3D study.

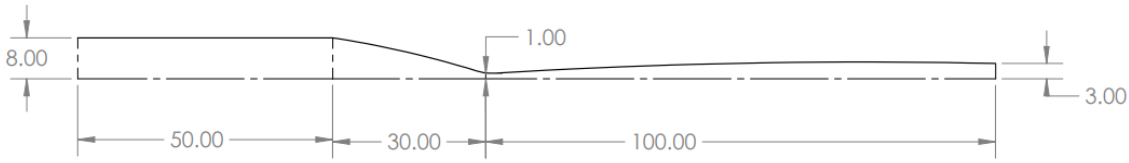

Figure 2. CS-2000 nozzle with installments.

Model Meshing

A type of mesh was used with a quadrilateral method for better ordering, in total 30465 nodes and 9712 elements were generated.

Selection of physical models and parameters

Two simulations were carried out in this study, the first one using the data from Ozdemir et al., 2019 and the second simulation using the data from Chen et al., 2018. It is worth mentioning that the third column of Table 1 refers to the high pressure cold spray process and was taken as a reference for the simulations in this work. .

Table 1. Models and parameters for the simulations.

Studied model [8]	Model Modified	Reference bibliography [6]
Standard model k-epsilon	Standard model k-epsilon	------
Discrete phase (Particle injection)	Discrete phase (Particle injection)	------
Parameters		
Gas: Nitrogen	Gas: Nitrogen	Gas: Nitrogen
Particles (nHAp): 22.3 µm	Particles (nHAp): 22.3 µm	--------
Ti6Al4V substrate	Ti6Al4V substrate	--------
Pressure: 22 bar	Pressure: 30 bar	Pressure: 30 bar
Gas temperature: 300°C	Gas temperature: 800°C	Gas temperature: 800°C

Results and analysis

This study provides an overview of the simplified analysis of the axisymmetric model to understand the design of cold spray nozzles for HAp ceramic particles. The results can allow to modify the nozzle geometry by using parametric variables. Figure 3 shows contour maps of the high pressure cold spray process. These contour maps show the evolution of gas velocity when it flows through the De-Laval nozzle. One can observe that gas velocity increases in the divergent area of the nozzle, reaching out velocity values between 700 m/s and 900 m/s. Moreover, when the gas gets the substrate surface, it is deflected. This fact promotes a decrease on its velocity due to the formation of a bow shock. Figure 3 also shows the temperature contour of the processing gas in the cold spray process. It reveals how the temperature increases in the impact zone of the particles. Under the conditions explored, the processing gas associates high velocities and temperatures.

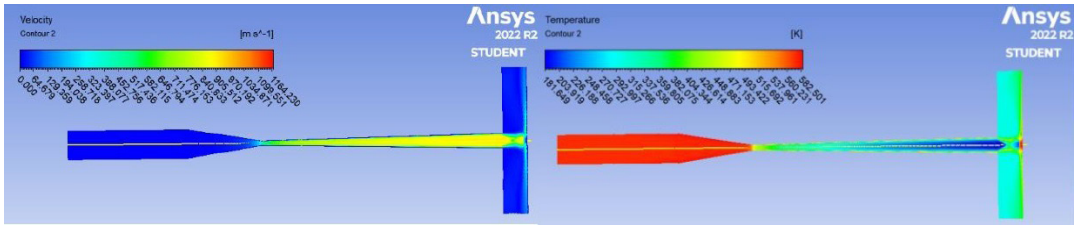

Figure 3. Velocity and temperature contours along the nozzle and upon impact on the substrate.

HPCGS process simulation data:

For the validation of the results, a second simulation was carried out by modifying the nozzle geometry with data reported in the reference [6]. Type 27 TC nozzle manufactured by KINETIK® 4000 was used with nozzle throat diameter (2.7 mm), outlet diameter (8.5 mm), standoff distance (35 mm), length of converging section (51.2 mm), length of divergent section (70.3 mm).

Next, the curves of the two experiments were overlapped in the same graph as shown in Figure 4. One can observe that gas velocity history is quite different in spite of using the same process. The geometry of the De-Laval nozzle is a key parameter that can drive either to increase the kinetic energy or reduced it. In terms of ceramic materials such as HAp, the design of non-conventional nozzles can be a solution.

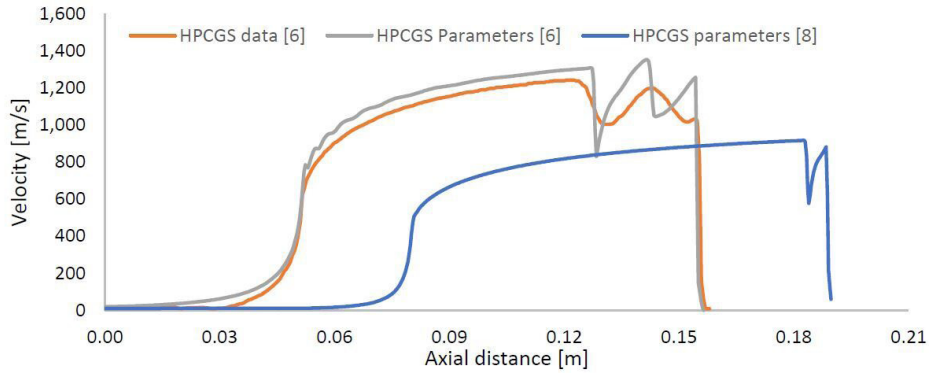

Figure 4. Comparative graph of Simulations of HPCGS processes

Conclusions

The present study was focused on the 2D axisymmetric analysis of the cold spray processing conditions used for the deposition of HAp particles. The results of this work confirm that finite element analysis and simulation are powerful tools for understanding thermal spray processes, in particular, the cold spray process. Regarding the results obtained, it is important to point out that the nozzle geometry is a key factor in the deposition of any material by cold spray since it has an important influence on the gas velocity and temperature. In terms of HAp particles deposition, the nozzle geometry can be a factor to explore in future studies since particle velocity and temperature can be adjusted to obtain optimal conditions leading to increase deposition efficiencies and to improve coating adhesion and mechanical properties.

Acknowledgment:

The authors thank the National Council for Science and Technology (CONACYT) for its support through the Call “Paradigms and Controversies 2022”, project FQPM-32018 with number 320126. They also thank the program “Investigadores por México” former “catedras” program for the support of the projects 848 and 881.

References

[1] Kubicki, G., Leshchynsky, V., Elseddawy, A., Wi´sniewska, M., Maev, R.G., Jakubowicz, J., Sulej-Chojnacka, J. (2022). "Microstructure and Properties of Hydroxyapatite Coatings Made by Aerosol Cold Spraying–Sintering Technology." Coatings 2022, 12, 535.

[2] Vilardell, A. M., Cinca, N., Dosta, S., Cano, I. G., and Guliemany, J. M. (2018). "Feasibility of using low pressure cold gas spray for the spraying of thick ceramic hydroxyapatite coatings." Applied Ceramic Technology., 16(1), 221-229.

[3] Özdemir, O. Ç., Conahan, J. M., & Müftü, S. (2020). Particle Velocimetry, CFD, and the Role of Particle Sphericity in Cold Spray. Coatings, 10(12), 1254.

[4] Hasniyati, M., Zuhailawati, H., Sivakumar, R., Dhindaw B. K. and Noor S. N. F. M. (2015). "Cold spray deposition of hydroxyapatite powder onto magnesium substrates for biomaterial applications." Surface Engineering. 31(11), 867-874.

[5] Cinca, N., Vilardell, A. M., Dosta S., Cano, I. G., Guilemany, J. M., Estradé, S., Ruiz, A. and Peiró F. (2016). "A New Alternative for Obtaining Nanocrystalline Bioactive Coatings: Study of Hydroxyapatite Deposition Mechanisms by Cold Gas Spraying." 99(4), 1420-1428

[6] Vadla, S. R. and Doom. J. (2018). "Analysis of Jet Characteristics Among Various Cold Spray Nozzles." Journal of Thermal Spray and Engineering, 1(1), 24-31.

[7] Ozdemir, O. C., Chen, Q., Muftu, S. and Champagne, V. K. (2019). "Modeling the continuous heat generation in the cold spray coating process." Journal of Thermal Spray Technology, 28(1), 108-123.

[8] Chen, X., Ji, G., Bai, X., Yao, H., Chen, Q. and Zou, Y. (2018). "Microstructures and properties of cold spray nanostructured HA coatings." Journal of Thermal Spray Technology, 27(8), 1344-1355.

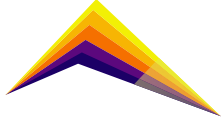

Study of thermal spray parameters through numerical simulations for ceramic powders

Juan Camilo Arango Galvez[1]
Alejandro Alvarez Uribe[2]
Alejandro Marulanda Tobón[3]
Claudia Constanza Palacio Espinosa[4]

E-mail: jarang71@eafit.edu.co

[1, 2, 3, 4] *EAFIT University*

Abstract

Atmospheric Plasma Spray (APS) is a highly developed process to produce high performant coatings and it is widely used in a lot of industrial applications. Comprehension of the different parameters involved in coatings fabrication through those techniques constitutes a key aspect tailoring developments. There are complementary computing tools that allow the prediction and modeling of this kind of processes. In this study the software *"Jets and Powders"* was used to simulate the behavior of ceramic particles in a plasma spray process used to fabricate a thermal barrier coating of Yttria-stabilized zirconia (ZrO_2 – Y_2O_3 8 wt.%). Comparisons seeking correlations were made with the experimental results obtained by an optical sensor (Accuraspray G3C) and the microstructural characterization of the coatings obtained. As a result, it was possible to establish the parameters of non-direct inputs of the software (turbulence model, thermal efficiency, and type of air barrier) that allow predicting the behavior of a plasma spray process that is carried out by a SinplexPro torch.

Correspondent author

Key words: Jets et Poudres, plasma spray, APS, simulation, YSZ.

Introduction

Thermal spraying comprises a group of coating techniques where metallic or non-metallic materials are deposited in a molten or semi-molten state to form a coating. Among these techniques, the Atmospheric Plasma Spray (APS) emerges as one of the most applicable and in which the material is projected by means of a gas flow that is subjected to continuous electric discharges leading to plasma jet generation jet [1-2].

In this class of processes, a wide variety of physical phenomena are involved, which can be predicted and modeled by means of computational tools that allow to establish the conditions of the gas flow, temperatures of the jet and projected particles, concentration of charge carriers (ions and electrons) in the discharge, kinetic parameters of particles in flight and the electromagnetic fields associated to the system. Authors such as S. Semenov and T.H. Van Steenkiste, performed simulations of the plasma jet behavior in this kind of processes, aided by complementary computational tools [3], [4]. Likewise, Y. P. Wan, M. Pasandideh-Fard and Huimin Liu have managed to simulate the thermo-kinetic behavior of particles in flight during projection processes. [5]–[7].

Methodology

Usually, the coatings used as thermal barriers, such as those manufactured in this study, consist of an internal anchor layer made of an alloy of the type MCrAlY, where M is usually Fe (Iron), Ni (Nickel), Co (Cobalt or NiCo) and an outer layer of the ceramic material, in this case YSZ; both layers are fabricated using the plasma thermal spray process [8]. However, this study is limited to the thermo-kinetic and microstructural analysis of the ceramic outer layers.

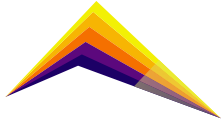

Materials and Methods

The powder used was ZrO_2 – 8 wt.% Y_2O_3 (YSZ) nanoparticles agglomerated and sintered. This was manufactured by Oerlikon Metco and named Metco 204NS-G whose thermodynamic properties are presented in Table 1.

Table 1. Properties of YSZ powder Metco 204NS 1[9] – [12].

Solid Specific Heat [J/kgK]	Mass Density [kg/m³]	Thermal conductivity [J/(msK)]	Melting point [K]	Latent heat [J/kg]	Molar mass [g/mol]
460	5938	1.26	2800	812400	131.429

The morphology of the particles was determined by images from a Scanning Electron Microscope (SEM). This powder exhibits spherical morphology particles, seen in Figure 1.

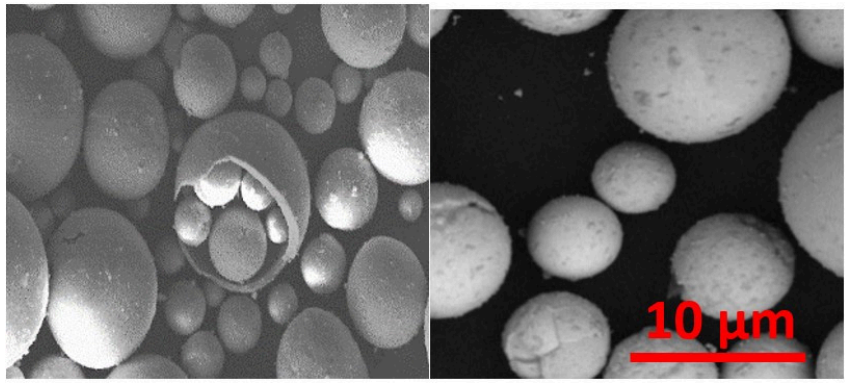

Figure 1. Morphology of Metco 204 NS-G particles.

The particle size distribution is determined by laser diffraction using water as a dispersing medium. The particles are dispersed by ultrasound and then placed in the laser-illuminated cell to generate diffraction and by means of lens arrays determine the size and size distribution of the particles. Particles have a micrometric particle size distribution in which the particle size is between 21.7 µm (d10) and 94.25 µm (d90) and that the corresponding particle size when the cumulative percentage reaches 50% is at a size of 53.31 µm (d50).

The substrates used for the study were stainless steel (AISI 304) discs with a diameter of 25 mm and a 5 mm thick.

Projection parameters:

The device to manufacture the samples consists of an Oerlikon Metco SinplexPro torch. Powders are introduced into the plasma jet using a 1.8 mm internal diameter injector powered by a distributor. The injector is located upstream (external injection) of the jet nozzle outlet. The samples are arranged on a rectangular samples holder that can receive up to six. The sample holder is static, and it is placed perpendicular to the jet axle which allowed the torch performing the relative movements of translation in face to the fixed samples. The projection parameters are shown in Table 2.

Table 2. Projection parameters for the outer layer from Metco 204NS-G powder.

Type of Torch		SinplexPro Oerlikon Metco
Nozzle diameter		9 mm
Powder injection	Type	External, perpendicular to the axis of the torch
	Rate	1.2 kg/h
	Injector diameter	1.8 mm
Projection distance		105 mm
Energy	Electric current intensity	500 A
	Voltage	96 V
	Electrical Power	48 kW
Gas mixture		$Ar + H_2$
Composition of the mixture 50 l/min – 7 l/min		88 - 12% Vol. 50 l/min – 7 l/min

Computational modeling of the in-flight particles' behavior:

Particles in-flight behavior through the plasma jet was evaluated by computational models using the software Jets & Poudres that allows to calculate a variety of parameters like temperature and velocity of the jet and particles, percentage of fusion and K Sommerfeld (dimensionless to be between 3 and 57.7) of particles in flight during the process. The input parameters to perform a plasma spray simulation include the type of turbulence model, the composition and flows of the plasma-forming gases, the composition of the atmosphere surrounding the jet, the projection distance, the characteristics of the torch like the electrical

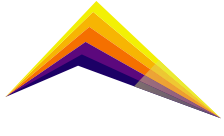

power and thermal efficiency of the torch or effective power, and the parameters of the powder that were presented in the Table 1 [13] – [15]. Some of these process variables were known (for this specific process) such as the composition and flows of the plasma-forming gases, the projection distance, the properties of the torch and the electrical power and can be seen in Table 2. Other parameters must be selected among different ranges:

1. The type of turbulence model: it can be mixing length or k-ε.
2. The composition of the surrounding atmosphere: this refers to whether the plasma jet and its temperature are confined within an air pressure, that is, a temperature cone may or may not be generated around the jet. This translates to Shield or No Shield to the jet.
3. The thermal efficiency of the torch or effective power: electrical power traduces the torch ability to convert electrical power to heat. It varies between 85 % and 95 % as effective power.

Experimental process for the diagnosis of particles in-flight:

The study of the thermokinetic state of the particles in-flight during the projections was carried out with the complementary information collected from the Accuraspray G3C that allows estimating the speed of the particles and offers orders of magnitude to the temperature. The sensor was located on the X axis at 105 mm from the torch nozzle and on the Y axis at 300 mm, in order to obtain information about the rapidity of the particles at the projection distance. For this study, two moments of measurements were conducted for each ceramic powder projection: before projecting and after projecting without the presence of substrate and with the static torch, when the flow of particles is maximum and stable.

Results and analysis

Results of the experimental measurements:

Experimental results of measurements of velocity and temperature of particles in-flight made by the Accuraspray system are shown in Table 3.

Table 3. Experimental measurements of velocity and temperature on particles in-flight.

Material	Particle velocity [m/s]	Particle temperature [K]
YSZ	220.2 ± 8.6	2892.2 ± 27.4

Microstructural analysis of the coatings generated

This analysis allows to observe on the surface of the fabricated coatings the presence of a large number of small splats which correspond to particles of very small sizes or splashes of slightly larger particles which could explain the high values of the dimensionless Sommerfeld K parameter obtained in the simulations. These formations can be seen in Figure *2*.

When analyzing the results corresponding to the first stage of the study, two hypotheses are proposed:

The coating is possibly only be formed from particles smaller than 50 µm and larger particles do not contribute to the formation of this and therefore there is a significant loss of material because the smallest particles are not capable to arrive to substrate, then a high proportion of the size distribution of the powder is not part of the coating.
The presence of a large number of small splashes can explain the high K value obtained when performing the simulations, since, as mentioned above, for a splat to form the value of the K Sommerfeld must be between 3 and 57.7.

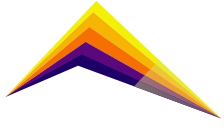

Conclusions or summary

To perform simulations with the “Jets et Poudres” software of a thermal spraying process using an Oerlikon Metco SinplexPro torch, the unknown input parameters of the process are:

1. The thermal efficiency of the torch.
2. The turbulence model.
3. The composition of the surrounding atmosphere.

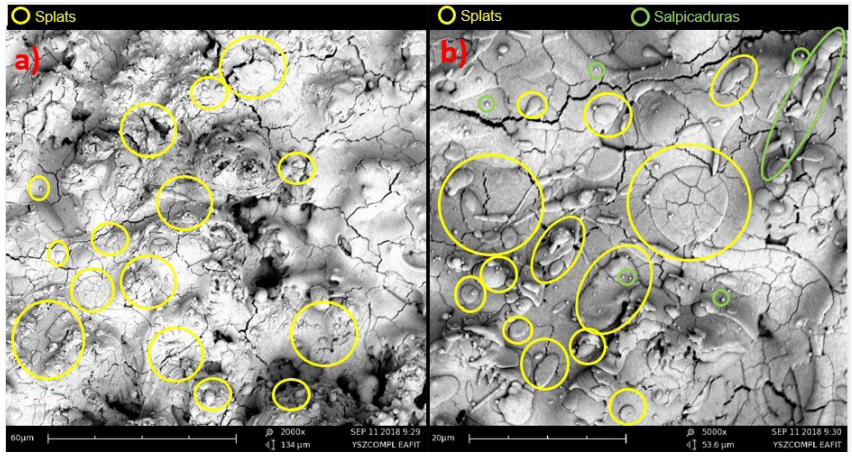

Figure 2. Microstructure evaluated by means of SEM on the surface of the generated coatings: a) 2000X, b) 5000X

During this study it was identified that the conditions of these parameters are:

The thermal efficiency value between 85 % and 95 % adjusts very well to experimental conditions of the plasma torch used. An exact value was not necessary because the variation of the results with one or another value is not mathematically relevant.

The turbulence model that best simulates the used plasma jet is the Mixing Length model, because it best describes the temperature profile generated with this type of torches.

The application of confinement barrier is not necessary because the results of the speeds and temperatures recorded do not make any physical sense and, in addition, these torches do not have an external air flow to keep the temperature confined within a range.

The software “Jets et Poudres” does not consider that particles can be porous or constituted by the accumulation of small particles, then this causes the simulation results to be farther away from the experimental results. It was observed that for particles greater than 45 µm simulations predicted they are not able to reach the substrate however the experimental

result is that a coating was formed when those sizes of particles were used. However, for particles below that size, the software is able to predict their behavior in good agreement to experimental results which could be verified through the characterizations.

It is possible to conclude that simulations of jet and spray process are useful tools to adjust experimental parameters with the aim of getting the maximum profit of raw materials and obtain specific expected characteristic within the coatings.

References

[1] P. L. Fauchais, J. V. R. Heberlein, and M. I. Boulos, *Thermal Spray Fundamentals*. 2014. doi: 10.1007/978-0-387-68991-3.

[2] L. Pawlowski, *The science and engineering of thermal spray coatings*, Second Edi. WILEY, 2008. doi: 10.1016/0263-8223(96)80006-7.

[3] S. Semenov and B. Cetegen, "Spectroscopic temperature measurements in direct current arc plasma jets used in thermal spray processing of materials," *Journal of Thermal Spray Technology*, vol. 10, no. 2, pp. 326–336, 2001, doi: 10.1361/105996301770349411.

[4] T. H. Van Steenkiste *et al.*, "Kinetic spray coatings," *Surface and Coatings Technology*, vol. 111, no. 1, pp. 62–71, 1999, doi: 10.1016/S0257-8972(98)00709-9.

[5] Y. P. Wan, V. Prasad, G.-X. Wang, S. Sampath, and J. R. Fincke, "Model and Powder Particle Heating, Melting, Resolidification, and Evaporation in Plasma Spraying Processes," *Journal of Heat Transfer*, vol. 121, no. 3, p. 691, 2008, doi: 10.1115/1.2826034.

[6] M. Pasandideh-Fard, V. Pershin, S. Chandra, and J. Mostaghimi, "Splat shapes in a thermal spray coating process: Simulations and experiments," *Journal of Thermal Spray Technology*, vol. 11, no. 2, pp. 206–217, 2002, doi: 10.1361/105996302770348862.

[7] H. Liu, E. J. Lavernia, and R. H. Rangel, "Numerical simulation of substrate impact and freezing of droplets in plasma spray processes," *Journal of Physics D: Applied Physics*, vol. 26, no. 11, pp. 1900–1908, 1993, doi: 10.1088/0022-3727/26/11/010.

[8] O. Metco, "Material Product Data Sheet Nickel Cobalt Chromium Aluminum [Tantalum , Hafnium Silicon] Yttrium (NiCoCrAl [Ta , HfSi] Y) Thermal Spray Powders." pp. 2–6, 2018.

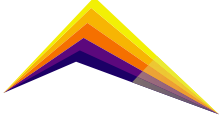

[9] J. Spišiak, M. Hartmanová, G. G. Knab, and S. Krcho, "Thermal properties of yttria-stabilized zirconia (YSZ)," *J Eur Ceram Soc*, vol. 11, no. 6, pp. 509–514, 1993, doi: 10.1016/0955-2219(93)90110-D.

[10] O. Metco, "Material Product Data Sheet High Yttria Percentage Stabilized Zirconia Agglomerated and Plasma-Densified Thermal Spray Powders," pp. 1–3, 2017.

[11] D. F. Zambrano *et al.*, "Thermal properties and phase stability of Yttria-Stabilized Zirconia (YSZ) coating deposited by Air Plasma Spray onto a Ni-base superalloy," *Ceramics International*, vol. 44, no. 4, pp. 3625–3635, 2018, doi: 10.1016/j.ceramint.2017.11.109.

[12] L. ZHU, N. ZHANG, C. CODDET, R. BOLOT, and H. LIAO, "Thermal Shock Properties of Yttria-Stabilized Zirconia Coatings Deposited Using Low-Energy Very Low Pressure Plasma Spraying," *Surface Review and Letters*, vol. 22, no. 05, p. 1550061, 2015, doi: 10.1142/s0218625x15500614.

[13] G. Delluc, G. Mariaux, A. Vardelle, P. Fauchais, and B. Pateyron, "A Numerical Tool for Plasma Spraying Part I: Modelling of Plasma Jet and Particle Behaviour," *16th International Symposium on Plasma Chemistry*, pp. 1–6, 2003.

[14] G. Delluc, G. Mariaux, and A. Vardelle, "A numerical tool for plasma spraying. Part II: Model of statistic distribution of alumina multi particle powder," *Proceedings of the 16th International Symposium on Plasma Chemistry*, no. June, pp. 1–6, 2003.

[15] G. Delluc, H. Ageorges, B. Pateyron, and P. Fauchais, "Fast modelling of plasma jet and particle behaviours in spray conditions," *High Temperature Material Processes (An International Quarterly of High-Technology Plasma Processes)*, vol. 9, no. 2, pp. 211–226, 2005, doi: 10.1615/hightempmatproc.v9.i2.30.

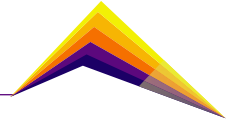

Fabrication of Hydroxyapatite/ Polyester composite coatings by high velocity oxygen fuel spray (HVOF)

Juan C. Jamboos[1] *E-mail: carlos.jamboos@ciateq.edu.mx*
John Henao[2] *E-mail: john.henao@ciateq.mx*
Astrid Giraldo[3] *E-mail: agiraldo@cinvestav.mx*
Carlos A. Poblano-Salas[4] *E-mail: carlos.jamboos@ciateq.edu.mx*

[1, 4] *Plastic and Advanced Materials Group, Center of Advanced Technology – CIATEQ A.C.*
[2] *CONACYT- Center of Advanced Technology – CIATEQ A.C.*
[3] *CONACYT-CINVESTAV*

Abstract

There are two aspects that regulate the bone biointegration process of joint implants, 1. The bone-implant relationship in the interfacial area and 2. The design of the implant. Bone interaction with the implanted material is governed by several variables that involve loading conditions, physical properties and composition of the host bone, thickness of the interface, local concentration of osteoblasts and osteoclasts, as well as chronic degenerative diseases (diabetes, rheumatoid arthritis, etc.) and smoking. The present work aims to explore the fabrication of hydroxyapatite/polyester (HA/PS) composite coatings as a first step to control the distribution of HA and a second polymeric phase in the volume of the coatings obtained. This work includes the preparation of powder mixtures as well as the HVOF spraying and characterization of the coatings obtained. This study seeks to evaluate the feasibility in the fabrication of HA/PS composite coatings by HVOF, which, at first glance, seems to be a challenge due to the high temperatures and velocities achieved in this process. The results obtained revealed that HA/PS coatings can be obtained by adjusting some key parameters with respect to those employed for the preparation of pure HA coatings.

Correspondent author

Key words: Thermal Spray, Coatings, Hydroxyapatite, Polyester.

Introduction

The high percentage of patients who require revision surgery before five years is a fact that has been widely reported by several authors, who show that the highest percentage of these surgeries have aseptic loosening as the main cause, which has several causes, among which is the lack of cohesion and osteointegration [1].

Currently, knowledge continues to be generated around improving the aspects that cause this and other failures that, with high recurrence, lead to patients being subjected to revision surgeries shortly after the primary surgery. In this sense, the plasma spray technique is of great importance because it is a process that provides protection against wear, friction and corrosion [2], but at the same time it experiences temperatures above 10,000 °C, which causes phase changes that, in the case of hydroxyapatite coatings, generate metastable phases that have high solubility in body media. On the other hand, the High-Velocity Oxygen Fuel – HVOF combustion technique, despite generating fairly dense coatings and presenting resistance with low residual tensile stresses, has not been sufficiently explored to position this technique as a potential resource in the design and production of coatings that seek to give the implant greater osseointegration and thus reduce failures that could speed up revision surgery in patients with low bone density.

Experimental studies have shown that the HA coating improves the fixation of unstable uncemented joint implants when there are spaces between the bone and the implant [3]. HA, together with the presence of porosity in the coating, makes it possible to overcome the loosening and mobility problems experienced by these implants, which reach rates up to 70% [4]. One way for introducing this feature in HA coatings by thermal spray is by adding a pore forming phase. Up to date, there are few investigations about introducing polymers as pore forming phase in thermal spray, in particular, there are not previous works related to explore this possibility using the HVOF process. In this way, the present study seeks to explore the feasibility in the preparation of HA/PS coatings by HVOF.

Materials and Methods

A commercial polymeric powder (Poly-4-Hydroxymethylbenzoate), polyester (PS) as nominal chemistry, with -124 +34 m of particle size distribution, rounded morphology and with 0.6 g/cm^3 of apparent density, was obtained from Oerlikon Metco, Mexico. The HA powder, was obtained commercially from Plasma Biotal Limited. Ceramic in a medical-grade, synthetic, high-purity, highly crystalline bioresorbable bone substitute material designed to closely mimic the properties and composition of natural bone. Powder with particle size of 31.6 m and a Ca:P ratio of 1.66-1.72.

In the manufacture of the coatings, titanium (Ti) was used as a substrate and titanium dioxide (TiO_2) as a bond coat to facilitate the anchoring of HA as well as to mitigate the differences between the thermal expansion coefficients of the materials, both materials known for their biocompatibility and bioactivity. The process was carried out by High Velocity Thermal Spray (HVOF – High Velocity Oxygen Fuel), which allows the ceramic particles of HA and the polymer (PS) to be melted and projected towards the substrate from the combustion of oxygen, reaching 2500 °C.

The mixture of these two powders was made in three different HA/PS weight percentage ratios that were 90/10, 80/20 and 70/30, respectively, in a rotary milling for four hours without balls. Then, HVOF spraying of the powder mixtures was carried out at 160 mm, 200 mm and 260 mm by using a KUKA robotic arm at a relative velocity spraying gun/substrate surface of 1 m/s.

Scanning Electron Microscopy – SEM

SEM analysis allowed the capture of cross-sectional images of the coatings, which facilitated the quantification of PS area using Image J software. Coating thickness was also calculated from SEM images.

X Ray Diffraction – XRD

XRD patterns from feedstock powders and coatings were obtained in the present study in order to corroborate the presence of the polymer in the coatings obtained.

Results and analysis

XRD shows that HA and PS are present in the coatings obtained at the different spray distances studied. However, regardless of the spray distance, the coatings obtained with the lowest polyester mixture in the HA/PS ratio (90/10) turned out to be the best, preserving the properties of the compounds together with the 80/20, while the 70/30 ratio showed signs of PS degradation. On the other hand, the coatings obtained at different angles only with HA showed not only that the coating loses thickness as the thermal spray angle decreases, but also there was no evidence that would allow selecting this variable as the most suitable in the purpose of get a better PS distribution as was the weight percentage in the HA/PS ratio.

Conclusions

It is possible to obtain a PS distribution inside HA coatings by HVOF thermal spraying, varying the percentage of the polymer in the mixture with the ceramic, despite the density of the coatings generated by this technique and preserving mechanical properties.

In addition, the best condition for this purpose was the spray distance of 160 mm, with blending for four hours without balls and a mixture of 10%w of the polymer with 90%w of the HA.

Finally, it is also important to note that further experimentation is required to determine the biological response to the coating, both in Simulated Body Fluid and live cell tests.

Acknowledgments

Plásticos y Materiales Avanzados Research Group at CIATEQ A.C. Unidad Querétaro and CIATEQ Unidad Estado de México. Cenaprot/CINVESTAV Querétaro. Investigadores por México Program (Cátedras). Projects 848 y 881.

References

[1] Annibali, S., Pranno, N., Cristalli, M. P., La Monaca, G., & Polimeni, A. (2016). Survival analysis of implant in patients with diabetes mellitus: a systematic review. *Implant dentistry*, *25*(5), 663-674.

[2] Odhiambo, J. G., Li, W., Zhao, Y. T. and Li, C. L. (2019). Porosity and Its Significance in Plasma-Sprayed Coatings. Coatings, 9, 460; doi:10.3390/coatings9070460.

[3] Önsten, I., Nordqvist, A., Carlsson, Å. S., Besjakov, J., & Shott, S. (1998). Hydroxyapatite augmentation of the porous coating improves fixation of tibial components: a volumened RSA study in 116 patients. *The Journal of Bone and Joint Surgery. British volumen*, *80*(3), 417-425.

[4] Beckmann, N. A., Bitsch, R. G., Gondan, M., Schonhoff, M., & Jaeger, S. (2018). Comparison of the stability of three fixation techniques between porous metal acetabular components and augments. *Bone & Joint Research*, *7*(4), 282-288.

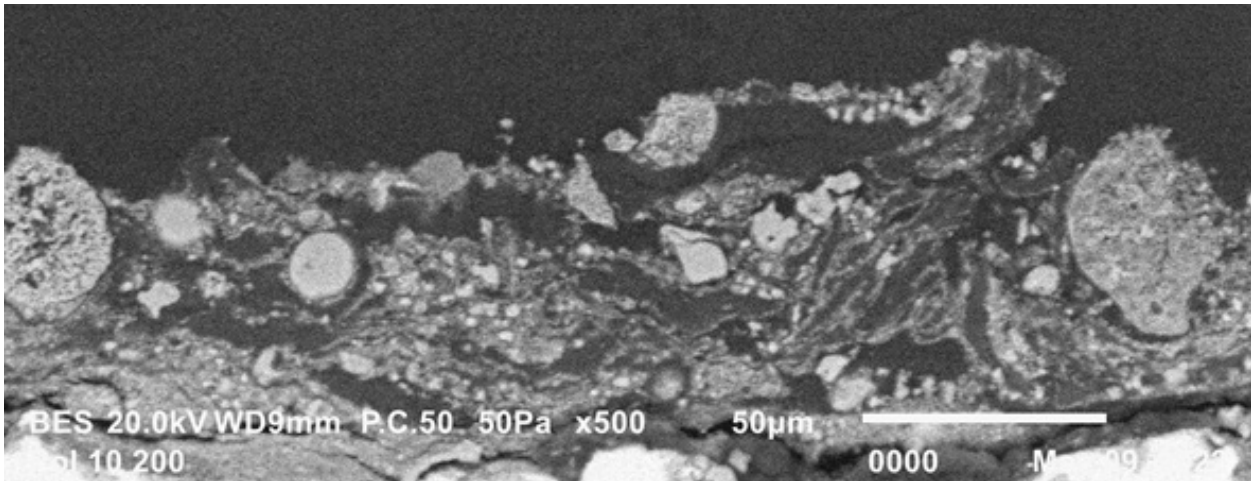

Scanning Electron Microscopy (SEM), of the cross-section of a HA/PS (90/10%w) coating at a spray distance of 160 mm, showing the distribution of the polymer corresponding to the darker areas.

Improvement of the structural quality of nicrbsife coatings elaborated by oxy-acetylene flame spraying from control of the main process parameters

Edward Restrepo[1] — E-mail: roger.cardona@udea.edu.co
Fabio Vargas[2] — E-mail: fabio.vargas@udea.edu.co
Roger Cardona[3] — E-mail: roger.cardona@udea.edu.co
Sebastian Carvajal[4] — E-mail: sebastian.carvajal@somosgrupo-a.com
Juan David Carvajal[5] — E-mail: juandavid.carvajal@somosgrupo-a.com

[1, 2] Ph.D
[3] Eng, Universidad de Antioquia, Grupo GIMACYR, Medellín, Colombia
[4, 5] Eng, Bonem S.A. Medellín-Colombia

Abstract

In this paper the effect of the oxyacetylene flame type, the feedstock powder flow and the relative velocity between the torch and the substrate, on the structural quality of NiCrBSiFe coatings, deposited on boron steel substrate, using a torch Eutectic- Castolin Castodyn 8000™, were studied. The results show the importance of the control of the feedstock flow powder and the contribution of the low relative speed between the torch and the substrate, on the compact structure of the thermally sprayed coatings.

Key words: Flame spraying process, structure of coatings, feedstock powder flow.

Correspondent author

Introduction

The structure of thermally sprayed coatings depends on the melting and stacking level reached by deposited particles when they impact the substrate. Therefore, the thermal energy supplied to the particles and the quantity of them among which this energy is distributed must be carefully controlled in order to achieve the melting level required to both good cohesion among them and their adhesion to the substrate. Likewise, the kinetic energy supplied to the particles and the relative speed between the torch and the substrate must be controlled to achieve good stacking and therefore a compact structure. The spraying distance is other controlling parameter of melting and stacking level of particles impacting the substrate [1, 2]. Nickel-based coatings elaborated by thermal spraying are used to protect substrates against abrasive wear conditions [3]. Oxyacetylene flame spraying is a low cost and high versatility process. However, the energy supplied by the flame to the particles could not be enough to manufacture coatings with low porosity. In this work, the effect of: *i)* the energy supplied by different oxyacetylene flames, *ii)* the quantity of fed particles, and *iii)* the relative speed between the torch and the substrate, on the structure of the sprayed coatings were evaluated.

Methodology

To manufacture the coatings, a nickel-based alloy powder from Eutectic–Castolin 5304 SF™ was thermally sprayed. The particle size distribution and morphology of the powder were analyzed using a Malvern Master Sizer 2000™ instrument and a JEOL JSM-6490LV scanning electron microscope, respectively. The particles were embedded in resin, subsequently they were cut using a Buehler Isomet 1000 equipment and finally they were polished in order to analyze their cross-section using the aforementioned scanning electron microscope. The chemical composition of the powder was determined by optical emission spectrometry using an Oxford Foundry-Master Pro equipment.

In order to evaluate the effect of the control of some parameters of the oxyacetylene flame spraying process on the structural quality of the coatings, two processes were carried out. The first of them was performed manually, using only the control system provided by the torch Eutectic-Castolin reference Castodyn 8000™ for both gas and feedstock powder flows. The second using the Areste chamber developed by the University of Antioquia, which allows controlling the spray speed and distance, as well as the gas flow, among other parameters. Boron steel substrates were used to deposit the coating. For the process carried out manually, the surface substrate was prepared applying a jet of metallic particles with a size distribution between 0.85 mm and 1.1 mm, while the coatings deposited using the Areste chamber were prepared using corundum particles whose size distribution is between 0.67 mm and 3.5 mm.

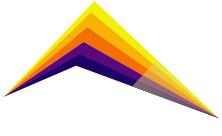

The measured surface roughness (Ra) of the substrates were 5.2±0.2 µm and 7.6±0.9 mm, respectively. The main parameters used for the coatings sprayed are described below.

- Manually deposited coatings: In order to control the gas flow rate, the Castodyn 8000™ torch is provided with a valve that allows to control the flow rate of acetylene supplied to its gas mixing chamber and then to its nozzle where the combustion will be carried out it. The tube that transports the oxygen has a bifurcation (Figure 1a) through which the amount of oxidizer provided is divided, one part is transported to the gas mixing chamber and the other part is used to create the Venturi effect that sucks the powders to the nozzle where they will be heated by the flame (Figure 1b). However, the original design of this equipment did not include flowmeters to measure the gas flow rate. Additionally, there are unknown factors such as the quantity of oxygen supplied to the torch, as well as the proportion of it that is divided to drag the powders to be sprayed and used for the mixing chamber where it is mixed with the acetylene before combustion. This does not allow controlling this parameter of thermal spraying process. Nevertheless, the coating was elaborated supplying acetylene at a pressure of 68.9 kPa and oxygen at 427.5 kPa and the quantity of acetylene was regulated until a flame with physical characteristics similar to the neutral flame was obtained [4]. Moreover, in order to control the amount of oxygen that produces the Venturi effect, the screw #10 that is part of the torch kit was used and the feedstock valve of powder was fixed at #4, in this way a powder flow of 55.7±4.5 g/min was obtained. The spraying distance was between 13 cm and 19 cm. The relative velocity between the torch and the substrate could not be measured because it was a manual process. For the manufacture of this coating the Rotojet was not used. The coating produced under these conditions was codified as M0.

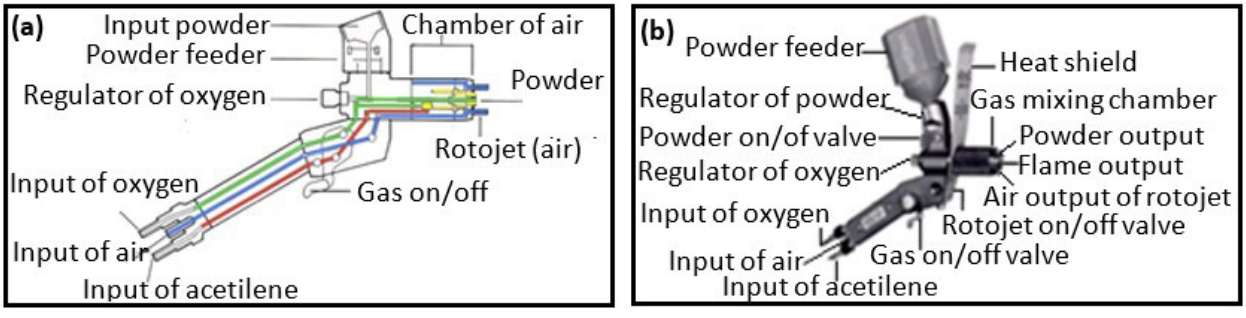

Figure 1. Eutectic-Castolin Castodyn 8000TM torch. a) Interior layout. b) Components.

- Coating process using the Areste chamber: Before installing the Castodyn 8000™ torch in the chamber, the screw that regulates the oxygen flow used to produce the Venturi effect was removed (Figure 2a), and the bifurcation through which this oxygen flow is transported to feed the particles to the nozzle was sealed (Figure 2b). This allows that all the fed oxygen to be carried to the gas mixing chamber, which allow the control of the oxidizer flow involved in the combustion. From this modification made to the torch it was possible to establish that the maximum flow of combustion gases of this equipment is ≈ 60 L/min, being the maximum flow of acetylene ≈20 L/min. The screw used to control the oxygen flow was replaced by coupling connector, see Figure 2c, which allows to connect a plastic tube that transport the powder from feeder reference Tumac CHTB10™.

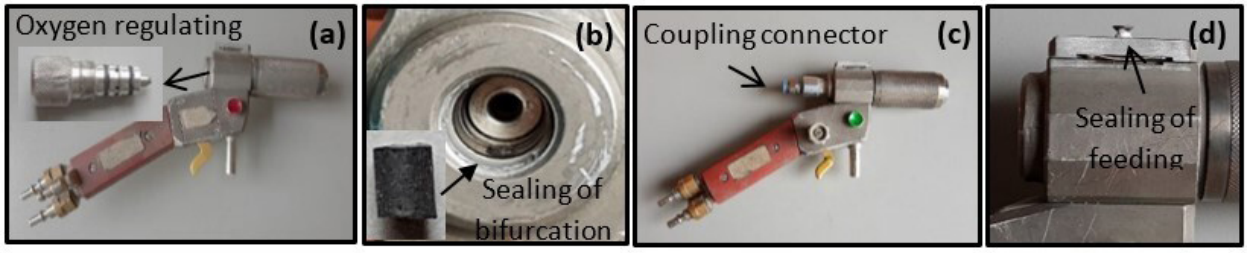

Figure 2. Modifications to the original design of the Castodyn 8000TM torch. (a) Removal of the regulating screw. (b) Sealing of the oxygen tube that produces the Venturi effect. (c) Connection of the external powder feeder. (d) Sealing of the original powder feed tube.

Then, the tube through which the powder is supplied was sealed, see Figure 2d and the coatings M1, M2 and M3 were deposited according to the parameters shown in Table 1. Due to the modifications carried out to the torch, when it is started suppling high flows of oxygen and acetylene to produce the combustion flame, backward of the flame is produced along the powder feeder tube, which can be counter by the nitrogen used as carrier gas powders. Then, this gas must be supplied before the oxygen and acetylene used as combustion gases.

Table 1. Oxyacetylene flame spraying parameters using the Areste chamber.

Flame spraying parameters		Coating codes		
		M1	M2	M3
Pressure combustion gases [kPa]	Acetylene	89.6		82.7
	Oxygen	358.5	427.4	
Combustion gases [L/min]	Acetylene	19.3	19.3	16.5
	Oxygen	31.7	39.1	41.3
Volumetric gases ratio	(C_2H_2:O_2)	1:1.6	1:2.0	1:2.5
Flame type		Neutral	Oxidizing	
Powder Flow rate [g/min]		21±5	25±7	34±11
Torch linear speed [cm/s]		0.36	0.51	
Substrate speed [cm/s]		35.7	46.3	

The coatings were obtained fixing some process parameters according to preliminary test results, such as: the surface substrate temperature was between 250 °C and 300 °C, the spraying distance was 9 cm, the pressure and flow of nitrogen used as carrier gas powders were 275.8 kPa and 17 L/min respectively, and the Rotojet air pressure was 206.8 kPa. Finally, the coatings deposited were embedded in epoxy resin, cut and polished according to ASTM E 1920-03 (2014) and their cross-section structure was analyzed by optical microscopy using a Nikon eclipse MA100 microscope.

Results and analysis

The results of the chemical analysis of the powder (Table 2) show that this material is a NiCrBSiFe alloy. It is a self-melting alloy, which allows deposited particles completely melted by heating after spraying, obtaining coatings with a dense structure and high adhesion to the substrate, thanks their metallurgical bonds [4, 5].

Table 2. Chemical analysis (wt.%) of the powder used to obtain the coatings.

Powder	Cr	B	Fe	Si	Mo	V	C	Ni
Eutectic Castolin 5304 SF™	13.7±0.2	3.3±0.2	3.1±0.1	3.4±0.1	0.6±0.0	0.1±0.0	0.4±0.0	Balance
Deloro 50	11	2.4	3	4 (max.)	--	--	0.4	
Deloro 60	15.5	3.5	4	4.3 (max.)	--	--	0.8	

The chemical composition of this powder is intermediate to that between Deloro 50 and Deloro 60 powders, which are self-fluxing alloys for hard dense corrosion resistant coatings with superior fusing characteristics. The coatings manufactured from Deloro 50 powder are machinable, while those from Deloro 60 are ground but they are not machinable.

For its part, the morphological analysis carried out to the particles showed that its surface is rounded (Figure 3a), and they have inserts in its cross-section, whose size is 2.5±0.2 µm (Figure 3b). The chemical analysis performed by X-ray energy dispersive spectroscopy showed that the composition of these insert is 42.4%Cr, 32.0%C, 22.3%Ni, 2.5%Fe and 0.8%Si (wt.%), while that of the matrix is 58.1%Ni, 32.8%C, 6.0% Cr and 3.1%Fe (wt.%). On the other hand, the analysis of the particles size distribution indicated that the size of this powder is between d_{10}=60.4 **µ**m y d_{90}=128.5 **µ**m.

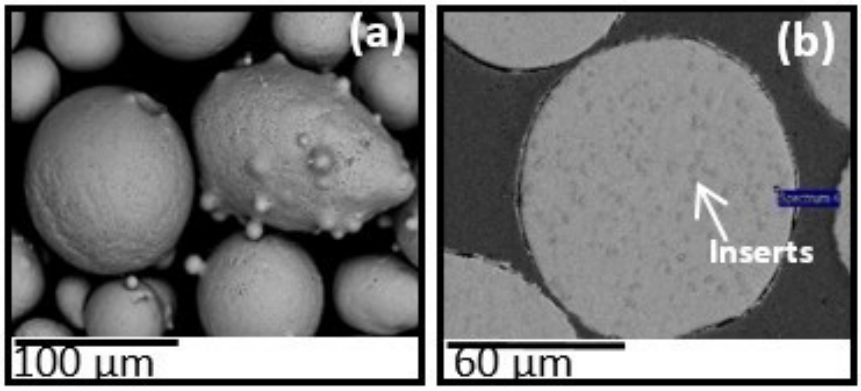

Figure 3. Morphology of particles used to manufacture the coatings. (a) Surface. (b) Cross section.

Meanwhile, the results of the structural analyses performed on the cross-section of coatings show that the M0 sample deposited manually using a neutral flame exhibits high porosity due to the poor stacking produced by partially melted particles (Figure 4a). On the other hand, the structure of the M1 coating, elaborated from a neutral flame and using the Areste chamber, contains less partially melted particles and then, its lamellae packing is higher than the M0 sample (Figure 4b). The difference between both coatings is due to mainly that the powder flow used to produce the M0 and M1 samples were 55.7±4.5 g/min and 21±5 g/min, respectively; then, the energy per unit mass of particles provided by the flame to M1 is greater. On the other hand, in the structure of M2 and M3 coatings sprayed with oxidizing flames was observed a progressive increment of partially melted particles and then, in their porosity (Figures 4c and 4d), regarding to M1 sample manufactured using neutral flame.

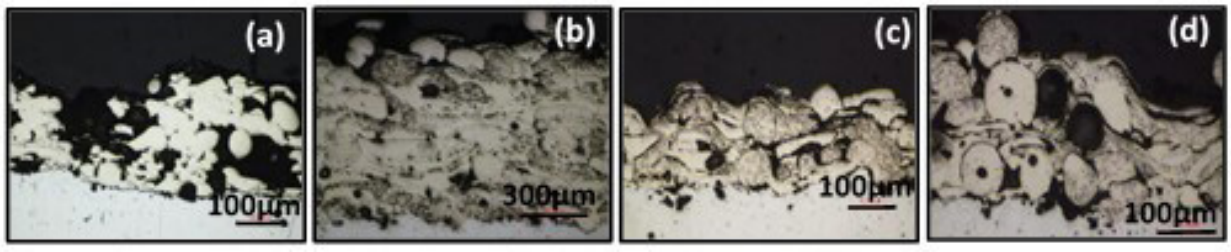

Figure 4. Cross-section structure of samples. (a) M0. (b) M1. (c) M2. (d) M3.

The decrease in the maximum temperature reached by the neutral flame, compared to the oxidizing one [6], and the greater amount of particles fed, would be the main causes of a less homogeneous structure in samples M2 and M3.

Conclusions

Coatings of a NiCrBSiFe alloy were manufactured on boron steel substrates, using oxyacetylene thermal spraying with an Eutectic-Castolin Castodyn 8000™ torch, from both a manually controlled process and using the Areste chamber, which allows controlling the spray speed and distance, powder and gas flow among other parameters. The results obtained allowed to establish that:

- The control of the relative speed between the torch and the substrate using the Areste chamber allowed to manufacture coatings with better homogenous structure than manually deposited coatings due to better particles stacking.
- The control of the adequate quantity of particles fed to the flame is essential to obtain coatings with a compact structure, from their good melting level. Therefore, it is important to implement feeding control systems in this type of torches.
- The maximum temperature in neutral flame is higher than that in oxidizing ones, then the particles sprayed along this flame can achieve higher heating, favoring their melting and consequently a better packing between them, to form coatings with a more compact structure.

Acknowledgements

The authors wish to thank to the tax benefits project 69067 presented to Colciencias by the company Bonem. Edward Restrepo, is grateful to Colciencias for the Doctoral Fellowship.

References

[1] L. Pawlowski. (2008). “The Science and Engineering of thermal spray coatings”. John Wiley and Sons. Second Edition. ISBN: 978-0-471-49049-4.

[2] P. L. Fauchais, J. V.R. Heberlein, M. I. Boulos. (2014). “Thermal Spray Fundamentals”. Springer. ISBN: 978-0-387-68991-3.

[3] Martha Ferrer, Fabio Vargas, Carlos Moreno, Gabriel Peña. (2017). “Effect of temperature and substrate roughness on the adhesion of coatings of Ni alloy deposited by flame spray”. Rev. LatinAm. Metal. Mat., 37 (2), 219-227, ISSN: 2244-7113.

[4] J.R. Davis. (2004). “Handbook of Thermal Spray Technology”. ASM International. ISBN 0-87170-795-0.

[5] P. Daram, C. Banjongprasert. (2020). “The Influence of post treatments on the microstructure and corrosion behavior of thermally sprayed NiCrMoAl alloy coating”. Surface and Coatings Technology., 384, DOI: 10.1016/j.surfcoat.2019.125166.

[6] Edwin Cadavid Iglesias, Carolina Parra Velásquez, Fabio Vargas Galvis. (2016).“Estudio de llamas oxiacetilénicas usadas en la proyección térmica”. Revista Colombiana de Materiales. No 9, 15-26, ISSN 2256-1013.

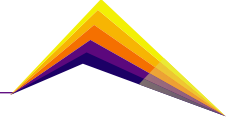

Thermal projection by flame, as a way to obtain ceramic coatings resistant to wear at high temperatures

M. Ferrer[1]
E. Vera
F. Vargas

E-mail: marthayasmidfp@ufps.edu.co
E-mail: luisemiliovd@ufps.edu.co
E-mail: fabio.vargas@udea.edu.co

1, 2 PhD, MSc, UFPS
3 PhD, UdeA

Abstract

Beehive ovens made of red clay or adobe bricks are used in the coal coking industry. In the process, the furnaces are subjected to sudden changes in temperature that range from 300°C to 1000°C on average, in the removal process a steel rake is used to remove the coke, which causes abrasive wear due to friction between the rake, the coke, and the floor, at elevated temperatures. Over time, flooring deteriorates and needs to be replaced, leading to high maintenance costs. To prolong the furnace floor service life, it can be lined with a material resistant to wear at high temperatures. One of the best performing materials under these conditions is zirconia, which when properly mixed with alumina provides excellent surface protection against wear and thermal shock. For the preparation of the coatings, the thermal projection technique with oxyacetylene flame is chosen, due to its versatility and economy. The coatings are morphologically characterized both with MO optical microscopy and SEM scanning electron microscopy, the wear resistance with a tribometer in ball-disk configuration at room temperature and at 500°C without abrasive, the microhardness with Vickers notches and the thermal shock resistance with heating cycles at 500°C and cooling at room temperature. It has been proved that all coatings exhibited much higher wear resistance than the uncoated substrate by at least one order of magnitude and that the coating protected the substrate

Correspondent author

through at least 30 thermal shock cycles.

Key words: thermal projection by flame, resistance to wear, resistance to thermal shock

Introduction

Surfaces exposed to thermal shock that undergo abrupt temperature changes from approximately 1000°C to 300°C, as is the case with the floor of coke ovens, require additional protection: a coating of a material resistant to wear at high temperatures. One of the materials that performs best under these conditions is zirconia, which properly mixed with alumina, provides excellent surface protection against wear and thermal shock.

FS flame thermal spraying is a low-cost, high-performance technique used to manufacture hard coatings. The process consists of atomizing particles, (that have been melted or semi-molten thanks to the energy released by a heat source, in this case the combustion of acetylene premixed with oxygen, which provides an oxyacetylene flame of high energetic power), with a compressed gas.

Generally, the particles have velocities below 100 m/s, (the lowest velocity experienced by the particles in flight compared to other thermal spraying techniques). These velocities are exploited to increase the dwell time of the particles inside the flame, making it easier for them to reach their melting temperature [1]. The flame temperature is in the range between 2727 and 3077°C, however, the particles only reach 70% of this temperature depending on their dwell time in the flame [2].

Among the many applications of thermal spraying, this has been used to apply wear and thermal shock resistant coatings on structures subjected to aggressive high-temperature wear environments, in order to protect them and increase their service life. This technique makes possible to obtain high melting point ceramic coatings, thanks to the proper selection of oxyacetylene flame composition, spray distance Dp and powder flow.

Materials and Methods

Zirconia-alumina coatings were made from the reference particulate material Eutectic Castolin (25088 ™) (MetaCeram 25088 ®) on red clay ceramic substrates, by means of the thermal spraying technique with oxyacetylene flame, carried out in the ARESTE I sputtering chamber of the University of Antioquia, using a modified Eutectic Castolin Terodyn (2000 ™) torch.

Obtaining the coatings

Four projections denominated P1, P2, P3 and P4 were carried out, in which the substrate preheating temperature and the projection distance (Dp) were varied. The projections denominated P1 and P2 were obtained with an oxidizing flame (O) while P3 and P4 with a superoxidizing flame (SO), with the oxygen-acetylene flux ratio shown in Table 1.

The samples were prepared metallographically according to ASTM E1920 [3] and sputter coated with gold. The free software ImageJ was used to determine the porosity percentage of the coatings; the percentage was measured for each sample in at least 5 micrographs. The thickness of each coating was determined by taking 20 measurements on the micrographs along its cross face.

Mechanical and tribological properties

The microhardness of the coatings was measured in cross section by Vickers microindentation, based on ASTM C1327[4]. The load selected for the evaluation of hardness by Vickers microindentation was determined from a calibration curve, performing indentations at 300, 200 and 100 gf.

Wear was performed by means of tribological sliding contact tests using a ball-disc tribometer developed by the University of Antioquia and applying a high-pressure air jet in the area adjacent to the contact between the sample and the counterbody, in order to eliminate the material worn during the test. The tests were carried out on a circumference of 5 mm in diameter, during 10000 cycles, applying a load of 500 g, at temperatures of 30 and 500°C. A 6 mm diameter alumina ball with a hardness of 18.5 GPa was used as a counterbody. The tests were performed according to the recommendations of ASTM G99[5].

The surfaces of the coated samples were polished according to ASTM E1920 [3] reaching an arithmetic mean roughness (Ra) less than or equal to 1 micrometer, which was measured with a Mitutoyo SJ201 roughness tester, following the recommendations of ASTM D7127-13 [6].

After the wear tests, the measurement of the tracks generated on the samples evaluated was taken. A Surtronic S125P profilometer was used to measure the cross-sectional area of the track, with a sensitivity of 0.1 micrometers. Ten profiles of each sample were analyzed, performing a radial sweep at different points of each footprint.

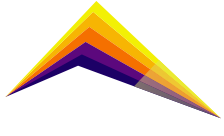

Equation (1) was used to calculate the wear rate.

$$TD=Ad/(C_n \times D) \quad (1)$$

Where TD is the wear rate in mm^3 /Nm, Ad is the volume of the wear track μm^3, Cn is the normal load applied in the test in Newton (N) and D is the linear distance traveled during the test in meters (m).

Thermal shock

Thermal shock tests were performed by heating and cooling the samples with water from a temperature of 500°C to a room temperature (20°C to 25°C). The samples were heated in an electric oven for 5 minutes and then quickly dropped into cold water, this same process was performed until approximately 10% of the coating surface was visibly destroyed, thus determining the thermal life cycle of the coating. Four samples of the same specification were used to reproduce the results. This type of thermal shock test has been performed by several researchers [7-9].

Results and analysis

Mechanical and tribological properties

The thickest coatings were obtained at a distance of projection, Dp=9 cm, this was due to the fact that the particles remained longer in the flame and got to melt even to evaporate, which justifies that the highest porosity is found in this same condition, as observed in P2 and P4 (see Table 2). On the other hand, the superoxidizing flame favors the thickness of the coatings, since by increasing the amount of oxygen in the flame, it gets cools slightly, and the length of the hot zone lengthens, this facilitates the melting process of the particles by remaining a little longer in the hot zone of the flame [2]. With respect to Vickers microhardness, all coatings have statistically similar microhardness, ranging from 9.6 ±0.9 to 10.5 ± 1 GPa, with a higher mean for the coating deposited with the SO flame at a PD=9 cm (P4), which could be associated with a higher percentage of porosity [10].

The wear tracks generated on each of the samples at a temperature of 500°C are shown in Figure 1. Table 3 shows the wear track rates at the two study temperatures. All coatings showed wear resistance far superior to that of the uncoated substrate (at least one order of magnitude). At room temperature, the surface damage produced on the specimens is much less than that generated when tested at 500°C. This may be associated with a transformation of the wear mechanism, from wear by ductile deformation (which usually occurs at room temperature in alumina coatings or materials containing this aluminum oxide), to wear by brittle deformation, which usually occurs in these same materials when they are tested at 500 °C [11-13].

Figure 2 shows the wear tracks of P4 at high magnifications (a) at room temperature, (b) at 500 °C and (c) elemental analysis of the track. The coating with the highest wear resistance at a temperature of 500 °C is the one deposited with the SO flame, P4. This shows the effect that hard particles present in coatings, exposed to severe conditions, can have, as they can easily detach and cause severe damage to the counterbody, and pass through the coating leaving tracks as shown in Figure 2(b). Damage to the counterbody results in the detachment of fine particles that often form a layer that partially protects the surface of the sample [11].

Thermal shock

Figure 3 shows the results of thermal shock performed on samples P1, a) at 30 cycles and b) at 50 cycles. The results of the thermal shock tests performed at 500 °C, showed that part of the coating detached from the samples, which is attributed to the cooling rate being high enough for the stresses between the coating and the substrate to generate its detachment.

Conclusions

Zirconia-alumina coatings are wear resistant at room temperature, even when subjected to aggressive high-temperature environments. The coatings also protect the substrate when subjected to sudden temperature changes for at least fifty continuous duty cycles.

Acknowledgment

The authors would like to thank the University Research Fund - FINU of the Universidad Francisco de Paula Santander and the company CARBOMAX**.**

References

[1] F. Fanicchia, D. A. Axinte, J. Kell, R. McIntyre, G. Brewster, and A. D. Norton, (2017). "Combustion Flame Spray of CoNiCrAlY & YSZ coatings". Surf. Coatings Technol, vol. 315.

[2] L. Pawlowski, (2008). "The Science and Engineering of Thermal Spray Coatings", Wiley, Hoboken, 2nd ed.

[3] ASTM E1920, (2014). "Standard Guide for Metallographic Preparation of Thermal Sprayed Coatings".

[4] ASTM C1327 - 15, (2003.) "Standard Test Method for Vickers Indentation Hardness of Advanced Ceramics".

[5] ASTM G99, (2017). "Standard Test Method for Wear Testing with a Pin-on-Disk Apparatus".

[6] ASTM D7127 - 13, (2013). "Standard Test Method for Measurement of Surface Roughness of Abrasive Blast Cleaned Metal Surfaces Using a Portable Stylus Instrument".

[7] A. N. Khan and J. Lu, (2003). "Behavior of air plasma sprayed thermal barrier coatings , subject to intense thermal cycling", Surf. Coatings Technology, vol. 166, pp. 37-43.

[8] A. N. Khan and J. Lu, (2007). "Thermal cyclic behavior of air plasma sprayed thermal barrier coatings sprayed on stainless steel substrates", Surf. Coatings Technol, vol. 201, no. 8, pp. 4653-4658.

[9] H. Jamali, R. Mozafarinia, R. S. Razavi, and R. Ahmadipidani, (2012). "Comparison of thermal shock resistances of plasma-sprayed nanostructured and conventional yttria stabilized zirconia thermal barrier coatings", Ceram. Int, vol. 38, no. 8, pp. 6705-6712.

[10] A. Rico, J. Rodriguez, E. Otero, et al, (2009). "Wear behaviour of nanostructured alumina-titania coatings deposited by atmospheric plasma spray", Wear, vol. 267, no. 5-8, pp. 1191-1197.

[11] D. Franco, H. Ageorges, E. Lopez and F. Vargas, (2019). "Tribological performance at high temperatures of alumina coatings applied by plasma spraying process onto a refractory material", Surface & Coatings Technology". 371, pp. 276-286.

[12] X. Dong, S. Jahanmir, S. M. Hsu, (1991). "Tribological characteristics of α - alumina at elevated temperatures", J. Am. Ceram Soc, vol.74, pp. 1036-1044.

[13] W. Stachowiak and A. W. Batchelor, (2013). "Wear of nonmetallic materials, in Engineering Tribology,chap 16", G. W. Stachowiak and A. W. Batchelor, Fourth ed. pp. 679-673.

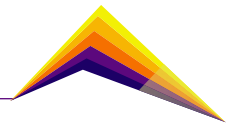

Table 1. Parameters for the elaboration of coatings.

Parameter	P1	P2	P3	P4
Torch speed (cm/s)	0.5			
Rotation speed (rpm)	92.2			
Pre-heating temperature (°C)	300	310	350	320
Projection passes	12			
Powder flow rate (g/min)	6.9	7.8	6.3	6.3
Projection distance	8	9	8	9
Flow rate N_2(L/min)	17			
Flow rate C_2H_2(L/min)	22			
Flow rate O_2(L/min)	55		70.5	

Table 2. Structural characteristics of coatings

Sample	Thickness(µm)	$HV_{0.2}$(GPa)	Porosity(%)
P1	146±2	9.9±2.0	9.4±0,8
P2	178±2	9.6±0.9	11.1±2.9
P3	154±2	9.9±1.4	7.6±1.3
P4	192±3	10.5±1.1	11.6±1.6

Table 3. Wear rate produced in the evaluated samples

Sample	TD at room temperature mm^3/Nm	TD at 500 °C mm^3/Nm
P1	Unmeasurable	1.06×10^{-3} ±5.08×10^{-4}
P2	Unmeasurable	1.26×10^{-3} ±2.92×10^{-4}
P3	$8,89\times10^{-5}$ ±$2,81\times10^{-5}$	Wear greater than the thickness of the coating
P4	4.64×10^{-4} ±1.27×10^{-4}	6.37×10^{-4} ±1.91×10^{-4}
Substrate	3.09×10^{-3} ±2.71×10^{-3}	2.20×10^{-2} ±7.27×10^{-3}

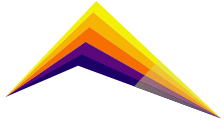

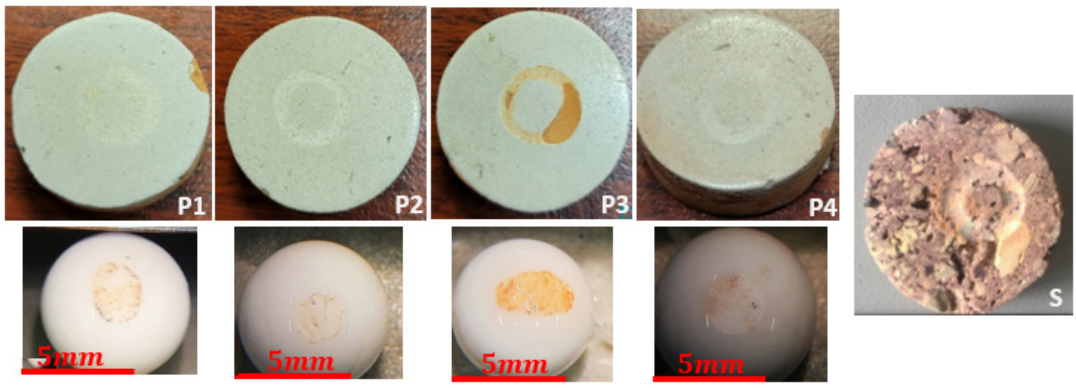

Figure 1. Wear tracks generated on the surface of coatings and substrate at a temperature of 500 ℃.

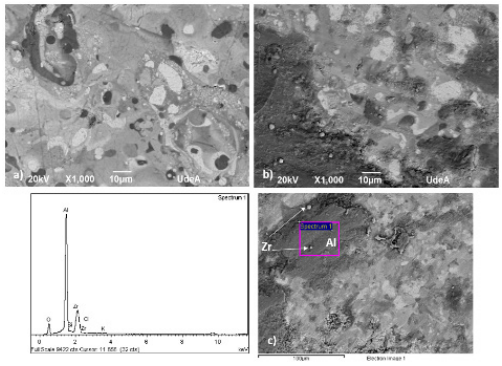

Figure 2. Enlargement of wear track at P4 a) at room temperature. b) at 500 ℃ c) elemental analysis on wear track.

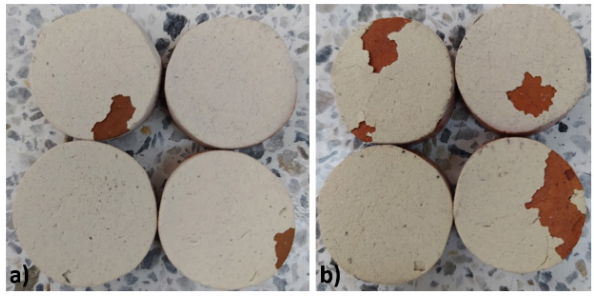

Figure 3. P1 coatings, after thermal shock tests. a) 30 cycles. b) 50 cycles.

Assessment of delaminated areas in Thermal Barrier Coating subjected to Thermal Cycling by Infrared Thermography

Andrés García[1] *E-mail: anfgarciare@unal.edu.co*
Sebastián Sánchez[1] *E-mail: seb.sanchez@pascualbravo.edu.co*
Manuel Ramos[1] *E-mail: ma.ramos@pascualbravo.edu.co*
Jhonatan Román[1] *E-mail: jromanr@unal.edu.co*
Alexander Arboleda[1] *E-mail: jaarboledag@unal.edu.co*
Pablo Gómez[2] *E-mail: Pablo.Gomez@epm.com.co*
Alejandro Restrepo[1] *E-mail: arestre5@unal.edu.co*
Alejandro Toro[1] *E-mail: altoro44@gmail.com*

1 Universidad Nacional de Colombia, Sede Medellín
2 Empresas Públicas de Medellín

Abstract

Thermal barrier coatings (TBCs) allow higher operating temperatures in thermal power plants as they provide insulation to hot gas path components such as blades, liners, combustion chambers, among others; therefore, they are key for increasing the overall thermal efficiency.

TBCs are usually produced by Atmospheric Plasma Spraying (APS), and when in operation, these coatings are subjected to thermomechanical cyclic loadings. As a result of the cyclic loading and the difference in the coefficient of thermal expansion between the ceramic layer and the metallic substrate, stresses are created between the TBC and the nickel-based superalloy in which the components are manufactured. This leads to the formation of cracks that grow progressively as the cycling increases and can ultimately

Correspondent author

cause the failure of the coating, leaving the substrate exposed to the high temperatures and corrosive environments of operation due to combustion process in the turbine. This mode of failure is known as delamination, and it is of great importance to detect this phenomenon before the coating completely fails.

Infrared Thermography (IRT) is a non-destructive technique used for early detection of delamination zones, using an energy source such as a flash lamp, which heats up the coating, and monitors the temperature evolution through time with an infrared camera.

In this work, APS-deposited TBCs were subjected to thermal shock testing as a mean to induce delamination through thermal cycles under controlled conditions, and then were evaluated by IRT with the aim of identifying delaminated areas. The samples used for this study consisted of: Yttria-Stabilized Zirconia (YSZ) Top Coat, NiCoCrAlY Bond Coat and Inconel 625 substrate. The thermal cycles were carried out by repeatedly heating the samples up in a muffle furnace up to 1020°C (5 minutes hold) and then quenching them in water at a temperature between 18 and 25°C.

The IRT evaluation consisted of heating the samples TBC surface with a halogen lamp, while the temperature evolution (in heating and cooling stages) was recorded with the use of a long-wave IR camera. The thermographic data obtained by the camera was processed with Matlab and Python to reduce noise and increase contrast, and delaminated areas were detected in zones where the coating looked sound to the bare eye. The results were related to the microstructure to discuss the feasibility of the use of IRT as a technique for delamination detection in early stages. Subsequent work is to be done in order to improve resolution, quality, better algorithms and have a broader experimental design.

Key words: TBC, Infrared Thermography, Thermal Shock, delamination, APS.

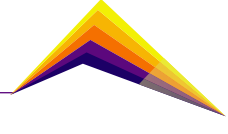

Introduction

In order to increase thermal efficiency in gas turbines, mechanical components made of superalloys are protected using Thermal Barrier Coating as a mean to decrease the temperature in the metallic component and to protect it from corrosive environments. Along with internal air-cooling systems, temperature reductions up to 300°C are achieved [1], allowing higher operation temperature and therefore higher thermal efficiency.

Thermal Barrier Coating consist of three layers (see ***Figure 1***): a ceramic layer in direct contact with combustion gases, called Top Coat (TC), typically ZrO_2 - Y_2O_3 or YSZ, which functions as a thermal insulator; a metallic layer, known as BC (Bond Coat-anchoring layer), typically NiCoCrAlY, in charge of controlling oxygen diffusion towards the substrate and mitigating thermal expansion differences between the TC and the substrate [2]; and finally, a ceramic layer that is formed between the TC and the BC, known as TGO (Thermal Grown Oxide), typically Al_2O_3 (alumina); this layer is formed due to the reaction between the diffusion of aluminum from the BC and the oxygen from the working atmosphere that migrates through the TC, and it is fundamental in the life of thermal barrier coatings [2], [3]. The failure of these coatings occurs due to several physicochemical, thermal and/or mechanical phenomena that occur simultaneously in cyclic operating conditions, this is one of the reasons why failure in TBCs is not completely understood [4]. Still, the main mechanisms have been identified.

In this study, it is of particular interest the failure mode known as delaminations, which consist of cracks parallel to the TBC/substrate interface which grow progressively with themal cycles until a separation from the TBC system occurs, leaving the sustrate exposed to high temperatures and corrosive/erosive envionments [5]. As a result of thermal cycling, particularlly during the compressive stages, stress fields are created along the TC/TGO/BC interface (see ***Figure 2***), the main cause of this being the difference in coefficient of thermal expansion. These stresses generate cracks which grow as the TGO thickness increases with total time at high temperature, this is known as partial delaminations. Finally, these cracks coalsce and failure of the coating occurs, leaving the subtrate exposed (total delamination). The aim of this work is to detect this delaminations at early stages prior to complete failure, the mean to achive this is the use of a technique known as Infrared thermography.

Active thermography is a non-destructive method that makes possible to detect the radiation emitted by objects in the infrared spectrum, which is not directly visible to the human eye, and relate this radiation to heat transfer inside the material and with its internal features. This requires special cameras to obtain the radiation and convert it into an electronic signal. Subsequently, a color is assigned to each energy level (within the infrared spectrum) and an image is obtained in the visible spectrum [6]. In active thermography, there is a source that thermally excites the object of study by sending a pulse of electromagnetic radiation (mainly in the visible area of the spectrum and partly in the IR) which by means of a photothermal effect results in a temperature increase on the surface of the coating and a subsequent heat transfer [7]. Rapidly after the pulse, the surface temperature changes, mainly due

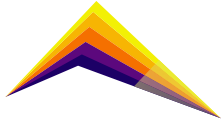

to heat conduction phenomena, although convection and radiation losses also occur [8]. The temperature distribution on the surface of the material will be uniform over time if the material is homogeneous, however, when there is a defect in the TBC system, there is a disturbance to this heat transfer due to an increase in the impedance at these points, and as a result there is a change in the temperature of this defective point concerning the sound areas of the coating. In the case of delaminations, it could be understood as a change in the resistance to thermal conductivity, since due to the high porosity of the YSZ, these delaminations are modeled as encapsulated air, which has a low thermal conductivity.

A thermographic camera evaluates the thermal response of the coating, a phenomenon in which heat transfer occurs from the surface to the interior of the coating. For quantitative analysis, different interpretation methods have been proposed based on algorithms that help to obtain quantitative data [9], in addition to filtering the relevant information for the study and allowing to differentiate, for example, between defects and coating thickness irregularities and increasing the visibility of defects [10], [11]. **Figure *3*** shows a schematic showing a solid with a defect and how the thermal response varies with respect to sound areas.

Methodology

Samples were cut and polished for characterization following ASTM E1920 (*Standard Guide for Metallographic Preparation of Thermal Sprayed Coatings*) guidelines. Cross sections were viewed for as-sprayed sample with optical and electron microscopes. Also, XRD was performed on the YSZ surface to identify phases. Further characterizations are to be done on thermally cycled probes.

Thermal Shock tests were performed in 1 in. x 1 in. samples coated with NiCoCrAlY BC and YSZ TC. The coatings were comercially obtained, produced by Woodgroup. Each thermal shock cycle consisted of placing the samples in a muffle furnace with a temperature of 1020°C, holding for 5 minutes and then quenching in water at a temperature between 18 and 22°C approximately. In order to perform the tests and the subsequent thermographic analysis 3 samples were used, labeled *A*, *B* and *C*. As part of the experimental planning, sample A was taken to total failure (184 cycles). This analysis allowed to know the behavior of the coating as the thermal cycles were performed. With the results obtained with sample A, sample B was subjected to 100 cycles with the objective of keeping a larger coated area with possible internal delaminations that could be detected by thermography. Sample C was not subjected to cycles and is taken as a reference for later comparisons by thermography between samples. Thermographic inspection was performed using a Fancier QI 500W Halogen lamp as thermal excitation source, a a FLIR T1020 camera for temperature recording. (see ***Figure 6***).

Results and analysis

X-Ray diffractograms and cross section images from optical and scanning electron microscopes are shown in figures 4 and 5 respectively. Nontransformable tetragonal phase (t') was detected in the YSZ X-ray diffractogram. A YSZ porosity of ~8.7% was calculated using image thresholding, and several cracks and defects were revealed in SEM Back-scatter electron images, this is a consequence of bad spraying conditions . Thermographic results obtained for sample B are shown in **Figure *7***. As it was expected, some delaminated areas are detected by IR thermography prior to detachment of the coating, but not detectable by visual insepction. In this case, a pulse of 15 seconds was used and the best contrast was obtained at 5 seconds after the beginning of the pulse. The delaminated area corresponds to the brighter zones, as brighter (more white) means higher temperature and this is related to defective zones.

Conclusions or summary

Thermal shock tests were performed in TBC systems to induce delaminated areas in laboratory conditions. Later, IR thermography was used to detect delaminations prior to complete failure and positive results were obtained in the process. However, due to the small size of the samples, the resolution of the camera lens and the low power used, some noise is still to be deal with as the thermographic data obtained is not clean enough to perform post-processing techniques and obtain better results. This is set as future work, done by the acquisition of better equipment, and using IR lens to improve resolution and focus the heat of the thermal source.

Acknowledgment

This work was possible thanks to the financial support given by Empresas Públicas de Medellín, EPM with base in Medellín, Colombia and Minciencias.

References

[1] H. L. Tsai and P. C. Tsai, "Microstructures and Properties of Laser-Glazed Plasma-Sprayed ZrO2-YO1.5/Ni-22Cr-10Al-1Y Thermal Barrier Coatings," *Journal of Materials Engineering and Performance 1995 4:6*, vol. 4, no. 6, pp. 689–696, Dec. 1995, doi: 10.1007/BF02646445.

[2] Z. Lu *et al.*, "Thermal stability and mechanical properties of thick thermal barrier coatings with vertical type cracks," *Transactions of Nonferrous Metals Society of China*, vol. 24, no. SUPPL. 1, pp. s29–s35, Jul. 2014, doi: 10.1016/S1003-6326(14)63284-2.

[3] J. D. Osorio Ramírez, "Propiedades de transporte en recubrimientos cerámicos utilizados en turbinas a gas," *Universidad Nacional de Colombia*, 2011. https://repositorio.unal.edu.co/handle/unal/9092 (accessed Apr. 11, 2022).

[4] R. Darolia, "Thermal barrier coatings technology: critical review, progress update, remaining challenges and prospects," *http://dx.doi.org/10.1179/1743280413Y.0000000019*, vol. 58, no. 6, pp. 315–348, 2013, doi: 10.1179/1743280413Y.0000000019.

[5] N. P. Padture, M. Gell, and E. H. Jordan, "Thermal Barrier Coatings for Gas-Turbine Engine Applications," *Science (1979)*, vol. 296, no. 5566, pp. 280–284, Apr. 2002, doi: 10.1126/SCIENCE.1068609.

[6] R. Usamentiaga, P. Venegas, J. Guerediaga, L. Vega, J. Molleda, and F. G. Bulnes, "Infrared Thermography for Temperature Measurement and Non-Destructive Testing," *Sensors 2014, Vol. 14, Pages 12305-12348*, vol. 14, no. 7, pp. 12305–12348, Jul. 2014, doi: 10.3390/S140712305.

[7] G. S. Ptaszek, "Investigation and development of transient thermography for detection of disbonds in thermal barrier coating systems," 2013, doi: 10.25560/11205.

[8] X. P. v. Maldague, *Nondestructive Evaluation of Materials by Infrared Thermography*. Springer London, 1993. doi: 10.1007/978-1-4471-1995-1.

[9] E. D'accardi, D. Palumbo, R. Tamborrino, P. Cavallo, and U. Galietti, "Pulsed Thermography: evaluation and quantitative analysis of defects through different post-processing algorithms," *14th Quantitative InfraRed Thermography Conference*, 2018, doi: 10.21611/qirt.2018.048.

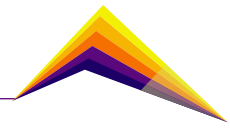

[10] S. Marinetti, D. Robba, F. Cernuschi, P. G. Bison, and E. Grinzato, "Thermographic inspection of TBC coated gas turbine blades: Discrimination between coating over-thicknesses and adhesion defects," *Infrared Physics & Technology*, vol. 49, no. 3, pp. 281–285, Jan. 2007, doi: 10.1016/J.INFRARED.2006.06.018.

[11] Franke. Barbara, "Nondestructive Evaluation Of Thermal Barrier Coatings With Thermal Wave Imaging And Photostimulated Luminescence Spectroscopy | Semantic Scholar," University of Central Florida, 2005. Accessed: Jun. 13, 2022. [Online]. Available: https://www.semanticscholar.org/paper/Nondestructive-Evaluation-Of-Thermal-Barrier-With-Franke/d3f0fe70272b751652e3fb7c370715c42c21f803

[12] S. Doshvarpassand, C. Wu, and X. Wang, "An overview of corrosion defect characterization using active infrared thermography," *Infrared Physics & Technology*, vol. 96, pp. 366–389, Jan. 2019, doi: 10.1016/J.INFRARED.2018.12.006.

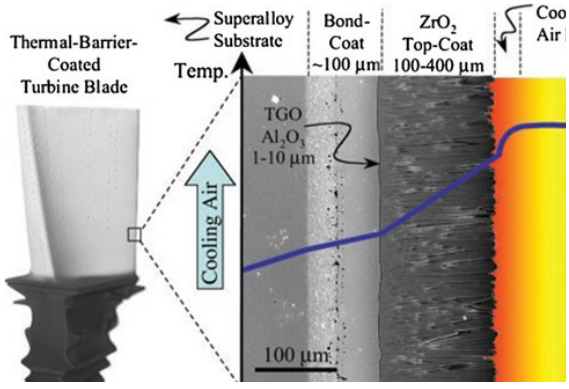

Figure 1. Schematic of TBC system on a turbine blade showing SEM micrograph of cross section, parts of TBC system and temperature reduction effect [5].

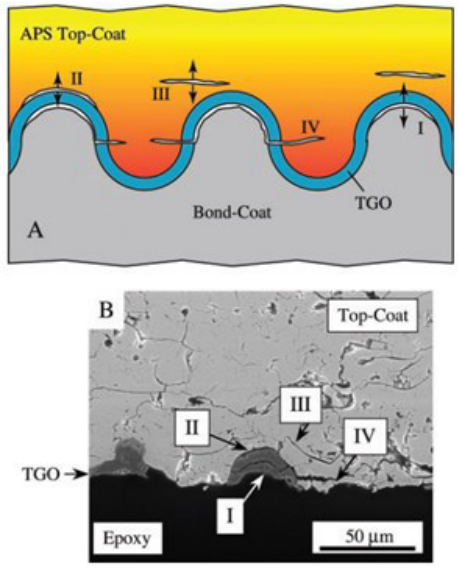

Figure 2. Failure mechanisms of a TBC system (A) and cross section example of a 240-cycled coating illustrating different crack locations [5].

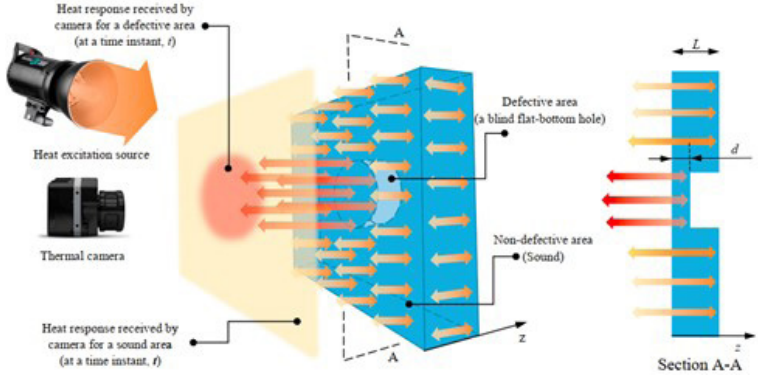

Figure 3. Schematic depicting heat transfer through the thickness of a solid with defected area [12].

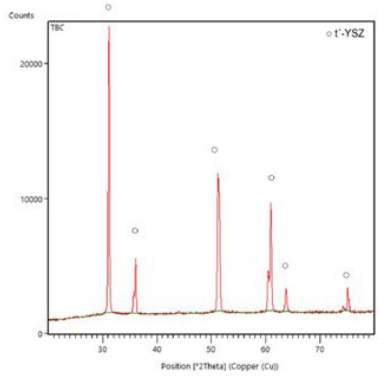

Figure 4. X-Ray diffractogram of YSZ as-prayed.

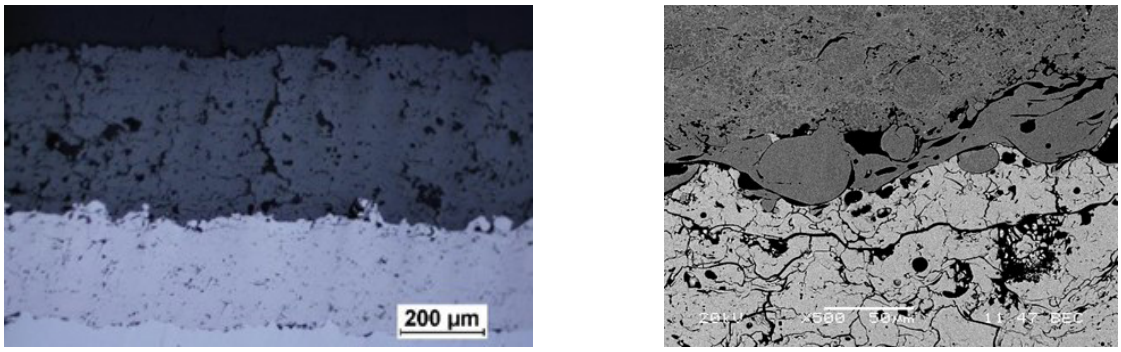

a) b)

Figure 5. Cross section showing TBC: a) optical, b) SEM.

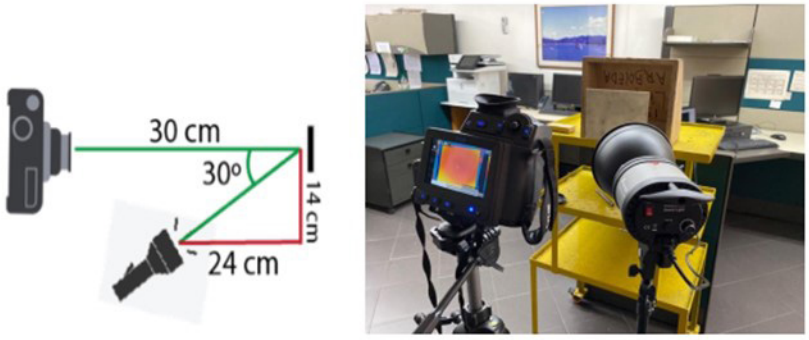

Figure 6. Schematic and photograph of assembly used for the thermographic data acquisition.

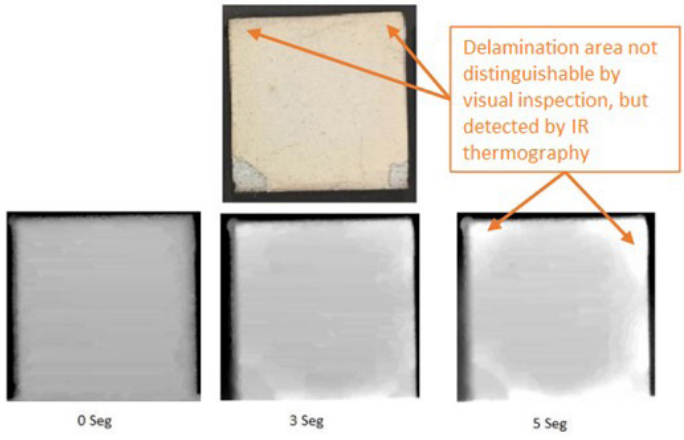

Figure 7. Thermographic images obtained after 0, 3 and 5 seconds of heating sample B (subjected to 100 cycles). Also, a photo in visible spectrum is shown and related to delaminations detected by IR thermography.

VITAL ENGINEERING

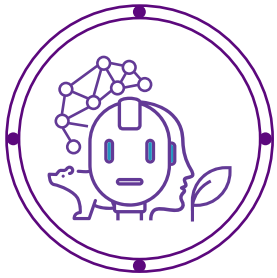

Variation of organic matter and aquatic macroinvertebrates associated with Eichhornia crassipes roots with flood pulse.

Vallejo, M[1] — E-mail: melanieg.vallejo@udea.edu.co
Serna, J[1] — E-mail: jpablo.serna@udea.edu.co
Aguirre, N[1] — E-mail: nestor.aguirre@udea.edu.co
Velez, F[1] — E-mail: fabio.velez@udea.edu.co
Fernández, D[1] — E-mail: david.fernandez@udea.edu.co

1Gepar-Geolimna research group, University of Antioquia.

Abstract

When variables such as those that occur with the change of the flood pulse are evaluated in an aquatic ecosystem, the specific behavior of the ecosystem can be determined, that is, a saturation by pollutants or a dilution can occur as the variation of the water surface is presented, as well as knowing the correlation between aquatic plants, aquatic macroinvertebrates and the influence of organic matter on their growth, in addition to estimate water quality using hydrobiological indices that use aquatic macroinvertebrates as bioindicators. Thus, determining the influence of the flood pulse on the distribution of Eichhornia crassipes and the aquatic macroinvertebrates associated with its roots in La Ciénega de Ayapel became the research problem through the analysis of physicochemical and environmental variables. The main objective of the study was to analyze the abundance of organisms assembled in the roots of the plant during the periods of drought and flooding, taking into account that during this year there is an atypical period due to the presence of an ENSO increasing rainfall in the sampling seasons. Then, considering the

Correspondent author

above, these are some partial results since the project is still in execution: regarding the aquatic macroinvertebrates associated with the roots of E. crassipes, the families that were present in greater quantity were Libellulidae and Dysticidae, for the atypical period when a drought should be occurring; and concerning water quality using hydrobiological indices, it is determined that there is deficient water quality in all sampling points. Given that the sampling was done in the littoral zone where there is population and discharge of organic matter, the results of the indices are accurate. However, it is necessary to wait to analyze the results of the aquatic macroinvertebrates, since, as a hypothesis, it is expected that when the flood pulse varies, the biomass of E. crassipes will change along with the assembly of aquatic macroinvertebrates, as well as the dilution of the organic matter present, because the second sampling is done during the rainy season. It is important to mention that the project being carried out is being financed by the Vice Rector's Office for Research under the SIMEVAM SIIU P2020-37870 project.

Keywords: Ciénega de Ayapel, hydrobiological indexes, dry and rainy seasons, biomass, biomass.

Introduction

The Ciénega de Ayapel, located in the department of Córdoba, municipality of Ayapel, is part of a swampy system It has been observed that thanks to climatic changes there has been a variation of the flood pulse and, as a consequence, a distinctive growth in terms of aquatic plants and distribution of aquatic macroinvertebrates [1], Therefore, it is established that there is a marked relationship between aquatic plants and macroinvertebrates since they increase positively because they find more efficient oviposition sites, food sources and nutrient utilization. In addition, through physicochemical analysis and taxonomic recognition of macroinvertebrate species, conclusions about the trophic state of the study site can be drawn, since evidence of dominance of organisms and low diversity, indicates the tendency of the water body to be eutrophicated, i.e., contaminated [2].

On the other hand, the flood pulse plays a very important role in the dynamics of the marsh because it allows the interconnection between the swamp system, allowing the transfer of pollutants or their dilution [3]. Together with the abovementioned, it can be stated that in the event of a precipitation, it will trigger a homogenization of the environmental characteristics and therefore affect the richness and vegetation cover; the opposite is the case for the dry season, showing dominance and a specific behavior in response to the temporal, spatial, biotic and biotic scales and the flood pulse present in the site[4].

Thus, maintaining the study of lentic water bodies allows identifying anthropic impacts and how these are reflected in changes and modifications in the abundance of organisms, as well as understanding how the dynamics of the same vary and help to take restrictive measures for the community in terms of good and bad development of daily habits. Given the above, it was decided to conduct the study in the Ciénega de Ayapel, using the collection of macroinvertebrates and aquatic plants to determine the available biomass and the assemblage of macroinvertebrates as well as to identify the variation of these when changing from dry to rainy season based on the fact that an abnormal ENSO period is occurring.

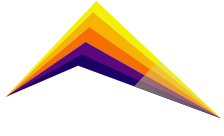

Methodology

The methodology used for the development of the project is divided into two parts, one in the field for the collection of samples and the second, in the laboratory where the respective analyses were carried out.

Field sampling

Initially, a field trip was made to Ciénega de Ayapel located in the municipality of Ayapel, department of Córdoba, as shown in Figure 1:

Figure 1. Site location: Ayapel swamp system, Colombia. Source: Google Earth

For field sampling a transect line was launched, this consists of marking a rope every two meters to take data at each mark in the littoral zone, the study site was in front of the headquarters of Corpoayapel - Mi ranchito, as shown in Figure 2. For sampling specimens of macroinvertebrates associated with the roots of E. crassipes, crassipes roots were collected and washed with water from the swamp on a tray, additionally, a triangular net was placed under the patch of plants to maximize the number of organisms; this procedure of trapping macroinvertebrates was repeated in all stations (10 points). On the other hand, two specimens of E. crassipes were taken at station two, that is, at two meters along the transect line. At this station, a water sample was also taken in a one-liter jar to later analyze nutrients such as phosphates, nitrites, nitrates, total hardness, ammonium and alkalinity employing a Visacolor nutrient kit that allows determining them once the water sample is in situ, i.e., insitu, a procedure that was repeated at all stations (10 points), and that using a spectrophotometer and specific reagents that come in the kit can determine the amount of nutrients contained in the water sample. It is important to emphasize that at least one liter

of water must be available for analysis. This sampling lasts two days, one day in the sampling area and another day analyzing nutrients in the field. The project aims to visit the wetland twice a year to analyze the dry season and the rainy season in March and September 2022, to analyze and validate the information provided.

Figure 2. Transect line location. Source: Fabio Vélez

Laboratory procedure

Once the macroinvertebrate samples are obtained, the respective analysis is made. The taxonomy of the organism is identified using a stereomicroscope, this means that the organism is assigned to the order, family, or species it belongs to, following as a guide the Manual of Limnology of Gabriel Roldan. After this, they are counted and determined employing diversity indexes that analyze the richness, diversity, and dominance of the species found and the BMWP index that assigns a value to the macroinvertebrates identified to determine the quality of the water present in the site. As for the aquatic plants, the specimens are burned in a muffle first at 105°C and then at 550°C to verify the organic part of the inorganic part and the available biomass of E. crassipes for macroinvertebrates, fish, or aquatic animals. And finally, through a drone flight, images were analyzed using ArcGIS to determine the approximate area covered by aquatic plants near the study site.

Results and analysis

To date, the study has partial results, i.e., there are results of the first sampling carried out on March 1, 2022; where for this time it was expected to go through a dry season, however, as it is going through an ENSO "girl", the results may have an atypical behavior and still need to perform the new sampling that allows correlating the variables, that will be held in September this year. Therefore, partial results are presented in Table 1 below, which provides an overview of the behavior of the marsh during this season.

Table 1. Results of the study

Variable evaluated	Información obtenida
Most dominant taxa	Libellulidae
Diversity index	Highly contaminated water
BMWP index %ETP index Available biomass Approximate area of vegetation cover	Critical water quality Poor water quality About 1% of the plant is inorganic material. 1522. 03 m^2

Table 2. Analysis of physico-chemical parameters

Physicochemical parameters		***RES 2115 of 2007***
Nitrites [mg/L]	0.01	0.1
Phosphates [mg/L]	2.1	0.5
Nitrate [mg/L]	<1.0	10
Total hardness HZ °d	2.95	300
Total hardness °d	3.0	
Ammonium [mg/L]	<0.4	<0.02
Alkalinity [mmol/L]	1.0	200

After obtaining the information, it is analyzed that, according to the indexes, the water quality is poor and there is dominance of the Libellulidae species, belonging to the Odonata order, that is resistant to contamination. As it is known, the fact that a species or organism remains in greater quantity in a site (is dominant) confirms the presence of organic matter and that the ecosystem conditions are altered. On the other hand, plants have about 99% of consumable matter both in roots and in their bodies, which makes them an indispensable site for the survival of macroinvertebrates, fish, and other animals that feed on them. Finally, when nutrients were evaluated, a comparison was made in terms of drinking water regulations, Resolution 2115 of June 22, 2007, to determine if it was suitable for human consumption; however, it was found that phosphates, ammonium, and alkalinity were not within the permissible limits, so the respective potabilization processes must be carried out to avoid public health problems in the population.

As for the flood pulse, the next sampling should be carried out to correlate all the variables and determine how it influences the variation in the growth of plants and macroinvertebrates.

Conclusions

The study of the growth and development of aquatic plants and the assemblage of macroinvertebrates and their variation with the flood pulse covers an environmental problem since the flood pulse naturally influences the ecosystem. However, the anthropic activity that occurs in the studied water body plays a fundamental role by introducing vectors that are reflected in the abundance of macroinvertebrate species and the patch of aquatic plants. Then, it is important to maintain the study of the water bodies from the biotic point of view since a direct alteration to the ecosystem can be evidenced, showing results such as those described above.

References

[1] Batzer, D., Wissinger, S., (1996) “Ecology of insect communities in nontidal wetlands” <10.1146/annurev.en.41.010196.000451>

[2] Zelnik, I., Gregoric, N., Tratnik, A. (2018) “Diversity of macroinverebrates positively correlates with diversity of macrophytes in karst ponds” <https://doi.org/10.1016/j.ecoleng.2018.03.019>

[3] Da Silva, F., Severino, S., Senteio, S., Schiavone, D., Da Cunha-Santino, M., Bianchini, I., (2020) “ An applied ecological approach for the assessment of anthropogenic disturbances in urban wetlands and the contributor river. <https://doi.org/10.1016/j.ecocom.2020.100852>

[4] Marchetti, Z., Scarabotti, P., (2016) “Macrophyte assemblages in relation to environmental, temporal and spatial variations in lakes of a subtropical floodplain-river system”. <https://doi.org/10.1016/j.flora.2016.10.004>

[5] Prüss, A., Kay, D., Fewtrell, L., Bartram, J., (2002) “Estimating the burden of disease from water, sanitation, and hygiene at a global level”. <doi: 10.1289/ehp.110-1240845>

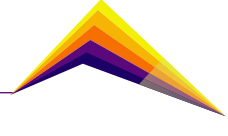

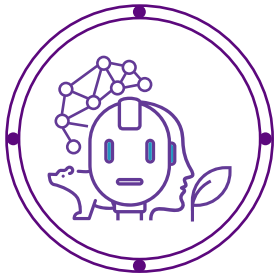

Capture of particulate matter of 1, 2.5 and 10 microns, with the use of microalgae in outdoor photobioreactors

Mazo, Santiago
Miranda Alejandra
Sáez, Álex

Email: smazoza@eafit.edu.co
Email: ammirandap@eafit.edu.co
Email: asaez@eafit.edu.co

Universidad EAFIT

Abstract

Particulate matter (PM), made up of a variety of organic and inorganic substances, is harmful to human health due to its small size (1, 2.5 and 10 microns) and its ease in entering the respiratory and circulatory systems, both so in Medellín in 2019, according to a study of the Metropolitan Area, 22,900 deaths were reported due to poor air quality (Valle de Aburrá Metropolitan Area 2019). As the problem grows, it seeks to propose the implementation of technologies that can mitigate this environmental problem in outdoor and human traffic areas. This study proposes the use of technology in outdoor conditions, using photobioreactors and microalgae to evaluate the capture potential of these microorganisms in the capture of this PM and how it affects their growth. As a conclusion of the experiment, it was shown that the microalga Scenedesmus Obliquus ATCC 457 (S. Obliquss ATCC 457) in conjunction with a photobioreactor system, grew up to 1.52 g/L and captured up to 61.07% of PM 1, 65.45% of PM 2.5 and 81.01 % PM10.

Keywords: Microalgae, photobioreactor, particulate matter, capture, Technology.

Correspondent author

Introduction

Air pollution due to the suspension of particles has become a general problem that many cities in the world face and try to mitigate. This pollution is characterized by being a mixture of various substances present in the atmosphere, such as carbon dioxide sulfur, nitrogen dioxide, ozone, carbon monoxide, and, of course, particulate matter (PM) (Ministry of the Environment, 2018), with the agricultural industry, manufacturing, and motor vehicles as the biggest emitters. The concern about the negative effects that poor air quality can cause on health has been increasing exponentially in recent decades where it is found that the high levels of pollutants in the air, a product of the high gas emissions that are related to the consumption of fossil fuels, cause severe public health problems, even generating respiratory diseases (Junping et al., 2020). In Colombia and especially in the city of Medellín, this problem arises, which is the unequivocal result of urban planning processes and the combustion of different types of poor-quality fossil fuels, caused by the accelerated growth of the vehicle fleet and development itself; thus, releasing the most critical pollutants for the Valle de Aburrá, such as PM of 1, 2.5 and 10 microns (Area Metropolitana del Valle de Aburrá, 2019). PM 2.5 and 10 are the pollutants with the greatest presence and frequency in open urban areas, and according to the studies conducted, they have the most detrimental effects on health in general (WHO 2017). In fact, the air pollution conditions in the Aburrá Valley in terms of PM 10 and PM 2.5 have not improved since 2012, although the monitoring stations show a stable concentration of these pollutants. The station located in the Caldas market square and the location of Éxito de San Antonio considerably increased the average value of their pollution records for PM 2.5 and 10, including 4 of the 10 stations with records per year between 2012 and 2015 They showed levels of contamination that exceed 50 µg/m3, that is, higher than those established by Resolution 610 of 2010 of Colombia concerning air quality (Medellín Quality of Life Report, 2016). In addition, and supported by the parameters of the World Health Organization for the minimum concentration of PM 2.5 (10 µg/m3), none of the stations complied with this parameter, it has been reported that only the station located in the Itagüí Council building presented a concentration of 25 µg/m3 which is accepted by Colombian air quality standards, however, it still does not comply with what is established by the World Health Organization. (WHO 2019).

In 2016, Medellin Quality of Life Report informed that the highest pollution by PM 2.5 and 10 is attributed to the participation of motor vehicles, being 1% 2t motorcycles, 13% 4t motorcycles, 6% cars, 2% taxis, 8% buses, 1% trucks, 22% dump trucks, 29% trucks and 18% fixed sources such as industries (figure 1). As viable solutions that have been determined to deal with this problem are social and transport measures, for which some laws restrict the use of vehicles on specific days and times and stop the industry for a few hours, especially if they are polluting above the allowed value.

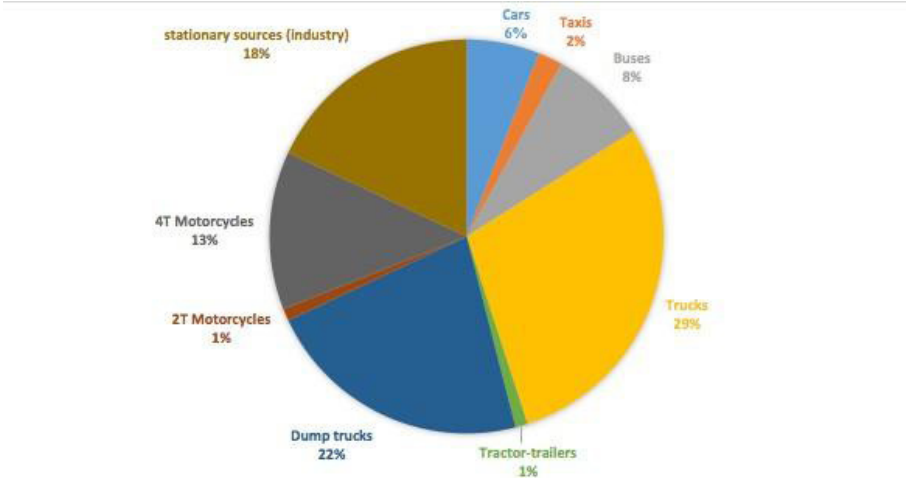

Figure 1. Participation, by source, in the annual emissions of PM 2.5. Source: Aburrá Valley Atmospheric Emissions Inventory, base year 2015.

As this problem became evident, different industries have tried to solve it by introducing machinery capable of separating waste, for example, the venturi scrubber is a separator that allows capturing very fine powders and aerosols, which is why it has been implemented on some occasions to mitigate pollution by PM, such as cyclones and multicyclones that have a similar operation by capturing substances dissolved in the air that can be pollutants. However, for all the above and given how harmful PM can be to human health, this study seek to evaluate the retention, assimilation, or digestion capacity of the microalgae S. Obliquss ATCC 457 for these compounds and make an approximation to the amount found in the sampling area. This phenomenon can be used to maintain healthy conditions and mitigate pollution in areas of the Aburrá Valley, also taking advantage of the biomass resulting from this process, since depending on its percentage of nitrogen, it becomes attractive for uses such as the manufacture of biocrudes as a product relevant to the industry.

Methodology

Five 20-liter photobioreactors (FBR) were used, these FBR were built with acrylic with approximately 1,10 meter in heigh, at the bottom, it has two ports, one for entry of gas and air and another to recover the sample to be analyzed. Each with Scenedesmus obliquss, a blower that captures ambient air, and a manifold that evenly distributes the air with carbon dioxide and surrounding particulate matter to each of the photobioreactors.

In terms of measurement, there are two OPC-N3 particulate matter meters, one at the air inlet (blower) and another that is placed at the air outlet (upper part of each FBR), this captures the particulate matter that enters and leaves to subsequently quantify how much

particulate material is retained in the system with microalgae, a control of the FBRs is made with only water and culture medium, to ensure that the retention is due to microalgae and not to the system itself.

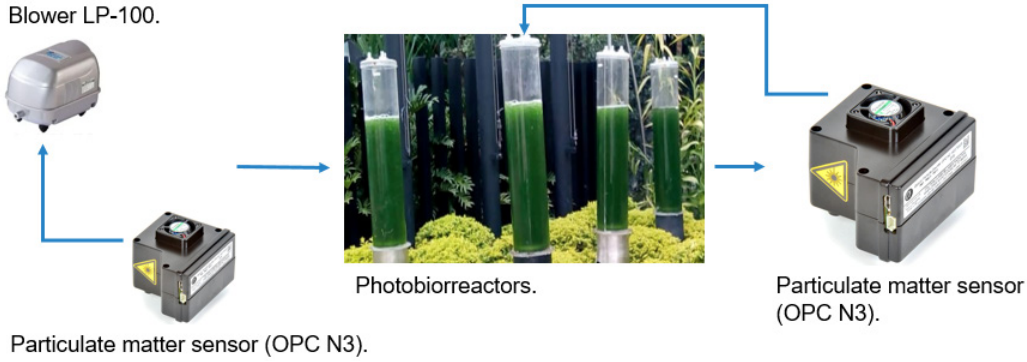

Figure 2. Diagram showing the location points of the particulate matter sensors, the first at the inlet of the blower ad the second at the output at the top of the FBR.

On the other hand, the cell concentration of the microalgae is measured with optical density and dry weight to contrast both techniques and have a more accurate approximation of the real growth of the microalgae, creating a kinetic profile that allows accounting for how thrives in the presence of these contaminants. Initially, the concentration of the sodium nitrate substrate varies as a nitrogen source between 0.25 g/L and 0.99 g/L, two FBR with 0.25 g/L and two with 0.99 g/L, the last FBR was used as a control, to contrast which is more optimal for its growth. It should be noted that these values were taken on the basis that in previous tests they are the ones that show the best growth rate in relation to the amount of reagent used and the expected final growth.

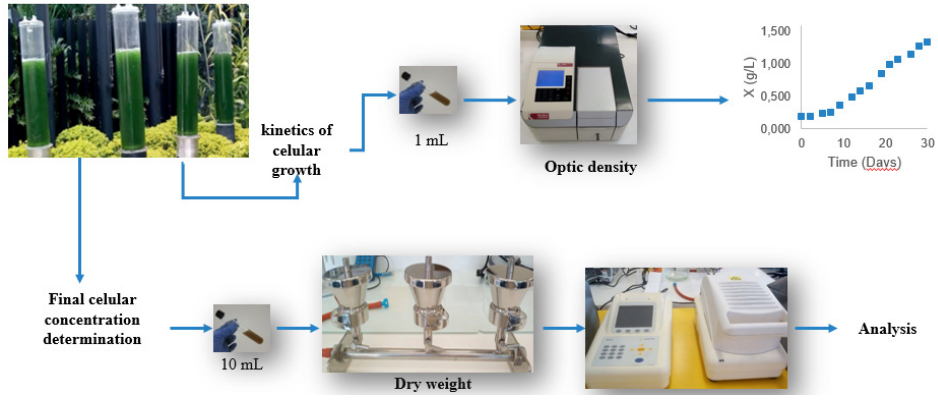

Figure 3. Diagram showing cell density analysis process by the dry weight technique.

Finally, the amount of total nitrogen in the collected biomass is measured by DUMAS.

Results and analysis

Regarding the growth kinetics, it was obtained that the best treatment for the microalgae was presented under a concentration of sodium nitrate (NaNO3) of 0.25 g/L, where growth of 1.52 g/L was reached while with 0.99 g /L at a concentration of 1.2 g/L. This can be explained as an inhibition due to excess substrate where the active site of the microalgae is disabled and presents failures when proceeding to protein synthesis, for example, to the dependent variable final cell concentration, an ANOVA analysis of variance was performed, where with a value of P=0.01 against an alpha of 0.05, the null hypothesis (Ho) is rejected, there is no significant difference between the final cell concentration of the two treatments, accepting the alternative hypothesis: there is a significant difference in the treatments used. In conclusion, there is an incidence of the levels of the factor (nitrogen source) and the best treatment to obtain a higher cell concentration is that of 0.25 g/L of NaNO3.

On the particulate material side, a capture of 61.07% of PM 1, 65.45% of PM 2.5 and 87.01% of PM 10 was obtained. During the test, the analysis was supported with micrographs to determine if there was a noticeable change in the particles. Microalgae handled in the laboratory did not show that the microalgae were physiologically affected by the presence of this particulate material. However, it is believed that its retention is a more physical and membrane permeability process than a metabolic one; that is, it captures this particulate material but does not metabolize it, or at least not to a great extent. Supported by Konstantin S., et al 2019, it is correct to say that the microalgae, because they are not in an environment where they can "enjoy" their carbon source without major problem, in this case CO_2, enters a state of stress and triggers internal reactions that affect the generation of extracellular polymeric substances and hyperpolarizes the membrane, making its concentration gradient becomes unbalanced and captures any substrate it finds in its surrounding environment, which is why most of the particulate material is believed to be physically trapped when trying to enter the interior of the membrane and that a little of it can be metabolized (nitrates and sulfates), in terms of the amount of nitrogen in the final biomass.

The resulting nitrogen quantification was conducted in the final biomass of the treatment with 0.25 g/L of nitrate since it was the one that obtained the highest growth and, consequently, the highest amount of biomass. The result by the Dumas method (AOAC 2005) showed a total of 4.57% nitrogen in the final biomass. In August 2019, laboratory tests were conducted to obtain nitrogen in the final biomass and these results range between 5.60 and 6.32%, being in greater quantity due to a constant CO2 injection, that at the outdoor level with "natural" CO2, this biomass with less nitrogen is better since it makes it attractive to produce biocrudes, as mentioned above.

Conclusions or summary

Scenedesmus Obliquus ATCC 457, together with a photobioreactor system, seems to be an alternative and effective method for the capture and retention of surrounding particulate matter in the environment, showing retention values of up to 61.07% of PM 1, 65.45% of PM 2.5 and 87.01% of PM 10. In turn, it shows that the interaction with these particles does not hinder normal cell growth and development, reaching an average growth of 1.52 g/L; in turn, the morphology of the membrane is not deformed. Adding to the above mentioned, the treatment with the concentration of 0.25 g/L of NaNO3 showed a significant difference in terms of the final cell concentration for the treatment of 0.99 g/L of NaNO3.

Finally, the amount of nitrogen in the final biomass is found in a lower proportion than in other tests carried out in the laboratory under more controlled conditions, with a total of 4.57% nitrogen; this increases the relevance of the study since the results suggest, due to the characteristics found in the membrane, that these particles cause more lipids to be produced than protein, which translates into a lower amount of nitrogen and positioning it as a relevant candidate for the development of important products in the commercial sphere such as biocrude.

Acknowledgment

We thank Argos Innovation Center (CApI) of EAFIT University and EAFIT University for financing the entire project, in addition to all the support in human talent and infrastructure.

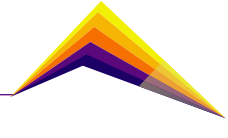

References

[1] Área metropolitana Valle de Aburrá 2019.

[2] AOAC (ASOCIACIÓN DE QUÍMICOS AGRÍCOLAS OFICIALES). (2005). Métodos Oficiales de Análisis. Método Dumas (990.03) . 15ª edición. Washington DC, Estados Unidos.

[3] Dean R. Appling, Spencer J. Anthony-Cahill, Christopher K. Mathews. (2016). Conceptos y conexiones de bioquímica. China: PEARSON, 8, pág. 267-269.

[4] Dean R. Appling, Spencer J. Anthony-Cahill, Christopher K. Mathews. (2016). Bioquímica.

[5] Junping Lv, Fei Zhao, Jia Feng, Qi Liu, Fangru Nan, Xudong Liu, Shulian Xie, The impact of particulate and soluble organic matter on physicochemical properties of extracellular polymeric substances in a microalga Neocystis mucosa SX, Algal Research, Volume 51,(2020),102064,ISSN 2211-9264.

[6] Konstantin S. Pikula, Valery V. Chernyshev, Alexander M. Zakharenko, Vladimir V. Chaika, Greta Waissi, Le Hong Hai, To Trong Hien, Aristidis M. Tsatsakis, Kirill S. Golokhvast, Toxicity assessment of particulate matter emitted from different types of vehicles on marine microalgae, Environmental Research, Volume 179, Part A,(2019), 108785, ISSN 0013-9351.

[7] Lodish, Berk, Kaiser, Krieger, Bretscher, Ploegh, Amon, Scott. (2016). Biologia celular y molecular. Ciudad autónoma de Buenos Aires: Panamericana, págs. 443-445.

[8] Pikula K, Kirichenko K, Vakhniuk I, Kalantzi OI, Kholodov A, Orlova T, Markina Z, Tsatsakis A, Golokhvast K. Aquatic toxicity of particulate matter emitted by five electroplating processes in two marine microalgae species. Toxicol Rep. 2021 Apr 16;8:880-887.

[9] Sabariswaran Kandasamy, Bo Zhang, Zhixia He, Narayanamoorthy Bhuvanendran, Ahmed I. EL-Seesy, Qian Wang, Mathiyazhagan Narayanan, Palaniswamy Thangavel, Mudasir A. Dar, Microalgae as a multipotential role in commercial applications: Current scenario and future perspectives,Fuel, Volume 308, (2022),122053, ISSN 0016-2361.

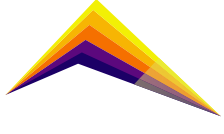

Analysis of Eichhornia crassipes root-associated protists and their relationship to the flood pulse

Naranjo, V[1]
Aguirre, N[1]
Serna, J[1]
Vélez, F[1]
Fernández, D[1]

E-mail: valeria.naranjo@udea.edu.co
E-mail: nestor.aguirre@udea.edu.co
E-mail: jpablo.serna@udea.edu.co
E-mail: fabio.velez@udea.edu.co
E-mail: david.fernandez@udea.edu.co

[1]Gepar-Geolimna research group, University of Antioquia.

Abstract.

The relationship between physicochemical and biological characteristics in marsh systems can determine the modification of the ecosystem, providing information on changes in the hydrological cycles. In addition, the abundance of microorganisms is essential to analyze the dynamics of the communities under the environmental conditions they face. The main objective of this research was to determine the different hydrobiological indices of "protoctists or protists", which refers to the eukaryotic algal organisms and free-living protozoa that are associated with the roots of Eichhornia crassipes in periods of drought and flooding, as well as to determine the primary productivity and chlorophyll a to quantify the autotrophic biomass of the study area. The field methodology was carried out for 10 different points, near the littoral area separated every 2 meters with a transect rope, recording the depth, dissolved oxygen (DO), pH, conductivity, water temperature, furthermore, to carrying out the assembly of primary productivity using the method of light and dark bottles, for 4 hours (Gaarder and Gran, 1927), as well as physicochemical and biological samples were taken, to afterwards be analyzed with the hydrobiological indices of diversity (Shannon and Weaver. 1949), Dominance (Simpson, 1949), Equity (Pielou.

Correspondent author

1996) and Richness. Besides, the data was compared with regulation 2115 of 2007, which corresponds to the quality of water for human consumption, since this marsh interacts directly with the population. As partial results, because the project is still in process, the algae with the highest diversity, but lower dominance for the drought period is the genera Synedra sp, Nitzschia sp, Fragilaria sp, representing the group of Diatoms, additionally, the only protozoa present in the samples were Tecamebas sp and Strombomonas sp, being these representative of lentic waters, moreover, taking into account these results, the water of the tested points was characterized as moderately polluted water. Considering that the sampling was carried out in the littoral region where there is a population and discharge of organic matter, as well as proliferation of E. crassipes, the results obtained are accurate. Indeed, it is necessary to have the analyses in both sampling periods to have a relationship with the limnimetric level, since, as a hypothesis, it is expected that by varying the flood pulse, any alteration will affect the biochemical processes in the E. crassipes assemblage in the short term.

Keywords: Marsh, Flood pulse, Epiphyton, Water quality

Introduction

According to Juank et. al, 2004, information in swamp systems have proven to be an integrative approach for studies of different ecological processes, because biota respond to flooding through morphological, anatomical, physiological, phenological and/or atological adaptations, forming characteristic structures that are produced by the modification of the flood pulse., The relationship between physicochemical and biological characteristics can determine the alteration of an ecosystem, providing information and determining if the flood pulse is the main modifier of these characteristics (Pinilla, G. 2006).

According to Neiff et. al,(2000), flood plains are characterized mainly as areas that are periodically flooded due to the lateral overflow of rivers or direct precipitation on the basin drainage, resulting in a change and dynamic physicochemical environment, in which hydrology and material flow limit the stability and diversity of the communities present there, In this sense, and according to research conducted in this type of environment, species vary and respond to the environmental conditions to which they are exposed by, whether in the water column, in the substrate or in any hydrological period (Montoya et al., 2012).; since it is well known that this system has a large number of habitats and it is

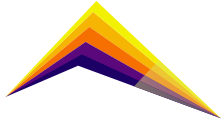

responsible for providing biological productivity in ecosystems, even in aquatic organisms such as periphyton, zooplankton and phytoplankton, which are the most abundant in the Ayapel marsh as indicated by Puerta et al, 2016.

In the Ayapel marsh, the determinant of the specific composition and abundance of the organisms that compose the epiphyton are fundamental for the community dynamics valuation in the stage of diverse environmental factors, for example, in relation to flood pulses (Montoya y Aguirre, 2013). At the micro and hydrobiological level, this community acts as an interface between the substrate and the water, so studying the productivity of these systems with protist organisms (algae and protozoa), are the next step in the strategy knowledge that "allows us to approach the energy flows understanding in the system's trophic chain" (Montoya Y Aguirre, 2008) and that in turn the taxonomic structure can indicate the abiotic conditions and signal the spatial and temporal heterogeneity, which justifies the possibility of using epiphyton as an indicator of biological water quality and relates it to the flooding pulse of the swamp system (Rodríguez et al, 2008, as cited in Montoya et al, 2013).

This is why it is important to monitor these systems that have a flood pulse and alter the ecosystem conditions, in order to find out a relationship between the physicochemical and biological characteristics of a hydrological cycle that can change according to environmental conditions and may also harm the different populations that inhabit the system, whether they are microorganisms, macroorganisms or communities in general.

Metodology

Study area

The research is being carried out in the Ayapel marsh system located in the department of Córdoba, Colombia; this system is distinguished characterized for being a highly studied system because it is slow and floodableflooding, which receives water supplies contributions from the overflow of the San Jorge river during rainy seasons and also has wastewater, agricultural, mining and livestock discharges, which makes the swamp the focus of different physical, chemical and biological processes.

The first analysis sampling for the analysis of protists associated with the root of Eichhornia crassipes was carried out specifically at coordinates 484817.33E-919380.44N, exactly on the banks of CorpoAyapel, where the patch of E. crassipes is located. The sampling points were distributed at a distance of 2 meters, for a total of 10 points where physical, chemical and biological characteristics were determined.

Physicochemical and biological characteristics

Physicochemical characteristics were evaluated at the initial sampling point (point 1), at the time of arrival, depth, dissolved oxygen (DO), pH, conductivity, water temperature, and primary productivity was recorded using the method of light and dark bottles, during 4 hours (Gaarder and Gran, 1927), additionally, 2 liter sample water liters samples were taken for laboratory determination determine of nutrients such as phosphate($PO3-$), nitrite($NO-$), nitrate($NO-$), total 4 2 3 hardness, ammonium($NH+$), alkalinity, turbidity and in turn chlorophyll a, filtering 500mL of sample (Talling and Driver,1963; APHA, 2017), this to relate it to the productivity of the area.

In each of the 10 sampling points pH, conductivity, DO and water temperature were recorded and likewise epiphyton samples were extracted from the roots of Eichhornia crassipes by 3 suctions of a Pasteur pipette (Aguirre, 2013), of which only protists such as algae and protozoa are of interest. The collected samples were fixed with 10% lugol, obtaining a total 10mL volume of 10mL, which were then observed in the laboratory in a Boeco BIB 100 reference tri-eyepiece inverted microscope with 40x objective, counting 30 randomly chosen fields in the Segdwick-Rafter chamber of 1 mL capacity.

The hydrobiological indexes of diversity (Shannon and Weaver, 1949), Dominance (Simpson, 1949), Equity (Pielou, 1966) and Richness, in order to characterize the water quality of the study area, in addition, the density of organisms wereas calculated according to the formula of Ross (1979), expressed in number of individuals per mL, and taxonomic keys and bibliographic references such as the Atlas of freshwater microorganisms (Heinz Streble), Der Kosmos-AlgenführerDie wichtigsten Süßwasseralgen (Linne, K et al 2004), among others, were used to determine morphotypes.

Results and analysis.

As partial results, due to the fact that the project is still in executionprogress, the first sampling was carried out during the dry season, but at the same time, the project was going through the “La Niña” phenomenon since November, which caused the results to have an atypical behavior. Table 1 shows the consolidated results found for the 10 sampling points.

Table 1. Results obtained

Variables evaluated	Information obtained
Physicochemical parameters	Oligotrophic zone
Most dominant taxa	*Synedra* sp
Diversity index	Moderately polluted
Dominance index	Lower dominance and higher diversity
Equity index	Maximum equity
wealth index	Low
Primary productivity (PP)	38,68$mgC/\ m^3 * h$
Chlorophyll a	7,60µ/L

For the physicochemical parameters, the concentrations obtained are relatively low, which indicates that there was a dilution of these concentrations thanks to the high rainfall that occurred in the place, these values characterize the study area as oligotrophic, however, when analyzing the biological parameters, it was determined that it is a moderately polluted area, since the Shannon diversity index gives values between 1-3, It was determined that it is a moderately polluted area, given that the Shannon diversity index gives values between 1-3, also with respect to the dominance, there are values that tend to 0, which indicates that there is less dominance and greater diversity, among these are the species Synedra sp, this being the one that tends to be more dominant; Nitzschia sp, Fragilaria sp, Tecamebas sp, Strombomonas sp, the last two on the list being the only protozoa found. At the same time, as the roots of the aquatic plant Eichhornia crassipes have the highest diversity, the equity index is obtained to be the maximum, which is corroborated by the fact that the values tend to 1.

These differences between parameters are mainly due to the fact that the physicochemical parameters were analyzed from a water sample near the patch of Eichhornia crassipes plants, which could have caused the macrophyte to retain a large amount of the nutrients present in the water, in addition to the dilution of these due to high rainfall; likewise, the primary productivity gives an oligoproductive environment, which is related to low production systems and therefore is associated to the fact that the organisms are found in greater proportion attached to the roots. In contrast, the hydrobiological indices were analyzed for samples attached to the root of the E. crassipes plant, so the great diversity of species is in agreement with the concentrations of nutrients that these can retain, given that the most abundant algal species (Synedra sp) develops better with the presence of nitrogen

and phosphorus so there is greater availability of these in the environment where they live (Reynolds, 2006), as well as other species such as Navicula sp, Nitzschia sp and Fragilaria sp that are found in sites of middle to high contamination.

With respect to the values obtained for chlorophyll a, being values less than 10 µg/L is categorized as a relatively low value, this may be because the water is highly degraded by brown algae and therefore the degradation products may be higher than chlorophyll, so there is not such a significant value of pigments.

It should be added that the density obtained for this environment is more or less high, because 40% of the analyzed samples had values greater than 30000 cells/mL, and the other 60% is in a range between 10000 and 30000 cells/mL, this is common for marsh environments.

Conclusions or summary

The obtained results are accurate, however, it is necessary to have the analyses in the two sampling periods to have a relationship with the limnimetric level, since, as a hypothesis, it is expected that, by varying the flood pulse, any alteration may affect in the short term the biochemical processes in the E. crassipes assemblage, in addition to the response of these organisms to the disturbance conditions.

Acknowledgement

Thanks to the support and funding of the Vice Rector's Office for Research under the SIMEVAM SIIU research project P2020-37870.

References

[1] Aguirre, N. (2013). *Hidrobiología Sanitaria*. (1 ed., Vol. 1, pp. 74-76). ude@.

[2] APHA, 2017. Standard Methods for the Examination of Water and Wastewater, 20th Editibon. American Public Health Association, Washington, DC.

[3] Gaarder, T., & Gran, H. H. (1927). Investigations of the Production of Phytoplankton in the Oslo Fjord. Rapports et procès-verbaux des réunions/Conseil international pour l'exploration de la mer, 42, 1-48.

[4] Juank, Wantzen.(2004). The flood pulse concept: new aspects, approaches and applications. Obtenido de https://www.researchgate.net/publication/274511459.

[5] Linne, VB. Hoef-Emden et al (2004). Der Kosmos-AlgenführerDie wichtigsten Süßwasseralgen. Traducción Aguirre, N y Hernandez, E. Universidad de Antioquia.

[6] Montoya, Y. Aguirre, N. (2008). Asociación de algas perifíticas en raíces de macrófitas en una ciénaga tropical colombiana. *Hidrobiológica 18(3): 189-198.*

[7] Montoya, Y. Aguirre, N. (2012)"Aproximación multivariada a la dinámica del ensamblaje algal epifítico en un sistema de planos inundables tropical".*Investigación, Biodiversidad y Desarrollo 2012; 31 (2): 83-95.*

[8] Montoya, Y. Aguirre, N. (2013). "Dinámica del ensamblaje algal epifítico en el sistema de planos inundables de Ayapel a través del pulso de inundación". Rev. U.D.C.A Act. & Div. Cient. 16(2): 491-500.

[9] Montoya, Y. Aguirre, N. Cano, M.(2013). Estructura del epifiton de diferentes macrófitas acuáticas de un sistema de planos inundables tropicales; Universidad Tecnológica del Chocó Diego Luis Córdoba.; Revista Institucional de la Universidad Tecnológica del Chocó; 32; 2; 7-2013; 85-105

[10] NEIFF, J. J. Aspectos conceptuales para la evaluación ambiental de tierras húmedas continentales de América del Sur.Programa de Ecologia e Recursos Naturais, UFSCar, Anais do VIII Seminario Regional de Ecología, Vol. VIII, São Carlos, Brasil, 2000

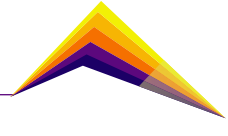

[11] Pielou, E C. 1996. Ecological Diversity. Wiley New York, 165 p

[12] Pinilla, G. (2006). Modelación del pulso de inundación en el lago Boa, Amazonía colombiana. Tomado dehttp://ecotropicos.saber.ula.

[13] Reynolds, C. (2006). Ecología del fitoplancton

[14] Ross J. 1979. Prácticas de Ecología. Barcelona. Ediciones Omega, SA.

[15] Simpson E H. 1949. Measurement of diversity. Nature 163 (4148):688.

[16] Shannon, C E. 1949 The mathematical theory ofcommunication. The University of Illinois Press.

[17] Streb H. Krauter, D. (sf). Atlas de los microorganismos de agua dulce. EdicionesOmega, SA.

[18] Talling, J.F. and Driver (1963) Some Problems in the Estimation of Chlorophyll a in Phytoplankon. US Atomic Energy Committee, Washington DC.

[19] Puerta, Y. Aguirre, N, Velez, F, (2016). "Sistema cenagoso de Ayapel como posible sitio Ramsar en Colombia". Gestión y ambiente, vol 19.(1): 110-122-xx.

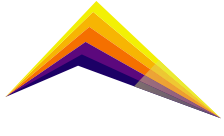

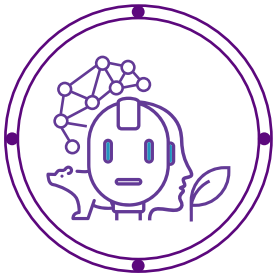

Social and environmental contributions to floriculture in the hydrangea sector through a life cycle assessment approach

María Alejandra González[1] E-mail: mariaa.gonzalezb@upb.edu.co
Mariluz Betancur[1] E-mail: mariluz.betancur@upb.edu.co
Juliana Miranda[1] E-mail: juliana.miranda@upb.edu.co
Cindy Natalia Arenas[1] E-mail: cindy.arenas@upb.edu.co
José Adrián Ríos[1] E-mail: jose.rios@upb.edu.co
Nicolás Fernando Molina[2] E-mail: nicolas.molina@upb.edu.co
Juliana Quintero[3] E-mail: qjuliana611@gmail.com
Jaime Botero[3] E-mail: jlbotero@elpoli.edu.co

[1] Environmental Research Group, Universidad Pontificia Bolivariana, Medellín, Colombia
[2] Projects, Programs and Portfolio Research Group, Universidad Pontificia Bolivariana, Medellín, Colombia
[3] Productivity and Quality Research Group, Politécnico Jaime Isaza Cadavid, Medellín, Colombia

Correspondent author

Abstract

The Colombian flower sector has been growing and consolidating as one of the country's main economic activities, representing every year between the second and third place of national agricultural exports and reaching markets in more than 90 countries. In the sub-region of La Provincia de La Paz in Eastern Antioquia, Colombia, hydrangea floriculture has been positioned as an important driver of economic and social development after the post-conflict situation, with a high-value generation in the territory. This study identified the social and environmental aspects of hydrangea cultivation by small and medium producers that trigger impacts and externalities throughout the life cycle of the crops, to contribute to the development of floriculture in harmony with ecosystems, protecting human health and generating value for the different stakeholders of the territory. As a methodological framework, the requirements and guidelines of

the ISO 14040 and 14044 series of standards for environmental life cycle analysis and the UNEP Methodological Guide were applied.

Some of the most significant results of the research have made it possible to identify the most significant environmental impacts that affect the performance of hydrangea production throughout its life cycle. These are associated with aspects such as the demand for natural resources, the intensive use of agrochemicals that can affect human health and ecosystems, the alteration of soil properties, and the requirement of fossil resources - plastics and fuels - at different stages of the process, which have a significant contribution to climate change. In addition, from the social point of view, stakeholders were identified, as well as the relevant aspects that need to be strengthened in terms of associative issues, occupational health and safety and agrochemical management, regulatory aspects, and substitution of systems that hamper transience, as well as the need for specialized technical support in new knowledge that allows producers to strengthen their activity through the implementation of lower-cost technologies contributing to a great extent to the reduction of some environmental impacts and associative models that can improve the conditions of hydrangea crops.

Keywords: Hydrangea cultivation, Carbon footprint, Life Cycle Assessment, Social analysis, Sustainable development

Introduction

The Colombian economy is mainly based on the production of the primary sector, with raw materials derived from mining and agriculture, such as floriculture, which is the second and third most traded non-mining energy product in the country every month [1] and represents the second largest agricultural export in terms of value, with 95% of the country's production exported [2]. Of the total of 8000 ha of flowers planted in Colombia, more than 1500 are planted with hydrangeas, 99% of which are produced in the eastern region of Antioquia [3]. Hydrangea cultivation for export is an important sector for economic and social development in La Provincia de La Paz in eastern Antioquia because it generates employment and improves the rural sector's quality of life.

Hydrangea floriculture presents socio-environmental gaps to be resolved to consolidate as a sustainable economic activity, mainly for small and medium-sized producers. This production process generates significant environmental impacts throughout its life cycle and there are challenges from the social point of view to strengthen the conditions under which the activity is developed.

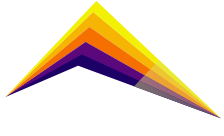

About 12 international research studies were identified and analyzed in which the environmental impacts of floriculture processes were evaluated under life cycle analysis. In Colombia, three studies have been done for hydrangea, chrysanthemums, and roses, while at the international level (especially in Italy) studies have been conducted for other species. The overall results show that the cultivation, flower transport, and raw material production stages are the ones that contribute the most to the environmental impacts of the life cycle.

The project "Evaluation of the environmental, economic and social life cycle for hydrangea agroindustrial enterprises as a strategy for the sustainable development of the Province of La Paz in Eastern Antioquia, Colombia" is being developed. This project has been identifying actions to reduce or mitigate socio-environmental impacts so that it can be implemented by producers to increase the value generation of their production chain in the territory. Thus, the environmental Life Cycle Assessment (LCA) approach and the Social Life Cycle Assessment (S-LCA) are tools that allow an objective, methodological, systematic, and scientific analysis of the impacts associated with a product or process during its production cycle, to provide information to identify the most significant impacts that must be addressed and at the same time prioritize actions to improve its performance.

Methodology

The carbon footprint analysis was performed under a life cycle approach, following the guidelines of ISO 14067:2018, which allows identifying and quantifying the direct and indirect emissions of Greenhouse Gases (GHG) of a product during its life cycle, in line with the International Standards for Life Cycle Assessment (ISO 14040:2007 and ISO 14044:2006) [4]. The analysis of the social aspects was performed following the guidelines of the UNEP (United Nations Environment Programme) in the Guide for the Social Life Cycle Assessment (S-LCA) of products and organizations, which is based on the ISO 14040:2007 standard [5].

Within the scope of the study, the product system was defined as the production process of hydrangeas for export on a small farm (0.45 ha) located in La Unión in La Provincia de La Paz in the department of Antioquia, Colombia. The functional unit was defined as 1 kg of hydrangea stems packed and transported to a trading company for export, from a crop of 0.45 ha in a production cycle of 36 weeks, equivalent to approximately 12 hydrangea stems.

The scope was defined from gate to gate, including the phases of prior activities to crop establishment (soil preparation, seeding, and infrastructure preparation), the cultivation phase (fertilization, stem selection, and phytosanitary management), harvesting (stem cutting), post-harvest (stems reception, monitoring, and make-up, hydration and packaging), transport to the marketer, some cross-cutting processes such as washing and disinfection, and for the crop end of cycle, removal of remaining stems, composting, and mulching of plant waste were taken into account.

The carbon footprint value was determined using the IPCC Global Warming Potential (GWP) values for a 100-year time horizon, from the Ecoinvent 3.8 database, using the Umberto software, which allows modeling each stage of the process system, correlating material

and energy consumption data with Ecoinvent process inventories, linking process data with characterization factors (impact indicators) and analyzing the complete results of the study. N_2O emissions from organic and synthetic fertilizers and CO_2 emissions from the lime application were determined following the Intergovernmental Panel on Climate Change (IPCC) methodology for national greenhouse gas inventories - Chapter 11. National and international emission factors were also used to calculate CO_2, N_2O, and CH_4 emissions from fuel and oil burning and electricity generation.

For the social analysis, the stakeholders associated with the hydrangea cultivation process in La Provincia de La Paz were identified and prioritized, and these were classified according to the categories defined by the UNEP [5], thus allowing the analysis of some qualitative and quantitative social indicators defined by the UNEP and complemented with GRI (Global Reporting Initiative) indicators. Finally, the indicators selected according to the context were evaluated using the SAM methodology proposed by Ramírez et al. [6], which shows the subcategory of social impact with the greatest influence on the production chain.

Results and analysis

The evaluation of the carbon footprint of the hydrangea production process resulted in 0.969 kg CO_2e for 1 kg of packaged hydrangeas, with the cultivation phase being the largest contributor with 64.62% of total emissions, followed by the prior activities phase (12.67%), post-harvest (11.99%) and crop end of cycle (9.90%), the harvesting and transport phases contribute less than 1% to the carbon footprint (Figure 1).

Figure 1 shows that the fertilization process is the largest contributor to the footprint with 0.464 kg CO_2e, which is due to the upstream process of NPK triple 15 fertilizer (0.243 kg CO_2e) and the direct emissions due to its application and the incorporation of compost (0.221 kg CO_2e). These results are generated because these products increase the nitrogen availability in the soil, promoting reactions that release nitrous oxide (N_2O), one of the main greenhouse gases. Similarly, the process of mulching plant waste on the soil of the crop (0.088 kg CO_2e), since N_2O is emitted during decomposition.

Phytosanitary management also has a significant contribution to the carbon footprint with 0.162 kg CO_2e, which is mainly associated with direct emissions from the use of fossil fuel in the pesticide spraying machine (0.062 kg CO_2e) and indirect emissions from the upstream process (0.014 kg CO_2e), as well as the use of pesticides, especially Mancozeb-based Dithane with 0.062 kg CO_2e (Figure 1).

Other aspects that contribute to a lesser degree to the carbon footprint are the use of polymeric materials such as the polypropylene of the hydrators used in the hydration process of the flower and the polyethylene of the saran and the tutoring mesh used in the preparation of the infrastructure due to its production and transport processes upstream, as well as the Bamboo poles, among other materials of the infrastructure.

The sustainability of the process can be improved by implementing cleaner production strategies to reduce the carbon footprint. In the agricultural sector at the international level, the actions implemented focus on good agricultural practices, technical solutions for the efficient use of resources, and waste management. Some of the most important actions include the implementation of biological controls to replace pesticides, the use of organic fertilizers instead of synthetic, the optimization use of natural resources, and the utilization and valuation of agricultural wastes.

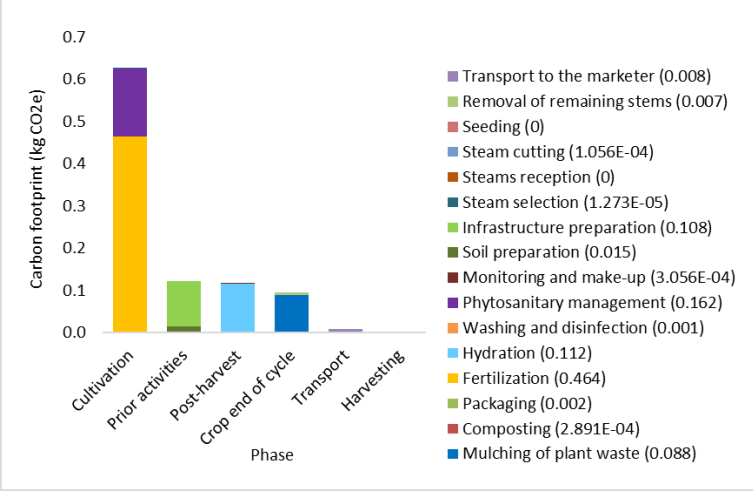

Figure 1. Contribution of processes to the carbon footprint in hydrangea production.

In social issues, the main areas for improvement were identified, with occupational health and safety being the issue requiring the most attention. Therefore, it is essential to implement education and training programs on the risks associated with the inappropriate use of agrochemicals for health and the environment, the importance of using personal protective equipment, and the management to minimize the use of these products, which are hazardous substances.

The above, considering that the crop workers are the main stakeholder group that potentially has the greatest influence and/or will be most affected by hydrangea production. In addition, the accompaniment and leadership of other important stakeholders such as hydrangea regulatory entities who can transfer knowledge on good agricultural practices, marketers as a strategy to strengthen sustainability in their value chain, and other crops through associative models.

Conclusions or summary

The sustainability of the hydrangea production process is affected by the generation of environmental impacts that contribute to climate change. Efforts to mitigate these impacts should focus on reducing the use of agrochemicals (fertilizers and pesticides) by seeking optimal application levels according to the crop needs or by introducing new organic and biological control products. Alternatives should also be sought to reduce the use of materials based on non-renewable resources such as fossil fuels and polymeric materials.

From the social point of view, efforts should focus mainly on occupational health and safety issues to reduce the impacts on human health and ecosystems caused by the use of agrochemicals, which can be strengthened through leadership, the generation and transfer of knowledge from educational and industry entities, and partnerships between producers.

References

[1] Sánchez, A. M. (2021). Colombia es el principal proveedor de flores de corte para el mercado de Estados Unidos. Agronegocios, <https://www.agronegocios.co/aprenda/colombia-es-el-principal-proveedor-de-flores-de-corte-para-el-mercado-de-estados-unidos-3167223> (May 11, 2021).

[2] Ministerio de Agricultura y Desarrollo Rural. (2021). Flores. Sistema de información de Gestión y Desempeño de Organizaciones de Cadenas, <https://sioc.minagricultura.gov.co/Flores/Pages/default.aspx> (May 11, 2021)

[3] González, X. (2019). Cultivo de hortensias, un negocio con gran potencial en el Oriente Antioqueño. Agronegocios, <https://www.agronegocios.co/agricultura/cultivo-de-hortensias-un-negocio-con-gran-potencial-en-el-oriente-antioqueno-2821240> (May 11, 2021).

[4] ICONTEC (Colombian Technical Standards and Certification Institute). (2007). NTC-ISO 14040. Gestión ambiental. Análisis de ciclo de vida. Principios y marco de referencia.

[5] UNEP (United Nations Environment Programme). (2020). Guidelines for Social Life Cycle Assessment of Products and Organizations.

[6] Ramírez, P.K., Petti, L., Haberland, N.T. and Ugaya, C.M.L. (2014). Subcategory assessment method for social life cycle assessm Part 1: methodological framework. Int J Life Cycle Assess, 19, 1515-1523.

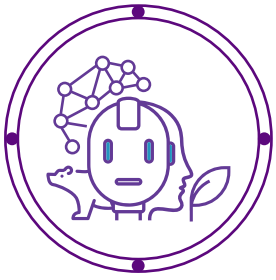

Car fleet growth model in Medellín city: Exploratory review of the implementation of public policies for the transportation demand management based on the restriction due to the use of plates and scrapping

José A. Zapata[1]
Yony F. Ceballos[2]
Julián A. Castillo[3]

E-mail: jalejandro.zapata@udea.edu.co

[1]Ingeniero Civil, Estudiante de Maestría en Ingeniería Universidad de Antioquia
Grupo Ingeniería y sociedad - Facultad de Ingeniería, Medellín Colombia
[2]Ph. D. en Ingeniería, Profesor Universidad de Antioquia
[3]MSc. en Ingeniería, Profesor Institución Universitaria Digital de Antioquia

Abstract:

The increase in the number of vehicles in highly dense areas with a limited road network has become a challenge for main cities worldwide. Recent decades' demographic and economic growth has generated a gradual increase in traffic congestion and the commutation times of inhabitants, which directly affects their productivity and quality of life. To counteract these impacts, governments have implemented Demand Management Measures (TDM) that restrict the circulation of private vehicles to reduce traffic congestion, while discouraging their acquisition and promoting the use of public transport. However, due to their coercive characteristics, the effectiveness of TDM to discourage the acquisition of private vehicles and their real long-term effect on controlling the growth of the vehicle fleet has been harshly questioned. This research presents a literature review and the recent scientific methodologies to estimate variations in automotive fleet growth. This work also identifies some estimation variables in Medellín city using publicly available databases, as well

Correspondent author

as one methodology proper for the selection of the appropriate evaluation model. These establish scenarios for projecting the vehicle fleet based on the implementation of public policies for demand management of demand such as the restriction due to license plate-based use and scrapping. This make it possible to evaluate the relationship between vehicle age allowed for the circulation of vehicles on the road network, demographic growth, and the trend increase for new vehicles.

Keywords: Model, Car Fleet, Transportation Demand Management, Public Policies.

Introduction

Peripheral expansion, densification, and overpopulation of cities, added to the increase in the purchasing power of their inhabitants, massify the ownership and use of private vehicles as a preferred mode of transport. The increase in vehicle units in a territory decreases the operating capacity of the roads to meet travel demand, thus generating a gradual increase in the traffic congestion of the territories, which affects the productivity and quality of life of citizens (Wang et al., 2021). High vehicle congestion indicators means inefficient use of the available road network, which deems necessary to invest public resources in strategies to control mobility indicators (Litman, 2006). Additionally, congestion levels have an impact on the quality of public transport service, thus making it more difficult for private vehicle owners to opt for modal change (CAF, 2011) In this sense, Medellín, like other cities in the world, has implemented various TDM, which seek to restrict the circulation of private vehicles as a strategy to manage and condition citizens' circulation using a private mode of transport, while aiming to discourage its acquisition and promote the use of collective public transport (AMVA, 2017) However, national economic policies for the acquisition and scrapping of vehicles seem to stand against regional objectives aiming to improve mobility conditions (Aydınalp Köksal et al., 2021) In the last 10 years, the study of the problems derived from the growth of the automotive fleet, traffic congestion and TDM has become increasingly relevant within the scientific field, in which statistical methodologies and modeling propose solutions to a generalized problem in cities with a high population concentration (Viri et al., 2015).

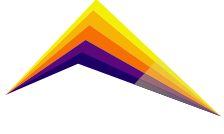

Methodology

Literature review: The last decade has seen an increasing interest in investigating the phenomenon of traffic congestion and its impact on the quality of life of citizens. Research has looked at models of systems and agents, as well as statistical analyses that respond to the variations of the automotive fleet and the implementation of TDM (Vidal et al., 2020)

(Luo et al., 2022) published his theoretical model to explore factors that influence public acceptance of LPRs. Based on the formulation of resident surveys of the city and a Partial Least Squares Structural equation model, the research found that the problem perception, perceived effectiveness, perceived value, and social norms exert a significant direct and indirect impact on the acceptance of a demand management policy. Likewise, (Aydınalp Köksal et al., 2021) in their research on the characteristics of the long-term vehicle fleet in Turkey, present a multivariate statistical analysis model. It has shown that several factors must be considered for the formulation of transport policies. To obtain the analysis model of these policies, the projected vehicle fleet until 2030 was determined by government indicators of mobility and public health associated with traffic congestion while defining five scenarios to conclude that the vehicle fleet is increasing rapidly and aging at a minimum scrapping rate.

(Viri et al., 2021), in their study on the renewal of the car fleet in Finland regarding the renewal rate of the vehicle fleet, provided a reference scenario for the development of the car fleet until 2040 from a model that combines sociodemographic data of the Finnish population and fleet average age . The study concluded that the areas in which growth models are carried out have an influence on the results, specifically between rural and urban areas. Similarly, (Adnan et al., 2021) published a research that aimed to establish scenarios for optimizing TDM for the cities of Hasselt, Belgium, and Bologna, Italy, based on models of automotive fleet growth. These models helped determine that the collective behavior of the travels made by citizens is related to their quality of life, while the optimization of public transport generates a shift of cyclists to it, bringing along undesirable results for sustainable mobility policies. The research used an Agent-Based Model (ABM) to simulate and analyze traffic variables that influence city mobility.

For its part, (Fridstrøm et al., 2016) sought to identify a mathematical model to mitigate the adverse effects of greenhouse gases and pollutants derived from the current vehicle fleet using a normal of vehicle renewal process towards cleaner vehicles. This mathematical model presented growth projections over the year 2050 horizon to Norway under a low-carbon fiscal policy scenario. It concluded that such a policy makes a big difference in terms of long-term fuel consumption and CO2 emissions. Finally, it highlights the importance of including key aspects like scrapping rate, traffic incidentality, and travel choice in new models of automotive fleet growth.

Finally, (Kim et al., 2004) and their research on optimal fleet conversion policy, from a life cycle perspective in the U.S., explores an optimal fleet conversion policy based on medium-sized internal combustion engine vehicles, which is defined as the minimization of the total lifecycle emissions of the whole new and used vehicle fleet. The study concludes that accelerated scrapping policies to reduce regulated emissions are recommended, although there is a risk of greenhouse gases increase.

Methodology and sources of available information: Based on the literature review, the methodology and variables used in different investigations to analyze the behavior of the vehicle fleet and design the growth model are defined. Some of the variables identified allow us to relate the behavior of the vehicle fleet with variables such as demography, traffic incidentality, and traffic control. To obtain this information, it was necessary to manage with the different entities and municipalities the information of the variables, through requests for formal information that allows validating the veracity of the information that was used in the research.

Model design: With the variables defined, it is determined that the objective sought by the research is possible to address from the design of an ABM since this type of model focuses on the individual and the global behavior arises as a result of interactions of many individual behaviors, allowing simulation scenarios to be generated with a graduated time scale and a defined geospatial interaction (Borshchev & Filippov, 2004; Crooks, 2015) The conceptual model of the proposal is made using the Overview, Design concepts, and Details (ODD) protocol. This protocol is a standard format that allows describing ABM and facilitates the interpretation of their structure, reading, and writing, allowing the replication of simple and complex models of different topics (Grimm et al., 2020)

The version of the model was developed in the Netlogo software 6.1.1. It establishes a relationship between the growth of the Automotive Park for each of the 16 Communes and 5 Corregimientos of the municipality of Medellín, based on the historical data of the automotive fleet in the last 10 years, the traffic incidentality of the last 2 years for each commune and the body of traffic agent available for the traffic control of the city in the last 10 years.

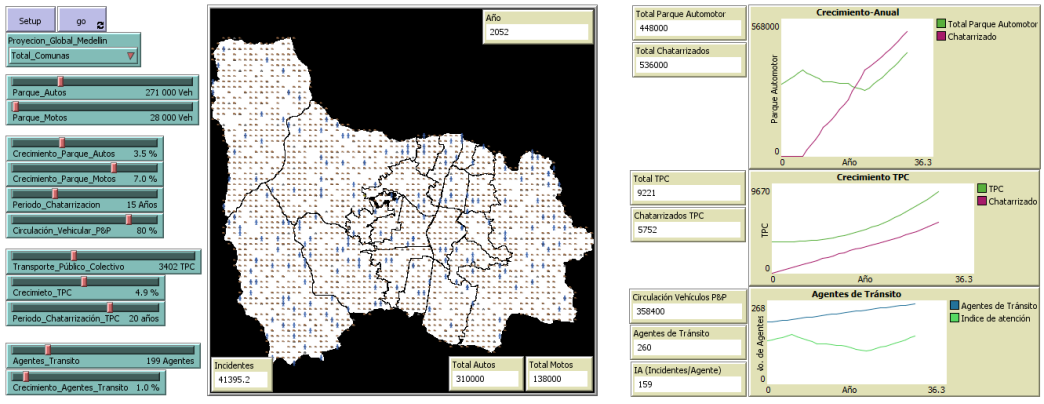

Figure 1. Graphic design of the model. Source: Compilation from Netlogo 6.1.1

The graphical interface of the ABM, allows the modeler to evaluate the projections of the growth of the automotive fleet and the requirements for traffic control within the next 30 years, from the definition of growth rates of cars, motorcycles, and Collective Public Transport (TPC), defining policies for its scrapping period and strategies to reduce the percentage of the vehicular volume that circulates through the city, as a result of the restriction by plate use.

Conclusions

In the scenario analyzed based on the information collected, Medellin has more than 300,000 registered passenger vehicle units (PCU), with an average vehicle fleet growth rate of 4% and with restriction policies for plate use that decreases daily traffic between 10% and 20%. In this scenario, the model considers the implementation of scrapping policies to be favorable for PCU that have a useful life of more than 15 years equivalent to kilometers traveled, with a grace period for the implementation of the policy of no less than 8 years, which will allow, according to the model, to have a variation in the growth of the vehicle fleet of less than 5% within the first 20 years, a period after which it will continue to increase due to the inevitable demographic growth. The projections of both population and automotive fleet growth in the neighborhoods of Medellín with a highly inclined topography, normalized road infrastructure, and limited traffic control represent an important challenge for future governments. They will have the challenge to implement effective public policies to limit the use of private vehicles, thus encouraging the modal shift towards a quality public transport offer. In this vein, it is necessary to promote public policies that reinforce the control of traffic in real time through technology, which allows supporting the traffic agents corps available, especially in peripheral and difficult access areas.

Bibliography

[1] Adnan, M., Outay, F., Ahmed, S., Brattich, E., di Sabatino, S., & Janssens, D. (2021). Integrated agent-based microsimulation framework for examining impacts of mobility-oriented policies. *Personal and Ubiquitous Computing*, *25*(1), 205–217. https://doi.org/10.1007/s00779-020-01363-w

[2] Area Metropolitana Del Valle De Aburrá. (2017). *Plan Maestro de Movilidad para el Valle de Aburrá*.

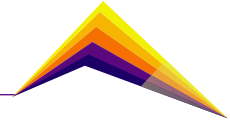

[3] Aydınalp Köksal, M., Tekeli, E., Ara Aksoy, S., Kızıltan, A., Kızıltan, M., Duran, N., Aslanoğlu, S. Y., Öztürk, F., Özyürek, N., Doğan, P., Yılmaz, A. G., Köksal, C. E., Çetintürk Gürtepe, İ., Yereli, A. B., Birpınar, M. E., & Güllü, G. (2021). Long term characterization of the vehicle stock in Turkey. *Transportation Research Part D: Transport and Environment*, *99*. https://doi.org/10.1016/j.trd.2021.102988

[4] Borshchev, A., & Filippov, A. (2004). From System Dynamics and Discrete Even to Practical Agent Based Modeling. *The 22nd International Conference of the System Dynamics Society*.

[5] Banco de Desarrollo de America Latina. (2011). *Desarrollo urbano y movilidad en américa latina*.

[6] Crooks, A. (2015). *Agent-based Models and Geographical Information Systems*. *January*.

[7] Fridstrøm, L., Østli, V., & Johansen, K. W. (2016). A stock-flow cohort model of the national car fleet. *European Transport Research Review*, *8*(3), 1–15. https://doi.org/10.1007/s12544-016-0210-z

[8] Grimm, V., Railsback, S. F., Vincenot, C. E., Berger, U., Gallagher, C., Deangelis, D. L., Edmonds, B., Ge, J., Giske, J., Groeneveld, J., Johnston, A. S. A., Milles, A., Nabe-Nielsen, J., Polhill, J. G., Radchuk, V., Rohwäder, M. S., Stillman, R. A., Thiele, J. C., & Ayllón, D. (2020). The ODD protocol for describing agent-based and other simulation models: A second update to improve clarity, replication, and structural realism. *Jasss*, *23*(2). https://doi.org/10.18564/jasss.4259

[9] Kim, H. C., Ross, M. H., & Keoleian, G. A. (2004). Optimal fleet conversion policy from a life cycle perspective. *Transportation Research Part D: Transport and Environment*, *9*(3), 229–249. https://doi.org/10.1016/j.trd.2004.02.004

[10] Litman, T. (2006). Mobility management innovative management strategies to transport problems. *25th Annual Southern African Transport Conference, SATC 2006 - 2010: Will Transport Infrastructure and Systems Be Ready*, *2006*(July).

[11] Luo, M., Ma, Z., Zhao, W., Enoch, M., & I-Jy Chien, S. (2022). An ex-post evaluation of the public acceptance of a license plate-based restriction policy: A case study of Xi'an, China. *Transportation Research Part A: Policy and Practice*, *155*(October 2021), 259–282. https://doi.org/10.1016/j.tra.2021.10.024

[12] Vidal, R. M., Duk, C. N., Guevara, Á., & Rubinstein, E. (2020). *Análisis del estado del arte y experiencias de gestión de demanda de transporte urbano en América Latina y el Caribe*. *1*, 67.

[13] Viri, R., Mäkinen, J., & Liimatainen, H. (2021). Modelling car fleet renewal in Finland: A model and development speed-based scenarios. *Transport Policy*, *112*(August), 63–79. https://doi.org/10.1016/j.tranpol.2021.08.012

[14] Viri, R., Mäkinen, J., Liimatainen, H., Kloess, M., Müller, A., Fridstrøm, L., Østli, V., Johansen, K. W., Madre, J. L., Bussière, Y. D., Grimal, R., Florent, Q., & Enrico, B. (2015). Modelling car fleet renewal in Finland: A model and development speed-based scenarios. *Transportation Research Procedia*, *48*(3), 1744–1751. https://doi.org/10.1016/j.tranpol.2021.08.012

[15] Wang, X., Rodríguez, D. A., & Mahendra, A. (2021). Support for market-based and command-and-control congestion relief policies in Latin American cities : Effects of mobility , environmental health , and city-level factors. *Transportation Research Part A*, *146*(February), 91–108. https://doi.org/10.1016/j.tra.2020.12.004

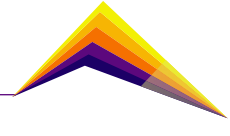

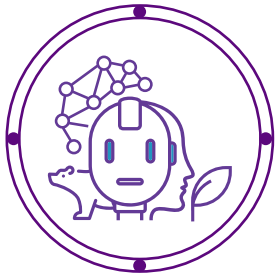

Emissions of criteria pollutants and greenhouse gasses from mobile sources in three main streets of an intermediate city in colombia.

Bush Felipe Uriah Aron — *Email: ubush@unicesar.edu.co*
Murillo Villamizar Alex Andrés — *Email: aamurillo@unicesar.edu.co*
Rodríguez Castilla José Luis — *Email: joselrodriguez@unicesar.edu.co*
Díaz Muegue Luis Carlos — *Email: luisdiaz@unicesar.edu.co*
Angulo Argote Luis Carlos. — *Email: lcangulo@unicesar.edu.co*

Abstract.

One of the most important markers of sustainable cities is air quality, which is largely affected by the emissions that come from mobile transport. These cities also have crucial problems with their public transport systems. This is the case with Valledupar, which has seen an accelerated and an exponential growth of its population in the last 10 years; its urban area has expanded remarkably but its public transport remains very deficient and inefficient. The objective of this study is to estimate the pollutants criteria emissions and greenhouse gasses from mobile sources in three streets of high vehicular flow in Valledupar's city. A vehicle characterization was carried out on the studied streets and the IVE model was implemented to estimate the emissions. At the end, contaminant path way scenarios were analyzed with the HYSPLIT model using WRF data. The results showed that in the case of pollutants criteria, the highest amount of CO and PM10 were emitted from motorcycles and the highest emissions of SOx and NOx from private cars. For GHG, private cars emitted the highest amount of CO2 and N2O while motorcycles were the ones that emitted the highest amount of CH4. The path way scenarios for the study days showed that in the morning hours the air pollutants move predominantly to NE and in the afternoon hours they move to SE, affecting the population located in the areas where the displacement of contaminants occurred.

Correspondent author

Key words: Vehicle Emissions, IVE, Greenhouse gasses, HYSPLIT, WRF, urban mobility.

Introduction

Currently air pollution in urban areas of the planet is mainly caused by mobile sources. In main Colombian cities such as Bogotá and Medellín, the contribution of vehicles to pollutant emissions is 78% and 81% respectively (Secretaría Distrital de Ambiente [SDA], 2014) (Área Metropolitana del Valle de Aburrá [AMVA], 2015). Colombian Intermediate cities , such as Valledupar, have significantly increased their population, which has led to a greater demand for transportation by their inhabitants. If we add to this an inefficient public transport system, the problem becomes much greater. Valledupar city´s vehicle fleet registered has increased by 74% from 2008 to the present day (RUNT 2008, 2022). The greenhouse gas emissions that came from mobile sources have their origin in the type of combustion used, by spark (gasoline) gasses which are emitted through the exhaust pipe, the carburettor, the crankcase and the fuel tank. The largest emissions come from the exhaust pipe for spontaneous ignition engines (Diesel) (Albornoz & Guerrero, 2019).

Methodology

For our study, three sectors of three main streets in the city were chosen (one sector for each street), the roads were Ave Sierra Nevada (north), Ave Carrera 19 (center), Ave Calle 44 (South). To stimate the emissions, it was necessary to characterize the flow of motor vehicles in the named sectors, to which a capacity was made with the help of video recordings in three points (one recording point for each section) for days 14 (Thursday), 15 (Friday), and 16 (Saturday) of October 2021. To make it ease handling the information, the recordings were done of an 1-hour long until completing the study schedule, which was from 08:00 am to 06:00 pm. The information obtained is representative only in the three study streets and for the entire year. Once the capacity was completed, the vehicles technical data sheets observed in the videos were searched, to classify them according to the type of fuel used like Gasoline (Sulfur 50 Ppm, lead 0.013g/l, benzene 1.0%) and Diesel (15ppm) (Ecopetrol 2021), type of injection, and mileage traveled on the study roads.

1208	Pt: SmlEng : Lt : 4Cyc Carb : None : None: >50K km	1.55
1316	Ds: SmlEng : Med : 4Cyc : None : None: >50K km	0.2
1214	Pt: SmlEng : Hv : 4Cyc Carb : None : None: >50K km	1.35
1211	Pt: SmlEng : Med : 4Cyc Carb : None : None: >50K km	1.55
1178	Pt: SmlEng : Hv : 2Cyc : None : None: >50K km	47.2
1175	Pt: SmlEng : Med : 2Cyc : None : None: >50K km	46.7
1172	Pt: SmlEng : Lt : 2Cyc : None : None: >50K km	1.55

Figure 1: Entered Technologies fleet file – Motorcycles.

Temperature (28.5°C) and Relative Humidity (67.2%) were obtained from IDEAM (2021) meteorology stations. Speed Emissions for the bins evaluation was used, together with the avenza maps app, which provided the speed data Second by Second, slope of the terrain.

To identify possible pollutant scenarios, three-dimensional trajectories (fwrd) were calculated and analyzed using the HYSPLIT model of the Air Resources Laboratory (ARL) of the National Oceanic and Atmospheric Administration (NOAA) (Stein, et al., 2015). In this model, the WRF (Weather Research and Forecasting) files (Skamarock, W. C., et al., 2019) with a resolution of 1 km were taken as the meteorological base, trajectories were obtained during the 14, 15 and 16 days of the month of October of the year 2021, at 13 UTC with a duration of one hour and at 23 UTC with a duration of one hour, at the 3 monitoring points.

Results and analysis.

On the three streets, a total of 267,936 vehicles were observed: Motorcycle 147,553 (55.10%); private Cars 80343 (30.00%); Taxis 28295 (10.60%); Boxcars 3850 (1.40%); Vans 2914 (1.10%); Special Service Taxis 1265 (0.50%); Buses 882 (0.30%); Trucks 546 (0.20%); Police Motorcycles 656 (0.20%); Dump trucks 543 (0.20%); Ambulances 338 (0.10%); Campers 310 (0.10%); Police Cars 184 (0.10%); Tractors 253 (0.10%); Backhoes 4 (0.001%).

For the pollutants criteria were obtained: CO 89090Kg (96.9%), NOx 1935Kg (2.1%), SOx 2Kg (0.002%), PM10 889Kg (1.0%); For greenhouse gases were obtained: CO2 110923Kg (97.1%), N2O 1Kg (0.001%), CH4 3294Kg (2.9%).

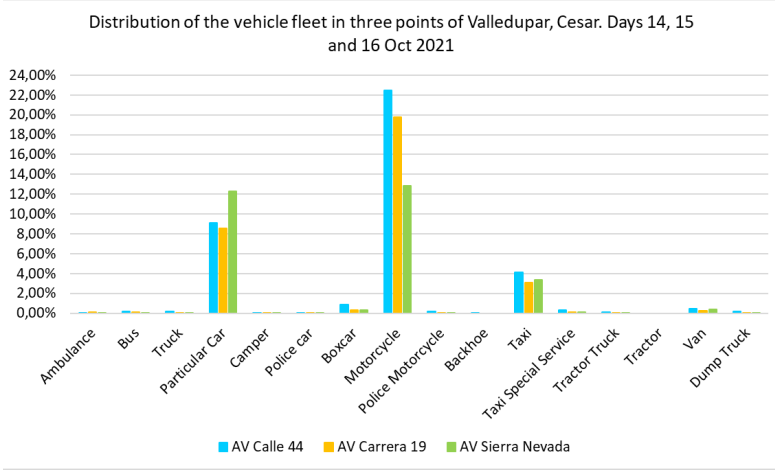

Figure 2. Vehicle fleet distribution in three points of Valledupar, Cesar. Days 14,15 and 16 Oct 2021.

Table 1. Specific contribution of each vehicle category.

	Criteria Pollutants				**Greenhouse Gases**		
Typology	**CO**	**NOx**	**SOx**	**PM10**	**CO2**	**N2O**	**CH4**
	96,9%	2,1%	0,002%	1,0%	97,1%	0,001%	2,9%
Ambulance	0,001%	0,04%	0,04%	0,10%	0,3%	0,2%	0%
Bus	0,007%	2,3%	0,3%	2,4%	2,0%	1,7%	0%
Truck	0,2%	1,1%	0,5%	0,8%	0,9%	1,1%	0,02%
Camper	0,1%	0,2%	0,3%	0,01%	0,2%	0,2%	0,03%
Particular Car	18,8%	49,8%	47,4%	5,6%	47,9%	53,6%	6,7%
Police Car	0,03%	0,1%	0,09%	0,04%	0,1%	0,17%	0,01%
Boxcar	0,02%	7,1%	1,1%	8,1%	7%	6,0%	0%

Motorcycle	72%	12%	29%	75%	19%	12%	90%
Police Motorcycle	0,2%	0,4%	0,1%	0,2%	0,2%	0,1%	0,1%
Backhoe	0,00003%	0,009%	0,001%	0,01%	0,008%	0,007%	0%
Taxi	7,9%	18,8%	19,1%	0,2%	15,7%	18,0%	2,8%
Taxi Special Service	0,1%	0,4%	0,4%	0,2%	0,7%	0,6%	0,1%
Tractor	0,002%	0,6%	0,08%	0,6%	0,5%	0,4%	0%
Van	0,2%	5,9%	1,3%	5,7%	4,9%	4,5%	0,1%
Dump Truck	0,1%	1,2%	0,3%	1,1%	1,0%	1,1%	0,01%

The motorcycles group that are presenting the greatest contamination is observed with concern. It is important to mention that according to RUNT figures, at national level, motorcycles have an evasion of 78% of mechanical technical inspection and polluting emissions (RTMyEC). In the total emissions of the pollutants criteria, the contribution of the motorcycles for CO was 72%, NO_X 12%, SO_X 29% and PM10 75%. Regarding the emission of greenhouse gasses emitted by motorcycles, CO_2 had an emission corresponding to 18.7%, N2O with a value of 12%, followed by CH4 with 90%.

The HYSPLIT model estimated the movement behavior of the air and the pollutants path way(fwrd) (CO, PM10, NOx, SOx, CO2, N2O and CH4) emitted at the studied streets. The model was simulated for the days 14, 15 and 16 in the month of October; a total of 18 route maps were obtained. For the route maps three emission points were established on the studied roads (Ave Sierra Nevada, Ave Carrera 19 and Ave Calle 44). In addition, the peak traffic hours corresponding to the hours from 08:00 am to 09:00 am and from 06:00 pm to 07:00 pm were taken into account. On days 14, 15 and 16 it was observed that the courses were directed mainly towards the city eastern part; specifically in the Ave Sierra Nevada where they can affect residential complexes and recreational parks located near to the avenue in that direction. For the Ave Carrera 19 the predominant pollutants movement direction was to the east, where they can affect hospitals, restaurants and business-related premises, finally, on the Ave Calle 44 with impacts on residential and school areas in the east-

southeast of the city. Figure 3 presents the case for October 14, it is observed that the impact of these paths is mainly in the east and northeast of the city.

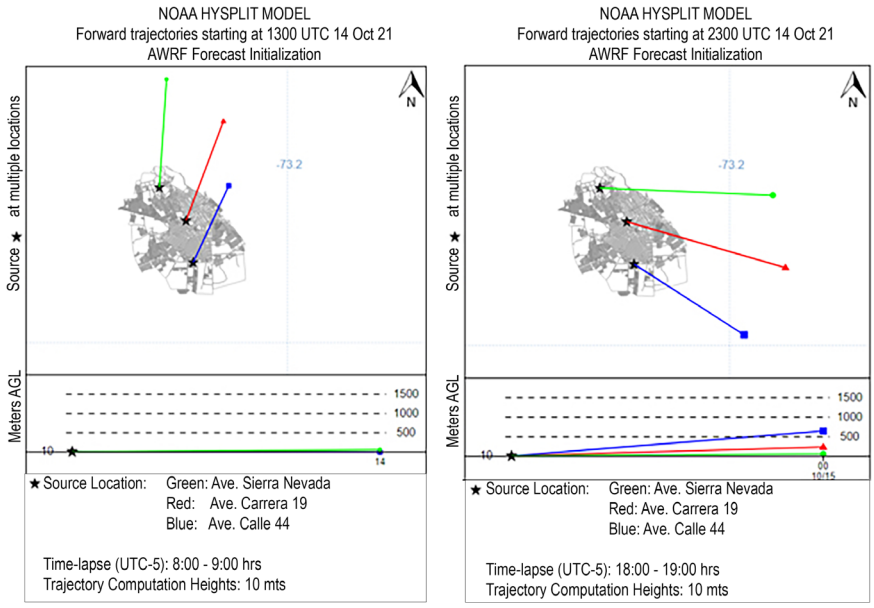

Figure 3.: Trajectories of air masses in the city of Valledupar. 14 Oct, 2021

Conclusions/summary.

Although different types of vehicles are analyzed to determine the pollutants criteria and greenhouse gasses, we observe that the greatest contribution is generated by motorcycles, this as mentioned before is aggravated by the lack of RTMyEC, so the community must be enabled and encouraged to perform the RTMyEC. In addition, to promote the use of green transport through the expansion of bike´s path network, also to increase the fleet of public buses so that the community uses less informal transportation.

Taking into account carbon sinks, which reduce GHG, the community and environmental authorities should be encouraged to plan reforestation and care for existing vegetation.

Acknowledgments

The authors thank the UNIVERSIDAD POPULAR DEL CESAR for financing the research project, agreement No. 062 - 2019. STUDY OF THE EMISSION AND DISPERSION OF PM10 PARTICULATE MATERIAL GENERATED BY VEHICULAR TRAFFIC ON THE MAIN ROADS OF THE CITY OF VALLEDUPAR, IMPLEMENTING THE HYSPLIT MODEL.

References

[1] Albornoz, A y Guerrero, B (2019) Inventario de emisiones atmosféricas de CO2 provenientes de fuentes móviles en el municipio de Mosquera por medio del modelo IVE. Tesis de pregrado. Universidad de Cundinamarca.

[2] AMVA. (2015). Inventario de emisiones. Obtenido de Área Metropolitana del Valle de Aburrá:http://www.metropol.gov.co/CalidadAire/isdocConvenio243/Informe_Inventario_emisiones_2015.pdf

[3] Registro Único Nacional de Tránsito (2008, 2022). Flota Vehicular registrada en la ciudad de Valledupar, Secretaría de tránsito de Valledupar.

[4] Registro Único nacional de tránsito, RUNT (2022). RUNT en cifras. Recuperado el 16 de Julio 2022. De: www.runt.com.co/runt-en-cifras

[5] Ecopetrol S.A (2021). Especificación Técnica del Catálogo de Productos de Ecopetrol S.A. Gasolina Básica Corriente (Gasolina Motor Regular). Recuperado de: www.ecopetrol.com.co/wps/portal/Home/multisitios/comercial/es/portafolio/productos-y-servicios/combustibles

[6] Ecopetrol S.A (2021). Especificación Técnica del Catálogo de Productos de Ecopetrol S.A. Diésel Extra B2/B0. Recuperado de: www.ecopetrol.com.co/wps/portal/Home/multisitios/comercial/es/portafolio/productos-y-servicios/combustibles

[7] Instituto de Hidrología, Meteorología y Estudios Ambientales, IDEAM (2021).

[8] Ramírez Hernández, O. J. (2014). Origen de masas de aire en cuatro ciudades de Colombia mediante el modelo HYSPLIT. *Revista De Investigación Agraria Y Ambiental*, *5*(1), 103–119. https://doi.org/10.22490/21456453.935

[9] Skamarock, W. C., J. B. Klemp, J. Dudhia, D. O. Gill, Z. Liu, J. Berner, W. Wang, J. G. Powers, M. G. Duda, D. M. Barker, and X.-Y. Huang, 2019: A Description of the Advanced Research WRF Version 4. NCAR Tech. Note NCAR/TN-556+STR, 145 pp.

[10] Stein, A.F., Draxler, R.R, Rolph, G.D., Stunder, B.J.B., Cohen, M.D., and Ngan, F., (2015). NOAA's HYSPLIT atmospheric transport and dispersion modeling system, Bull. Amer. Meteor. Soc., 96, 2059-2077, http://dx.doi.org/10.1175/BAMS-D-14-00110.1

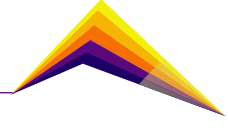

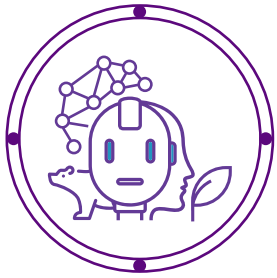

Comparison of extreme precipitation and temperature events between El Niño Southern Oscillation and neutral years in the Colombian Andes

Acero. I,C[1]
Vieira. S,C[2]

E-mail: cristina.acero@udea.edu.co
E-mail: sara.vieira@udea.edu.co

[1]Estudiante de Maestría en Ingeniería Ambiental, Grupo de Investigación y Gestión Ambiental
[2]Grupo de Investigación y Gestión Ambiental (GIGA). Escuela Ambiental, Facultad de Ingeniería, Universidad de Antioquia.

Abstract

Extreme precipitation and temperature events (EPTE) cause devastating impacts on ecosystems and society. The diversity of climates worldwide does not allow a single definition of extreme events, given the multiplicity of conditions in which each event develops. In regions of complex topography, interactions with vegetation have numerous atmospheric circulation patterns and various phenomena at different spatial and temporal scales, which prevents homogeneity of distribution, frequency, and intensity of extreme events. It is known that El Niño Southern Oscillation (ENSO) influences the interannual variability of precipitation and temperature in different regions around the world. However, it is unclear how this phenomenon interacts with the frequency and intensity of EPTE in areas with complex topography gradients and diverse climates. Here we focus on the Colombian Andes Mountain range in northern South America because it occupies a quarter of the territory, gathers most of the socio-economic development, and concentrates most of the country's population. This work uses statistical analysis to characterize EPTE during La Niña, El Niño, and neutral years. We also compare the frequency and intensity of EPTE between La Niña and neutral years and El Niño and neutral years.

Correspondent author

Unlike other studies, we want to know if there is any increase pattern or decrease of EPTE when an ENSO phase is active. We discuss the months in which there is an increase or decrease in EPTE according to the interannual variability of precipitation and temperature, as well as the months in which there is a significant relationship between the sea surface temperature of the Niño 3.4 region with precipitation and temperature. Our results showed that the highest intensities and frequent extreme precipitation events occurred in the rainy seasons March-April-May and September-October-November for both the 95th and 99th percentile. The difference in the analysis showed that during the La Niña periods, extreme precipitation events are more frequent, but their localization is variable in time and space. The behavior of extreme temperatures are more marked from the most intense and frequent events occur during El Niño from January to March. These results provide the basis for the design of adaptation and mitigation policies in the face of natural variability and climate change and to improve hydrometeorological forecasts.

Keywords: extreme events, ENSO, climate variability, Andes.

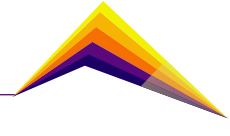

Introduction

The Colombian Andes, part of the extensive mountain range across South America, is influenced by numerous atmospheric circulation patterns and climatic phenomena at different scales due to complex interactions with topography and vegetation (Poveda, 2004). Moreover, the Andes occupy a quarter of Colombia's territory and are the main center of economic activity, containing most of the population (67%) (Etter & Wyngaarden, 2016). In this sense, the region's increased vulnerability to multiple natural hazards triggered by extreme precipitation and temperature events imposes a high cost in socio-economic terms.

Several studies show the effects of ENSO on precipitation and temperature variables, explaining the relationship between the ENSO phenomenon and the annual cycle of these variables; however, few studies have focused on analyzing the effect of this phenomenon on extreme events.

Negative precipitation anomalies are observed throughout most of the Colombian tropical Andes during El Niño (EN) events. Consequently, EN adversely impacts agriculture, energy production, water supply, and other economic activities. For example, the EN events of 1991 - 1992 and 2015 - 2016 produced significant impacts on society and considerable financial losses (Erfanian et al., 2017)with profound eco-hydrological and socioeconomic impacts. In 2015-2016, both regions were hit by another drought. Here, we show that the severity of the 2015-2016 drought (2016 drought hereafter. In contrast, La Niña (LN) stands out for heavy rains that cause flooding, landslides, and mudflows, to name a few.

This research aims to study the influence of the ENSO phenomenon on extreme precipitation and temperature events in the Colombian Andes. Therefore, the general question summarizing the problem is: How does ENSO affect extreme rainfall and temperature events in the Colombian Andes? Thus, it is essential to define an extreme event for this study, to characterize the EPTE during EN, LN, and neutral years, and to compare the occurrence of EPTE between the active phases of ENSO and the neutral phase.

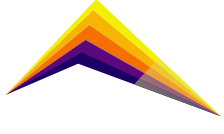

Methodology

This study was performed in northern South America (Figure 1), the thresholds of 95th and 99th percentiles were chosen to characterize extreme daily precipitation events. Moreover, the threshold of the 90th percentile was used to characterize extreme daily temperature events. Characterization was performed using a satellite-based precipitation product, which is uncertain in regions of complex topography like the Andes (Barlow et al., 2019; Condom et al., 2020).

The Tropical Rainfall Measuring Mission (TRMM-3B42-V7) Multi-satellite Precipitation Analysis (TMPA) product was used to identify extreme daily precipitation events (Huffman et al., 2010). This product has a spatial resolution of 0.25°, data since 1998, and is available at https://gpm.nasa.gov/data/directory. On the other hand, the daily temperature at 2m from the European Centre for Medium-Range Weather Forecasts reanalysis 5th generation - ERA5, which has a resolution of 0.25°, was used to identify extreme temperature events; this database has a record since 1981.

The purpose of this study is to characterize EPTE in the active phases of ENSO. We used the Oceanic Niño Index (ONI) (https://origin.cpc.ncep.noaa.gov/products/analysis_monitoring/ensostuff/ONI_v5.php) to classify La Niña, El Niño, and neutral year events. Based on the ONI index, we estimated two types of composites using the intensity and frequency of EPTE during LN, EN, and neutral years. The first consists of the monthly combination and the second is estimated considering the totality of the events. On the other hand, the differences between ENSO and neutral years and LN and EN were calculated to determine during which event the extremes increase or decrease. The parametric t-test was used to determine the significance of the differences.

Results and analysis

The study of extreme events in the northern region of South America has focused mainly on the evaluation of trends in the context of climate change. However, there is a lack of understanding of the spatial and temporal variability of these events in the Colombian Andean region, and it is not clear if these events are affected by synoptic-scale phenomena such as ENSO. Figure 1a shows the combination of precipitation intensity for the 95th percentile during EN, LN, and neutral years for the September - October - November quarter. The spatial pattern is generally similar for the warm, cold, and neutral stages. In the Andean region, the intensity values present little variability and lower magnitudes compared to the surroundings, such as the Pacific coast. The low values in the Andes may be due to problems in the precipitation representation in the inter-Andean valleys by the TRMM database. On the other hand, results showed that the spatial pattern is similar to the one depicted in the 99th percentile (not shown).

Analysis of precipitation frequency for the 95th percentile shows that extreme events are more frequent during LN events than during EN or neutral events (Figure 1b). Moreover, the difference analysis shows significant values for LN event (Figure 1c). The positive values for LN-neutral and LN-EN differences indicate that more extreme events characterized at the 95th percentile occurred during LN than during EN or neutral years. It is worth noting that the positive values cover the entire study region. These magnitudes are similar when monthly values are analyzed. The pattern also holds for the 99th percentile (not shown). In contrast, precipitation intensity values show high heterogeneity throughout the region.

Figure 2a shows the composite of temperature intensity for the 90th percentile during LN, EN, and neutral years for the December - January - February quarter. Temperature intensity is lower in the Andean region than in the inter-Andean valley region. This pattern is affected by the inadequate representation of the temperature variable in high-altitude areas in ERA5. Additionally, the spatial pattern of temperature intensity is similar during the LN, EN, and neutral events. On the other hand, the high values of extreme events in the Colombian northern area and the Colombian and Venezuelan plains are not worthy.

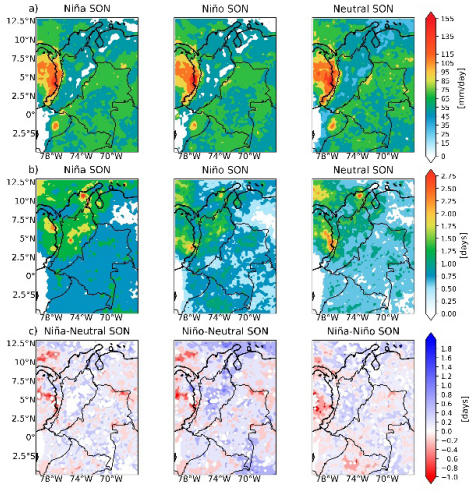

Figure 1. Characterization of extreme precipitation events 95th percentile. **a)** Intensity, **b)** frequency, and **c)** difference between ENSO - neutral years and LN-EN with 95% CI. The shading in Figures **1a** and **1b** means that there was no extreme event in the season and area plotted.

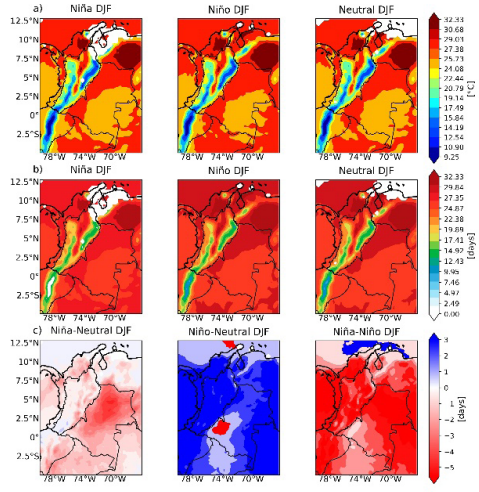

Figure 2. Characterization of extreme temperature events 90th percentile. **a)** Intensity, **b)** frequency, and **c)** difference between ENSO - neutral years and LN-EN with 95% CI. The shading in Figures **2a** and **2b** means that there was no extreme event in the season and area plotted.

The frequency of extreme temperature events shows that during ENSO there is a high activity of extremes in the eastern Andes and the Colombian plains (Figure 2b). Figure 2c shows the difference between EN-neutral years and LN - EN. Positive values in LN-EN indicate a higher extreme temperature events frequency for EN. Negative values between LN – EN also indicate a higher frequency of events for EN.

The results presented above showed that the precipitation and temperature extremes depict a pattern consistent with the temporal behavior of dry and rainy seasons in the Andes region. In addition, the effect of ENSO in these seasons is consistent with Poveda et al. (2011) findings. Figures 3a and 3b show intensity and frequency composites for precipitation events. LN, EN, and neutral years display higher intensities on the Pacific coast and lower in the Andes. However, frequency values indicate that during LN, there is an increased activity of extreme precipitation events in the Andes and lower frequency values in EN and neutral years.

Consequently, Figures 4a and 4b show the composites for extreme temperature. The inter-Andean valley region shows higher values of extreme temperature. However, the spatial pattern of magnitudes in the Andes and surroundings is similar in ENSO and neutral years. The frequency composite presented in Figure 4b shows a higher number of events during EN than during LN and neutral years.

Conclusions or summary

We characterized precipitation and temperature extremes using the 95th and 99th percentiles for precipitation and the 90th percentile for temperature. Results show that intensity values for extreme precipitation and temperature events have a similar pattern for EN, LN, and neutral years. However, frequency values show a different pattern, since, during LN, a larger number of extreme precipitation events occur compared to EN or neutral years. Furthermore, frequency temperature values are lower during LN and neutral years; on the contrary, during EN increases the frequency of events. The composite analysis gives us information on the spatial distribution of the events in intensity and frequency.

Our results show that extreme precipitation and temperature events are more frequent during ENSO. However, these events are not necessarily more intense when interannual variability phenomena such as ENSO occur. The increase in the frequency of precipitation and temperature extremes is an effect of natural variability and cannot avoid adverse impacts on population; however, understanding the phenomenon will allow the implementation of risk management plans focused on adaptation and disaster prevention.

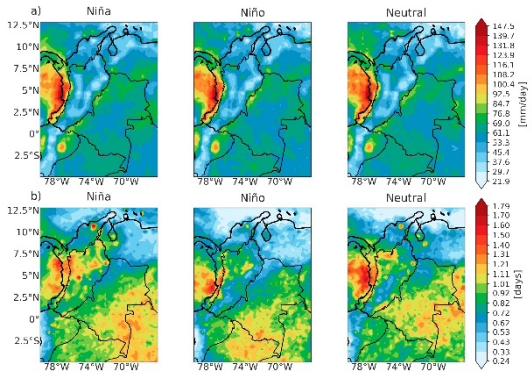

Figure 3. Composite analysis of extreme precipitation events for the 95th percentile during El Niño, La Niña, and neutral years, **a)** intensity and **b)** frequency.

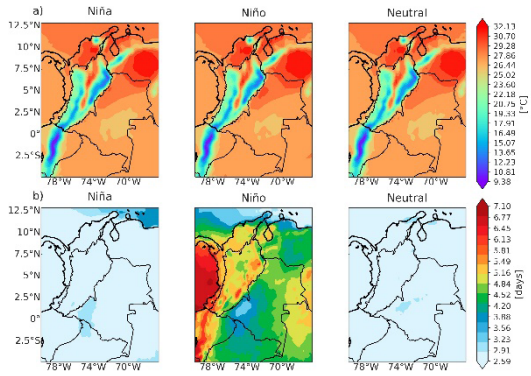

Figure 4. Composite analysis of extreme temperature events for the 90th percentile during El Niño, La Niña, and neutral years, **a)** intensity and **b)** frequency.

References

[1] Barlow, M., Gutowski, W. J., Gyakum, J. R., Katz, R. W., Lim, Y. K., Schumacher, R. S., Wehner, M. F., Agel, L., Bosilovich, M., Collow, A., Gershunov, A., Grotjahn, R., Leung, R., Milrad, S., & Min, S. K. (2019). North American extreme precipitation events and related large-scale meteorological patterns: a review of statistical methods, dynamics, modeling, and trends. *Climate Dynamics*, *53*(11), 6835–6875. https://doi.org/10.1007/s00382-019-04958-z

[2] Condom, T., Martínez, R., Pabón, J. D., Costa, F., Pineda, L., Nieto, J. J., López, F., & Villacis, M. (2020). Climatological and Hydrological Observations for the South American Andes: In situ Stations, Satellite, and Reanalysis Data Sets. *Frontiers in Earth Science*, *8*(April). https://doi.org/10.3389/feart.2020.00092

[3] Erfanian, A., Wang, G., & Fomenko, L. (2017). Unprecedented drought over tropical South America in 2016: Significantly under-predicted by tropical SST. *Scientific Reports*, *7*(1), 22–24. https://doi.org/10.1038/s41598-017-05373-2

[4] Etter, A., & Wyngaarden, W. van. (2016). Patterns of Landscape Transformation in Colombia , with Emphasis in the Andean Region Patterns of Landscape Transformation in Colombia , with Emphasis in the Andean Region. *Royal Swedish Academy of Sciences*, *29*(June), 432–439.

[5] Huffman, G. J., Adler, R. F., Bolvin, D. T., & Nelkin, E. J. (2010). The TRMM Multi-Satellite Precipitation Analysis (TMPA). In M. Gebremichael & F. Hossain (Eds.), *Satellite Rainfall Applications for Surface Hydrology* (pp. 3–22). Springer Netherlands. https://doi.org/10.1007/978-90-481-2915-7_1

[6] Marengo, J. A., Jones, R., Alves, L. M., & Valverde, M. C. (2009). Future change of temperature and precipitation extremes in South America as derived from the PRECIS regional climate modeling system. *International Journal of Climatology*, *29*(15), 2241–2255. https://doi.org/10.1002/joc.1863

[7] Poveda, G. (2004). LA HIDROCLIMATOLOGÍA DE COLOMBIA : *Revista de La Academia Colombiana de Ciencias Exactas, Fisicas y Naturales*, *January 2004*.

[8] Poveda, G., Álvarez, D. M., & Rueda, Ó. A. (2011). Hydro-climatic variability over the Andes of Colombia associated with ENSO: a review of climatic processes and their impact on one of the Earth's most important biodiversity hotspots. *Climate Dynamics*, *36*(11–12), 2233–2249. https://doi.org/10.1007/s00382-010-0931-y

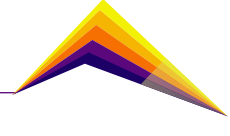

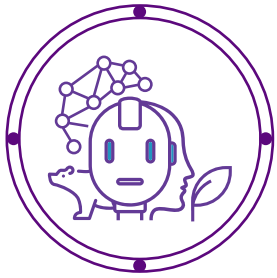

Life cycle analysis of a perovskite photovoltaic mini-module developed in Colombia with a PIN meso-superstructured configuration

Camilo A. Valderrama Benítez[1] *E-mail: candres.valderrama@udea.edu.co*
Francisco José Molina Péreza[1] *Email: francisco.molina@udea.edu.co.*
Juan Felipe Montoya Arango[2]
Jaime-Andrés Becerra[3]
Aída Luz Villa[3]
Diana Catalina Rodríguez[4]

[1]Universidad de Antioquia, Facultad de ingeniería, Escuela ambiental, Grupo de Investigación en Gestión y Modelación Ambiental (GAIA), Medellín, Colombia, 050010.
[2]Universidad de Antioquia, Facultad de ingeniería, Departamento de ingeniería de materiales, Grupo Centro de Investigación, Innovación y Desarrollo de Materiales (CIDEMAT), Medellín, Colombia, 050010.
[3] Universidad de Antioquia, Facultad de ingeniería, Departamento de ingeniería de química, Grupo Catálisis Ambiental, Medellín, Colombia, 050010.
[4] Universidad de Antioquia, Facultad de ingeniería, Escuela ambiental, Grupo Diagnóstico y Control de la Contaminación (GDCON), Medellín, Colombia, 050010.

Abstract

This paper presents a cradle–to–door Life Cycle Analysis (LCA) of a Perovskite Solar Cell (PSC) mini-module with meso-superstructured PIN architecture developed by the CIDEMAT group of the University of Antioquia. The evaluation of the environmental impact of manufacturing 1 cm2 active cell area showed that the layer with the highest impact is the electrode layer due to the use of silver; a mineral that has been linked to high environmental impact because of the associated extraction and purification processes. Additionally, the largest contributor is the energy requirement in all layers; this high contribution is generated through the disposal methods used in the laboratory such as spin coating and thermal evaporation. In this case, the substances with the greatest contribution were isopropanol, indium, and distilled water. The environmental impact

Correspondent author

categories with significant contributions are ranked from highest to lowest: freshwater ecotoxicity, human carcinogenic and non-carcinogenic toxicity, and depletion of mineral, fossil and renewable resources. Finally, the layers that had the least contribution in the evaluated categories were the hole transport layer, alumina support layer, and electron transport layer. For this type of architecture, the energy requirement may be the main limiting factor due to its relevance in the environmental impact categories. The requirement to implement other types of materials for the back electrode layer and the modification of the amount of substances used compared to other commercial cells is highlighted herein.

Keywords: Perovskite Solar Cell, Life Cycle Analysis, PIN architecture.

Introduction

Perovskite Solar Cells (PSC) are part of the third generation of photovoltaic technologies and are characterized by their low manufacturing cost and high conversion efficiency, reaching values of 25.2%. [1,2]. There are two PSC architectures, the conventional structure of PSC - referred to as regular Negative-Intrinsic-Positive (NIP) - consists of a glass substrate coated with Fluorine-Doped Tin Oxide (FTO) or Indium-doped Tin Oxide (ITO) that collects electrons and is known as a Forward Electrode Layer (FEL), an Electron Transport Layer (ETL), a Perovskite layer (PER) that serves as a light absorber, a Hole Transport Layer (HTL), and a back-electrode layer (BEL). In the second type of structure, the positions of the ETL and HTL layer are exchanged and it is called inverted structure or Positive-Intrinsic-Negative (PIN). Both architectures can be mesoporous or flat. [3,4].

The most used cells are the NIP-type architecture. These are easy to process and currently report the highest energy conversion efficiency, which may be attributed to the fact that the PIN architecture still has a lower open circuit voltage [5,6]. The meso-superstructured PIN architecture presents multiple advantages such as better film deposition, low temperature in the manufacturing processes (< 150 °C), low operating cost, and efficiencies of up to 22.3 % [7,8,9]. However, the environmental impact of this type of architecture needs to be understood since potentially toxic, rare, and expensive materials are used in the process. LCA is an environmental management tool that allows quantifying, analyzing, and comparing the environmental impact caused by the manufacture of a PSC [10]. Based on the above analysis, CIDEMAT, a research group of the University of Antioquia, proposed to conduct the LCA of a PSC mini-module - which corresponds to a meso-superstructured pin solar cell architecture; the discrete environmental impact was estimated by layer.

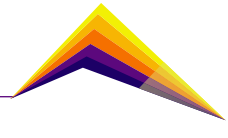

Methodology

The LCA was carried out using SimaPro 9.2.0.2, following the guidelines established in ISO 14040 and 14044 (2006) for its structuring and implementation. The determined scope of this study ranges from the phase of acquisition of raw material to the manufacture of the cell (cradle-to-door), the functional unit of study was indicated as 1 cm2 of PSC active area. The quantification of the environmental impact assumed that 90%of the material used in the manufacturing method is disposed of by spin coating and the remaining 10%, through thermal evaporation. The transport in all phases was excluded [11].

The primary data, in terms of matter and energy required for the manufacturing process, was provided by the CIDEMAT group [12]. When primary data was not available, it was extracted from Ecoinvent 3.8 database and scientific literature. If the information on materials or processes that contributed less than 5% of the mass, cost, or impact of the cell was not available, it was not considered. [13]. The International Life Cycle Data System (ILCD) method was used to calculate the environmental impact in this study; 10 environmental categories were selected: Climate Change (CC), Human Carcinogenic Toxicity (HTC), Human Non-Carcinogenic Toxicity (HNTC), Particulate Matter (PM), Acidification (Ac), Freshwater Eutrophication (FE), Water Ecotoxicity (WE), Land Use (LU), Water Resource Depletion (WRD), Mineral Resource Depletion, Fossils and Renewables (MRDFR). In addition, the environmental impact of using the Globe Box (GB) to manufacture Perovskite and the Alumina Support Layer (ASL) was quantified.

Results and analysis

The environmental impact of the extraction process, raw material handling, and manufacturing of 1 cm2 of PSC was obtained across 10 categories. The results were characterized by the impact of the layer that integrates the PSC, and normalized for the manufacturing of PSC as a whole (see Table 1). This evaluation identified the most significant impact – from highest to lowest – in the following order: WE, HTC, MRDFR, and HNCT respectively.

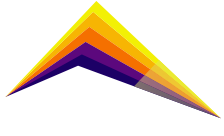

Table 1. Environmental impact of manufacturing 1 cm^2 PSC, discriminated by layers.

Category from impact	Unit	FEL	HTL	ASL	PER	ETL	BEL	GB	Total	Total Normalized
CC	kg CO_{2eq}	2.51E-03	2.20E-05	1.33E-05	6.05E-04	2.42E-04	6.49E-03	5,29E-03	1,52E-02	1,65E-06
HNCT	CTUh	6.36E-10	5.65E-12	4.00E-12	1.71E-10	3.65E-11	1.32E-09	8.79E-10	3.06E-09	5.73E-06
HTC	CTUh	1.21E-10	1.00E-12	2.31E-12	2.39E-11	7.50E-12	2.67E-10	1.82E-10	6.05E-10	1.64E-05
MP	kg $PM_{2.5\ eq}$	1.36E-06	1.51E-08	8.32E-09	3.93E-07	1.42E-07	2.73E-06	2.31E-06	6.96E-06	1.83E-06
Ac	molc $H+_{eq}$	1.53E-05	2.70E-07	9.59E-08	4.23E-06	1.10E-06	4.59E-05	3.89E-05	1.06E-04	2.24E-06
FE	kg P eq	8.13E-07	5.37E-09	4.06E-09	1.58E-07	4.85E-08	1.41E-06	9.40E-07	3.37E-06	2.28E-06
WE	CTU_e	5.28E-02	9.97E-04	5.88E-04	7.49E-03	2.46E-03	2.73E-01	1.80E-01	5.17E-01	5.92E-05
LU	kg C deficit	1.79E-03	1.26E-05	9.31E-06	4.81E-04	1.98E-04	2.99E-03	2.03E-03	7.50E-03	1.00E-07
WRD	m^3 water eq	2.33E-05	1.29E-08	9.58E-09	1.05E-06	4.51E-07	2.60E-06	2.15E-06	2.95E-05	3.63E-07
MRDFR	kg Sb eq	6.45E-07	4.23E-10	1.03E-09	1.39E-07	2.42E-09	1.41E-07	3.96E-08	9.68E-07	9.58E-06

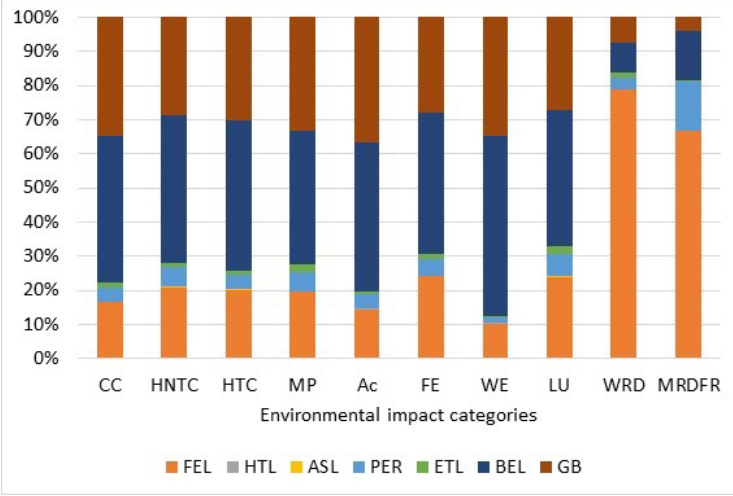

Figure 1. Results of cradle-to-gate environmental impacts of manufacturing a solar cell with an active area of 1 cm^2.

The fact that the most significant categories are toxic impact on freshwater aquatic species and impact on human health. This demonstrates the influence that can be caused by the manufacture of these cells. In the case of WE, the layers that generated the highest impact are BEL, GB, and FEL with 52.8%, 34.8%, and 10.2%, respectively (see Figure 1). This is attributed - upon further analysis within the SimaPro tool-b - mainly to the use of energy (93 %), indium (1.72 %), silver (1.26 %), deionized water (0.68 %), acetonitrile (0.57 %), isopropanol (0.45 %) and other processes.

In the case of HTC and HNCT, a similar behavior in the contribution of the layers was observed, with the BEL, GB, FEL, and PER layers being the largest contributors with an average value of 43.7%, 29.4%, 20.4%, and 4.78%, respectively. It was determined that this is mainly attributed to the use of energy for HTC and HNCT, with 80.3% and 74.7% respectively. For both categories, the substances that contribute the most are indium, isopropanol, diethyl ether, silver, acetone, deionized water, and acetonitrile among others.

Finally, the MRDFR category represents a relevant contribution due to the FEL (66.7 %), BEL (14.5 %), and PER (14.3 %) layers. Upon detailed review, it was found that the use of indium is the main contributor with 57.1 %, followed by electricity (10.2 %), silver (8.98 %), lead (6.47 %) diethyl ether (6.08 %), and isopropanol (5.7 %). The results presented for the evaluated categories are in agreement with those reported in the literature [11,12,14].

Conclusions or summary

This study identified the BEL layer as the layer that generates the highest environmental impact due to the use of a silver cathode. On the other hand, the process that has the highest contribution is the use of GB in most layers. Among all categories, the energy requirement was the main contributor, except in the MRDFR category. The use of chemical substances presents a higher contribution in the toxicity categories excluding lead, that had a contribution close to zero except in MRDFR. These results enable the identification of materials or processes that can be optimized from an environmental and technical perspective and exacerbates the need to establish a comparison amongst solar cells to estimate their environmental competitiveness.

Acknowledgment

The authors would like to express their gratitude to the Colombian Scientific Program for the financial support provided within the framework of the Scientific Ecosystem call for proposals (Contract No. FP44842-218-2018).

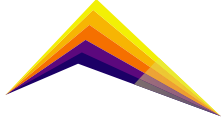

References

[1] Jeong, J., Kim, M., Seo, J., Lu, H., Ahlawat, P., Mishra, A., ... & Kim, J. Y. (2021). Pseudo-halide anion engineering for α-FAPbI3 perovskite solar cells. Nature, 592(7854), 381-385.

[2] Peters, I. M., Gallegos, C. D. R., Sofia, S. E., & Buonassisi, T. (2019). The value of efficiency in photovoltaics. Joule, 3(11), 2732-2747.

[3] Momblona, C., Gil-Escrig, L., Bandiello, E., Hutter, E. M., Sessolo, M., Lederer, K., ... & Bolink, H. J. (2016). Efficient vacuum deposited pin and nip perovskite solar cells employing doped charge transport layers. Energy & Environmental Science, 9(11), 3456-3463.

[4] Hussain, I., Tran, H. P., Jaksik, J., Moore, J., Islam, N., & Uddin, M. J. (2018). Functional materials, device architecture, and flexibility of perovskite solar cell. Emergent Materials, 1(3), 133-154.

[5] Best Research-Cell Efficiencies Chart. Available online: https://www.nrel.gov/pv/assets/pdfs/best-research-cell-efficiencies-rev220630.pdf (accessed on 16 July 2022).

[6] Lemercier, T., Perrin, L., Planès, E., Berson, S., & Flandin, L. (2020). A Comparison of the Structure and Properties of Opaque and Semi-Transparent NIP/PIN-Type Scalable Perovskite Solar Cells. Energies, 13(15), 3794.Garrett, D. L. (2003). "Coupled analysis of floating production systems." Proc., Int. Symp. on Deep Mooring Systems, ASCE, Reston, VA, 152-167.

[7] Haider, S. Z., Anwar, H., Manzoor, S., Ismail, A. G., & Wang, M. (2020). A theoretical study for high-performance inverted pin architecture perovskite solar cells with cuprous iodide as hole transport material. *Current Applied Physics*, *20*(9), 1080-1089.

[8] Dagar, J., Fenske, M., Al-Ashouri, A., Schultz, C., Li, B., Köbler, H., ... & Unger, E. (2021). Compositional and interfacial engineering yield high-performance and stable pin perovskite solar cells and mini-modules. ACS applied materials & interfaces, 13(11), 13022-13033.

[9] Saxena, K., Gayathri, J., Gupta, N., & Mehta, D. S. (2022). Progress in Organic-Inorganic Hybrid Perovskite Solar Cells: Architecture, Efficiency and Stability. Indian Journal of Pure & Applied Physics (IJPAP), 60(4), 367-376.

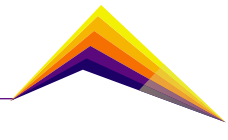

[10] Vidal, R., Alberola-Borràs, J. A., Sánchez-Pantoja, N., & Mora-Seró, I. (2021). Comparison of Perovskite Solar Cells with other Photovoltaics Technologies from the Point of View of Life Cycle Assessment. Advanced Energy and Sustainability Research, 2(5), 2000088.

[11] Gong, J., Darling, S. B., & You, F. (2015). Perovskite photovoltaics: life-cycle assessment of energy and environmental impacts. Energy & Environmental Science, 8(7), 1953-1968.

[12] Ramirez, D., Velilla, E., Montoya, J. F., & Jaramillo, F. (2019). Mitigating scalability issues of perovskite photovoltaic technology through a pin meso-superstructured solar cell architecture. Solar Energy Materials and Solar Cells, 195, 191-197.

[13] Krebs-Moberg, M., Pitz, M., Dorsette, T. L., & Gheewala, S. H. (2021). Third generation of photovoltaic panels: A life cycle assessment. Renewable Energy, 164, 556-565.

[14] Espinosa, N., Serrano-Luján, L., Urbina, A., & Krebs, F. C. (2015). Solution and vapour deposited lFE perovskite solar cells: Ecotoxicity from a life cycle assessment perspective. Solar Energy Materials and Solar Cells, 137, 303-310.

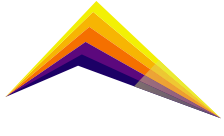

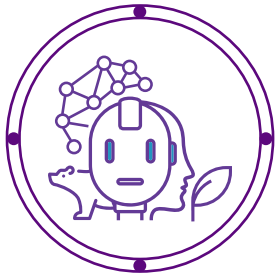

Mathematical model for the tactical planning of the supply chain of supplementary cementitious materials

Camacho, Camila[1] — *Email: camila.camacho@udea.edu.co*

Álvarez, Germán[2] — *Email: juan.villegas@udea.edu.co*

Villegas, Juan G.[1] — *Email: germanalvarez@itm.edu.co*

[1] *Universidad de Antioquia, Medellín, Colombia. Grupo ALIADO, Analítica e Investigación para la toma de decisiones.*

[2] *Instituto Tecnológico Metropolitano, Medellín, Colombia. Grupo de Investigación Calidad, Metrología y Producción.*

Abstract

In recent years, the technical feasibility and sustainability benefits of including biomasses as supplementary cementitious materials have been demonstrated. Due to the physical and chemical characteristics (pozzolanic properties) of these materials, they can be used efficiently to produce economic and sustainable concrete. However, challenges such as costs, plant location, distances between origins/destinations, and waste availability over time persist. The existing literature shows there is no research focused on supply chains of biomasses as supplementary cementitious materials that consider stochasticity comes from seasonal crops and uncertain volumes. This work seeks to plan the supply chain necessary to take advantage of biomasses as additional cementing materials considering the seasonality and uncertainty associated with the supply of these wastes, therefore we propose an optimization model for the decision-making of material quantity to be sent from each biomass between the process nodes and their storage over regular periods, considering the load and transport capacities of each of the processes, and meeting the minimum demand. Finally, it seeks to analyze and evaluate different scenarios of supply chain operation to determine the relevant

Correspondent author

characteristics and possible economic and environmental benefits of using rice husk, cane bagasse, and palm rachis simultaneously in Colombia.

Currently, the model adequately incorporates multiple residues, but uncertain parameters are in development.

Keywords: Supply chain, Mixed integer linear programming, Biomass, Supplementary cementitious materials

Introduction

Concrete is the most used artificial material in the world, and the most used in the construction sector (Jin et al., 2015). This is obtained from a mixture of fine and coarse aggregates, some additives, water, and cement (Aprianti S, 2017). Globally, the cement industry contributes 5-10% of total anthropogenic greenhouse gas emissions, and 12-15% of total industrial energy use (Hossain et al., 2018).

One strategy aimed at reducing the emissions generated by this industry is the use of supplementary cementitious materials (SCM) that come from other industries' wastes. It is also possible to obtain SCM from biomasses such as oil palm ashes, cane bagasse, wood waste, bamboo leaves, wheat straw, corn cob, or rice husk (Aprianti S, 2017).

Despite the interest in exploring different alternatives for SCM from biomasses, preview research has not focused on the supply chain (SC) that takes advantage of these wastes in concrete production. For this reason, we carried out this work for the design of an SC that uses biomasses as SCM with optimization models. Three residues are considered: (i) rice husk, (ii) cane bagasse, and (iii) palm rachis, which, as shown in Figure *1*, are grown in different areas of Colombia.

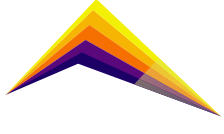

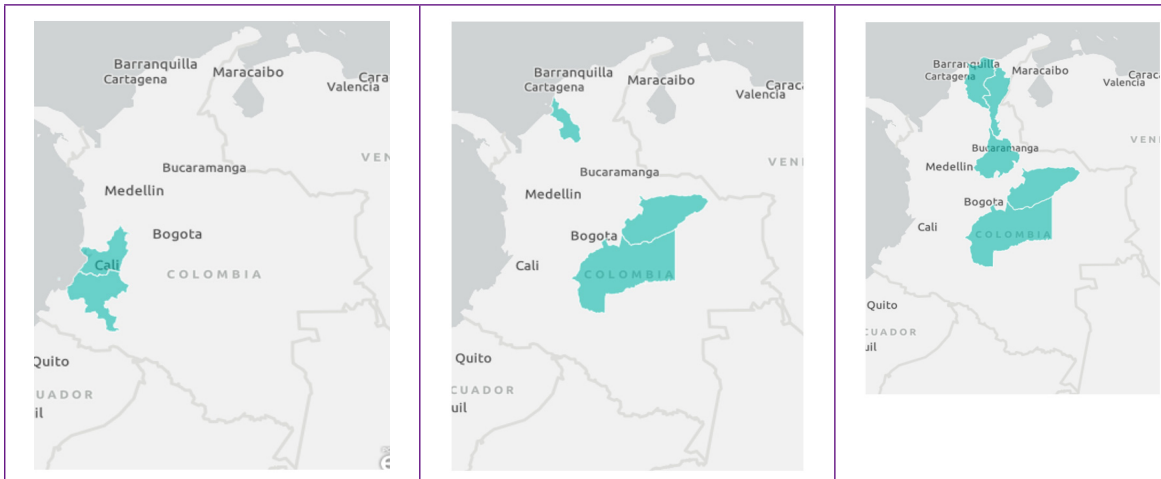

Cane Bagasse	Rice husk	Palm Rachis

Figure 1. Geographical dispersion of biomasses for the production of SCM.
Source: Múnera et al., (2020)*donde se destacan las emisiones de CO2. Como alternativa para reducir las emisiones, esta industria explora el reemplazo de sus componentes por materiales alternativos. En este trabajo se utiliza el Proceso Analítico Jerárquico (AHP.*

Related to the literature review, we consulted works from 2009 to 2021 in the Scopus database, analyzed ninety-one papers related to the optimization of biomass supply chains that considered stochastic parameters mainly in the International Journal of Production Economics, Computers and Industrial Engineering, and the Journal of Cleaner Production, among others, and found that stochastic programming is a predominant method to treat uncertainty, followed by Robust Optimization and Simulation. In recent years, Stochastic Optimization stands out, as well as the use of multiple solution methods for the different stages of the supply chain design.

Through the literature review, we could verify there is a research opportunity associated with the planning of a supply chain of supplementary cementitious materials that consider stochasticity coming from waste availability, due to its seasonality and uncertain volume.

Materials and Methods

SCM Supply Chain

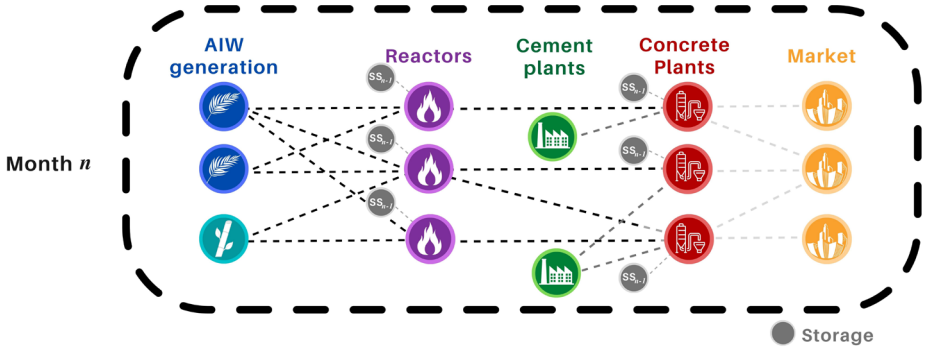

Figure 2. Supply chain to produce SCM

The biomass supply chain that will be considered as SCM begins with the generation of these wastes: palm rachis, cane bagasse, and rice husk, which are generated in different geographical areas of the country. They are then moved to some reactors in which the biomasses are transformed into ash (Supplementary Cementitious Material). After this process, the Material is taken to the concrete plants where is received SCM and conventional concrete from the cement plants.

Finally, the chain considers the markets as a parameter that it seeks to meet, despite not making tactical decisions on transportation between concrete plants and markets.

Mathematical Model

Through this model, the aim is to minimize the total costs of the chain. For this, the following sets are considered: AIW type ($a \in A$), where AIWs are generated ($w \in W$), planning periods ($t \in T$), supply chain nodes ($n \in N$), locations of the reactors ($r \in R$), cement plants ($k \in K$) and concrete plants ($p \in P$).

The parameters that vary through time $t \in T$ are: AIW purchase cost ($AICOST_{at}$ [$/ton]), amount of AIW generated at each location $w \in W$ (Q_{awt} [ton]) and concrete demand (DEM_t [ton]); while those that remain constant are: fixed storage cost of AIW at nodes $n \in N$ ($CALM_n$ [$/ton]), safety stock at nodes $n \in N$ ($SSEG_n$ [ton]), Conversion rate of AIW to SCM in the reactors ($RCONV_a$ [%]), unit cost of converting AIW to SCM (UNITCOST_a [$/ton]), reactor capacity $r \in R$ ([[CAP]]_r [ton]), cement plant production capacity $k \in K$ (CEM_CAP_k [ton]), unit production

cost per ton of cement in the cement plant $k \in K$ (CEM_COST_k [$/ton]), cement consumption per cubic meter of concrete produced without SCM and with SCM ($CON_CEMCONV$ y CON_CEMSCM [ton/m^3]), SCM consumption per cubic meter of concrete ($CONS\_SCM$ [ton/m^3]), production capacity of each concrete plant $p \in P$ (CON_CAP_p [m_3]), unit production cost per cubic meter of conventional concrete in each concrete plant $p \in P$ (CON_COCOST_p [$/$m^3$]), Unit production cost per cubic meter of concrete with SCM in each concrete plant $p \in P$ ($CON\_SCMCOST_p$ [$/$m^3$]), distances between sources of AIW and reactors ($DIST_{wr}$ [km]), cost per ton of AIW transported per km between sources and reactors ($COSTT$ [$/(ton*km)), distance between each location ion of reactors $r \in R$ and each concrete plant $p \in P$ ($DISTA_{rp}$ [km]), cost per ton of SCM transported per km between reactors and concrete plants ($COSTTR$ [$/(ton*km)]), distance between the cement plant $k \in K$ and the concrete plant $p \in P$ ($DISTAN_{kp}$ [km]) and the cost per ton of cement transported per km between the cement plants and the concrete plants ($COSTTRA$ [$/(ton*km)])

All the decision variables can vary through time $t \in T$: amount of AIW $a \in A$ to buy at each source $w \in W$ (q_{awt} [ton]), amount of SCM $a \in A$ to store at node $n \in N$ (alm_{ant} [ton]), amount of AIW $a \in A$ to be sent from each source $w \in W$ to each reactor $r \in R$ ($sent_{awrt}$ [ton]), binary variable that shows if an AIW $a \in A$ is received in each reactor $r \in R$ ($aireac_{art}$ [-]), Amount of AIW $a \in A$ o be processed in each reactor $r \in R$ ($proc_{art}$ [ton]), Amount of SCM to be sent from each reactor $r \in R$ to each concrete plant $p \in P$ ($sentt_{rpt}$ [ton]), Quantity of cement to be shipped from each cement plant $k \in K$ to each concrete plant $p \in P$ (sen_{kpt} [ton]), Quantity of conventional concrete to be manufactured in each plant concrete plant $p \in P$ ($conprod_{pt}$ [m_3]) and Quantity of concrete with SCM to be manufactured in each concrete plant $p \in P$ $e(conscm_{pt}$ [m^3]).

The objective is to minimize the total costs of the chain, so the objective function is Min

$$Z=Total\_Cost=\sum_{(i=1)}^{9}\sum_{t\in T}c_{it}$$

The total cost includes: the cost of acquiring AIW from each source during a period, the cost of transporting AIW between the sources and reactors during a period, the cost of processing each AIW in each reactor during a period, the cost of transporting the SCM from the reactors to the concrete plants during a period, the cost of production of the cement plants during a period, costs of transporting cement from the cement plants to the concrete factories during a period, the cost of manufacturing conventional concrete during a period, The cost of manufacturing concrete with SCM during a period and the cost of storage during a period.

$c_{1t}= \sum_{a\in A}\sum_{w\in W}AICOST_{at}*q_{awt}$

$c_{2t}=COSTT\ (\sum_{w\in W}\sum_{r\in R}DIST_{wr}*\ sent_{awrt})$

$c_{3t}=\sum_{a\in A}\sum_{r\in R}UNIT_{COSTa}*proc_{art}$

$c_{4t}= COSTTR\sum_{r\in R}\sum_{p\in P}DISTA_{rp}sentt_{rpt}$

$c_{5t}=\sum_{k\in K}\sum_{p\in P}CEM_{COSTk}*sen_{kpt}$

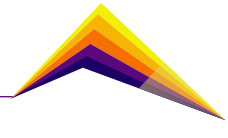

$c_{6t}=COSTTRA\sum_{k\in K}\sum_{p\in P}DISTAN_{kp}sen_{kpt}$

$c_{7t}=\sum_{p\in P}CON\_COCOST_{p}\ conprod_{pt}$

$c_{8t}=\sum_{p\in P}CON\_SCMCOST_{p}\ conscm_{pt}$

$c_{9t}=\sum_{n\in N}CALM_{n}\ alm_{ant}$

The restrictions present in the model are on the capacities of the processes: (1) AIW generation capacity, (2) Reactor capacity, (3) Production capacity in the cement plants and (4) Production capacity in the concrete plants; on balance restrictions: (5) The amount of AIW sent to the reactors must be equal to the amount of AIW purchased (6) The amount of AIW processed in each reactor must be equal to the amount received (7) Inventory balance in the reactors (8) Inventory balance in the concrete plants; on compliance with requirements: (9) The amount of cement received by each concrete plant must be sufficient for the manufacture of conventional concrete and with SCM, (10) The amount of SCM received in each concrete plant must be sufficient for the manufacture of concrete with SCM according to its formulation, (11) The amount of concrete produced by the plants must satisfy the market in general. Are:

$$q_{awt}\leq Q_{awt}\quad \forall\ a\in A,\forall\ w\in W,\forall\ t\in T \tag{1}$$

$$\sum_{a\in A}proc_{art}\leq CAP_{r}\ \forall\ r\in R,\forall\ t\in T \tag{2}$$

$$\sum_{p\in P}sen_{kpt}\leq CEM\_CAP_{k}\ \forall\ k\in K,\forall\ t\in T \tag{3}$$

$$conprod_{pt}+conscm_{pt}\leq CON\_CAP_{p}\quad \forall\ p\in P,\forall\ t\in T \tag{4}$$

$$\sum_{r\in R}sent_{awrt}=q_{awt}\ \forall\ w\in W,\forall\ t\in T \tag{5}$$

$$proc_{art}=\sum_{w\in W}sent_{awrt}\ \forall\ r\in R,\forall\ t\in T \tag{6}$$

$$\sum_{a\in A}alm_{a,r,t-1}+RCONV_{a}\sum_{a\in A}proc_{art}\geq\sum_{p\in P}sentt_{rpt}+SSEG_{r} \tag{7}$$

$$\sum_{a\in a}alm_{a,p,t-1}+\sum_{r\in R}sentt_{rpt}\geq\sum_{k\in K}sen_{kpt}+SSEG_{p}\ \forall\ p\in P,\forall\ t\in T \tag{8}$$

$$\sum_{k\in K}sen_{kpt}\geq CON\_CEMCONV\ conprod_{pt}+CON\_CEMSCM\ conscm_{pt}\ \forall\ p\in P,\forall\ t\in T \tag{9}$$

$$\sum_{r\in R}sentt_{rpt}\leq CONS\_SCM\ conscm_{pt}\quad \forall\ p\in P,\forall\ t\in T \tag{10}$$

$$\sum_{p\in P}conprod_{pt}+conscm_{pt}\geq DEM_{t}\quad \forall\ t\in T \tag{11}$$

Finally, the domain restrictions of the decision variables:

$$q_{awt}\geq 0\ \forall\ a\in A,\forall\ w\in W \tag{12}$$

$$alm_{ant}\geq 0\ \forall\ a\in A,\forall\ n\in N,\forall\ t\in T \tag{13}$$

$$sent_{awrt}\geq 0\ \forall\ a\in A,\forall\ w\in W,\forall\ r\in R,\forall\ t\in T \tag{14}$$

$$proc_{art}\geq 0\ \forall\ a\in A,\forall\ r\in R,\forall\ t\in T \tag{15}$$

$$sentt_{rpt}\geq 0\ \forall\ r\in R,\forall\ p\in P,\forall\ t\in T \tag{16}$$

$$sen_{kpt}\geq 0\ \forall\ k\in K,\forall\ p\in P,\forall\ t\in T \tag{17}$$

$$conprod_{pt}\geq 0\ \forall\ p\in P,\forall\ t\in T \tag{18}$$

$$[\![conscm]\!]\_pt\geq 0\ \forall\ p\in P,\forall\ t\in T \tag{19}$$

Data and Computational implementation

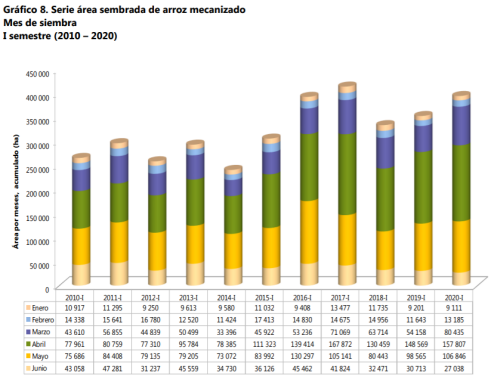

Figure 3. Source: DANE & FEDEARROZ, (2020) como parte del convenio entre las dos entidades, la Encuesta Nacional de Arroz Mecanizado (ENAM

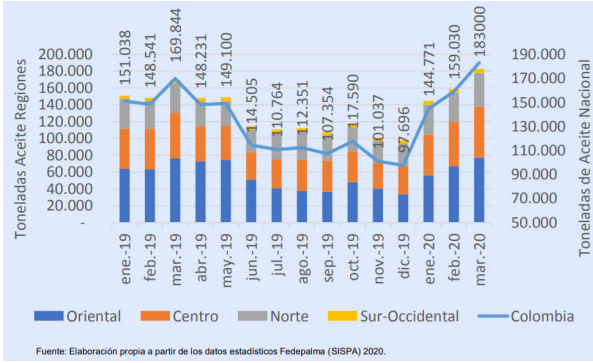

Figure 4. Source: Ministerio de Agricultura y Desarrollo Rural, (2020)

One of the characteristics of the biomass is seasonality and regionality, which is seen in Figure 3, with the planted area of mechanized rice from 2010 to 2020, and Figure 4 with the National production of palm oil during the first semester of 2019 in different regions of Colombia.

With this model, this characteristic of biomasses, whose production is variable over time, is properly incorporated. Nevertheless, the problem presented in this article has research opportunities that may be developed in the future related to the stochastic analysis of the origins of biomass, aimed at supporting strategic decision-making on the supply chain.

Conclusions and future work

In this model, we represent an algebraic procedure to obtain the minimum supply chain cost.

This document provides a model for the design of the supply chain necessary for the use of AIW as SCM in the production of concrete, considering the differences that may exist in some parameters in different periods, so the model is a multi-period mixed integer linear program that minimizes the operating costs of the Supply Chain.

The proposed model can also have applications in other areas in which the principle of multiple sources of resources in the supply chain is preserved, as well as a variable behavior over time.

Additionally, the opportunity for this model to be used in multiple contexts is presented, since it has the characteristic of incorporating multiple origins of the resources of the supply chain, which could be seen in other contexts as multiple suppliers of a resource located in different places.

For future research, it is proposed to study other optimization methods that adequately integrate the stochasticity of the parameters to the model and allow it to support strategic decision-making considering this.

Funding

This work was funded by Colombian Ministry for Science, Technology and Innovation-Minciencias- through the project 115080863589 (166-2019 contract).

References

[1] Álvarez, G., Jaramillo, L. Y., Pérez Blair, R., Vanegas, V., & Villegas, J. G. (2021). Designing the supply chain for supplementary cementitious materials from agro-industrial wastes with an optimization model.

[2] Aprianti S, E. (2017). A huge number of artificial waste material can be supplementary cementitious material (SCM) for concrete production – a review part II. Journal of Cleaner Production, 142, 4178–4194. https://doi.org/10.1016/j.jclepro.2015.12.115

[3] DANE, & FEDEARROZ. (2020). Boletín Técnico: Encuesta Nacional de Arroz Mecanizado. https://sioc.minagricultura.gov.co/DocumentosContexto/A964-bol_arroz_Isem20.pdf

[4] Hossain, M. U., Poon, C. S., Dong, Y. H., & Xuan, D. (2018). Evaluation of environmental impact distribution methods for supplementary cementitious materials. Renewable and Sustainable Energy Reviews, 82(May 2016), 597–608. https://doi.org/10.1016/j.rser.2017.09.048

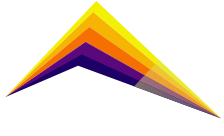

[5] Jin, R., Chen, Q., & Soboyejo, A. (2015). Survey of the current status of sustainable concrete production in the U.S. Resources, Conservation and Recycling, 105, 148–159. https://doi.org/10.1016/j.resconrec.2015.10.011

[6] Ministerio de Agricultura y Desarrollo Rural. (2020). CADENA DE PALMA DE ACEITE: Indicadores e Instrumentos. https://sioc.minagricultura.gov.co/Palma/Documentos/2020-03-30 Cifras Sectoriales.pdf

[7] Múnera, A., Álvarez, G., Villegas, J. G., Arango, K., Romero, M., Jaramillo, L., Martínez, J. D., & Arenas, C. (2020). Aplicación del proceso analítico jerárquico para la selección de residuos agroindustriales en la obtención de materiales cementantes suplementarios. XXXIII Encuentro Nacional de Docentes de Investigación Operativa.

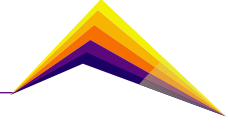

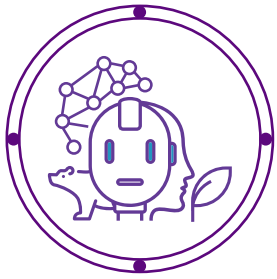

A Mixed Integer Linear Programming Model for Facility Location in Disaster Relief Operations Using Georeferenced Data

Kevin Palomino
Carmen Berdugo
David García

E-mail: krpalomino@unnorte.edu.co
E-mail: cberdugo@uninorte.edu.co
E-mail: davidgarciabarrios@gmail.com

Industrial Engineer, Universidad del Norte, Barranquilla, Colombia.
Industrial Engineer, Universidad del Atlántico, Colombia.

Abstract

A facility location model to support humanitarian logistics operations was designed using Mixed Integer Linear Programming, in which a finite number of demand nodes could be satisfied by a set of supply nodes, considering not only the costs related to these locations but also constraints aimed at complying with timely humanitarian attention in an operation of this type. Also, an integrated solution scheme was proposed, which includes the use of a GeoJSON API, along with a branch and cut algorithm. Subsequently, a case study was executed analyzing the operation of the water supply through water tanks during a natural disaster, which occurred in 2017 in Mocoa, Colombia. The results reflected positive effects on the prioritization of the average distance traveled and on the satisfaction of shelter demand, along with the costs associated with the implementation of the optimal solution.

Correspondent author

Keywords: Operation research; Optimization; MILP; Spatial analysis.

Introduction

Natural disasters are becoming more severe, conflict is on the rise, and populations across the world are being impacted by the global financial crisis, high food prices, energy and water shortages, population growth, and urbanization [1]. Humanitarian aid is a response to situations in which the security, rights, and well-being of certain communities, groups, or collectives are at risk. There are many important and successful contributions in the literature to treat emergencies in humanitarian logistics using different approaches. For instance, some authors solve location problems using an operation research approach based on the concept of the center of gravity method for the identification of the optimum location of a temporary or fixed facility in a certain geographic area [2]–[4]. In addition, some research is based on programming that investigated multi-criteria modeling frameworks for discrete stochastic facility location problems [5]–[7], or optimization models [8]–[10]. However, these designs are complex in large-scale humanitarian response efforts. This is a research gap because the location of facilities plays a fundamental role in synchronizing activities across the logistics network to facilitate a more agile response in any humanitarian aid situation. When considering the problem of locating facilities for humanitarian attention after a disaster situation, operational needs change on the fly as the emergency develops and multiple organizations open and close facilities in short time frames, considering dynamic needs and resource levels.

Therefore, the purpose of this article was to design a model for facility location in disaster relief operations, which would provide a realistic and effective solution for the design of a supply network. The design of the model was based on an integrated scheme involving a Mixed Integer Linear Programming (MILP) model solved using a branch and cut algorithm and input data related to distance values taken from the web mapping service developed by Google Maps. The results of the validation presented positive benefits in relation to implementing the proposed model for facilities located in disaster relief operations, proposing a methodology that considers a list of candidate facilities provided based on a prior analysis of the affected zone. Similarly, not only was it possible to establish in this allocation model a prioritization of the costs associated with this operation, but also constraints were considered oriented to the distance between supply and demand nodes and to the percentages of this satisfied demand, but also an integrated scheme that works synergistically with real data from a GIS system to collect distance information.

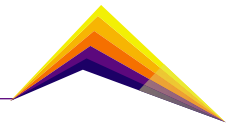

Methodology

The problem of designing a facilities network to support humanitarian logistics operations was analyzed considering a list of candidate locations, to avoid the unrealistic scenario of selecting these locations within a continuous surface by traditional methods such as the Center of Gravity or Weber's method. With these considerations in mind, this model was designed as an allocation model in which a finite number of demand nodes for humanitarian assistance could be satisfied by several supply nodes. Therefore, the goal was to find an optimized network of humanitarian aid facilities that satisfy the demand for a certain number of facilities in an area. Although these concepts may seem simple, solving an optimization problem of this type that involves real case studies can be a complicated task. If, for example, a humanitarian operation has 50 shelters dispersed in each area and has 10 candidate locations to open collection centers, it would be necessary to analyze 500 different combinations that may involve distance variables and demand flows. Therefore, an integrated solution scheme was proposed, focused on the design of a Mixed Integer Linear Programming Model (MILP) solved using a branch and cut algorithm. First, indexes ii and $j\,j$ were defined, denoting a specific supply node and a demand node, respectively. The arc of a node ii to a node jj is represented by the notation $x_{ij}\,x_{ij}$. In addition, there is a total of nn supply nodes and mm demand nodes. The objective function (zz) was defined to minimize total costs. The two most important components in deciding to open new facilities were considered: a fixed cost. (C_iC_i) incurred by locating or "opening" a supply node (B_iB_i) and a variable cost $c_{ij}c_{ij}$ depending on the flow through the arc. For example, $c_{ij}c_{ij}$ could be characterized by a transportation cost that depends on the number of emergency kits that are being delivered to a shelter. Then, this function assumes for all possible arcs, a particular cost multiplied by the flow through $x_{ij}x_{ij}$: $Min\ z = \sum_{i=1}^{n}\sum_{j=1}^{m} c_{ij}x_{ij} + \sum_{i=1}^{n} C_iB_iMin\ z = \sum_{i=1}^{n}\sum_{j=1}^{m} c_{ij}x_{ij} + \sum_{i=1}^{n} C_iB_i$. Equally important, B_iB_i is a binary variable. That means that it can only take two values, either 0 or 1. The model used this variable to indicate whether to open or not open a facility, and this is for all the ii nodes that are in the supply set. Now, this variable was added to the objective function, and it is multiplied by the fixed cost for opening an ii supply node. This could be for flow over a week, a month, a year, etc., then this fixed cost (C_iC_i) is the cost of opening this facility for that period. A supply constraint was also required. That is making sure that everything from the supply nodes does not exceed what is available there for all the ii nodes within the supply set (S_i)S_i): $\sum_{j=1}^{m} x_{ij} \le S_i\ \ \forall i \in S\sum_{j=1}^{m} x_{ij} \le S_i\ \ \forall i \in S$.

In the same way, a demand constraint ensures that all the flows coming into a certain $j\,j$ node must exceed or be equal to the demand at each one of those (D_j)(D_j): $\sum_{i=1}^{n} x_{ij} \ge D_j\ \forall j \in D$ $\sum_{i=1}^{n} x_{ij} \ge D_j\ \forall j \in D$. Similarly, two constraints were introduced in the model, these limit the number of facilities open. One is setting a minimum value $F_{min}F_{min}$ and the other an upper bound, $F_{max}\,F_{max}$. These values are the number of facilities that could be opened: $\sum_{i=1}^{n} B_i \le F_{max}\ ;\sum_{i=1}^{n} B_i \ge F_{min}\sum_{i=1}^{n} B_i \le F_{max}\ ;\sum_{i=1}^{n} B_i \ge F_{min}$. In addition, link constraints were considered. It is not possible to supply from a supply node unless it is open. Thus, $W_{ij}W_{ij}$ is a big number and the binary variable B_iB_i can take two values, either 0 or 1. Considering the options and choosing these WW's, it is not recommended to make it excessively big

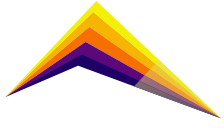

because it slows down the solution time. It was proposed to set it equal to the sum of all the demand because the flow on each arc can never be greater than the total demand required: $x_{ij} - W_{ij}B_i \leq 0 \ \forall j i x_{ij} - W_{ij}B_i \leq 0 \ \forall j i$. On the other hand, humanitarian aid organizations want to ensure that the affected population is effectively served and want to mitigate the impact of the disaster and its consequences as soon as possible. Therefore, a constraint for the maximum allowed average distance was included, where each $x_{ij} x_{ij}$ is multiplied by its distance $d_{ij} d_{ij}$ which corresponds to the distance from a node ii to a node $j\ j$. This operation involves the calculation of a weighted distance. This favors areas or facilities that may be distant but have the highest volumes of demand. Also, this value is divided by the sum of the total demand ($D_j D_j$) to calculate the percentage represented. The constraint sums all arcs x_{ij} x_{ij} and obtains a weighted average distance: $\sum_{ij}(d_{ij}x_{ij}/\sum_j D_j) \leq \phi \sum_{ij}(d_{ij}x_{ij}/\sum_j D_j) \leq \phi$.

In addition, an input value $\varphi\ \varphi$ was defined in another distance constraint as the minimum percentage of demand that must be met within a minimum distance value: $\sum_{ij}(a_{ij}x_{ij}/\sum_j D_j) \geq \varphi$ $\sum_{ij}(a_{ij}x_{ij}/\sum_j D_j) \geq \varphi$. The left side of this constraint includes an $x_{ij} x_{ij}$ arc multiplied by a new input data, a constant $a_{ij}\ a_{ij}$. This value is equal to 1 if a demand node jj served by a supply node ii is within a given distance value, and it is equal to 0 otherwise. For example, consider a network with collection centers and shelters, where the first ones are the supply nodes and the second ones are the demand nodes, a value of 50 miles is considered to determine $a_{ij} a_{ij}$, and the value $\varphi\varphi$ is 80%. Then, if a collection center $i\ i$ supplies a shelter jj, $a_{ij} a_{ij}$ will have the value of 1, if the distance between ii and jj is less than or equal to 50 miles; otherwise, it will be 0. The constraint will only consider those combinations that are within 50 miles and divide that value by the total demand. Therefore, the percentage of total demand that is within 50 miles must be greater than or equal to a minimum percentage value $\varphi\ \varphi$, which in this case is 80%. In other words, 80% of the demand supplied must be at a distance less than or equal to 50 miles. This constraint is very important to ensure a short distance on humanitarian supply trajectories. Furthermore, it was necessary to have a restriction that limits the attention in the facilities. While a facility may have enough capacity, this feature may not be conducive to providing quick attention. If a humanitarian attention facility is responsible for several shelters, the waiting rate for attention may increase considerably per person. Similarly, storage systems depend on the volume of people sheltered and the frequency with which demand is supplied to this community. An example of this can be illustrated if a person requires 15 liters of water per day for basic needs and has a water supply tank with a capacity of 10,000 liters, but with a current base of 7.5 liters per minute. Thus, this tank could supply water to over 650 people, but it would take more than 21 hours, which is counterproductive. Therefore, it is recommended to establish a value to limit the maximum flow of attention ($\delta\delta$): $x_{ij} \leq \delta \ \forall i j x_{ij} \leq \delta \ \forall i j$. Finally, there are non-negativity constraints for the flows. The model cannot flow negative volume: $x_{ij} \geq 0 \ \forall i j x_{ij} \geq 0 \ \forall i j$.

Computing the distance between combinations of supply nodes and demand nodes was an input required by the model. In addition, a network structure defined on maps and routing optimization algorithms is required. However, the availability of this data and the price of adequate mapping can be a challenge. To overcome these limitations, a VBA code was written and integrated with the GeoJSON API., These distance values are extracted by iterative calls to Google Maps API, which provides real traveling distances between each

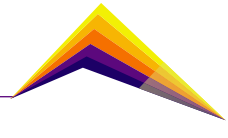

pair of locations. Also, distance values may be subject to certain restrictions by choosing what Google should avoid when calculating travel time. If units are not specified, the origin country of the query determines the units to use. The MILP was solved using a branch and cut algorithm. In simple terms, this divide-and-conquer approach attempts to solve a problem by solving linear programming relaxations of a sequence of smaller subproblems. The solver also executes advanced techniques such as pre-solving, generating cutting planes, and applying heuristics to increase the efficiency of the overall algorithm. The basic idea of branch-and-cut is breaking a problem into subproblems (sequences of LPs) that are easier to solve. Consider MILP: $J^* = min\, c^T x + d^T y J^* = min\, c^T x + d^T y;\ s.t.(x,y) \in Xs.t.(x,y) \in X$, where X is the set of feasible solutions, $X = \{(x,y)\epsilon\, \mathbb{R}_+^n \times \mathbb{Z}_+^p : Ax + By \geq b\} X = \{(x,y)\epsilon\, \mathbb{R}_+^n \times \mathbb{Z}_+^p : Ax + By \geq b\}$. Let $X = X_1 \cup X_2 \cup \ldots \cup X_k X = X_1 \cup X_2 \cup \ldots \cup X_k$ be a decomposition of the feasible solution set XX into smaller sets $X_k X_k$, and let $J^k = min\{c^T x + d^T y : (x,y)\epsilon\, X_k\} J^k = min\{c^T x + d^T y : (x,y)\epsilon\, X_k\}$ for $k = 1, \ldots, K k = 1, \ldots, K$. Then $J^* = \max_k J^k . J^* = \max_k J^k$. The mathematical procedure for solving a particular mode is well-known, and hence can be entirely omitted.

Results and analysis

In this case study, the proposed model was implemented within the context of the natural disaster that occurred in the municipality of Mocoa (Colombia) on March 31, 2017, due to the sudden overflow of the Mocoa, Sangoyaco, and Mulato rivers, and the Taruca, Taruquilla, and La Mision streams. The situation report, prepared by OCHA (United Nations Office for the Coordination of Humanitarian Affairs) in collaboration with UMAIC (Colombia Information Management and Analysis Unit) [11], [12] was studied. During this emergency, water services were suspended, and demand was met with the help of water tank cars, drinking water plants, and water tanks in various sectors of the municipality. During the humanitarian operation, these tanks were located at different points in the affected areas. Thus, the goal was to find the locations of these tanks that would minimize the associated costs and, at the same time, improve response time. The supply tanks used were of four types, defined according to their capacity in liters: 250 L, 5,000 L, 10,000 L, and 20,000 L. Based on the above information, a total of 35 candidate locations were considered. In addition, because each location had the possibility of establishing a tank of any of the four types, a total of 140 location possibilities were considered. According to the National Shelter Management Manual of the Colombian Red Cross Society [13], the community must be guaranteed a minimum of 15 liters of water per inhabitant per day to carry out basic activities. As of the date of the report, 12 shelters had been opened serving nearly 726 families, for a total of 2462 people approximately. Regarding the objective function, fixed costs were determined by the unit value of establishing a water supply tank of a certain capacity. The variable cost corresponded to the transportation cost incurred in the supply operation. The water treatment plants keep the supply in tank cars that supply water tanks, the value was calculated according to the liters of water transported.

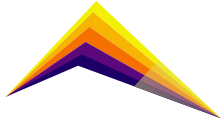

Since the problem included 12 shelters and 140 possible locations for the tanks, the GeoJSON API was applied to calculate these 1680 distance combinations using Google Maps. The exact geographical coordinates of the nodes were considered in the model to achieve a realistic solution. Concerning the entry data of constraints related to short response time, the maximum allowed distance was set at 0.5 km, then the weighted average distance was less than this value. Similarly, the minimum permissible demand within this distance was required to be greater than or equal to 85%. This was based on the guidelines of the National Manual for Shelter Management of the Colombian Red Cross Society, which states that the distance between any shelter and the nearest place of supply must not exceed 500 meters. Also, for the attention limit constraint, the manual indicated a maximum of 250 people per water source, which is equivalent to a supply limit of 3750 liters. Thus, people do not have to wait too long to fill their containers. First, the problem was solved without varying any of the established input parameters. Therefore, in this first run, the model tried to find the optimal values. Table 1 shows the characteristics of the model, along with the total cost and the calculation of a set of metrics: the average distance, the weighted average distance associated with the distance by the amount of volume supplied, and the maximum distance (representing which shelter is farthest from any supply tank). Also, the percentage demand within different distance intervals is presented, by computing what percentage of the demand is supplied within 0.1 km; 0.1 km to 0.25 km; 0.25 km to 0.50 km; 0.50 km to 0.75 km; 0.75 km to 1.0 km; and more than 1 km of distance.

Therefore, the total cost of the operation was approximately 10,533 USD, with 12 tanks or supply nodes supplying 12 shelters. The results were favorable, not only because an optimal response was obtained that met all the constraints described at the beginning of this section, but also because 81.2% of the demand was supplied from a distance less than or equal to 0.5 km. This guarantees an effective response in this humanitarian operation. Subsequently, several scenarios were tested where the minimum requirements of the weighted average distance were modified. It is important to mention that there was no other change in the model except for the variation of this value. Remember that according to the guidelines of the National Manual for Shelter Management of the Colombian Red Cross Society, the distance between any family space and the nearest place of supply should not exceed 500 meters (0.5 km). Therefore, small modifications of this distance were made to study its variation and the sensitivity of the model. The analysis of Table 2 showed that the maximum distance to supply a shelter was between 5.63 and 6.28 km, then there was no significant variation. In addition, the percentage of demand met that exceeded one kilometer of distance did not have a large participation in the total value in any scenario, concentrating between 11.4% and 13.6%. Correspondingly, no value was recorded greater than 0.75 km and less than 1 km. As expected, the scenario that established 0.49 km as the maximum value of weighted average distance presented the best result, with 86.5% of demand met at a distance less than or equal to 0.25 km. In contrast, the last scenario that set 0.61 km as the maximum value of weighted average distance presented 62.7% in this same distance range. Overall, it is possible to mention that the proposed objectives of designing a model that prioritizes timely attention in humanitarian operations were adequately accomplished.

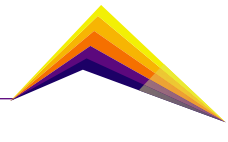

Table 1. Optimal solution.

Summary	**Objective Sense:**	**Minimization**	**Algorithm:**	**Branch and Cut**
	Objective Function:	Total Cost	Solution Status:	Optimal
	Objective Type:	Lineal	Objective Value:	10533
	Number of Variables:	1820	Iterations:	1466
	Number of Constraints:	3516	Pre-solve Time (s):	0.22
	Solver:	MILP	Solution Time (s):	0.64
Results	Enabled supply nodes:	12	Distance ≤ 0,1 km	22.4%
	Total Cost (USD):	$10,533	0.1 km < Distance ≤ 0.25 km	58.8%
	Average distance (km):	0.56	0.25 km < Distance ≤ 0.50 km	6.0%
	Weighted average distance (km):	0.50	0.50 km < Distance ≤ 0.75 km	1.4%
	Maximum recorded distance (km):	5.63	0.75 km < Distance ≤ 1 km	0.0%
			1 km < Distance	11.4%

Table 2. Comparing scenario results.

Maximum weighted average distance (km)	0.49 km	0.50 km	0.51 km	0.53 km	0.55 km	0.57 km	0.59 km	0.61 km
Enabled supply nodes	11	12	12	9	8	8	18	15
Total Cost (USD)	$12,843	$10,533	$9,551.8	$9,397.2	$8,367.3	$8,367.3	$7,908	$7,756.5
Average distance (km)	0.57	0.56	0.54	0.61	0.62	0.62	0.94	0.95
Weighted average distance (km)	0.490	0.499	0.509	0.514	0.546	0.546	0.586	0.610
Maximum recorded distance (km)	5.63	5.63	5.63	5.63	5.63	5.63	6.28	6.28
Distance ≤ 0.1 km	22.4%	22.4%	19.3%	22.4%	22.4%	22.4%	13.9%	13.9%

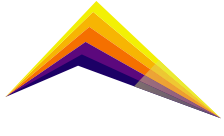

0.1 km < Distance ≤ 0.25 km	64.1%	58.8%	58.1%	58.1%	48.2%	48.2%	48.8%	48.8%
0.25 km < Distance ≤ 0.50 km	2.0%	6.0%	9.8%	6.0%	16.0%	16.0%	22.2%	22.2%
0.50 km < Distance ≤ 0.75 km	0.0%	1.4%	1.4%	2.0%	2.0%	2.0%	3.5%	1.4%
0.75 km < Distance ≤ 1 km	0.0%	0.0%	0.0%	0.0%	0.0%	0.0%	0.0%	0.0%
1 km < Distance	11.4%	11.4%	11.4%	11.4%	11.4%	11.4%	11.5%	13.6%

Conclusions or summary

It was possible to design a model using Mixed Integer Linear Programming (MILP) to solve facility selection problems in humanitarian assistance operations proposing a methodology that considers viable location options resulting from an analysis of an affected area in a disaster situation. Furthermore, the solution scheme to collect distance information using Google Maps and a branch-and-cut algorithm worked synergistically. For this model, the level of timely humanitarian attention is the top priority for the location of facilities. In the case study, several scenarios were tested where the maximum weighted average distance was modified, and the percentage of the demand satisfied within 0.1 km; 0.1 km to 0.25 km; 0.25 km to 0.50 km; 0.50 km to 0.75 km; 0.75 km to 1.0 km; and more than 1 km of distance, was calculated. Overall, the results of the validation presented positive benefits. First, the largest percentage of satisfied demand was generated when locating the supply nodes at a distance greater than 0.1 km and less than or equal to 0.25 km, reaching values between 48.2% and 64.1% in the different scenarios analyzed. Additionally, the next largest percentages were recorded when locating supply nodes at a distance inferiorthan 0.1 km. Thus, the percentages of demand satisfied at this distance reached values between 13.9% and 22.4% in the different scenarios. In contrast, the lowest percentages of satisfied demand were found by locating supply nodes at distances greater than 0.75 km away. Regarding the total cost, we noted that it increased as the maximum weighted average distance and the maximum recorded distance were reduced. This is important because the results showed that the model allows allocating humanitarian funding in proportion to costs and aligning the constraints according to local priorities in different ways in different contexts. In addition to these inferences, depending on the institutions or bodies involved, it is possible to present other ways of using this model in practice. For example, regarding the case study, it would be possible to go back and establish that 85% of the demand should not be within 0.5 km of the supply nodes; perhaps another value could be set. As the complexity of the problem increases, it is possible to alter these numbers and analyze how much these changes cost

and the level of humanitarian attention. In the case study, the solution of having 12 supply nodes within the established distance conditions can be slightly more expensive compared to other scenarios. Indeed, it may not be entirely appropriate to implement such an optimal solution at a lower cost. Other constraints may also be imposed, this is the advantage of the model because it can be adapted to many hypothetical scenarios.

References

[1] B. S. Sahay, S. Gupta, and V. C. Menon, *Managing Humanitarian Logistics*. New Delhi, India: Springer India, 2015.

[2] Y. Chen, Q. Zhao, L. Wang, and M. Dessouky, "The regional cooperation-based warehouse location problem for relief supplies," *Comput. Ind. Eng.*, vol. 102, pp. 259–267, 2016, doi: https://doi.org/10.1016/j.cie.2016.10.021.

[3] R. Maharjan and S. Hanaoka, "Warehouse location determination for humanitarian relief distribution in Nepal," *Transp. Res. Procedia*, vol. 25, pp. 1151–1163, 2017, doi: https://doi.org/10.1016/j.trpro.2017.05.128.

[4] N. Cotes and V. Cantillo, "Including deprivation costs in facility location models for humanitarian relief logistics," *Socioecon. Plann. Sci.*, vol. 65, pp. 89–100, 2019, doi: https://doi.org/10.1016/j.seps.2018.03.002.

[5] Y. Liu, N. Cui, and J. Zhang, "Integrated temporary facility location and casualty allocation planning for post-disaster humanitarian medical service," *Transp. Res. Part E Logist. Transp. Rev.*, vol. 128, pp. 1–16, 2019, doi: https://doi.org/10.1016/j.tre.2019.05.008.

[6] M. Haghi, S. M. T. F. Ghomi, and F. Jolai, "Developing a robust multi-objective model for pre/post disaster times under uncertainty in demand and resource," *J. Clean. Prod.*, vol. 154, pp. 188–202, 2017, doi: https://doi.org/10.1016/j.jclepro.2017.03.102.

[7] W. J. Gutjahr and N. Dzubur, "Bi-objective bilevel optimization of distribution center locations considering user equilibria," *Transp. Res. Part E Logist. Transp. Rev.*, vol. 85, pp. 1–22, 2016, doi: https://doi.org/10.1016/j.tre.2015.11.001.

[8] A. Sebatli, F. Cavdur, and M. Kose-kucuk, "Determination of relief supplies demands and allocation of temporary disaster response facilities," *Transp. Res. Procedia*, vol. 22, pp. 245–254, 2017, doi: 10.1016/j.trpro.2017.03.031.

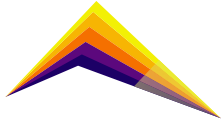

[9] N. Loree and F. Aros-Vera, “Points of distribution location and inventory management model for Post-Disaster Humanitarian Logistics,” *Transp. Res. Part E Logist. Transp. Rev.*, vol. 116, pp. 1–24, 2018, doi: https://doi.org/10.1016/j.tre.2018.05.003.

[10] C. Boonmee, M. Arimura, and T. Asada, “Location and allocation optimization for integrated decisions on post-disaster waste supply chain management: On-site and off-site separation for recyclable materials,” *Int. J. Disaster Risk Reduct.*, vol. 31, pp. 902–917, 2018, doi: https://doi.org/10.1016/j.ijdrr.2018.07.003.

[11] OCHA. The United Nations Office for the Coordination of Humanitarian Affairs, “Colombia: Creciente súbita y deslizamientos en Mocoa, Putumayo. Reporte de Situación No. 03 (al 11.04.2017),” 2017.

[12] OCHA, “The United Nations Office for the Coordination of Humanitarian Affairs. Colombia – Avalancha e inundaciones en Mocoa (Putumayo). Flash Update No. 4 (04/04/17).,” 2017.

[13] Cruz Roja Colombiana, *Manual Nacional para el manejo de Albergues Temporales*. Bogotá: Sociedad Nacional de La Cruz Roja Colombiana: Dirección General del Socorro Nacional, 2008.

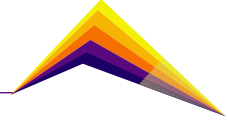

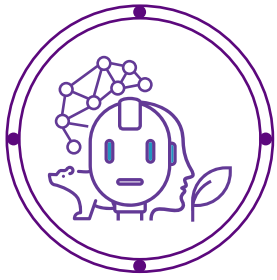

CATESID: Software for identifying alluvial gold mining areas, their characteristic coverages, and their multitemporal analysis

Maura Melissa Herrera[1] — E-mail: maura.herrera@udea.edu.co
David Stephen Fernández[2] — E-mail: david.fernandez@udea.edu.co
Fabio de Jesús Vélez[3] — E-mail: fabio.velez@udea.edu.co
Néstor Jaime Aguirre[4] — E-mail: nestor.aguirre@udea.edu.co

[1] Master's student, Universidad de Antioquia
[2,3,4] University professors, University of Antioquia, Engineering Faculty

Abstract

Currently, remote sensing offers the potential to develop several lines of ecological restoration. The most studied line is the "spatial mosaic", or land cover change identification at a spatial and temporal level. This line seeks out, for the mining areas case, to evaluate vegetation cover changes that an area has undergone to estimate how long vegetation growth is evident and in which specific areas. The software CATESID (Temporal Characterization of Cover using Satellite Images) was developed to achieve this objective. This software fulfills the primary function of classifying and quantifying the area of each land-cover usually observed in alluvial gold mining areas.

For the classification stage, CATESID initially calculates the SAVI index (Soil Adjusted Vegetation Index), and based on the contrasts generated by the index, the classification of the different types of cover land is applied through the unsupervised K-Means classification method, which application generates the distinction of four categories: "Waste land", "High vegetation", "Medium vegetation",

Correspondent author

and “Low vegetation”. The user selects these depending on the color he/she considers belongs to a specific group.

After the classification stage, post-processing is applied for the inclusion of additional categories such as “Clouds”, “Water bodies”, and “Mining areas”. Finally, in the multitemporal analysis stage, the sequential mining method pattern SPADE (Sequential Pattern Discovery Using Equivalent Classes) is applied, which allows the identification of a series of sequences for each spatiotemporally located pixel, a sequence being understood as a set of categories. This process makes it possible to identify what changes occurred between the different categories and how often and on what dates those changes occurred.

Keywords: Remote sensing, satellite images, Landsat, mining areas, alluvial gold mining, software.

Introduction

In Ayapel, the San Pedro River basin and the three basins that feed the Ayapel swamp, present this deforestation condition due to mining activities [8]. The Quebradona, Escobillas, and Trejos streams, upstream of the Ayapel swamp are in a particularly critical situation. The entire gallery forest has been destroyed and deforested throughout the three watersheds, and the stream beds have been modified [4].

As with other types of mining, alluvial mining transforms the landscape to a significant degree, so monitoring these changes is essential to quantify the impact of these activities on terrestrial ecosystems. Therefore, as mining activity has increased, interest in monitoring it has also grown for the sake of conservation and governance [3]. Remote sensing offers excellent possibilities for monitoring land and open water changes, which is critical in natural resource management, environmental policy, and administration. Although it is common to use satellite images for those purposes, software development provides advantages in terms of simplicity of analysis. Such is the case of CATESID software, developed throughout this research, from which good results were obtained that allow a general approach to the situation of a mining area in a simple way and with little computational cost.

Currently, methods based on advanced artificial intelligence are used, such as the case of Deep Learning, which offers excellent advantages in relation to accuracy in the classification

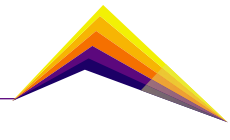

of mining areas coverage [1][3][9]. However, these methods require a large amount of training data and a higher computational cost. On the other hand, the creation of a simple software in its use and operation represents a valuable tool for governmental entities, for example, those in charge of environmental and territorial management, since it allows a general approach to the mining situation in a particular area. The CATESID software is developed to use free data such as those offered by the USGS [11] through the images captured by the Landsat satellite. It also offers the possibility of having a multitemporal follow-up of the changes that occurred over several years from the time that the Landsat satellite records data.

The development of this software is based on the analysis of spectral indices such as SAVI and NDVI [2][10], which have been widely used for remote sensing of land use or vegetation monitoring. The commonly used methods do not track multi-temporal changes in pixels over time [3]. Therefore, Ibrahim, 2020 applied sequential pattern mining [6], which this study uses to do multitemporal tracking of land cover changes. This study had satisfactory results in such multitemporal tracking. Therefore, it is also applied in the development of this software.

CATESID, therefore, offers simplicity, low computational cost, multitemporal analysis, and accuracy that exceeds 70%, which allows an approach and general evaluation of the territory with the presence of alluvial mining.

Methodology

Study area

The study area consists of a polygon located to the southeast of the Ciénaga de Ayapel, an area where the Quebradona micro-watershed is located. The Ciénaga de Ayapel is located in the Córdoba department, Colombia. It is part of the macro-system of wetlands and alluvial plains known as the La Mojana region. It is considered one of the most important within the San Jorge River flooding system due to its total area (45 km^2) and importance for the fishing sector in the local economy. In Ayapel, since approximately 2005, alluvial mining has been carried out intensively and with machinery in the Escobillas, Quebradona, and Trejos streams, which contribute to the swamp [4]. The Quebradona micro-watershed has been one of the micro-watersheds most affected by alluvial gold mining.

Image acquisition

For this analysis, Landsat T1 images were obtained from the Google Earth Engine database [5], corresponding to the study area's Landsat 4, 5, and 8 missions. The downloaded images had a preprocessing at the atmospheric level (TOA), which already has a radiometric correction at the atmospheric surface level.

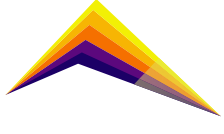

After obtaining the Landsat images, the classification stages, post-processing, and multitemporal analysis of the study area were started with the purpose of proving the change in land cover over time (Figure 1).

For the first "classification" stage, the different Landsat satellite bands $\{B_{i,j,1}, \ldots, B_{i.i.X}, B_{i.i.OA}\}$ $\{B_{i,j,1}, \ldots, B_{i,j,X}, B_{i,j,QA}\}$ are introduced, and a preliminary classification $C_{i,j,SAVI}C_{i,j,SAVI}$, is obtained, based on the Soil Adjusted Vegetation Index (SAVI). Subsequently, the "post-processing" stage begins, where the classified image obtained in the previous stage and additionally a raster type image $V_{i,j,W}V_{i,j,W}$ obtained from the vectorization of rivers and streams are entered. In this stage, new categories are added, such as the "Clouds" category, the "Water" group, and the "Mining Soil" category, obtaining the classified image $C_{i.i}C_{i.i}$. Finally, for the "multitemporal analysis", a set of images $\{C_{i,j,1}, \ldots, C_{i,j,t}\}\{C_{i,j,1}, \ldots, C_{i.i.t}\}$ are introduced where t refers to a specific capture date for the image, and where $C_{i,j,1}C_{i,j,1}$ is an *mxn* matrix. Each pixel *i, j* has a number equivalent to a coverage category. In this set of input images, the "Clouds" group is excluded since it is considered an information void. After applying the Sequential Pattern Discovery Using Equivalent Classes (SPADE) method, support "*Sup*" and confidence "*Conf*" values are obtained for each of the sequences found by the method, a sequence being understood as an ordered set of categories.

1208	Pt: SmlEng : Lt : 4Cyc Carb : None : None: >50K km	1.55
1316	Ds: SmlEng : Med : 4Cyc : None : None: >50K km	0.2
1214	Pt: SmlEng : Hv : 4Cyc Carb : None : None: >50K km	1.35
1211	Pt: SmlEng : Med : 4Cyc Carb : None : None: >50K km	1.55
1178	Pt: SmlEng : Hv : 2Cyc : None : None: >50K km	47.2
1175	Pt: SmlEng : Med : 2Cyc : None : None: >50K km	46.7
1172	Pt: SmlEng : Lt : 2Cyc : None : None: >50K km	1.55

Figure 1. Summary of phases for satellite image processing.

The classification based on the SAVI index, digital image processing, and the application of the unsupervised K-means classification method yielded a total overall accuracy of 74.37%±0.10. The total overall accuracy was calculated as the average of the overall accuracies yielded by each classified image. In general, it was observed that the images corresponding to Landsat 4 and 5 missions showed lower results in the overall accuracy compared to Landsat 8 images, which could be due to the differences in the radiometric images resolution, which is better for Landsat 8. On the other hand, the calculated Kappa coefficient, known as a concordance index, was 0.658, a value interpreted as a good classification [7]. Conversely, regarding the results, the software's difficulties with the presence of high cloudiness were evidenced, even though the selected images contained maximum cloudiness of 20%. The software underestimated the presence of bare ground due to the clouds and their shadows when there was a high presence of clouds in the images.

In some cases, pixels corresponding to the bare ground were overestimated due to the similarity in reflectance levels between the categories. Therefore, the contrast between the

images was increased in the software. However, it is recommended to preprocess the images before classifying them with the software so that there is a better contrast between tonality and more significant differentiation between reflectance levels and, therefore, between categories.

Conclusions

Although the software's accuracy does not reach percentages very close to 100% (as it is achieved from methods that use Deep Learning or complex statistics), CATESID software offers an excellent approximation to changes in mining over time. In addition to other relevant coverages such as vegetation, useful to measure land use change over time, environmental impact on the territory, forest loss, and even forest recovery. CATESID offers a quantification of these changes, which represents a tool for land management, easy to access and use, using free information such as Landsat images.

Future enhancement opportunities for the software include a more complete image processing. Image processing should include the generation of higher contrast between pixel shades to facilitate the distinction between land cover types. It would also be expected to include the analysis of Sentinel images with a higher spatial resolution.

Acknowledgment

Thanks to Engineers Nicolás Albornoz and Esteban Chaverra for their vital support to the development of this software.

References

[1] Abaidoo, C., Osei, E., Arko-Adjei, A., Kwesi Prah, B. “Monitoring the Extent of Reclamation of Small-Scale Mining Areas Using Artificial Neural Networks” Heliyon., 5, 4. https://doi.org/10.1016/j.heliyon.2019.e01445.

[2] Caballero Espejo, J.; Messinger, M.; Román-Dañobeytia, F.; Ascorra, C.; Fernandez, L.E.; Silman, M. Deforestation and Forest Degradation Due to Gold Mining in the Peruvian Amazon: A 34-Year Perspective. Remote Sens. 2018, 10, 1903. https://doi.org/10.3390/rs10121903.

[3] Camalan, S.; Cui, K.; Pauca, V.P.; Alqahtani, S.; Silman, M.; Chan, R.; Plemmons, R.J.; Dethier, E.N.; Fernandez, L.E.; Lutz, D.A. (2022). “Change Detection of Amazonian Alluvial Gold Mining Using Deep Learning and Sentinel-2 Imagery”. Remote Sens., 14, 1746. https://doi.org/10.3390/rs1407174.

[4] Defensoría del pueblo (2015). La Minería sin control, un enfoque desde la vulneración de los Derechos Humanos. https://www.defensoria.gov.co.

[5] Gorelick, N., Hancher, M., Dixon, M., Ilyushchenko, S., Thau, D., & Moore, R. (2017). “Google Earth Engine: Planetary-scale geospatial analysis for everyone”. Remote Sensing of Environment. https://doi.org/10.1016/j.rse.2017.06.031.

[6] Ibrahim, E., Lema, L., Barnabé, P., Lacroix, P., & Pirard, E. (2020). “Small-scale surface mining of gold placers: Detection, mapping, and temporal analysis through the use of free satellite imagery”. International Journal of Applied Earth Observation and Geoinformation, 93, 102194. https://doi.org/10.1016/j.jag.2020.102194.

[7] Landis, J. R., & Koch, G. G. (1977). “The Measurement of Observer Agreement for Categorical Data”. Biometrics. https://doi.org/10.2307/2529310.

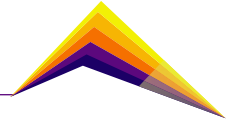

[8] Pérez-Rincón, M., (2014). Conflictos ambientales en Colombia: inventario, caracterización y análisis. Minería en Colombia: control público, memoria y justicia socio-ecológica, movimientos sociales y posconflicto.

[9] Suárez, Heinner., (2019). “Satellite image processing protocol for the training and testing of a neural network for the prediction of ecological damage due to illegal mineral extraction within the framework of the celebration of the 100th anniversary of the Colombian Air Force”. Universidad Distrital Francisco José de Caldas.

[10] Swenson, J.J.; Carter, C.E.; Domec, J.-C.; Delgado, C.I. Gold Mining in the Peruvian Amazon: Global Prices, Deforestation, and Mercury Imports. PLoS ONE 2011, 6, e18875. https://doi.org/10.1371/journal.pone.0018875.

[11] USGS (United States Geological Survey). “Landsat missions”. Available at: https://www.usgs.gov/landsat-missions.

Customized Ti6Al4V implants by EBM: design, manufacturing and surface treatments

Enrique Quiceno[1,4] *Email: enriquequiceno@itm.edu.co-enrique.quiceno@upb.edu.co*
Carlos Botero[2]
Lars-E. Rännar[2]
Angie Ramirez[3]
Juan Castaño[3]
Maryory Gomez[3]
Libia Baena[4]
Carlos A. Vargas[5]
Nicolás Bedoya[1]
Alejandro Zuleta[1]
José A. Tamayo[4]

[1]Grupo de Investigación de Estudios en Diseño - GED, Facultad de Diseño Industrial, Universidad Pontificia Bolivariana, Sede Medellín, Circular 1 No 70-01, Medellín, Colombia.
[2]Department of Quality Technology and Mechanical Engineering, Mid Sweden University, Kunskapens väg 8, SE-831 25 Östersund, Sweden.
[3]Centro de Investigación, Innovación y Desarrollo de Materiales – CIDEMAT, Facultad de Ingeniería, Universidad de Antioquia UdeA, Calle 70 No 52 – 21, Medellín, Colombia
[4]Grupo Calidad metrología y producción, Instituto Tecnológico Metropolitano –ITM-, Medellín, Antioquia 050034, Colombia
[5]Grupo Materiales Avanzados y Energía, Instituto Tecnológico Metropolitano –ITM-, Medellín, Antioquia 050034, Colombia

Abstract

Subtractive manufacturing methods such as machining have been conventionally used to produce standard metallic implants for bone replacement in materials such as Co-Cr and Ti-based alloys. The production of a customized implant with complex geometries using conventional machining techniques such as CNC requires specification equipment (5 or 6 axes), where the manufacturing process is difficult, limiting the mass production of customized products. New advanced metal additive manufacturing (AM) methods allow patient-specific implants obtaining, in which the

Correspondent author

implant geometry can be designed to fit to a specific patient from the information of a CT scan. Besides this flexibility in the design, AM offers a cleaner production with less generation of scrap, low energy consumption and lower CO_2 release. Electron Beam Melting (EBM) is one of the most used AM methods in the implant industry. In EBM, an electron beam is used to melt metal powder layer by layer in a vacuum protective environment, following a digital 3D model. Titanium alloys, specifically Ti6Al4V, have been the most widely used biomaterial in biomedical applications of orthopedic implants. In general, implants for biomedical applications require post-manufacturing surface modification to improve their performance, biocompatibility and fixation with the surrounding tissues in the area where they are implanted. Formation of anodic layers is one of the surface modifications that have become essential due to the high demands of implant applications and in order to enhance chemical and mechanical properties of the surface specimen. The most common anodizing developments were performed on Ti6Al4V alloy surfaces manufactured by conventional technologies such as forging and conventional machining. The project explores the feasibility of EBM of metal implants prototypes manufacturing for the Colombian healthcare market. 3D implant models were obtained, and then manufactured using EBM in Ti6Al4V alloy. A PEO process to surface modification with the aim to improve the biocompatibility of the manufactured implants by EMB process were demonstrated.

Key words: Additive manufacturing (AM); Electron Beam Melting (EBM); Ti6Al4V implants, customized; PEO process.

Introduction

Devices manufacturing for the biomedical industry has conventionally been performed by traditional subtractive methods. In recent decades, manufacturing has evolved towards additive techniques, which have great advantages in terms of obtaining parts of high geometric complexity and completely customizable, thanks to the processes associated with the techniques such as software-assisted modeling, tomography and three-dimensional scanning [1]. In additive manufacturing, the design, analysis and optimization stages are integrated in the prototype's development or medical devices [2]. As its name suggests, additive manufacturing adds material to create an object, unlike other traditional manufacturing techniques such as machining, where it is necessary to remove layers of material [3], which represents an advantage in terms of additive manufacturing being a cleaner and more environmentally friendly technique. In particular, for metal additive manufacturing techniques, the most used group of techniques is known as Powder Bed Fusion (PBF). In PBF, a fine metal powder is consolidated layer by layer to obtain the desired 3D object. This layer-by-layer shaping and consolidation can be achieved by agglutination, melting and/or sintering of powders [4]. For metal PBF methods, an energy source is necessary for the sintering or melting of the metal particles. The energy sources used to melt the metal powders can be a laser; such as in selective laser melting (SLM) or electron e-beam, such as in Electron beam melting (EBM). SLM and EBM are the most used techniques in the medical field, supported by the amount of research, applications and patents developed in this area [5].

For the Ti6Al4V alloy there are some concerns regarding the release vanadium and aluminum ions which can originate inflammatory responses and the probability of developing Alzheimer's disease, respectively [6]. For this, different techniques have been used to modify the surface of the alloy in order to improve the material corrosion behavior while improving biocompatibility. Anodizing is one of the surface modifications that have become crucial due to the high demands of implant applications. The first anodizing developments were performed on Ti6Al4V alloy surfaces manufactured by conventional technologies such as forging and conventional machining. A variation of conventional anodizing is plasma electrolytic oxidation, PEO (or microarc oxidation), which differs in the application of potentials of higher level with respect to conventional anodizing presenting the dielectric breakdown potential, allowing to obtain oxide ceramic coatings, oriented in improving at a higher-level resistance to corrosion, wear, biocompatibility and other surface requirements [7]. The aim of this work is to show the followed process to obtain printed parts in the Ti6Al4V alloy superficially modified. The electron beam melting (EBM) technique is used for the fabrication of the substrates and plasma electrolytic oxidation (PEO) for the formation of anodic films on their surface.

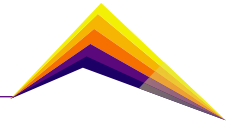

Methodology

For the morphological definition of the implant, the procedure of extraction of the reference points in a generic femur is followed and reverse engineering methodology was applied in the definition of the geometry of the femoral stem. Diagnostic aids such as X-rays, computed tomography or electromagnetic resonance imaging are used to proceed to dimension an object using design software. X-ray diagnostic images were used to extract the dimensions of the femoral component (Figure 1. a), once the component, in the case of this work a femoral part was modeled in solid works to obtain the CAD model (Figure 1. b), its different design elements are detailed and defined: femoral neck axis, diaphyseal axis, neck axis angle, anteversion angle, femoral length and femoral canal width. Finally, with the characteristics detailed above, reference measurements of the femur are obtained and the geometry of the stem are defined for further manufacturing by EBM.

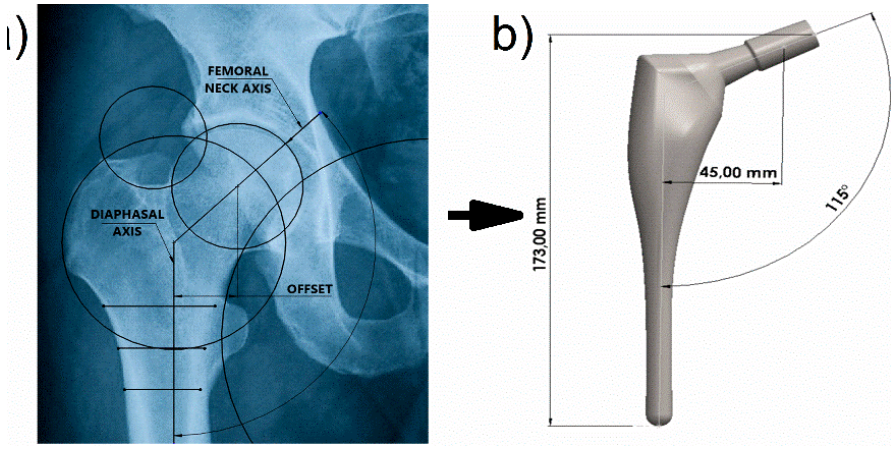

Figure 1. a) anteroposterior X-ray of the hip, b) CAD model of the femur.

The specimens were manufactured in Ti6Al4V alloy using the ARCAM A2 machine by ARCAM EBM installed at the facilities of Mid Sweden University, departing from the stl models of the parts. In the EBM process an electron beam melts the metal powder, layer by layer, in a vacuum environment. A rake system spreads a powder layer that is first preheated and presented by a defocused electron beam, and subsequently melted using a focused beam. Thereafter, a new powder layer is spread, and the process repeats layer upon layer until the parts are completed. Layers of 70 µm in thickness were used with a process temperature of 760°C. After the printing process, the powder ad-sintered to the parts is removed in a PRS (powder recovery system). For surface modification by PEO process, cylinders of EBM specimens were cut into coupons of 20 mm in diameter and 4mm thick and then polished using successive grades of SiC paper up to # 2000, cleaned with ethanol and rinsed with distilled water, finally, the specimens were processed according to the conditions described in Table 1 using a stainless-steel beaker as cathode and the specimen as anode.

Table 1. PEO process conditions applied on Ti6Al4V substrate.

Electrolyte	Current density [mA/cm²]	pH	Conductivity [ms/cm¹]	Time [s]
$Na_3PO_412H_2O$ (10 g/L) $Na_2SiO_35H_2O$ (2 g/L) $EDTANa_2$ (3,72 g/L) NaOH (2 g/L)	50	13.0-13.3	17.90	1000

Finally, the PEO-treated specimens were analyzed using a JEOL JSM-7100 scanning electron microscope.

Results and analysis

Figure 2 shows the process to obtain the prosthesis prototypes (femur) and samples manufactured in Ti6Al4V alloy using the Electron Beam Melting (EBM) technique, starting from adequate placement and orientation of the different parts from STL files and to take advantage of the full capacity of the printing equipment (Figure 2 a). Subsequently, the final result of the manufacturing process of the different parts is presented (Figure 2b), and the femoral stem (Figure 2c) in Ti6Al4V alloy.

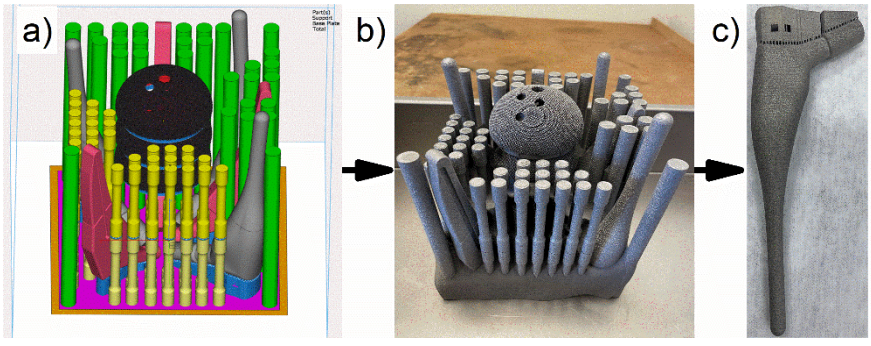

Figure 2. a) Parts in stl digital format, b) after printing process and c) Femoral stem with customized morphology and optimized surfaces.

Production of complex geometries in implants, typical of customized shapes in the femoral stem used for the treatment of hip arthroplasty, was simplified with the application of the EBM additive manufacturing technique, reducing the manufacturing times of the femoral stem and achieving the dimensional characteristics determined in the morphology of the implant.

A surface modification by PEO on a substrate fabricated by EBM is presented below (Figure 3). The morphology of the anodic layer obtained shows the formation of pores where it is possible to distinguish a group of pores of sizes between 1 to 3 μm (3.09 μm average) and another group of pores of sizes less than 1 μm (0.67 μm average), Yan and coworkers have also evidenced in a recent study this formation of pore sizes [8]. It can also be seen that the larger pores generate a protrusion on the surface of the anodic layer, while the small pores occur at the lower level of the anodic layer. In Figure 3 (a), the presence of cracks can be observed, which can be attributed to the time of current application that allows releasing more energy on the layer [9]. The formation of pores favors the increase of the surface area of the substrate allowing cell adhesion and proliferation processes, which are essential for implants in the human body [10]. However, high or non-uniform porosity can disfavor physicochemical properties of the substrate, which are also important for implant applications [8]. The thickness and phase composition of the oxide layer generated during the PEO process confer additionally, good wear and corrosion resistance [11].

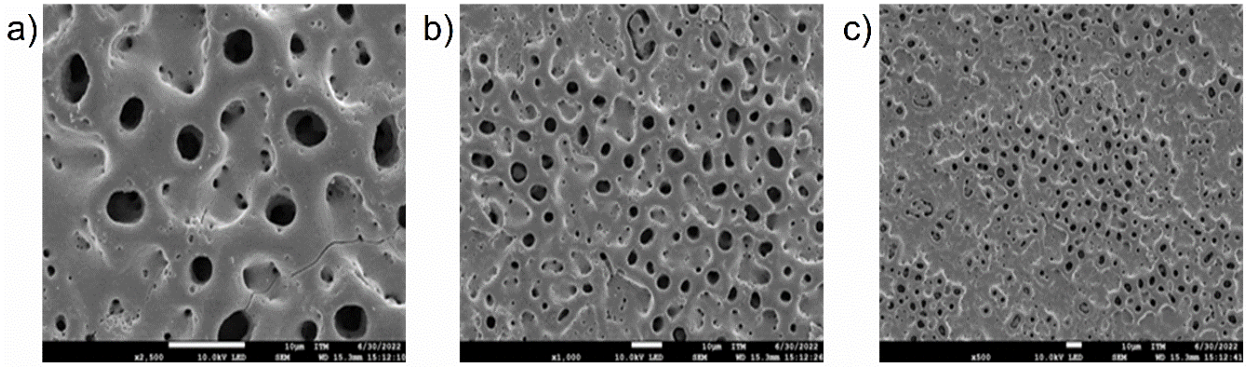

Figure 3. Secondary electrons image of the anodic films obtained by PEO process on Ti6Al4V substrate obtained by EBM. (a) 2500X, (b) 1000X, (c) 500X

Conclusions

- It was possible to obtain the morphology design and fabrication by additive manufacturing of prototypes for personalized (customized) implants in Ti6Al4V titanium alloy with complex geometry, usual in the femur and hip joint and with characteristics for their possible application in the biomedical industry, in the region. It was found with the additive manufacturing technique it is possible to obtain such geometries which are difficult with other conventional manufacturing techniques such as CNC.

- With the surface modification tests by PEO of the printed samples, an anodic layer morphology was observed with the formation of two groups of pores with sizes between 1 to 3 mm and pores of sizes less than 1 mm, respectively. This pore formation favors the increase of the surface area of the substrate allowing cell adhesion and proliferation processes, which are indispensable in biomedical prostheses.

Acknowledgment

The authors are grateful to 'PROYECTOS DE I+D+i EN EL MARCO DE LA AGENDA REGIONAL DE I+D + i (Project #49), Instituto Tecnológico Metropolitano Project (PE21101), Universidad de Antioquia, Mid Sweden University, Centro de Investigación para el Desarrollo y la Innovación (CIDI) from the Universidad Pontificia Bolivariana (Rad: 636C-11/20-35) and Corporación Ruta N.

References

[1] V. V. Popov et al., "Design and 3D-printing of titanium bone implants: brief review of approach and clinical cases," Biomed. Eng. Lett., vol. 8, no. 4, pp. 337–344, 2018, doi: 10.1007/s13534-018-0080-5.

[2] R. Noorani, *Rapid prototyping: principles and applications*. John Wiley & Sons Incorporated., 2006.

[3] General Electric, "What is Additive Manufacturing? | GE Additive." https://www.ge.com/additive/what-additive-manufacturing (accessed Oct. 25, 2021).

[4] P. K. Gokuldoss, S. Kolla, and J. Eckert, "Additive Manufacturing Processes : Selective Laser Melting , Electron Beam Melting and Binder," *Materials (Basel).*, vol. 10, 2017, doi: 10.3390/ma10060672.

[5] J. A. Tamayo, M. Riascos, C. A. Vargas, and L. M. Baena, "Additive manufacturing of Ti6Al4V alloy via electron beam melting for the development of implants for the biomedical industry," *Heliyon*, vol. 7, p. 26, 2021, doi: 10.1016/j.heliyon.2021.e06892.

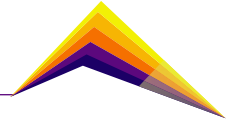

[6] A. L. Martinez, D. O Flamini,., & S. B. Saidman,. (2022). Corrosion resistance improvement of Ti-6Al-4V alloy by anodization in the presence of inhibitor ions. Transactions of Nonferrous Metals Society of China, 32(6), 1896-1909.

[7] M. Molaei, M. Nouri, K. Babaei abd A. Fattah-Alhosseini,. "Improving surface features of PEO coatings on titanium and titanium alloys with zirconia particles: A review." Surfaces and Interfaces 22 (2021): 100888.

[8] Yan, Q., Xue, T., Liu, S., Wang, W., Wang, Y., Song, X., Yang, X., & Shang, W. (2022). A comparative study of surface characterization and corrosion behavior of micro-arc oxidation treated Ti–6Al–4V alloy prepared by SEBM and SLM. Journal of Iron and Steel Research International.

[9] Han, I., Choi, J. H., Zhao, B. H., Baik, H. K., & Lee, I. S. (2007). Changes in anodized titanium surface morphology by virtue of different unipolar DC pulse waveform. Surface and Coatings Technology, 201(9–11), 5533–5536.

[10] Paital, S. R., & Dahotre, N. B. (2009). Calcium phosphate coatings for bio-implant applications: Materials, performance factors, and methodologies. Materials Science and Engineering: R: Reports, 66(1–3), 1–70.

[11] Kaseem, M., & Choe, H. C. (2021). Simultaneous improvement of corrosion resistance and bioactivity of a titanium alloy via wet and dry plasma treatments. Journal of Alloys and Compounds, 851, 156840.

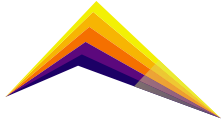

Numerical study of microwave hyperthermia for the treatment of breast cancer

Gabriel Cardona[1]
Bryan Rodriguez [2]
Waira Murillo[3]
Marcela Mercado-M[4]

E-mail: gabrielcardona282407@correo.itm.edu.co
E-mail: bryan.rodriguez@udea.edu.co
E-mail: waira.murillo@udea.edu.co
E-mail: marcela.mercadom@insilicose.com

[1, 2, 3, 4] Researcher, In Silico UdeA Research Incubator, In Silico SE SAS
[1]Biomedical Engineering Student, ITM, 2 Physician, Universidad de Antioquia
3 Physics Student, Universidad de Antioquia, 4 CEO, In Silico SE SAS

Abstract

Heat treatment or hyperthermia is one of many cancer treatments that are being used nowadays. The advantages of this treatment over others are its non-invasive, low-price, and accessibility characteristics for some specific cases, also reducing side effects and improving wellness in the long term. COMSOL Multiphysics is used in this study to simulate microwave hyperthermia therapy in a simplified 3D breast model and compare the results with those reported in another paper with the same problem formulation. The replication of the paper was successful. This study includes additional results showing the temperature inside the breast and high dangerous temperatures reached above 47 °C. This study is the base for multiple investigations with regression models, more realistic geometries, calibrated tissue properties, tissue necrosis measurement, etc.

Keywords: Numerical Analysis, Hyperthermia, Breast Cancer, Electromagnetic heating

Correspondent author

Introduction

Breast cancer is the world's leading cause of cancer, with 1.671.149 new cases and 521.907 deaths each year [1] being a disease in which cells grow out of control. Studies have shown that the main risk is a combination of multiple factors; which includes being a woman and getting older. Most of them are found in women who are 50 years old or older.[2] It's the most common among women and with it, so many treatments have been developed. There are invasive treatments like surgery where the tumor is removed manually; also, chemotherapy, whose purpose is damaging the tumor genes using medicines. Radiotherapy can be invasive or no-invasive; The non-invasive type consists of the usage of an ionizing radiation-focused beam through an external device focusing on the cancer zone. The invasive one consists of radioactive seed introduced in the tumor [3].

Hyperthermia consists of rising temperatures focused on the tumor reducing the tumoral tissue. It can be applied by inserting catheters and applying heat to the tumor, reducing, and destroying it, or applying an external heat source (non-invasive), like dipoles generating microwaves [4]. Hyperthermia has been widely investigated over the last decades, one of its main characteristics is its raising temperature and control through electromagnetic (EM) phenomena, some recent studies show possibilities by implementing a mixed method with nanoparticles, which could improve the actual cancer treatments [5]. Others are using technologies like Quantum Dots with a Core-Shell structure to improve the treatments, these efforts represent the main issue that this treatment has alongside, damage to healthy tissue on the peripheries of the tumor [6],

Numerical analysis is commonly used for the solution of electromagnetics, heat transfer, and other phenomena such as that involved in microwave hyperthermia for breast cancer. In [7], the authors suggested a simple model using eight half wavelength linear dipoles to calculate the temperature distribution on a simplified breast model. In addition, the effect of changing the stages of the array elements on the temperature distributions was studied. In a more realistic approach, [8] developed 3D electromagnetic and thermal simulations to evaluate the selective heating effectiveness in four numerical breast phantoms with different breast tissue densities.

This paper is aimed to model and simulate using COMSOL Multiphysics 5.6 the microwave hyperthermia therapy in a simplified 3D breast model. The waves are generated with an 8-half wavelength array at 6GHz, with 20V amplitude and variable stages, to replicate the study case reported by [7] and establish a base point for further investigation. Also, to report and discuss additional results other than those given by the authors, such as the temperature distributions in different planes and locations.

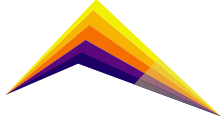

Methodology & Methods:

The CAD model in Figure 1 shows the computational domain with the breast as a truncated cone whose major basis has a diameter of 5 cm, minor basis has a diameter of 3 cm and height is 5 cm; the tumor is a 4 mm radio sphere. Eight dipoles are evenly distributed around the breast, each dipole is formed by two arms with lengths of 2.5 cm and a radius of 0.125 cm separated by a 0.5 mm gap. The breast is surrounded by an air sphere with a radius of 0.1 m with a Perfectly Matched Layer (PML), used to truncate computational regions into numerical methods. This layer absorbs all outgoing wave energy in frequency-domain problems, without any impedance mismatch causing spurious reflections at the boundary. In this case, the PML has a thickness of 2.5cm.

$$\nabla \times \mu^{-1}(\nabla \times \vec{E}) - k_0^2(\epsilon_r - \frac{j\sigma}{w\epsilon_0})\vec{E} = 0 \quad \textbf{[Eq. 1]}$$

In this study, there are two physics involved, microwave propagation, which is generated for each dipole and is governed by the frequency domain electromagnetic wave equation[Eq. 1]; where **E** is the electric field intensity (V m^{-1}), μ is the magnetic relative permeability, ε_r is the electric relative permittivity, ε_0 is the vacuum electric permittivity (8.85 F m^{-1}), K_0 is the wave number, σ is the electrical conductivity (S m^{-1}) and ω is the wave frequency (rad s^{-1}).

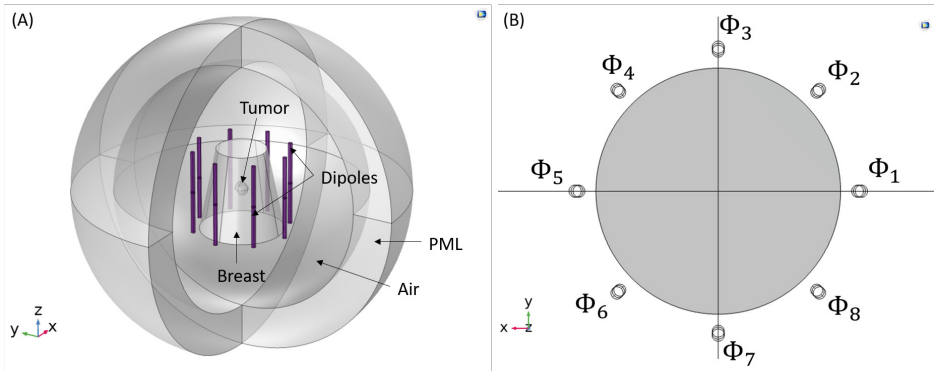

Figure 1. Computational domain. (A) 3D view and (B) Stages assigned to each dipole.

The wave's superposition, coming from the array, produces an electromagnetic field, whose magnitude depends on the wave amplitude, frequency, and dipole phases.

$$\rho Cp\frac{\partial T}{\partial t} - \nabla \cdot (k\nabla T) = Qbio + Qem \quad \textbf{[Eq. 2]}$$

For the heat transfer in biological tissues, in this case with the human body, whose behavior is governed by the Pennes Bioheat transfer equation (Eq. 2). Where T is the temperature (K), ρ is the density (kg m^{-3}), C_p is the heat capacity (J kg^{-1} K^{-1}), k is the thermal conductivity (W m^{-1} K^{-1}), Q_{bio} is the biological heat source and Q_{em} is the electromagnetic heat source.

The heat transfer analysis is only considered in the breast and tumor domains and in the stationary state, so the first term in Eq.2 is set to zero. The expression for biological heating Q_{bio} can be divided into perfusion heat source and metabolic heat source. On the other hand, the expression for electromagnetic heating Q_{em} can be divided into resistive heating and magnetic losses.

The Lumped Port boundary condition available in COMSOL was applied at the dipoles gap. This feature avoids the need for the actual port geometry, by lumping it in terms of its height, width, and direction between its terminals. Each port is established with a wave voltage excitation as $V(t) = A\,sin(\omega t + \Phi)$. Where A is the voltage amplitude (V), ω is the wave frequency (rad s^{-1}), and is the wave phase (rad or °). A is set to 20 V, the same as reported in [9] which leads the temperature to rise around 43 °C, which is the desired temperature to achieve tissue necrosis with hyperthermia. The frequency was set to 6 GHz and 5 combinations of the dipole stages were considered according to Table 1, where $\Phi_1, \Phi_2, \ldots \Phi_8$ are the stages of dipoles 1, 2, ... 8 respectively, as shown in Figure 1.

Table 1. Simulation cases with varying stages of the dipoles.

Case	$_1$(°)	$_2$(°)	$_3$(°)	$_4$(°)	$_5$(°)	$_6$(°)	$_7$(°)	$_8$(°)
Control	0	0	0	0	0	0	0	0
5° shift	0	5	10	15	20	25	30	35
10° shift	0	10	20	30	40	50	60	70
20° shift	0	20	40	60	80	100	120	140
Neg 2,3	0	-40	-50	60	70	80	90	100

The thermal boundary condition was set as Dirichlet T = 37 °C at all the breast surfaces, except at the breast base, in which thermal isolation (no flux) Neuman boundary condition was applied. The electromagnetic and thermal material properties for each domain are specified in Table 2 [8].

Domain	ρ (kg m^{-3})	C_p (J kg^{-1} K^{-1})	k (W m^{-1} K^{-1})	μ_r	ε_r	σ (S m^{-1})
Breast	1020	2348	0.37	0.99	4.49	0.59
Tumor	1000	3421	0.5	0.99	50	4

Results and analysis

The comparison between this study's results and Elkayal et. al. [7] presented in Figure 2 makes evident the similarity between the ranges and the distributions of temperature reached for both studies with all the cases considered: around 43 °C maximum. Nevertheless, it is observed that in other planes considering the inside of the breast and the tumor, and reported for this study in Figure 2, the maximum temperatures are considerably higher than 43°C (target value), reaching dangerous temperatures with a maximum of 47.77 °C in the control case. Also, the maximum heating is occurring in the healthy tissue instead of the tumor. The last suggests a lack of proper post-processing from the authors before concluding which voltage amplitude to apply to burn the specific regions of the tissue also considering that this is a 3D distribution, and both behavior and analysis are different from that reported by the authors, that just consider the heating on the breast base like this study was developed over a 2D distribution.

This study is like Elkayal et. al as the stage variation suggested little deviations of the maximum point depending on the phase shift. These deviations were more visible when the stage shift increased, but also led to lower values of maximum temperature. The negative stages applied to dipoles 2 and 3 remarkably moved the maximum temperature location towards these 2 electrodes, but again, compromising the maximum temperature reached.

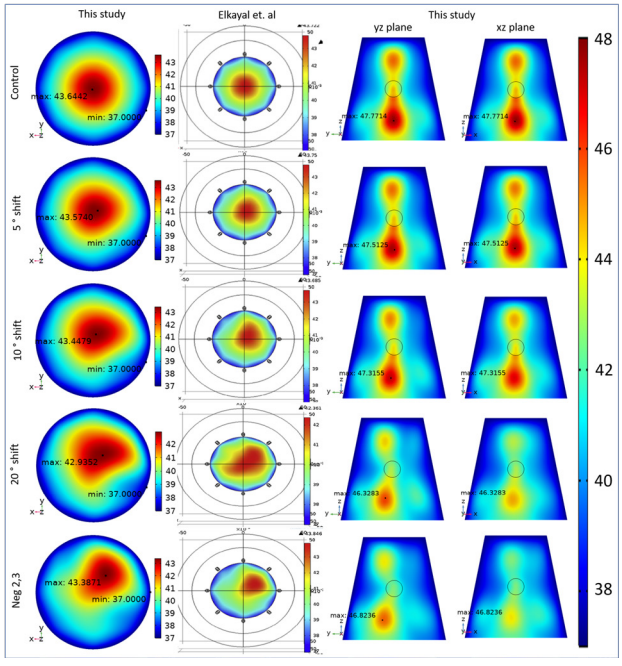

Figure 2. Results for this study compared to Elkayal et. al.

Conclusions or summary

The reproduction of the model and simulation developed by Elkayal et. al. in [7] was successfully achieved. Some discrepancies were found that can be due to some geometrical or material properties that were not reported in the original publication and had to be found in additional references. The current study goes deeper into the postprocessing and finds an incorrect conclusion in the original model, as the maximum temperature reached is much higher in other planes than the only one considered by the authors.

This study is the base for further investigation that includes using regression models based on simulation data to find the proper combination of stages that lead to the desired location of maximum temperature and then, improve the efficacy and selectivity of hyperthermia for breast cancer. The model also allows for calibrating the parameters to consider anatomic variation, different tissue and cancer properties, more realistic geometries from medical images, account for the tissue necrosis by using Arrhenius approximation, test different wave characteristics, and generation equipment, to mention some of the many possibilities that will be developed.

References

[1] Guerrero, E., Ballesteros, H., & Torres, L. F. (2018). Respuesta clínica en pacientes con tumores de mama tratadas con radioterapia conformacional postmastectomía en el Instituto Nacional de Cancerología, Colombia. Revista Colombiana de Cancerología, 22(4), 132–137.

[2] Division of Cancer Prevention and Control, & Centers for Disease Control and Prevention. (2021, September 20). What Are the Risk Factors for Breast Cancer? https://www.cdc.gov/cancer/breast/basic_info/risk_factors.htm.

[3] Bull, C., Malipatlolla, D., Kalm, M., Sjöberg, F., Alevronta, E., Grandér, R., Sultanian, P., Persson, L., Boström, M., Eriksson, Y., Swanpalmer, J., Wold, A. E., Blomgren, K., Björk-Eriksson, T., & Steineck, G. (2017). A novel mouse model of radiation-induced cancer survivorship diseases of the gut. American Journal of Physiology-Gastrointestinal and Liver Physiology, 313(5), G456–G466.

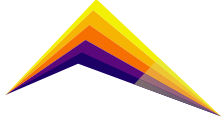

[4] Sales, A. R. K., Negrão, M. V., Testa, L., Ferreira-Santos, L., Groehs, R. V. R., Carvalho, B., Toschi-Dias, E., Rocha, N. G., Laurindo, F. R. M., Debbas, V., Rondon, M. U. P. B., Mano, M. S., Hajjar, L. A., Hoff, P. M. G., Filho, R. K., & Negrão, C. E. (2019). Chemotherapy acutely impairs neurovascular and hemodynamic responses in women with breast cancer. American Journal of Physiology-Heart and Circulatory Physiology, 317(1), H1–H12.

[5] Tajabadi, M., Rahmani, I., Mirkazemi, S. M., & Goran Orimi, H. (2022). Insights into the synthesis optimization of Fe@SiO2 Core-Shell nanostructure as a highly efficient nano-heater for magnetic hyperthermia treatment. *Advanced Powder Technology*, *33*(1), 103366.

[6] Nizam-Uddin, N., Abdulkawi, W. M., Elshafiey, I., & Sheta, A.-F. A. (2022). Towards an efficient system for hyperthermia treatment of breast tumors. *Biomedical Signal Processing and Control*, *71*, 103084.

[7] Elkayal, H. A., Ismail, N. E., & Lotfy, M. (2015). Microwaves for breast cancer treatments. *Alexandria Engineering Journal*, *54*(4), 1105–1113.

[8] Zastrow, E., Hagness, S. C., & van Veen, B. D. (2010). 3D computational study of non-invasive patient-specific microwave hyperthermia treatment of breast cancer. *Physics in Medicine and Biology*, *55*(13), 3611–3629.

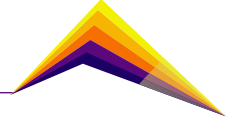

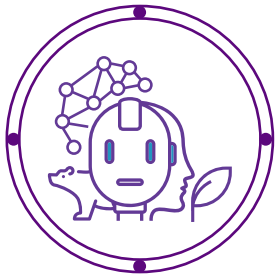

Automated semantic annotator for information retrieval, based on biomedical ontologies

Josue Santiago Cano-Pulgarin[1] *E-mail: josue.cano@udea.edu.co*
Fernando Mora-Ángel[2] *E-mail: fernando.mora@udea.edu.co*
Mónica Pineda-Gaviria[3] *E-mail: monica.pineda@udea.edu.co*
Jesenia Avendaño-Ramírez[4] *E-mail: ester.avendano@udea.edu.co*
Astrid Duque-Ramos[5] *E-mail: astrid.duquer@udea.edu.co*

[1, 2, 5] *Ingeniería y Tecnologías de las Organizaciones y de la Sociedad ITOS, Departamento de Ingeniería de Sistemas, Universidad de Antioquia UdeA, Calle 70 No. 52-21, Medellín, Colombia*
[3, 4] *Sistema de Bibliotecas, Universidad de Antioquia UdeA, Calle 70 No. 52-21, Medellín, Colombia*

Abstract

This paper presents an automated semantic annotation tool based on biomedical ontologies, applying Natural Processing Language (NLP) techniques and technologies based on the Semantic Web. All these have the purpose of identifying relevant concepts in a set of scientific articles. This can contribute to the classification and information retrieval available in data resources in the areas of health and parallel disciplines. The annotation was created in five stages: selection of a set of scientific articles and the preprocessing with NLP techniques; selection of the ontology (COVID-19) for the classification available in the repository of biomedical ontologies, BioPortal; creation of the automated annotator; validation of the annotator against the annotations of the Bioportal annotator and manual verification of the annotations by domain experts. Automated semantic annotators can be applied to retrieve key information for decision-making in different biomedical areas and scenarios, as they present a greater degree of relevance because the concepts of the ontology are created by experts in the health domain and constantly updated when new concepts are included.

Correspondent author

Keywords: Biomedical Ontology, Semantic Annotator, Information Retrieval

Introduction

The progress of science has produced an exponential increase in biomedical publications that are stored in digital information resources. Consequently, from it emerges the necessity to recover efficiently appropriate information [1], to make decisions in different scenarios. The Semantic Web use to search and classify information has improved. Semantic Web centers on ontology which are structures that represent and contextualize expert knowledge in a specific area. Ontology, from the artificial intelligence point of view, was defined in 1993 by Gruber, and then in 1997 Borst complemented this definition and Studer *et al* combined both definitions in 1998 like this: "an ontology is an explicit formal specification of a shared conceptualization" [2], in other words, ontology is a formal representation of a domain through its set of concepts and the hierarchy and semantic relation between them.

Ontologies contribute to recovering the data because it allows us to identify and contrast the terms found in a scientific article with their related concepts. To extract this information, a semantic annotator that extracts entities from the text and link them to a semantic description present in an ontology [3] has been developed.

Ontologies contribute to the recovery of information because they allow to label an article text and the related concepts using semantic annotation. Those are text entities with a link to a semantic description [3]. The semantic annotation with ontologies was applied in some approximations such as AeroDAML [4] or KIM [5] Another approximation is Ont-O-Mat [6], which is based on machine learning. Finally, Sanchez-pi *et al,* proposed a classification algorithm that uses ontologies to implement a text preprocessing stage. They search for the words in the text that match with the ontology to assign a label and determine the correspondence position of the label [7]. This algorithm was useful as supplies to implement the semantic annotator present in this article.

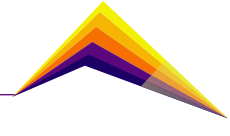

Methodology

The semantic annotator was developed in five main stages:

i) Data characterization: specific parser from JSON to a Pandas data frame was created from the JSON data extracted from the *Covid-19 Open Research Dataset Challenge (CORD-19)* [8].

ii) Ontology selection: elements for ontology selection defined in [9] were applied. Eight COVID-19 ontologies published on the Bioportal platform [10] created by the National Center for Biomedical Ontology were studied and the COVID-19 was chosen. This ontology contains 2.270 classes and 641, related to" molecular and cellular entity information, in the virus-host interactions of the virus life cycle, and a wide specter of medical and epidemiological concepts related".

iii) The preprocessing step had some stages and was made with RegexpTokenizer, stopwords, WordNetLemmatizer y Snowball Stemmer (implementation of Porter Stemmer) libraries from the NLTK package [11]:

   a. Remotion of abbreviations, punctuation signs, URLs, and null text. Replacing "\n" with simple space.

   b. Tokenization process (text segmentation by words), stopwords deleting (words without meaning from NLTK dictionary).

   c. Lemmatization uses vocabulary and morphological analysis of words and tries to remove inflectional endings, thereby returning words to their dictionary form. Its purpose is to make sure that things are done properly by analyzing if query words are used as verbs or nouns [9].

   d. Stemming removes derivational suffixes as well as inflections so that word variants can be conflated into the same roots or stems [9].

   e. Conversion of the text in plain to be received by the annotator.

iv) Annotator implementation: every ontology class went through the same preprocessing as the abstracts. Afterwards, the special regular expressions for the class searching and counting were applied. In addition, each class, was searched for the correspondent synonyms. As a result, the annotator gives the original class name and the synonyms give the base class name.

v) Test and validation, the annotation of ten abstracts from the CORD-19 database were obtained, applying six versions of the same annotator with different combinations of lemmatization and stemming. Then, experts manually validated those annotations. Additionally, 8013 abstracts annotations with one annotation were done; then, results of those from the BioPortal annotator were compared.

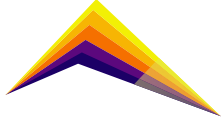

Results and analysis

Six versions of the automated annotator were created. For those versions, lemmatization and stemming over the abstract and the biomedical COVID-19 ontology were combined. Then, 8013 abstracts were annotated and ten of them were randomly selected to make a manual verification of the annotations with two experts in biomedical literature.

Figure 1. shows an abstract with the annotations, on the left side, and one fragment of the COVID-19 ontology on the right side. The annotations of this text are highlighted. In blue are the ontological concepts ("viral infections," "antiviral agents," "pandemic"), and in yellow the synonyms as well. For instance, in the text there are such terms as "SARS-2", "coronavirus", "SARS-COV-2", and "coronaviruses" however, they do not appear in the nodes of the ontology (right side) because they are not concepts in the ontology, but they are synonymous of the ontology concept "severe acute respiratory syndrome coronavirus 2" as is shown in the class description box. Therefore, the annotation identifies that those terms in the abstract are related to the same concept in the ontology and its frequency is 7 (Coronavirus (2), COVID-19 (2), SARS (3). This allows to identify a concept showing a correct use of the annotator.

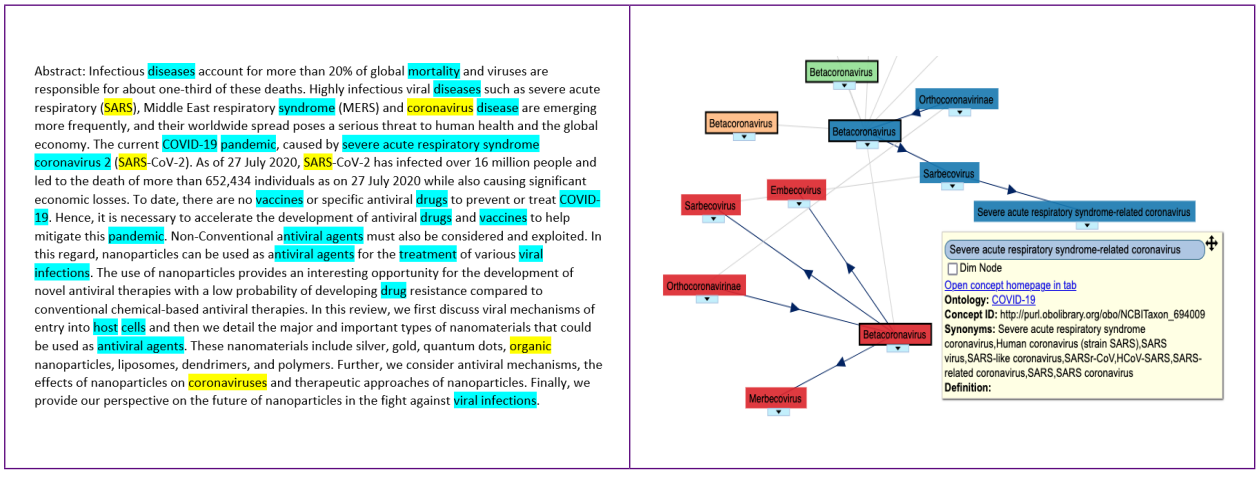

Fig 1. Summary of an article (left); A portion of the Covid-19 ontology with its synonyms (right).

Ten abstracts were annotated with the six annotator versions and a detailed analysis of the resultant annotations per abstract was done and presented in Table 1. In the manual verification, the experts identified that articles 1 and 9 did not present COVID-19 terms, in consequence, they were excluded from the study.

To compare the outcomes obtained, two versions of Bioportal annotator were used, one of them considers synonyms detection and the other one detects just categories. In this test, the developed annotator identified at least the same number of concepts as the annotator of the Bioportal reference. In table 1, the scenario with a higher number of average annotations per abstract was D.

Table 1: Total annotations by annotator version on chosen abstract.

Annotator Version	2	3	4	5	6	7	8	10	
	Number of annotations								**Average**
A: BioPortal with synonyms	6	18	2	20	11	28	11	32	14.1
B: BioPortal without synonyms	3	9	1	15	11	11	11	12	8.0
C: Lemmatized abstract, unlemmatized classes	8	20	5	22	15	40	16	38	17.6
D: Unlemmatized abstract, lemmatized classes	10	22	7	23	15	42	19	41	19.2
E: Abstract with stemming, classes without Stemming	8	12	3	17	6	24	14	14	10.8
F: Abstract without stemming, classes with Stemming	6	11	3	19	6	22	16	25	11.9
G: Abstract stemmed and lemmatized, classes without stemmed and lemmatized	8	5	3	17	6	24	14	14	10.1
H: Abstract without stemmed and lemmatized, classes with stemmed and lemmatized	15	15	8	20	15	35	26	30	17.8

Table 2 shows the outcomes for the eight remaining abstracts. True Positives (TP) are concepts that were annotated correctly; False Positives (FP) are those annotated but not present in the abstract; True Negatives (TN) are concepts that were excluded correctly, and False Negatives (FN) are those that were excluded incorrectly. For instance, in abstract 10 some of the concepts were TP: host, viruses, treatment; FP: Homo sapiens, TN: organ and FN: cell, vaccine, T cell). The rest of the concepts can be seen at https://3c5.com/v3pq0.

Table 2: Percentage of occurrence of TP, FP, TN, and FN in each scenario

VERSION/RESULT	TP	FP	TN	FN
A	58,17%	12,72%	8,20%	20,91%
B	51,86%	1,27%	15,75%	31,13%
C	71,20%	15,95%	6,48%	6,37%
D	78,18%	15,08%	5,93%	0,82%
E	45,28%	16,63%	7,89%	30,19%
F	45,22%	15,48%	9,14%	30,16%
G	47,15%	11,67%	8,86%	32,32%
H	76,95%	18,21%	2,32%	2,52%

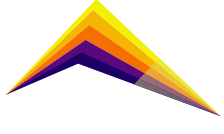

Finally, a comparison between the BioPortal annotator and the D annotator was done, through the creation of a weight metric defined in the formula (1), in which one unit of weight is added when annotator D has a concept that the BioPortal does not, or when both have the concept, but annotator D has it more frequently. If the BioPortal is the unique annotator with the concept or if this has more frequency, one unit of weight is subtracted from the metric.

$$\frac{\sum_{i=0}^{n} \frac{\sum_{j=0}^{c_i} p_j}{c_i}}{n} \quad (1)$$

Weights are normalized, where values near –1 indicate better performance for BioPortal, and a value near 1 indicates better performance for annotator D, while values near zero indicate equality in the annotators. Once the metric was applied to the 8013 annotated abstracts, its average was 0.418. Figure 2 represents the abstract distribution according to the metric; a higher number of annotated concepts have values in the range 0, 0.5, which means a moderated tendency with a higher frequency of concepts in annotator D.

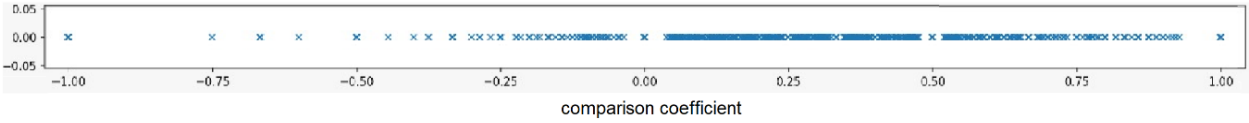

Figure 2: Comparison coefficient distribution of the annotations in Bioportal vs Version D of the annotator

Conclusion

1. This automated semantic annotator allows the identification of relevant concepts from articles, from any domain of knowledge, with a better degree of pertinence, because of the use of an ontology which is created by experts in that domain and constantly updated.
2. Lemmatization and stemming processes helped the annotator to be more efficient. In the manual verification, it was found that BioPortal identified ontology terms that corresponded to a higher level of the hierarchy, but they did not appear in the abstract.

3. The manual verification also showed that, in general, the use of stemming in the abstracts or the categorizes decreases the number of annotations, whereas the lemmatization either in the abstract or in the groups increases it. Then, a more complete analysis was done through the comparison coefficient which showed that annotator D identified more annotations than Bioportal, as future work a bigger manual verification would be done to demonstrate the performance of the classification.
4. The automated annotator can be applied for decision-making in any biomedical scenario with the selection of an adequate domain ontology.

References

[1] B. Xu *et al.*, "A supervised term ranking model for diversity enhanced biomedical information retrieval," *BMC Bioinformatics*, vol. 20, no. 16, pp. 1–11, Dec. 2019, doi: 10.1186/S12859-019-3080-2/TABLES/8.

[2] N. Guarino, D. Oberle, and S. Staab, "What Is an Ontology?" *Handbook on Ontologies*, pp. 1–17, 2009, doi: 10.1007/978-3-540-92673-3_0.

[3] H. N. Talantikite, D. Aissani, and N. Boudjlida, "Semantic annotations for web services discovery and composition," *Computer Standards & Interfaces*, vol. 31, no. 6, pp. 1108–1117, Nov. 2009, doi: 10.1016/J.CSI.2008.09.041.

[4] P. Kogut and W. S. Holmes, "AeroDAML: Applying Information Extraction to Generate DAML Annotations from Web Pages," *undefined*, 2001.

[5] I. Ismail, W. Gad, M. Hamdy, and K. Bahnsy, "Text document annotation methods: Stat of art," *2015 IEEE 7th International Conference on Intelligent Computing and Information Systems, ICICIS 2015*, pp. 634–640, Feb. 2016, doi: 10.1109/INTELCIS.2015.7397289.

[6] S. Handschuh, S. Staab, and A. Maedche, "CREAM-Creating relational metadata with a component-based, ontology-driven annotation framework," *Proceedings of the international conference on Knowledge capture - K-CAP 2001*, 2001, doi: 10.1145/500737.

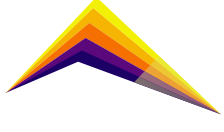

[7] N. Sanchez-Pi, L. Martí, and A. C. Bicharra Garcia, "Improving ontology-based text classification: An occupational health and security application," *Journal of Applied Logic*, vol. 17, pp. 48–58, Sep. 2016, doi: 10.1016/J.JAL.2015.09.008.

[8] L. L. Wang *et al.*, "CORD-19: The COVID-19 Open Research Dataset," *ArXiv*, Apr. 2020, doi: 10.48550/arxiv.2004.10706.

[9] V. Balakrishnan and E. Lloyd-Yemoh, "Stemming and lemmatization: A comparison of retrieval performances," *IACSIT*, pp. 174–179.

[10] A. Sargsyan *et al.*, "The COVID-19 ontology," *Bioinformatics*, vol. 36, no. 24, pp. 5703–5705, Dec. 2020, doi: 10.1093/BIOINFORMATICS/BTAA1057.

[11] "NLTK : Natural Language Toolkit." https://www.nltk.org/ (accessed Aug. 07,2022)

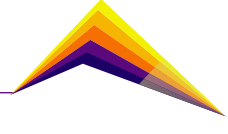

Biotribological behavior of Ti6Al4V alloy fabricated by EBM and subsequently anodized

Angie Ramírez[1] E-mail: alizeth.ramirez@udea.edu.co
Alexander Zuleta[2] E-mail: alexanderzuleta@itm.edu.co
Camila Zapata[3] E-mail: maria.zapatal@udea.edu.co
Carlos Vargas[4] E-mail: carlosvargas@itm.edu.co
Adrián Tamayo[5] E-mail: josetamayo@itm.edu.co
Libia Baena[6] E-mail: libiabaena@itm.edu.co
Juan G. Castaño[7] E-mail: juan.castano@udea.edu.co
Carlos Botero[8] E-mail: Carlos.Botero@miun.se
Alejandro Zuleta[9] E-mail: alejandro.zuleta@upb.edu.co
Nicolás Bedoya[10] E-mail: nicolas.bedoyao@upb.edu.co
Enrique Quiceno[11] E-mail: enriquequiceno@itm.edu.co
Maryory Gómez[12] E-mail: maryory.gomez@udea.edu.co

[1, 3, 7, 12] Universidad de Antioquia
[2, 4, 5, 6, 11] Instituto Tecnológico Metropolitano – ITM – Medellín
[8] Mid Sweden University
[9, 10] Universidad Pontificia Bolivariana

Abstract

Hip joints can be damaged by metabolic (degenerative disease) or mechanical (fracture) causes, limiting their functioning. To restore joint movement, the joint must be replaced by a hip prosthesis. Lubrication, friction and wear phenomena occur in the joints, which, in turn, are often responsible for the failure of the prosthesis, causing its loosening.

The aim of the present study is to evaluate the biotribological behavior of a prototype Ti6Al4V hip prosthesis made-up by electron beam melting (EBM) additive manufacturing and subsequently surface modified by anodizing. Once the prototype was obtained,

Correspondent author

some samples were polished for biotribological tests and others for anodizing. The biotribological tests were performed in a ball-on-disk tribometer using 6 mm diameter alumina counterbodies. Wear tracks of 2 mm in diameter were obtained, using SBF solution at a temperature of 37 °C as the medium.

The samples fabricated by EBM and subsequently anodized showed the highest values of friction coefficients, while the samples made-up by forging and EBM showed similar friction coefficients, while the anodized samples showed the lowest wear rate followed by the samples manufactured by EBM.

Key words: Biotribological behavior, Hip prosthesis, Joint movement, EBM, Anodizing

Introduction

Additive manufacturing processes have several associated benefits such as: material application, great design flexibility and property tailoring. These benefits are mainly maximized when using powders as raw materials due to their flexibility in localized handling and low material waste [1].

On the other hand, Ti6Al4V alloy is used for the manufacture of hip prostheses and hence the interest in studying its biotribological behavior. Ti6Al4V is widely used in biomedical applications considering its corrosion resistance, high specific strength, low density and low modulus of elasticity, however, when used as implant due to the biotribological surfaces formed, the passive layer surface is broken and thus its passivity, allowing the release of metal ions exacerbating the corrosion of the implant creating a synergy with the biotribological phenomenon [2-5].The fragments generated in hip implants can cause adverse reactions that lead to bone loss around the implant and therefore to loosening of the prosthesis, pushing a new revision surgery [6-8].

Taking into account the need to improve the performance of the materials used in implants, the present work studies the effect of the manufacturing process of Ti6Al4V prosthesis prototypes on their biotribological behavior when manufactured by conventional forging, EBM and anodizing on the prototypes manufactured by EBM.

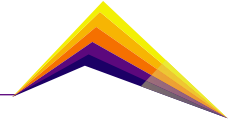

Materials and Methods

Samples of Ti6Al4V alloy were manufactured by electron beam melting (EBM) and subsequently anodized under the following parameters: pH=13.22, conductivity (ms/cm)=17.91, current density (mA/cm^2)=50 and time (s)=1000, the composition of the bath was: $Na_3PO_412H_2O$(g/L)=10, $Na_2SiO_35H_2O$(g/L)=2, EDTANa_2(g/L)=3.72 and NaOH(g/L)=2. For comparison purposes, samples of the same alloy obtained by conventional forging were also prepared. The samples were cut into disks of 18.02 mm in diameter and 3.77 mm in thickness, then the samples were polished using SiC emery paper with different grit sizes.

Biotribological tests were conducted in a ball-on-disk tribometer using 6 mm diameter alumina counterbodies (21GPa), wear tracks with 2 mm diameter were obtained, using SBF solution at a temperature of 37 °C as medium, with a load of 5 N, a speed of 30 rpm and a test time of 40 minutes. The friction coefficients were measured directly on the tribometer.

The samples were cleaned with ethanol in an ultrasonic bath for 5 min and then weighed in order to determine the mass loss during the tribometer tests, this procedure was performed before and after each test to find the wear rate. A Mettler Toledo UMX5 micro-balance with an accuracy of ± 0.1 µg was used to calculate the mass loss. The roughness (Ra) of the samples were measured with a BRUKER Dektak XT profilometer using longitudinal runs of 1500 µm at a speed of 100 µm/s.

In addition, the tribological surfaces of both the samples of interest and the counterbodies were analyzed by optical microscopy (Nikon Eclipse MA 100) in order to identify possible wear mechanisms in the different tribological pairs.

Results and analysis

Friction and wear

Table 1 shows the samples roughness and hardness values obtained by the used different methods, it can be seen that the anodized samples have the highest roughness, followed by the forged samples, while the samples prepared by EBM show the lowest roughness of all. The high roughness of the anodized samples could favor cell growth on the implants. The samples processed by EBM show higher hardness than the forged ones.

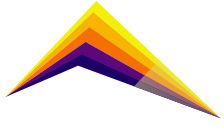

Table 1. Roughness and hardness of the samples tested.

Sample	Roughness (nm)	Hardness (HV)
Forged	125.52 ± 11.31	275.92
EBM	67.06 ± 5.62	381.34
Anodizing	1594.60 ± 359.81	--

Figure 1 shows typical results of friction coefficients as a function of test time for all-samples prototypes. Two stages of friction coefficients behavior were identified after 2400 s, an initial transient behavior (running-in) exhibited high fluctuation on friction coefficients values with a short period of continuous increment followed by a steady-stage regime. Generally, during the period of running-in period, plastic strain occurs in the subsurface region, such friction work is mainly due to plastic deformation.

The running-in period for the forged and EBM samples occurred for t < 100 s, followed by the steady-stage period with a friction coefficient of approximately of 0.40, which was observed in all two repetitions. EBM + Anodizing samples presents a higher coefficient of friction value than other samples of tribological test. The running-in period for this sample was approximately 300 s, followed by a steady-stage period with a coefficient of friction approximately of 0.70 with a slight decreased along the test time.

Figure 2 shows different samples wear rates, as can be appreciated the forged samples present the highest wear rate ($3.65x10^{-9}$ kg/Nm), while the samples prepared by EBM exhibit an ostensible decrease in wear rate ($0.59x10^{-9}$ kg/Nm). The lowest wear rate value was obtained in the anodized samples ($0.29x10^{-9}$ kg/Nm), showing a significant effect of EBM manufacturing in decreasing the friction coefficients and wear rates with respect to conventional forging processing. The anodizing, in spite of increasing the friction coefficient, shows a very important decrease in the wear rate. These apparently contradictory results are probably due to the ceramic nature of the anodized surface, which, by being harder, increases the friction value and at the same time is more protective against wear.

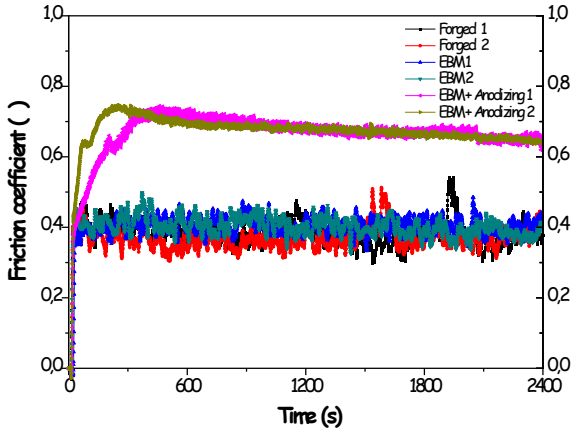

Figure 1. Records of friction coefficients as a function of test time.

Surface analysis

The wear tracks obtained after biotribological tests were characterized using optical microscope to explore the wear mechanisms.

Figure 3, shows comparative images of worn surfaces obtained after 2400 s, using SBF solution at a temperature of 37 °C as a method and a load of 5 N. The regions within the dashed lines correspond to the wear tracks of disk specimens, showing that the main wear mechanism in the Ti6Al4V forged, Ti6Al4V EBM and Ti6Al4V anodized samples is abrasion, with characteristic scratches in slip direction, probably caused by debris. Indeed, the wear tracks show more severe wear on the wrought formed alloy, followed by the EBM processed alloy while the anodized alloy after EBM processing reveals the same abrasive wear mechanism, but less severe. Additionally, the higher roughness resulting from this treatment probably makes it more suitable for implants by facilitating cell adhesion.

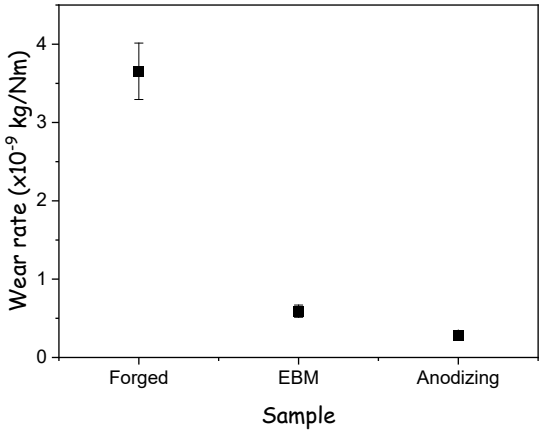

Figure 2. Different samples Wear rate.

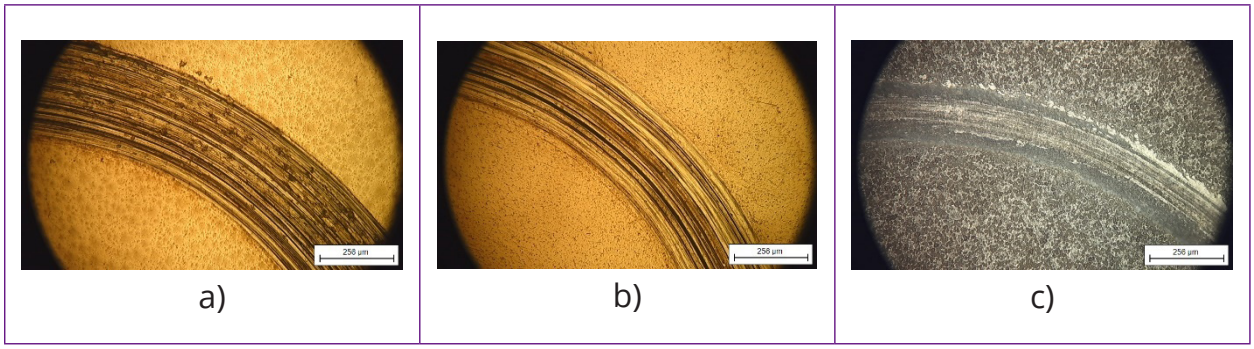

Figure 3. Optical microscope images of surface wear after biotribological test.
a) Forged, b) EBM and c) Anodized.

Conclusions or summary

The prototypes obtained by EBM manufacturing process of Ti6Al4V alloy showed an ostensible decrease in the wear rates under the evaluated conditions in the present study, while the friction coefficients remained similar to the samples obtained by forging.

The samples obtained by EBM and subsequently anodized by PEO exhibited wear rate values corresponding to half of the wear values found in the samples made-up by EBM without anodizing.

Acknowledgment

The authors are grateful to PROYECTOS DE I+D+i EN EL MARCO DE LA AGENDA REGIONAL DE I+D + i (Project #49), Instituto Tecnológico Metropolitano Project (PE21101), Universidad de Antioquia, Mid Sweden University, Centro de Investigación para el Desarrollo y la Innovación (CIDI) from the Universidad Pontificia Bolivariana (Rad: 636C-11/20-35 and Convocatoria becario de formación investigativa) and Corporación Ruta N.

References

[1] Scherillo, F, Manco, E, El Hassanin, A, Franchitti, S, Pirozzi, C. and Borrelli, R. (2020). "Chemical surface finishing on electron beam melting Ti6Al4V using HF-HNO_3 solutions." J. Manu. Processes, 10.1016/j.jmapro.2020.10.033, 400-409.

[2] Mathew, M.T, Barão, V.A, Yuan, J.C-C, Assunção, W.G, Sukotjo, C. and Wimmer, M.A. (2012). "What is the role of lipopolysaccharide on the tribocorrosive behavior of titanium?" J. Mech. Behav. Biomed. Mater., 10.1016/j.jmbbm.2011.11.004, 71-85.

[3] Mathew, M.T, Srinivasa, P.P, Pourzal, R, Fischer, A. and Wimmer, M.A. (2009). "Significance of tribocorrosion in biomedical applications: Overview and current status." Adv. Tribol., https://doi.org/10.1155/2009/250986, 1-12.

[4] Yan, Y, Neville, A, Dowson, D. and Williams, S. (2006). "Tribocorrosion in implants—assessing high carbon and low carbon Co–Cr–Mo alloys by in situ electrochemical measurements." Tribol. Int., https://doi.org/10.1016/j.triboint.2006.01.016, 1509-1517.

[5] Ríos, J.M, Quintero, D, Castaño, J.G, Echeverría, F. and Gómez, M.A. (2022). "Effect of EDTA addition on the biotribological properties of coatings obtained from PEO on the Ti6Al4V alloy in a phosphate-based solution." Surf. & Interfaces, 10.1016/j.surfin.2022.101857, 101857.

[6] McGee, MA, Howie, DW, Costi, K, Haynes, DR, Wildenauer, CI, Pearcy, MJ and D McLean, J. (2000). "Implant retrieval studies of the wear and loosening of prosthetic joints: a review." Wear, 10.1016/S0043-1648(00)00370-7, 158–65.

[7] Yan, Y, Neville, A. and Dowson, D. (2007). "Tribo-corrosion properties of cobaltbased medical implant alloys in simulated biological environments." Wear, 10.1016/j.wear.2007.01.114, 1105–1111.

[8] Brown, SS. and Clarke, IC. (2006). "A review of lubricant conditions for wear simulation in artificial hip joint replacements." Tribol. Trans., 10.1080/05698190500519223, 72–8.

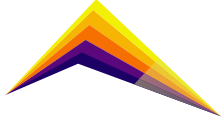

Bioengineering of Structured Lipids Microencapsulated as an Alternative of Healthy Oil

Angie Vanessa Caicedo Paz[1] Email: angie.caicedo@udea.edu.co
Marta Beatriz Mediavilla Quintero[2] Email: qmarta338@gmail.com
Aída Luz Villa[2,3] Email: aida.villa@udea.edu.co
Diego M. Sánchez-Osorno[1] Email: diego.sanchez@pascualbravo.edu.co
Victoria Mesa[1] Email: Victoriamesa@gmail.com
Julián Paul Martínez Galán[1] Email: Julian.martinez@udea.edu.co

1Laboratory of Human Nutrition and Feeding, School of Nutrition and Dietetic, Universidad de Antioquia, Medellín, Antioquia, Colombia
2Environmental Catalysis Research Group, Chemistry Engineering Department, Engineering Faculty, Universidad de Antioquia, Medellín, Antioquia, Colombia
3Applied Chemistry Department, Engineering Faculty, Venezuela Central University, Venezuela

Abstract

Structured lipids (SLs) are lipids modified by chemical reactions using 1,3 regio-selective lipases to the aim of modifying the fatty acid positions. This work is aimed in food bioengineering by enzymatic incorporation of capric acid in grape oil to obtain structured MLM lipids, which are alternative healthy oils. Furthermore, these lipids have functional properties, and metabolic or physiology effects used in prevention and treatments of several untransmissible chronic diseases (UCD) such as obesity, diabetes and cardiovascular diseases.

Grape seeds oil were selected as a raw material to obtain SLs due to the 80% of polyunsaturated fatty acids content, principally linoleic and linolenic acid. The biocatalyst used was *Rhizopus oryzae*, an uncommercial enzyme immobilized in corn cob powder, a low-cost support, the medium change fatty acid was capric acid; the synthesis of structured lipids was carried out by acidolysis reactions between the grape seed oil and capric acid using a stirred tank system as a

Correspondent author

bioreactor during 24 h, a molar ratio of 1:3 ratio (oil: acid), 45°C, and 10% of enzymatic load. The obtained incorporation degree was 35% which is very beneficial to improve the health lipid indices which define the SLs from grape seed as potential preventer of UCD.

SLs were microencapsulated to preserve their characteristics, using fibers as encapsulating material, obtaining 80% of the encapsulation degree. Controlled release tests of the encapsulated SLs by simulating gastrointestinal conditions showed a constant liberation at pH of 1 and 5.8. Grape seed oil, SLs and microcapsules were analyzed by gas chromatography to determinate the profile of fatty acids; grape seed oil had not capric acid on the profile, while for SLs the value was 44%, for microcapsules the profile remained constant due to the conservation of fatty acid composition. The effect of microencapsulated on the changes in the intestinal microbiota and on the metabolic alterations will be evaluated in the murine model of obesity.

Key words: Structured lipids, enzyme, *Rhizopus oryzae,* microcapsules.

Introduction

To satisfy the demand of health-conscious consumers, triacylglycerols or lipids have been developed in a way that modifies the positions and composition of fatty acids from the native state, originating structured lipids. Among these, dietary triglycerides stand out, which have a lower caloric value than conventional oils and fats (FERREIRA-DIAS et al., 2013). Designed primarily for special nutritional applications to meet the growing need for healthier foods (CAO et al., 2013). Its small size has the advantage of greater solubility compared to long-chain fatty acids, so short- and medium-chain fatty acids are transported directly to the liver, providing a quick source of energy (LEE et al., 2012).

MLM-type dietary triglycerides can be synthesized chemically or enzymatically. Depending on the type of substrate available, the following production methods can be used: (i) alcoholysis; (ii) acidolysis and (iii) interesterification (YANG T et al., 2005). Enzymatic synthesis of structured lipids is normally catalyzed by specific 1,3 lipases. The acidolysis reaction, catalyzed by these lipases, has been widely used to introduce capric and caprylic fatty acids into the sn-1 and sn-3 positions of different vegetable oils (FERREIRA-DIAS et al., 2013), while

maintaining long-chain unsaturated fatty acids in the sn-2 position, making their absorption more efficient (WANG et al., 2012).

The choice of *Rhizopus oryzae* lipase as an immobilized enzyme will improve industrial application, limited by its high cost, loss of stability under reaction conditions and difficulty in reuse in new cycles. A strategy used to minimize these inconveniences is the immobilization technique, which helps to increase stability and useful life of the immobilized form, and facilitate the recovery from the reaction medium (AMINI et al., 2017). Thus, support selection is an essential step in the development of a reaction system using immobilized biocatalysts.

Grapeseed oil has high content of monounsaturated fatty acids (MUFA), and polyunsaturated fatty acids (PUFA) (TANGOLAR et al., 2009) which make it ideal for synthesis of structured lipids. These fatty acids have been associated with health benefits such as antimicrobial, cardiac protector, anti-inflammatory, and anticancer (KAPOOR et al., 2021). It is possible to improve the nutritional value of some food products by incorporating grape seed oil in various matrices, thus taking advantage of the beneficial effects it has on health. However, some industrial processes such as the use of high temperatures, other compounds present in food, light and oxygen, could generate a degradation or modification of grape oil since it is chemically unstable and susceptible to oxidative degradation giving result to unwanted flavors, colors or aromas, in addition to the loss of its nutritional value (ZHONG et al., 2019).

Microencapsulation is a technology that seeks to protect bioactive compounds. In the case of lipids, it can delay oxidation, reduce volatility and improve the stability of oils and aromas.

Methods

Characterization of the grape seed oil

Fatty acid composition was determined by gas chromatography according to the American Oil Chemists' Society Method Ce 2-66 (AOCS 2011) before and after the acidolysis reaction A Gas Chromatography–Mass Spectrometry (GC–MS) was used to investigate the composition of the oil samples prior to and after encapsulation. The grapeseed oil analysis was performed using a Varian CP-3800 gas chromatograph equipped with a CP-Sil 8 CB Low Bleed/MS (length 30 m × Inner diameter 0.25 mm x film thickness 0.5 µm) column. Equipment conditions were set as follows: injector temperature at 250°C; flow rate of helium as the carrier gas was 1.5 mL/min; oven temperature initially at 50°C and then raised to 240°C at 3°C/min. Essential oil composition was then determined by mass spectrometry (ion trap temperature at 220°C; different temperature at 80°C, transfer line temperature at 240°C). The percentage of fatty acid incorporation degree was calculated according to the following equation: [*% ID = (MFA/MT) *100]* (CASAS-GODOY et al. 2013).

Enzymatic immobilization

The support selected was corn pop power as an agroindustry waste, it was chosen by the OH groups which allowed the activation of support for the immobilization , it was carried out using the methodology described by Bassan et al. (BASSAN et al. 2016). The enzymatic immobilization was realized as following: for each gram of activated support, 10 mL of 50 mmol/L sodium phosphate buffer (pH 7.0) containing enzymatic solution (25 mg/mL) was added. The suspension was submitted to agitation for 24 h at 25°C in a roll bed. The protein quantification was measured by the Bradford method (Bradford 1976) on the supernatant before starting the contact time and at the end to calculate the immobilization percentage of the enzyme on the support.

Acidolysis reaction on stirred tank reactor operated in batch mode

The acidolysis reaction was carried out between a sample of Grape seeds oil and capric acid in a stirred tank reactor operated in batch mode for 24 hours at 40C, 1:3 molar ratio (oil: acid) with 10% enzyme loading of the whole medium and constant stirring. After 24 hours of reaction, 3 g of sample was weighed, then 60 mL of hexane and 20 mL of 0.8 M KOH hydroalcoholic solution (30% ethanol) were added to remove the free FAs produced during the reaction (WANG ET AL. 2012).

Microencapsulation of grape seeds oil

Emulations were carried out by dissolving whey protein (WPI) and crystalline microcellulose (MCC), both under stirring by using an Ultra-Turrax T-25 homogenizer (IKA model Bioblock Scientific, Medellín, Colombia) for 5 min at room temperature and then the grape seed oil was added. For the emulsion preparation, the lipid core was incorporated into the aqueous phase using an Ultra-Turrax operated at 25000 rpm for 10 min and immediately after, the solution was spray dried. The encapsulating agent vs grapeseed oil ratio (w/w) was 3: 1. The emulation was spray dried, microcapsules were collected and analysed by electronic microscopy SEM and TEM, there was also carried out a gas chromatography analysis to compare the fatty acid profile whit the original oil.

Spray-drying conditions

Immediately after the preparation of the feed solution, encapsulation was carried out using a laboratory-scale Mini Spray Dryer (Buchi B-290), with a nozzle orifice diameter of 0.5 mm. The solution was fed at 25 °C into the main drying chamber through a peristaltic pump, and the feed rate was controlled by a rotary pump. The drying chamber was a glass cylinder with a diameter of 35 cm and a height of 90 cm. The following parameters were fixed: pump (10%), aspirator (100%), flow rate (600 L/h), inlet temperature (180 °C) and outlet temperature (100 °C).

Results and analysis

Characterization of the grape seeds oil

Table 1 shows the fatty acid profile of grape seed oil, where the fatty acid was estimated in 96%, 15% saturated fatty acid, 83% unsaturated fatty acid, linoleic acid was the most representative (48%) which makes an oil of great nutritional interest. The second most representative fatty acid was oleic (33%) followed by palmitic (10%).

Values for structured lipid were: linoleic (35%), oleic (15%), palmitic (6%); the incorporation degree was 35%. It was observed a diminution of the most representative fatty acids on the original oil due the incorporation of capric acid as it was expected, the new conformation of structured lipid makes it healthier and beneficial to human health due the behavior on the metabolism.

The profile of microencapsulation of grape seed oil shows that the composition of fatty acids remains constant. The fatty acid compositions of the non-encapsulated and encapsulated oil were 16.5% and 21.6% saturated fatty acids (SFAs); 25.67% and 25.47% monounsaturated fatty acids (MUFAs); 57.81% and 52.89% polyunsaturated fatty acids (PUFAs). The proportion of total fat in the microcapsule is accord to the encapsulation degree (85%)

Enzymatic immobilization

R. oryzae lipase was immobilized by covalent coupling to the glutaraldehyde-corn cob powder support and the amino group of the terminal lysine of the enzyme. The immobilization yields by protein quantification show values closer to 100% corroborating success of immobilization due to physicochemical characteristic of the support.

Acidolysis reaction on stirred tank reactor operated in batch mode.

A characterization of *R.O* enzyme was carried out, aimed to find optimum conditions for temperature, time of reaction, molar ratio, enzymatic load to the acidolysis reaction as described above. After 24 hours of reaction, the incorporation degree (35%) was calculated by gas chromatography which indicates a success of incorporation, this percentage is very significative according to literature reports because it improves the protector effect of the lipid on the development of UCD, decreasing saturated long chain fatty acids, which were replaced by medium chain fatty acid and improve the metabolism of lipids on the organism.

Microencapsulation of grape seeds oil

Figure 1 shows the different micrographs (SEM) (A, B ,C and D) of the microcapsules. All the samples observed show a superficial shrinkage of the particles, similar to the illustrations described by other authors (YANG & SHAN, 2021). It has been reported that the use of

optimal encapsulation conditions produces particles with smooth surfaces. However, when changing the encapsulating materials, it is necessary to modify the encapsulation conditions. The cellulose fiber used in the encapsulation processes produce rough surfaces (MENEGUIN et al., 2020) which would explain the roughness present in the obtained particles.

Additionally, it is believed that there is an incidence of temperature on surface roughness and particle shrinkage as reported by Yang 2021, where three states associated with temperature are identified. At the beginning of the drying process, in the water drop formed, there is a greater evaporation of water from the drop compared to the wall material; at this point the pressure inside the drop increases and the volume expands. The microcapsules do not show cracks or fractures which is important for the protection and retention of the encapsulated oil. However, when evaluating the internal morphology there was a fractured microcapsule (Fig. 1D). A correct wall formation is observed due the encapsulation fibers were completely homogeneous and in the hollow part, there is evidence of droplets embedded in the matrix, this being typical of the spray-drying process (RAMOS, SILVEIRA JÚNIOR, & PRATA, 2021). The wall thickness obtained is consistent at the drying temperatures used, exhibiting a good thickness in the wall material (RAMOS et al., 2021).

Transmission electron microscopy (TEM) can allow for a qualitative understanding of the internal structure, spatial distribution, and particle dispersion within the matrix of the wall material. Figure 1 (E and F) show the TEM micrographs for grapeseed oil microparticle, representing the cross-section of the particles in which the distribution of grapeseed oil inside the green polymers (WP and MCC) can be observed. As it can be seen, the grapeseed oil (light gray color) was concentrated in the centre of the particle, being surrounded by the wall material (dark gray color) as observed on the magnification of one microcapsule figure 1 (F) (FERNANDES et al., 2021)which are essential for the human body. However, their high degree of unsaturation (double bonds. These results are according with SEM results where the formed wall has a good formation.

Conclusions or summary

SLs enriched with capric acid were successfully produced by immobilized lipase *Rhizopus oryzae* on corn cob powder, using grape seed oil is an alternative raw material which will be beneficial for human health due to the advantages in the fatty acid composition and the improving at the digestion process and high nutritional value. The obtained incorporation degree was 35% which is very beneficial for improving the health lipid indices which define the SLs from grape seed as potential preventer of UCD. Matrices made by using whey protein and microcrystalline cellulose as green polymers with WP:MCC of 3:1 offer important possibilities for microencapsulation of grapeseed oil with higher encapsulation degree of 85%.

References

[1] AEMADI, F., AMINI, A., GHOLAMI, A., & GHASEMI, Y. 2017. Functionalized graphene oxide with chitosan for protein nanocarriers to protect against enzymatic cleavage and retain collagenase activity. *Scientific Reports*, *7*(1), 1-13. BASSAN, JULIANA CRISTINA, THAÍS MILENA DE SOUZA BEZERRA, GUILHERME PEIXOTO, CLARIANA ZANUTTO PAULINO DA CRUZ, JULIÁN PAUL MARTÍNEZ GALÁN, ALINE BUDA DOS SANTOS VAZ, SAULO SANTESSO GARRIDO, MARCO FILICE, & RUBENS MONTI. 2016. «Addendum: Immobilization of trypsin in lignocellulosic waste material to produce peptides with bioactive potential from whey protein. [Materials, 9, 5, (357)]». *Materials* 9 (8).

[2] BRADFORD, MARION M. 1976. «A rapid and Sensitive Method for the Quantitation of Microgram Quantites of Protein Utilizing the Principle of Protein- Dye Binding» 254: 248-54.

[3] KIM, B H, Y C ASIMIR C A AKOH. 2005. «Modeling of Lipase-Catalyzed Acidolysis of Sesame Oil and Caprylic Acid by Response Surface Methodology : Optimization of Reaction Conditions by Considering Both Acyl Incorporation and Migration AND», 12-15.

[4] CAO, Y.; QI, S.; ZHANG, Y.; WANG, X.; YANG, B.; WANG, Y. 2013. Synthesis of structured lipids by Lipase-Catalyzed interesterification of triacetin with camellia oil methyl esters and preliminary evaluation of their plasma lipid-lowering effect in mice. Molecules, v. 18, p. 3733 – 3744.

[5] FERNANDES, S. S., GREQUE, L., SANTOS, M. DE F. C., DE NOVAIS, L. M. R., D'OCA, C. D. R. M., PRENTICE, C., & SALAS-MELLADO, M. DE LAS M. (2021). Effect of the spray drying conditions on the physicochemical and structural characteristics and the stability of chia oil microparticles. *Journal of Applied Polymer Science*, *138*(39), 1–14.

[6] FERREIRA-DIAS, S.; SANDOVAL, G.; PLOU, F.; VALERO, F. 2013. The potential use of lipases in the production of fatty acid derivatives for the food and nutraceutical industries. Electronic Journal of Biotechnology. v. 16, n. 3, p. 1-38,

[7] KAPOOR, B., KAPOOR, D., GAUTAM, S., SINGH, R., & BHARDWAJ, S. 2021. Dietary Polyunsaturated Fatty Acids (PUFAs): Uses and Potential Health Benefits. *Current Nutrition Reports*, *10*(3), 232–242.

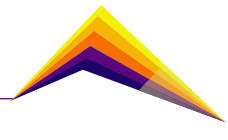

[8] LEE, YEE YING, TECK KIM TANG, AND OI MING LAI. 2012. "Health Benefits, Enzymatic Production, and Application of Medium and Long-Chain Triacylglycerol (Mlct) in Food Industries: A Review." *Journal of Food Science* 77 (8): 137–44.

[9] MENEGUIN, A. B., DA SILVA BARUD, H., SÁBIO, R. M., DE SOUSA, P. Z., MANIERI, K. F., DE FREITAS, L. A. P & CHORILLI, M. 2020. Spray-dried bacterial cellulose nanofibers: A new generation of pharmaceutical excipient intended for intestinal drug delivery. *Carbohydrate Polymers*, *249*(August), 116838.

[10] MISHRA, M. 2015. *Handbook of Encapsulation and Controlled Release*.

[11] Mohammed, N. K., Tan, C. P., Manap, Y. A., Muhialdin, B. J., & Hussin, A. S. M. 2020. Spray Drying for the Encapsulation of Oils—A Review. *Molecules*, *25*(17).

[12] NUNES, P.A.; PIRES-CABRAL, P.; GUILLÉN, M.; VALERO, F.; FERREIRA-DIAS, S. 2012. Optimized production of MLM triacylglycerols catalyzed by immobilized heterologous *Rhizopus oryzae* lipase. Journal of the American Oil Chemists' Society, v. 89, n. 7, p. 1287-1295.

[13] WANG, L.; PANPAN, Z.; YU, G.; JING, Z.; Xu, Q.; YONGKANG; G.; MINGXUN, Y.; Hongli, Z.; QITU, Z. 2019. The effect of ZnCl2 activation on microwave absorbing performance in walnut shell-derived nano-porous carbon. RSC Advances, 9(17), 9718– 9728.

[14] YANG, W., & SHAN, Z. 2021. Application of wool keratin: an anti-ultraviolet wall material in spray drying. *Journal of Food Science and Technology*, Vol. 58, pp. 4235–4244. https://doi.org/10.1007/s13197-020-04897-2YANG T, REBSDORF M, ENGELRUD U, XU X. 2005. Monoacylglycerol synthesis via enzymatic glycerolysis using a simple and efficient reaction system. J Food Lipids. 12(4):299–312.

[15] ZHONG, S., LI, L., SHEN, X., LI, Q., XU, W., WANG, X., & YIN, H. 2019. An update on lipid oxidation and inflammation in cardiovascular diseases. *Free Radical Biology and Medicine*, *144*(February), 266–278. https://doi.org/10.1016/j.freeradbiomed.2019.03.036

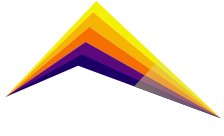

Table 1. Fatty acid profiles of grape seed oil, structured lipid and encapsulated grape seed oil.

Fatty acid (%)	Grape seeds oil	Structured lipid	Microcapsule of grape seeds oil
C10 **C16**	- 11.11	**35,54** 6,54	- 13,41
C18	3.77	2,22	4,58
C18:1 **C18:2** **C18:3**	25.37 51.64 6.17	15,09 30,82 3,66	25,08 47,30 5,60

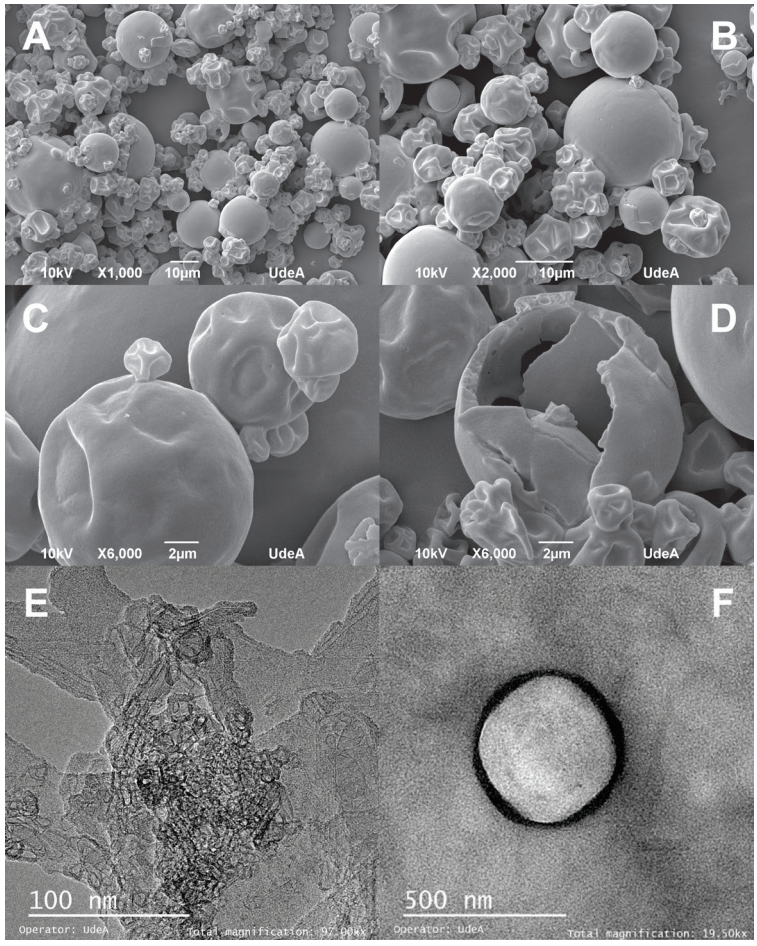

Figure 1 A) X 1000; B) X 2000; C) X 6000; D) Microcapsules Internal morphology. E) 100 mn and F) 500 nm Microcapsules TEM micrograph.

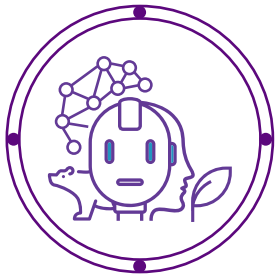

Analysis of Sustainability of Nopol Catalytic Production Using Non-Wood Forestry Biomass

Saleth Causil Durango[1] *Email: saleth.causil@udea.edu.co*
Aída Luz Villa[1] *Email: aida.villa@udea.edu.co*

[1]*Grupo de Investigación Catálisis Ambiental, Departamento de Ingeniería Química, Facultad de Ingeniería, Universidad de Antioquia*

Abstract

Currently, a large amount of chemicals and fuels is produced from fossil nonrenewable resources such as oil and natural gas. However, nowadays there is a great interest in the use of biomass as a source of energy and chemicals because of expected worldwide shortages of easy-to-access oil and gas. Furthermore, it is necessary to mitigate the harmful environmental impacts that are generated within the chemical industry that uses fossil sources as raw materials. Turpentine oil is one of the best-known and most exploited non-wood pine products, one of the products that can be obtained from turpentine oil is nopol which is a homoallylic alcohol. The use of clean catalytic technologies, especially with heterogeneous catalysts, is becoming increasingly important for the development of environmentally benign chemical processes; therefore, in this research, the technical, economic, and environmental feasibility of the nopol catalytic production process using turpentine oil as a source of β-pinene was studied. The best reaction conditions to obtain nopol from turpentine oil as a source of β-pinene were: 0.7 M β-pinene solution (a component of turpentine oil) in ethyl acetate, a catalyst loading of 17.6 % (mg catalyst/mg β-pinene), 90 °C, and a reactant molar ratio of 1:1. At these conditions, the highest conversion of β-pinene in turpentine oil was 56 %, and nopol

Correspondent author

selectivity was 79%. A process conceptual design was specified, through simulations using experimental data of nopol synthesis. In addition, the operating conditions, type, characteristics, and energy consumption of the different equipment involved in the proposed process were detailed. The environmental evaluation, carried out using the life cycle assessment methodological tool that employs the SimaPro software and the ReCiPe methodology, allowed to identify the main categories of impact generated by the process under study: climate change and human toxicity, particulate matter formation, and land use/transformation.

Keywords: nopol, life cycle assessment, feasibility, process design, environmental, green chemistry.

Introduction

Pine constitutes a major worldwide tree crop, providing an array of products to several industrial sectors [1]. Turpentine oil is one of the best-known and most exploited non-wood pine products, which is a complex mixture of terpenes produced by specialized cells responsible for the tree defense [2]. Terpenes are an important renewable feedstock for various applications, including chemical, pharmaceutical, agrochemical, food additive, and bioenergy industries [3]. Within terpenes, β-pinene, α-pinene, and limonene are of great commercial interest due to the possibility of being transformed into value-added chemicals by reactions such as hydration, isomerization, hydrogenation, oxyfunctionalization, epoxidation, hydrolysis, high-pressure thermolysis, ozonolysis, photo-oxidation, isomerization, and dimerization. Nopol, a homoallylic alcohol, is obtained by the reaction of Prins between β-pinene and the anhydrous formaldehyde polymer, known as paraformaldehyde, in the presence of a Lewis acid [4]. This alcohol is used for obtaining household and food products, as an intermediate in the synthesis of polymers, and in the formulation of active molecules in the pharmaceutical industry.

The life cycle assessment (LCA) is a robust methodology for environmental assessment internationally recognized, that is based on the collection of all the materials and energy resources from the raw material extraction until the product's final disposal, that are necessary for obtaining the product [5]. In this methodology, it is estimated and analyzed the environmental impacts attributable to the life cycle of a product. LCA has been applied to compare the environmental impacts of different catalytic reaction processes because they allow for more efficient, less energyintensive, more costeffective, and environmentally benign processes that promote significant energy savings in the chemical industry.

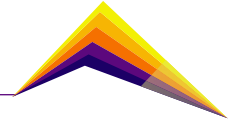

The use of turpentine oil as a source of β-pinene arises with several challenges related to the increase in process complexity, the presence of side reactions, and the increase of operating costs. However, the benefits are also noticeable: reduction in raw material costs, use of a resource available at the national level, and use of a by-product of the agroindustry. Therefore, this research work proposes to evaluate the sustainability by technical, economic, and environmental analysis of the nopol catalytic production process using turpentine oil as a source of β-pinene. The appropriate reaction conditions were evaluated at a laboratory scale and the LCA methodology was used for the environmental assessment of the process.

Methodology

Materials

Myristyltrimethylammonium bromide (Aldrich, 99%), tetraethyl orthosilicate (Sigma Aldrich, 98%), tin (II) chloride dihydrate (Alfa AEAR), ammonium hydroxide (Merck), ethyl acetate (Panreac, 99.5%), turpentine oil (ProtoKimica; 69.8 %p/p α-pinene, 12.3 %p/p β-pinene, and other terpenes), paraformaldehyde (Aldrich, 95%).

Methods

Catalytic tests. MCM-41 [6] and Sn/MCM-41 [4] were synthesized according to the reported methodology. The catalytic tests were carried out in 2 mL glass vials closed with silicone septa and provided with a magnetic stirrer. The reaction temperature was reached by introducing the vials in an oil bath, whose temperature was kept constant with the help of an EKT Hei-Con Heidolph temperature controller, under a magnetic stirring of 1000 rpm. Before separating the catalyst from the reaction mixture by centrifugation, the vials were introduced in a cold bath to stop the reaction. Reactants and products were identified and quantified using a GC-MS Agilent 7890.

Technical-economic analysis. The technical-economic analysis of the proposed process was carried out following the guidelines, well-established paradigms, and techniques used in chemical engineering process design [7]. This analysis allows evaluation of an investment alternative, in which the costs associated with total investment capital and operating costs must be calculated. The cash flow of the project was projected in an established period (10 years) and the profitability of the project was obtained through and Net Present Value analysis.

Environmental analysis. The LCA was carried out following the guidelines of the ISO 14040 standard [8], which involves four phases: definition of objective and scope that also includes system limit and functional unit; inventory data collection and analysis for explaining and presenting life cycle inventory data; life cycle impact assessment for selecting of impact

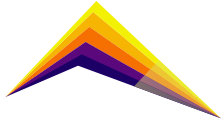

categories for energy and resource, as well as the emission generated, and interpretation and presentation of results. SimaPro® software, the Ecoinvent® database, Excel®, and Matlab® software were used. The LCA software SimaPro® 9.0 by PRé Sustainability and Ecoinvent v.3.5 were used, respectively, for the LCA model and to evaluate the impact assessments using the mass and energy balances obtained from the techno-economic analysis.

Results and analysis

Catalytic tests

The results of the catalytic test show that from turpentine oil, it is feasible to obtain nopol from β-pinene (oil component), using the catalyst Sn/MCM-41. Up to 56.3% conversion and 78.3% yield towards nopol production were achieved, at moderate reaction conditions (8 h, 0.7 M β-pinene solution (a component of turpentine oil) in ethyl acetate, a catalyst loading of 17.6 % mg catalyst/mg β-pinene, 90 °C, reactant molar ratio of 1:1); the above conditions minimize the presence of secondary reactions and adsorption of the solvent on the surface of the catalyst. To minimize the processes of repolymerization of formaldehyde is recommended to use a stoichiometric molar ratio of reactants. A reaction rate mechanism based on the Langmuir–Hinshelwood approach was adjusted to nopol experimental initial reaction rates data with ethyl acetate as solvent.

Technical-economic analysis

A conceptual design of the nopol production process from turpentine oil was established, which involves the stages of obtaining and treating raw materials, synthesis, and purification of the product of interest, using the information collected at laboratory scale, design algorithms in engineering, and software specialized in simulation of chemical processes (Matlab® software and Aspen Tech® suite software). The nopol production process begins with the entry of the raw materials, the catalyst, and the solvent (fresh and recirculated ethyl acetate mixture) to the reaction unit that operates in batch mode. The reaction process is carried out isothermally at 90 °C, with constant stirring for 8 h. At the end of the batch process, the reactor effluent, a liquid-solid suspension, is separated employing filtering equipment. The liquid phase is sent to a sequence of 3 distillation columns and the solid filter cake is dried and sent to the reaction unit. In the first column, the solvent is separated and recirculated to the reaction unit; in the second tower, the monoterpenes are separated from the sesquiterpenes and alcohols obtaining a stream rich in pinene; and in the third tower, nopol is obtained. The economic evaluation of the proposed process showed that through a 10-year projection of the project's cash flow and using the Net Present Value analysis, the process is profitable if the product has a minimum market price of 37 USD$/kg.

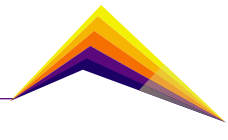

Environmental analysis

For this analysis, 1 kg of synthesized nopol with a purity greater than 95% was selected as the functional unit. As nopol is an intermediate product within fine chemistry that has a wide range of possible uses and transformation and for fine chemical processes, it is recommended to work up to the synthesis stage of the product of interest, therefore, the scope of the work was defined as "cradle to gate". Figure 1 shows the boundaries of the system.

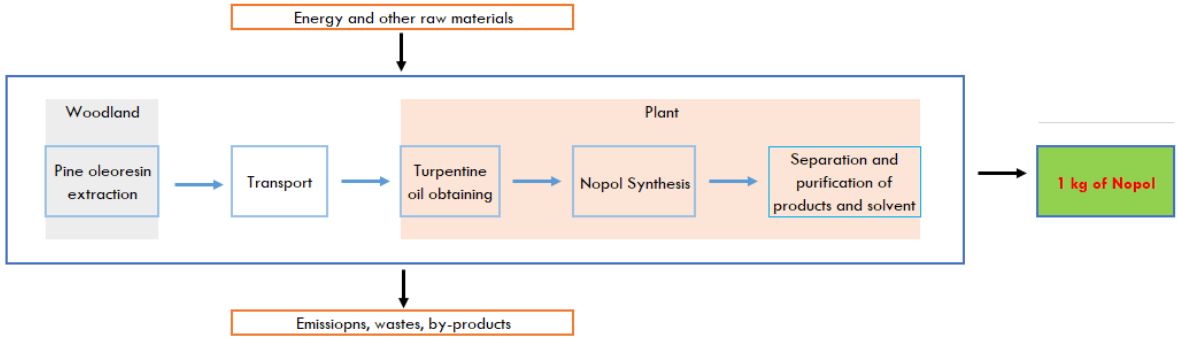

Figure 1. Production of nopol from turpentine oil – System boundaries.

Table 1. ReCiPe Environmental Impact Categories results, per 1 kg of nopol.

Impact Categories - Midpoints	Characterization		Normalization
	Unit		
Global warming	$kg_{eq}\ CO_2$	75.7	0.00946
Stratospheric ozone depletion	$kg_{eq}\ CFC\text{-}11$		7.66
Ionizing radiation	$kBq\ Co\text{-}60_{eq}$	4	0.00832
Ozone formation, Human health	$kg_{eq}\ NO_x$	0.369	0.0179
Fine particulate matter formation	$kg_{eq}\ PM_{2.5}$	0.166	0.0065
Ozone formation, Terrestrial ecosystem	$kg_{eq}\ NO_x$	0.39	0.0219
Terrestrial acidification	$kg_{eq}\ SO_2$	0.336	0.0082
Freshwater eutrophication	$kg_{eq}\ P$	0.0957	0.147

Impact Categories - Midpoints	Characterization		Normalization
	Unit		
Marine eutrophication	kg_{eq} N	0.00764	0.00166
Terrestrial ecotoxicity	kg_{eq} 1,4-DCB	569	0.0374
Freshwater ecotoxicity	kg_{eq} 1,4-DCB	2.75	0.109
Marine ecotoxicity	kg_{eq} 1,4-DCB	3.88	0.0892
Human carcinogenic toxicity	kg_{eq} 1,4-DCB	11.4	1.1
Human non-carcinogenic toxicity	kg_{eq} 1,4-DCB	72.2	0.00231
Land use	$m^2_{(annual\ cropland\ eq)}$	187	0.0302
Mineral resource scarcity	kg_{eq} Cu	0.208	1.73
Fossil resource scarcity	kg_{eq} oil	22.7	0.0231
Water consumption	$m^3_{sagua\ eq}$	3.65	0.0137

Table 1 shows that the most relevant impact categories are: Human carcinogenic toxicity, freshwater eutrophication, freshwater ecotoxicity, and marine ecotoxicity. These results are related specifically to the use in the process stages of some chemical reagents such as ethyl acetate, formaldehyde, and catalyst precursors, which would have a direct impact on these categories. The energetic costs of the process and its interrelation with the use of fossil fuels is another process parameter that has a high impact. Another relevant category is land use, basically because the raw material for the process is turpentine oil, which is obtained from coniferous crops that require a large amount of planted land to obtain good yields. Since the process has already been extensively studied, no changes in the reagents used in the reaction are proposed. One alternative is to recirculate the solvent or to use conditions that decrease the generation of by-products.

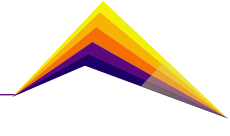

Conclusions

The results of this work show the viability of obtaining nopol from turpentine oil; nopol was obtained using turpentine oil as β-pinene source (ethyl acetate, SnMCM-41 loading of 17.6 mg catalyst/mg β-pinene, 90 °C, a reactant molar ratio of 1:1), with 56 % conversion and nopol selectivity of 79%. A positive effect was established in the economic field of the integration of the process units, specifically regarding the recirculation of the solvent. Preliminary sales values of the product of interest, nopol, were established that guarantee economic returns and make the project attractive to investors. It was possible to specify a process, through simulations using experimental data, of relatively simple nopol synthesis. In addition, the operating conditions, type, characteristics, and energy consumption of the different equipment involved in the proposed process were detailed. The LCA results showed that in general, the phase of raw materials extraction contributes to a much greater extent to the environmental burdens than the production process phase. Furthermore, it was determined that ethyl acetate is the hotspot in the process.

Acknowledgment

The authors thank funding from Ministerio de Ciencia, Tecnología e Innovación, Ministerio de Educación Nacional, Ministerio de Industria, Comercio y Turismo, and ICETEX, Programme Ecosistema Científico-Colombia Científica from Fondo Francisco José de Caldas; Grant RC-FP44842-212-2018.

References

[1] Aryan, V., Maga, D., and Kraft, A. (2019). J. Clean. Prod., 224, 766–778.

[2] Neis, F., Fett, J., de Costa, F., Fett-Neto, A., and de Araújo, A. (2019). Ind. Crops Prod., 130, 248.

[3] Rubulotta, G., and Quadrelli, E. A. (2019). In Horizons in Sustainable Industrial Chemistry and Catalysis, vol. 178, Albonetti, S., Perathoner, S., and Quadrelli, E., (Eds.), Amsterdam, Elsevier, 215.

[4] Casas-Orozco, D., et al. (2017). Ind. Eng. Chem. Res., 56, 6590–6598.

[5] Nuss, P. (2016). In Catalysis for Sustainability Goals, Challenges, and Impacts, Umile, T. Ed. Boca Raton - FL: Taylor & Francis Group, 177–194.

[6] Grün, M., Unger, K., Matsumoto, A., and Tsutsumi, K. (1999). Microporous Mesoporous Mater., 27, 207.

[7] Seider, W., Seader, J., Lewin, D., and Widagdo, S. (2009). Product and Process Design Principles, 3rd ed. John Wiley & Sons, New Jersey, EE.UU.

[8] Instituto Colombiano de Normas Técnicas y Certificación. (2022). NTC-ISO 14040:2022. Bogota, 1–25.

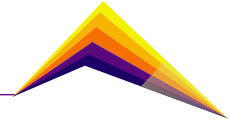

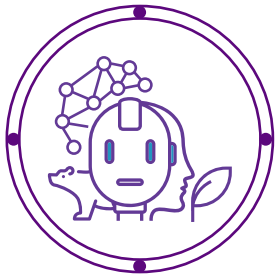

Transformation of monoterpenes through one-pot pathways over heterogeneous catalysts

Luis A. Gallego-Villada[1]
Edwin A. Alarcón[2]

E-mail: alfonso.gallego@udea.edu.co
E-mail: edwin.alarcon@udea.edu.co

[1,2] Chemical Engineering Department, Environmental Catalysis Research Group, Universidad de Antioquia, Calle 70 N° 52-21, Medellín 050010, Colombia

Abstract

β-Pinene is one of the main components of turpentine oil, which can be extracted from different Pinus species. In this way, the study of its valuation towards high added-value products such as myrtanal is a significant challenge in fine chemistry. In the present work, MCM-41 was synthesized according to the traditional methodology using the sol-gel procedure. xFe/MCM-41 materials were prepared by wetness impregnation using Fe (III) nitrate nonahydrate as a salt precursor. Commercial MgO was used, together with xFe/MCM-41, as heterogeneous catalysts for the transformation of β-pinene towards myrtanal through a one-pot pathway (epoxidation and epoxide isomerization in one vessel). The highest selectivity to myrtanal (75%), with complete conversion of β-pinene, was achieved using 1: 1.2: 0.72: 30.2: 19.7: 15.6: 0.8 as weight ratios for **β**-pinene: MgO: 1Fe/MCM-41: H_2O: acetone: acetonitrile: H_2O_2, after 48 h at 50 °C.

Correspondent author

Keywords: β-Pinene, Myrtanal, MgO, Fe/MCM-41, One-Pot.

Introduction

A significant contemporary challenge in organic chemistry is the search for alternative cleaner, safer, and environmentally friendly technologies, which are addressed to contribute to the goals of sustainable development and the principles of green chemistry [1]. Therefore, reducing waste and using renewable feedstocks, environmentally friendly reagents, and catalysts are significant to achieve more sustainable processes. An effective approach is synthesizing the target molecule in a single reaction vessel, often termed 'one-pot', to apply to a multi-step reaction, method, or synthesis. This approach is promising and effective because the transformations can be carried out in a single pot, avoiding several intermediate purification processes, minimizing chemical waste, saving time, and simplifying practical aspects [2].

One-pot catalytic reactions are not yet in general application because the control of these kind of reactions are quite difficult because the interactions that arise between different active species and components involved in the overall synthetic sequence can cause deactivation. A possible approach to address the problem is the preparation of multi-site solid catalysts in which a series of well-optimized isolated active sites are immobilized on support to catalyze different reactions but also it is possible to use the catalysis-in tandem approach, which is related to the use of multiple catalysts, achieving control and optimization of selectivity, as is presented in this contribution since MgO and Fe/MCM-41 are used as catalysts [1].

Turpentine oil, derived from coniferous forests, especially of the *Pinus genus*, is a colorless liquid of low viscosity that is mainly composed of α- and β-pinene monoterpenes [3]. The composition and its properties depend significantly on the species of the pine tree, the cultivated area climate, the geographical location, and the soil conditions [4]. The functionality of terpene epoxides to high-added value products have promoted the research towards the oxidation of monoterpenes, which is one of the most important organic transformations that can occur through two competitive pathways: i) double bond epoxidation and ii) allylic oxidation, whose predominance of each reaction pathway depends on the olefin nature, the oxidizing agent, the catalyst, and the reaction conditions [5].

The epoxidation of β-pinene has been reported over different heterogeneous catalytic systems such as ZnCo-MOF, CoOx/mordenite, $FeCl_3 \cdot 6H_2O$, $PdCl_2$ and $[(nBu_3Sn)_2MoO_4]$, which have shown yields to β-pinene epoxide of 44.3%, 34.3%, >46%, 11%, and 28%, respectively. However, MgO has been reported as a highly active and low-cost catalyst for the epoxidation of β-pinene with complete conversion and 74% of selectivity towards myrtanal under mild conditions (50 **°C, 2 h,** $\mathbf{H_2O_2}$ and acetonitrile as combined oxidant, acetone as solvent and excess H_2O as improver) [6]. This is a promising material because of its simplicity, as well as low environmental impact, health risk, and cost, which are desirable properties of a heterogeneous catalytic system [6]. On the other hand, Sánchez-Velandia et al. reported Fe/MCM-41 materials as promising for the isomerization of β-pinene epoxide towards myrtanal because it is favored in catalysts with high content of Lewis acid sites [7].

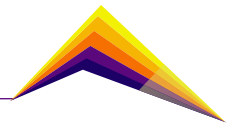

Up to date, there have not been reports on carrying out the transformation of β-pinene towards myrtanal through a one-pot catalytic route (Figure 1). In that way, the most important aim of this research is to establish suitable reaction conditions for the selective synthesis of myrtanal from β-pinene using mild conditions.

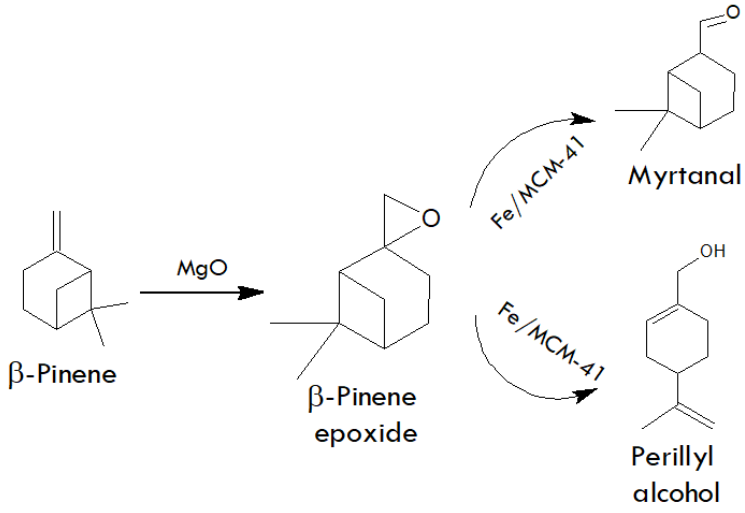

Figure 1. β-pinene Transformation through a one-pot catalytic pathway.

Materials and Methods

Materials

Business-related reagents were used as received. Reagents for catalysts preparation were myristyltrimethylammonium bromide (MTAB, 99 wt %, Sigma-Aldrich), tetraethyl orthosilicate (TEOS, 98 wt %, Sigma-Aldrich), ammonium hydroxide (NH_4OH, 29 wt %, Merck), iron (III) nitrate nonahydrate ($Fe(NO_3)_3.9H_2O$, 99.5 wt. %, PanReac AppliChem) and magnesium oxide (MgO, 99.6 wt. %, J.T. Baker). Reagents for catalytic tests were β-pinene (99 wt %, Sigma-Aldrich), hydrogen peroxide (H_2O_2, 30 % w/v, PanReac AppliChem), acetone (99.9 wt. %, PanReac AppliChem) and acetonitrile (99.5 wt. %, Merck).

Synthesis of Fe/MCM-41

MCM-41 support was obtained according to the methodology reported by Grün et al. [8]. The template, MTAB, was dissolved in deionized water under magnetic stirring (750 rpm), for getting a concentration of 0.055 mol L^{-1}. Then, the basic pH was controlled with NH_4OH and subsequently, TEOS was added dropwise, using a Masterflex model 77200-60 peristaltic pump (0.7 mL min^{-1}). The molar ratio of the mixture was 1 TEOS: 0.1380 MTAB: 1.6280 NH_4OH: 147.0995 H_2O. This syrup was constantly stirred at room temperature for 1 h. The

precipitate was filtered and dried overnight at 100 °C. Finally, the solid was burned at 1 °C min^{-1} up to 550 °C for 5 h, under static air. Typical conditions of synthesis were: 22.43 g MTAB, 101.71 g TEOS, 104.60 mL NH_4OH, and 1.2 L of deionized water. Fe loading was anchored to MCM-41 using the wetness impregnation procedure where the salt precursor, in deionized water (1 wt. %), was added to the support and the mixture was constantly stirred for 2 h and afterward dried at 60 °C overnight. Finally, the solid was burned at 1 °C min^{-1} up to 550 °C for 5 h, under static air.

Catalytic tests

Reactions were performed in 2 mL capped vials as reactors, covered with silicone septa. The reaction temperature was maintained by immersing the vias in a well-stirred oil bath with an EKT Hei-Con Heidolph controller. After removal, samples were cooled in an ice bath to subsequently separate the catalysts from the reaction mixture by centrifugation at 3000 rpm for 15 min. In a typical test, 0.10 mmol of β-pinene is used and 1:1.2:0.72:30.3:19.7:15.7:0.8 as weight ratios for **β**-pinene: MgO: Fe/MCM-41: H_2O: acetone: acetonitrile: H_2O_2, were poured in the reactor at 50 °C. The reaction products were identified by gas chromatography using a GC-MS Agilent 7890 N with a DB-1 column (30 m, 320 **µ**m, 0.25 **µ**m), equipped with an FID detector and autosampler. The carrier gas was He (30.462 cm s^{-1}), the split ratio 15:1. The oven temperature was kept at 70 °C for 2 min and then, heated up to 130 °C (10 °C min^{-1}) for 1 min, and finally heated up to 180 °C at 20 °C min^{-1}. The detector temperature, injection volume, and carrier gas (He) flow were 250 °C, 1 **µL**, and 30 mL min^{-1}, respectively. Substrate conversion, product selectivity, and product yield were calculated with Eqs. (1)-(3), respectively.

$$\%\ \text{Conversion}\ (X) = (A_i - A_f)\_\beta\text{-pinene}/A_{i,\beta\text{-pinene}} * 100 \qquad \text{Eq.(1)}$$

$$\%\ \text{Selectivity j}\ (S) = A(f,j)/(\sum A_{products}) * 100 \qquad \text{Eq.(2)}$$

$$\%\ \text{Yield j}\ (Y) = A_{f,j}/A_{i,\beta\text{-pinene}} \qquad \text{Eq.(3)}$$

Where A_i and Af correspond to areas at the initial and final time, respectively.

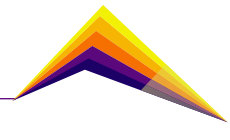

Results and analysis

The effect of the Fe loading in the catalyst xFe/MCM-41 (x = 1 wt. %, 3 wt. % and 5 wt. %, Figure 2.A), catalyst concentration (weight ratio for xFe-MCM-41/β-pinene = 0.72, 1.27, 1.81 and 2.36, Figure 2.B), H_2O_2 concentration (weight ratio for H_2O_2/β-pinene = 0.40, 0.80, 1.20 and 1.60, Figure 2.C), and temperature (50 **ºC**, 60ºC and 70 ºC, Figure 2.D) were evaluated in the oxidation reaction of β-pinene with H_2O_2. Conversion profiles are not shown in Figures A and D because a complete conversion was achieved at all times under different conditions.

Figure 2.A shows a significant similarity in the selectivity profiles towards epoxide and myrtanal with the three Fe loadings, although slightly higher selectivity towards myrtanal and lower towards epoxide is observed. On the other hand, Blank (there is no Fe-based catalyst but only MgO) shows that it is possible to produce myrtanal but with a lower selectivity than it is used a Lewis acid catalyst as xFe/MCM-41, which improves the isomerization of the epoxide. Therefore, 1Fe/MCM-41 was chosen for evaluating the effect of the other variables, which allow achieving complete conversion and selectivities around 75% and 23% towards myrtanal and epoxide, respectively, after 48 h.

Figure 2.B shows complete conversions except in 1 h of reaction for 1Fe-MCM-41/β-pinene weight ratios of 1.27, 1.81, and 2.36, which suggests that the catalytic activity in a system is not always improved by a greater amount of catalyst. When this ratio is 0.72, the highest selectivities to myrtanal (75%) and epoxide (23%) are achieved, while when that ratio is increased (there is more acid catalyst in the reaction medium), the selectivity to both myrtanal and epoxide decreases, giving an increase to the formation of other products of the epoxide rearrangement such as myrtenol and perillyl alcohol and oxidized products such as diols.

Figure 2.C shows that a β-pinene conversion of around 50% is achieved in 1 h of reaction when an H_2O_2/β-pinene weight ratio of 0.40 is used but complete conversions are observed for higher times and the other weight ratios. On the other hand, with a ratio of 0.80, the best selectivities towards myrtanal after 8 h, 24 h, and 48 h are achieved, while a ratio of 0.40 allows obtaining the lowest and highest selectivity to myrtanal and epoxide, respectively, after 24 h and 48 h. Selectivities very close to zero are achieved after 48 h when ratios of 1.20 and 1.60 are used, due to other products such as perillyl alcohol and diol are obtained under that conditions.

Figure 2.D shows that the **β**-pinene epoxide ring-opening is favored at high temperatures (60 ºC and 70 ºC) because selectivity to epoxide is close to zero after 24 h, while that selectivity at 50 ºC is around 50% and 23% after 24 h and 48 h, respectively. However, the best selectivity to myrtanal is achieved at 50 ºC, which is a temperature that avoids the formation of many products in comparison with the other two. Furthermore, the selectivity to myrtanal remains almost constant after 24 h when the reaction is carried out at 60 ºC and 70 ºC.

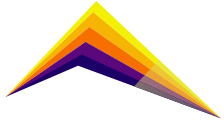

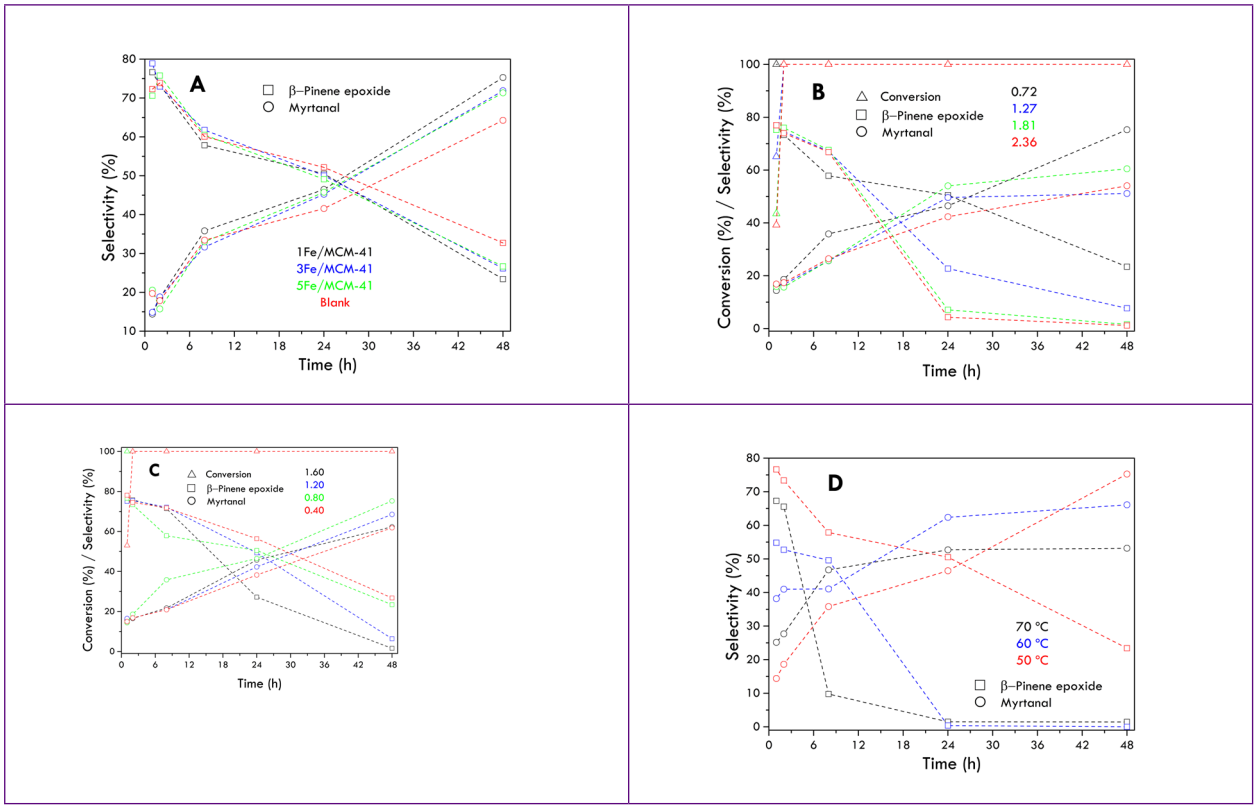

Figure 2. Different variables effect on catalytic measurements: conversion and selectivity towards epoxide and myrtanal, in the **β**-pinene oxidation with H_2O_2. Reaction conditions: 0.10 mmol **β**-pinene, 1:1.2:30.3:19.7:15.7 as weight ratios for **β**-pinene: MgO: H_2O: acetone: acetonitrile, 50 **ºC**. **A.** Effect of the Fe loading onto MCM-41 (xFe-MCM-41/β-pinene = 0.72). **B.** Effect of the 1Fe/MCM-41 concentration (1Fe-MCM-41/β-pinene weight ratio = 0.72, 1.27, 1.81, 2.36). **C.** Effect of the H_2O_2 concentration (H_2O_2/β-pinene weight ratio = 1.60, 1.20, 0.80, 0.40). **D.** Effect of the temperature (70 **ºC, 60 ºC, 50 ºC**).

Conclusions

The oxidation reaction of **β-pinene with H_2O_2** was studied under mild reaction conditions, evaluating the effect of four variables such as Fe loading in MCM-41, catalyst concentration, H_2O_2 concentration, and temperature. Results showed that Fe loading does not have a significant effect on the selectivity towards β-pinene epoxide and myrtanal; in addition, the tests without the Fe/MCM-41 catalyst (Blank = only MgO as a catalyst) showed that it is possible to produce myrtanal but it can be improved with the presence of a Lewis acid catalyst such as Fe/MCM-41. On the other hand, with high amounts of 1Fe/MCM-41 in the reaction mode , the selectivity towards myrtanal decreased but the formation of perillyl alcohol, myrtenol, and diols is observed. Therefore, the highest selectivity to myrtanal is

obtained with a 1Fe-MCM-41/β-pinene weight ratio of 0.72. Similarly, the formation of other products of epoxide rearrangement is favored with high weight ratios for H_2O_2/β-pinene (1.6 and 1.2), while a ratio of 0.8 allows obtaining the best selectivity towards myrtanal. The β-pinene epoxide ring-opening is favored at high temperatures, whose results showed the highest selectivity to myrtanal at 50 °C.

Acknowledgments

Authors thank funding from the Ministry of Science, Technology, and Innovation, the Ministry of Education, the Ministry of Industry, Commerce and Tourism and ICETEX, programme Ecosistema Científico – Colombia Científica, from the Francisco José de Caldas Fund, Grant RC-FP44842-212-2018. The authors also thank Universidad de Antioquia for the fund "Beca Doctoral UdeA".

References

[1] M. J. Climent, A. Corma, and S. Iborra, "Heterogeneous Catalysts for the One-Pot Synthesis of Chemicals and Fine Chemicals," *Chem. Rev.*, vol. 111, no. 2, pp. 1072–1133, Feb. 2011, doi: 10.1021/cr1002084.

[2] Y. Hayashi, "Pot economy and one-pot synthesis," *Chem. Sci.*, vol. 7, no. 2, pp. 866–880, 2016, doi: 10.1039/C5SC02913A.

[3] L. A. Gallego-Villada, E. A. Alarcón, and A. L. Villa, "Evaluation of nopol production obtained from turpentine oil over Sn/MCM-41 synthesized by wetness impregnation using the Central Composite Design," *Mol. Catal.*, vol. 498, p. 111250, Dec. 2020, doi: 10.1016/j.mcat.2020.111250.

[4] R. Vallinayagam, S. Vedharaj, W. M. Yang, W. L. Roberts, and R. W. Dibble, "Feasibility of using less viscous and lower cetane (LVLC) fuels in a diesel engine: A review," *Renew. Sustain. Energy Rev.*, vol. 51, pp. 1166–1190, Nov. 2015, doi: 10.1016/j.rser.2015.07.042.

[5] J.-A. Becerra, Ó. F. Arbeláez, and A.-L. Villa, "Transformation of monoterpenes and monoterpenoids using gold-based heterogeneous catalysts," *Brazilian J. Chem. Eng.*, vol. 37, no. 1, pp. 1–27, Mar. 2020, doi: 10.1007/s43153-020-00013-1.

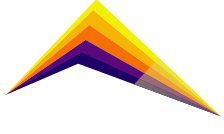

[6] D. García, M. Jaramillo, F. Bustamante, A. L. Villa, and E. Alarcón, "Epoxidation of β-pinene with a highly-active and low-cost catalyst," *Brazilian J. Chem. Eng.*, vol. 38, no. 1, pp. 89–100, Mar. 2021, doi: 10.1007/s43153-020-00078-y.

[7] J. E. Sánchez-Velandia and A. L. Villa, "Isomerization of α- and β-pinene epoxides over Fe or Cu supported MCM-41 and SBA-15 materials," *Appl. Catal. A Gen.*, vol. 580, no. April, pp. 17–27, Jun. 2019, doi: 10.1016/j.apcata.2019.04.029.

[8] M. Grün, K. K. Unger, A. Matsumoto, and K. Tsutsumi, "Novel pathways for the preparation of mesoporous MCM-41 materials: control of porosity and morphology," *Microporous Mesoporous Mater.*, vol. 27, no. 2–3, pp. 207–216, 1999, doi: 10.1016/S1387-1811(98)00255-8.

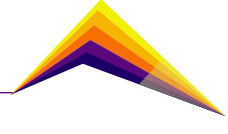

4.0 TECHNOLOGY

Q-means clustering coherent noise tolerance analysis

David A. Quiroga[1]
Javier F. Botia[2]

E-mail: daq3@rice.edu
E-mail: javier.botia@udea.edu.co

[1] Computer Science PhD student, Department of Computer Science, Rice University, 6100 Main St, Houston, TX 77005, United States
[2] Prof. System Engineering, Faculty of Engineering, Dept. of System Engineering, GITA Research Group, Universidad de Antioquia (UdeA), Calle 50 No. 73-21, Medellin, Colombia

Abstract

The use of cluster validity indices has long been the classical strategy to find the optimal number of clusters when clustering algorithms are applied to a dataset. While the k-means algorithm is the most commonly used unsupervised learning approach to obtain a set of labels, advances in quantum computing have enabled the implementation of a quantum version of the k-means called the quantum k-means (q-means) algorithm. Although q-means has a lower computational complexity than k-means, the amount of noise Noisy Intermediate-Scale Quantum (NISQ) quantum computers have generated an increase of epistemic uncertainty when using a Quantum Machine Learning (QML) model and therefore, the performance of q-means clustering may be lower than expected. For this paper, we apply cluster validity indices to evaluate the performance of q-means clustering for the Iris dataset when coherent noise in the form of is applied. By means of the Elbow method and cluster validity indices, the optimal number of clusters is found for each database with varying values for ϵ ranging from 0 to $\pi/6$, where evidence suggests that the q-means is robust against coherent noise up to an angle of $\pi/6$. Results from the clustering processes are then compared to clustering using the classical k-means for the same datasets, and very similar scores can be observed on the validity indices used for the study. The validity indices on setups using the

Correspondent author

q-means hint towards the same optimal number of clusters for any value of ϵ between 0 and $\pi/6$. We concluded that validity indices can be efficiently used to determine the optimal amount of clusters in a dataset when using q-means for the fitting process, with a tolerance on the amount of coherent noise up to an angle of $\pi/6$. By inspecting the cluster validity indices we also determine influence based on the number of shots, instead of on coherent noise.

Key words: Machine Learning, Quantum Machine Learning, Quantum Computing, Q-Means, Coherent Noise, Cluster Validity Index

Introduction

Since its conception, finding patterns from a dataset in order to group data points together has been a challenging task due to the difficulty of evaluating the validity of results obtained from unsupervised learning methods. Unlike supervised learning, there is no universal mechanism for performing cross-validation or validating results in unsupervised learning [1], and this has been a lasting problem. The increasing relevance of quantum computing and QML have led us to adapt classical machine learning algorithms onto quantum computers in order to make use of possible quantum advantages [2]. These advantages are showing that QML is in fact the next big step for ML. Despite such a statement, it remains true that adapting a quantum version of a classical ML algorithm may lead it to inherit some of the difficulties of its classical counterpart, as well as troublesome characteristics that need to be considered when using quantum computers in the Noisy Intermediate-Scale Quantum (NISQ) era such as noise and state preparation and measurement (SPAM) errors. One important type of noise is coherent noise, which affects each application of a quantum gate by adding an over-rotation of ϵ with respect to a specific axis and thus having the potential of a quadratic effect on computation results [3]. On the other hand, incoherent noise has a time-dependent linear effect that could be significantly lower [4] but may also have a profound effect on deeper quantum circuits. With important problems for both quantum computing algorithms and unsupervised learning techniques, the issue goes on to become: how results will we validate from a QML unsupervised learning algorithm?

In this paper, we look into assessing results retrieved from our implementation of the k-means algorithm, the quantum k-means or q-means, on a quantum computer. We determine the optimal number of clusters for datasets using validity indices of different nature with our q-means implementation when computations suffer the effects of coherent noise in the

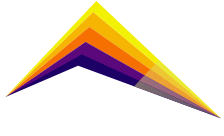

form of an over-rotation of ϵ, and compare them to results from a noiseless scenario and when performing the same task using the classical k-means.

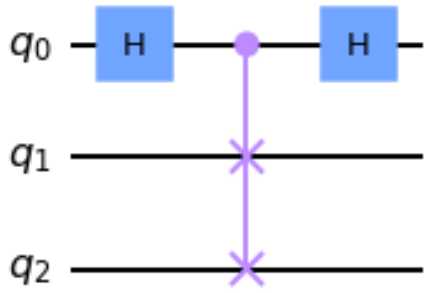

Figure 1. SwapTest circuit for measuring distances between qubit 1 (second line) and qubit 2 (third line).

Methodology

We began by specifying the dataset from which we wish to determine the optimal amount of clusters. We chose the iris dataset [5] to perform the experiments, as it has been widely studied and provides sufficient data for an in-depth analysis. The iris dataset has 4 features and 150 samples, and its main use is to group types of Iris flowers according to length and width from their sepal and their petals. In order to utilize the Iris dataset on an IBMQ quantum simulator, we encode the data onto qubits with encoding amplitude. features are encoded using qubits with the relation , and thus only 2 qubits are required for each sample. We then perform clustering using the q-means algorithm, the quantum counterpart of the k-means that uses the SwapTest circuit in order to calculate distances. The SwapTest circuit is shown in Figure 1, and a more in-depth explanation of the circuit and the algorithm can be found in this paper [6].

We used Jupyter Notebooks and the Qiskit, numpy and Scikit-learn libraries for the q-means algorithm, the k-means algorithm and conducting experiments. The experiment and relevant source code can be found in this Github repository [7]. This implementation of the q-means algorithm has a complexity of with being the number of samples, the number of clusters, the number of features, the number of iterations and the number of batched circuits [6]. We performed a fitting process to both the classical k-means and the q-means on a range of $c \in [2, 10]$ clusters and calculated the final inertia values of each clustering process. This process is repeated by using the q-means algorithm but applying coherent noise in the form of RY(ϵ) to each basis gate through the use of a local simulator. We performed a total of 4 iterations of experiments using q-means, one for each value of $\epsilon \in \{0, \pi/24, \pi/12, \pi/8, \pi/6\}$,

and an additional iteration using k-means for a sum of 5 iterations of 9 experiments. We used 2048 shots for all q-means setups.

The inertia values are used to perform an Elbow analysis which consists of plotting a curve to the inertia value of each clustering on *c*-clusters and finding the first point from which the slope remains constant. The Elbow test criterion denotes such a point as the optimal number of clusters as no sudden change in inertia occurs. Further clustering of the dataset into a larger number of clusters will only provide a slight improvement to inertia that is not enough to consider a larger number of clusters as the optimal number. Afterwards and using the 9 fitted models for each set of experiments, we applied cluster validation indices to each k-means and q-means instance and decided on the optimal amount of clusters, *c-opt*. We used the Davies-Bouldin (DB) score [8], the Calinski-Harabasz (CH) score [9], and the Silhouette Coefficient (SC) [10] in order to base our decision on different aspects of the clusters. We then compared the optimal number of clusters *c-opt* on each set of experiments to determine both the effectiveness of the q-means algorithm against the k-means, and the tolerance the q-means has over coherent errors in the form of an over-rotation of an angle ϵ around the Y axis.

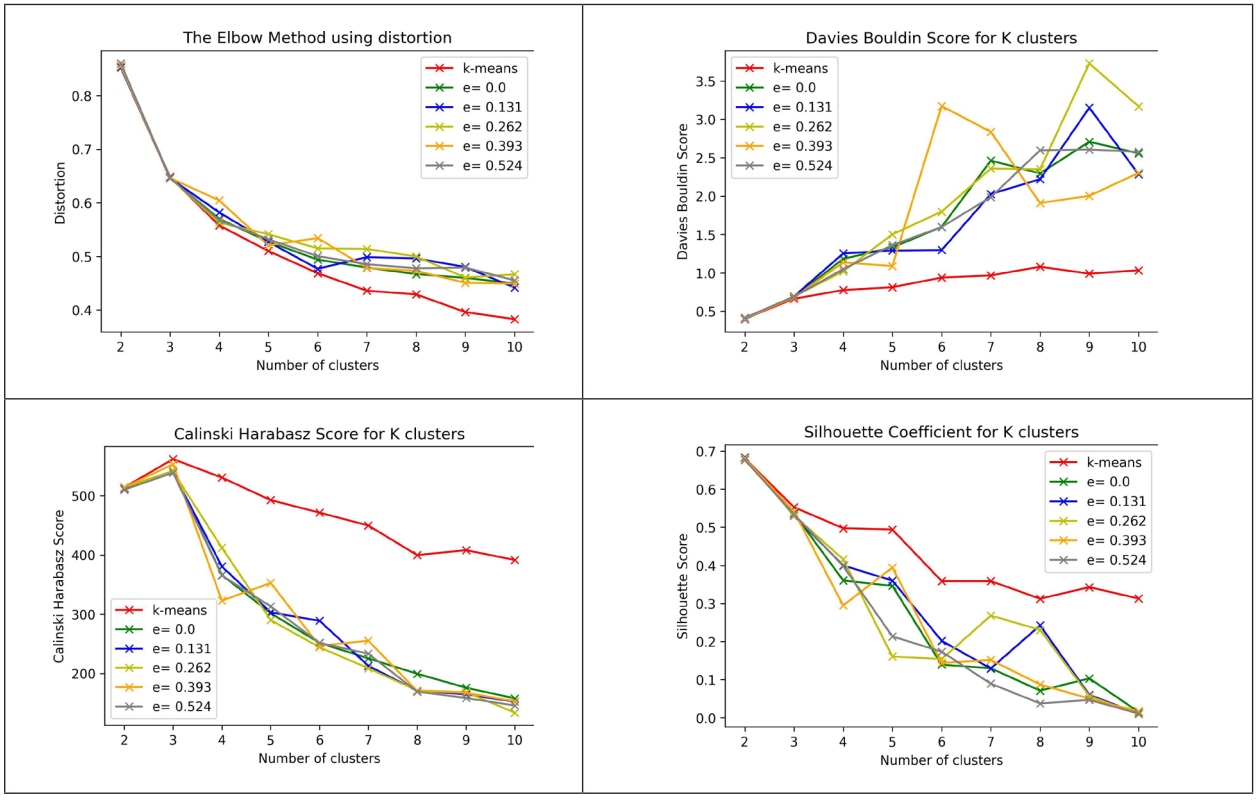

Figure 2. Elbow analysis using distortion (upper left) and validity indices DB (upper right), CH (lower left), and SC (lower right) for the k-means (red line), noiseless q-means with $\epsilon = 0$ (green line), and noisy q-means for $\epsilon \in \{\pi/24, \pi/12, \pi/8, \pi/6\}$ (blue, yellow, orange, and gray lines respectively). Each set of experiments was performed for $c \in [2, 10]$ clusters with the number of clusters, *c*, against the score in each plot.

Results and analysis

We first obtained the k-means and q-means instances from training on $c \in [2, 10]$ clusters for each setup to apply the inertia Elbow analysis, the DB scores, the CH scores and the SC scores on the trained instances. The results from the Elbow analysis and each validity index (DB, CH and SC) can be seen in Figure 2 (upper left, upper right, lower left, and lower right, respectively), for the k-means and the q-means with $\epsilon \in \{0, \pi/24, \pi/12, \pi/8, \pi/6\}$. The graphs show very similar values for the Elbow analysis and the validity indices in each q-means setup, and that the same conclusion can be drawn on the optimal number of clusters using the Elbow analysis and the validity indices for each setup (classical and quantum). Particularly, the DB and SC scores hint towards the optimal number of clusters being 2 with a second best score of 3 clusters, the CH scores hinting towards 3 clusters with a second best score of 2 clusters, and the Elbow method hinting towards 4 clusters. It is important to note that the Elbow method showed the least consistent results, with the slope varying on q-means instances with $\epsilon > 0$ due to the coherent noise included in those setups. Because of this, we will refer to the validity indices to determine the optimal number of clusters. Since all validity indices are naturally prone to assign better scores to a lower number of clusters, it is common for 2 to be the predominant result. Despite this, the CH index showed 3 to be the best number of clusters for all cases (even those influenced by the most noise), by a margin. Also, it is possible to visually determine that between 2 and 3 clusters, the data seems to group better into 3 clusters. Based on the collected evidence, we determined 3 to be the best number of clusters, and it aligns with the real number of clusters with the clusters being Iris Setosa, Iris Versicolour, and Iris Virginica. We can observe that in a general sense, the use of validity indices to determine the optimal number of clusters remains stable regardless of the amount of coherent noise the quantum computer has with the exception of the Elbow method, since an increase in the uncertainty of the algorithm yields a varying slope and therefore it is more error-prone. Nonetheless, it is possible to evaluate the performance and quality of a clustering process using validity indices when coherent noise is present, and there tends to be an agreement with clustering results from the classical k-means.

Conclusions or summary

We performed a clustering analysis on our implementation of the q-means by using the DB, HC, and SC scores, and the Elbow method using an inertia metric. We found that the Elbow method had a tendency to yield results from which determining the optimal number of clusters was difficult when coherent noise is generated. The validity indices were a more helpful approach as a simple analysis was possible when considering global maximums on the scores for both classical and quantum setups. We found that the cluster validity indices showed the same results on all setups (classical, noiseless quantum and noisy quantum), and therefore, we concluded that cluster validity indices can be efficiently used to determine

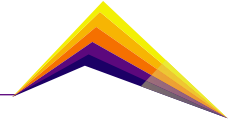

the best number of clusters on the q-means algorithm, regardless of the amount of coherent noise present in the quantum device. Future work for this research is to simulate all kinds of noise available in Qiskit to test tolerance to different noise sources such as incoherent noise and SPAM errors, and to determine the magnitude error order . Also, new specific quantum validity indices should be provided for unsupervised learning algorithms as many of such algorithms have different ways of mapping data onto qubits and clustering data. Therefore, more accurate ways to map data onto qubits are also needed, since many state preparation techniques require a large number of gates that ultimately inject more errors onto a quantum circuit.

Acknowledgment

Special thanks to staff scientists Prasanna Date in the Beyond Moore group and Raphael C. Pooser in the Quantum Information Sciences group from Oak Ridge National Laboratory for useful conversations on the algorithm.

References

[1] James, G., Witten, D., Hastie, T., and Tibshirani, R. (2013) An introduction to statistical learning: With applications in R. Springer New York, NY.

[2] Y. Wu, et al. (2021) Strong quantum computational advantage using a superconducting quantum processor. arXiv 2106:14734.

[3] Quiroga, D. (2021) Pulse-level characterization of qubits on quantum devices. B.S. Systems Engineering, Universidad de Antioquia.

[4] Bravyi, S., Englbrecht, M., Konig, R., and Peard, N. Correcting coherent errors with surface codes. npj Quantum Information, 4(1), Oct 2018.

[5] Dua, D. and Graff, C. (2019). UCI Machine Learning Repository: iris Data Set [https://archive.ics.uci.edu/ml/datasets/iris]. Irvine, CA: University of California, School of Information and Computer Science.

[6] Quiroga, D., Date, P., and Pooser, R (2021). Discriminating quantum states with quantum machine learning. In: 2021 IEEE Int. Conf. on Quantum Computing and Engineering (QCE), pp. 481–482.

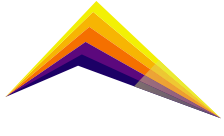

[7] Raijeku/qmeans-coherent-noise. Available in: https://github.com/Raijeku/qmeans-coherent-noise

[8] Davies, D. L. and Bouldin, D. “A cluster separation measure,” IEEE Transactions on Pattern Analysis and Machine Intelligence, vol. PAMI-1, pp. 224–227, 1979.

[9] Caliński, T. and J.A., Harabasz, “A dendrite method for cluster analysis,” Communications in Statistics - Theory and Methods, 3, pp. 1–27, 01 1974.

[10] Rousseeuw, P. J. “Silhouettes: A graphical aid to the interpretation and validation of cluster analysis,” J. Computational and Applied Mathematics, 20, pp. 53–65, 1987.

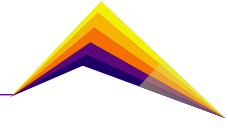

Towards Anomaly Classification on IIoT Edge Devices Using Statistical Variable Selection

Martha Rodriguez[1] *E-mail: mlucia.rodriguez@udea.edu.co*
Diana Tobon[2] *E-mail: dtobon@udemedellin.edu.co*
Danny Munera[3] *E-mail: danny.munera@udea.edu.co*

[1,3] Universidad de Antioquia
[2] Universidad de Medellín

Abstract

The fourth industrial revolution (Industry 4.0) provides real-time, secure, and autonomous manufacturing environments where Industrial Internet of Things (IIoT) affords enhanced wireless connectivity for data collection and processing in interconnected plants. Quality data is required to make smart decisions in industrial systems. One way to identify poor-quality data is through anomaly detection systems. An early IIoT anomaly detection reduces maintenance costs, minimizes machine downtime, increases safety, and improves product quality. A multi-class classifier that detects events, failures, or attacks is much more efficient than a simple binary classifier that only detects the presence or absence of anomalies, thus relieving a human operator of identifying the anomaly's cause, which generates wasted time that could compromise the performance process and security. With these issues in mind, this paper attempts to determine whether it is possible to statistically differentiate between a failure that generates a temperature increase in the IIoT device processor, a denial-of-service attack on the MQTT broker, and an event caused by an application executing on the IIoT edge device. This work tries to find out which variables are essential to make this differentiation. Data used to perform the statistical analysis comes from a sensor that measures the current consumption of a Raspberry

Correspondent author

PI 3 operating as an edge device and some internal data from its CPU (temperature, load, frequency, voltage). The results show that all the analyzed variables indicate a statistical difference between normal operation and anomaly events. In comparison, CPU temperature is the only one that shows a statistical difference between normal operation and the data generated when a temperature failure occurs. At the same time, the CPU voltage, frequency, and load indicate that normal data is significantly different from those generated during the denial-of-service attacks on the MQTT broker. The results obtained in this work will be used to design a fast and simple anomaly classifier.

Keywords: Anomaly Detection, Anomaly Classification, ANOVA, IIoT, Industry 4.0.

Introduction

Industrial Internet of Things (IIoT) offers wireless connectivity for data collection and processing in interconnected plants and provides real-time, secure, and autonomous manufacturing environments [1]. Improving production value requires reliable and accurate computing and communication tools to deal with security threats caused by high interconnection among subsystems [2]. Additionally, IIoT objects use heterogeneous technologies and collect data of all kinds, without structure, with noise, and highly redundant [3]. Security flaws and data collection issues are factors affecting data quality. This situation can make data gathered by IIoT systems unsuitable for providing relevant services to users [4]. One way to identify poor-quality data is through anomaly detection systems. Gosh et al. [5] define an anomaly as an observation (or a subset) that appears inconsistent with the rest of the data set. Ghosh et al. [5] also classify anomaly as an event, failure, and attack. They use the term “failure” to refer to data coming from a faulty sensor measurement due to a lack of calibration or device malfunction [6]. At the same time, an “event” is a situation that changes the state of the real world, such as a natural phenomenon that alters some monitored variables [4]. In addition, a “malicious attack” is an action that comprises one or more nodes in an IIoT network, tricking others into interacting with them and compromising the entire network’s security [5].

Early detection of anomalies in an industrial process is crucial to implementing decisions based on real-time information, thus reducing maintenance costs, minimizing machine downtime, increasing safety, and improving product quality [7]. Knowing the anomaly source (event, failure, or attack) helps choose appropriate recovery actions to minimize abnormal behavior [8]. This work aimed to determine whether it is possible to statistically differentiate between a failure that generates a temperature increase in the IIoT device processor, a

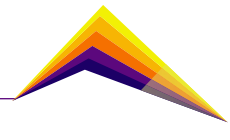

denial-of-service attack on the MQTT broker, and an event caused by an application executing on the IIoT edge device. This report looks for the variables that are essential to make this differentiation. The remainder of this paper is organized as follows. Section 2 describes the materials and methods used for data collection and analysis. Section 3 shows the variables that differentiate between event, failure, attack, and normal operation. Finally, section 4 describes the report's conclusion.

Materials and Methods

The experimental purpose is to determine if it is possible to differentiate between a temperature failure, a denegation-of-service attack, and normal operation of an Industrial Internet of Things edge device. An IIoT system was selected to simulate events, failures, and attacks in its edge device. This system consists of several low-cost sensors that monitor a three-phase motor. Each sensor sends the motor current, temperature, sounds, speed, or vibration data through a microcontroller (ESP32) low-cost development system using MQTT to a Raspberry PI edge device. Raspberry processes motor data and activates alarms when a value exceeds a normal range. Then, the processed information is sent to a cloud application that stores and displays statistics on a website. An Edge device was monitored to detect some electronic component failures or cyberattacks. To differentiate between high-temperature failure or denial of service (DoS) attacks on an edge device processor, the Raspberry current consumption and some edge device internal data such as temperature, CPU load, frequency, voltage, and free memory were selected. The Raspberry pi collects the data. A fan regulates the edge device processor temperature. Moreover, the DoS attack is controlled by a computer running Kali Linux in a local network.

The edge device is a Raspberry Pi3 model B+ using micro-SD format for loading the operating system and data storage and input power 5V/2.5A DC via micro-USB connector. Raspberry Pi3 B+ consumes about 400 mA of current at 5.0 V when it is in an idle state, 690mA loading graphical user interface, and 980mA at 400% CPU load. Temperature failure or a DoS attack is expected to be reflected in power consumption. Some internal parameters such as voltage, temperature, average CPU load in the last minute, and free memory are used to determine if a failure, event, or attack occurs. Edge device takes information from itself through a sensor and an application. An INA219 is a low-cost current sensor with an I2C interface, a current range of ±3.2A, and a current resolution of ±0.8mA. This sensor is connected to the Edge device power supply. Raspberry PI samples the current every approximately 10 milliseconds (ms), and internal data every 50ms on average. In addition, RPImonitor is an application that reads internal information from the edge device. This information is written in a CSV file by a Python script. It has not been possible to determine internal data accuracy.

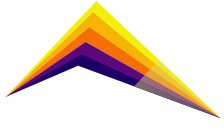

Several data samplings were performed. In each of them, normal operation data from the system were taken for 5 minutes. Likewise, anomaly data were taken for 3, 5, and 10 minutes. According to the sampling frequency, 6000 current samples were taken per minute, and 1200 samples were taken from RPIMonitor. Each test was repeated four times to reduce the inter-sample error. This collected data was averaged. Separate sampling is explained as follows.

- Failure. Temperature failure was simulated by turning off the fan that cools the edge device. The 24 watts AC fan was placed 20 centimeters above the Raspberry.
- Attack. A Python script runs on a local computer that subscribes 1024 clients to "#" topic and publishes a short message every second to make a Denegation-of-Service attack on MQTT Mosquitto broker running on the same edge device.
- Event. A Python script calculating the average time to make 100.000 division operations in two processes simultaneously.

To analyze the data collected, it used an analysis of variance (ANOVA) with RStudio Cloud (https://rstudio.cloud/). First, a linear regression was performed between each variable and treatments (normal, 3-, 5-, and 10-minutes anomaly). Before determining whether the treatments are statistically different from each other using Duncan's test, it is necessary to apply some tests to verify the assumptions of independence (Runs test, Durbin-Watson test), normality (Shapiro test) and homoscedasticity (Bartlett test) of the residuals. The following section describes the results obtained.

Results and analysis

Figure 1 shows boxplot graphics for each variable. Excluding free memory, the remaining variables help to differentiate between normal behavior and some anomaly occurring in the edge device. For example, current consumption data can differentiate between an event and an attack but confuse normal data with temperature failures. However, the above is clearly differentiated with the help of the internal temperature data of the microprocessor.

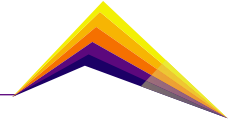

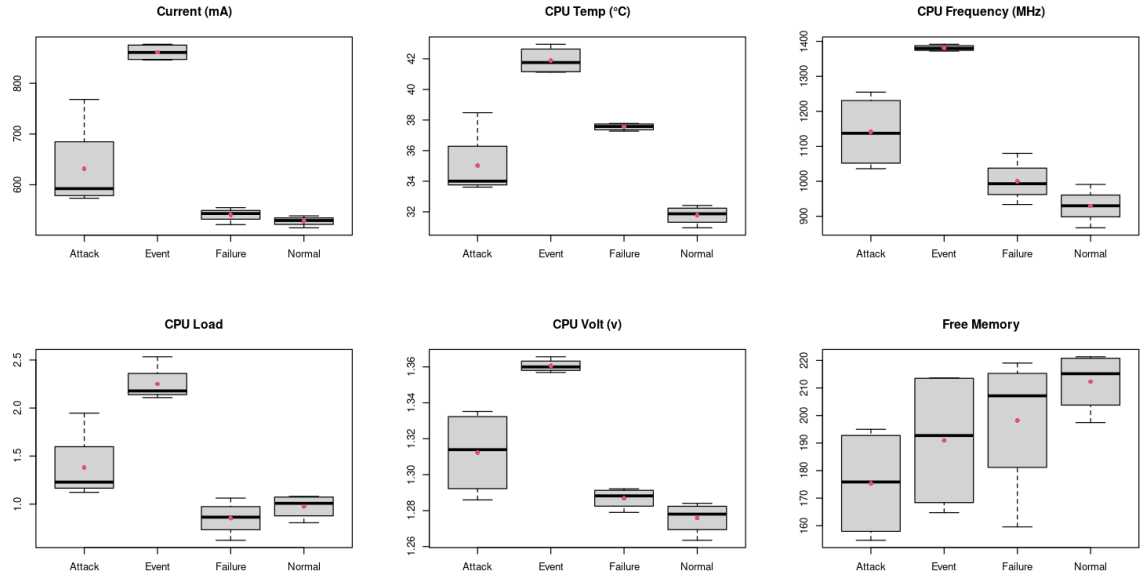

Figure 1. Boxplot to differentiate between anomalies.

Duncan's test was used to confirm that the observations derived from the boxplots are correct. Duncan's multiple range test makes various comparisons of group means; it allows comparing the means of the t-levels of a factor after rejecting the null hypothesis of equality of means using the ANOVA technique, with a significance level equal to 0.01. Table 1 shows the comparison. The same letter indicates that the test considers identical means of the compared data sets.

While current, frequency, and voltage clearly distinguish between event and attack, the internal temperature is necessary to differentiate failure from normal operation. Otherwise, free memory does not provide any information. On the other hand, CPU frequency and voltage show the same conclusions as current, so it may be unnecessary to include this sensor in anomaly monitoring.

Table 1. Duncan's multiple range test results

Anomaly	Current	Temp	Freq	Load	Volt	Memory
Event	a	a	a	a	a	a
Attack	b	b	b	a	b	a
Failure	c	ab	c	b	c	a
Normal	c	c	c	b	c	a

To find out if anomaly duration had any effect on the measured variable, each anomaly was applied for 3, 5, and 10 minutes. Figure 2 shows the results. It is observed that the current increases with the attack duration and decreases slightly as the fault duration extends, remaining almost constant for normal operation and the event. The above may be related to the frequency and voltage behavior of each anomaly type. It is also observed that the temperature increases as the duration of attack or failure increases. The free memory is less in any anomalies compared to normal system operation.

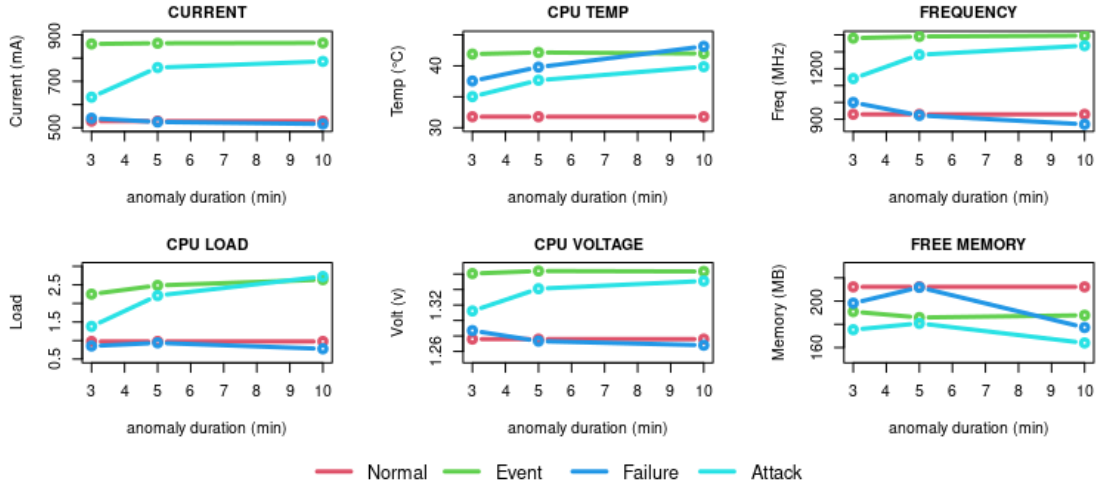

Figure 2. Effect of anomaly duration on variables

Conclusion

This work found that it is possible to differentiate a temperature fault, a denial-of-service attack on the MQTT broker, and an additional script execution event on an IIoT edge device using low-cost solutions. In this case, a current sensor and the internal data of the microcontroller were used. The analysis of variance (ANOVA) showed that it is not even necessary to include the current sensor as it gives the same results as the CPU frequency and voltage, further decreasing the cost and complexity of anomaly monitoring. It also found that while current, frequency, and voltage differentiate between event and attack, temperature allows differentiation between fault and normal system operation. Finally, it is relevant to mention that the duration of the attack or failure influenced the magnitude of all the variables recorded. Future works should explore the behavior of other internal variables in the presence of anomalies. Likewise, they should extend the statistical analysis to different other types of events, failures, and attacks.

References

[1] A. Angelopoulos *et al.*, "Tackling Faults in the Industry 4.0 Era-A Survey of Machine-Learning Solutions and Key Aspects," *SENSORS*, vol. 20, no. 1, pp. 1–34, 2020, doi: 10.3390/s20010109.

[2] A. Modern and T. Iot, "Combinatorial Analysis for Securing IoT-Assisted," vol. 18, no. 1, pp. 3–15, 2022.

[3] Y. Wu, H. Dai, and H. Tang, "Graph Neural Networks for Anomaly Detection in Industrial Internet of Things," *IEEE Internet Things J.*, 2021

[4] A. Karkouch, H. Mousannif, H. Al Moatassime, and T. Noel, "Data quality in internet of things: A state-of-the-art survey," *J. Netw. Comput. Appl.*, vol. 73, pp. 57–81, 2016, doi: 10.1016/j.jnca.2016.08.002.

[5] N. Ghosh, K. Maity, R. Paul, and S. Maity, "Outlier detection in sensor data using machine learning techniques for IoT framework and wireless sensor networks: A brief study," *Proc. - 2019 Int. Conf. Appl. Mach. Learn. ICAML 2019*, pp. 187–190, 2019, doi: 10.1109/ICAML48257.2019.00043.

[6] N. Mohamudally and M. Peermamode-Mohaboob, "Building An Anomaly Detection Engine (ADE) for IoT Smart Applications," *Procedia Comput. Sci.*, vol. 134, pp. 10–17, 2018, doi: 10.1016/j.procs.2018.07.138.

[7] Y. Wang, M. Perry, D. Whitlock, and J. W. Sutherland, "Detecting anomalies in time series data from a manufacturing system using recurrent neural networks," *J. Manuf. Syst.*, 2020.

[8] G. Tertytchny, N. Nicolaou, and M. K. Michael, "Classifying network abnormalities into faults and attacks in IoT-based cyber physical systems using machine learning," *Microprocess. Microsyst.*, vol. 77, 2020, doi: 10.1016/j.micpro.2020.103121.

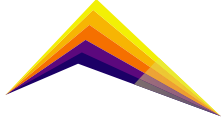

Method for analyzing morphological traits of chrysanthemum cuttings based on computer vision

Juan Guillermo Pavas-Henao[1] *E-mail: guillermo.pavas@udea.edu.co*
David Fernández-Mc Cann[2] *E-mail: david.fernandez@udea.edu.co*
Dagoberto Castro-Restrepo[3] *E-mail: investigacion.dir@uco.edu.co*

[1]M.Sc. Student of Engineering
[2]Ph.D. of Telecommunications; GEPAR Research Group, Universidad de Antioquia
[3]Ph.D. of Agricultural Sciences; Development and Innovation, Universidad Católica de Oriente

Abstract

In this paper, a computer vision method is proposed to determine and analyze the morphological traits of venation and leaf lobes of chrysanthemum cuttings, which can contribute to the quality control of the conventional cuttings propagation process. For this, a set of 650 cuttings leaf images of the "Baltica" cultivar was formed. Then, for its implementation, digital image processing methods for feature extraction and machine learning models with a semi-supervised approach for labeling and classification were used. The procedure carried out for the feature extraction consisted of the following stages: (i) segmentation of veins, petiole, and leaf blade of the leaf with the largest area of the cutting, (ii) lobes identification, (iii) feature extraction such as area, perimeter, length, and diameter of each morphological part, and (iv) building of a dataset with the features of all the images. On the other hand, to label the dataset, a K-means unsupervised learning model was fitted using the leaf area and perimeter features. In this way, three clusters corresponding to the leaves with the smallest area, the intermediate area, and the largest area were found, which allowed assigning of the labels of the dataset samples. At once, to determine the relationship between the morphological traits of veins, petiole, and lobes with the leaf,

Correspondent author

different supervised models like Logistic Regression (LR), Support Vector Machine (SVM), Random Forest (RF), and K-Nearest Neighbors (KNN) were trained, using all the features (excluding the leaf area and perimeter) and those of each morphological part separately for the training. Accordingly, with all features, accuracies above 90% were obtained for almost all models except KNN with 76%. Then, excluding the remaining features of the leaf blade, percentages of 70% to 81% were achieved for the same models. Next, using only the vein features, accuracy percentages of 63% to 71% were obtained. Subsequently, with petiole features, accuracies of 52% to 56% were obtained. Later, combining vein and petiole features, percentages from 67% to 74% were achieved. Finally, when training with lobe features, accuracies from 74% to 80% were obtained.

Keywords: Computer vision, image processing, machine learning, chrysanthemum, cuttings, leaf morphology.

Introduction

Chrysanthemum, whose flowers are in high commercial demand worldwide, is a genus of perennial plants native to China, consisting of approximately 40 species and more than 20,000 cultivars, which are mainly used for ornamental purposes due to their diversity of shapes, sizes and colors [1], [2]. Its reproduction is mainly done through cuttings, which are small parts of the plant composed of a piece of stem, a bud containing a meristem and one or more leaves, and are used as a vegetative propagation technique to produce new plants identical to the mother plant [3], [4].

Successful propagation of new plants is achieved when they are capable of producing roots in the rooting banks, so cuttings must meet criteria such as: having at least one developed leaf, their stem must have a certain length, and they must not have leaves near their base [3], [5]. In practice, the last two criteria are feasible to apply using a cut artifact as a measurement guide. However, for the first criterion, no instrument is available to determine the stage of development of the leaf —based on its area [3]—, so it is established according to the visual estimation of the collector or quality inspector.

Knowing the state of leaf development is essential to ensure successful rooting, as it will determine the growth way of the plant. Nevertheless, further the leaf area, there are other characteristics that could more accurately indicate its state of development, due to

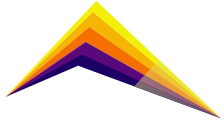

influencing the execution of its fundamental processes —photosynthesis and transpiration [6]—. These are the morphological traits of the veins, petiole, and lobes [6]–[8], which could be visible and measurable for a computer vision system.

In the literature, there are diverse studies that have approached venation or lobes of leaves, but none have related them to the cuttings lifecycle in their rooting stage until now. Likewise, in the specific case of chrysanthemum, it has not worked with vein traits yet; however, petiole and lobes have been used for other purposes like variety classification, although at advanced stages of their development [9], [10]. Furthermore, despite the peak of computer vision in recent years and the multiple methods proposed for leaf vein identification in other plant genera —which are highlighted [11]–[13]—, they have not been combined with petiole and lobe traits so far. Even so, the petiole has been theoretically linked to the venation structure as a fundamental piece [7].

The above shows that there is a gap in the literature, so a new computer vision method is proposed to analyse the contribution of morphological traits of venation (including petiole) and leaf lobes of chrysanthemum cuttings to determine their quality for optimal rooting of plants.

Materials and Methods

The realization of this work began with data acquisition, so a set of 650 images of cuttings leaves belonging to "Baltica" chrysanthemum cultivar was formed. The images were obtained through a controlled illumination setup, designed with a 33x28x22 cm plastic box, two 20x27 cm white acrylic sheets, and 9 12 V white led light modules, which were connected to an adapter with 100-240 V input and 12 V output. Thus, the sheets were placed one below the other to place the cuttings and the lighting respectively, placing the latter at the bottom of the box. Next, a hole was drilled in the lid of the plastic box to place a Xiaomi Redmi 6A mobile device with a 13 MP camera and an aperture of f/2.2. Images were then taken by applying a 1.6 zoom.

On the other hand, due to the chrysanthemum cuttings included one or more leaves, it was determined to use the leaf with the largest area to segment its morphological parts and extract the features of each of these. Thus, the defined morphological parts were: leaf blade H, petiole P, veins V, and lobes L; whereas the defined features were: area, perimeter, length, and diameter.

Given the above, the proposed method was composed of two main stages that were image processing and machine learning, which were divided into six phases that were represented in the flowcharts of Figure 1. In this way, the image processing stage was made up of the phases: veins segmentation, petiole segmentation, leaf segmentation, and lobes identification,

which corresponded to the flowcharts of Figures 1a-d. While the machine learning stage consisted of the remaining phases: labeling by clustering and classification model, which were plotted in the flowcharts of Figures 1e-f. To develop the phases of the flowcharts of Figures 1a-d, traditional digital image processing techniques were applied, in order to get a feature vector EC{v(x,y)+p(x,y)+h(x,y)+L} for each input image f(x,y), where v(x,y), p(x,y), and h(x,y) corresponded to the segmentation of veins, petiole, and leaf blade respectively, L to the lobes identification, and EC to the feature extraction method. Regarding the phases of the flowcharts of Figures 1e-f, unsupervised and supervised learning methods were used. Thus, to implement the first learning method defined in Figured 1e, a feature vector dataset EC{v(x,y)+p(x,y)+h(x,y)+L}→$\vec{X}$ that included all the images f(x,y) was formed, which allowed fitting a K-means [14] unsupervised learning model, where the data were grouped into different clusters C. This enabled assigning the classes Y and labels LB of the dataset samples $\vec{X}$. Then, to effect the second learning method described in the flowchart of Figure 1f, the feature vector dataset $\vec{X}$ was used again, but in this case, using it with the respective classes Y, to train different supervised learning models such as Logistic Regression (LR) [14], Support Vector Machine (SVM) [14], Random Forest (RF) [14], and K-Nearest Neighbors (KNN) [14]. Thereby, distinct classifiers CL{($\vec{X}$)} would be found to determine the criterion of leaf development.istinct classifiers would be found to determine the criterion of leaf development.

Results and analysis

Initially, using the implemented image processing method, the feature vectors of all images were obtained, forming a dataset of 650 samples. For this, the flowcharts described in Figures 1a-d were run with each image to segment the morphological parts of veins, petiole and, leaf blade, and identify the lobes. The features of each morphological part were then extracted to obtain the respective feature vector for each image.

Then, using the dataset and based on the criterion that determines that a leaf is developed, since its area is known [3], a K-means model was fitted through the leaf blade area and perimeter features —given their relationship—. This allowed the samples to be divided into three clusters, where the first had the leaves with the smallest area —immature—, the second those of intermediate area —ideal—, and the third those with the largest area —mature—. From these clusters, the labels of the samples were assigned.

Subsequently, with the labeled dataset, different supervised models of LR, SVM, RF, and KNN types were trained, defining the scenarios in Table 1 to evaluate the relationship between the leaf features and the other morphological parts. Thus, in scenario N° 1 of Table 1, all the features of the dataset were used except the leaf blade area and perimeter features, because they were used to find the clusters. Thereby, after training, accuracy percentages of 92% for LR, 91% for SVM and RF, and 76% for KNN were obtained, being the highest accuracies of

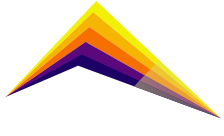

the scenarios (with an exception of the KNN model), which indicates that these features represent the leaf and would allow checking its development state. However, that scenario kept part of the leaf information with the length and diameter features. For this, scenario N° 2 of Table 1 was defined, where all the features of the leaf blade were excluded, reaching accuracies of 81% for LR, 79% for SVM, and 70% for RF and KNN, being high percentages even to determine that veins, petiole, and lobes together can describe the leaf. Next, scenarios with separate morphological parts were proposed, starting with scenario N° 3 of Table 1, where the vein features were only taken, obtaining percentages of 71% for SVM, 66% for LR, 64% for KNN, and 63% for RF, which showed that venation still preserves the leaf information. Then, in scenario N° 4 of Table 1, with petiole features, accuracies of 56% for KNN, 55% for SVM, 53% for RF, and 52% for LR were obtained, acquiring the lowest percentages of the scenarios and showing that there is no clear correspondence between petiole and leaf. Therefore, based on [7], who insinuates the petiole as part of the venation, scenario N° 5 of Table 1 was evaluated, combining vein and petiole features, achieving percentages of 74% for LR, 72% for SVM, 69% for RF, and 67% for KNN. This improved the accuracies reached in the training of the separate morphological parts, showing that they are linked. Finally, with scenario No. 6 in Table 1, lobe features were used for training, achieving accuracy percentages of 80% for SVM, 78% for RF, 77% for LR, and 74% for KNN, which showed that it is the morphological part that best represents the leaf.

Conclusions

The models trained with the characteristics of the venation (including the petiole) and the lobes showed that these can determine the developmental stage of the leaf, without knowing the specific characteristics of the leaf blade. As for the models trained with the characteristics of the morphological parts separately, they showed that these can also represent the leaf, especially the lobes and veins (using the SVM classifier). In the case of the petiole, good results were only obtained when it was included as a part of the venation. Finally, with the results obtained, it is concluded that it is possible to propose more robust models in the future, either with machine learning or deep learning, increasing the number of samples, and involving other chrysanthemum cultivars.

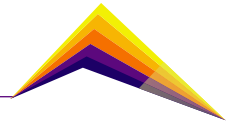

References

[1] T. Hoang, Y. Wang, Y. Hwang, and J.-H. Lim. (2020). "Analysis of the morphological characteristics and karyomorphology of wild Chrysanthemum species in Korea". Horticulture, Environment, and Biotechnology, 61 (2), 359–369. https://doi.org/10.1007/s13580-019-00222-9

[2] F. Wang, F. J. Zhang, F. Di Chen, W. M. Fang, and N. J. Teng. (2014). "Identification of chrysanthemum (chrysanthemum morifolium) self-incompatibility". The Scientific World Journal, 2014, Article 625658. https://doi.org/*10.1155/2014/625658*

[3] P. McMillan Browse. (1979). "Plant Propagation: Seeds, roots, bulbs and corms, layering, stem cuttings, leaf cuttings, budding and grafting". Littlehampton Book Services Ltd.

[4] D. Vince-Prue and R. Yeomans. (2014). "The Fundamentals of Horticulture: Theory and Practice". Cambridge University Press.

[5] H. B. Creighton and E. P. Christopher. (1959). "*Introductory Horticulture*". AIBS Bulletin, 9 (1), 47–48. https://doi.org/10.2307/1292762

[6] J. C. Schilletter and H. W. Richey. (1940). "*Textbook of general horticulture*". McGraw-Hill Book Company, Inc.

[7] L. Sack and C. Scoffoni. (2013). "Leaf venation: structure, function, development, evolution, ecology and applications in the past, present and future". New Phytologist, 198 (4), 983–1000. https://doi.org/10.1111/nph.12253

[8] M. Semchenko and K. Zobel. (2007). "The role of leaf lobation in elongation responses to shade in the rosette-forming forb Serratula tinctoria (Asteraceae)". Annals of Botany, 100 (1), 83–90. https://doi.org/10.1093/aob/mcm074

[9] D. Warren. (2000). "Image analysis in chrysanthemum DUS testing". Computers and Electronics in Agriculture, 25 (3), 213–220. https://doi.org/10.1016/S0168-1699(99)00069-1

[10] F. C. Jiangmin Wang Weimin Fang, Sumei Chen, Zhiyong Guan, Haiyan Tang. (2013). "Differentiation of Cut Chrysanthemum Cultivars Based on Multiple Foliar Morphological Parameters". *Chinese Bulletin of Botany*, 48 (6), 608–615. https://doi.org/10.3724/SP.J.1259.2013.00608

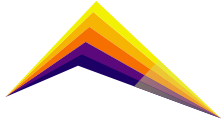

[11] J. Mounsef and L. Karam. (2012). “Fully automated quantification of leaf venation structure”. Proceedings of the 2012 International Conference on Artificial Intelligence, ICAI 2012, 2, 820–825. http://worldcomp-proceedings.com/proc/p2012/ICA3681.pdf

[12] J. Bühler *et al.*. (2015). “phenoVein—a tool for leaf vein segmentation and analysis”. Plant physiology, 169 (4), 2359–2370. https://doi.org/10.1104/pp.15.00974

[13] P. Wilf, S. Zhang, S. Chikkerur, S. A. Little, S. L. Wing, and T. Serre. (2016). “Computer vision cracks the leaf code”. Proceedings of the National Academy of Sciences, 113 (12), 3305–3310. https://doi.org/10.1073/pnas.1524473113

[14] T. Hastie, R. Tibshirani, J. Friedman, and J. Franklin. (2005). “The elements of statistical learning: data mining, inference and prediction”. The Mathematical Intelligencer, 27 (2), 83–85. https://hastie.su.domains/Papers/ESLII.pdf

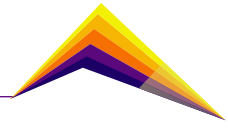

Table 1. Classification models

Scenario		Classifier accuracy (%)			
N°	Description	LR	SVM	RF	KNN
1	All features except the leaf blade area and perimeter	92	91	91	76
2	All features excluding the leaf blade	81	79	70	70
3	Vein features	66	71	63	64
4	Petiole features	52	55	53	56
5	Vein and petiole features	74	72	69	67
6	Lobe features	77	80	78	74

Figure 1. Flowcharts of the proposed method.

Image characterization of coral reefs using computer vision techniques and convolution neural networks (CNNs)

Sebastian Guzman Obando[1] E-mail: sebastian.guzman@udea.edu.co
Daniela Cuartas Marulanda[2] E-mail: daniela.cuartasm@udea.edu.co
David Stephen Fernandez Mc Cann[3] E-mail: David.fernandez@udea.edu.co

[1] MSc student in Telecommunications Engineering,
[2] Electronic Engineering Student, GEPAR Research Group, University of Antioquia
[3] Ph.D. in Telecommunications, GEPAR Research Group, University of Antioquia

Abstract

Coral reef communities are important for the marine ecosystem because they are home to species such as fish and algae that help balance the ecosystem and the economy of coastal communities. Climate change and human action are negatively affecting the benthic communities -A set of organisms that live in the water bottoms- of coral reefs in the Colombian Caribbean, either due to the deterioration of water quality, pollution, sedimentation, or overfishing [1][2][3]. In recent years, to learn about the state of the marine ecosystem and collect information on coral reefs, strategies have emerged such as taking digital images using divers, satellites -such as IKONOS [4]- and remotely guided underwater vehicles; This task of automating the getting of samples allows a sweep of much larger areas in less time, but at the same time increases the number of samples and the time needed for a marine biologist to analyze an area. For this, the authors have proposed ways to partially automate the image analysis process, to reduce the processing time.

In this work, data was collected from the Morea Labeled Dataset [5] coral reef image bank, which is one of the most extensive with more than two million annotations on coral reef images, to compare

Correspondent author

architectures of convolution neural networks or CNN. The work was made with comparisons that show how the CNNs in the state of art achieved percentages of success greater than 96% for coral from non-coral differences, but when these topologies were run, replicating the training with the ELIAT and RMAS databases [6] on the Beijbom database [5] percentages of success around 82% were obtained. The training made in this work for comparing with other topologies was done using nets such as Resnet-152 with success percentages of 94%, SquezeeNet with 93%, VGGnet (VGG-19) topology with 94%, which compared with the results of Marcos et-al [7] with their database and Beijbom et-al [6] and Modasshir et-al [8] experiments on the Moorea database, which shows that novel approaches with larger databases are promising.

Keywords: Automated recognition, CNN, Resnet, VggNet, SqueezeeNet, Coral reef annotation

Introduction

Coral reef communities are essential for the marine ecosystem because they are home to a large number of species such as fish and algae that are necessary for the balance of the ecosystem and the economy of coastal communities, providing ecological services at the level of physical structures such as natural protection against the erosion of the coasts caused by waves and storms. It also offers biotic services making the exchange with other ecosystems and organisms that coexist, and it offers cultural and economic services for fishers and tourists, these services were described by Moberg [1] and Heber [2]. Climate change and human action are negatively affecting the benthic communities -A group of organisms that live in the water bottoms- of coral reefs, either due to the deterioration of water quality, pollution, sedimentation, or overfishing documented in Moberg [1] and Chin et-al [3].

In recent years, for marine biologists to know the status and health of coral reefs, strategies that use image processing techniques to assist biologists in these processes have emerged. The process begins with the acquisition of image banks taken in transects [9][10] either by taking photographic records with satellites [4], divers, or autonomously guided vehicles (ROVs) [11]. The authors have been able to perform classification tasks from the different image banks as shown in table 1.

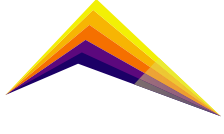

This work intends to show the behavior of convolutional neural network topologies over the Morea Labeled Coral MLC dataset described on Beijbom et-al [5], such as SqueezeNet, Resnet 152, DarkNet, DenseNet 201, and VggNet 19, after comparing with MLC database works as shown in table 2.

Materials and Methods

Database

It starts from the MLC (Moorea Labeled Coral) [5] database that was introduced in 2012 by Oscar Beijbom at the CVPR in his work Automated Annotation of Coral Reef Survey Images. It consists of about 2055 images, each with 200 points random, each point has its respective annotation belonging to 9 selected classes of which 5 are from the genus of corals: Acropora, Pavona, Montipora, Pocillopora, Porites, and 4 belong to other classes such as Sand, Macroalgae, Grass-type Algae, Sponge Algae, and Crustose Coralline Algae. The reference images database was taken on the island of Moorea in French Polynesia with a camera set to a 50x50 cm frame to keep the distance and camera orientation constant. From each of the 2055 images, a subset of images was extracted for training and testing called fi(x,y) whose measurements were 100x100 pixels and whose center corresponded to the classification made by marine biologists.

Method Overview

Step 1: Separate database to train with their respective classification, where $f_i\,(x,y)$ will be the training images and c_k the outputs and $g(x,y)$ the set of tests.

Step 2: Apply pre-processing to the set of images $f_i\,(x,y)$ applying scale transformations and rotations to increase the acropora class that is unbalanced with less than 1000 samples compared to the CCA class that has more than 80000 samples, to later obtain obtaining a new set $f_{i,j}\,(x,y)$.

Step 3: Train the different models with the set of samples. $\mathrm{Model}_i=\mathrm{Train}[\mathrm{CNN}_l\,(f_{i,j}(x,y),\, c_k]$

Step 4: Eval the models with new samples $\hat{c_k}=\mathrm{Model}_i\,[g(x,y)]$

The general method was illustrated in Figure 2.

Results and analysis

Analyzing the results of the experiment conducted and contrasting them with those of the authors Beijbom et-al [5], Modasshir et-al [8], and Pierce [12] on all the classes of the reference database taken from Beijbom et-al [5], the highest result was obtained with Resnet-152 topology with an accuracy of 94.5% followed by the result obtained using Darknet topology with an accuracy of 93.5% as shown in Table 2. Augmenting data on the Acropora class, going from having 300 samples to 1200 improved the accuracy by an additional 5 to 10% compared to the works of Beijbom[5] and Modasshir[8] and Pierce[12], this augmenting data show that the CCA class with more than 90,000 samples have a great imbalance with the other classes such as Acropora that are being affected, and the data augmentation technique can help improving this data imbalance. Finally, sorting corals from non-corals yielded a 97% success rate improving on Beijbom[5] with 89% and Metha[7] with 95% as show in table 1.

Conclusions or summary

The annotation process using the new convolutional neural network topologies and performing augmenting data on the most unbalanced classes, it is possible to increase the percentage of success on test data, and even though the database, in general, has many samples and is ideal for training a CNN Sometimes it can play against a class having few samples and that is where data augmentation techniques can help improve the database for improving the elements for a class with a low level of samples.

Acknowledgment

Thanks to the GEPAR research group for the resources provided for the training and other support.

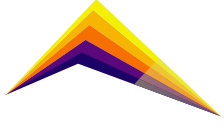

References:

[1] F. Moberg and C. Folke, "Ecological goods and services of coral reef ecosystems," Ecol. Econ., vol. 29, no. 2, p. 215–233, 1999.

[2] K. Heber, "Ecosystem services and community based, coral reef management institutions in post blast-fishing Indonesia," Ecosyst. Serv., vol. 16, p. 1–14, 2014.

[3] A. Chin, T. Lison De Toma, K. Reytar, S. Planes, K. Gerhardt, E. Clua, L. Burke, and C. Wilkinson, "Status of Coral Reefs of the Pacific and Outlook: 2011," p. 260, 2011.

[4] SJ Purkis, "A 'reef-up' approach to classifying coral habitats from IKONOS imagery," IEEE Trans. Geosci. Remote Sens., Vol. 43, no. 6, p. 1375–1390, 2005.

[5] O. Beijbom, PJ Edmunds, DI Kline, BG Mitchell, and D. Kriegman, "Automated annotation of coral reef survey images," Proc. IEEE Computer. Soc. Conf. Comput. Vis. Pattern Recognition., pp. 1170–1177, 2012.

[6] Raphael, A., Dubinsky, Z., Iluz, D. et al. Deep neural network recognition of shallow water corals in the Gulf of Eilat (Aqaba). Sci Rep 10, 12959 (2020). https://doi.org/10.1038/s41598-020-69201-w

[7] MSA Marcos, M. Soriano, and C. Saloma, "Classification of coral reef images from underwater video using neural networks.," Opt. Express, vol. 13, no. 22, p. 8766–8771, 2005.

[8] M. Modasshir, AQ Li and I. Rekleitis, "MDNet: Multi-Patch Dense Network for Coral Classification," *OCEANS 2018 MTS/IEEE Charleston,* 2018, pp. 1-6, DOI: 10.1109/OCEANS.2018.8604478.

[9] R.-RA Garzón-Ferreira, J, Reyes-Nivia, MC, "SIMAC Methods Manual," INVEMAR, St. Marta, p. 61, 2002.

[10] J. Garzón-Ferreira and A. Rodríguez-Ramírez, "SIMAC: Development and implementation of a coral reef monitoring network in Colombia," 2010.

[11] FJ Corpuz, PN Jr, EC Jr, J. Jauod, RJ Judilla, and M. Soriano, "Coral Reef Mosaicking using Teardrop and Fast Image Labeling," 2012.

[12] JP Pierce, Y. Rzhanov, K. Lowell and JA Dijkstra, "Reducing Annotation Times: Semantic Segmentation of Coral Reef Survey Images," Global Oceans 2020: Singapore – US Gulf Coast, 2020, pp. 1-9, DOI: 10.1109/IEEECONF38699.2020.9389163.

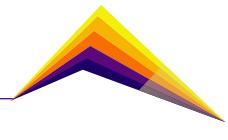

[13] A. Mehta, E. Ribeiro, J. Gilner, and R. van Woesik, "Coral reef texture classification using support vector machines," pp. 302–310, 2007.

[14] Gonzalez. and Woods, Digital image processing, 4th ed. Global Edition - New York: Pearson, 2018.

Table 1. Related work

First Author	Classes	Related work	Accuracy Test (%)
Beijbom [5]	9	Uses a k-means grouping per channel in the L*a*b color space with fifteen centers to generate dictionaries and with these train a support vector machine using a radial basis function as the kernel for making an annotation process over random points on the image. Publish the public bank of image Morea Labeled Coral (MLC) [5] with more than four hundred thousand annotations between corals, sand, and algae.	89% for coral to the rest. 83% All classes. 89% Crustose Coralline Algae, 46% Algae, 19% Macroalgae, 83% Sand, 62% Acropora, 60% Pavona, 42% Montipora, 60% Pocillopora, 76% Porites
Raphael [6]	11	Use a VGG-16 with raw images of EILAT and RMAS image bank (<2000 annotations)	The results show an accuracy of 80.13% over all classes. And accuracy of 67% to 93% between classes
Marcos [7]	5	Uses Local binary patterns (LBP) [14] and neural networks for detecting alive coral and dead coral.	86% for coral dead and coral
Modasshir [8]	9	Use the MLC database with raw images as features. Use CNN topologies: VGGNet, ResNet, DenseNet, MDNet	68% CF, 65% VGGNet, 79% ResNet, 73% DenseNet, 81% MDNet.

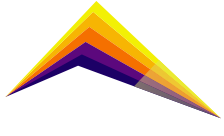

Pierce [12]	9	uses raw images and proposes a segmentation process using convolution neural networks (CNN). create the masks for training from images in the MLC database [5].	83,9% with DenseNet.
Mehta [13]	2	Uses a support vector machine and RGB color space to make classification over your private database	95% for coral and non-coral

Table 2. Results

Model	Accuracy Train (%)	Accuracy Test (%)	Comparative with Beijbom et-al [5], Modasshir et-al [8] and Pierce [12] over all classes
SqueezeNet	94.2	90.1	> to [5][8][12]
Resnet152	97.0	94.5	> to [5][8][12]
dark net	97.0	93.9	> to [5][8][12]
DenseNet201	86.2	82.9	< to [5][12]
VggNet19	84.3	83.1	< to [12] and > to [5]

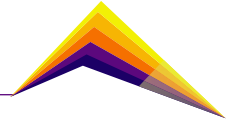

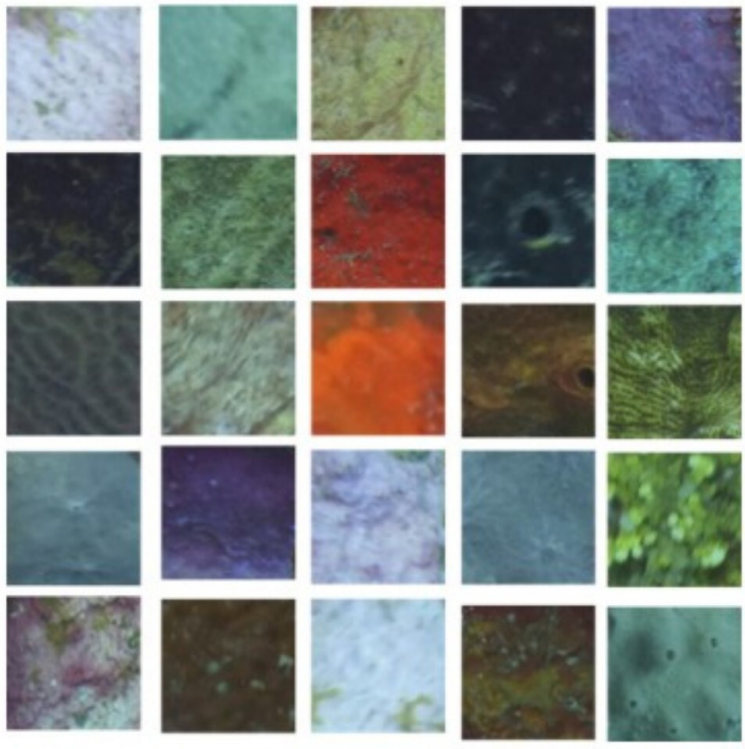

Figure 1. Database samples.

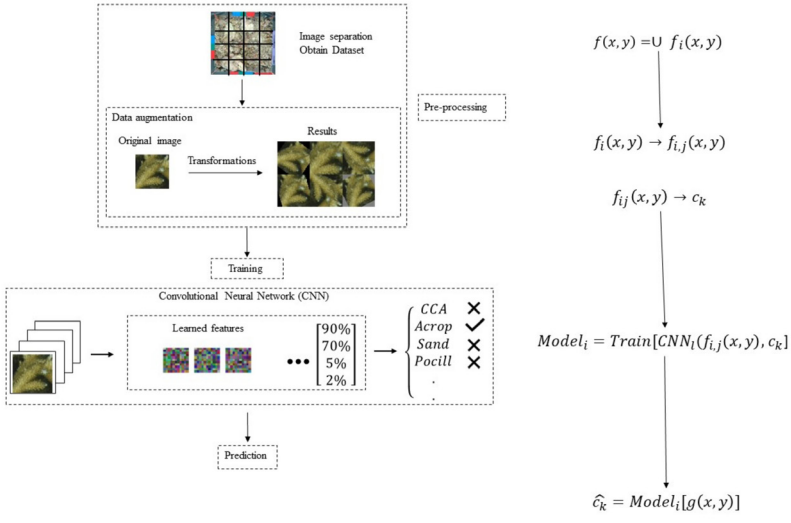

Figure 2. Generic Model Training.

Effect of pressure and time on green compaction of UHMWPE powder by uniaxial pressure

Jennifer J. González M
Félix Echeverría E
Maryory A. Gómez B
David A. Quintero G

E-mail: jennifer.gonzalezm@udea.edu.co
E-mail: felix.echeverria@udea.edu.co
E-mail: maryory.gomez@udea.edu.co
E-mail: dalberto.quintero@udea.edu.co

Centro de Investigación, Innovación y Desarrollo de Materiales - CIDEMAT, University of Antioquia, Medellin – Colombia

Abstract

Ultra-high molecular weight (UHMWPE) is a material widely used in the manufacture of joints for arthroplasty prostheses. In this case, it is interesting to know the effect of pressure and time on the green compaction of UHWMPE powder by uniaxial pressure. The UHMWPE powders were previously characterized by SEM and compacted in a hydraulic press. A completely randomized factorial design was used. Two factors were analyzed at three levels (Pressure: 200, 300 and 400 MPa; Time: 5, 10 and 15 minutes). Two replicates were made for each treatment, for a total of 27 experimental runs. The compacted specimens were weighed, and their dimensions were measure, in order to calculate the respective density values. The results showed a significant effect of pressure on the green compaction percentage of the UHMWPE powders. Although the significance level of the time factor was less than 0.05, SEM analysis was important to determine the best green densification condition to reach 80% of green compaction.

Keywords: Green compaction, uniaxial pressure, UHMWPE powder.

Correspondent author

Introduction

Compactibility can be defined as the ability of any powder to densify by applying pressure during a given time[1]. It is generally known as the green density and is expressed in units of . The traditional method of compaction is uniaxial pressing. Currently, there is great interest in strengthening the knowledge about the UHMWPE powder processing route by hot isostatic pressing (HIP) for the manufacture of bearings for use in arthroplasty[2]. For this reason, it is first necessary to transform the powder into a preform, which will be later processed in a HIP equipment. Some advances are known in this regard, including pre-densification by cold isostatic pressing (CIP), but it is very expensive specialized equipment that is not available at the moment. Therefore, it is proposed to use a hydraulic press at different pressures (200, 300 and 400 MPa) and times (5, 10 and 15 minutes), to evaluate the degree of densification of UHMWPE powders and determine the working condition at which the highest degree of compaction is achieved. Similarly, the current study includes a morphological evaluation by SEM microscopy of the raw material and processed material. This work is expected to provide information that will be helpful for the processing routes of UHMWPE powder.

Methodology

Ultra-high molecular weight polyethylene (UHMWPE) medical grade powder, reference GUR 1020, supplied by Sigma Aldrich (USA) was used. The average particle size reported by the supplier was 125 µm, with a size range between 105 µm and 145 µm. The theoretical density of the powders is 0.94 g/mL at 25 °C and the chemical formula . First, a representative sample of material was selected. Subsequently, the morphology and particle size distribution of the virgin powders were determined by scanning electron microscopy and Image J software. Then, the UHMWPE loose powder was poured into a metal mold and compressed using a Ferton hydraulic press. Uniaxial pressure was applied under the conditions of each treatment. A green compacted piece was obtained in the shape of a parallelepiped with dimensions of 60 x 12 x 8 mm. It was not necessary to use any lubricating agent to extract the pieces thanks to the low coefficient of friction of the material. The compacted samples were weighed on a Mettler Toledo-UMX5 brand electronic microbalance with a precision of 0.1 µg and the dimensions were measured using a Mitutoyo brand digital micrometer with a precision of 0.001 mm. Finally, with the data obtained, the green density of each specimen was determined and the degree of compaction (%) achieved was calculated. The methodology described is shown in Figure 1.

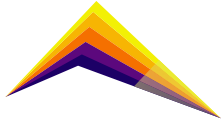

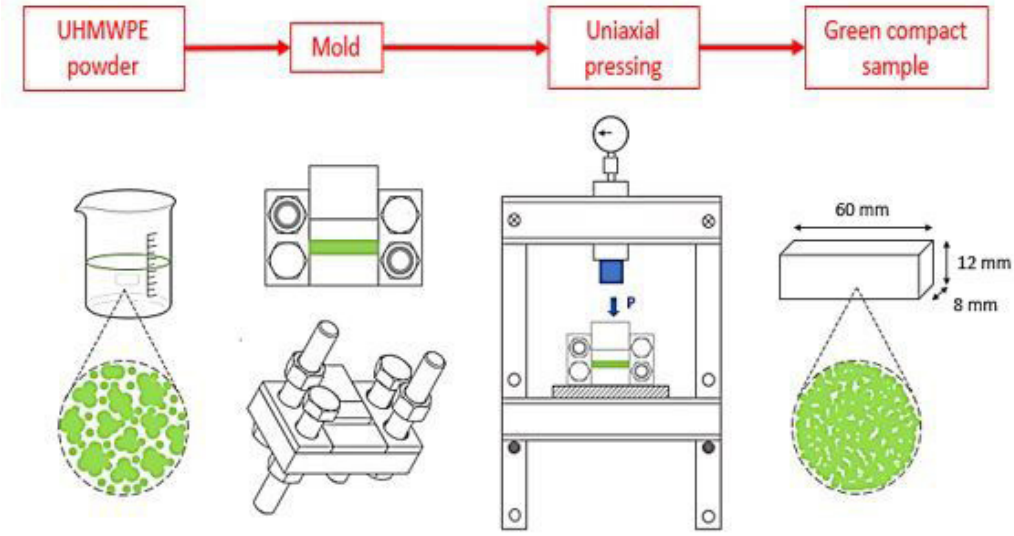

Figure 1. General scheme of the methodology used.

Results and analysis

The particle morphology of the virgin UHMWPE powder is shown in Figure 2. In the micrographs, the UHMWPE powder particles do not exhibit a completely spherical morphology, instead it is rather irregular. According to literature reports, this granular surface characteristic is related to the manufacturing process of UHMPWE powders by ZIegle-Natta polymerization mechanism[3][4]. At higher magnifications, there is a certain agglomeration of smaller particles and the presence of porosity in the structure. The particle size distribution of the virgin UHMWPE powder is shown in Figure 3. The particles of the representative sample evaluated have a normal size distribution. The average particle size (d50) was 114 µm. Minimum particle sizes of 8 µm and maximum of up to 220 µm were recorded.

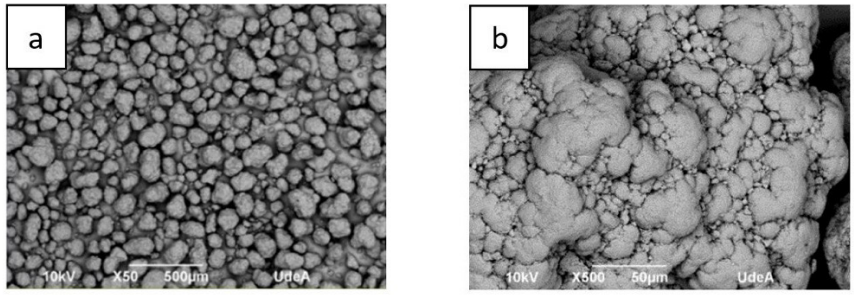

Figure 2. SEM micrographs of virgin UHMWPE powder, magnification: (a) 50X and (b) 500X.

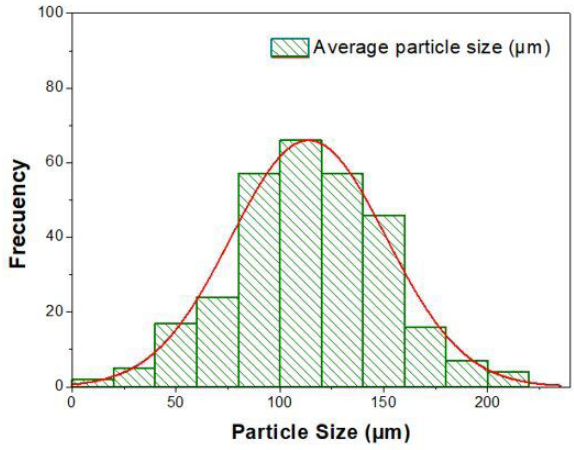

Figure 3. Curve of particle size distribution of UHMWPE powder as purchased.

Different densities were calculated from mass and volume measurements. The bulk density of the loose, uncompacted powder was 0.34. The green compaction percentages of the UHMWPE powder were determined by the real density of each of the compacted samples and the theoretical density. The green compaction percentages of the UHMWPE powder were determined by the real density of each of the compacted samples and the theoretical density. The Statgraphics 18 program was used to process the data and to calculate the statistical parameters associated with the experimental design. The Box-Plots of the degree of green compaction of UHMWPE (%) with respect to the levels of each factor, are shown in Figure 4.

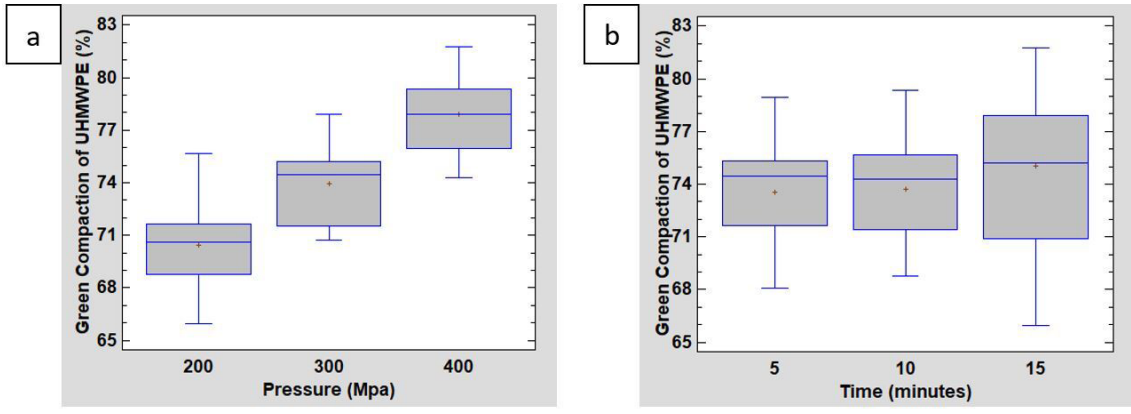

Figure 4. Box-Plot graph of the degree of green compaction of UHMPWE powder with respect to pressure (a) and time (b).

In figure 4(a), it is observed that there was a moderate dispersion of data, the means, and medians for levels 200 and 400 MPa were very close, but for 300 MPa there is a slight positive bias. In general, it was observed that the green compaction percentage of UHMWPE increased with the compaction pressure. On the other hand, in figure 4(b), the dispersion of data at level 15 minutes with respect to levels 5 and 10 minutes was greater.

Table 1 shows that the time factor did not present a very appreciable difference between the mean values for its different levels. While the difference between means of each level of the pressure factor was highest. The maximum average value of green densification was 78.93% at 400 MPa and 15 minutes. Likewise, the average minimum value was 68.96% at 200 MPa and 15 minutes.

Table 1. Experimental Data

Factor	Level	Min.	Mean	Max.
Pressure [MPa]	200	65.96	70.96	75.69
	300	71.70	74.28	77.91
	400	73.63	78.11	81.76
Time [min]	5	68.06	73.52	78.93
	10	68.78	74.28	79.32
	15	65.96	75.05	81.76

The ANOVA table below tests the statistical significance of each effect by comparing its mean square against an estimate of experimental error. The result obtained showed that the pressure factor has a P-value less than 0.05, indicating that, with a confidence level of 95.0%, pressure has a significant effect on the response variable. In contrast, the time factor and the interaction of both factors had no significant effect on the degree of green densification of UHMWPE.

Table 2. ANOVA analysis for green compaction of UHMWPE (%)

Source	Sum of Squares	Df	Mean Square	F-Value	P-Value
A:Pressure (MPa)	248.348	1	248.348	43.54	0.0000
B:Time (minutes)	10.4729	1	10.4729	1.84	0.1886
AB	20.856	1	20.856	3.66	0.0684
Error	131.197	23	5.7042		
Total (corr.)	410.873	26			

The adjusted lineal regression model obtained was:

Green Compaction (%)=69.3426+0.0107778*Pressure (Mpa)-0.638444*Time(minutes)+0.00263667*Pressure(Mpa)*Time(minutes)

The p-values of the pressure and time factors were 0.0000 and 0.1886, respectively. This indicates that the pressure factor had a great influence on the green compaction of the

UHMWPE powders. Therefore, at higher pressure values, a higher percentage of densification is reached. Although the time factor apparently had no significant effect on the green densification percentage of the UHMWPE powders, a scanning electron microscopy analysis revealed some slight differences in the distribution and compaction of the powder particles. The result can be seen in figure 5.

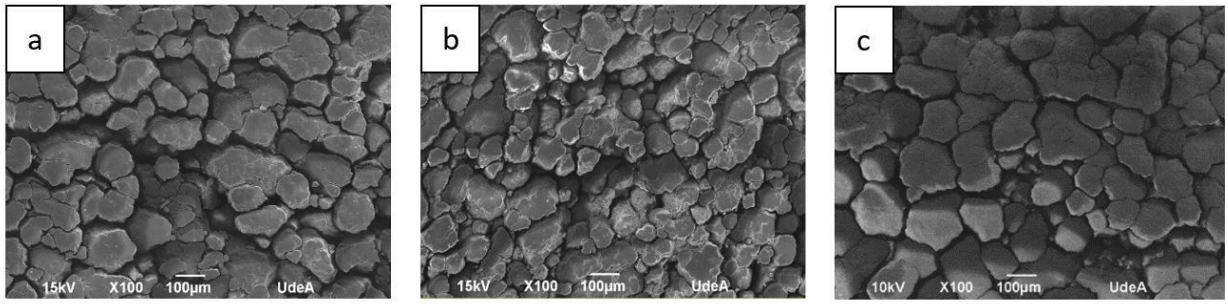

Figure 5. SEM micrograph of UHMWPE compacted at 400 MPa for: (a) 5 minutes, (b) 10 minutes and (c) 15 minutes.

Likewise, when comparing the micrographs of the loose and densified green UHMWPE powder, it is evident that during the pressing process, the particles are repacked and the porosities are reduced, which generates an increase in the densification of the material.

Conclusions or summary

The powder morphology characterization and the size distribution were carried out using a scanning electron microscope and Image J software. It showed granular particles with a normal size distribution and the average size was 113.89 µm. The pressing process of UHMWPE powder for the different pressures (200, 300 and 400 MPa) times (5, 10 and 15 minutes) was carried out in the hydraulic press. After making the respective descriptive and regression analysis of all the experimental data and contrasting them with SEM images, the maximum pressure and the maximum time evaluated were chosen as the working condition to reach the maximum percentage of densification of the UHMWPE powders by means of uniaxial pressing. The foregoing, given that under this treatment an average green densification value reached was of 80.34%, greater than 80% as required. It is expected that this work will provide knowledge and continue the processing route of UHMWP powders.

Acknowledgment

The authors thank the Microscopy Services unit for their collaboration. In the same way to the Faculty of Engineering of the University of Antioquia and to Jaimes Rueda & Precimec Company SAS for being the source of financing for the project “Desarrollo de los procesos requeridos para la obtención del espaciamiento en UHMWPE necesario en prótesis de reemplazo total de rodilla” within the framework of the 75th anniversary of the Faculty of Engineering.

References

[1] A. Y. C. Nee, *Handbook of manufacturing engineering and technology*. 2015.

[2] S. M. Kurtz, “Ultra-High Molecular Weight Polyethylene in Total Joint Replacement and Medical Devices,” in *UHMWPE Biomaterials Handbook*, Second edi., 2009, p. 532.

[3] R. M. Gul and F. J. Mcgarry, “Processing of ultra-high molecular weight polyethylene by hot isostatic pressing, and the effect of processing parameters on its microstructure,” *Polym. Eng. Sci.*, vol. 44, no. 10, pp. 1848–1857, Oct. 2004, doi: 10.1002/pen.20186.

[4] K. Patel, S. H. Chikkali, and S. Sivaram, “Ultrahigh molecular weight polyethylene: Catalysis, structure, properties, processing and applications,” *Progress in Polymer Science*, vol. 109. Elsevier Ltd, 01-Oct-2020, doi: 10.1016/j.progpolymsci.2020.101290.

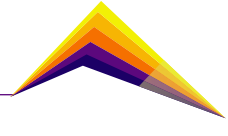

Implementation of a graphene nanocompound to reduce energy consumption as measured with a current sensor using real-time data analysis through the internet

Jorge M. Patiño[1]
Diego Giraldo[2]

E-mail: jorge@phima.co

[1]CEO, Phima S.A.S.
[2]CEO, Helo

Abstract

Tech, contact centers and all type of companies can increase their competitiveness on many fronts, not only improving their products or services, but also through improving processes. One such important process improvement is to reduce energy consumption. This in turn helps to reduce climate impact that each business makes to the environment. Two technologies out of the fourth industrial revolution (4IR) which we were interested in leveraging were cloud computing and graphene material nanotechnology. This nanomaterial has previously been shown to have high thermal conductivity, to an extent that when it is added to a thermal interface material its heat transfer rate increases . In this study we used an external current sensor plugged to a PC power cord and uploads energy usage statistics to the cloud, which showed decreased energy consumption when applying a thermal interface material (TIM) made with graphene. A four-hour testing periods showed a 10% energy consumption decrease compared to original TIM. Furthermore, subsequent studies in daily office work with PCs using this TIM showed 25% average energy savings values .

Correspondent author

Keywords
Energy saving, graphene, computer cooling, IoT, cloud computing, nanotechnology.

Introduction

Nanotechnology is the development, imaging, measurement, modeling, manufacturing and materials measuring less than 100 nm [1] use. Nanomaterials acquire unique properties, but also require specialized skills and engineering to work at this scale. Nanotechnology today is essential to all the fourth industrial revolution technologies, specifically in that the development of nanomaterials and nanodevices has promoted products and services manufacture which consume fewer resources and have characteristics that could not have been achieved previously. This has led to the massive manufacture of more efficient and tiny devices that we carry everywhere, making us more efficient, providing us with valuable information and decisions making help. Here it is where another of the fourth industrial revolution technologies , the Internet of Things, IoT (for its acronym in English) comes in, by providing decision making tools with data analysis previously uploaded to the cloud by ordinary devices.

Graphene [2] is a nanomaterial developed in the past decade by Russian scientists Kostantine Novoselov and Andre Geim, who were awarded the Nobel Prize in Physics in 2010 for their studies that gave evidence of how the properties of graphite were altered [3] when its thickness is from 10 atoms to 1 atom, that is, from 8 nanometers to 0.8 nanometers thick. Their first discovery was to find much higher electrical conductivity at this scale than had ever been measured [4] in another material at normal environmental conditions. After this discovery, research, development and applications of this surprising material, which is 200 times stronger than steel and conducts heat and electricity about 10 times more than gold and silver, increased enormously. Only three years later a thermal paste was developed, which is used as a thermal interface material in heat sinks and which contains graphene nanoplates [5] 0.08% in weight. This development, which today is one of the many nanotechnological products that are sold worldwide, has been reducing the effects of overheating and lengthening the computer equipment life , video game consoles and other electronic devices that require thermal control for their correct operation. Additionally, by reducing the effects of overheating, energy consumption is reduced. The present work compared the energy consumption data of an office computer in real time by changing the factory thermal paste for one with graphene. We measured power versus time through a standard test to show the advantages of applying nanotechnology and the IoT in an everyday business test environment.

Materials and Methods

Room temperature was measured with an Elitech GSP-6 Thermohygrometer. To measure energy consumption, we used a Helo® ONE energy meter based on current sensors (Figure 1) provided by the company Helo (Technical data sheet at helo.com.co). This sensor reports data to the internet platform helo.com.co, where data is synthesized and drawn to be viewed an analyzed. The collected and reported data were power (in W) versus time (in format day hh:mm:ss). The equipment for which we determined energy consumption is a laptop with Intel® Core ™ i5 8250U 1.6GHz 1.8GHz processor, 64-bit operating system with x64-based processor, 8Gb of RAM, nVIDIA GeForce MX 130 3D Accelerator and SSD Drive ADATA SU800NS38 (SATA-III) (Figure 2). We compared two thermal interface materials (MIT) between the processor and the heat sink: the factory thermal paste of an unknown brand, with short service time since the computer was recently unpackaged; and a Fres One® brand thermal interface nanomaterial with a high-speed cooling formula [6] that contains graphene nanoplates (GNP) (Figure 3), 0.08% in weight, provided and manufactured by Phima S.A.S.company

Figure 1. IoT current sensor energy plug device.

Figure 2. Laptop PC and setup for testing power consumption.

Figure 3. Graphene based on high performance thermal

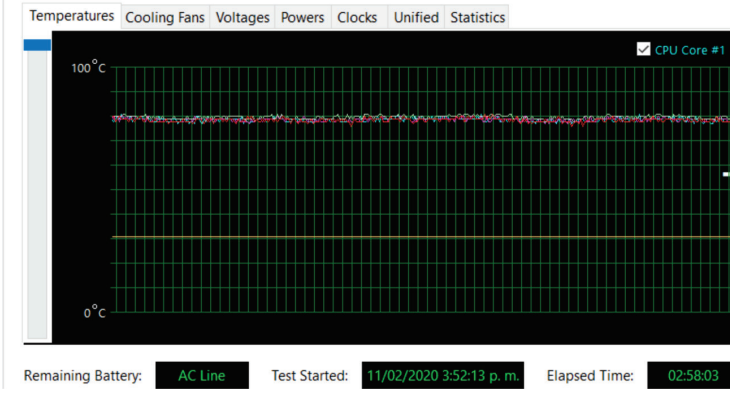

Figure 4. Screen shot of stability test software where identical moments of constant power consumption were produced.

The tests were carried out by selecting an operational environment for which the Fres One® graphene nanoplate composite is intended to work, namely a business office in the center of the Aburra Valley, Colombia, at 1477 meters above sea level (masl), with open windows and without the use of air conditioning. The temperature during test periods were 27.9+/-1.5 ˚C remaining with a very similar temperature on both test days, with both tests performed starting at 2:00 pm. The consumption measurement method was proposed by the Helo company, who are experts in acquiring signals and data in the cloud that are used to make strategic decisions. These consumption tests consisted of connecting the Helo® ONE to a standard 110V connector and waiting 30 seconds for it to connect to the internet on the Helo® internet platform. We then selected to show the data of this device, after which we connected the cable of PC power to the Helo® ONE in the arrangement seen in Figure 2 above. To start the standard tests, we ran on the PC the AIDA 64 program to start the stress test (figure 4), which puts the processors at 100% constantly. The start time was

recorded and the test was left to run for four hours. The following day, the factory thermal paste was changed to the new Fres One® thermal paste in the computer, after which it was reconnected to the meter and in the afternoon same stress test was run again with identical start and end time. This test was repeated 3 more times using a different thermal paste as factory paste.

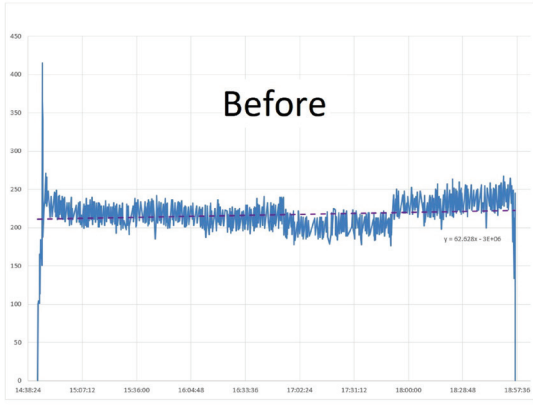

Figure 5. Data graph of electrical power consumed vs. test time with regular factory thermal paste.

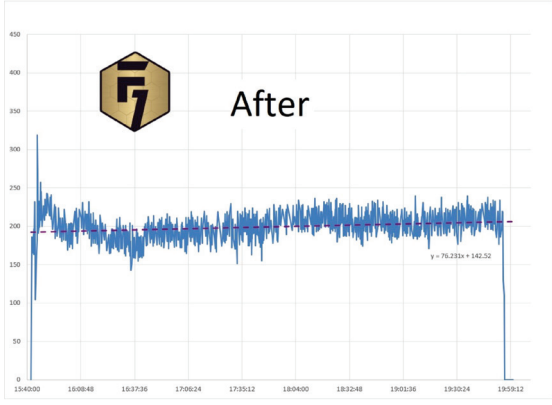

Figure 6. Data graph of electrical power consumed vs. test time with thermal paste containing graphene nanoplatelets.

Results and analysis

From the internet and in real time, energy consumption values were acquired during the time of both tests and downloaded in spreadsheet format after they were finished. Figure 5 shows the graph of consumption at each instant of time for the computer with factory thermal paste and figure 6 for the Fres One®. Subsequently, this consumption was converted at each instant to energy expressed in Watt x hour (W h) in order to be able to compare it with the commercial consumption parameters in the local electrical network and was made a summary of statistical data (table 1). Change in energy consumption was likely due to high surface area and high thermal conductivity of nanoplatelets dispersed on the paste applied between CPU and heatsink.

Table 1. Comparative PC´s energy consumption with and without graphene composite.

	Factory thermal paste	Graphene thermal paste
Test length (HH:MM:SS)	04:13:01	04:18:21
Average consumption (W)	216.42	199.18
Total energy consumption (W)	930.17	850.68
Energy consumption per hour (W/h)	**220.58**	**197.56**

Conclusions

We found that the energy consumption per hour saving (initial consumption - final consumption) was 23.02 W/h. This means an approximate of 10% consumption energy savings, since the price per hour of thermal paste maintenance during a year of use is below 0.01% of the total cost of the energy consumed by the PC equipment. These values are minimum savings that can be reached, because a PC after a year of use and near to its maintenance date can reach more than 20% energy saving, proved by further data analysis investigation.

Standardized PC tests are used widely by information technology departments and technology magazines to make comparative performances so that conditions can be easily replicated. As energy consumption is measured directly from the PC energy plug and uploaded to the internet with third party energy public services acquiring the data, long time lapses to get information and data errors are avoided.

Furthermore, if we do constant monitoring with the current sensor connected to the Helo® internet platform, we can detect when our equipment needs maintenance, which involves changing the thermal paste and thus keeping consumption to a minimum. This has the benefit of improving PC performance and maximizing equipment durability, resulting in fewer failures and emergency shutdowns due to overheating.

Acknowledgment

CollaboraTec coworking space for promoting creation between Helo and Phima startups, Alejandro Patiño computer maintenance technician, Helo, PHIMA S.A.S., Ruta N and the Business Laboratory program.

References

[1] J. Doran and G. Ryan, "Does nanotechnology research generate an innovation premium over other types of research? Evidence from Ireland," *Technology in Society,* vol. 59, no. 101183, pp. 1-8, 20 Agosto 2019.

[2] A. Valencia, "El Grafeno," *Revista Colombiana de Materiales,* no. 1, pp. 1-24, 2011.

[3] A. Geim and K. Novoselov, "The Rise of Graphene," *Nature Materials,* vol. 6, pp. 183-191, marzo 2007.

[4] A. Geim, K. Novoselov, S. Morozov, D. Jiang, Y. Zhang, S. Dubonos, I. Grigorieva and A. Firsov, "Electric Field Effect in Atomically Thin Carbon Films," *Science,* vol. 306, pp. 666-669, 22 octubre 2004.

[5] J. Patino, "Fabricación de Nanocompuesto de Matriz Polimérica Usado como Material de Interfase Térmica," *Revista Colombiana de Materiales,* pp. 10-16, 2013.

[6] J. M. Patiño Acevedo, H. Villar Vega, R. Isaza Escobar and S. Matta L., "APPLICATION: GRAPHENE NANOCOMPOSITE FOR IMPROVEMENT OF VACCINE TRANSPORTATION COLD CHAIN," *Revista EIA/ English version,* vol. 12, no. 2, pp. 59-67, Mayo 2016.

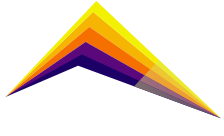

Graphene based Erbium doped fiber laser's design guidelines for ultra short pulse generation

Jaime Arturo Bedoya Correa[1] *E-mail: 1jarturo.bedoya@udea.edu.co*
Ana María Cárdenas Soto[2] *ana.cardenas@udea.edu.co*
Juan Diego Zapata Caro[3] *juan.zapata@udea.edu.co*

1M.Sc. on Telecommunication Engineering; 2Ph.D. on Telecommunications; 3Ph.D. on Electronics Engineering - GITA Research Group, Universidad de Antioquia

Abstract

In this paper, some guidelines useful to design an Erbium-doped fiber laser (EDFL) that uses graphene as a saturable absorber for ultrashort pulse generation are presented. These guidelines are the result of the study of formation and propagation mechanisms of such pulses and, the analysis of the evolution of a Gaussian noise seed passing through a saturable absorber based on graphene in each turn of a cavity, modeling this behavior by the Ginzburg-Landau equation. It was found that graphene's linear absorption coefficient q_0; fiber-based cavity length and erbium-doped fiber gain length influence the pulse formation. All of these parameters can be handled by the designer to achieve wider spectral width sources, as a previous step for a feasible implementation of broadband fiber lasers in local labs, which are the base for custom-made tunable lasers and colorless devices , with a special interest in optical communications.

Keywords: Graphene, erbium-doped fiber laser, ultra-short pulse generation.

Correspondent author

Introduction

Although optical communication systems can transport large amounts of data, new challenges in capacity address the research agendas. Mode-locking EDFL (erbium-doped-fiber-laser) ultrashort pulse generation can be a solution to the problem of sending large amounts of data due to it is high stability, high repetition rate, high power, easy integration to the fiber optic-based components, and low cost [1,2]. There are two different mechanisms for mode-locking EDFL ultrashort pulse generation: active and passive [1-3]. Passive mode-locking uses a nonlinear material as a self-modulator, driving the absorption depending on optical power. By passive mode-locking, it is possible to generate pulses from picoseconds to femtoseconds with large spectrum width, and repetition rate of the order of MHz [1-5]. Novel techniques use graphene as a saturable absorber in EDFL ultrashort pulse generation, due to its ultrafast recovery time, high modulation deep, and low linear loss. Graphene performance in EDFL cavities depends on light-graphene interaction, existing two types: by evanescent field and normal incidence. Recent reported experimental works use graphene on optical fiber D as a saturable absorber in EDFL cavities, whose interaction between light-graphene is via evanescent field, achieving pulse duration between 168 and 599 fs [3 - 5]. In previous works [5-7], the interaction light-graphene by normal incidence in a EDFL cavity has been studied, observing pulse duration dependence of turns in the cavity. To derive some key recommendations for designing optical sources based on this configuration, in this paper, the incidence of graphene´s linear absorption coefficient q_0; fiber-based cavity length, and erbium-doped fiber gain length, in the ultra-short pulse generation is analyzed.

Methodology

The simulated setup is a cavity EDFL with a variable length from 12 to 1500 m, as depicted in [7]. The cavity consists of 1-m length Erbium-doped fiber (-33.8 dB/m absorption coefficient, -57 ps/nm/km dispersion coefficient at 1550 nm), a 980 nm semiconductor pump laser coupled in co-propagation configuration through a 980/1550 nm WDM, a polarization controller, a 50-dB optical isolator, a 15.3% - coupler output connected to graphene at the optical fiber tip as a non-linear material; and a 50/50 beam splitter for oscilloscope and OSA measurements. Firstly, two important elements in the simulation setup are modeled: the Saturable absorber (graphene on the tip of optical fiber) and the gain medium (erbium-doped fiber). The other elements in the proposed setup only contribute with linear losses in the simulation. To analyze the impact of fiber length in the cavity performance different fiber lengths between Er-doped fiber and the saturable absorber were included.

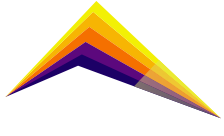

The Saturable absorber (graphene on the tip of optical fiber)

In the model, graphene was simulated as a fast saturable absorber [6,7] due to its recovery time being faster than the repetition rate in the cavity. The equation that describes the saturable absorber rate q for each turn in the cavity is $q = q_0 / \left(1+\left(|A|^2 \tau_A / E_A\right)\right)$; where q_0 is the linear absorption coefficient, E_A is saturation energy of the saturable absorber, τ_A is the saturable absorber's recovery time, and $|A|^2$ is the electric field power.

In the simulations, typical values for graphene on substrate were used [7]. Two different q_0 values have been included to analyze their effect on pulse generation and shape: q_0=0,05 (few overlapping layers of graphene), q_0=0.02 (monolayer Graphene), τ_A = 100 fs, E_A = 1.34x10^{-12} J.

Gain medium (erbium-doped-fiber)

Erbium-doped fiber (EDF) is used for optical signal amplification. The medium gain G is mathematically expressed through the following equation:

$$G(n)\widetilde{A}_n = \left\{1 + g\left[1 - \frac{(n\Delta\omega)^2}{\Omega_g^2}\right]\right\}\widetilde{A}_2 \qquad (1)$$

Where g is the saturable gainis the order of the n longitudinal mode, is the gain bandwidth, is the separation between longitudinal modes, is the relationship between the amplitude of longitudinal n-mode and the central mode, A_n is small signal gain, Ps is the saturation power of erbium and Pm is average power. This study's characteristic Erbium parameters used in the simulations are g0=3.5, Ps = 0.538x10-3W, g =3.75[7]. The next step will be to simulate the EDFL behavior using the Ginzburg-Landau (G-L) equation.

W_g =3.75[7]. The next step will be to simulate the EDFL behavior using the Ginzburg-Landau (G-L) equation.

Ginzburg-Landau differential equation

The ultrashort pulses generation and propagation were investigated from the numerical solution Ginzburg-Landau differential equation (G-L), written as:

$$\frac{\partial A}{\partial z} = \left[-\beta_1 \frac{\partial A}{\partial t} - i\frac{\beta_2}{2}\frac{\partial^2}{\partial^2 t} + \gamma|A|^2 A - \frac{\alpha_T}{2}\right] + \left[g\left(1 + \frac{1}{\Omega_g^2}\frac{\partial^2}{\partial^2 t} - q\right)\right]A \qquad (2)$$

Where A is cross electric field, is fiber losses, group speed, second-order dispersion, nonlinear parameter, g Er peak gain, W_g gain bandwidth, and q is saturable absorption parameter [7]. The polarization controller and the output coupler generate linear losses, which are added to the fiber optic losses, introduced in the G-L equation (2) as a total α_T. To solve this equation, the method of finite differences Split Step Fourier and MATLAB as simulation tool were chosen.

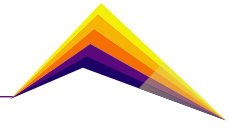

Results and analysis

After simulating equation (2), the pulse generation dynamic was studied in function of turns in the cavity, and subsequently, the pulse duration and spectrum width under cavity length changes were investigated.

Role of graphene as saturable absorber in EDFL

To start the simulation, the initial optical signal in the cavity is produced from the evolution of the noise components, generated by the EDF amplified spontaneous emission. The first question to solve is related to the effect in pulse generation due to changes in graphene's linear absorption parameter and the number of turns needed to obtain pulse stability, i.e., the effect of graphene and EDF interaction in the pulse generation was analyzed. It is possible to see in figures 1a (q_0=0.05) and 1b (q_0=0.02) a pulse generation after 500 turns passing through graphene in the cavity. Graphene exhibits some particular characteristics: it becomes transparent in the presence of intense electromagnetic fields. This means that in a saturated state, it stops absorbing radiation. At this moment, the gain is greater than the losses

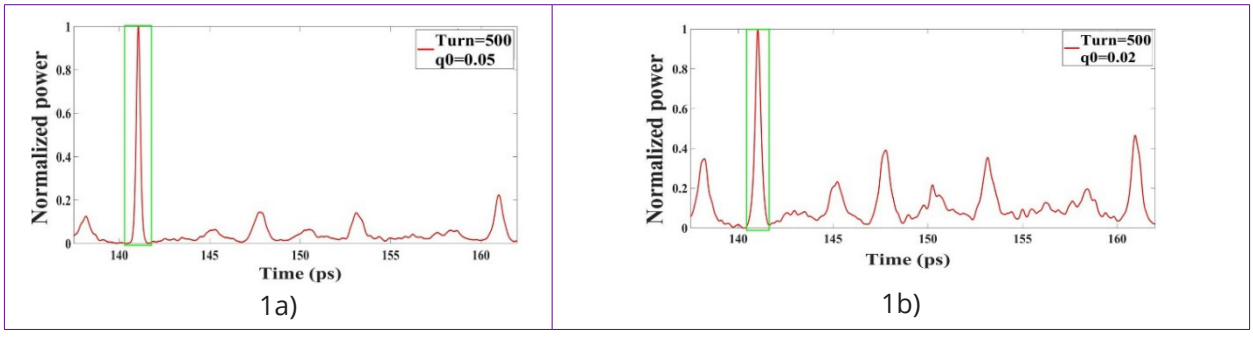

Figure 1. Effect of graphene and EDF interaction in the pulse generation. Pulse generation after 500 turns in the cavity, for a) q_0 =0.05 and b) q_0 =0.02.

In the cavity, generating a time-lapse which allows the passive coupling of modes and therefore a pulse generation [1-7]. On the other hand, thanks to the tip configuration, it is not polarization depending due to the normal incidence of the light. when q_0 decreases, the pulse takes more time to form, and in both cases, it is needed more than 100 turns to form the pulse. The pulse duration stability in function of turns in the cavity is shown in Fig. 2a and 2b. For two values of linear absorption q_0 = 0.05 and q_0 = 0.02, different stabilities values were found. In fact, when q_0 = 0.05, the pulse duration was stabilized after 2200 turns in the cavity with an approximately pulse duration of 0.180 ps. On the other hand, for q_0 = 0.02 the pulse duration stability was around 6000 turns with a pulse duration of 0.153 ps.

Erbium Doped Fiber Laser performance in function of gain length

The EDF gain length limit for which a pulse is formed was studied. In figure 4 the gain length varied between 0.4m and 2m, keeping the pumping power constant Pp = 0.02mW. Figures 3a (q_0=0.05) and 3b (q_0=0.02) show the minimum turns and gain lengths upper than 0.3m and 0.4 m approx. respectively, for the ultrashort pulse formation with stability.

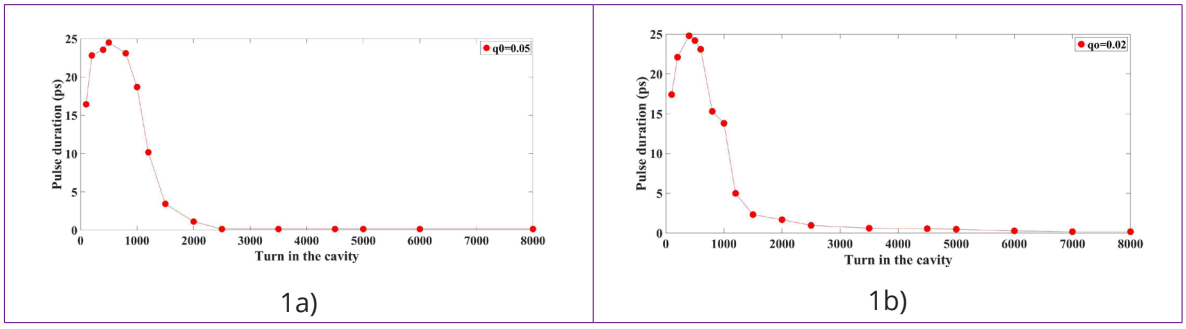

1a) 1b)

Figure 2. Pulse duration in function of turns in the cavity at absorber saturable output. a) q_0 =0.05 and b) q_0 =0.02.

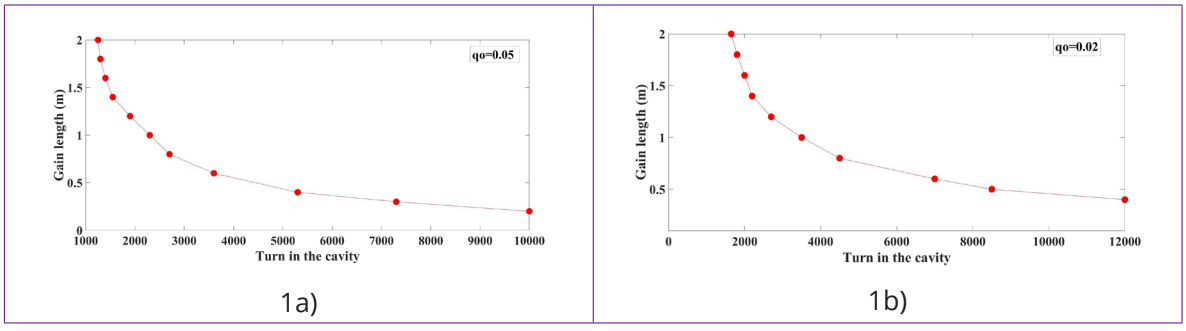

1a) 1b)

Figure 3. Gain length vs. turns required for pulse formation in the cavity: a) q0 = 0.05, and b) q0 = 0.02.

Cavity length effects in the pulse duration

Fig. 4 shows the cavity performance, setting q_0 = 0,05 and 2500 turns, and varying the fiber length from 50 m to 1500m. The bandwidth (blue curve) decreases from 14.2 nm to 0.57nm when the cavity length increases from 50m to 1500m; and the pulse duration (red curve) increases from 0.178 ps to 4.69 ps, respectively. The pulse duration stabilizes for values higher than 600 m-fiber length in the cavity when for long cavities the laser mode-locking performance is determined by soliton and large dispersion effects.

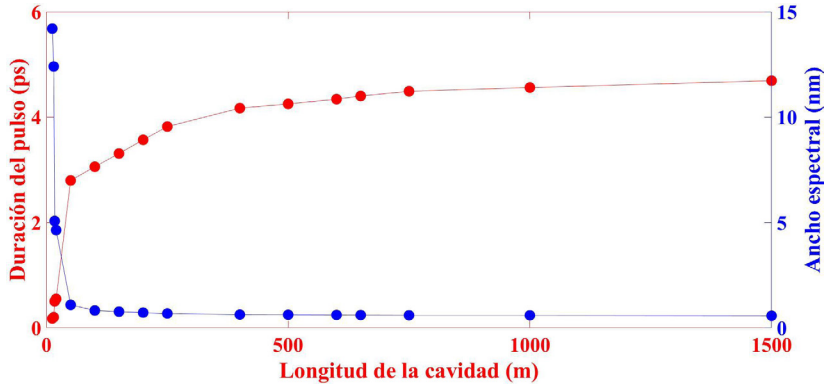

Figure 4. Bandwidth and pulse duration as function of cavity length.

Conclusions or summary

In summary, three parameters that allow a tailored bandwidth design of a broadband source at 1550 nm based on a passive mode- locking Erbium doped fiber laser, using graphene on a tip, as a saturable absorber have been analized. The results obtained by simulation show high dependence on graphene linear absorption q_0: higher values up to $q_0 = 0.05$ allow better performance in pulse stability, requiring fewer turns to pulse generation. It was observed that around 2200 turns in the cavity are needed to pass from noise to stable optical pulse for this q_0. The pulse duration also depends on the cavity length: the shorter the length the shorter the pulse duration and the larger bandwidth. When $q_0 = 0,05$, the pulse duration was stabilized after 2500 turns in the cavity with an approximately pulse duration of 0.178 ps, for a 50m-cavity length. On the other hand, it was found that for $q_0 = 0,05$ there is a limit in the EDF length of 0,4m, needed to provide enough gain to compensate for the losses in the cavity. This is a previous step for a feasible local deployment of broadband sources, useful for tunable and colorless lasers with application in optical communication systems.

Acknowledgment

We thank the UDEA's support through **SOS-21-1-05 Project granted to GITA Group.**

References

[1] Rui Zhu *et al* (2022). Novel nanomaterials based saturable absorbers for passive mode locked fiber laser at 1.5 μm. *Nanotechnology* 33 182002

[2] Ya-ni Zhang et al (2022). 2D van der Waals materials for ultrafast pulsed fiber lasers: review and prospect. *Nanotechnology* 33 082003

[3] Zapata, J. D., Steinberg, D., Saito, L. A., De Oliveira, R. E. P., Cárdenas, A. M., & De Souza, E. A. (2016). Efficient graphene saturable absorbers on D-shaped optical fiber for ultrashort pulse generation. *Scientific reports*, *6*(1), 1-8.

[4] Zapata, J. D., Saito, L. A. M., Cárdenas, A. M., & de Souza, E. T. (2016). Sub-150 fs mode-locked Erbium doped fiber laser based on monolayer graphene on a D-shaped optical fiber. In *CLEO: Science and Innovations* (pp. JTu5A-71). Optica Publishing Group.

[5] Henrique Guimaraes Rosa et al (2015). Transfer of an exfoliated monolayer graphene flake onto an optical fiber end face for erbium-doped fiber laser mode-locking. *2D Mater*. Vol.2 031001

[6] Henrique G. Rosa, et all (2015), "Raman Mapping Characterization of All-Fiber CVD Monolayer Graphene Saturable Absorbers for Erbium-Doped Fiber Laser Mode Locking," *J. Lightwave Technol*. 33, 4118-4123

[7] Bedoya, J. A., Cardenas, A. M., & Zapata, J. D. (2020). Numerical study of noise evolution for ultrashort pulses generation using graphene as saturable absorber. In *2020 IEEE Colombian Conference on Communications and Computing (COLCOM)* (pp. 1-4).

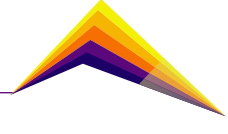

Evaluation of the application of suspensions of iron oxide magnetic nanoparticles functionalized with quaternized chitosan on maize seeds

Yessica A. Montoya Giraldo[1] — E-mail: ymontoy2@eafit.edu.co
Adriana. R. Portela Davila[2] — E-mail: adriana.portela@udea.edu.co
Danna Susunaga Gómez[3] — E-mail: dmsusunagg@eafit.edu.co
Jeaneth P. Urquijo[4] — E-mail: jurquijo@udem.edu.co
Álvaro A. Velásquez[5] — E-mail: avelas26@eafit.edu.co
Diego Villanueva Mejia[6] — E-mail:dvillanu@eafit.edu.co

[1, 3, 6] *Grupo de Ciencias Biológicas y Bioprocesos, Área de Sistemas Naturales y Sostenibilidad, Universidad EAFIT, Medellín, Colombia.*
[2] *Grupo Interdisciplinario de Estudios Moleculares, Ciencias Naturales y Exactas, Universidad de Antioquia, Medellín, Colombia.*
[4] *Grupo de Estado Sólido, Instituto de Física, Universidad de Antioquia, Medellín, Colombia*
[5] *Grupo de Electromagnetismo Aplicado, Área de Ciencias Fundamentales, Universidad EAFIT, Medellín, Colombia*

Abstract

Nanoparticles are material structures with sizes between 1 and 100 nm. Recently, they have been of a great interest for their study in different areas. For example, in the agriculture field there are sustainable developments such as nanofertilizers, which main function is to adsorb and release micro or macronutrients necessary for plants nutrition. However, there are still many concerns about the effects that these nanofertilizers could cause on plant growth and development. Therefore, in this research we evaluated the effect of the application of iron oxide spinel type magnetic nanoparticles syrups functioning with quaternized chitosan on morphological parameters of maize (*Zea mays* L.) plants (variety FNC31AC), at *in vitro* and microstation levels. As preliminary results, it was evidenced that upon exposing maize seeds to different syrup iron

Correspondent author

concentrations at *in vitro* level, the biomass and root length variables of germinated seeds had a statistically significant relationship with the iron concentrations. Likewise, it was observed that, for iron concentrations higher than 50 ppm, the values of these variables decreased. As a result of this trial, three iron concentrations below 50 ppm were chosen and subsequently evaluated on maize seeds. The variables of seedling height, germination percentage and seedling dry biomass did not show statistically significant differences among the iron concentrations evaluated. Likewise, none of the treatments showed any phytotoxic effect on maize plants. These preliminary results suggest that for nanoparticle syrups with iron concentrations below 50 ppm there is no evidence of negative effects on the seed germination process and on the growth of maize seedlings, which would indicate that this nanofertilizer could be suitable to be use in the evaluated crop.

Key words: Iron oxide magnetic nanoparticles – Maize seeds – Nanofertilizers – Germination process

Introduction

Nanoparticles (NPs) are defined as particles less than 100 nm in size [1]. The use of NPs in different areas has increased rapidly [2], in particular, the application of NPs in agriculture can have a transforming effect on food production techniques as it can enable the delivery of bioactive agents (growth factors, pesticides, and fungicides) directly to plants [3]. Within the classification of NPs is the category of metal NPs that are synthesized from essential metals and belong to the most commonly manufactured types of nanomaterials since they have unique physical and chemical properties [4, 5]. At present, many kinds of metal oxide NPs, such as iron oxide NPs, have been applied in agriculture, specifically in plant protection and fertilization [4,6]. Several studies have reported that iron oxide NPs can increase seed germination [3,7], seedling vigour, plant biomass, and yield and also enhance physiological function [3,8]. In order to achieve biocompatibility, biodegradation and stability of the NPs, as well as to modulate any toxic or agglomerative effect in physiological environments, their surface must be covered with embedding materials such as chitosan, which chemical structure must be modified to improve their solubility at physiological pHs [9,10]. However, the majority of the published nanotoxicology articles have focussed on mammalian cytotoxicity or impacts to animals and bacteria, and only a few studies have considered the toxicity of NPs to plants system [11]. Furthermore, to our knowledge, there are not enough studies that

examine the impact of iron oxide NPs on maize (*Zea mays* L.), a crop of great importance for humankind food security. In this work, we evaluated the effect of the application of syrups of iron oxide spinel type magnetic NPs functioning with quaternized chitosan on morphological parameters of *Z. mays* plants (variety FNC31AC).

Materials and Methods

Iron oxide NPs

The iron oxide NPs used were synthesized and characterized at the Instrumentation and Spectroscopy Laboratory of the Universidad EAFIT [12]. The structural and magnetic characterization of the particles obtained was carried out by Electron Transmission Microscopy (TEM), Infrared spectroscopy (FTIR), Mössbauer transmission spectroscopy (TMS) and vibrating sample magnetometry (VSM) at room temperature, indicating that the sample is composed by particles with a magnetic-polymer core-shell structure, with a diameter smaller than 20 nm. The iron content in the syrup of magnetic NPs functioning with quaternized chitosan was obtained by visible spectrophotometry, obtaining a value of 454 ppm. The stock syrup of iron oxide NPs was diluted in deionized water to obtain the desired concentrations for the different tests.

In vitro and Microstation tests

Seeds of maize were acquired by "Federación Nacional de Cultivadores de Cereales, Leguminosas y Soya (FENALCE)" with an average germination rate of 90%. The *in vitro* experimental trials consisted of an incubation of maize seeds in a humid chamber, which consisted of placing 10 maize seeds per Petri dish (100 mm x 15 mm) with a cellulose filter paper at the bottom impregnated with 3 mL of deionized water (control) or with a syrup at different iron concentrations (3.12 ppm, 6.25 ppm, 12.5 ppm, 25 ppm, 50 ppm, 75 ppm, 100 ppm for the first trial, and 25 ppm, 35 ppm and 45 ppm for the second one). Petri dishes were stored in a dark place at 23°C for 8 days. After this time, the biomass and root length of germinated seeds were recorded. Each treatment was carried out by triplicate. For the microstation test, maize seeds were sown in seedling trays using fine-textured heterogeneous soil as substrate. The soil was moistened with the treatment to be evaluated: deionized water (control), 25 ppm, 35 ppm or 45 ppm of the syrup. The tray with the sown seeds was taken to the microstation of Universidad de Antioquia, under uncontrolled environmental conditions for 28 days. After this time, the dry biomass, seedling length and germination percentage were measured. There were 20 replicates per treatment.

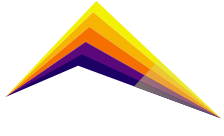

Statistical analysis

The results of the *in vitro* assay were analyzed by regression analysis, where the value of the parameters was considered. Results of microstation assay were performed using the analysis of variance (ANOVA) with 95% of confidence, previously verifying the assumptions. The statistical analysis was made by Statgraphics centurion software (version 19).

Results and analysis

From the evaluation at the *in vitro* level, a statistically significant relationship was observed between the dependent variables of biomass and root length with the different iron concentrations evaluated. In the case of biomass, a positive relationship was observed for a syrup with iron concentrations below 50 ppm, while, at concentrations above that value, the relationship was negative (Figure 1a). As for the root length variable, it presented higher values with respect to the control between 3.12 ppm and 50 ppm iron concentrations, but above 50 ppm the root length value decreased (Figure 1b). Furthermore, at the qualitative level, it was observed that the roots exposed to a concentration higher than 50 ppm of iron were thinner and weaker than those exposed to lower concentrations, and some of them even showed necrosis.

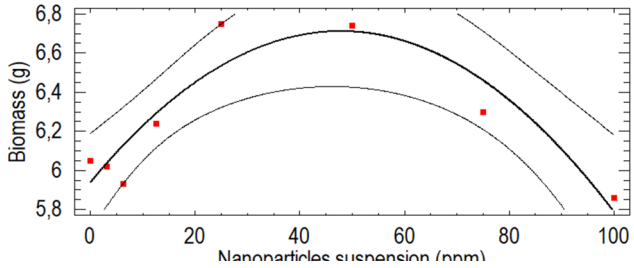	Polynomial model grade 2 Y = 5,939 + 0,032*X-0,000338*(X)^2 R2:84.3% R2(adjusted): 77,9% ANOVA of model: 0.0098
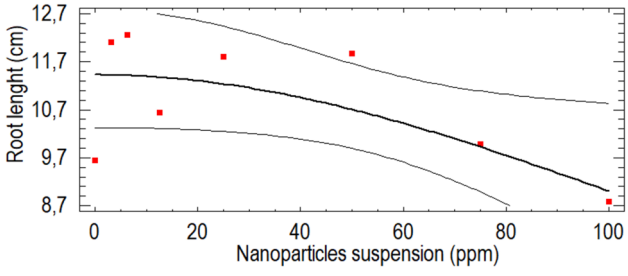	Reciprocal Y-Squared X model Y = 1/(0,0875 + 0,00000235*(X)^2) R2:52.4% R2(adjusted): 44,5% ANOVA of model: 0.0424

Figure 1. Regression analysis of different iron concentrations in germination of maize seeds. a) Evaluation of variable Biomass, b) evaluation of variable Root length. The red Squares represent the points of the graphics, the thin black lines define the confidence limit and the center black line represents the fitted model.

According to the results in this first trial, it was determined that the syrup of iron oxide NPs began to have a negative effect on maize seeds at iron concentrations above 50 ppm. For this reason, three concentrations below 50 ppm were defined for subsequent evaluations (25 ppm, 35 ppm and 45 ppm). In order to analyze the effect of these three iron concentrations, two new tests were carried out. The first was an *in vitro* wet chamber test, where the seeds were in contact with the established iron concentration during the whole germination process. As a result of this test, it was observed that all seeds exposed to the iron concentrations presented a good germination percentage, higher than 90%, but none of them matched the control, which was 100%. In addition, the root length of all treatments was similar to that of the control, with the exception of the seeds subjected to 25 ppm syrup, which presented a higher value than the control. However, according to the ANOVA analysis, there were no statistically significant differences between the different treatments in the variables evaluated (Table 1). The second test performed was the sowing of maize seeds in a substrate moistened with NPs syrups, where the seeds germinated and grew until day 28 after sowing. After this time, the morphological evaluations of the seedlings showed that in comparison with the *in vitro* test, the seeds of all the treatments reduced their germination percentage, the lowest being 60% obtained under the 35 ppm treatment and the highest being 85% for the seeds of the control treatment. As for seedling length and dry biomass, similar values were obtained among all treatments, which was confirmed by the analysis of variance, since they did not present statistically significant differences between them (Table 1).

Table 1. Evaluation of three iron concentrations (25 ppm, 35 ppm, 45 ppm) on maize seeds. * *in vitro* trial, ANOVA analysis with 95% confidence, root length *p-value*: 0.123. **microstation trial, ANOVA analysis with 95% confidence, seedling length *p-value*: 0.9910, dry biomass *p-value*: 0.1029, germination percentage *p-value*: 0.4485

	In vitro trial*		Microstation trial**		
Treatments	Germination percentage (%)	Root length (cm)	Germination percentage (%)	Seedling length (cm)	Dry Biomass (g)
Control	100	8,03 ± 0,98	85	15,71 ± 2,87	0,19 ± 0,01
25 ppm	90	10,34 ± 1,57	70	15,46 ± 1,59	0,16 ± 0,04
35 ppm	83	7,40 ± 2,74	60	14,71 ± 3,83	0,13 ± 0,06
45 ppm	90	9,88 ± 2,32	80	14,50 ± 2,35	0,11 ± 0,04

Finally, based on the results from the *in vitro* and tray assay, as well as the absence of necrosis and inhibition of germination, we ruled out any possible phytotoxic effect of the NPs suspension at the concentration of 25 ppm, 35 ppm and 45 ppm on maize seeds and in their growth and development.

Conclusions

This study demonstrates that there is not phytotoxic effect on maize seeds (FNC31AC) and plants at iron concentrations below 50 ppm, but at concentrations above that value a negative effect is beginning to be seen. Additionally, seed sowing confirmed that the iron concentrations 25 ppm, 35 ppm and 45 ppm are not phytotoxic for the variable's germination, height and dry biomass of exposed seedlings. However, it is necessary to carry out a new experiment at greenhouse level, which will allow confirming this premise with greater precision.

References

[1] Mangalampalli, B., Naresh, D., and Paramjit, G. (2018). "*Allium Cepa* Root Tip Assay in Assessment of Toxicity of Magnesium Oxide Nanoparticles and Microparticles." Journal of Environmental Sciences (China)., 66, 125-137.

[2] Roco, M.C. (2003). "Broader Societal Issues of Nanotechnology." Journal of Nanoparticle Research., 5 (3), 181–189.

[3] Elizabeth, C.H.T., Carvalho, L.B., Pereira, A.E.S., Montanha, G.S., Corrêa, C.G., Carvalho, H.W.P., Ganin, A.Y., Fraceto, L.F., and Yiu, H.H.P. (2020). "Localization of Coated Iron Oxide (Fe3O4) Nanoparticles on Tomato Seeds and Their Effects on Growth." ACS Applied Bio Materials., 3 (7), 4109–4117.

[4] Yang, Z., Jing, C., Dou, R., Gao, X., Mao, C., and Wang, L. (2015). "Assessment of the Phytotoxicity of Metal Oxide Nanoparticles on Two Crop Plants, Maize (*Zea Mays* L.) and Rice (*Oryza Sativa* L.)." International Journal of Environmental Research and Public Health., 12 (12), 15100–15109.

[5] Ruttkay-Nedecky, B., Krystofova, O., Nejdl, L., and Adam, V. (2017). "Nanoparticles Based on Essential Metals and Their Phytotoxicity." Journal of Nanobiotechnology., 15 (1), 1–19.

[6] Gogos, A., Knauer, K., and Bucheli, T.D. (2012). "Nanomaterials in Plant Protection and Fertilization: Current State, Foreseen Applications, and Research Priorities." Journal of Agricultural and Food Chemistry., 60 (39), 9781–9792.

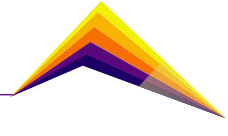

[7] Sundaria, N., Singh, M., Upreti, P., Chauhan, R., Jaiswal, J.P., and Kumar, A. (2018). "Seed Priming with Iron Oxide Nanoparticles Triggers Iron Acquisition and Biofortification in Wheat (*Triticum aestivum* L.) Grains." Journal of Plant Growth Regulation., 38, 122-131.

[8] Rui, M., Ma, C., Yi, H., Guo, J., Yukui,R., Tang, X., Zhao, Q., Fan, X., Zhang, Z., Tianqi, H., and Zhu, S., (2016). "Iron Oxide Nanoparticles as a Potential Iron Fertilizer for Peanut (*Arachis hypogaea*)." Frontiers in plant science., 7 (815), 1-10.

[9] Frank, L.A., Onzia, G.R., Morawskib, A.S., Pohlmanna, A.R., Guterresa, S.S., and Contri, R.V., (2020). "Chitosan as a coating material for nanoparticles intended for biomedical applications." Reactive and functional polymers, 147, 1-14.

[10] Shuklaa, S., Jadaunb, A., Arorac, V., Sinha, R.K., Biyani, N., and Jaina, V.K., (2015). "In vitro toxicity assessment of chitosan oligosaccharide coated iron oxide nanoparticles." Toxicology Reports, 2, 27-39.

[11] Sarvendra, K., Patra, A.K., Datta, S.C., Rosin, K.G., and Purakayastha, T.J. (2015). "Phytotoxicity of Nanoparticles to Seed Germination of Plants." International Journal of Advanced Research., 3 (3), 854–865.

[12] Velásquez, A.A., Marín, C.C., and Urquijo, J.P. (2018). "Synthesis and characterization of magnetite-maghemite nanoparticles obtained by the high-energy ball milling method." J Nanopart Res., 20 (72), 1-13.

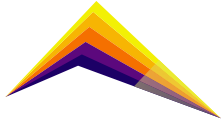

Mechanical characterization of bioinspired composite materials produced via additive manufacturing

Liliana Bustamante Góez[1]
Junes Villarraga Ossa[2]
Pablo Zavattieri[3]

E-mail: liliana.bustamante@udea.edu.co
E-mail: junes.villarraga@udea.edu.co
E-mail: zavattie@purdue.edu

[1] Ph. D. (c), Ingeniería Mecánica, Universidad de Antioquia, Colombia
2 Ph. D., Ingeniería Mecánica, Universidad de Antioquia, Colombia
3 Ph.D., Purdue University, EEUU

Abstract

Nature has evolved over millennia to produce composite materials with excellent mechanical properties despite the poor properties of the base materials; as a result, they are a good source of inspiration for material optimization for applications, such as increasing toughness and damage resistance. Eight structural elements are identified in biological materials: fibrous, helicoidal, gradients, layered, tubular, cellular, suture, and overlapping. Helical structures consist of stacks of ordered fibers that form layers that are rotated at a constant angle of inclination. Bouligand structures consist of an helicoidal arrangement of fibrous laminates that completes a 180° turn and provides increased strength and toughness in multiple directions and exceptionally high fracture toughness. Traditional methods used to make fiber-reinforced polymer composites (FRPC) have a restriction on specific fiber alignment and demand expensive molds, dies, or lithographic masks. Additive manufacturing has the potential to replace many conventional manufacturing processes due to its ability to create complex geometries with customizable material properties, low cost, low energy input, material consumption and employ several materials simultaneously. Fused deposition modeling (FDM) is the most widely used manufacturing

Correspondent author

additive technique for manufacturing FRPC. This work presents three-dimensional models mimicking the Bouligand structures by turning the pitch angle of the layers. The specimens were fabricated using the FDM technique. A thermoplastic polyurethane (TPU) was used for the matrix and polylactic acid (PLA) of the fibers. Tensile tests were used to mechanically characterize both the raw materials and the manufactured composites to examine the impact of the helical angle and the contribution of the matrix and fiber materials to the stiffness and toughness of the composite. Experiments and analysis revealed that high rotation angles improve the stiffness and toughness of the composite.

Key words: Biomimetic, Bouligand structures, fiber reinforced polymer composite, additive manufacturing, stiffness, toughness.

Introduction

Nowadays, biomimetics plays a very important role in the research to create materials with a better mechanical performance. The result of the observation and imitation of the solutions that nature employs throughout the evolutionary process can contribute to areas such as the creation of protective structures, aerodynamic elements, weight reduction, thermal transfer, and optimization of materials, among others. It has been established that hierarchical structures provide an adequate distribution, dimensions, and properties to the components of a system so that it responds optimally to a particular need of a specie [1]. There are several types of hierarchical structures, some are formed by fibers, plates, particles or inclusions, pores, multilayer configuration, organic and inorganic interface, and depending on the organization we can classify them as unidirectional, orthogonal, and helical or Bouligand [2], [3]using Oryctes rhinoceros and five other species of beetles. The precision of orientation of each specific endocuticle layer at a given location is shown by the low variation (± 3·3° for 10 measurements. Bio-inspired structures have been employed in a wide range of applications such as in the design of automobiles and trains, for building structures, aircraft wings, missile structures, protective armor, and unmanned aerial vehicle (UAV) design, among others[3], [4]. The optimal performance of these structures has been achieved by a high degree of organization ranging from the molecular to the macro scale. Fiber reinforced composites (FRC) are the materials that structurally resemble bio-inspired structures the most, since they can be manufactured to have better properties than the sum of their parts.

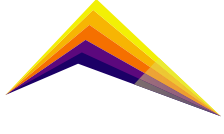

Currently, additive manufacturing is a highly employed manufacturing process due to its multiple benefits and the decrease in its costs. Additionally, it allows the elaboration of complex structures with an adequate dimensional control and the use of different materials, even simultaneously. All these conditions make additive manufacturing an appropriate tool in the research process for the optimization of materials in engineering [5].

In this work, we combine two architectures: the Bouligand [6], [7] and the "brick and mortar" [3], [8] to investigate, discontinuous fiber helicoids (DFH) composites as function of helicoidal angle between layers. The fiber helicoid is found in the dactyl club of the Peacock mantis shrimp (Stomatopod) [9], the cuticle of arthropods [9], [10] and fish scales [11]. The brick and mortar is found in sea shells, e.g., the innermost layers of red abalone (Haliotis ufescens) [12]. It has been proposed that helicoidal arrays of fibrils, adapt to the loading environment through laminae rotation towards the loading direction, whereas other laminae, with large off-axis angle, rotate away from the loading direction [13]. Also, this fiber reorientation has been found to contribute in the enhancement of ductility and toughness in fish scales [11]. For this reason, here, we fabricated a discontinuous Bouligand assembly composed by fibers of PLA in embedded in a TPU matrix to investigate the effect the angle between layers on strength, stiffness and toughness of helicoidal composite.

Methodology

The primary objective of this research is to increase the material toughness, and as a result, a Bouligand-type structure was chosen. This type of configuration significantly increases the toughness and ductility of the armor or shell by reorienting layers towards the axis of stress and deforming by stretching, sliding, and delamination mechanisms while other layers rotate away from the tension and compression axis.

The DFH composites specimens are 3D printed with two materials. The material used for the matrix was thermoplastic polyurethane (TPU) and polylactic acid (PLA) for the fibers, with these materials is possible to simulate the materials used by nature. The fibers were printed with a square cross-section area. The stiff fibers have a length of 10 *mm*, a square cross-section with a width of 1.2 *mm*. The matrix wraps the fibers in all directions by a thickness of 1.2 *mm*. The matrix thickness is a function of the number of necessary layers to complete a Bouligand structure unit (180°), see Figure 1.

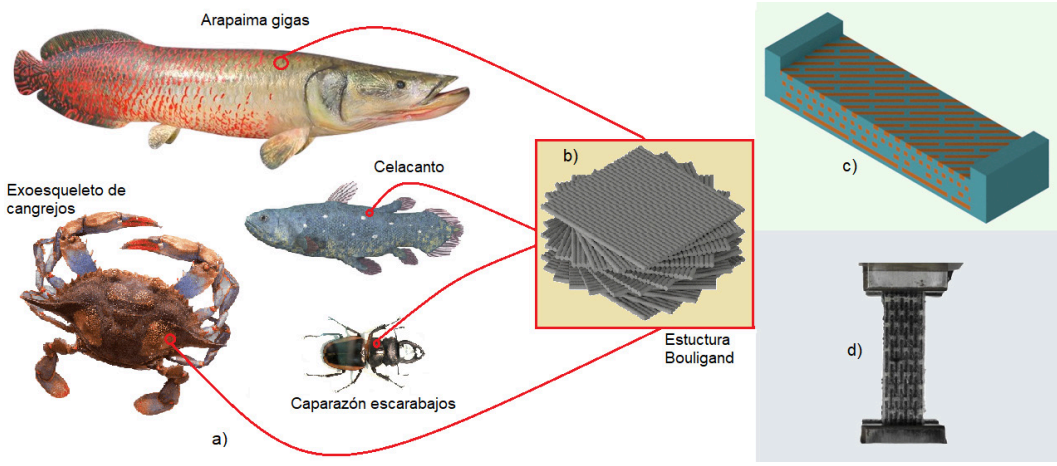

Figure 1. *a) Examples of animals with Bouligand type arrangement, b) Bouligand structure c) CAD sectional view of a Bouligand type test specimen with discontinuous fibers for a pitch angle of 45°* and d) Specimen assembly in the test machine

The printed composites were tested under quasi-static tensile loading at a strain rate of 2.77×10^{-4} s^{-1} in a universal testing machine equipped with a 30kN load cell. The mechanical characterization of the bulk materials was carried out according to ASTM D638 and an Epsilon axial extensometer. The loading direction was parallel to fibers of the first layer printed in the helicoid. Fiber orientation in subsequent layers is defined by the pitch angle of each specimen. The studied pitch angles were 30°, 45° and 60°.

Results and discussion

Materials used for the matrix and fibers were characterized. The Young's modulus values obtained were 16.67 *MPa* and 1303.4 *MPa* for the matix (TPU) and fibers (PLA), and Poisson's ratio values were 0.45 and 0.37 respectively.

The stress-strain relationships obtained for the angles of 30°, 45° and 60° can be seen in the figure 2, these angles were measured from the loading axis. For all the tested specimens, two zones were observed, zone 1 with a close to linear behavior, where the contribution in the resistance is given by the fibers and zone 2 with a plastic behavior, with a little strain hardening due to the realignment of the fibers, this result has already been observed and discussed by other authors [3], [14].

The strength of the test specimen in contrast to the bulk material used as the matrix and fibers is shown in Figure 2. A combination of the matrix and fiber strengths was obtained, and it was observed that the resistance of this Boluligand structural composite material

fabricated via additive manufacturing complies with the mechanics of materials [5][6]. For the angles analyzed, the pitch angle with the highest toughness was 45° and the one with the lowest toughness was 60°. Currently, there are many differences among researchers regarding the optimal pitch angle to improve energy absorption. Wenting et al, Sha Yin et al., Kaijin Wu et al., Yuan et al, and Jiahua et al., [15], reported optimum pitch angle values of 9.1°, 16°, 20°, 25°, 30° and 36° respectively. These variations could result from a variety of factors, including the materials employed, the composite scale (nano, micro and macro) and the sorts of testing carried out. The types of tests performed include fracture mechanics [14], impact resistance[16], and tensile strength [17].

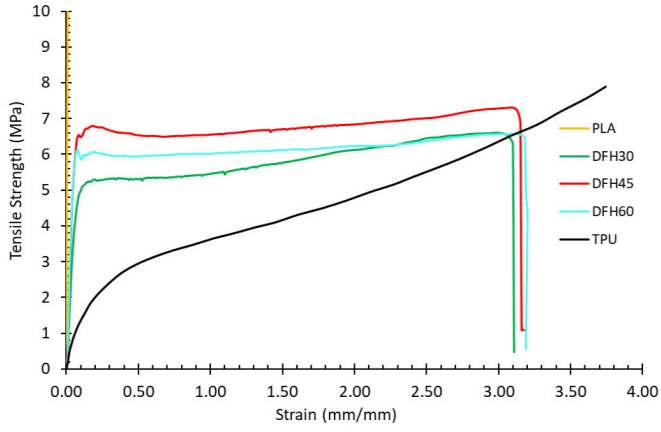

Figure 2. Stress comparison results for each pitch angle and matrix and fibers materials

Stiffness, tensile strength, and toughness according to pitch angle can be seen in figure 3. This graph shows the influence of the fibers angle on the behavior at zone 1 of a DFH material. An increase in stiffness of composite can be observed as the angle increases while the highest value for the strength was obtained for an angle of 45°. This can be explained by the fact that this angle is the one that evenly distributes the properties in both the direction of the applied load and perpendicular to it. Similar findings were reported by [18] for most of their tests. In specimens with a helical structure printed using the same FDM technology but with a polyamide and polypropylene matrix, the pitch angle was adjusted from 10° to 45°. Additionally, it was noted that the fluctuation of the plateau stress decreased as the angle increased.

Toughness is a mechanical property that is crucial when designing materials that must exhibit excellent penetration resistance and fracture toughness characteristics. In this study, toughness showed comparable values in all cases, but the greatest average values were reached by 45° pitch angle, and these values increased by around 10%. When the pitch angle between layers increase, the soft matrix material contributes more, which causes this increase. This finding may help designers to develop materials with superior mechanical properties.

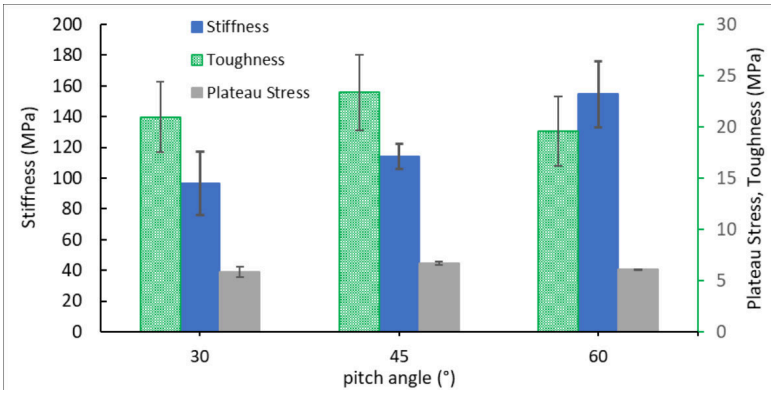

Figure 3. Stiffness, Plateau stress and Toughness vs pitch angle variation

Conclusions

For testing and research on two-material composites, additive manufacturing is a good alternative. Significant information for the design of bioinspired materials is provided by mechanical tests of these printed specimens.

The mechanical properties of composite materials manufactured via FDM are significantly influenced by the pitch angle between layers. By incorporating discontinuous fibers in a composite with a Bouligand structure, a composite material with two remarkable defined deformation zones was obtained. A plastic zone where the realignment and geometric rearrangement of the fibers produce a strain hardening effect and a nearly linear zone where the fibers offer the resistance. As a result, for custom - built material, it is possible to improve toughness, stiffness, and strength.

An increase of toughness was obtained by the 45° pitch angle, which also presented an increase in plateau stress and an improvement in resistance compared to fibers oriented at 30°. In applications where higher toughness values are needed, it is recommended to use 45° as helicoidal angle. As the pitch angle increased, an increase in the resistance of composite was obtained. The fiber contribution is stronger for smaller pitch angle values.

References

[1] T. Ikoma, H. Kobayashi, J. Tanaka, D. Walsh, and S. Mann, "Microstructure, mechanical, and biomimetic properties of fish scales from Pagrus major," *J. Struct. Biol.*, vol. 142, no. 3, pp. 327–333, Jun. 2003, doi: 10.1016/S1047-8477(03)00053-4.

[2] B. Zelazny and A. C. Neville, "Quantitative studies on fibril orientation in beetle endocuticle," *J. Insect Physiol.*, vol. 18, no. 11, pp. 2095–2121, Nov. 1972, doi: 10.1016/0022-1910(72)90243-0.

[3] D. Wang, A. Zaheri, B. Russell, H. Espinosa, and P. Zavattieri, "Fiber reorientation in hybrid helicoidal composites," *J. Mech. Behav. Biomed. Mater.*, vol. 110, no. June, p. 103914, 2020, doi: 10.1016/j.jmbbm.2020.103914.

[4] C. Hu, D. Ashok, D. R. Nisbet, and V. Gautam, "Bioinspired surface modification of orthopedic implants for bone tissue engineering," *Biomaterials*, vol. 219, no. June, p. 119366, 2019, doi: 10.1016/j.biomaterials.2019.119366.

[5] Y. Yang *et al.*, "Recent Progress in Biomimetic Additive Manufacturing Technology: From Materials to Functional Structures," *Adv. Mater.*, vol. 30, no. 36, p. 1706539, Sep. 2018, doi: 10.1002/ADMA.201706539.

[6] P.-Y. Chen, A. Y.-M. Lin, J. McKittrick, and M. A. Meyers, "Structure and mechanical properties of crab exoskeletons," *Acta Biomater.*, vol. 4, no. 3, pp. 587–596, May 2008, doi: 10.1016/j.actbio.2007.12.010.

[7] M. A. Meyers and A. M. Hodge, "Advances in Biological Materials and Biomaterials Science," 2008.

[8] M. A. Meyers, P.-Y. Chen, A. Y.-M. Lin, and Y. Seki, "Biological materials: Structure and mechanical properties," *Prog. Mater. Sci.*, vol. 53, no. 1, pp. 1–206, Jan. 2008, doi: 10.1016/j.pmatsci.2007.05.002.

[9] L. K. Grunenfelder *et al.*, "Bio-inspired impact-resistant composites.," *Acta Biomater.*, vol. 10, no. 9, pp. 3997–4008, Sep. 2014, doi: 10.1016/j.actbio.2014.03.022.

[10] J. R. C. Dizon, A. H. Espera, Q. Chen, and R. C. Advincula, "Mechanical characterization of 3D-printed polymers," *Addit. Manuf.*, vol. 20, pp. 44–67, Mar. 2018, doi: 10.1016/J.ADDMA.2017.12.002.

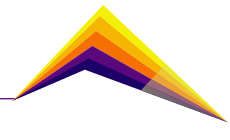

[11] W. Yang, H. Quan, M. A. Meyers, and R. O. Ritchie, “Arapaima Fish Scale: One of the Toughest Flexible Biological Materials,” *Matter*, vol. 1, no. 6, pp. 1557–1566, 2019, doi: 10.1016/j.matt.2019.09.014.

[12] F. Barthelat, Z. Yin, and M. J. Buehler, “Structure and mechanics of interfaces in biological materials,” *Nat. Rev. Mater.*, vol. 1, no. 16007, pp. 1–16, 2016, doi: 10.1038/natrevmats.2016.7.

[13] N. Suksangpanya, N. A. Yaraghi, R. B. Pipes, D. Kisailus, and P. Zavattieri, “Crack twisting and toughening strategies in Bouligand architectures,” *Int. J. Solids Struct.*, Jun. 2018, doi: 10.1016/J.IJSOLSTR.2018.06.004.

[14] K. Wu *et al.*, “Discontinuous fibrous Bouligand architecture enabling formidable fracture resistance with crack orientation insensitivity,” *Proc. Natl. Acad. Sci. U. S. A.*, vol. 27, no. 117, p. 8, 2020, doi: 10.1073/pnas.2000639117/-/DCSupplemental.

[15] W. Ouyang, B. Gong, H. Wang, F. Scarpa, B. Su, and H. X. Peng, “Identifying optimal rotating pitch angles in composites with Bouligand structure,” *Compos. Commun.*, vol. 23, p. 100602, Feb. 2021, doi: 10.1016/j.coco.2020.100602.

[16] Y. Yuan *et al.*, “Manipulating impact damage modes in composite laminates by helical pitch angle and ply thickness,” *Eng. Fract. Mech.*, vol. 265, no. December 2021, p. 108383, 2022, doi: 10.1016/j.engfracmech.2022.108383.

[17] Z.-M. Huang, W.-J. Guo, -B Huang, H, and C. C. Zhang, “Tensile Strength Prediction of Short Fiber Reinforced Composites,” *Materials (Basel).*, vol. 14, no. 2708, pp. 1–22, 2021, doi: 10.3390/ma14112708.

[18] S. Yin *et al.*, “Tough Nature-Inspired Helicoidal Composites with Printing-Induced Voids,” *Cell Reports Phys. Sci.*, vol. 1, no. 7, p. 100109, Jul. 2020, doi: 10.1016/j.xcrp.2020.100109.

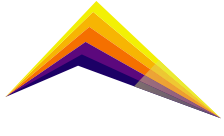

Design and Construction of a Low-Cost Test Bench for Thrust Vector Control Systems in Experimental Rockets

Sebastian L. Serna[1] *E-mail: sebastian.leons@udea.edu.co*
Jaider J. Alzate[1] *E-mail: jaider.alzate@udea.edu.co*
Sergio A. Gómez[1] *E-mail: sergio.gomezv@udea.edu.co*
Felipe A. Obando[2] *E-mail: felipe.obando@udea.edu.co*

[1]Bachelor student, Ingeniería Aeroespacial, Facultad de Ingeniería, Universidad de Antioquia, Km 6 via Rionegro-La Ceja, El Carmen de Viboral, Antioquia, Colombia
[2]Departamento de Ingeniería Mecánica, Facultad de Ingeniería, Universidad de Antioquia, Calle 70, No. 52-21, Medellín, Antioquia, Colombia

Abstract

Rocket attitude control and stabilization systems require extensive testing before implementation. New control techniques and algorithms can be simulated from mathematical rocket models. However, for their application in real devices it is necessary to determine all the dynamics of rocket operation, although this involves considerable risk and economic investment. Given this, the development of a two-degree-of-freedom test bench for the characterization of low-cost experimental rocket attitude control systems, in which thrust vector control (TVC) is implemented to modify the rocket attitude, is described in this paper. The structural components of the bench were fabricated by fused deposition 3D printing. a pneumatic propulsion system was used to simulate the rocket thruster. Two servo motors were used to change the position of the rocket nozzle, modifying the pitch and yaw angle of the rocket. An accelerometer and a gyroscope were used as an inertial measurement unit (IMU) to determine the attitude of the rocket. The control system of the bench was implemented in the ESP32 microprocessor module, which calculates the attitude of the rocket

Correspondent author

and modifies the position of the servo motors according to the desired conditions. This, in turn, sends the information wirelessly via Wi-Fi to a user interface for monitoring the bench, the interface was developed using the open-source platform Node-RED, using the MQTT communication protocol through the open-source message broker Eclipse Mosquitto, which are one of the most used tools in the development of Internet of Things (IoT) devices. The initial tests of the bench operation, implementing a PID feedback control, demonstrated that this is a viable option for the experimentation of rocket attitude control algorithms using the vector thrust control technique. This development proves to be a necessary component to encourage experiential learning in engineering programs.

Key words: Thrust Vector Control, Experimental Rockets Control, Low-Cost Test Bench, Internet of Things.

Introduction

With the development of rocket technology, the efficiency of these vehicles has increased considerably. One of the systems that have contributed the most to the efficiency and proper functioning of rockets is called the Thrust Vectoring System (TVS), which consists of obtaining control over the direction of the exit gases that produce thrust, generating moments that allow, from increasing the stability of the flying rocket to the controlled landing of stages that used to be lost at sea or its recovery that represented a significant effort in all areas of the rocket [1]. The developments of TVS test benches are focused on full-size engines test [2] and the research about TVC applied to amateur or scale rockets is limited. About this topic, Miloš et al. developed a novel 6-degree-of-freedom TVC test bench based on the 6-degree-of-freedom parallel manipulator to measure the spatial distribution of the reaction forces of the rocket engine and concluded that it is not necessary to have a test bench with more than two-degree of freedom [3]; and recently, Moraes et al. developed a vertical static test bench for amateur rocket engines to measure the thrust of the propellant, without including TVS. The present article fills this lack of knowledge about Thrust Vectoring Control (TVC) System test benches [4]. Allowing to develop, improve and test innovative control strategies and algorithms in academic and research environments.

Materials and Methods

Implementing additive manufacturing (3D printing), low-cost materials such as wood and commercial-off-the-shelf (COTS) components [5], a test bench was manufactured in which the rocket is in its launch configuration, i.e., vertically, supported on a gyroscope that allows it to have two degrees of freedom on the horizontal plane, being able to perform pitch and yaw movements (Figure 1a and Figure *1b*) allowing to control the attitude of the rocket [6]. The TVC system chosen is based on a gimbal system [7] (Figure 2), where external and internal gimbal space is left for the servomotors, which will give movement by arms in the perpendicular axes to the inner tube that simulated the nozzle of the engine rocket. In the final part of the inner tube, a coupling is designed to fix internally a hose by a quick coupling as shown in Figure *3*, to connect a pneumatic system that provides thrust, like the nozzle of a real engine. The the parts design of weremade in Autodesk Inventor software [8].

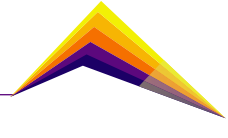

(a) Lateral view.

(b) Isometric view.

Figure 1. Gyroscope mechanism assembled on main structure.

Figure 2. TVC system mechanism.

Figure 3. Final exhaust gas coupling.

An electronics module altogether complements the test bench. The onboard computer oversees obtaining acceleration data, controlling the system through the TVC, and sending the data to the ground base to visualize the behavior quantitatively. The ESP32 Devkit V1 development board was chosen due to its low cost, high capacity compared to the other boards investigated, and the advantage of having an integrated Wi-Fi communication module. The pitch and yaw angles were determined by an IMU, which measures the accelerations in the three main axes. The accelerometer chosen was the IMU GY-89 due to its programming simplicity and wide bibliography it has. A PCB was designed in Autodesk EAGLE software [9] and manufactured using a CNC router to integrate the electronic components (Figure 4). With the integration of these components, the final cost of the test bench was around 50 USD, including manufacturing and materials, as described in Table 1. This cost is below other developed prototypes that exceed 500 USD [10].

Table 1. Cost analysis.

System	Cost (USD)
Main structure	3
Gyroscope mechanism	3.5
TVS	7.5
Pneumatic system	20
Onboard computer and communications	16
Total	~50 USD

Based on the ESP32 Devkit V1 development board, a control algorithm based on this board was implemented, and at the same time, its integrated Wi-Fi module was programmed to see the data collected and calculated by the system. A flowchart of the control algorithm operation is presented in Figure 5, which was programmed in the Arduino IDE. After determining the yaw and pitch angles, a set-point is established to which the rocket will be maintained, thus,

by means of a PID control for the TVS movement, and the actuation of the pneumatic system within a range of pitch and yaw angles, the attitude of the rocket is controlled [6].

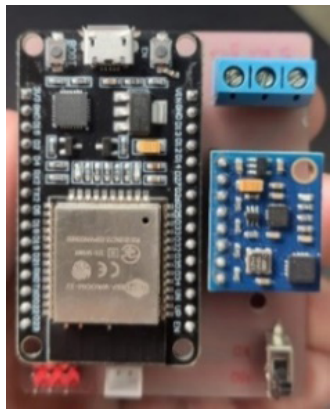

(a) Top view.

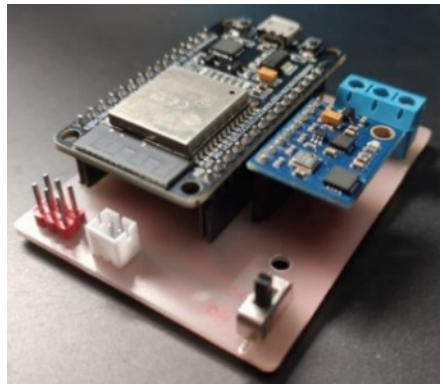

(b) Isometric view.

Figure 4. Final onboard computer.

A graphical interface was created using the open—source software *NodeRED* to visualize the data measured by the test bench. The wireless communication between the developed interface and the ESP32 was made through the MQTT protocol. For this, a *message broker* was implemented in the computer using the open-source software *Mosquitto*. The interface designed to check and store the data delivered by the results can be seen in Figure 6.

Results and Analysis

After having described the systems that make up the test bench, the results of all the integrated systems are shown in Figure 7. A step response was tested to see the performance of the PID controller and the integrity of the bench. The test bench was connected to the compressor and the power outlet. The compressor was turned on and the working pressure was set to 50 PSI. After the desired pressure was achieved, the electronics were turned on using the built-in switch. The PID response to a step change in the pitch angle is shown in Figure 8. The PID control changes the position of the pitch angle servomotor until the pitch angle of the rocket reaches the desired value. A delayed response from the PID control response was observed for the PID parameters used. This indicates that a review of the sampling time and computing new PID gains should be performed.

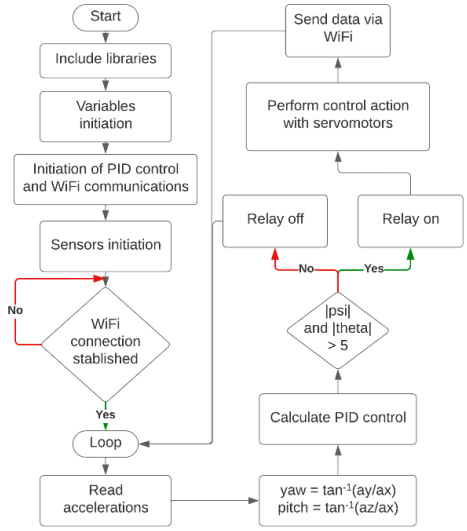

Figure 5. Flowchart of the implemented control algorithm.

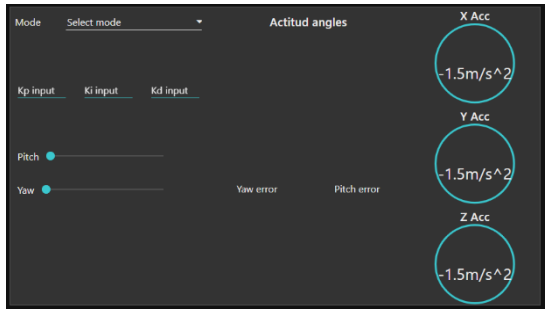

Figure 6. User interface in NodeRED.

Figure 7. Test bench

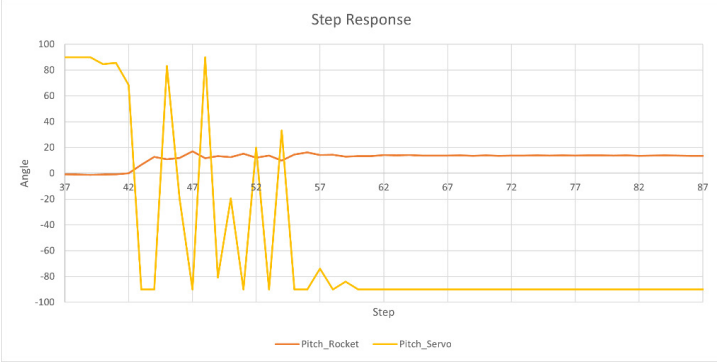

Figure 8. PID controller step response.

During testing, the base did not show any sway or decay due to structural stresses. Also, the gyroscope, electronic module, and TVC moved freely without obstructions. The onboard computer measured the accelerations and calculated the Euler angles. Also, the library implemented for the PID control sent the appropriate signals to the servomotors within the set values, as well as the actuation of the pneumatic system by the relay.

Conclusions

This type of system supplies the possibility of putting into practice much of the knowledge acquired previously and opens the door to new control practices and process optimized, as in the case presented, the stability of rockets by PID controllers. This type of test bench also allows the analysis of other types of control systems, without the need to build a complete rocket and launch it to obtain data on its operation, which entails greater investments just to choose components or working systems.

It was proved that it is possible to integrate systems with COTS-type components for the construction of test benches for rocket attitude control systems, reducing the costs that a more robust test bench could have. This was also proved through different manufacturing techniques such as CNC machining of PCBs and 3D printing, components that are readily available today.

Although the test bench is still under construction and constant improvements, this work allows seeing the wide potential of this type of practices in terms of strengthening new topics and learning related to measurement, instrumentation, and process control.

References

[1] O. B. G. P. Sutton, Rocket Propulsion Elements.

[2] e. a. Ahmel Ünal, "Design and Implementation of a Thrust Vector Control (TVC) Test System," *Journal of Polytechnic ·,* 2018.

[3] e. a. Milos Predrag, "A NOVEL 6 DOF THRUST VECTOR CONTROL TEST STAND," *Technical Gazette,* 2015.

[4] e. a. Moraes Soares Douglas, "Development of a vertical static test bench for amateur," *International Journal of Advanced Scientific and Technical Research,* 2018.

[5] I. Archive, "2.000 Scope of part," January 2017. [Online]. Available: https://web.archive.org/web/20170130041945/https://www.acquisition.gov/far/html/Subpart%202_1.html.

[6] A. M., PID Control. Control Systems, Robotics, and Automation..

[7] J. Banard, "BPS Space, TVC," 2021. [Online]. Available: https://bps.space/tvc.

[8] Autodesk, "Inventor," 2021. [Online]. Available: www.autodesk.com.sg/products/inventor/overview.

[9] Autodesk, "EAGLE," 2021. [Online]. Available: autodesk.com/products/eagle.

[10] R. e. a. Linsen, "Optimal Thrust Vector Control of an Electric Small-Scale Rocket Prototype," Switzerland, 2022.

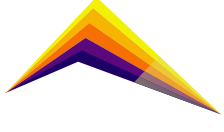

Prototype of a 3D indoor anemometer based on MEMS thermopile sensors

Elizabeth Ospina-Rojas[1] E-mail: elizabethospina251455@correo.itm.edu.co
Juan Sebastián Botero-Valencia[1] E-mail: juanbotero@itm.edu.co

[1] Instituto Tecnológico Metropolitano, Medellín, Colombia

Abstract

The behavior of air is characterized by its speed and direction. Wind speed measurement is heavily used in climate analysis activities, meteorological research, infrastructure construction, wind power generation, agriculture, and ventilation systems, among others. Monitoring wind behavior is essential for indoor air quality control as wind acts as a carrier of gases, chemicals, and pollution. In recent years, researchers have focused on the development of devices to measure wind speed and direction, mainly in two dimensions of space. The most common instrument for measuring wind speed is the cup anemometer, whose measurement method is based on a mechanical system that rotates at the same speed as the wind; this system has the disadvantage of mechanical wear over time, limitations in the speed of rotation, Overspeed, and is not designed for indoor use. Cup anemometers do not usually measure wind direction and those that do are limited to two dimensions. In this work, an anemometer based on an array of three hot-wire sensors is proposed, this device measures wind speed and direction in three dimensions. The hot-wire sensors used in this work are part of the microelectromechanical systems (MEMS), they are based on a metal filament that is cooled by the airflow in the environment, thus, the variation in the temperature of the filament is related to the wind speed. To characterize the wind in three dimensions and to know the direction of the flow, an arrangement of three sensors

Correspondent author

is proposed, one pointing to the x-axis, one pointing to the y-axis, and the last one pointing to the z-axis direction, all sensors at 90° to each other. This anemometer measures wind speed in the range of 0 and 7.2 m/s, the wind direction measurement range is 90° for each axis. IoT technology is added to visualize the data via the internet. As wind behavior influences air quality, the main application of this anemometer is in indoor air control and monitoring, this device can also be used to evaluate the performance of ventilation, heating, and air conditioning systems.

Keywords: Anemometer, Internet of Things (IoT), Wind speed, Micro Electro Mechanicals Systems (MEMS).

Introduction

Anemometers are meteorological devices used to measure wind speed and, in some cases, wind direction. Wind measurement has been used mainly to predict weather conditions, but also in the areas of engineering, health, agriculture, wind power generation, and others.

These devices are widely used to monitor the air in wind power generation fields to increase energy efficiency and make the best use of the wind source [1]. Wind speed and direction must be constantly monitored to improve the safety of sea and air transport [2]. In autonomous maritime navigation, anemometers are used to monitor weather conditions and make decisions about navigation routes [3]. As well as in maritime navigation, in the world of aviation anemometers are used to know if the wind conditions are suitable for the landing or take-off of vehicles and thus avoid fatal accidents [4]. In countries such as China, anemometers are used to assess the load generated by strong winds on structures such as transmission towers, wind turbines, and bridges [5]. The measurement of wind speed is used in the construction field to determine whether a construction site is safe due to the impact of wind on infrastructure.

There are different kinds of anemometers, mechanical and electronic anemometers, and electronic anemometers including ultrasonic and thermal anemometers [6]. Mechanical anemometers are used to measure high wind speeds but have some disadvantages such as Overspeed, mechanical limitations, or reading delays due to inertia [7]. Electronic anemometers are used to measure low wind speeds, so their applications are focused on indoor spaces. The wind is the medium through which a gas flows from its origin to a point, odor detecting robots use anemometers to determine the possible source of odor produced

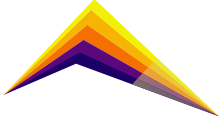

by gas in indoor spaces [8], this application focuses on the detection of gas sources that may be toxic to human health. Wind not only transports gases but also microparticles and pollution, wind conditions in an enclosed space can affect human health and comfort, for this reason, anemometers are used to monitor indoor wind conditions and to control refrigeration and air conditioning systems [9]. Indoor wind measurement applications are mainly focused on the comfort, care, and health of people, so the development of indoor anemometers has been the focus of researchers in recent years. Although electronic anemometers are the best tool for monitoring indoor wind, most of them eliminate the measurement of vertical wind movement and only measure wind speed and direction in two dimensions. Characterizing the wind in three dimensions allows us to determine wind flow conditions more accurately and thus improve indoor air quality and temperature monitoring systems.

In this work, we propose an anemometer to measure wind speed and direction in three dimensions. This anemometer is based on the arrangement of three unidirectional flow sensors that measure wind speeds between 0 and 7.2m/s. IoT technology is used to send and read the data from the cloud.

Materials and Methods

The operation of thermal flow sensors is based on capturing the temperature change of a heater and relating that change to the velocity of the air that cools the system [10]. In this work the SparkFun FS3000 flow sensor was used (Figure 1a), this sensor is based on the hot wire principle where a metal filament is heated to a constant temperature, the cooling of the hot wire is related to the flow velocity. The FS3000 can measure wind speed unidirectionally, reaches a measurement range of 0 to 7.2m/s, and is connected via I2C to the MCU.

To measure the wind in three dimensions and to obtain the direction, we propose a set of three FS3000 sensors. The sensors are positioned perpendicular to each other and are labeled according to their measurement axis (Figure 1b). One sensor points to the positive X-axis, the other points to the positive Y-axis, and the last one to the positive Z-axis, in this way the wind speed can be measured in three dimensions. Since wind speed is a vector, by obtaining the three components in which the flow moves and using vector calculation methods, the angle at which the predominant flow is moving can be obtained.

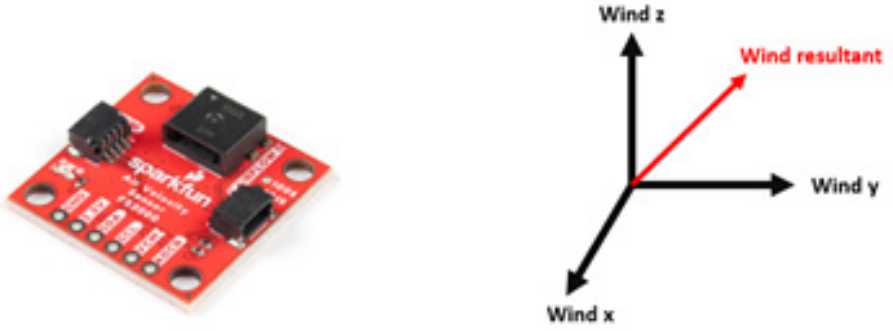

(a) (b)

Figure 1.a. SparkFun Air Velocity Sensor FS3000, 1b. Wind flow components.

The structure supporting the sensors was designed in 3D using Inventor and printed with polylactic acid (PLA). The 3D anemometer design is divided into different pieces for easy assembly. The complete anemometer is an assembly of 3D-printed parts. Each of the three sensors used is mounted on a rectangular piece, in addition, each sensor is covered with another piece that functions as a protective cover called *"sensor cap".* The assembly resembles a cube, it has a top, a front, and a side face. On the front face is placed the sensor pointing towards the y-axis, this piece is called *"y-axis support"*. On the front face is located the sensor pointing towards the x-axis, this part is called *"x-axis support".* Finally, on the side face is located the sensor pointing towards the z-axis, this part is called *"z-axis support".* All sensors are pointing in the positive direction of the Cartesian plane and form an angle of 90° to each other.

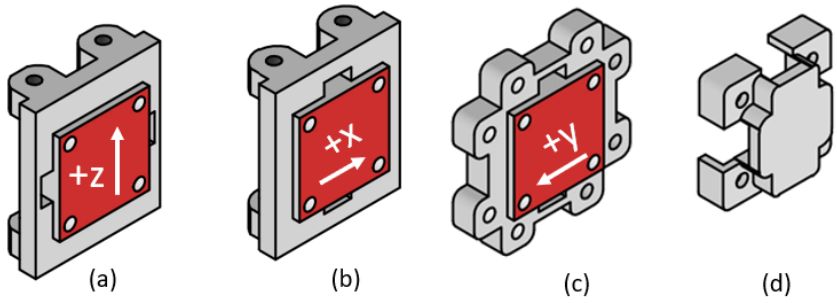

Figure 2a. Z-axis support, 2b. X-axis support, 2c. Y-axis support, 2d. sensor cap.

The X-axis and Z-axis support pieces hold the sensors pointing towards the X and Z axis respectively, both pieces are 3.7 cm x 4.3 cm in size. The x-axis support piece is the front face of the assembly, the z-axis support piece is the side face of the assembly. Both pieces are attached to the y-axis support piece. The sensor cap piece is designed to protect the FS3000 sensors from dust or humidity in the environment, this piece has openings on the sides to allow airflow through the sensor without affecting the measurement.

Finally, the design of a lightweight and compact anemometer is shown. The complete structure has a size of 6 cm x 6 cm, all parts are easy to assemble and are fixed with M3 screws. Supports at the bottom were added to give height to the anemometer.

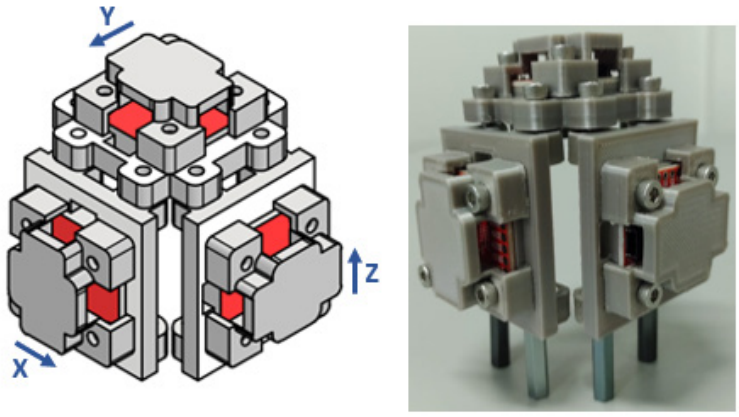

Figure 3. Anemometer assembly.

To store the anemometer measurements, IoT technology was implemented. The Ubidots IoT cloud platform was used in this project. To send the data, the MQTT protocol was used.

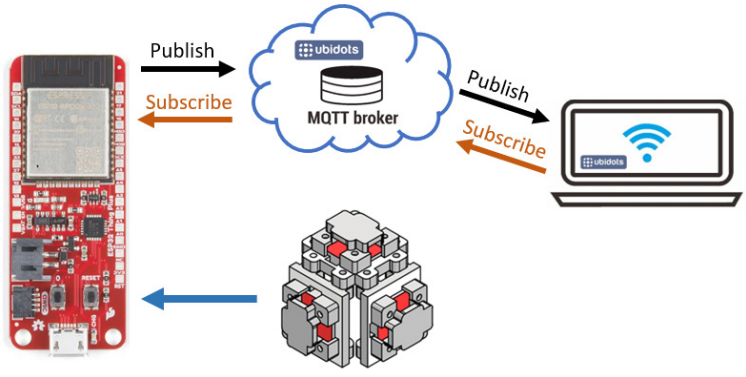

Figure 4. Sending data to the cloud.

Results and analysis

Experimental tests were performed with different wind speeds in different directions. The anemometer was tested with 2m/s and 3m/s winds parallel to the x-axis, parallel to the y-axis, and parallel to the z-axis. To correct the wind speed measurements and minimize errors, simple linear regression techniques were applied to approximate the data measured by the sensors to the reference wind speeds of 2m/s and 3m/s. The linear equation obtained for the wind speed is (1) where x represents the resultant speed measured from the three sensors and V is the corrected speed. Table 1 summarizes the results obtained. The wind speeds measured by the anemometer in different directions and the error for each measurement are shown.

$$V = 0.7523 * x + 0.1529 \quad (1)$$

Table 1. Experimental results with 2m/s and 3m/s winds.

Wind velocity (m/s)	Wind direction (°)	Wind speed (m/s)	X-angle (°)	Y-angle (°)	Z-angle (°)	Error (m/s)
2	Parallel to x	2.1164	0.51	90	89.50	0.1164
	Parallel to y	2.0036	90	0.5	89.49	0.0036
	Parallel to z	1.9058	75.88	86.87	21.16	0.0942
3	Parallel to x	3.0267	9.9	90	80.09	0.0267
	Parallel to y	2.9515	90	1.66	88.33	0.0485
	Parallel to z	2.9966	87.91	89.53	2.51	0.0034

This anemometer can accurately measure wind speed and direction over a range of 90° for each plane axis, a maximum error of 0.1164m/s was obtained. Wind against the direction of the sensors cannot be measured. The accuracy of the wind speed measurement is good; however, it is recommended to add more sensors to extend the measuring range and eliminate blind spots of the anemometer. Due to the electronic configuration, this anemometer can only be used indoors. Exposing this anemometer outdoors may cause damage to the sensors.

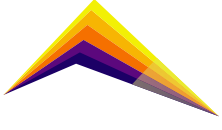

Conclusions

A 3D anemometer based on three hot-wire flow sensor arrays is presented. As the sensors used can only measure the flow in one direction, the device only measures the wind speed in a range of 90° for each axis. This anemometer detects winds in a range of 90° with a maximum error of 0.1164 m/s, its applications are focused on indoor air monitoring. The IoT technology implemented in this anemometer allows data to be accessed from the cloud. In future work, it is proposed to extend the measurement range.

Acknowledgment

This study was supported by the Sistemas de Control y Robótica (GSCR) Group COL0123701, at the Sistemas de Control y Robótica Laboratory, attached to the Instituto Tecnológico Metropolitano, the program "Sistemas inteligentes para el monitoreo de cultivos agricolas permanentes y transitorios" 70107, the project "IoT para el monitoreo de variables agroclimáticas en cultivos agrícolas permanentes y transitorios" 70706.

References

[1] M. Güçyetmez, S. Keser, and Ş. E. Hayber, "Wind speed measurement with a low-cost polymer optical fiber anemometer based on Fresnel reflection," *Sens Actuators A Phys*, vol. 339, Jun. 2022, DOI: 10.1016/j.sna.2022.113509.

[2] Z. Chen, Y. Wang, and L. Zhou, "Predicting weather-induced delays of high-speed rail and aviation in China," *Transp Policy (Oxf)*, vol. 101, pp. 1–13, Feb. 2021, DOI: 10.1016/j.tranpol.2020.11.008.

[3] D. Fernandes, L. Gomes, and A. Costa, "Wind speed and direction measurement based on time of flight ultrasonic anemometer," in *IEEE International Symposium on Industrial Electronics*, Aug. 2017, pp. 1417–1422. DOI: 10.1109/ISIE.2017.8001453.

[4] A. O. Connor and D. Kearney, "Evaluate the effect of turbulence on aircraft during landing and take-off phases," *International Journal of Aviation, Aeronautics, and Aerospace*, vol. 5, no. 4, 2018, DOI: 10.15394/ijaaa.2018.1284.

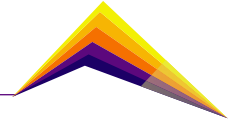

[5] G. Huang, Y. Jiang, L. Peng, G. Solari, H. Liao, and M. Li, "Characteristics of intense winds in mountain area based on field measurement: Focusing on thunderstorm winds," *Journal of Wind Engineering and Industrial Aerodynamics*, vol. 190, pp. 166–182, Jul. 2019, DOI: 10.1016/j.jweia.2019.04.020.

[6] Yongqing Bai, Xiangyu Meng, Haiyan Guo, Dechuan Liu, Yucjun Jia, and Peng Cuf, "Design and validation of an adaptive low-power detection algorithm for three-cup anemometer," 2021.

[7] Á. Ramos-Cenzano, E. López-Núñez, D. Alfonso-Corcuera, M. Ogueta-Gutiérrez, and S. Pindado, "On cup anemometer performance at high altitude above ground," *Flow Measurement and Instrumentation*, vol. 79, Jun. 2021, doi: 10.1016/j.flowmeasinst.2021.101956.

[8] H. Widyantara, M. Rivai, and D. Purwanto, "Wind direction sensor based on thermal anemometer for olfactory mobile robot," *Indonesian Journal of Electrical Engineering and Computer Science*, vol. 13, no. 2, pp. 475–484, Feb. 2019, DOI: 10.11591/ijeecs.v13.i2.pp475-484.

[9] E. Arens *et al.*, "Measuring 3D indoor air velocity via an inexpensive low-power ultrasonic anemometer," *Energy Build*, vol. 211, p. 109805, 2020, DOI: 10.1016/j.enbuild.2020.109805.

[10] Bo Han, Fu-dong Zhou, Mei Chen, Ke Lu, Xu Wang, and Ya-nan Zhang, "Design of highly-sensitive fiber thermal anemometer based on reflective photonic crystal fiber loop mirror".

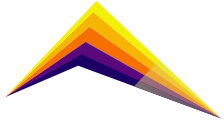

Design and improvement of a wireless energy harvesting rectenna operating at 2.4 GHz

Gustavo Urrea-Castaño — E-mail: gustavourrea314860@correo.itm.edu.co
Sebastian Montoya-Villada — E-mail: sebastianmontoya@itm.edu.co
Juan Botero-Valencia — E-mail: juanbotero@itm.edu.co
Erick Reyes-Vera — E-mail: erickreyes@itm.edu.co

1, Instituto Tecnológico Metropolitano, Medellín, Colombia

Abstract

The growth of information and communication technologies has recently extended to the Internet of Things (IoT). This has favored the research, monitoring, and control of processes improving their operational and productive capacity. As a result, electronic equipment requires energy consumption controls because wireless and electronic sensors must be installed outdoors in most cases, and have enough energy charge which allows their continuous operations. That is why energy harvesting has received a lot of attention in recent years since electromagnetic energy is now easily generated from several sources. Furthermore, they enable the provision of electricity wirelessly, i.e. the construction of wiring-free power distribution systems. As a result, the design of electromagnetic energy collectors such as rectenna (antenna and rectifier) systems is critical in the capture and conversion of this energy for use in sensing nodes. In this study, a rectenna was designed and optimized to operate at 2.4 GHz. The computational analysis and optimization of the suggested structure were carried out using the program CST STUDIO. The rectifier system consists of an impedance-matching circuit, an RF-to-DC rectifier, and an output load that transforms ambient RF energy into DC voltage capable of powering low-power devices. Moreover, the rectifier size was optimized to have a total

Correspondent author

size of 6 cm x 2.7 cm. On the other hand, a directive microstrip Yagi antenna with a gain of 7.8 dBi and a bandwidth of 220 MHz was used to capture the energy in combination with the rectifier system from a specific direction. Numerical results demonstrated that the overall system exhibited an efficiency of 76.56% with 6.58 V of the output voltage, for an input power of 21 dBm and a load of 1 kΩ. In addition, other characteristics and criteria were also analyzed. This demonstrates that the suggested rectenna system has good electrical performance and may be used to capture electromagnetic energy to power wireless sensor networks or other electronic devices.

Key words: Rectenna, Internet of Things (IoT), Energy harvesting, Wireless Power Transfer (WPT).

Introduction

The number of wireless sensing networks (WSN) has recently increased, owing mostly to the introduction of new technologies such as the internet of things (IoT), and 5G networks [1],[2]. Because electronic sensors must be deployed outside in most circumstances, energy harvesting systems to gather energy from the environment and deliver power to low-energy electronic devices or replenish their batteries have become important. Thermal energy, wind energy, solar energy, and electromagnetic energy (EM) have all been investigated as energy harvesting systems [3]. This last option has received a lot of attention in recent years since EM energy is ubiquitous in our surroundings, due to the availability of EM signals accessible from many sources like mobile stations, Wi-Fi signals, or television antennas [3], [4]. The rectenna is essential for this form of wireless power transfer. A rectenna is a device that combines a rectifying circuit and an antenna. The antenna receives electromagnetic power, which is converted to electric power by the rectifying circuit.

A rectenna's performance is determined by several variables. The radiation efficiency, gain, and beamwidth of the antenna impact the power received by the rectenna from an incident electromagnetic wave [3], [5]. A broad beamwidth is especially important when harvesting ambient radiation or powering mobile wearable receivers when angular alignment between transmitter and receiver is difficult. Furthermore, a compact size is generally desirable for unobtrusive IoT systems [2]. On the other hand, the RF to DC Power Conversion Efficiency (PCE) of the rectifier is governed by the source and load impedances of the rectenna and it is restricted at low power levels by the diode's forward voltage. In fact, several rectenna systems have recently been proposed, in which these problems have been addressed.

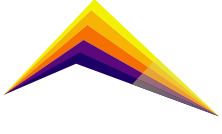

However, the main limitations of these systems are the PCE and the distance that they can reach [3], [6]–[8].

In this work, we propose to design and improve a rectenna system to capture EM radiation at the 2.4 GHz ISM band. When compared to prior research, the suggested has a high energy conversion efficiency. Likewise, the current study improves both the antenna and the signal rectification system, whereas most previous studies employ commercial antennas and solely focus on rectifier improvements. First, a 2.4 GHz-resonant directive Yagi microstrip antenna was designed and optimized. Second, a microwave circuit was designed to convert the alternating energy to a direct current signal, allowing the gathered energy to be used to power IoT devices efficiently. In fact, we achieve an efficiency of more than 75%.

Methodology

A method for creating a rectenna that can absorb electromagnetic energy and convert it to electrical energy is proposed and numerically analyzed in this work. This system is made up of two key components: an antenna that collects energy and a rectifier that converts the alternating current signal into a direct current signal that may be utilized to power electronic components. Figure 1 depicts the fundamental scheme of this system. First, the antenna was designed to operate at 2.4 GHz because there are many devices and technologies in this band, thus, it is more likely to pick up energy. To carry out the design of this antenna, CST STUDIO 2021 was used. Then, a microstrip Yagi antenna was implemented whose geometric shape is illustrated in Figure 2 (top and bottom layers). The material used for the design of this antenna was FR4, which has a dielectric permittivity of 4.3, a tangent loss of 0.025 and a thickness of 1.6 mm. This antenna has 7 directors to increase the directivity of the antenna, an input impedance of 50 Ω, the total width (W) and the total length (L) are 70 mm and 76 mm respectively, which offer a compact solution. The other dimensions of the antenna are summarized in Table 1.

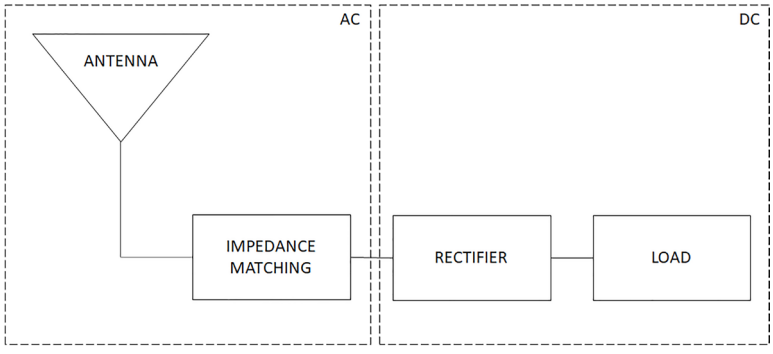

Figure 1. Block diagram of the proposed rectenna system.

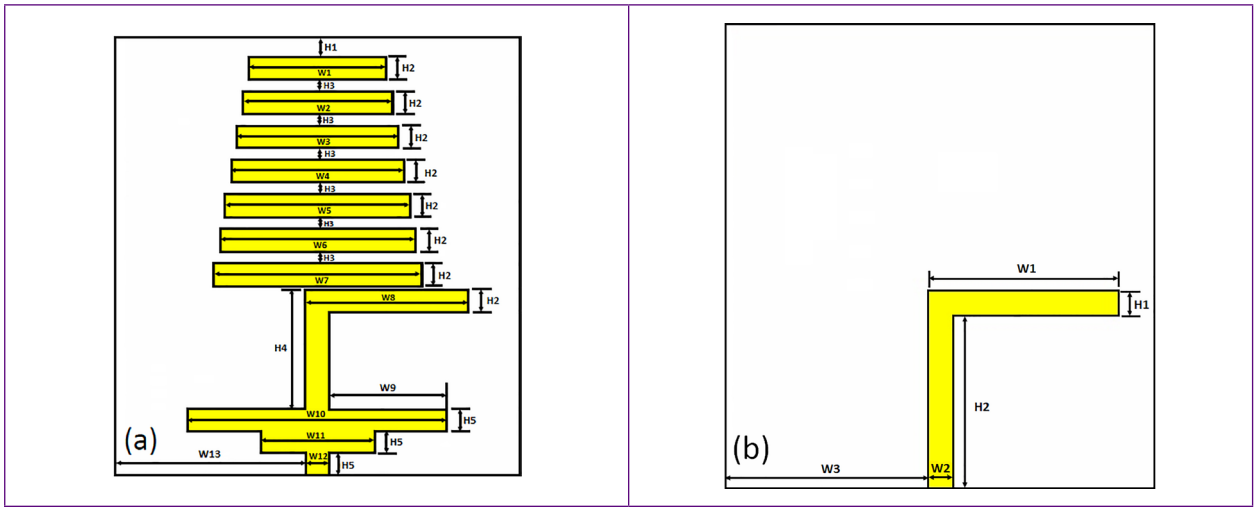

Figure 2. Diagram of the structure of the Yagi microstrip antenna used.
(a) Front view. (b) Bottom view.

The rectifier was simulated using Advance Design System (ADS) and it has three components: a matching impedance, a DC converter, and a resistive load. The first one was designed to have an-input impedance of 50 Ω at 2.4 GHz to guarantee a good match with the microstrip Yagi antenna. Moreover, the RF to DC converter was established by means of a Cockcroft-Walton voltage doubler rectifier circuit. Thus, two Schottky diodes HSMS-2860 were combined with an array of capacitors of 150 pf. Finally, due to the non-linearity of the diodes, it is preferable to run a load resistance parallel to the condenser of 500 pf to perform a low-pass filter. At that point, the load will vary to maximize the RMS voltage of departure. Figure 3 depicts the schematic of the correction system.

Table 1. Yagi microstrip antenna dimensions.

Parameter	Value (mm)	Parameter	Value (mm)	Parameter	Value (mm)
W1	24	W10	45	H3	2
W2	26	W11	20	H4	21
W3	28	W12	4	H5	3.75
W4	30	W13	33	H1b	4
W5	32	W1b	31	H2b	28.25
W6	34	W2b	4	L	76
W7	36	W3b	33	W	70
W8	28.1	H1	3.25	Z	1.6
W9	20.5	H2	4	t	0.035

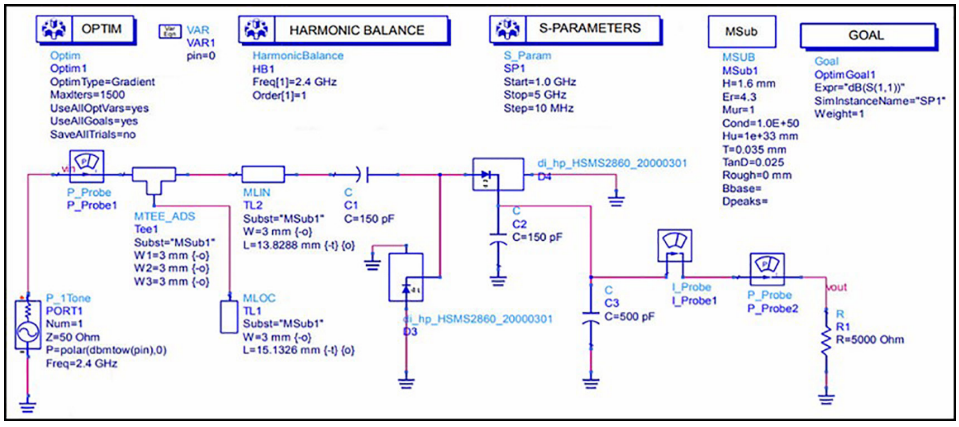

Figure 3. Advance Design System (ADS) schematic of the proposed rectifier design.

Results and analysis

The Yagi antenna to test the performance of the rectenna system has a directive radiation pattern, a gain of 7.86 dBi at 2.4 GHz, a bandwidth of 220.2 MHz (from 2.285 to 2.505 GHz), and a radiation efficiency of 99.97 %. The S11 parameter of the rectifier input impedance matching is presented in Figure 4(a). Thus, it is possible to validate that the rectifier is coupled with an impedance of 50Ω at a frequency of 2.4 GHz. On the other hand, the performance of the rectifier was examined to demonstrate its ability to convert EM energy into electrical current. First, the output voltage was evaluated as a function of the input power as depicted in Figure 4(a). The results show that using the proposed RF circuit (see Figure 3) yields a maximum voltage of departure when the power at the circuit's input power is equal to 21 dBm. As a result of this entry power, the system's response stabilizes at 6.58 VDC, and so the optimal operating zone is reached. Note that this voltage can be used to power a wide variety of electronic components.

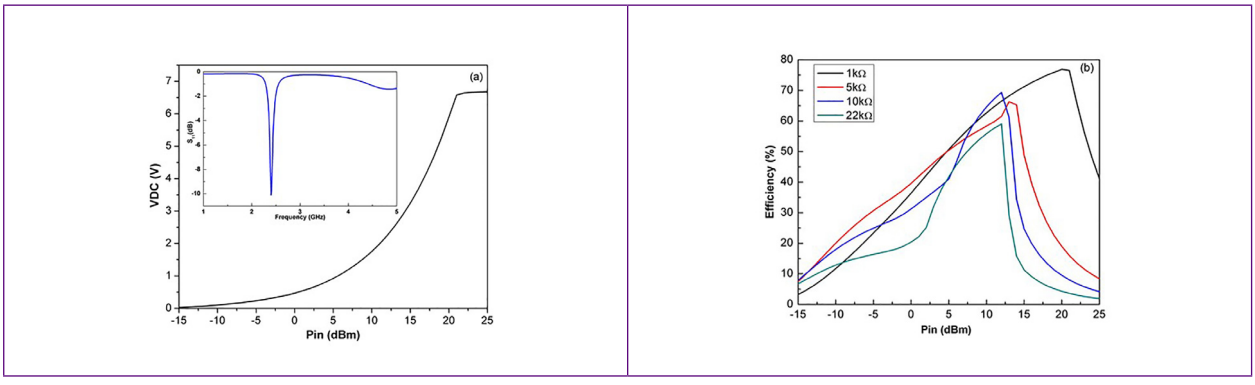

Figure 4. (a) Simulated output voltage of rectenna system with 1 kΩ load at 2.4 GHz. Inset in Figure shows the S11 parameter of the Yagi antenna, which was employed to test the performance of the entire rectenna. (b) Simulated energy radiation efficiency using different loads.

Finally, simulated conversion efficiency as a function of input power for 1 kΩ, 5 kΩ, 10 kΩ, and 22 kΩ are depicted in Figure 4(b) (these loads were selected since they are the most commonly employed in WPT systems). It is clear from the results that the efficiency is low at low input power levels and increases with the increase of RF input signal power. Below 50% conversion efficiency is observed for 5 dBm input power. On the other hand, the peak conversion efficiency is affected by the load and the input power. For example, when a load of 1 kΩ and an input power of 21 dBm were employed, an efficiency of 76.56% was obtained. In a similar way, maximum efficiencies of 65.26%, 69.34%, and 59.03% were obtained when the system was simulated using loads of 5 kΩ, 10 kΩ, and 22 kΩ respectively. Thus, the operating conditions of the rectenna system were optimized based on the load, and the input power.

Conclusions

A rectenna system comprising of an efficient antenna with a peak gain of 7.86 dBi and Schottky diode HSMS-2860 based rectifying circuitry is designed and tested at 2.4 GHz frequency band. Likewise, a simple impedance matching network is designed to match the rectifier input impedance to the impedance antenna to guarantee the maximum radiation conversion. On the other side, the results reveal that the rectifier achieved conversion efficiency of 76.56% and a maximum voltage of 6.58 VDC with a load resistance of 1 kΩ, which is adequate to function for most of the handheld electronic devices such as sensors or batteries. As a result, we may conclude that incorporating this EM energy harvesting method into electrical devices will minimize the load needs of low power IoT devices.

Future work will connect the created system with a wireless sensor network, demonstrating the proposed system's potential to harvest electromagnetic energy and utilize it to recharge the batteries of IoT components. This would address one of the key issues with IoT systems in open spaces.

Acknowledgment

This study was supported by the AE&CC Group COL0053581, attached to the Instituto Tecnológico Metropolitano and the project "FORTALECIMIENTO Y CONSOLIDACIÓN DEL GRUPO AUTOMÁTICA, ELECTRÓNICA Y CIENCIAS COMPUTACIONALES PARA RESPONDER A LAS NECESIDADES DE LAS INDUSTRIAS 4.0" code P21101.

References

[1] Reyes-Vera, E., Senior, D. E., Luna-Rivera, J. M., and López-Giraldo, F. E. (2018). "Advances in electromagnetic applications and communications." *TecnoLógicas*, 21(43), 9-13, 10.22430/22565337.1052.

[2] Liu, D., Hong, W., Rappaport, T. S., Luxey, C., and Hong, W. (2017). "What will 5G Antennas and Propagation Be?" *IEEE Trans. Antennas Propag.*, 65(12),6205-6212, 10.1109/TAP.2017.2774707.

[3] Wagih, M., Weddell, A. S., and Beeby, S. (2020). "Rectennas for RF Energy Harvesting and Wireless Power Transfer: A Review of Antenna Design." *IEEE Antennas Propag. Mag.*, 62(5), 95-107, 10.1109/MAP.2020.3012872.

[4] Umaña-Idarraga, F., Cataño-Ochoa, D., Montoya-Villada, S., Valencia-Balvin, C., and Reyes-Vera, E. (2021). "Design of a perfect and multi-resonant metamaterial absorber for electromagnetic energy harvesting applications." *J. Phys. Conf. Ser.*, 2118(1), 10.1088/1742-6596/2118/1/012005.

[5] Vandelle, E. *et al.* (2019). "Harvesting Ambient RF Energy Efficiently with Optimal Angular Coverage." *IEEE Trans. Antennas Propag.*, 67(3), 1862-1873, 10.1109/TAP.2018.2888957.

[6] Da Silva, E. F., Gomes Neto, A., and Peixeiro, C. (2019). "Fast and Accurate Rectenna Design Method." *IEEE Antennas Wirel. Propag. Lett.*, 18(5), 886-890, 10.1109/LAWP.2019.2904795.

[7] Lu, P., Song, C., and Huang, K. M. (2020). "A Compact Rectenna Design with Wide Input Power Range for Wireless Power Transfer." *IEEE Trans. Power Electron.*, 35(7), 6705-6710, 10.1109/TPEL.2019.2963422.

[8] Visser, H. J., Keyrouz, S., and Smolders, A. B. (2015). "Optimized rectenna design." *Wirel. Power Transf.*, 2(1), 44-50, 10.1017/wpt.2014.14.

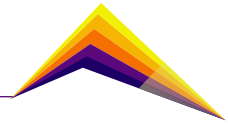

Key enablers: measuring digital transformation in companies located in ocaña norte de santander

Luis Fernando Morales Martínez[1] E-mail: lfmoralesm@ufpso.edu.co
Byron Cuesta Quintero[2] E-mail: byroncuesta@ufpso.edu.co
Magreth Rossio Sanguino Reyes[3] E-mail: mrsanguinor@ufpso.edu.co

Magister1, Magister2, Magister3, University Francisco de Paula Santander sectional Ocaña/ Faculty of Engineering / Engineering Technology and Development Research Group

Abstract

Today, it is essential to improve enterprise architecture based on a clear and precise vision of business objectives. The structuring of new architectural components must be based on a holistic approach, determining in principle the current state of an organization and thus detailing a coherent and organized system among all its elements. The incorporation of new information and communication technologies (ICT) requires a methodological accompaniment that allows the execution and control of digital transformation actions in the business context; in this sense, researchers have focused their efforts on knowing the appropriate model to implement and generate new configurations in organizations from the development of new technologies that are transforming the ways of doing business, supported by the provision of services that are supported by information technologies (IT). During the studies, through a systematic review, the researchers were able to analyze information that allowed them to know the current status (use and implementation of IT) of some companies located in Ocaña Norte de Santander; through the development of the thesis, they deduced the requirement to transform or adapt organizational processes based on key enablers for the realization of significant changes in the ICT environments, in addition, these measurements were elementary for the approach of important strategies for the improvement of

Correspondent author

business capabilities in the region, looking for organizations to orient their services through the implementation of emerging technologies that improve their marketing conditions.

Keywords: Digital transformation, Information technologies, Enablers, Connectivity, Big data.

Introduction

Nowadays, the implementation of information technologies offers different opportunities to companies, but at the same time these organizations have differentiated use the acquisition and use of this type of technology [2]; On the other hand, another study refers to digital transformation as a trending topic that concerns commercial, management, and operating companies, determining in its analysis that companies in the financial sector have had a successful takeoff through this practice, to which other sectors such as retail, industry and even mining have adhered [8]. Under the dynamics of a practical environment, the digital transformation promotes a series of benefits to small developing companies, analysts suggest that PYMES must adopt this process to keep up in a global market, and several companies reflect the need to migrate to new technologies to consolidate more efficient business processes and it is emphasized that this work could be somewhat intimidating for this type of companies [6]. According to some studies, digital transformation emerges as a relevant topic for both the scientific and the business communities; in organizations the technologies adhered to these transformations are increasingly generating greater efficiency along the entire value chain, at every moment it is more necessary to customize the user experience about the hyper-connectivity environment, being that organizational changes at the digital level relate multiple edges where the systematization of knowledge is a crucial activity for the entire transformation process [3]. In times of the COVID-19 pandemic, human beings faced new challenges, being information technologies essential for the development of activities in a changing way, during this period people learned the importance of being related between different sectors, and aspects such as self-management and training were essential to deal with the situation at the time, the technologies that helped to connect society were fundamental resources of interaction [7]; The COVID 19 pandemic generated a series of needs in international trade, and logistics processes were affected to such an extent that it triggered an accelerated logistics digitalization; CEPAL promoted transformation policies among different Latin American countries in order to configure logistics processes, strengthening interoperability and reinforcing the integration of technological solutions, based on collaborative schemes [10]. Other research contributions show that one of the benefits of digital transformation can be the improvement of the quality of life of people, as

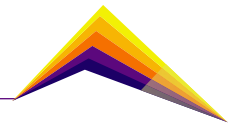

well as the promotion of critical industries for the development of a country, for this reason, it is essential to move from rhetoric to the implementation of plans that guide the necessary projects for continuous improvement [9]. On the other hand, a study conducted on Chilean companies, reveals that despite implementing new software for the administration and operation of processes in areas of people management, these companies have made little progress in the use of new emerging technologies, in addition, the needs of cultural and socio-emotional change that workers must face due to the processes of digital transformation, aligned to new orientations of service delivery, based on technologies based on artificial intelligence, Big data, and analysis methodologies [5].

Methodology

During the research and under a quantitative approach, the researchers used the descriptive methodology, supported by the method of analysis, seeking to understand the object of study, analyzing and indicating its main characteristics and properties [4]. In the process, a roadmap was drawn up in line with the stages proposed by PMBOK, which generated the following milestones: 1 Start: Pre-feasibility studies were conducted to understand the problems that the project would address and its feasibility; 2 Planning: The objectives to be achieved, the schedule, budget, among others, were set; 3 Execution: Tasks were carried out to specify the critical enablers for digital transformation, for this it was essential to recognize the appropriation of information and communications technologies in companies of the context (approximately 2500 companies according to data source provided by the chamber of commerce of Ocaña, of which 34 were studied), in addition, researchers consulted 21 experts in computer science on enablers of digital transformation; 4 Monitoring and control: a partial report that evidenced the measurement of the achievements; 5. Closing: Final acceptance under the confirmation of the research and extension division based on the validation of the deliverables that certify the fulfillment of the objectives.

Results and analysis

Use and implementation of technologies

Currently, there is a wide variety of new IT products on the market that support digital transformation processes; Some researchers recommend a framework to carry out these change processes and not only have a technical perspective; Currently, organizations must provide services 24 hours a day, 7 days a week throughout the year, where activities must be planned from a methodology that helps guide the strategy [1]. Below are some deductions about the use and implementation of ICT in Ocaña Norte de Santander:

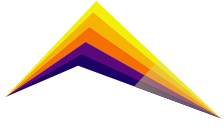

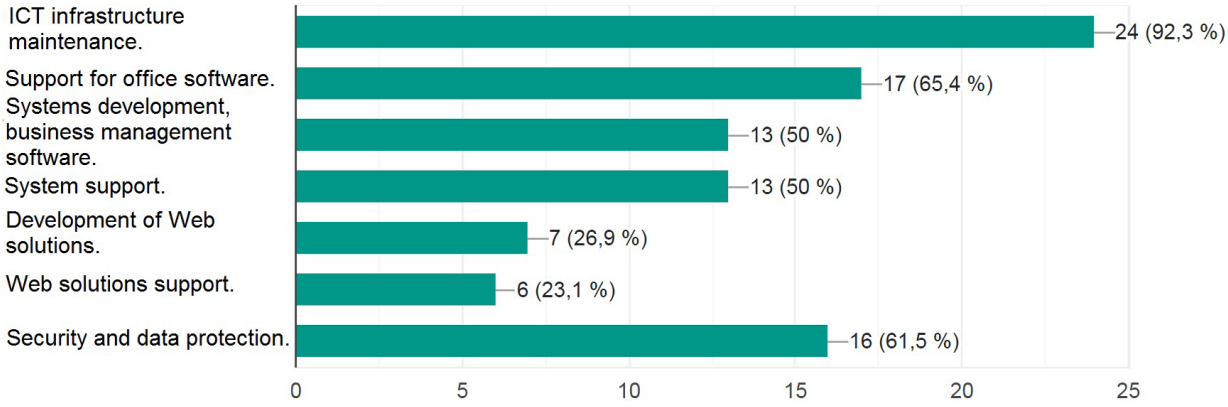

Figure 1. ICT support or implementation activities

Figure 1 shows a low percentage of 23.1% for companies that support web and e-commerce solutions, and 26.9% indicate that they do not develop this type of technology; a high and satisfactory 92.3% is also reflected for companies that perform infrastructure maintenance.

Digital transformation enablers

As mentioned above, digital transformation is a relevant dynamic for continuous improvement in the business context, so it is important to investigate which are the key enablers that could be significant for companies located in Ocaña Norte de Santander; according to [11] "enablers are transversal elements that facilitate and accelerate digital transformation in an organization since they allow transforming the business by aligning technology with the business strategy"; during data collection, for the researchers, it was essential to know the perceptions of different IT experts about digital transformation enablers, for which a sample of 21 individuals was extracted who selected a range of enablers classified into three categories. The first, technological enablers, i.e., current technologies needed to develop digital transformation processes are taught below:

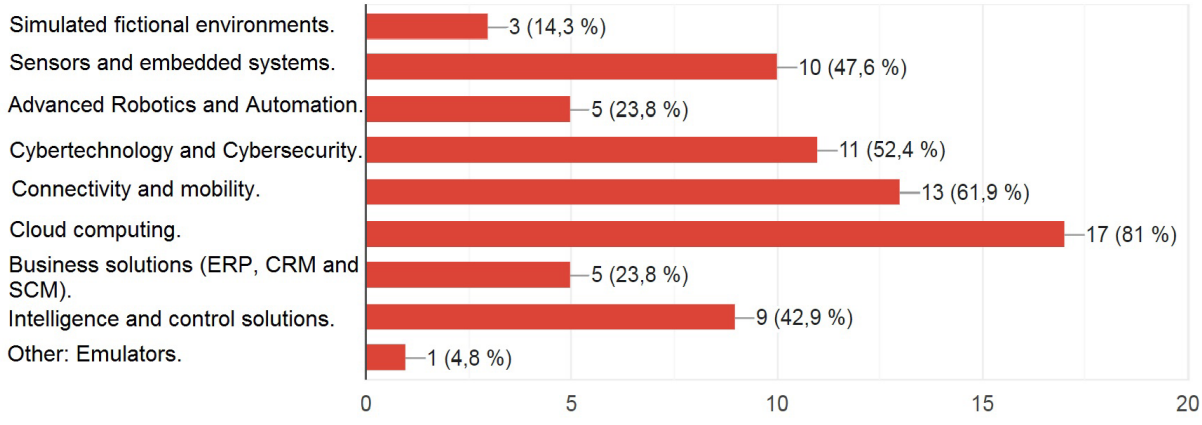

Figure 2. Technological enablers

As shown in Figure 2, 81% of IT experts agreed that one of the most necessary technologies for digital transformation is Cloud computing, followed by technologies related to Connectivity and mobility with a percentage of 61.9%, close to the average percentage we find technologies such as sensors and embedded systems and others such as cyber technology and cybersecurity, with a much lower selection and located at the bottom of the list we find technologies such as Emulators. The second classification is called conceptually based enablers, i.e., current concepts necessary to develop the transformation processes:

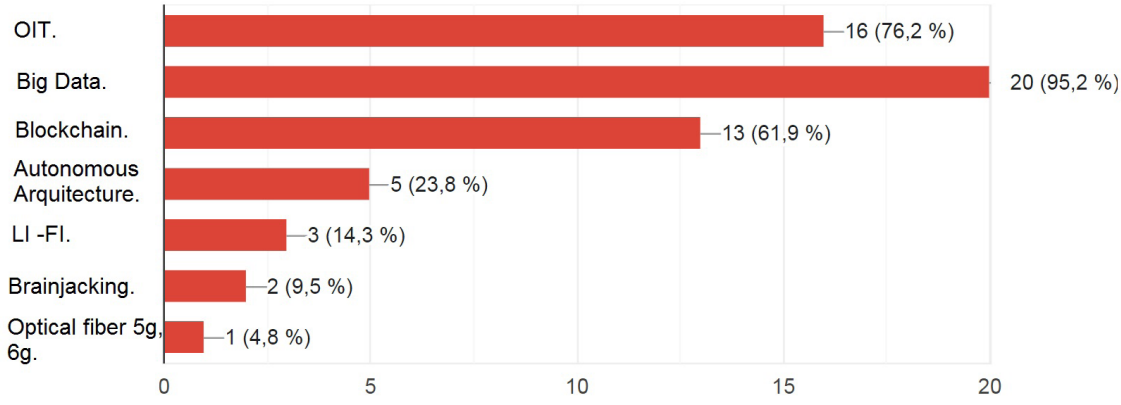

Figure 3. Conceptual basis enablers

As shown in Figure 3, 95.2% of IT experts agreed that the conceptual basis for digital transformation is based on the concepts of Big data, followed by IoT with 76.2%; another conceptual basis that exceeds the percentage average with 61.9% is Blockchain, in the last of Figure 7 we find Fiber optics, 5g, and 6g, of which the researchers consider an erroneous perception by one of the computer experts because it would be classified in the previous categorization, i.e., it would be part of the technological enablers specifically those of Connectivity and mobility. The third classification, strategic enablers, i.e., strategies necessary to develop digital transformation processes, is shown below:

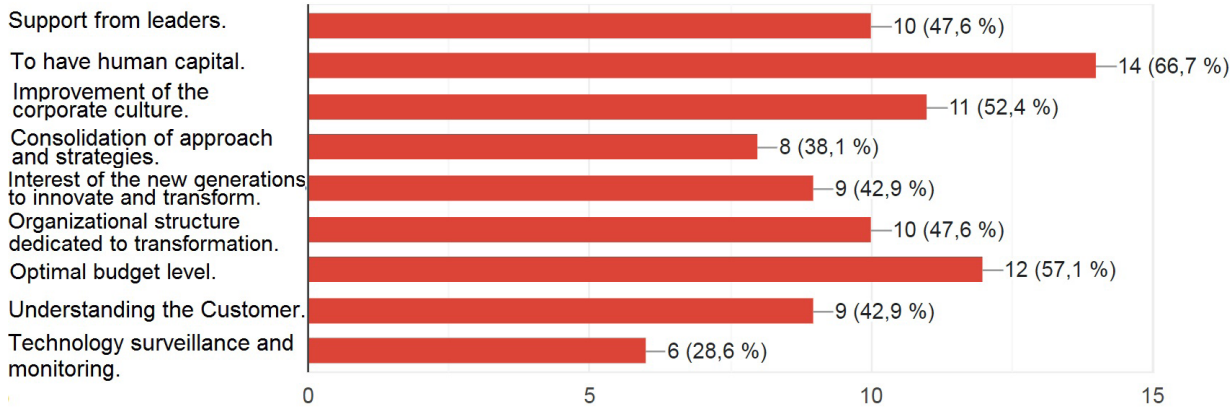

Figure 4: Strategic base enablers

As shown in Figure 4, 66.7% of IT experts agree that one of the relevant enabling strategies for transformation is to have human capital, followed by the optimal budget level with 57.1% and above average with 52.4% to improve corporate culture; at the end of the list is surveillance and monitoring of technology with a value of 28.6%; at a general level, Figure 4 shows a balance in the selections, in general, it is observed that all strategies could be valid for digital transformation processes according to the experts' perspectives.

Conclusions or summary

The results obtained in the course of this research, show different perceptions of thesis authors, people who work in business environments located in Ocaña, and experts in information technologies, it is deduced an orientation by those involved towards the structuring of new strategies to execute real processes of digital transformation; to perform these changing processes it is not enough to acquire traditional transactional systems, rather the proposal must be more dynamic and go far beyond, towards predictive intelligent systems that help decision making and that are simulators of agile environments. From the diversity of technologies that are available in the current market, it is necessary to select

The most appropriate for the context, it is necessary to choose those technologies that generate competitive advantages for the wholesale and retail trade that is developed in the context of the research; on the other hand, the studies showed significant data that indicate the backwardness in companies located in this region, which reduces the availability of services in these organizations, for which it is advisable the orientation towards key enablers, which allow activating coherently and safely the transition processes. Taking into account the information collected and analyzed about the business environments that are developed in the municipality of Ocaña Norte de Santander, the researchers conclude in the first instance that these environments are somewhat behind in actions that promote digital transformation, they also deduce the lack of knowledge in relation to the technologies that do promote digital transformation, They state that just building a website or promoting their products and services through social networks is not digital transformation, the issue must go further and it is necessary to have human capital specialized in the development of intelligent, secure and versatile ICT, as well as to propose strategies to guide aspects of change towards a true and safe digital transformation.

References

[1] Albán Díaz, E. E., Mesa Fernández, J. M., García González, J., and Valdeón Junquera, A. M. (2021). Analysis of maximum availability IT services in public administrations

[2] Castro, W. R. A. A., Suarez, C. A. H., and Suarez, A. A. G. (2022). Information technologies and business growth. Redipe Bulletin Magazine, (07-005, pp.1917-1930)

[3] Fernández, T. D. (2020). Taxonomy of digital transformation. Cuban Journal of Digital Transformation, (Vol. 1(1), pp.4-23)

[4] Hernández-Sampieri, R., & Torres, C. P. M. (2018). Research methodology (Vol. 4, pp. 310- 386). Mexico D. F DF: McGraw-Hill Interamericana. production systems." Proc., Int. Symp. on Deep Mooring Systems, ASCE, Reston, VA, 152-167

[5] Maliqueo Pérez, C., González Candia, J., Mardones Espinosa, R., and Ardiles Briones, M. (2021). People management and the barriers to innovate in digital transformation. Venezuelan Management Magazine, (Vol.26 (94), pp. 510-532)

[6] Pinzón Vigoya, C. A. (2020). Digital transformation of the business model of the SME Mi Merienda SAS (Master's thesis, University de La Sabana, Chía - Colombia)

[7] Ramírez-Montoya, M. S. (2020). Digital transformation and educational innovation in Latin America in the framework of CoVId-19. Virtual Campus, (Vol. 9(2), pp.123-139)

[8] Ríos, J. L. (2019). Keys to digital transformation in Peruvian companies. Peru: Top Publications SAC, Peru.(pp.1-12)

[9] Salinas, C. E. C., Vela, D. A. R., Parra, C. J. C., Torres, C. R. R. R., and Reina, C. F. (2021). Digital Transformation Plan for Tourism Promotion in the Vice Ministry of Tourism. Case study: Department of Boyacá /Digital transformation plan for tourism promotion in the vice ministry of tourism. Case study: department of Boyacá. Tourism and Society, (pp. 151 - 185).

[10] Valdés Figueroa, L., and Pérez, G. (2020). Digital transformation in Latin American and Caribbean logistics. FAL Bulletin No. 381

[11] Wilches Durán, J. M. (2021). Digital transformation policies in Colombia. ICT and digital society: twelve years after the law. Volume II, digital ecosystem in its different developments and disruptive technologies, (pp.381-417)

Selecting a Data Platform to Support the Development of Applications Oriented to Improve Citizen Security

Luis Germán García M.[1] — E-mail: german.garcia@udea.edu.co
Jaime Alberto Vergara T.[2] — E-mail: jalberto.vergara@udea.edu.co
Ricardo A. Velásquez[3] — E-mail: randres.velasquez@udea.edu.co
José Edinson Aedo[4] — E-mail: jose.aedo@udea.edu.co

[1, 2, 3, 4] *Faculty of Engineering, Universidad de Antioquia*

Abstract

Citizen security is an issue that repeatedly appears in different opinion polls as one of the major concerns of the Colombian population. In response to this problem, government entities have established various initiatives to improve citizen security in their development agenda. One initiative is to deploy solutions supported by smart technology to support the security forces in fulfilling their obligation to protect the citizen's rights. Different world cities have recently adopted smart technology to face security issues and other challenges such as population growth and aging, climate change, and aspirations for better living. This adoption has led to the appearance of the term "smart city," which refers to a modern urban zone that uses smart technology to help solve urban problems and thus enable people to use city resources effectively.

We can strengthen citizen security using tools employed in smart cities based on electronic perception technologies and computational intelligence, helping security forces to make better decisions. It requires flexible architectures to cope with various aspects that coexist and numerous actors that interact. Currently, architects and developers propose to employ a piece of software called a data platform to manage the system. A data platform must collect and

Correspondent author

store data from multiple sources, process and analyze it for decision making, and present the outcomes to proper stakeholders. They must also scale with the growing number of users, services, and devices that make up the smart city.

Some data platforms in the state-of-the-art can manage IoT devices, cope with big data volumes, and perform data analysis to make predictions and produce suggestions/alerts to citizens and operators. In this paper, we evaluated three available data platforms (Snap4City, VirIoT, and MiFiware) to determine which best ease the application development to improve citizen security. The experimental results showed that Snap4City not only complies with our proposed architecture but also offers specialized services and tools to help developers build applications regarding other data platforms.

Key words: Internet of Things (IoT), Big Data, Machine Learning, Citizen Security.

Introduction

According to [1], smart cities are complex ecosystems where numerous aspects coexist, and various actors of diverse types interact among them. In developing these complex ecosystems, many functional and non-functional requirements appear and evolve in diverse contexts and environments. Therefore, we require flexible architectures that allow us to tackle them and provide an effective solution. A data platform is a piece of software that adopts the concept of flexible architecture. It manages IoT devices, collects and retrieves data from IoT sensors and edge devices to internal databases, makes the collected data available to data analytics algorithms for decision making, and presents the algorithm outcomes to interested stakeholders. Currently, data platforms such as Snap4City [2], VirIoT [3], and MiFiware [4] provide developers with a set of protocols, interfaces, services, and tools to ease application development in various contexts within the smart cities field. They can even scale up to the increasing number of users and resources. All these features help developers to reduce the implementation of numerous verticals. Since this work focuses on strengthening citizen security, we must choose a data platform that best fits our proposed architecture.

This work describes the proposed architecture for developing an ecosystem oriented to strengthening citizen security. It also presents the analysis and evaluation performed on the mentioned platforms to choose the one that best suits the architecture established.

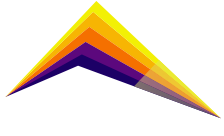

We organized the rest of this paper as follows: In Section 2, we describe the architecture proposed and the analysis and evaluation performed on the platforms. Section 3 presents the assessment results achieved on the platforms and discusses the selection of Snap4City. Finally, we provide a conclusion in Section 4.

Methodology for selecting a proper data platform

The purpose of this section is twofold: first, we explain the architecture proposed for choosing the data platform. Then, we show the analysis and experiment to determine the platform that best fits our proposed architecture.

a. System architecture for data platform selection

The system architecture is supported by a project currently being developed by Universidad de Antioquia and Universidad Nacional de Colombia, whose main aim is to propose different solutions to challenges in citizen security. We start by describing a common scenario. When a security incident occurs, we require a distributed system to gather as much information as possible. The collected information is then processed using data analysis algorithms. Based on the outcomes, the system can send alerts to security agencies and citizens so they can approach the situation appropriately. According to this scenario and different works in the state-of-the-art, we proposed a microservice-based multi-layer architecture, as shown in Figure 1.

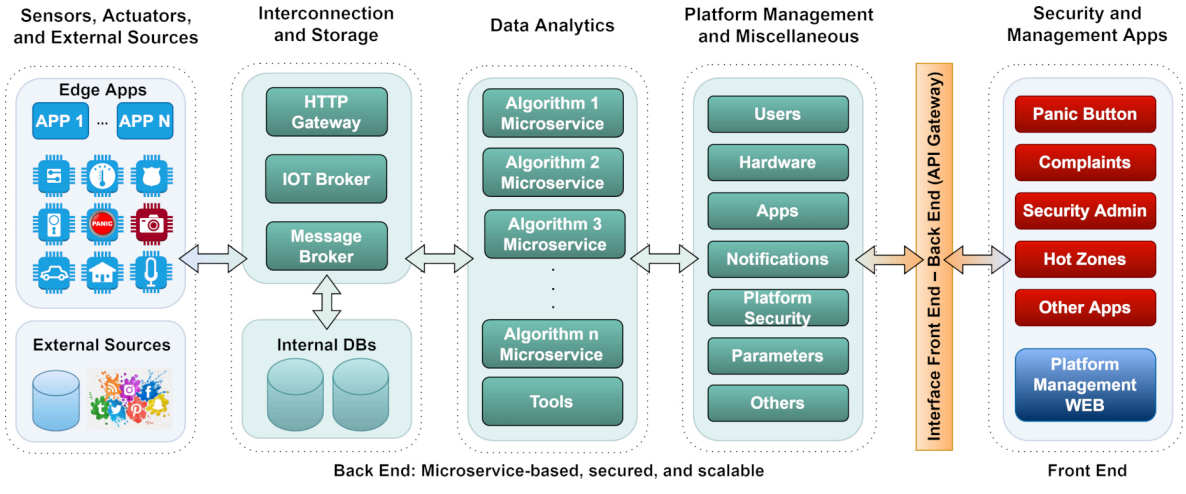

Figure 1. System Architecture of the Ecosystem

The architecture layers and their components are described below:

- **Sensors, actuators, and edge:** it is composed of different sensors, actuators, and IoT edge devices to collect data, execute particular actions, and process collected data to send events to the platform's core for decision making, respectively.
- **Interconnection**: it contains different types of brokers in charge of performing message transactions between many data producers and consumers.
- **Storage**: it keeps the internal database (context) and information collected from public or available datasets used for data analysis algorithms and applications.
- **Processing and data analytics**: this layer encloses services that mainly implement data analysis models for decision-making.
- **Platform management and miscellaneous**: it includes all the components that allow authorized users to modify the platform configuration, security, and more.
- **Frontend**: it contains all the applications and dashboards oriented to the end users.

Several works in the state-of-the-art have proposed different data platforms for smart cities. We made a pre-selection from a pool of platforms before evaluating them: Promenade [5], MiFiware [4], VirIoT [3], ITrade [6], Snap4City [2], Sentilo [7], and Sapparchi [8]. The main aspects considered in the pre-selection were: 1) microservice-based architecture, 2) open-source, 3) deployment using virtual machines or containers, 4) written in well-known programming languages, 5) manage IoT devices with different protocols and interfaces, 6) the ability to handle context information and large volumes of data, 7) the possibility of adding new resources or modules, and 8) being part of one or more projects with real scenarios. Finally, the chosen platforms were VirIoT, MiFiware, and Snap4City.

b. Data platforms analysis and experiment performed

Firstly, we analyzed each platform's documentation and source code to determine if they support the following capabilities or features for each of the layers proposed in the system architecture:

1. **Sensors, actuators, and edge:** standard data formats, protocols, and *edge* processing.
2. **Interconnection**: various brokers (data formats and protocols), scalability, and security.
3. **Storage**: manage relational and non-relational databases exposing CRUD operations.
4. **Data analytics**: algorithms and tools integrated or capability to incorporate new ones.
5. **Platform miscellaneous**: user management, scalability, and security.
6. **Frontend**: tools integrated to build apps or the ability to incorporate new ones.

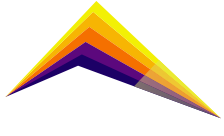

Secondly, we performed an experiment to develop two simple applications using the platforms to determine how straightforward the process was. The two applications were:

1. Collect data from sensors through available context brokers, process it to perform some filtering, and display the results on some dashboards.
2. Capture data from external sources (databases related to security incidents), perform some filtering, and display them on some dashboards.

For the first application, we used temperature sensors connected to single board computers SBC (VIM3 from Khadas) available in our labs. In Snap4City, we used the Fiware Broker to collect data from the SBCs. Then, we used Node-Red (available in Snap4city) to filter and visualize the data through available dashboards. Figure 2 shows the application structure built (on the left) and the visualization of the collected data (on the right). We developed the same application using VirIoT and MiFiware. Still, we had to integrate a few external components (Python and Kibana) to process and visualize the collected data into dashboards for these platforms. Since VirIoT and MiFiware do not have a management application, we manually used Postman to create entities and relationships (Fiware broker).

For the second application, we used Node-Red in Snap4City again to collect data from an external Mongo database, process it, and visualize it on the dashboards available. For VirIoT and MiFiware, we used the components integrated to build the previous application to read the database and visualize the data. Figure 3 shows the application's structure built using Node-Red (on the left) and the visualization of the collected data (on the right).

Results and analysis

From the analysis of each platform's documentation and source code, we determined the availability of the different layers and their components shown in Figure 1 to select the platform that best fits our architecture. We used the following policy to assign the scores:

- 0: layer or some capabilities inside the layer are not available.
- 1-2: layer or some capabilities inside the layer are partially available.
- 3: layer and its capabilities inside the layer are available.
- 4-5: layer provides extra tools, services, or other elements to ease the development.

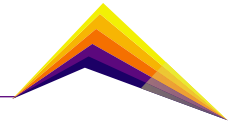

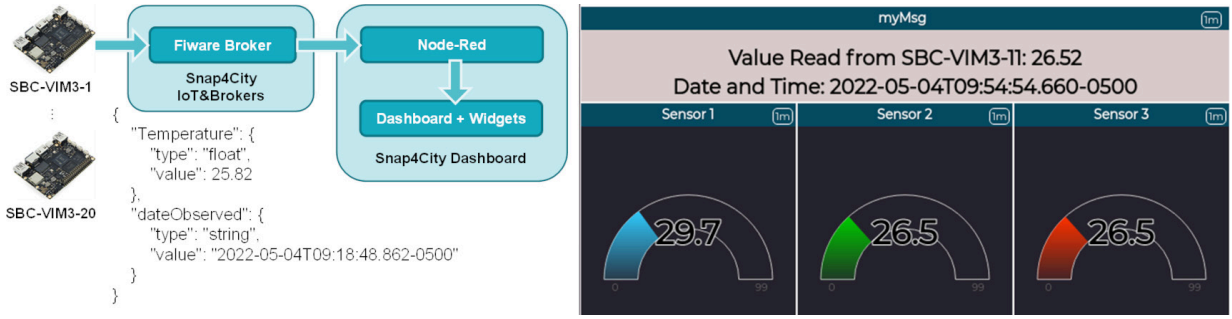

Figure 2. First application using Snap4City platform

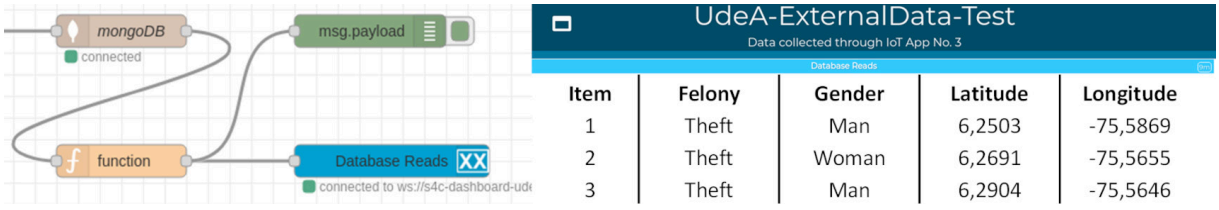

Item	Felony	Gender	Latitude	Longitude
1	Theft	Man	6,2503	-75,5869
2	Theft	Woman	6,2691	-75,5655
3	Theft	Man	6,2904	-75,5646

Figure 3. Second application using Snap4City platform

Table 1 shows the final scores given to each platform's layer based on the capabilities available. On the other hand, the experiment showed that the application development was straightforward with Snap4City as it has all the required resources. With VirIoT and MiFiware, although we managed to build the applications, we were required to incorporate external modules and take more time to complete the development. Based on the analysis performed and the experiment, we selected Snap4City as the project platform.

Conclusion

In this work, we analyzed and evaluated three data platforms available in the state-of-the-art: VirIoT, MiFiware, and Snap4City, to determine the one that best fits the proposed architecture. We selected Snap4City to develop an application ecosystem oriented to strengthening citizen security, as it complies with most of the elements established in the proposed architecture. In future work, we will develop a set of applications, including microservices, to improve citizen security, using Snap4City as a core platform.

Table 1. Evaluation based on the analysis performed to select the data platform

Architecture layer	MiFiware	VirIoT	Snap4City
Sensors, actuators, and edge	3.0	3.5	4.3
Interconnection and Storage	3.0	3.3	4.3
Processing and data analytics	1,5	1.5	3.5
Platform miscellaneous	3.0	3.0	4.0
Frontend	3.5	3.3	4.3

Acknowledgment

This research was supported by the General System of Royalties from Colombia (Project "Administración inteligente de problemas de seguridad ciudadana a través de modelos y herramientas generadas a partir de plataformas para territorios inteligentes apoyadas por estrategias de participación ciudadana en la ciudad de Medellín" BPIN 020000100044).

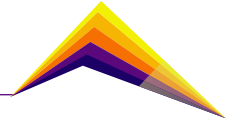

References

[1] Nicola Mitolo et al. “Snap4City Platform to Speed Up Policies”. In: Smart and Sustainable Planning for Cities and Regions. Springer International Publishing, 2021, pp. 103–114.

[2] Claudio Badii et al. “MicroServices Suite for Smart City Applications”. In: Sensors 19.21 (2019). issn: 1424-8220. doi: 10.3390/s19214798.

[3] Andrea Detti et al. “VirIoT: A Cloud of Things That Offers IoT Infrastructures as a Service”. In: Sensors 21.19 (2021). issn: 1424-8220. doi: 10.3390/s21196546.

[4] Juan Alberto Llopis et al. “MI-FIWARE: A web component development method for FIWARE using microservices”. In: 2021 IEEE 45th Annual Computers, Software, and Applications Conference (COMPSAC). 2021, pp. 1058–1065. doi: 10.1109/COMPSAC51774.2021.00144.13.

[5] Antonio De Iasio et al. “A Microservices Platform for Monitoring and Analysis of IoT Traffic Data in Smart Cities”. In: 2019 IEEE International Conference on Big Data (Big Data). 2019, pp. 5223–5232. doi: 10.1109/BigData47090.2019.9006025.

[6] Sina Rafati Niya et al. “ITrade: A Blockchain-based, Self-Sovereign, and Scalable Marketplace for IoT Data Streams”. In: 2021 IFIP/IEEE International Symposium on Integrated Network Management (IM). 2021, pp. 530–536.

[7] Júlia Camps Farrés. “Barcelona noise monitoring network”. In: Proceedings of the Euronoise. 2015, pp. 218–220.

[8] Arthur Souza et al. “Sapparchi: An Architecture for Smart City Applications from Edge, Fog and Cloud Computing”. In: 2019 IEEE International Smart Cities Conference. 2019, pp. 262–267.

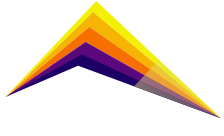

Additive manufacturing: an opportunity for innovation and sustainability

Henry A. Colorado L.[1] — E-mail: henry.colorado@udea.edu.co
Geovanna Girondi[2] — E-mail: geovanagirondi@pq.uenf.br
Gustavo Xavier[2] — E-mail: gxavier@uenf.br
Carlos Maurício Vieira[2] — E-mail: vieira@uenf.br
Afonso Azevedo[2] — E-mail: afonso@uenf.br

[1]Universidad de Antioquia, Facultad de Ingeniería. Bloque 20, Calle 67 No. 53 - 108, Medellín, Colombia
[2]State University of the Northern Rio de Janeiro, UENF, Rio de Janeiro, Brazil

Abstract

This research shows the main technologies and investigations in additive manufacturing, also known as 3D printing, as well as case studies using the technology towards sustainable development. Additive manufacturing is a revolution worldwide in almost all sectors of materials and processing because of its adaptability to materials, shapes, and processes. This technology allows to print almost any material type, such as food, rubber, concrete, metals, plastics, soils, ceramics, etc. Also, the most recognized advantage of this technology is the feasibility to fabricate the most unimaginable complex shapes and to change the design of parts. Some case studies involving inexpensive and highly adaptable techniques, such as fused deposition modeling, stereolithography, and direct ink writing are discussed. At the University of Antioquia, projects with educational, materials and manufacturing technologies have been developed in multidisciplinary projects, with participation of the engineering school, a primary local school, companies, and our university museum. The first case study is about the use of fused deposition modeling, the most worldwide widespread additive

Correspondent author

manufacturing technique, in teaching and learning, not only at the university level, but also in the university museum, and in a local primary school. In the university museum, several models of small local animals were selected from an artist collection, scanned, and printed, and combined with our proper designs to educate the public from the museum in the sustainability these species, and in the technology and materials involved. Also, a case study using the direct writing technique, an extrusion based additive manufacturing technology, is presented. In this case, cementitious materials were used and successfully printed. Then, some examples of materials adapted for additive manufacturing are presented and disused.

Keywords: additive manufacturing, 3D printing, fabrication.

Introduction

Additive manufacturing (AM), most popularly known as 3D printing (3DP), is a fabrication technique that has revolutionized almost all fields with the possibilities of making the most complex geometries [1]. AM is particularly powerful for printing complex shapes, changing areas in product design and rapid prototyping to a new level of possibilities [2]. The materials that can be printed are basically limitless: food [3], clays [4][5], cements [6], composites [7], polymers [8], metals [9], and more. AM is an advanced manufacturing technology, which starts from a 3D cad model, later to be sliced via software, and after further programming of the fabrication, the manufacturing is conducted by adding material layer by layer, consolidating plane by plane, a 3D part. AM has also been explored as sustainable technique, with possibilities to even give solutions to other technologies [10]. AM has also been used in learning activities [11] and played an important role in the current COVID 19 pandemic [12].

AM has been classified in seven technologies by ASTM F42, see Figure 1. VAT photopolymerization process is a technology in which a photopolymer liquid resin is cured with an ultraviolet light, hardened layer by layer until consolidate a 3D part [13]. Material jetting [14] and binder jetting [15] are two technologies where either the material or the binder are dispensed from a print head. Material extrusion is very versatile as fused deposition modeling (FDM) [16] or direct ink writing (DIW) [17], the most worldwide widespread technologies due to their relatively low costs and simplicity of the process. Powder bed fusion [18] is a technology in which a bed of powder with a source of heat can create metal parts. Sheet lamination [19] uses material sheets, cut in the demanded shapes typically by a laser beam, and thereafter bound with adhesives or welding to form a 3D part. Finally, direct energy

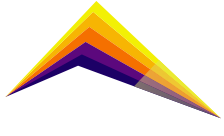

deposition [20] is a technology in which the material and heat are added simultaneously, where the heat source typically is provided by laser or electron beams.

This research presents results regarding the use of extrusion-based techniques applied in teaching and learning objects to be used in the university museum for sustainability of animal species printed with FDM technology; and the fabrication of structural traditional ceramics materials printed with DIW technology. Both projects have been conducted at the University of Antioquia.

Materials and Methods

First, for the teaching and learning activities, a common ant from the Medellin-Colombia area was selected as animal to model for several important reasons: first, there is an artwork, a sculpture located in the university museum of the University of Antioquia (Museo Universitario), made of balsa wood by the local artist A. Berrio, in 2003. This ant, particularly known as wood ant, the formica Spp, is important for the ecosystem as pathogen control.

Therefore, the artwork has been scanned using a 3D scanner EinScanPro + 3D scanner, with 0.05 mm of single-shot accuracy. Then, the 3D STL file was sliced with the slicer software Cura. Further process parameters were determined to be printed in PLA and TPU, two very common thermoplastic polymeric materials: speed of 40 mm/s, bed temperature of 60 °C, and a printing temperature of 200 °C and 220 °C for PLA and TPU, respectively. Subsequently, several activities were conducted to show students, children, and professionals, the artwork, technical information, and the manufactured part, for teaching and learning purposes. On the other hand, many parts have been printed with the direct ink writing (DIW) technique, an extrusion-based technology, where a material such a slurry can be extruded using a piston and deposited following the CAD model and slicing program as described above for the FDM process. Portland cement mortar and clays from local manufacturers were tested and combined with water in different formulations to show the versatility of the machines. Further mechanical, chemical, and performance tests, which are no presented in this paper, were conducted for characterizing the optimized formulations. The DIW technique was used at room temperature. Cement, as normally, was set at room temperature, while clay was fired in a furnace at 1000 °C for 1 h.

Results and analysis

Figure 2 shows the process for the ant manufacturing. The artwork is presented in Figure 2A, made in balsa wood, a very light and fragile material, not even able to handle due to the aging effects of the piece in the museum. Carefully, this piece was scanned, and the corresponding 3D image was post processed for the printing process, for instance, the legs and other thin structures were quite difficult to print due to the lack of support and rigidity, which was solved with the support showed in the image below STL files image, presented in Figure 2B. Then, the part was printed in two materials, one showed in Figure 2C.

On the other hand, several parts were successfully printed with tailored chemical compositions in collaboration with local industries of the traditional ceramics sector. Figures 2D and E respectively show parts printed with the DIW method in cement mortar (Portland cement with sand) and kaolinite clay. The rheology of slurries for the printer were controlled with DI water, showing the adaptability of this method to any material in a paste configuration. Further mechanical and many other characterizations were conducted and not presented here. Several forms were also printed aiming always to teach sustainability topics, not only from the design point of view, but from recycling or circular economy goals, by mixing with solid wastes to enable people to see how garbage can be reused. In the two case studies, the parts were presented to several groups of people, such as high school kids, see Figure 3, undergraduate and graduate students, professionals, and experts. In all cases, people were curious about many aspects such as the materials and manufacturing methods, a new hands-on experience, more interactive when is compared with the solely information given for artwork explanation in the museum, in books, or just told by a guide or professor. The motivation, particularly when people can touch and play physically with the object, is very significant in learning. In general, people were interested in how to use this technology in other applications, which certainly is important for innovation.

Summary

This research summarizes several experiences of using AM with different materials and goals, from teaching and learning to materials solutions. In all cases, the parts were successfully created and the hands-on experience of people who interreacted with them was quite positive, consequently, revealing a new method of teaching sustainability at all level of education, from children to adults. In developing countries, these two technologies represent an opportunity for innovation, not only to teach but also to improve in circular economy and sustainability issues, due to the wide spectrum of inexpensive materials that can be used and their potential impact in many manufacturing processes.

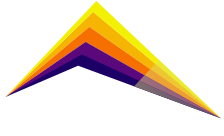

Acknowledgment

The author acknowledges the university museum and Vicerrectoría de extensión from the university of Antioquia for their support in this research.

References

[1] Bandyopadhyay, A., & Bose, S. (Eds.). (2019). *Additive manufacturing*. CRC press.

[2] Attaran, M. (2017). The rise of 3-D printing: The advantages of additive manufacturing over traditional manufacturing. *Business horizons*, *60*(5), 677-688.

[3] Javaid, M., & Haleem, A. (2019). Using additive manufacturing applications for design and development of food and agricultural equipments. *International Journal of Materials and Product Technology*, *58*(2-3), 225-238.

[4] Revelo, C. F., & Colorado, H. A. (2018). 3D printing of kaolinite clay ceramics using the Direct Ink Writing (DIW) technique. *Ceramics International*, *44*(5), 5673-5682.

[5] Revelo, C. F., & Colorado, H. A. (2019). 3D printing of kaolinite clay with small additions of lime, fly ash and talc ceramic powders. *Processing and Application of Ceramics*, *13*(3), 287-299.

[6] Vergara, L. A., & Colorado, H. A. (2020). Additive manufacturing of Portland cement pastes with additions of kaolin, superplastificant and calcium carbonate. *Construction and Building Materials*, *248*, 118669.

[7] Restrepo, J. J., & Colorado, H. A. (2020). Additive manufacturing of composites made of epoxy resin with magnetite particles fabricated with the direct ink writing technique. *Journal of Composite Materials*, *54*(5), 647-657.

[8] Ligon, S. C., Liska, R., Stampfl, J., Gurr, M., & Mülhaupt, R. (2017). Polymers for 3D printing and customized additive manufacturing. *Chemical reviews*, *117*(15), 10212-10290.

[9] Herzog, D., Seyda, V., Wycisk, E., & Emmelmann, C. (2016). Additive manufacturing of metals. *Acta Materialia*, *117*, 371-392.

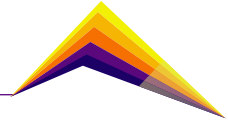

[10] Colorado, H. A., Velásquez, E. I. G., & Monteiro, S. N. (2020). Sustainability of additive manufacturing: the circular economy of materials and environmental perspectives. *Journal of Materials Research and Technology*, *9*(4), 8221-8234.

[11] Colorado, H. A., Mendoza, D. E., & Valencia, F. L. (2021). A combined strategy of additive manufacturing to support multidisciplinary education in arts, biology, and engineering. *Journal of Science Education and Technology*, *30*(1), 58-73.

[12] Colorado, H. A., Mendoza, D. E., Lin, H. T., & Gutierrez-Velasquez, E. (2021). Additive manufacturing against the Covid-19 pandemic: A technological model for the adaptability and networking. *Journal of Materials Research and Technology*.

[13] Pagac, M., Hajnys, J., Ma, Q. P., Jancar, L., Jansa, J., Stefek, P., & Mesicek, J. (2021). A review of vat photopolymerization technology: Materials, applications, challenges, and future trends of 3d printing. *Polymers*, *13*(4), 598.

[14] Gülcan, O., Günaydın, K., & Tamer, A. (2021). The state of the art of material jetting—A critical review. *Polymers*, *13*(16), 2829.

[15] Ziaee, M., & Crane, N. B. (2019). Binder jetting: A review of process, materials, and methods. *Additive Manufacturing*, *28*, 781-801.

[16] Samykano, M., Selvamani, S. K., Kadirgama, K., Ngui, W. K., Kanagaraj, G., & Sudhakar, K. (2019). Mechanical property of FDM printed ABS: influence of printing parameters. *The International Journal of Advanced Manufacturing Technology*, *102*(9), 2779-2796.

[17] Lewis, J. A. (2006). Direct ink writing of 3D functional materials. *Advanced Functional Materials*, *16*(17), 2193-2204.

[18] Sun, S., Brandt, M., & Easton, M. J. L. A. M. (2017). Powder bed fusion processes: An overview. *Laser additive manufacturing*, 55-77.

[19] Gibson, I., Rosen, D., Stucker, B., & Khorasani, M. (2021). Sheet lamination. In *Additive Manufacturing Technologies* (pp. 253-283). Springer, Cham.

[20] Dass, A., & Moridi, A. (2019). State of the art in directed energy deposition: From additive manufacturing to materials design. *Coatings*, *9*(7), 418.

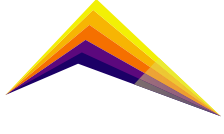

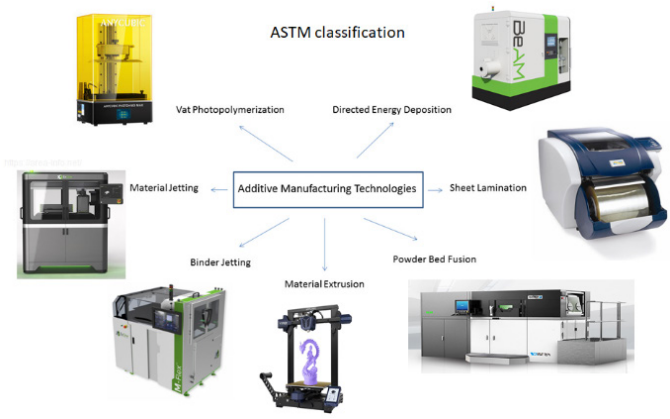

Figure 1. The seven categories of additive manufacturing given by ASTM F42.

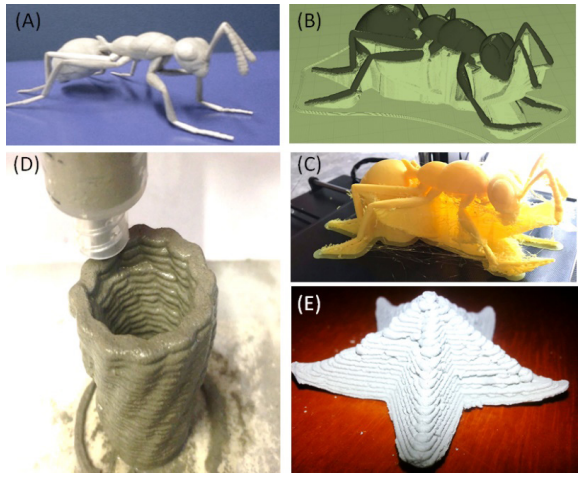

Figure 2. (A) Artwork from the University museum, (B) 3D model after scanning process, (C) 3D printing of (B), (D) detail of a cement part during the printing process, (E) object printed in clay material.

Figure 3. Detail of a teaching activity in the classroom in a local high school.

ORGANIZADORES

CENTRAL PROMOTORA DE MEDIOS S.A.S

ImaGroup Soluciones inteligentes

PLAZA MAYOR MEDELLÍN CONVENCIONES Y EXPOSICIONES

UNIVERSIDAD DE ANTIOQUIA

ALIADOS

Túnel Guillermo Gaviria Echeverri

Alcaldía de Medellín Distrito de Ciencia, Tecnología e Innovación

GOBERNACIÓN DE ANTIOQUIA

UNIDOS

MAIN SPONSOR

Fundación Universidad de Antioquia

Comfenalco Antioquia

Ingeni@ Soluciones TIC

INSTITUCIÓN UNIVERSITARIA PASCUAL BRAVO

SAPIENCIA Agencia de Educación Superior de Medellín

CO SPONSOR

isa

UNIVERSIDAD EAFIT

GRUPO sura

JDB

SUPPORT SPONSOR

CAMPUS FRANCE COLOMBIE

CESET Centro de Extensión Académica

Componentes Electrónicas

UNIVERSIDAD ICESI

intekgroup PROVEEDORES DE EQUIPOS PARA LABORATORIO

Investigación y Posgrados

Laboratorio de Estudios Ambientales

Nukke

ubicua

UNIVERSIDAD COOPERATIVA DE COLOMBIA

UNIVERSIDAD DEL NORTE

Laboratorio GIGA

ACOFI Asociación Colombiana de Facultades de Ingeniería


Expo
Ingeniería
Engineering for
Transformation